ABSTRACT

Title of thesis: FLOW CONTROL USING
PLASMA AND SYNTHETIC JET
ACTUATORS ON BLUFF BODIES

Sarah Haack
MASTER OF SCIENCE, 2007

Thesis directed by: Professor Alison Flatau
Department of Aerospace Engineering

This thesis shows the time-averaged effect of plasma and synthetic jet actuators on flow over bluff body shapes for delaying flow separation and, therefore, reducing pressure drag. The percentage of pressure drag reduction is used to evaluate the effectiveness of these two unique actuators for varied applied voltage, actuator position and flow velocity on a circular cylinder and 2D extrusion of a rotorcraft tail boom cross section. Two non-dimensional parameters were used to evaluate the effect of the actuators: coefficient of momentum ($C\mu$) and non-dimensional surface distance between the location of the actuator and the flow separation point (SD). Both actuation techniques beneficially affect the pressure distribution by decreasing the pressure near the location of the actuators and increasing the pressure in the separated flow region. Contour plots displaying the variation of the percentage of drag reduction as $C\mu$ and SD vary illustrate optimal operating conditions based on these parameters.

FLOW CONTROL USING PLASMA AND SYNTHETIC JET ACTUATORS ON BLUFF BODIES

by

Sarah Jo Haack

Advisory Committee:
Professor Alison Flatau, Chair/Advisor
Professor Inderjit Chopra
Professor James Hubbard

Dedication

To past, present and future family.

Acknowledgements

First, I would like to acknowledge my advisor, Dr. Alison Flatau, for her continual guidance through the last four years, initially, when I was an undergraduate transfer student and then a graduate student. None of this work nor collaboration between the six organizations would have been possible without the dedication from Dr. Alison Flatau at the University of Maryland and Dr. James Hubbard at the National Institute of Aerospace. This work involved the cooperation from the NASA Langley Research Center, Army Research Laboratory, Eagle Aviation, the Boeing Company, the National Institute of Aerospace, and the University of Maryland at College Park. From each organization, there were many generous people involved in the completion of this research for whom I am very grateful.

From NASA Langley, I would like to thank Steve Wilkinson for his unending patience, support and guidance, especially with understanding plasma physics and experimental testing techniques. I would also like to thank Anthony Washburn for

watched as a kid her push through and excel at all of the steps to her PhD against all odds and her efforts have inspired me. Thank you, Mom.

Table of Contents

List of Tables

x

xiii

List of Abbreviations

μ — Air viscosity

ρ — Air density

ρ_j — Air density of the synthetic jet

θ — Angular position on the cylinder

θ_a — Actuator angular position

θ_s — Flow separation angle

θ_{ta} — Tail boom actuator angular position

θ_{ts} — Tail boom flow separation angle

$\%_{CD}$ — Percentage of Pressure Drag Reduction $\left(\frac{C_{Doff} - C_{Don}}{C_{Doff}} \times 100 \right)$

A — Orifice area

b — Orifice width

c — Tail boom chord length

C_μ — Momentum coefficient $\left(\frac{2\rho_j U_j^2 b}{\rho U_\infty^2 d} \right)$

C_D — Drag coefficient

C_{Doff} — Actuator off drag coefficient

C_{Don} — Actuator on drag coefficient

C_p — Pressure coefficient $\left(\frac{P_s - P_\infty}{q} \right)$

d — Cylinder diameter

f — frequency

f_{act} — Actuator frequency

F^+ — Non-dimensional frequency $\left(\frac{f}{f_{act}} \right)$

$\dot{m}$ — Mass flow rate

P_s — Static pressure

P_∞ — Freestream static pressure

q — Dynamic pressure $\left(\frac{1}{2}\rho U_\infty^2 \right)$

Re — Reynolds Number $= \frac{\rho U_\infty}{\mu}$

r — Large tail boom radius

SD_c — Non-dimensional cylinder surface distance $\left(\frac{\theta_s - \theta_a}{\theta_s} \right)$

SD_{TB} — Non-dimensional tail boom surface distance $\left(\frac{\theta_{ts} - \theta_{ta}}{\frac{180}{r\pi} + \theta_{ts}} \right)$

St — Strouhal Number $\left(\frac{fd}{U_\infty} \right)$

U_∞ — Freestream velocity

U_j — Synthetic jet cross-stream velocity

x — Chordwise location

AFC	Active Flow Control
ARL	Army Research Laboratory
DBD	Dielectric Barrier Discharge
GPIB	General Purpose Interface Bus
IEEE	Institute of Electrical and Electronics Engineers
NASA	National Aeronautics and Space Administration
NIA	National Institute of Aerospace
PIV	Particle Image Velocimetry
SAS	Statistical Analysis Software
SJA	Synthetic Jet Actuator
SLA	Stereolithography Apparatus

Chapter 1

Introduction

The goal of this thesis is to obtain and present data showing the time-averaged effect of plasma and synthetic jet actuators on flow over bluff body shapes for delaying flow separation and, therefore, reducing pressure drag. The effect of the actuators on the pressure distribution will be evaluated to give an indication of how best to use the actuators for reducing pressure drag. Parameters to be varied to achieve this objective include the bluff body shape placed in the flow, Reynolds number, the type of actuator used, position of the actuators on the bluff body and the voltage applied to the actuators. Also, this work will give insight into trends in actuator performance associated with varying these parameters providing other groups with the basis for a first approximation as to actuator selection, placement, and operation to control flows over similar bluff body shapes.

1.1 Motivation

A rotorcraft fuselage is designed to meet utility and mission specific requirements which usually leads to sacrifices in the aerodynamic design. This is the case in designing the shape of the tail boom. There are two adverse effects associated with flow over a rotorcraft tail boom: 1) separated flow leads to pressure drag and a net downward force on the helicopter and 2) the aerodynamic forcing from the

rotor and resultant pressure drag is time varying leading to structural fatigue.

The original motivation for this thesis research was an interest in assessing the effectiveness of active flow control for reducing pressure drag on a rotorcraft tail boom. In collaboration with the Army Research Laboratory's (ARL) Vehicle Dynamics Directorate, the target application selected was an AH-64 Apache tail boom. The cross section of this tail boom is similar to a vertical teardrop in shape. Flow from the rotor hits the top of the teardrop and separates from the surface before reaching the bottom. A time varying forcing occurs at a frequency of n/rev, where n is the number of blades (n=4 for the AH-64 Apache), and induces excess fatigue in some structural parts of the helicopter and on the crew. The goal behind using the active flow control is to reduce (and ideally completely alleviate) the downward dynamic force and the vibrations associated with the 4/rev (121 Hz) forcing from the rotor. Reducing the download on the tail would likely, in turn, increase payload capability, range, net thrust and vertical climb velocity. Because the flow over the tail boom is three dimensional and highly variable in direction and velocity, an array of actuators around and along the length of the tail boom would be necessary to achieve continuous flow control during flight. Eventually, command over the aerodynamic forces would require the development and implementation of a feedback control algorithm. The first step toward this goal is observing how the active flow control (AFC) devices affect the pressure distribution under various steady conditions.

To determine the potential effectiveness of AFC for this application, two types of AFC devices and two cases of flow over a bluff body will be studied. The flow

cases consist of flow over 1) a circular cylinder and 2) a representative extruded 2D cross section of the AH-64 tail boom (shown in Figure 1.1). Both of these shapes are considered bluff bodies because there is a significant adverse pressure gradient in the pressure distribution which leads to instabilities in the boundary layer and, eventually, flow separation. A circular cylinder is a common platform for studying bluff body flow because it has been well characterized and modeled through many experimental and theoretical studies for over a century [17]. The AFC devices used are 1) synthetic jet and 2) plasma actuators, both of which have been shown to reduce pressure drag by delaying flow separation. These two devices were chosen for several reasons. They employ very different operating mechanisms and introduce flow perturbations at very different frequencies (typically O(100) Hz for synthetic jet actuators and O(1000) Hz for plasma actuators). Plasma actuators are also a relatively new to AFC applications compared with SJAs, and this study is believed to be the first in which these two devices will be used on the same bluff body surfaces and under the same flow conditions. Extension of the results from these bluff body tests should aid in guiding plans for applying the use of these types of actuators to other bluff body shape such as a fuselage, external weapons or fuel stores.

1.2   Overview of Flow Over Bluff Bodies

Significant pressure drag is usually associated with bluff bodies due to flow separation over a large region of the surface. Understanding what causes the flow to separate from the surface helps provide insight for understanding how AFC devices
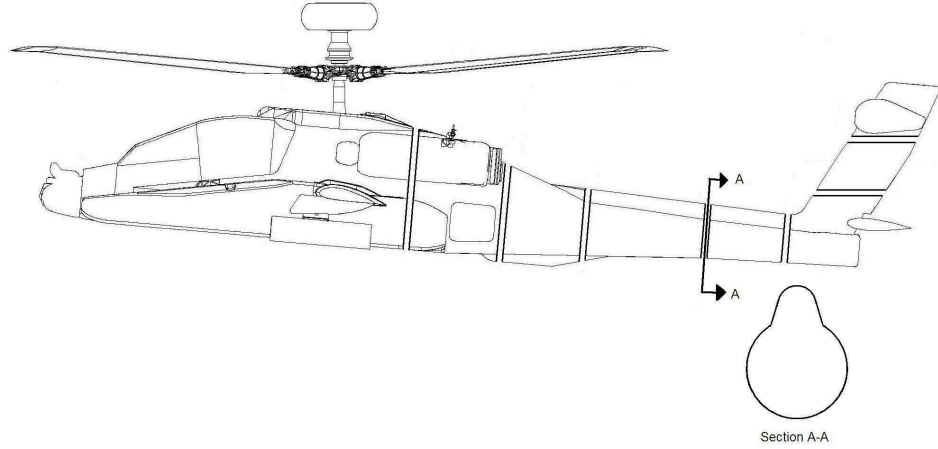
Figure 1.1: Sketch of an AH-64 Apache helicopter and location of the representative cross section of the tail boom labeled as Section A-A.

work to delay flow separation. In this section, a background review of fluid dynamics associated with flows over bluff bodies is presented.

1.2.1   Inviscid Theoretical Cylinder Flow

In ideal conditions, air flow is assumed to be inviscid and incompressible such that, when considering flow over a circular cylinder, there is no flow separation and, therefore, no net lift, drag or moment. The streamline pattern around a circular cylinder can be described as the superposition of uniform flow and doublet flow (Figure 1.2a). The corresponding ideal pressure distribution (Figure 1.2b) is given by

$$C_p = 1 - 4\sin^2(\theta) \tag{1.1}$$

4

in terms of the non-dimensional pressure coefficient $\left(C_p = \frac{P_s - P_\infty}{\frac{1}{2}\rho U_\infty^2}\right)$. There are two stagnation points at $\theta = 0°$ and $180°$ where the tangential surface velocity is zero and $C_p = 1.0$. At $\theta = 90°$ and $270°$, the surface velocity is twice the freestream velocity and $C_p = -3.0$ [1]. In real flow conditions, however, viscous forces are present and result in the thickening of the boundary layer, flow separation and drag.

Uniform Flow
$\Psi = V_\infty r \sin\theta$

Doublet
$\Psi = -\dfrac{\kappa}{2\pi}\dfrac{\sin\theta}{r}$

Flow over a cylinder
$\Psi = V_\infty r \sin\theta - \dfrac{\kappa}{2\pi}\dfrac{\sin\theta}{r}$

(a)

(b)
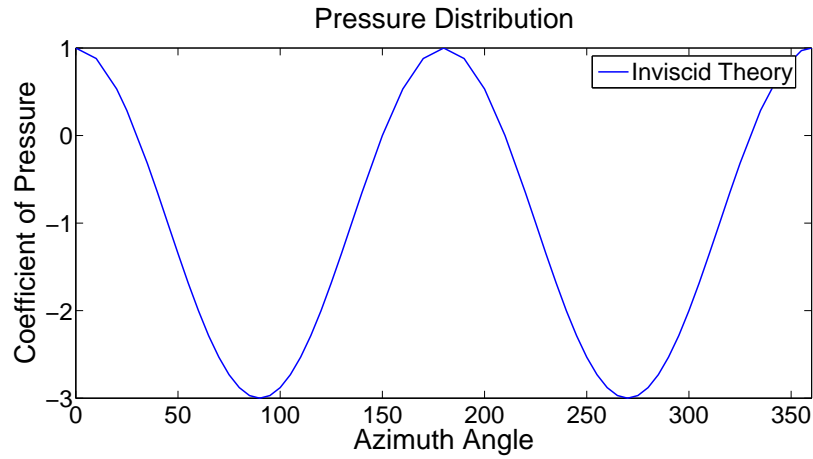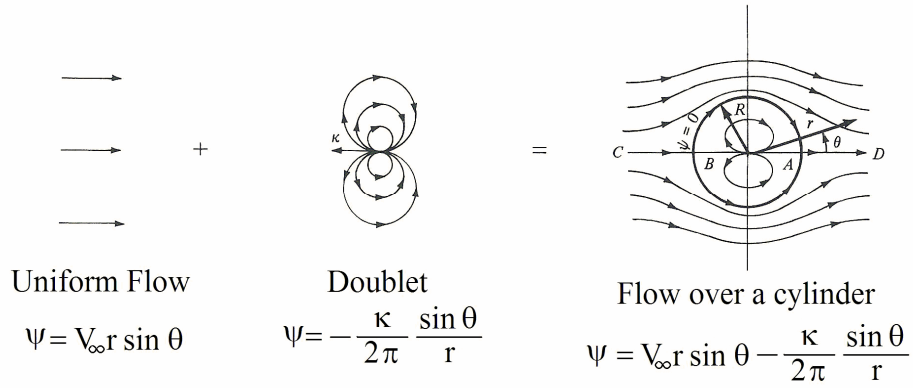
Figure 1.2: Theoretical inviscid and incompressible a) flow model of a circular cylinder [1] and b) the corresponding pressure distribution.

The corresponding pressure drag coefficient is found by integrating the compo-

nents of the pressure coefficient parallel to the flow direction over the entire pressure distribution (Equation 1.2). For the inviscid theoretical pressure distribution, the flow is assumed to be attached to the cylinder surface at all locations and symmetrically distributed on the upstream and downstream surfaces. This produces a result of $C_D = 0$. For a viscous flow pressure distribution, this value is greater than zero due in large part to what is called "flow separation" in which the flow literally separates from a portion of the cylinder's downstream surface. In this thesis, the effectiveness of the AFC devices is evaluated by calculating the percentage of pressure drag reduction from the actuator off to the actuator on cases (Equation 1.3).

$$C_D = \int_0^{2\pi} C_p cos(\theta) d\theta \qquad (1.2)$$

$$\%_{CD} = \frac{C_{Doff} - C_{Don}}{C_{Doff}} \times 100 \qquad (1.3)$$

On bluff body shapes in subsonic flow, there are two main types of drag: pressure drag, as described above, and skin friction drag. For this study, only pressure drag is evaluated because it is typically the more significant source of drag. Skin friction drag results from viscous interaction between the external flow and the bluff body surface. In attached flow, skin friction is the dominant source of drag whereas, in separated flow, pressure drag is the dominant source of drag. Because flow control attempts to maintain attached flow and reduce separated flow, there is typically a reduction in pressure drag but an increase in skin friction drag.

1.2.2 Viscous Cylinder Flow

At subsonic flow conditions, there are two main types of flow, laminar and turbulent, which are largely determined by surface roughness and the Reynolds Number (Re), i.e. the local ratio of inertia forces to viscous forces. Laminar flow is characterized by the absence of mixing between the fluid layers near the surface which makes the fluid susceptible to momentum losses and early flow separation due to viscous forces. In turbulent flow conditions, however, mixing between fluid layers exists such that momentum from the external flow is transferred to flow near the surface, raising the momentum of flow near the surface, thereby allowing the flow to stay attached to the surface longer. On a circular cylinder, a delay in flow separation results in reduced pressure drag by potentially both decreasing the net pressure component acting downstream on the upstream surface of the cylinder and increasing the net pressure component acting upstream on the downstream surface of the cylinder. As Re increases, the transition from laminar to turbulent flow on a smooth circular cylinder occurs around Re $= 4 \times 10^5$, at which point the drag coefficient drops significantly as seen in Figure 1.3.

Based on boundary layer development and Re, there are three main flow regimes around a cylinder: subcritical, supercritical and transcritical [3]. In all of these flow regimes, the flow separates from the cylinder surface and exhibits unstable, but periodic and alternating, three dimensional vortex shedding (Figure 1.4a). The Strouhal number $\left(St = \frac{fd}{U_\infty}\right)$ is a dimensionless frequency used to predict the cylinder shedding frequency and varies with Re (Figure 1.4b). Subcritical flow oc-
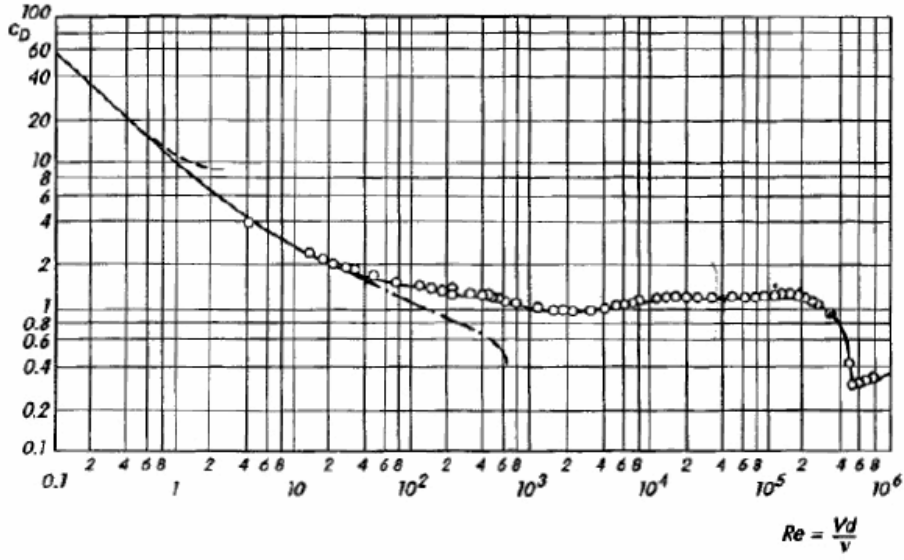
Figure 1.3: Circular cylinder: drag coefficient vs. Reynolds Number measurements [2].

curs between $300 < Re < 3 \times 10^5$ where the flow over the cylinder is completely laminar including laminar flow separation with a Strouhal number of 0.21 [2]. Supercritical flow occurs between $3 \times 10^5 < Re < 1.5 \times 10^6$ where the flow over the cylinder starts laminar and transitions to turbulent flow between the stagnation and separation points and the vortex shedding frequency is irregular [2]. Transcritical flow occurs when $Re > 4.5 \times 10^6$ where the flow over the cylinder is completely turbulent and the Strouhal number is between 0.25 and 0.3 [2].

1.2.3 Laminar Flow

When Re is below 2×10^5, the flow is typically laminar given a smooth surface and the interaction between the air and cylinder surface retards the motion of the air within the boundary layer. Moving from the freestream air to the surface, viscous

(a)

(b)
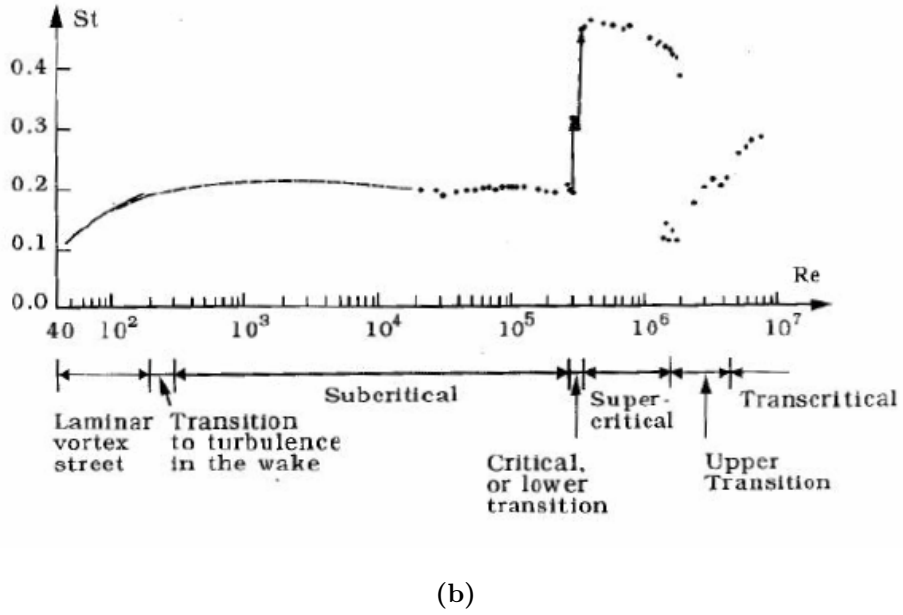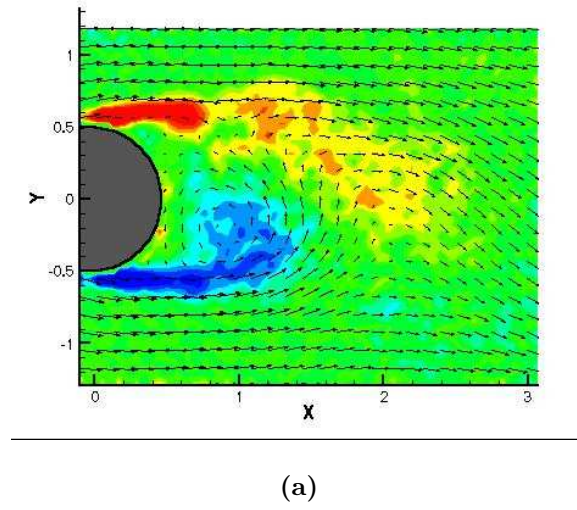
Figure 1.4: Vortex Shedding over a circular cylinder as shown using (a) PIV
and (b) the change in St as Re increases and the corresponding flow
regimes [3].

forces cause the air particles to gradually lose momentum until the no-slip condition
(surface velocity $= 0$) is met and there is no momentum in the air at the surface [2].
The velocity of the air corresponding to the loss in momentum forms a boundary

layer velocity profile as shown in Figure 1.5. The thickness of the boundary layer is defined by the distance from the surface where the profile velocity is 99% of the freestream velocity (δ_{99}).
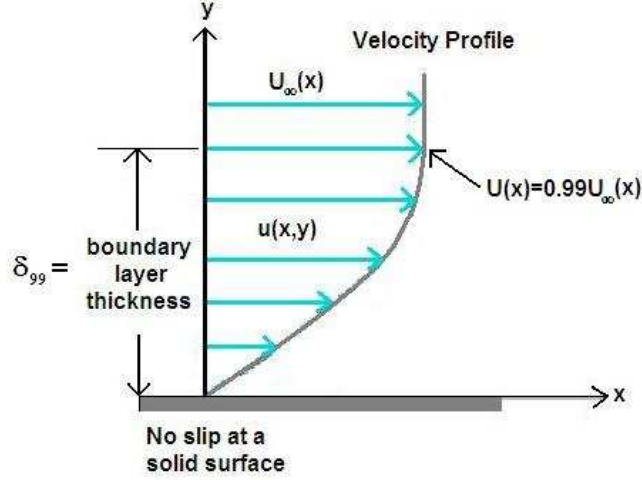
Figure 1.5: Laminar boundary layer over a flat plate [4].

As the air travels over the surface, viscous effects build and the velocity profile deforms until the flow at the surface reverses direction (Figure 1.6); at this point, flow separation has occurred. For laminar flow over a cylinder, flow separation usually occurs at $70° - 90°$, depending on Re. As shown in Figure 1.7, the separation angle, θ_s, moves upstream with increasing Re up to 1×10^5 and then moves downstream until the supercritical flow regime is reached. The location at which flow separation is said to occur is defined as the point on the surface above which the inverse slope of the velocity profile equals zero $\left(\frac{\partial u}{\partial y=0}\right)$ which corresponds to zero shear forces on the surface $\tau_w = \left(\frac{\partial u}{\partial y=0}\right)\mu = 0$. A paper by Achenbach [5] presents a high resolution progression of the shear stress and pressure distribution around the cylinder. Tracking the shear force and pressure distributions in Figure 1.8 shows

10
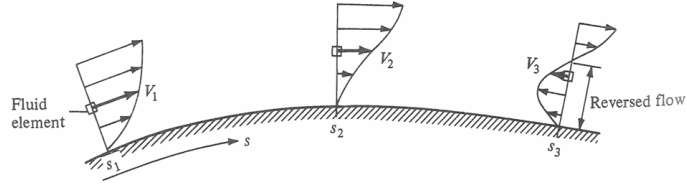
Figure 1.6: Viscous forces cause the boundary layer velocity profile near the surface to deform such that it transitions into separated flow [1].

that, at the front of the cylinder where flow is attached, shear stress values increase from zero at $\theta = 0°$ and the pressure coefficient decreases from one at $\theta = 0°$. At $\theta = 50°$, viscous effects begin to dominate momentum effects and cause the shear stress to decrease indicating a deformation of the boundary layer profile (middle image of Figure 1.6). As deformation progresses, the shear forces drop through t_w equals zero, corresponding to total flow separation, and level off indicating separated flow (right image of Figure 1.6). The angular positions on the cylinder surface where there is a constant shear force distribution correspond to a constant pressure distribution plateau over the rear half of the cylinder.

1.3   Previous Work

The application of AFC devices on circular cylinders, specifically plasma and synthetic jet actuators, is limited. The majority of the research relies on flow visualization and dynamic pressure sensors to monitor the pressure fluctuations in the flow and the effect of the actuators on the shedding frequency. Only papers on synthetic jet actuators used pressure distribution data to analyze the time-averaged
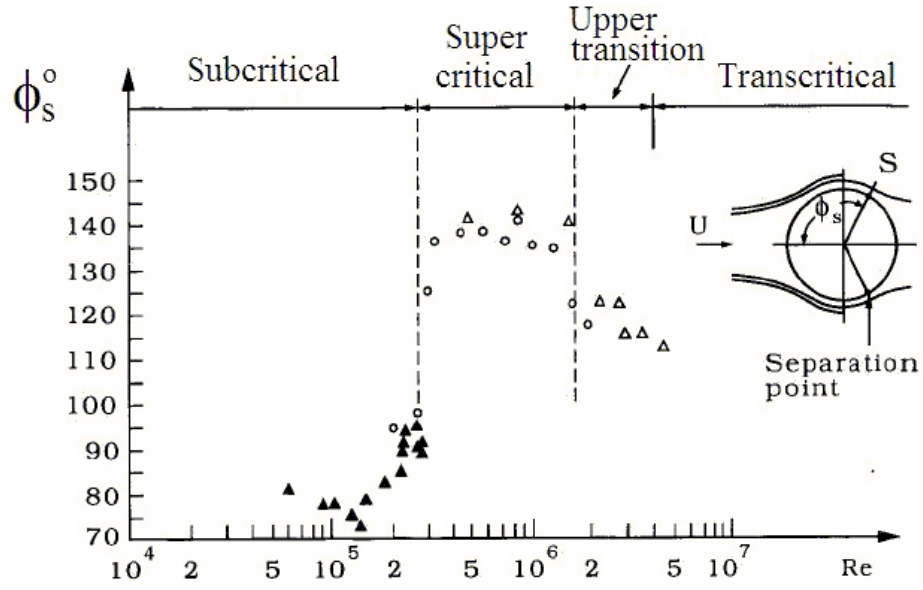
Figure 1.7: Position of the separation point as a function of the Reynolds number for circular cylinder [5].
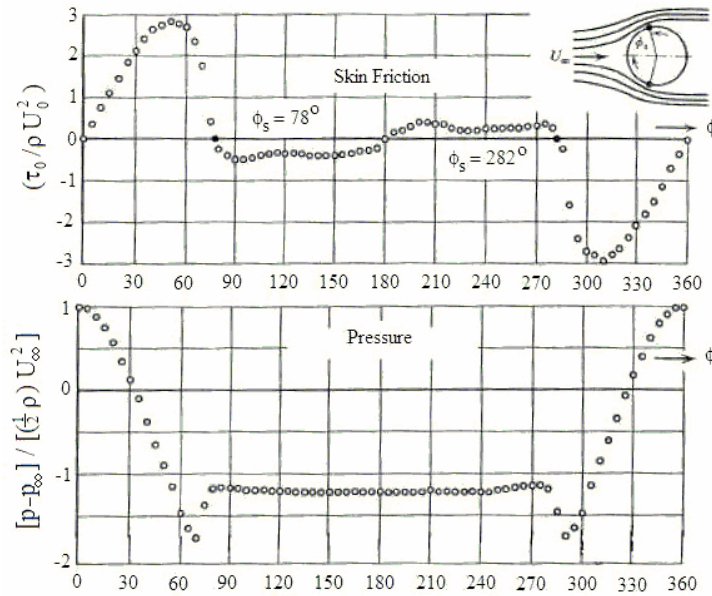
Figure 1.8: Shear force (τ_w) and pressure distribution over a circular cylinder in laminar flow at Re $= 10^5$ [5].

12

effect of the actuators.

1.3.1 Synthetic Jet Actuators and Flow Over Cylinders

In a paper by Amitay [6], the location of a synthetic jet was varied on one half of the cylinder and the change in the pressure distribution was observed. The position varied from 0° to 180° and the synthetic jet was produced by two adjacent synthetic jet actuators. This allowed for a strong single jet and the ability to vector the jet. At low Reynolds number (Re = 4,000), flow visualization was used to show the effect of the synthetic jet on the streamlines. These images (See Figure 1.9) show that the jets have a strong affect on the streamlines on the forced side of the cylinder. For some actuator locations toward the rear of the cylinder, the streamlines on the unforced side are also affected. The jet was also used to successfully delay flow separation almost completely when placed at 180°. When the jet at this location was vectored at 180°, the streamlines resembled those of flow over a rotating cylinder.

At a slightly higher Reynolds number (Re = 7.5×10^4), the pressure distribution was presented to show the time-averaged effect of the actuators. When the actuators were placed from 15° to 90°, the change in the pressure distribution resulted in a decrease in pressure at the top of the cylinder and a slight increase in the base pressure (the pressure in the separated flow region). When placed from 90° to 130°, the pressure starts to decrease on the unforced side of the cylinder as well as the forced side. The apparent global effect of the synthetic jet was explained as being due to suction forces from the forced side drawing the streamlines on the
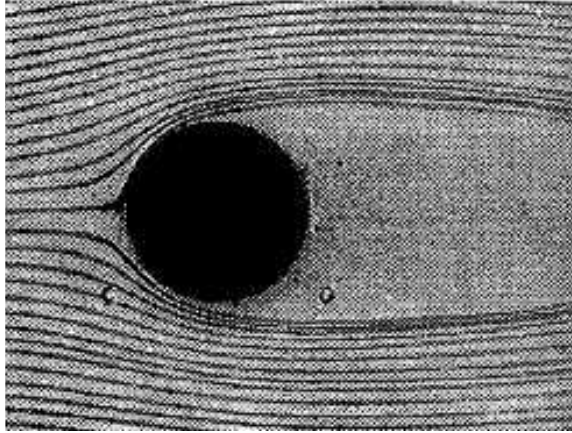
(a) Unforced flow.
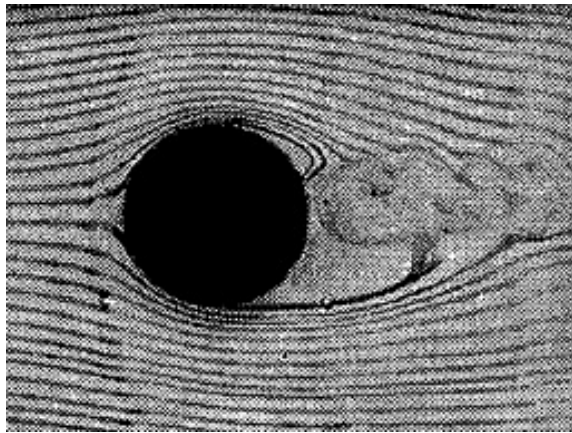
(b) Actuators at 150°.
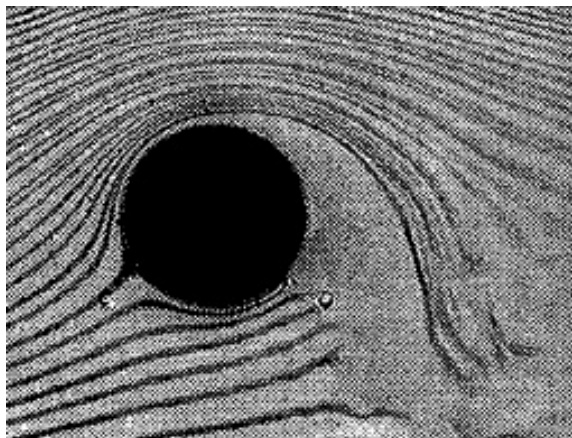
(c) Actuators vectored at 180°.

Figure 1.9: Flow visualization over a circular cylinder. [6]

14

(a) Actuator at 45°.　　　　　　(b) Actuators at 100°.
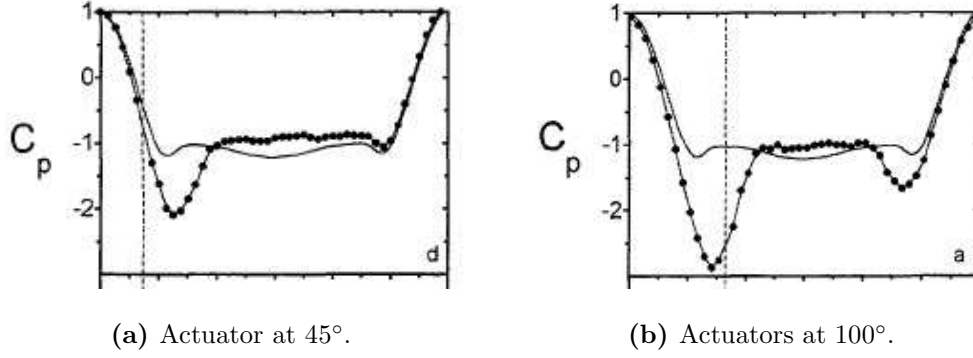
Figure 1.10: Pressure distribution with the actuators at the location of the vertical dashed line [6].

unforced side closer to the cylinder leading to the decrease in pressure shown in Figure 1.10.

As part of the data analysis, Amitay et al. looked at the variation in the lift (C_L) and drag (C_D) coefficients at different angular positions of the jet with the momentum coefficient, C_μ, a commonly identified parameter used to relate the jet velocity to the freestream velocity (Section 2.1 provides more information on C_μ). In these tests, with Re = 75,000 and F^+ of 2.6 (F^+ is discussed further in Chapter 2), both lift and drag coefficients improve as C_μ increases until C_μ equals 1×10^{-4} where the maximum improvement is achieved and maintained as C_μ continues to increase (Figure 1.11). The largest increases in C_L and decrease in C_D occur when the jet is located at 100°. Based on the pressure distributions, actuation at this location results in the largest drops in pressure on both sides of the cylinder with a slight increase in the base pressure. This work is very closely related to the work presented in this thesis and supports some of the findings presented in Chapter 4.

Another paper [7] examined the effect of the actuation frequency relative to
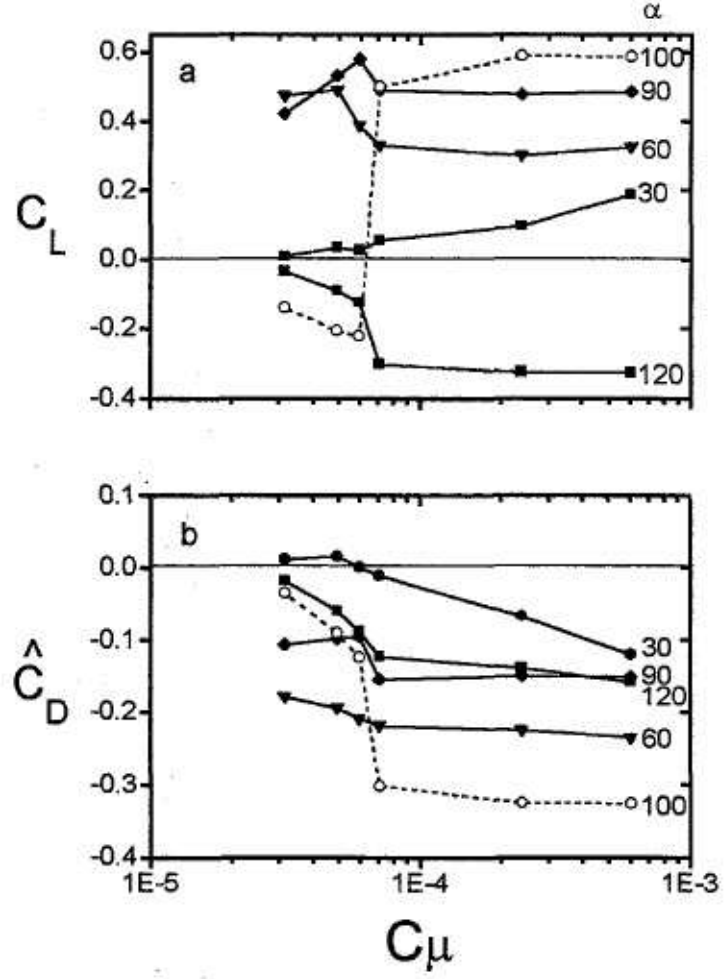
Figure 1.11: Variation in lift and drag coefficients with the momentum coefficient at various angular positions of the actuators for $Re = 7.5 \times 10^4$ and $F^+ = 2.6$ [6].

the natural shedding frequency by looking at the pressure distribution. The synthetic jets were tested at Re = 75,500 and at $C_\mu = 6 \times 10^{-4}$. The Strouhal number was varied from 0.24 to 4.98 and all values below 1.0 were considered low-frequency actuation results and all values above 1.0 were considered high-frequency. When the actuators were placed at 60°, low-frequency actuation produced a sharp pressure decrease at 60° and the flow separated between 110° and 135° whereas high-frequency actuation produced a broader pressure decrease and the flow separated consistently at 135°. The corresponding changes in the coefficients of lift and drag level off for $St > 1.0$ such that drag is at a minimum and lift is at a maximum (Figure 1.12).

A paper by Wygnanski et al. [8] showed the effect of using a single actuator using instantaneous PIV images of the suction and blowing phases of actuation (Figure 1.13). During the suction phase, streamlines are drawn toward the slot location and, therefore, reduce the thickness of the boundary layer. During the blowing phase, a vortex is clearly visible which is characteristic of synthetic jet actuation. They also presented results which show the effect of varying the actuator location and C_μ on the lift-to-drag ratio. This paper showed that there are optimal operating conditions for the actuators to achieve the best lift to drag ratio which can be achieved by varying actuator position, blowing velocity and actuation frequency.

1.3.2 Plasma Actuators and Flow Over Cylinders

Most of the plasma actuator research on circular cylinders centers on controlling the shedding frequency by placing two actuators at ±90° and exciting them
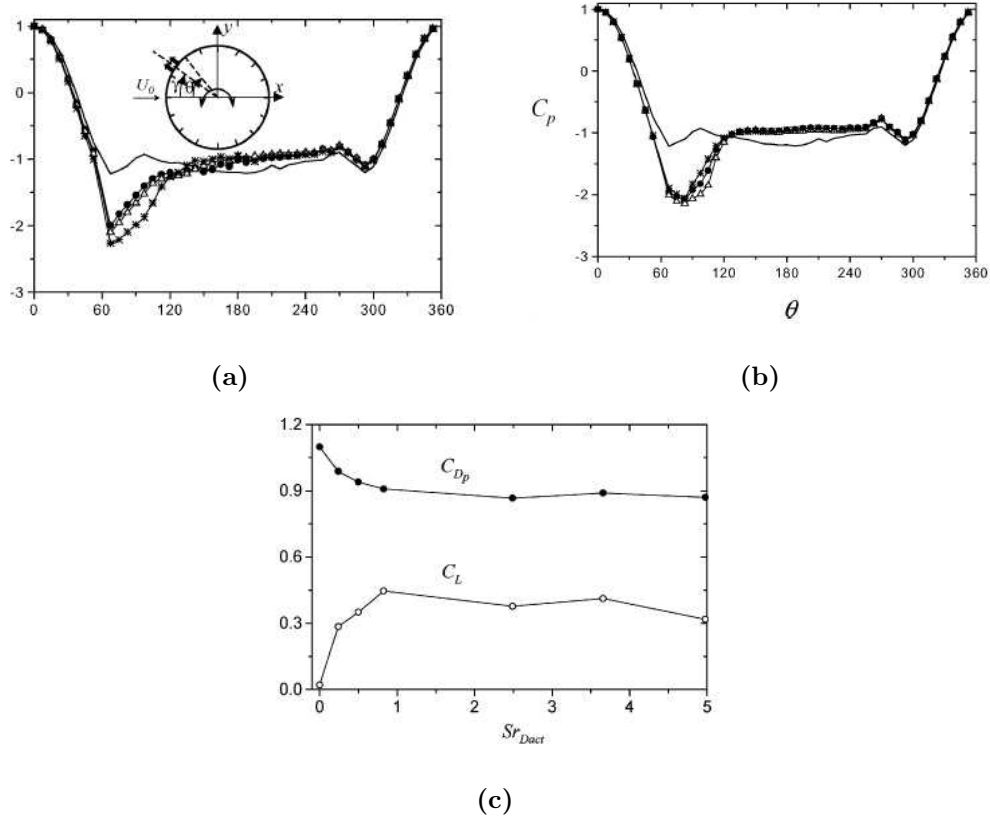
Figure 1.12: Frequency effects (based on St_{Dact}) on the pressure distribution at
(a) low frequencies ($St_{Dact} = 0.24\bullet, 0.50\triangle, and 0.83*$) and (b) high
frequencies ($St_{Dact} = 2.50\bullet, 3.66\triangle, and 4.98*$) and (c) the variation
of the lift and the pressure drag coefficients with St_{Dact} for the
actuators at $60°$ [7].

out-of-phase. In a paper by McLaughlin et al. [18], plasma actuators were used to
control and change the vortex shedding frequency by 10%. In a later paper pre-
sented by the same group [19], the same actuation techniques were used to control
vortex shedding at much higher Reynolds numbers such that there was no periodic
shedding of vortices from the cylinder without actuation. The actuators were able
to reestablish a regular shedding frequency and also showed command authority

18
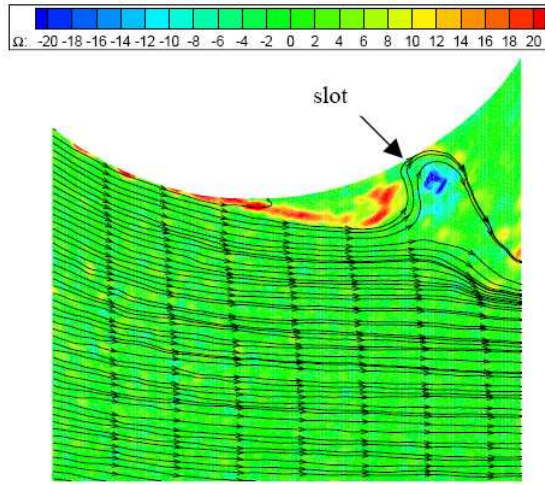
Figure 6c: Instantaneous data, suction phase
Slot at 120°, F^+_r=0.7, C_μ=0.07
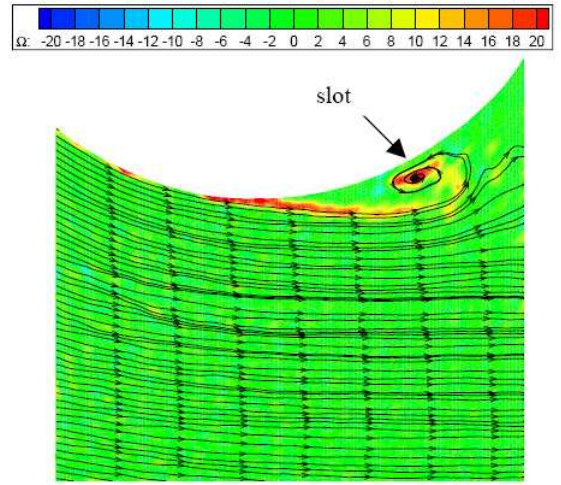
Figure 6d: Instantaneous data
Slot at 120°, F^+_r=0.7, C_μ=0.07

Figure 1.13: Instantaneous PIV data for a slot at 120°, $F_r^+ = 0.7$ and $C_\mu = 0.07$ [8].

above 500 Hz. This paper supports the idea for using plasma actuators to control the aerodynamic forcing on the helicopter tail boom.

These papers present the most closely related research to the thesis work presented. However, to the author's knowledge, there is no published work presenting the effect of two synthetic jets or any plasma actuators on the pressure distribution over a circular cylinder. This thesis will provide such data and also the effect on a similar, yet unique, bluff body shape.

Chapter 2

Active Flow Control Devices

Flow separation is a boundary layer phenomenon that affects the lift and drag characteristics of flow over aerodynamic surfaces. To avoid *adverse* effects, flow control devices have been used on aircraft to delay flow separation. There are two types of flow control devices: passive and active.

Passive devices are fixed alterations on the surface of a body in a flow. Some examples of these devices are vortex generators, chevrons, fences, dimples, and riblets [20]. While these devices improve flow characteristics, they are point-design devices; therefore, when the aircraft is in off-design flight conditions, the devices are still on the surface in the external flow and may induce adverse effects.

A more recent development in engineering research and development is *active* flow control devices. These devices have the unique ability to operate only when needed to improve flow characteristics. Some examples of these devices are trailing edge flaps, blown flaps, suction or blowing through orifices, thermal riblets, synthetic jets, electrostatic and plasma interactions with flows, acoustic cavities or forcing, surface deformation, and rapid transverse strain [20]. This thesis research uses synthetic jet and plasma actuators.

2.1 Synthetic Jet Actuators

Synthetic jet actuators have been developed for and applied to aerospace applications over the last several decades. A synthetic jet actuator (SJA) creates a synthetic jet by periodically discharging air mass into a boundary layer [10]. It creates the "synthetic" jet by drawing in low momentum boundary layer air from the external flow and pumping it out as higher momentum flow that may thicken or punch through the boundary layer. It is a unique device because the net effect is that of a blowing device but with zero-net-mass flux [10]. SJAs are advantageous because other blowing devices use engine bleed or another source of air which requires extra tubing and weight whereas this actuator only needs an electric power source.
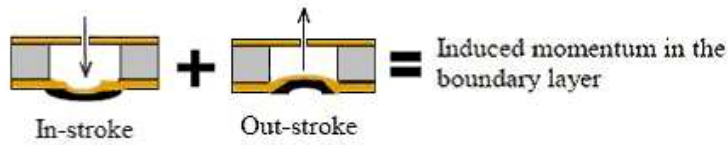
Figure 2.1: Concept of a synthetic jet actuator [9].

The basic design of a synthetic jet actuator (SJA) includes a closed cavity with a small orifice for air to be drawn in and forced out. The cavity volume and pressure change using, for example, a piston, a piezoceramic diaphragm or an acoustic source. During the in-stroke (Figure 2.1), the cavity expands, pressure decreases and low momentum air from the boundary layer above the orifice is drawn into the cavity. During the out-stroke, the volume is contracted and the cavity pressure increases

forcing air out of the cavity. With the appropriate combination of geometry and actuator parameters, vortices form as the air passes the edges of the orifice as shown in Figure 2.2 [9]. The vortices move away from the actuator due to the momentum of the flow out of the orifice.
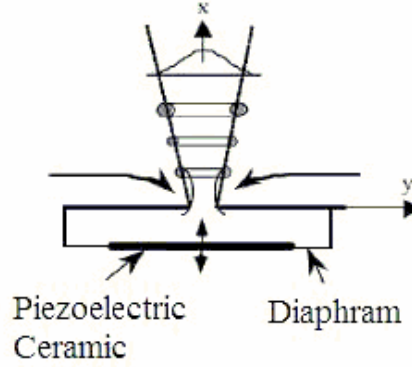
Figure 2.2: Flow concept for a synthetic jet [10].

To construct an actuator capable of producing a useful synthetic jet, certain physical design parameters, such as the size of the orifice and cavity, are used to optimize the interaction of the synthetic jet with the external flow environment. From the continuity equation for incompressible flows, $\dot{m} = \rho A U = const$, a large orifice would produce a very slow synthetic jet while a very small orifice would produce a high speed jet. The combination of these design parameters determine the velocity of the flow from the orifice. The coefficient of momentum, C_μ (Equation 2.1), is a commonly identified parameter used to relate the jet velocity to the freestream velocity and typically ranges from $O(10^{-4})$ to $O(10^{-1})$. SJA effectiveness correlates well with the magnitude of C_μ until a maximum effectiveness is achieved.

23

$$C_\mu = \frac{2\rho_j U_j^2 b}{\rho U_\infty^2 d} \qquad (2.1)$$

Another measure of the effectiveness of SJA performance is associated with their influence on flow above the orifice. A detailed view of the vortices shed from an SJA is presented in Jabbal et al. [11] where the type of vortex formation responsible for delaying flow separation is identified. There are three types of vortices produced by a synthetic jet depending on the actuator stoke length and blowing velocity: hairpin vortex, stretched vortex ring and turbulent vortex ring. Based on flow visualization looking at the vortex shedding from above and on the side of the actuator orifice as shown in Figure 2.3, Jabbal et al. identify that, hairpin vortices are responsible for producing the vortex pairs that delay flow separation. These vortices can be seen at least 50 orifice diameters downstream of the orifice. The dimensionless stroke length is important for the formation of hairpin vortices. Figure 2.4 shows the values of the jet-to-freestream velocity ratio (VR) and the dimensionless stroke length (L, Equation 2.2) for which the hairpin vortices are formed. In the presence of a cross flow, the vortices produced during the out-stroke are carried downstream but not without affecting the pressure distribution and streamlines [10]. By producing hairpin vortices, the SJA can be used to *virtually* change the contour of the surface to improve its overall aerodynamic characteristics.

$$L = \frac{L_0}{D_0} = \frac{\bar{U}_0}{f D_0} \qquad (2.2)$$

The frequency of actuation is another very important aspect of actuator de-
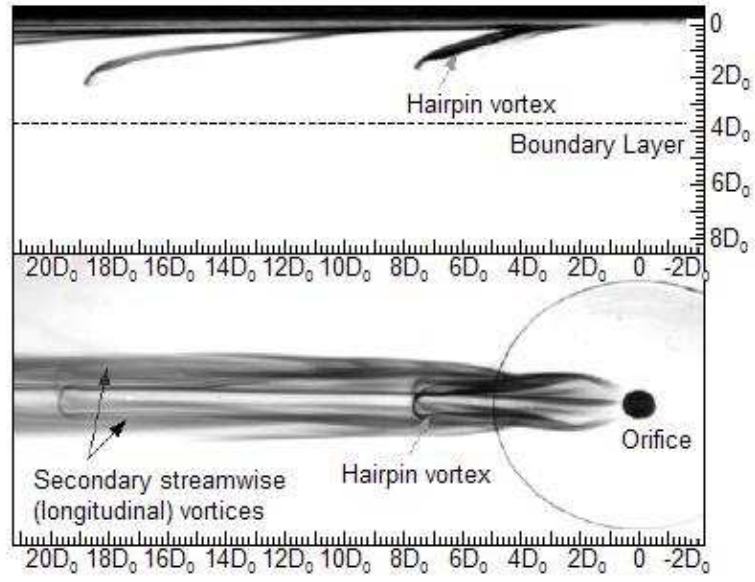
Figure 2.3: Near field stereoscopic dye flow and instantaneous surface liquid crystal data of a synthetic jet at VR = 0.11, Re_L = 29 and L = 1.1 [11].
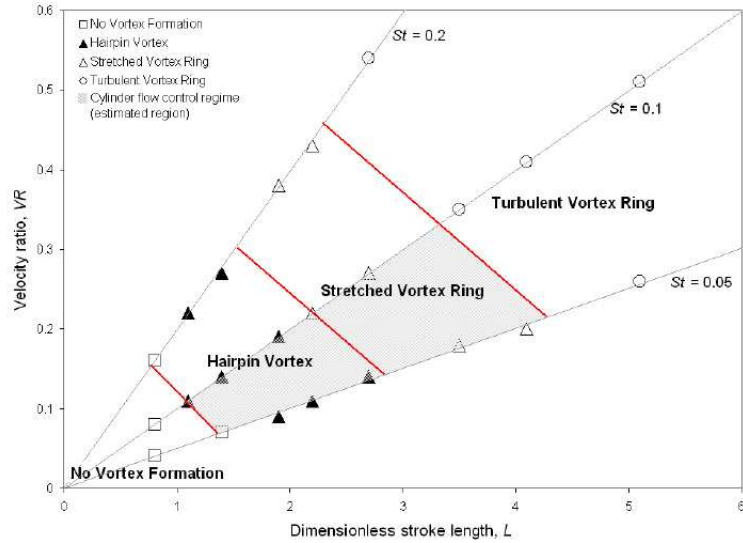
Figure 2.4: Parameter space of the different vortical structures seen as a result of the interaction between the synthetic jets and a boundary layer [11].

sign for efficient operation. The dimensionless frequency parameter F^+ is given in Equation 2.3 [21].

$$F^+ = \frac{f_{act}D}{U_\infty} \qquad (2.3)$$

To achieve control of vortex shedding and delay flow separation, F^+ should be O(1) in order to match the natural instabilities associated with vortex shedding within the lock-in range. The lock-in range is the range of actuation frequencies to which the flow will respond with periodic shedding of vortices [22]. Some researchers use F^+= O(10) for vortex shedding suppression. Current designs for synthetic jet actuators include devices that have a resonance frequency different (usually much higher) than their application demands. In such designs, the resonance frequency is used as a carrier frequency and the actuator is pulsed at the shedding frequency for modulated actuation.

Many experiments have been conducted using SJAs to affect the aerodynamic flow characteristics of airfoils and bluff bodies. The most significant work with circular cylinders that is related to this research comes from Amitay in the late 1990s [6] as described in Chapter 1. A thorough review of synthetic jets and their applications is presented in a paper by Amitay and Glezer [10]. Because SJAs have been thoroughly studied, research has progressed to the point of applying the actuators on full scale aircraft models to determine their command authority compared to conventional control surfaces. Closed loop feedback control models have been developed to achieve such goals.

2.2 Plasma Actuators

A plasma actuator is an aerospace application of the technology behind ozonizers and plasma TVs that was developed in 1998 by Roth and Wilkinson [23]. Ozone (ozonizer) and light (TV) are two products associated with ionizing air by applying a high voltage to electrodes that are separated by a dielectric. Another product that is generally not used is the body force on the air near the electrodes. By changing the position of the electrodes in relation to one another, this body force can be used to direct the flow of the air adjacent to the electrode surface. The ability to move air with a plasma-generated body force has led to interest in the use of plasma actuators as an active flow control device in a wide variety of aerospace applications.

Dielectric barrier discharge (DBD) plasma actuators have been used to improve aerodynamic characteristics in subsonic to hypersonic flows; however, the mechanism by which the plasma affects the flow is different for low and high speed flows. In supersonic flow, it is thought by some [24–26] to locally heat the air on the surface of the actuator, thereby creating small pressure perturbations. However, there are others [27] who believe the mechanism that influences shock wave dispersion and propagation in plasma is related to some "anomalous" effects such as the presence of an electric double layer [28]. A double layer is a structure in plasma where two layers of opposite electric charge create a strong electric field in which ions and electrons are accelerated rapidly [29]. There is still debate over which phenomenon is responsible for the changes in shock wave propagation and dispersion, yet regardless of the mechanism, they show improvements in the aerodynamic characteristics such

as wave drag reduction, sound attenuation and shock wave modification [27].

In low Re flows, plasma actuators are used to add energy to low momentum boundary layers and, therefore, delay flow separation. The actuator is typically constructed in an asymmetric configuration with an upper, exposed and lower, covered electrode separated by a dielectric material (see Figure 2.5). Offsetting the electrodes from each other allows the body force to give a preferred direction to the resulting induced velocity tangential to the surface directed toward the lower electode. Typically, the electrode is made of a metal, copper or aluminum, and the dielectric is made from Kapton tape or fiberglass epoxy (printed circuit board).
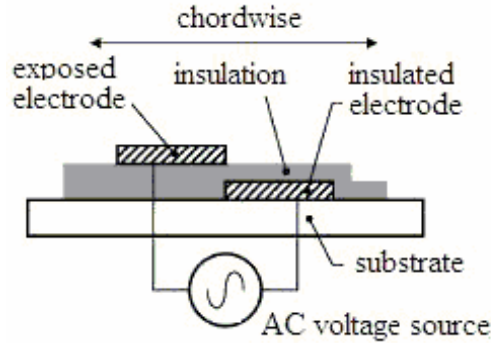
Figure 2.5: Plasma actuator setup [12].

The mechanism by which a plasma actuator imparts momentum into the flow has been carefully examined using several methods and has become clearer. Most of the efforts into discovering the intricacies of the actuator have been directed by Enloe [12, 30–33] at the US Air Force Academy.

A simulation of the forward and backward strokes is shown in Figure 2.6 where the dark particles are electrons and the white particles are ionized air particles

[13]. A high positive voltage is applied to the exposed electrode and at a specific voltage, the electrode emits free electrons and the plasma is ignited. These electrons accelerate toward the lower electrode in the electric field and collide with surrounding air molecules. The collisions release more electrons (hence the term "avalanche") through Lorentzian collisions [34], a process which weakly, positively ionizes the surrounding air. The continuing collisions causes the plasma to expand, covering the buried electrode. At the same time, the presence of a voltage differential between the two electrodes results in a body force opposite of the electric field on the ionized air particles. The ionized air particles are attracted to the negatively charged upper electrode while the electrons are drawn to the encapsulated electrode, however, because this electrode is buried, the electrons stay on the surface of the dielectric. This process, the "forward stroke" [13], ends when the accumulated charge on the dielectric cancels the charge from the exposed electrode and the voltage differential is too small to sustain the plasma and it is quenched.

The "backward stroke" [13] begins when the direction of the applied electric field changes such that the exposed electrode is more negative than the buried electrode. The plasma is reignited and the electrons embedded in the dielectric during the forward stroke are now drawn out by the upper exposed electrode. Again, through Lorentzian collisions, the air is ionized and the ionized air particles are drawn toward the lower electrode (plasma expansion). When the voltage differential in this direction becomes too small to sustain the plasma, which typically happens once all of the buried electrons have reached the upper electrode, the plasma is, again, quenched and turns off. Dielectric barrier discharge is self-limiting because
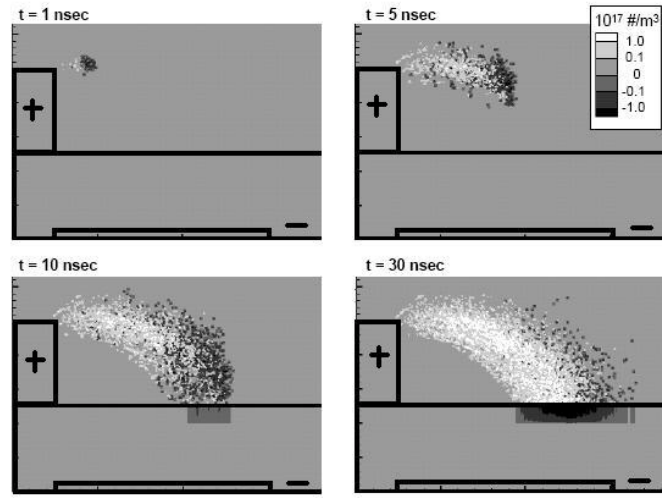
(a)
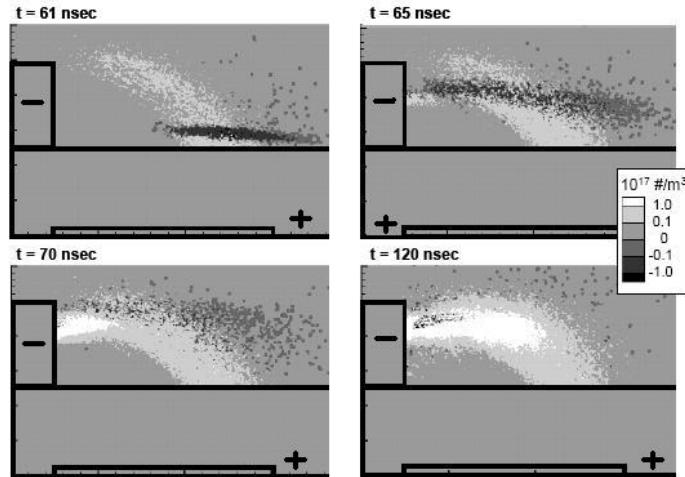
(b)

Figure 2.6: Charge Density contours of the a) forward and b) backward strokes [13].

charge buildup on the dielectric surface above the buried electrode opposes the voltage applied across the plasma. When the voltage reverses, the charge transferred

through the plasma is limited to the electron charge deposited on the dielectric surface as the buried electrode does not emit free electrons into the air. The self-limiting behavior makes an AC applied voltage necessary to continually reignite the plasma.

This simulation also shows that even though the voltage signal (unbiased sine wave) is symmetric, the time duration of the presence of plasma during the forward and backward strokes is different. The average ion density is higher and the presence of plasma is longer during the backward stroke than in the forward stroke suggesting that the backward stroke is more important for creating the induced flow. However, this results contradicts previous observations [31] where there is a net force downstream and a positive sawtooth waveform produced more thrust than for a negative sawtooth waveform.

Because the plasma structure exists in such a small time period, there are few actual experimental observations of the temporal and spatial structure of the plasma. Until recently, experimental results had shown that the *net* induced flow of plasma actuators was directed from the exposed electrode toward the buried electrode. However, because the plasma is created in an alternating electric field, it was unclear whether or not the magnitude and direction of the body force on the air changed between the forward and backward strokes. A paper by Enloe et al. [35] determined that one stroke produces a large "PUSH" on the air and the other stroke produces a small "push" in the opposite direction.

Laser deflection measurements were used to observe the temporal air density changes over the plasma actuator during the actuation cycle [33]. These observations

show that the action of the actuator is to pressurize the region near the electrode edge and to establish a favorable pressure gradient so that the air flow is directed downstream. Based on the images in Enloe's paper [33], the pressure gradient pulls in air from 10 mil above the surface, above the exposed electrode, toward the lower electrode. This action brings high energy freestream flow down from above the boundary layer thickness into the low momentum boundary layer resulting in delayed flow separation. These results explain the previous apparent contradictions stated above. This model suggests that the dominating factor controlling the net force on the neutral air is the low pressure void near the electrode and resultant pressure gradient, rather than the body force on the ionized air in the electric field.

Plasma actuators are attractive for aerospace applications because they are lightweight, rugged and can be applied easily to a curved surface such as a wing. They also have an advantage over synthetic jet actuators because they have a higher operating frequency which can be used as a carrier frequency in modulated operation. Therefore, in high velocity flows when the inherent flow instabilities occur at higher frequencies, operation of the plasma actuators can be modulated at frequencies higher than the operating frequency of most synthetic jet actuators. However, current actuator designs produce only small body force magnitudes/pressure gradients. Actuator development research has focused on improving force levels. Another drawback to these actuators is the high voltage (1-10kV_{rms}) and frequency (3-20kHz) requirements typically drawing up to 0.2A of current. While the power required is low (up to 1.34 Watts), the high voltage at a high frequency means a very heavy power supply, a considerable disadvantage for an aerospace platform. Therefore,

another part of the actuator development research has focused on optimizing the physical design by returning to the electronic model to maximize the output force and minimize power requirements [30, 36].

Actuator geometry and electrical inputs have been varied to find the best combination that produces the highest induced velocity. Research at the US Air Force Academy found that, for the same resulting induced velocity, the power dissipated by the actuator is independent of its width but the thrust to weight ratio is better with a smaller upper electrode; therefore, a narrow electrode will be more efficient [30]. The upper electrode can be either a small diameter wire or narrow strip of foil tape; there is no apparent difference in thrust produced between using wire and foil tape. The optimal size of the lower electrode depends on the maximum applied voltage because the lower electrode stores charged particles until it is saturated. If it is too small, the maximum potential of the actuator can not be reached. If it is too large, there is wasted material and weight. Therefore, the streamwise width of the lower electrode is optimized to accommodate the desired saturation charge [36]. At saturation, the plasma discharge turns itself off; therefore, the actuator is considered self limiting and usable at atmospheric pressures [31]. Another way to maximize actuator effectiveness has been to arrange them in a sequential configuration, or array. This setup combines the added momentum individually to the flow to create an overall higher thrust, lower drag, and higher induced velocity [30].

The AC voltage has been applied using a variety of waveforms while holding frequency constant. Of the square, triangle, positive and negative sawtooth slopes, the positive sawtooth and triangle waveforms provide the most thrust when actuated

because more of the waveform is positive-going which corresponds to the backward stroke. Also, the frequency and voltage are very dependent on the application and should be optimized for each experimental setup [36]. Similar to synthetic jet actuation, plasma actuation has been modulated to match the vortex shedding frequency of the external flow such that $F^+ = O(1)$ or $O(10)$. In fact, amplitude modulated actuation has produced better results than when the actuator was operated with no modulation [36].

Similar to the synthetic jet actuators, plasma actuators have been tested on aerodynamic surfaces such as airfoils and cylinders. Because the actuation frequency for plasma is much higher than for synthetic jets, plasma actuators have been tested in oscillatory as well as steady flow cases. Plasma actuation was first applied to supersonic flows to reduced drag by increasing the local Mach number and thereby increasing the drag divergence Mach number. This delays the sharp increase in drag that occurs at the drag divergence number, also known as wave drag [28]. One specific application is the improved mixing in a jet nozzle due to streamwise vortices [27].

Testing plasma actuators in the low Reynolds number regime has been producing promising results. Most of the experiments consist of two goals: 1) maximizing thrust or induced velocity on a flat plate and 2) reattaching otherwise separated flow on an aerodynamic shape (airfoil or cylinder). Through the flat plate experiments at the NASA Langley Research Center with the University of Tennessee, researchers realized that it was possible to induce unidirectional induced flow by the asymmetric configuration shown in Figure 2.5. At first, the configuration was such that the

induced flow created drag but it was soon realized that changing the orientation of the electrodes would reduce drag [23]. In 2004, the University of Kentucky applied an array of electrodes and phased them to create a traveling wave in the electric field [37].

As the potential of plasma actuators was exposed, universities explored their potential further by applying the actuators to airfoil shapes. The goal of the experiments was to maintain attached flow up to angles of attack further than the static stall angle, at which the flow separates from the surface and there is a significant loss of lift. Researchers at the University of Notre Dame were able to maintain attached flow up to 8° past the stall angle on several NACA airfoils [38] by delaying flow separation.

Another application of interest involved low pressure turbine engines. Until the development of the plasma actuators, no available active flow control device was small enough to fit on turbine blades. With plasma actuators, the device can be adhered to the surface of the blade with small electric leads. The Glenn Research Center found that the actuators are effective in reattaching separated flow at low Reynolds numbers and, specifically, in laminar flow on Pak-B turbine blades [39].

Plasma actuator technology has also been applied to bluff body (cylinder) flow control. At the US Air Force Academy, the actuators were used to attach the flow beyond the normal separation point. The actuators effectively influenced the flow to shed vortices further on the surface of the cylinder, thereby reducing the pressure drag on the cylinder [22].

In a similar experiment, the University of Notre Dame used plasma actuators

to control the vortex shedding on multiple cylinders. These cylinders were close enough in proximity that the wake shed from one cylinder influenced the wake from the other cylinder. Typically, the wakes from each cylinder would shed out of phase but the experiments at Notre Dame showed that the actuators could influence the wakes to shed in phase [40]. This ability could be very useful for controlling vibration and noise.

Through the evaluation of many papers on plasma actuator research, it can be seen that plasma actuators are still well within the research and development phase. Research is still continuing in order to understand the plasma discharge and apply that understanding toward further optimization. After the actuators are fully optimized, they can be applied to more and more flow control regimes.

Chapter 3

Experimental Setup

3.1 Wind Tunnel and Equipment

The wind tunnel facility used for the current test is the NASA Langley Research Center 20″ x 28″ shear flow wind tunnel (Figure 3.1). It is a low speed, open circuit facility with a maximum speed of 150 ft/s and low freestream turbulence due to a series of screens and large contraction ratio settling chamber. The test section is 15′ long and has a cross section 20″ high by 28″ wide with an adjustable upper wall to control the pressure gradient over the long test section [14].

Figure 3.1: 20″ x 28″ Wind Tunnel Facility [14]

Wind tunnel and room atmospheric conditions were measured. This included temperature, relative humidity, barometric pressure, wind tunnel entrance velocity and velocity profile at the position of the tunnel where the models were located. The barometric pressure was acquired using a Mensor Digital Barometer Model 2104 with a reading accuracy of 0.01% and temperature range of 15 to $45°C$. The temperature was read by two instruments: a Fluke Digital Thermometer and a General Eastern 800LC Digital Thermo-Hygrometer which measures relative humidity and, therefore, included a temperature sensor. The pitot static tubes at the entrance of the tunnel and at the test section were measured using separate Datametrics Barocel Digital Manometers Model 1174. Each manometer has a Datametrics 525 Thermal Base to maintain a temperature of $120°F$ to prevent changes in the room temperature from affecting the pressure reading and the manometer was calibrated at $120°F$. To acquire the velocity profile for the empty test section ensuring 2D flow, a pitot static probe was traversed in a plane (illustrated in Figure 3.2) perpendicular to the flow using an Aerotek Unidex 511 system. As shown in Figure 3.3, the velocity in the core of the test section $\pm 5''$ above and below the location of the pressure ports and $\pm 7''$ to each side of the center of the test section (illustrated in Figure 3.2) varies less than 1%.

A System 8400 High Performance Pressure Data Acquisition System and two Electronic Pressure Scanning modules were used to simultaneously measure the differential static pressure of all 58 pressure ports on the models. The physical experimental setup required the length of the pressure port tubing to be $4'$ long. To ensure the length of the tubes did not compromise the dynamic response of

38
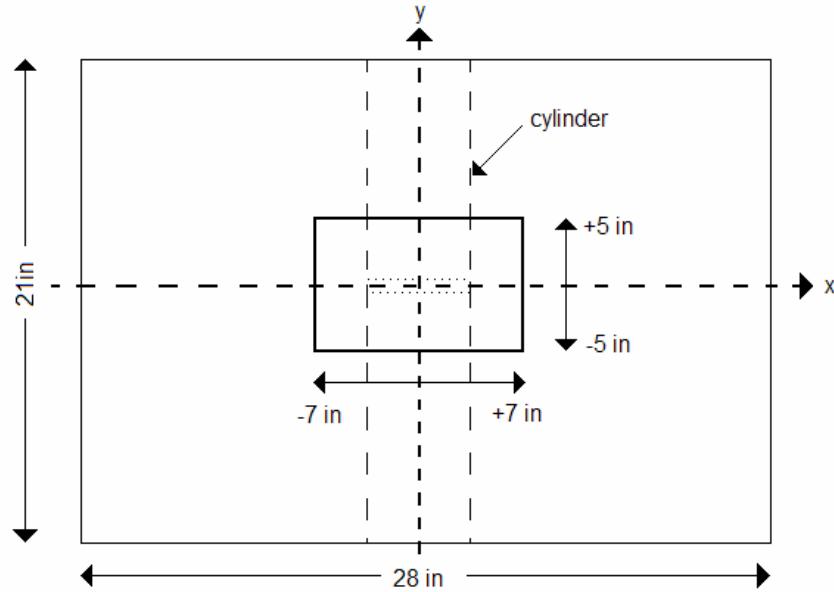
Figure 3.2: Diagram of Test Section Grid.
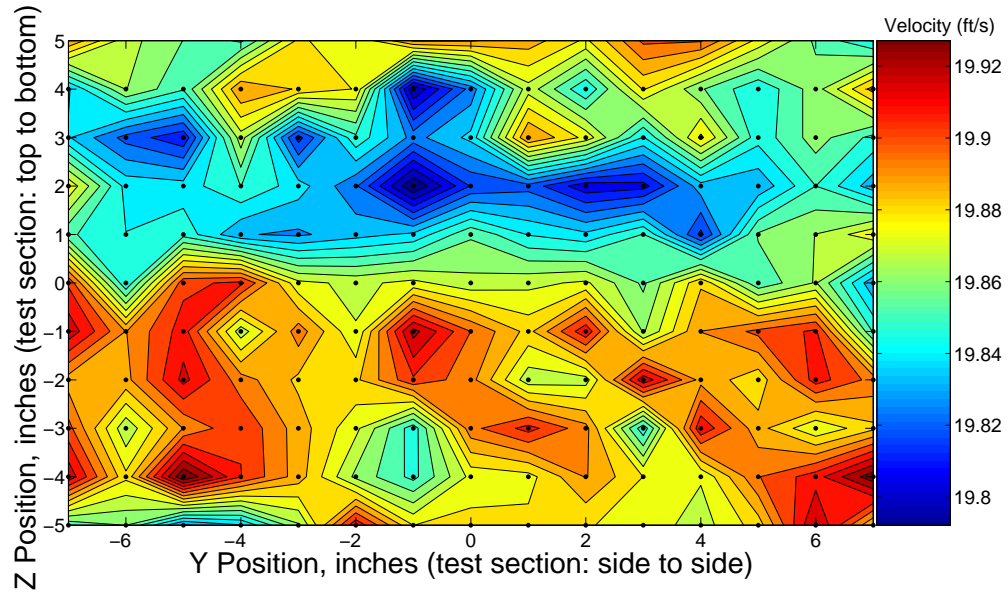
Figure 3.3: Velocity samples at grid locations.

the data, tube lengths of $2'$, $4'$, $8'$ and $20'$ were tested. A single pressure port in the area of the cylinder where the vortex shedding would create highly oscillatory pressure variations was monitored. Figure 3.4 shows that the effect of the tube

length is insignificant below 8′ of length. All instruments were read remotely through GPIB (General Purpose Interface Bus) connections and all of the data from these instruments were taken using Labview data acquisition programs.
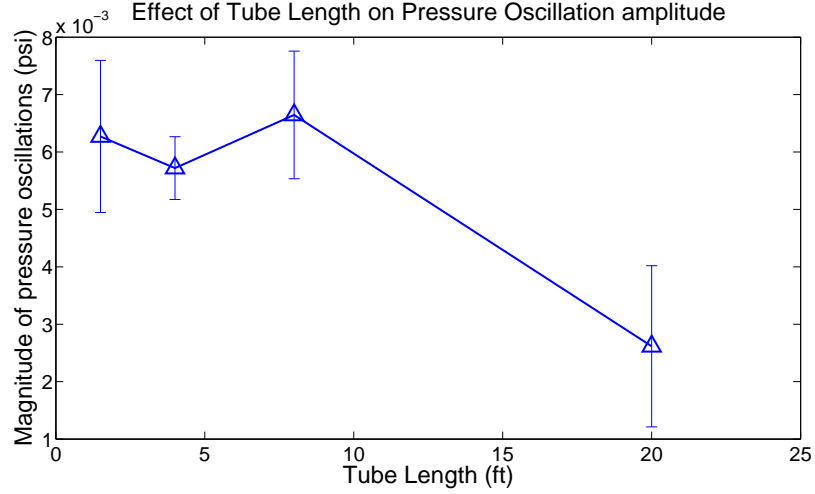
Figure 3.4: Variation of pressure oscillation magnitude with pressure port tube length.

3.2 Bluff Body Models

To observe the actuator effectiveness in laminar flow, two bluff body models were used in this experiment: a circular cylinder and a representative 2D extruded cross section of an AH-64 tail boom.

3.2.1 Circular Cylinder

The circular cylinder model, designed to be tested in laminar flow conditions, has a 4.5″ outer diameter, 4.0″ inner diameter, and length of 21″ (to accommodate the change in height of the wind tunnel ceiling). There are 58 pressure ports (Fig-

ure 3.5) on each cylinder but the actual number of useable ports decreased because the synthetic jet actuators blocked access to 4 ports each and the plasma actuators covered 3 ports each. The 58 ports are spaced such that they are more concentrated where flow separation is expected to provide high resolution pressure distribution measurements in that area. The cylinder was constructed out of cast acrylic, more commonly known as Plexiglass, giving the cylinder a smooth exterior surface. Aluminum support rings were used inside the cylinder to maintain the circular shape and to support the synthetic jet actuators. Because the plasma actuators required small holes for wiring to power the actuators and the synthetic jets required 6″ long spanwise slots to be machined into the surface of the cylinder, two separate models were made, as shown in Figures 3.6 and 3.7. With a dielectric strength from 450-550 Volts/mil, the 0.25″ thick plexiglass wall can withstand 112kV to 137kV before a spark from the plasma actuator could arc through the cylinder to the Aluminum rings. Thus, the plasma actuators could be operated safely at $12kV_{p-p}$. Additionally, the cylinders were sufficiently supported such that they did not bend or vibrate during testing.

3.2.2 AH-64 Tail Boom Section

A representative cross section of an AH-64 Apache helicopter tail boom was extruded to test the effectiveness of the actuators on a more realistic shape applicable to rotorcraft. The model was created by Eagle Aviation in Hampton, VA by the Rapid Prototyping method of Stereolithography Apparatus (SLA). Figure 3.8 shows
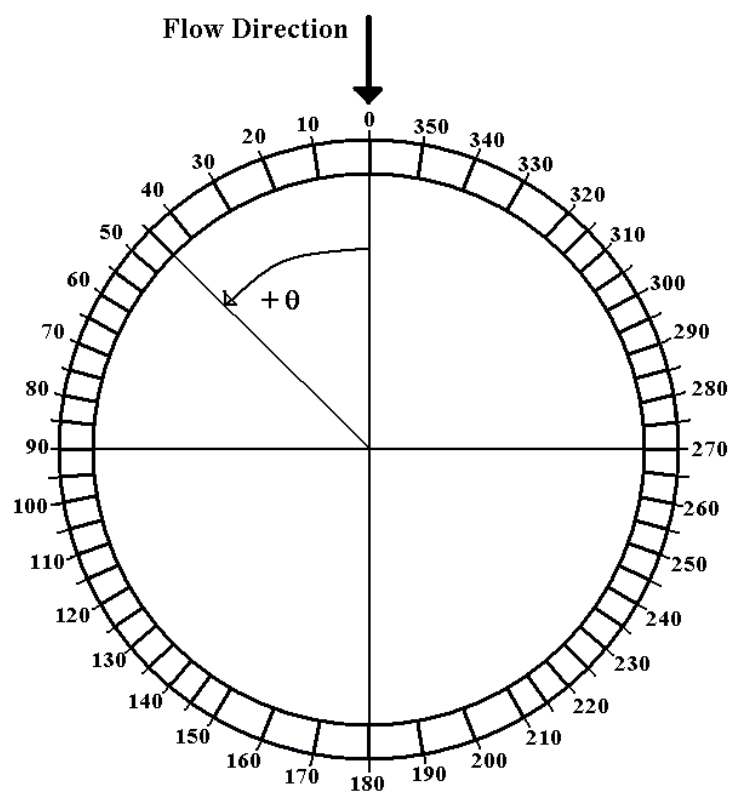
Figure 3.5: Port locations on the circular cylinder model.
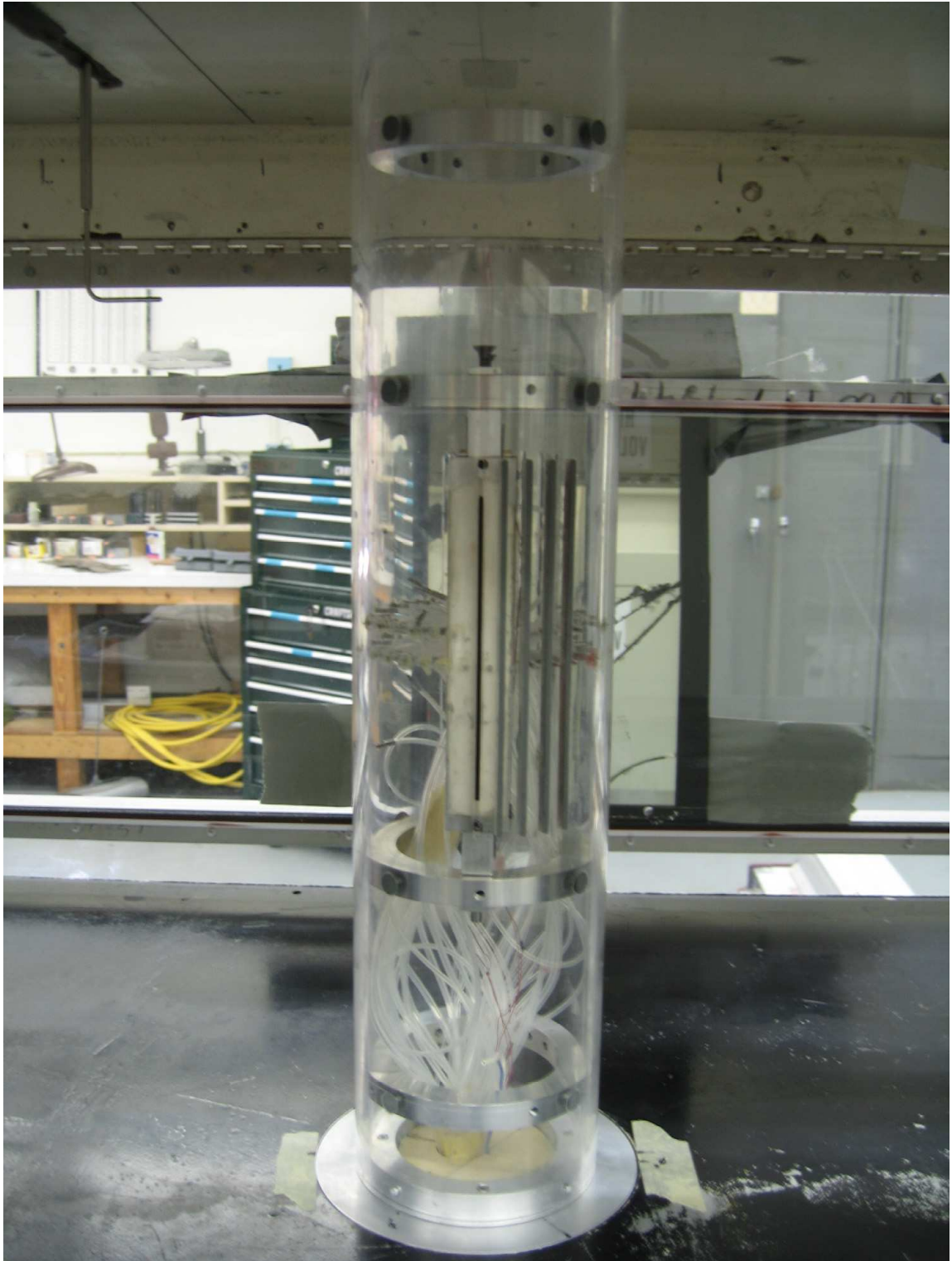
Figure 3.6: Circular cylinder model with synthetic jet actuators installed.

Figure 3.7: Circular cylinder model with plasma actuators installed.

the shape of the model and the pressure port locations. The 58 pressure ports are spaced such that they are more concentrated where flow separation is expected to provide a high resolution pressure distribution measurement over the tail boom in that area. The same physical alterations were made to this model as the circular cylinder (small holes for wires and slots for the SJAs), thus requiring fabrication of two models as shown in Figures 3.9 and 3.10. This design also included black carbon SLA constructed bulkheads to hold the two sections together and provide the support structure needed for synthetic jet installation.

3.3   Actuator Construction, Installation and Operation

3.3.1   Synthetic Jets

The design for the synthetic jets was provided by The Boeing Company in Seattle, WA. The actuators were positioned to energize the boundary layer through spanwise radially cut slots such that the SJAs ejected air perpendicular to the surface of the cylinder. The ends of the two actuators were attached to the centermost aluminum rings inside the models. The overall dimensions of the actuator were 1″ x 1″ x 8.875″ and they weighted 143.7 grams each. When the actuators were installed in the cylinder and tail boom model (illustrated in Figure 3.12), they were capable of producing velocities of up to 11 m/s when excited at their fundamental frequency which varied from 95 - 105Hz (Figure 3.11). The actuators also produce an audible noise at the operating frequency.
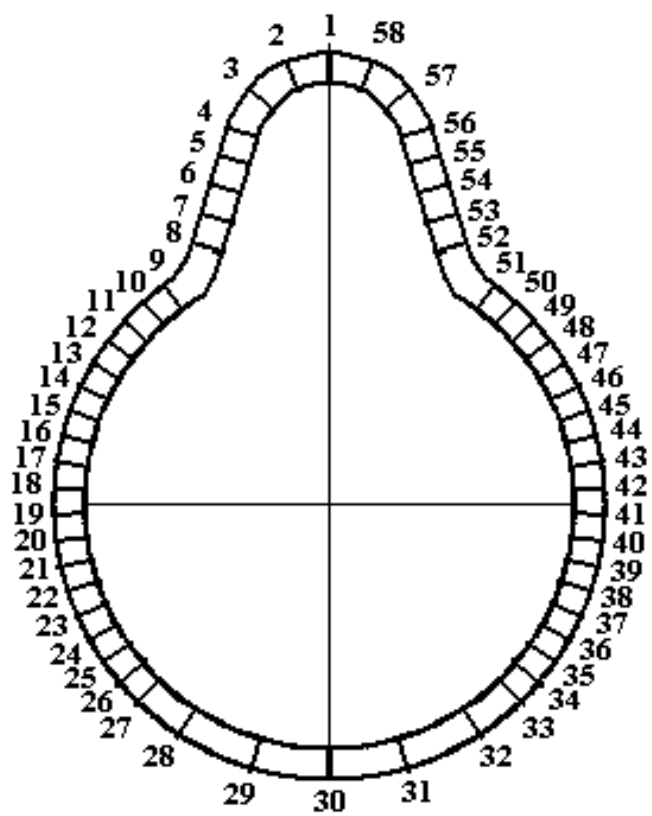
Figure 3.8: Port locations on the tail boom model.

Figure 3.9: Tail boom model with synthetic jet actuators installed.
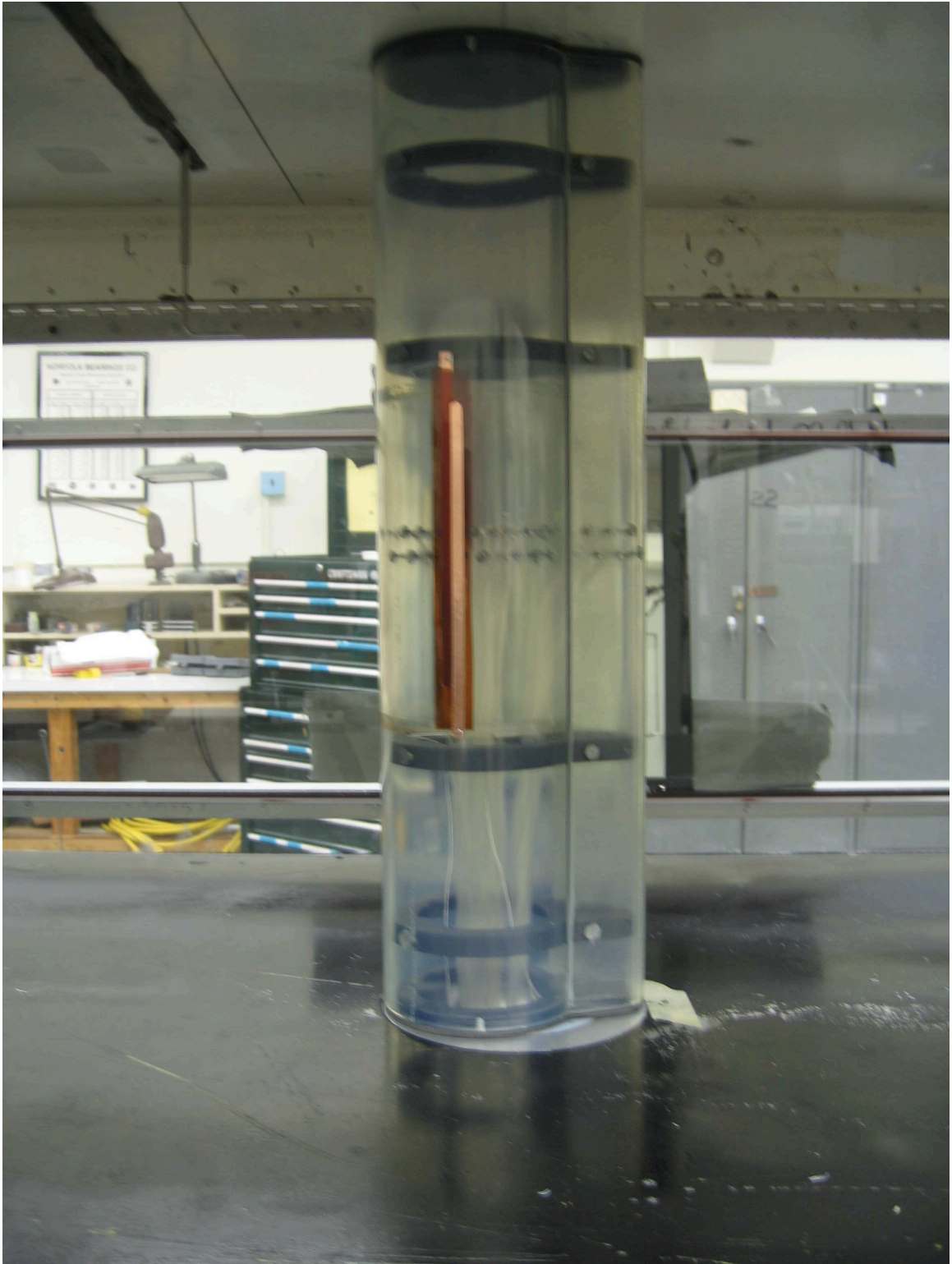
Figure 3.10: Tail boom model with plasma actuators installed.
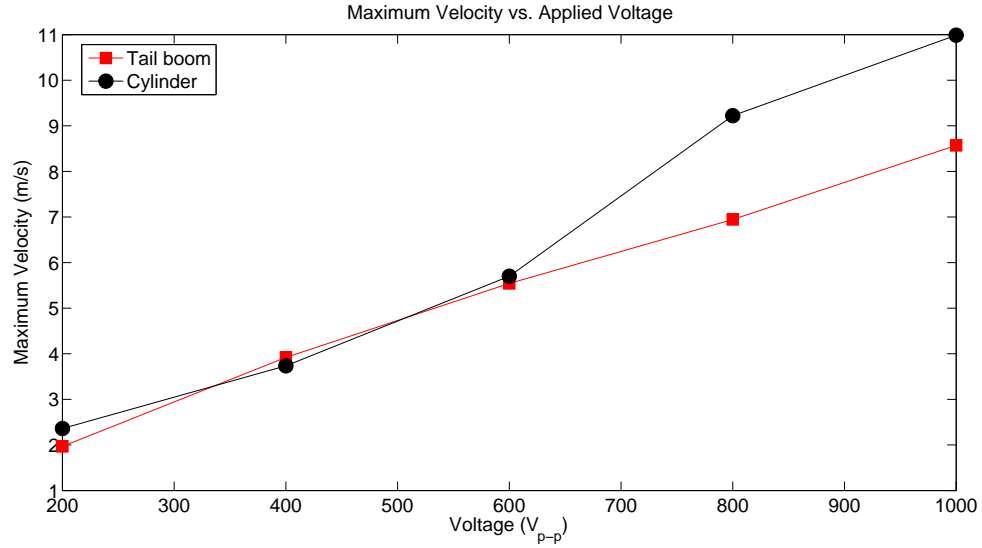
Figure 3.11: Synthetic jet velocities for each applied voltage when installed in the circular cylinder and tail boom models.

3.3.2 Plasma Actuators

The materials used for the actuator construction are two $1/4''$ strips of 2.5-mil thick copper tape and one $3/4''$ wide strip of 5.0-mil thick Kapton tape. The ends of the copper strips were rounded to prevent plasma from collecting at the corners and causing the actuators to short before reaching the maximum voltage. Figure 3.13 shows the three simple steps for constructing the actuators. The actuators are directly applied to the bluff body model by first laying a copper strip such that the upstream edge of the tape is just overlapping the desired angular position. Next, a $3/4''$ strip of Kapton tape is applied over the first strip and centered on the desired angular position. Finally, the second copper strip is placed on top of the Kapton tape so that the downstream edge just overlaps the upstream edge of the lower copper strip resulting in a small (1-mm) overlap of the upper and lower
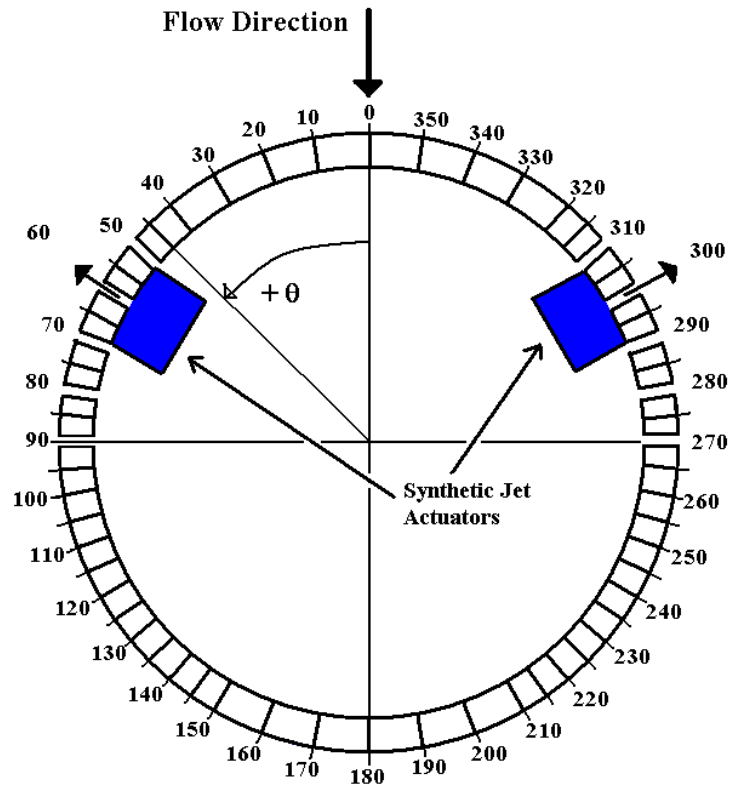
Figure 3.12: Pressure port and synthetic jet actuator angular position definitions.

electrodes. The upper electrode is wired to ground while the lower electrode is wired to the high voltage signal. A diagram showing the final configuration is illustrated in Figure 3.14. The resulting induced flow is downstream and tangential to the surface.

(a)   (b)   (c)
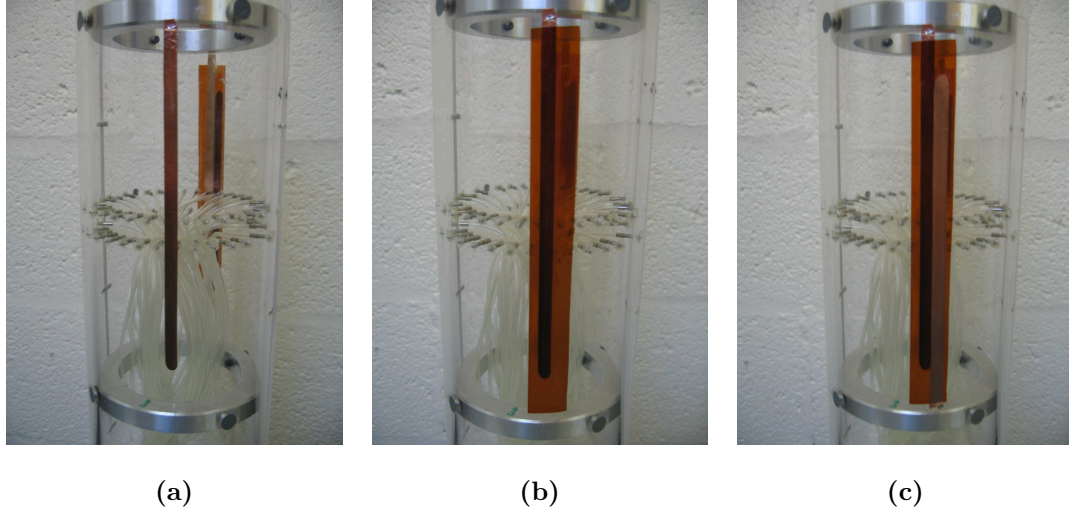
Figure 3.13: Images showing the three simple steps for constructing a plasma actuator directly on the circular cylinder model surface by a) placing the lower electrode, b) dielectric Kapton tape, and finally, c) the upper electrode.

3.3.3   Actuator Electronics

The electronic setup for the plasma actuator includes a signal generator, intermediate amplifier and step up transformer. A Wavetek Model 278 signal generator produces a continuous sine wave input to be split into two Compact Power Company Titan Series high voltage amplifiers, each with a maximum output of $260V_{rms}$ at 4Amps. Finally, each signal passes through a Corona Magnetics 1:25 turns ratio
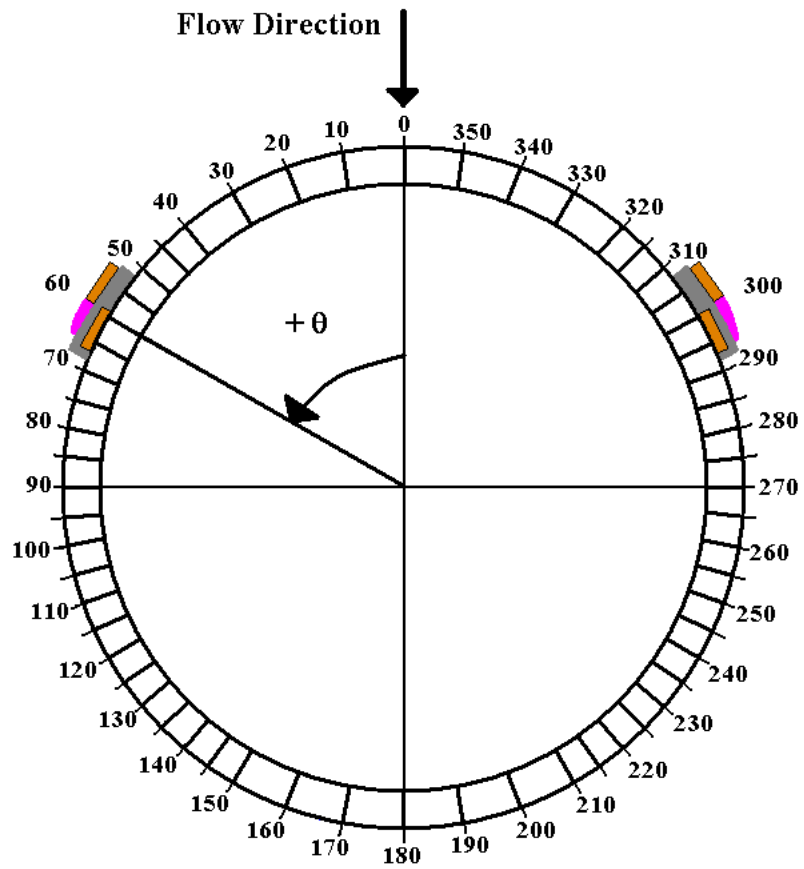
Figure 3.14: Pressure port and plasma actuator angular position definitions.

step up transformer designed to be used with signals with frequencies ranging from 400Hz to 40kHz (See Figure 3.16a). During operation, the transformers produced an audible tone at the operating frequency (5kHz for these tests).

A maximum voltage of $1000V_{p-p}$ at 5mA was used to operate the SJAs; therefore, only a waveform generator and voltage amplifier were necessary. The Wavetek signal generator produces the 95 - 105 Hz continuous sine wave and the signal is passed to a Trek Model 609E-6 high-voltage DC-stable power amplifier and then to the actuators (See Figure 3.15a).

For both actuator setups, the applied voltage and current drawn from the actuators was read and recorded using a LeCroy 9100 Series Oscilloscope. The voltage was run through a 1/1000 voltage divider before reaching the oscilloscope. An example of the signal for the applied voltage and current across the synthetic jet and plasma actuators are shown in Figures 3.15b and 3.16b, respectively. The current was read by passing the signal through a current transformer. Neither actuator was tested for endurance but the lifespan of the actuators exceeded the requirements of this testing unless the applied voltage exceeded the recommended maximum. A new pair of plasma actuators was constructed for each angular position and operated for a maximum of 10 minutes each. The same synthetic jets were used for all of the tests and were operated for a maximum of several hours.

(a)

(b)
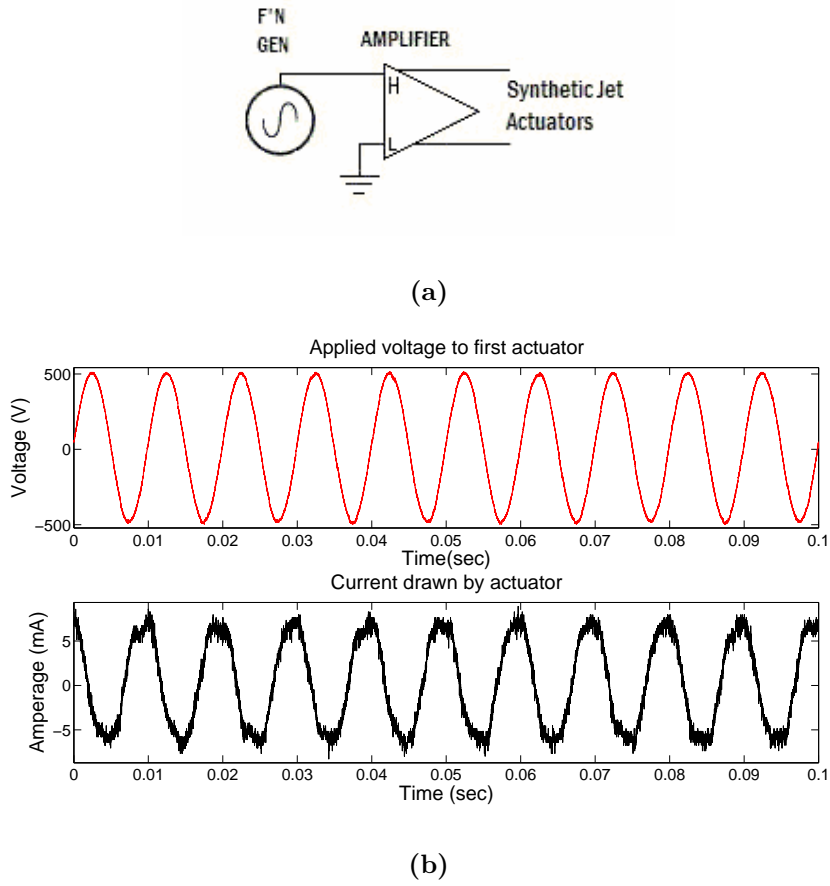
Figure 3.15: Actuator electronic setup for a) synthetic jet actuators and b) the

voltage and current signals for actuation at $1000V_{p-p}$ (0.7 Watts).

3.4   Test Matrix

The goal of this thesis research is to observe the effectiveness of the plasma

and synthetic jet actuators as certain parameters were varied. Test conditions were

selected to observe the effect of varying Re, angular position of the actuators, volt-

age applied, bluff body shape, number of working actuators and actuator type. The

two bluff body shapes were tested to see if results from the circular cylinder could

be extrapolated to other bluff body shapes, such as the tail boom shape. Three

(a)

(b)
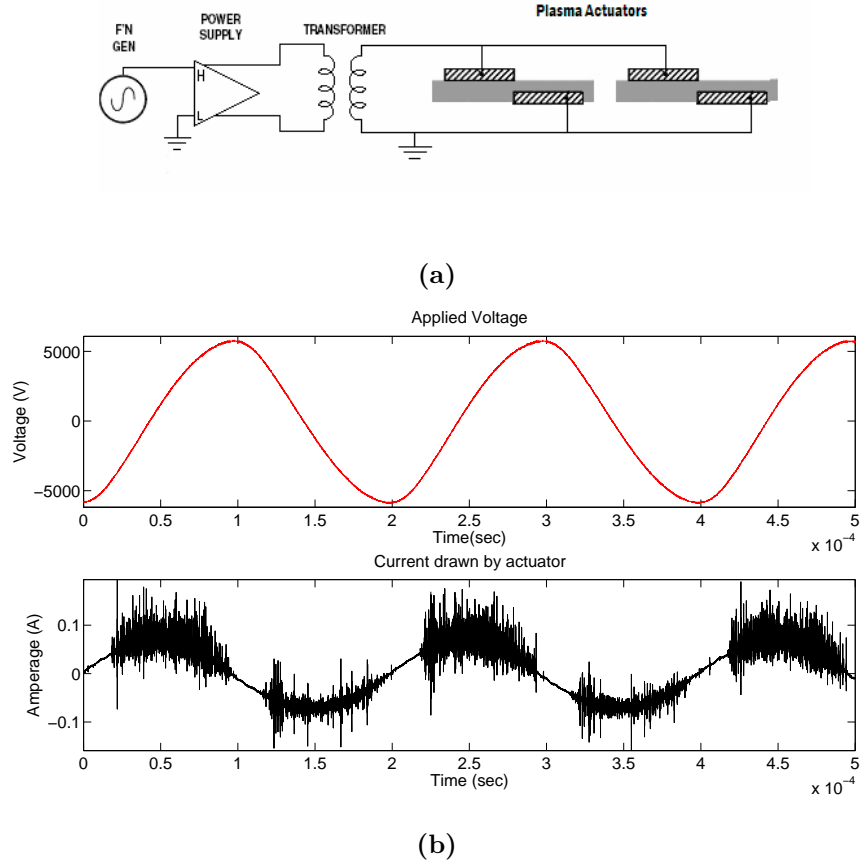
Figure 3.16: Actuator electronic setup for a) plasma actuators and b) the voltage and current signals for the plasma actuators at $11kV_{p-p}$ (1.34 Watts).

freestream velocities were used, corresponding to Reynolds Numbers of 2.48×10^4, 4.8×10^4 and 7.3×10^4 and flow separation angles of $\pm100°$, $\pm95°$ and $\pm85°$, respectively. On the circular cylinder, the angular position of the actuators in the single actuator case was varied at increments of $10°$ from $50°$ to $90°$. The angular position of the two actuators case was varied at increments of $10°$ from $\pm50°$ to $\pm90°$. On the tail boom model, the same Reynolds numbers were used and they correspond to flow velocities of 7.3 ft/s, 14.6 ft/s and 22.2 ft/s and flow separation

Pressure Port Locations			
Side 1	Side 2	x/c	Angle
13	38	0.4271	59.1°
15	40	0.4925	70.1°
17	42	0.5627	81.1°
19	44	0.6350	92.1°
21	46	0.7069	103.1°

Table 3.1: Pressure Port and corresponding x/c values for the actuator locations on the tail boom model.

at $(x/c)_s$ locations 0.67, 0.67 and 0.74, respectively. Actuator placement locations were chosen such that, at most, four locations were upstream of the separation point and at least one location downstream of the separation point. The port locations and corresponding $(x/c)_s$ values are shown in Table 3.1.

Voltage variations depended on the voltage requirements and limitations of each device. The synthetic jets were operated at the SJA resonance frequency of 95 - 105 Hz (depending on slight variations in actuator construction) and at voltages between $200V_{p-p}$ and $1000V_{p-p}$ at $200V_{p-p}$ increments. Plasma discharge occurs above voltages of $2.8kV_{p-p}$; therefore, the applied voltage varied at increments of $1.4kV_{p-p}$ from $2.8kV_{p-p}$ to $11.8kV_{p-p}$. Beyond $11.8kV_{p-p}$, the Kapton tape (dielectric) breaks down and the actuator shorts for this design (Figure 3.17). A summary of the test matrix parameters is given in Table 3.2. Each device provided noteworthy results that are described in Chapters 4, 5 and 6.

Test Matrix		
Parameter	DF	Parameter Values
Bluff Body Shape	2	Circular Cylinder, Tail Boom Model
Actuator Type	2	Synthetic Jet and Plasma Actuator
Reynolds Number	3	2.4×10^4, 4.8×10^4, 7.3×10^4
Actuator Location (Cylinder) (θ_a)	5	50, 60, 70, 80, 90
Actuator Location (Tail Boom) ($(x/c)_a$)	5	0.43, 0.49, 0.56, 0.64, 0.71
SJA Voltage (V_{p-p})	5	200, 400, 600, 800, 1000
Plasma Actuator Voltage (kV_{p-p})	7	2.8, 4.3, 5.8, 7.3, 8.8, 10.3, 11.8

Table 3.2: Test matrix parameters, degrees of freedom and the parameter values.

Figure 3.17: When the applied voltage is above 11.8kV_{p-p}, the dielectric breaks down and the actuators short burning through the dielectric tape and the copper tape for the upper electrode disintegrates. The top example is at a later stage in the breakdown than the lower example.

3.5 Data Processing and Error Analysis

All data post processing was performed using MATLAB and the statistical analysis of the results was performed using Statistical Analysis Software (SAS). Each pressure distribution plot presented in the results chapters of this thesis is a time-averaged mean distribution of more than 20 iterations of the instantaneous pressure distribution. For the coefficient of pressure, the differential pressure values from the ESP system are normalized by the dynamic pressure, q. The standard deviation of the coefficient of pressure is evaluated for each pressure port location. In addition, the pressure port locations were assigned an error of $\pm 1°$ due to variability associated with port placement during the manufacturing process. If there are blocked pressure ports (as is the case for the installed actuator pressure distributions), the experimental data points corresponding to these pressure ports are replaced by interpolated points calculated by the cubic spline interpolation method. Figure 3.18 shows the pressure distribution with the calculated error bars for the pressure distribution values and pressure port locations. For the interpolated data, no error bars are shown because they are not experimental values. The data presented in the remainder of the thesis will not include the error bars to make the plots easier to read. However, the collection of pressure distribution plots in Appendix A includes error bars on all data plots.

The coefficient of pressure drag was calculated using the relationships described in Equations 3.1 and 3.2. Equation 3.2 is based on the Trapezoidal Rule for integrating the drag distribution to find the total pressure drag coefficient. For
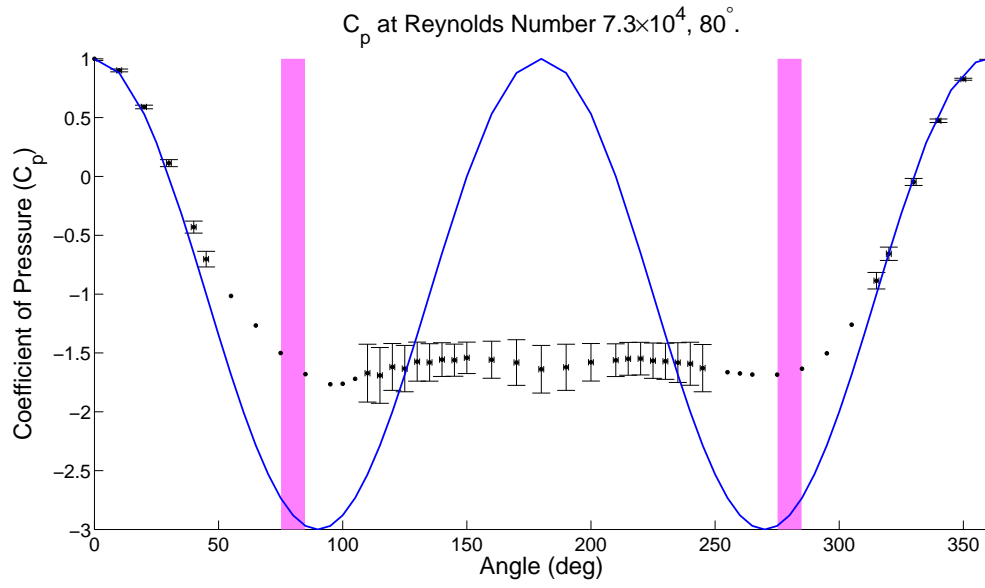
Figure 3.18: A sample plot of the pressure distribution with the standard deviation for the coefficient of pressure values (vertical error bars) and the pressure port locations (horizontal error bars). The points about the actuator location (solid magenta band) without error bars are interpolated.

each case in the test matrix, the coefficient of drag was calculated for four replications using a resampling method called "bootstrapping" used for statistical analysis. Eight of the instantaneous pressure distributions were selected randomly to calculate a pressure drag coefficient and percentage of pressure drag reduction four times. These results were evaluated using a 3-way factorial design method. The main effect of each of the three parameters (actuator position, freestream velocity and applied voltage) were evaluated, then interaction effects between all combinations of two parameters and, finally, the interaction effects between all three parameters. Using SAS, interactions between each test case, a mean percentage of pressure drag reduction value and an analysis of variance (ANOVA) table were returned. The goal of using an ANOVA table is evaluate the probability that the means are similar or unique results. There is one ANOVA table for each bluff body model and actuator combination (4 combinations). An example ANOVA table is shown in Table 3.3.

$$C_d(\theta) = C_p(\theta)cos(\theta) \tag{3.1}$$

$$C_D = \int_0^{2\pi} C_p cos(\theta)d\theta \approx \frac{1}{2}\sum_{i=1}^{n}[(C_d(i+1) + C_d(i))(\theta(i+1) + \theta(i))] \tag{3.2}$$

In the first column of the ANOVA table, the parameters evaluated are listed for the following main and interaction effects. The second column lists the degrees of freedom for each effect. The second column is the Type I SS (Sum of Squares), as opposed to Type III SS because this experiment is balanced (i.e. no missing data) and the third column is the Mean Square. The second and third columns are

60

ANOVA Table					
Source	DF	Type I SS	Mean Square	F Value	Pr > F
Position	4	11166.27010	2791.56753	1590.71	<.0001
Voltage	4	15481.04595	3870.26149	2205.38	<.0001
Velocity	2	3370.77903	1685.38952	960.38	<.0001
Position*Voltage	16	1660.35593	103.77225	59.13	<.0001
Position*Velocity	8	3394.87112	424.35889	241.81	<.0001
Voltage*Velocity	8	955.29778	119.41222	68.04	<.0001
Position*Voltage*Velocity	32	3626.98877	113.34340	64.59	<.0001

Table 3.3: Sample analysis of variance (ANOVA) Table.

used to compute the fourth column, F = SS/MS. F shows how strong the variations in the pressure drag reduction are compared to the experimental error, therefore, large F values are good. The last column show the probability that the variations in the results are a due to background experimental error. This number ranges from 0.0001 to 1. If Pr>F is 0.0001, the variations are unique and independent of the background experimental error. As Pr>F increases, this indicates that there is a higher probability that the results are similar and any variation is within the bounds of experimental error.

As mentioned, a result of running the three-way factorial design analysis is the mean square error (MSE) which can be used to find a confidence interval as shown in Equations 3.3 and 3.4.

$$CI_{99\%} = 3\sqrt{\frac{MSE}{N}} \tag{3.3}$$

$$CI_{95\%} = 2\sqrt{\frac{MSE}{N}} \tag{3.4}$$

The 99% and 95% subscripts indicate that the confidence interval represents 99% and 95% confidence that the mean value that would be obtained from a series of measured results lies within that range of $\pm CI$, respectively. Figure 3.19 shows an example of how the confidence intervals are used. The four data points represent the four repetitions for calculating the percentage of pressure drag reduction. The solid triangles represent the means of those four data points. The solid line is a quadratic polynomial fit of the mean values. The dashed lines above and below the mean line are the bounds for 99% confidence interval.

Based on the pressure drag reduction results in the test matrix, one consideration addressed in the post processing is that the changing Re affected the location of the flow separation point. The approach taken to normalize results associated with different separation angle locations was to identify a non-dimensional surface distance parameter, SD. SD is the surface distance between the flow separation point (θ_s) and the actuator location (θ_a) normalized by the surface distance from 0° to the flow separation point. For the circular cylinder, SD_c (c subscript for "cylinder") is calculated in Equation 3.5.

$$SD_c = \frac{\theta_s(\pi D \setminus 360°) - \theta_a(\pi D \setminus 360°)}{\theta_s(\pi D \setminus 360°)} \tag{3.5}$$
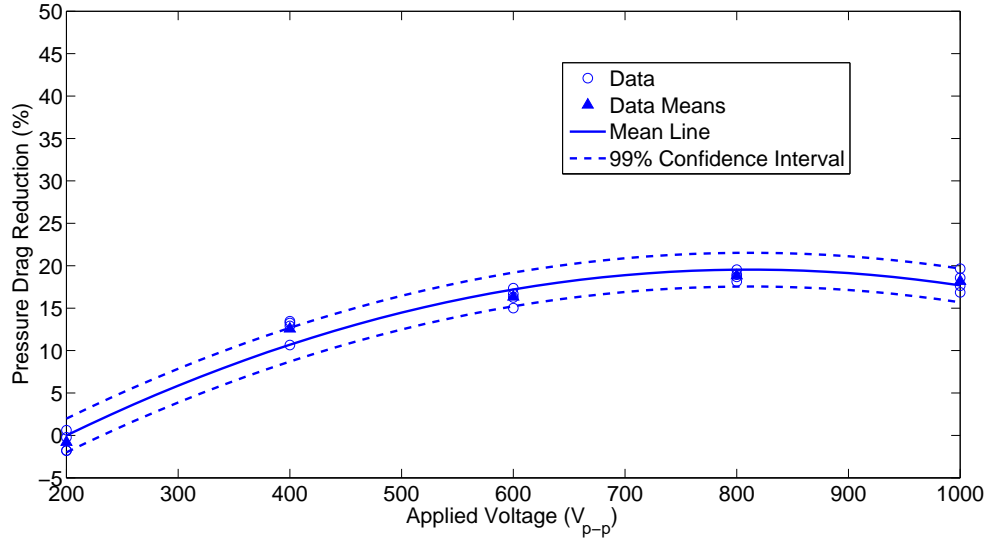
Figure 3.19: Sample figure illustrating the use of confidence intervals for a variation in the percentage of pressure drag reduction as the applied voltage increases.

The angle is converted to surface distance by $(\pi D \setminus 360°)$, the total circumference, where D is the cylinder diameter, but this quantity cancels out resulting in Equation 3.6.

$$SD_c = \frac{\theta_s - \theta_a}{\theta_s} \tag{3.6}$$

For the tail boom model, the total surface length of the model is found knowing that the front radius (r_s) is $0.862''$ (22mm) and is circular up to $73°$ (θ_1), the rear radius(r) is $2.25''$ (57mm) and is circular up to $148.43°$ (θ_2), and the chord length of the tail boom (c) is $5.95''$ (151mm) (as illustrated in Figure 3.20 and Equations 3.7 - 3.10).

$$l_1 = \theta_1 \left(\frac{2\pi r_s}{360} \right) = 1.10'' = 28mm \tag{3.7}$$

$$l_2 = \sqrt{[r \sin \theta_2 - r_s \sin \theta_1]^2 + [(c - r(1 + \cos \theta_2)) - (r_s(1 + \cos(180 - \theta_1)))]^2} \tag{3.8}$$

$$l_2 = 1.23'' = 31mm \tag{3.9}$$

$$l_3 = \theta_2 \left(\frac{2\pi r}{360} \right) = 5.83'' = 148mm \tag{3.10}$$

For calculating the surface length to the actuator location and flow separation point, θ_2 is the angular location of each port on the rear portion of the tail boom model. To distinguish between the two values, the angular position of the actuators is defined as θ_{ta} and the angular position of the separation point is θ_{ts}. Since the actuator position and flow separation points are always on the rear cylindrical half of the tail boom model, the surface distance on the first half is a constant value and $l_1 + l_2 = 2.23'' = l_f$. By algebraic manipulation, the non-dimensional distance (SD_{TB}, TB subscript for "tail boom") for the tail boom model can be simplified into Equation 3.11.

$$SD_{TB} = \frac{\theta_{ts} - \theta_{ta}}{\frac{180}{\pi r} l_f + \theta_{ts}} \tag{3.11}$$
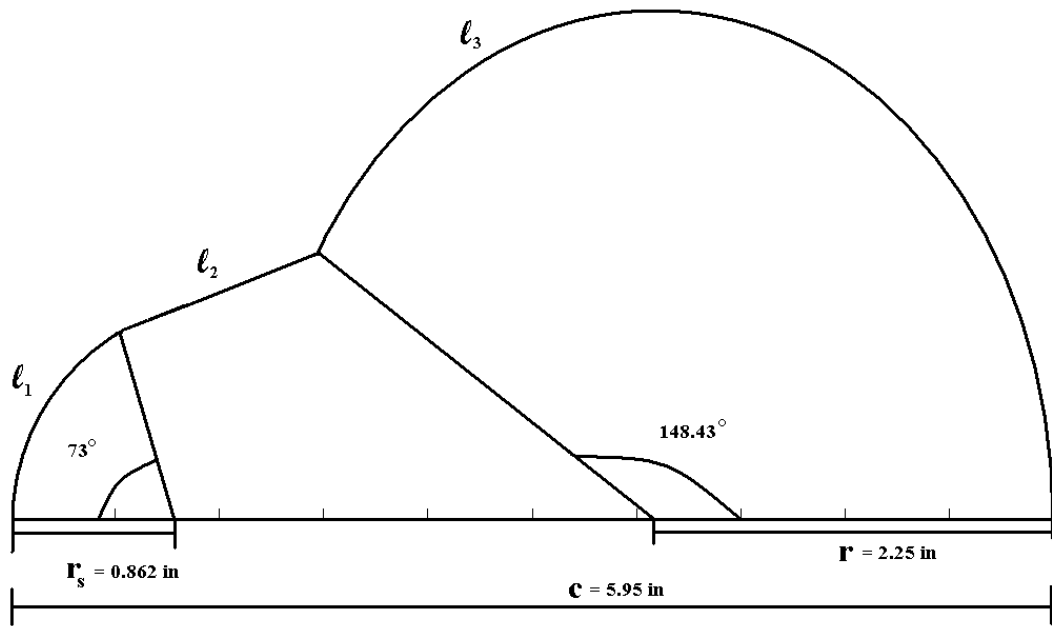
Figure 3.20: Illustration of the geometric variables used to calculate the surface length corresponding to actuator location and the flow separation point.

3.6 Addition Notes and Lessons Learned

During the course of taking the experimental data, there were a few issues that would have further improved the quality of the data acquired if they were addressed from the beginning of the experimentation. The most significant problem was with the asymmetries between the actuators. Because the goal of this research was to reduce pressure drag, two individual actuators were used on opposite sides of the bluff body shapes. It was very difficult to construct two identical actuators. The plasma actuator construction involved cutting 1″ wide pieces of tape (copper or Kapton) to the appropriate size but the processes for measuring and cutting were not precise. Also, when applying the tape pieces to the models, their alignment with the length of the model and for the overlap between the upper and lower electrodes was based on an "eyeball" approximation along with . Slight differences in the actuator construction could have resulted in the asymmetries as shown in Figure 3.21. To solve this problem, an actuator design should have been sent to an electronics company for consistent construction with the proper geometric sizing and electrode alignment. Also, the angular position of the actuators was based on the location of the pressure ports and because the actual position of the ports varied by a degree or two, so did the actuator position. As shown in the results, this could easily result in further asymmetries in the pressure distributions.

The synthetic jet data also showed unexpected asymmetries in the pressure distribution data which could have been a result of inconsistencies in the actuator construction and the physical alignment of the model and actuator lid slots. The
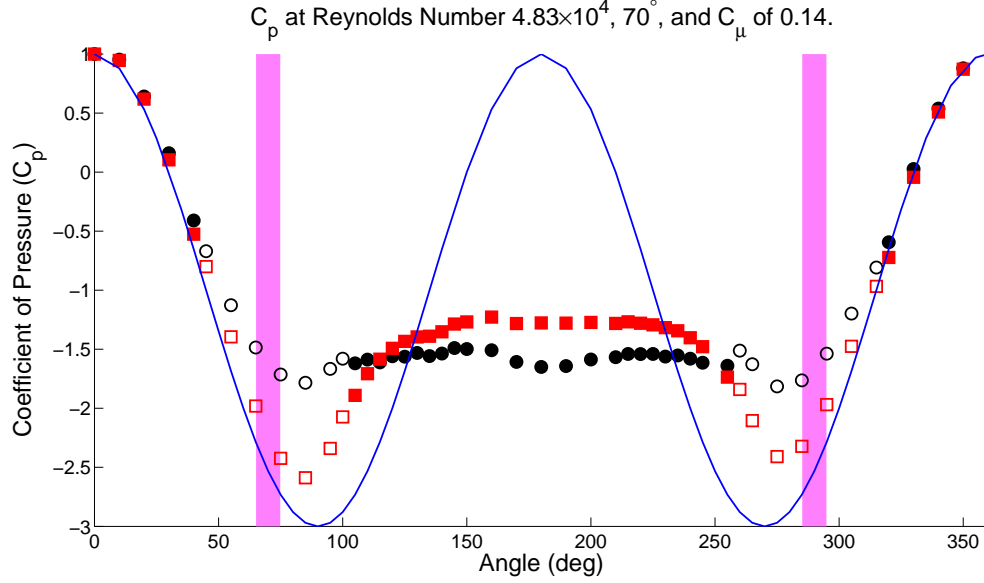
Figure 3.21: Asymmetries in the pressure distribution are caused by small difference in the position and actuator construction.

actuator design included many parts and there was a lot of room for variations in construction. In fact, there was a slight variation in the resonance frequency (95-105 Hz) of the actuators which could only be a result of construction related differences. This resulted in a reduced maximum velocity from the slot of one actuator or a change in the phase of actuator response in relation to each other when excited at 95 Hz and, hence, the interaction between the synthetic jet and the external flow were not the same.

The installation of the actuators blocked the pressure ports near the actuators preventing a full evaluation of the pressure distribution and resulting pressure drag coefficient. One suggestion is to use SLA construction to allow the pressure port tubing to be carried through the wall of the models. This method would allow all pressure ports near an installed SJA to be measured. Another possible solution is to
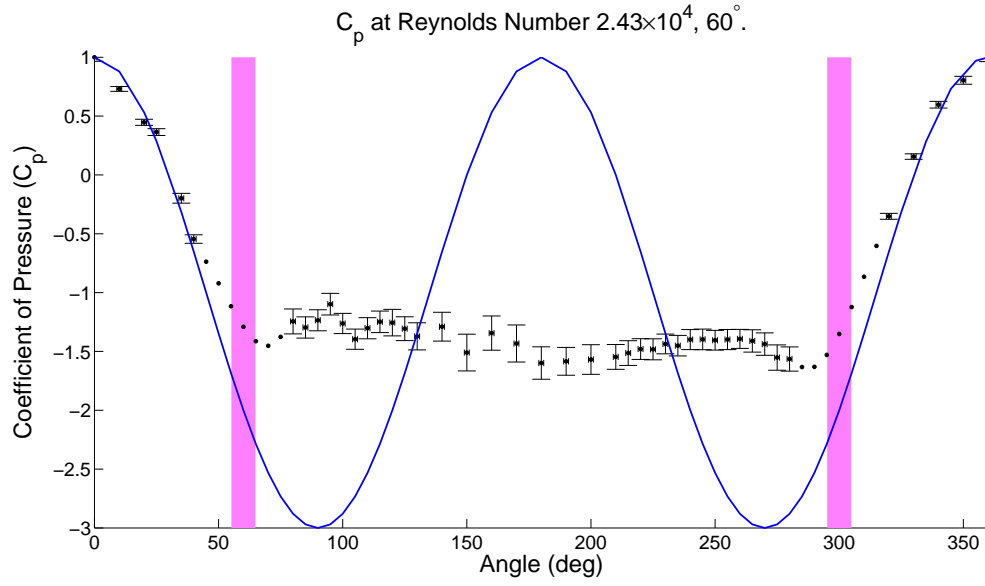
Figure 3.22: This pressure distribution at 10 ft/s shows the irregularity of the pressure measurements for the angles between 0° and 180° as compared to the measurements for 180° to 360°.

measure the pressure distribution on the wind tunnel walls rather than the surface of the model.

At low flow velocities, one of the modules in the ESP system used to measure the pressure distribution returned irregular data (See Figure 3.22) due to the failure of the ESP system to correctly calibrate the module. At higher velocities, this irregularity was reduced (eliminated in most cases) because the pressure coefficient (C_p) is the pressure differential divided by the dynamic pressure which increases by the velocity squared. The increase in velocity would reduce the irregularity in the pressure distribution. The irregular data has led to calculating the percentage of drag reduction based on the half of the cylinder surface from 180° to 360°.

Before testing the synthetic jet actuators in the circular cylinder model, the

baseline flow around the cylinder was observed. Based on the separation angle and the pressure in the separated flow region, the flow was turbulent. At first, it was thought that the size of the actuator slots were tripping the flow and the size of the slot was reduced to a width that was used by other researchers. However, the flow was still turbulent. During testing, a whistling noise was coming from the model and it turned out that flow was coming from the room (higher pressure) into the test section through the bottom opening of the model and out of the slots into the test section (lower pressure). This flow out of the slots was similar to constant blowing which has been used in experiments to transition the boundary layer to turbulent flow for active flow control. Once the bottom of the model was sealed, the baseline flow resembled laminar flow conditions. This problem was specific to the synthetic jet actuator design because the cavity is not sealed like most other actuator designs.
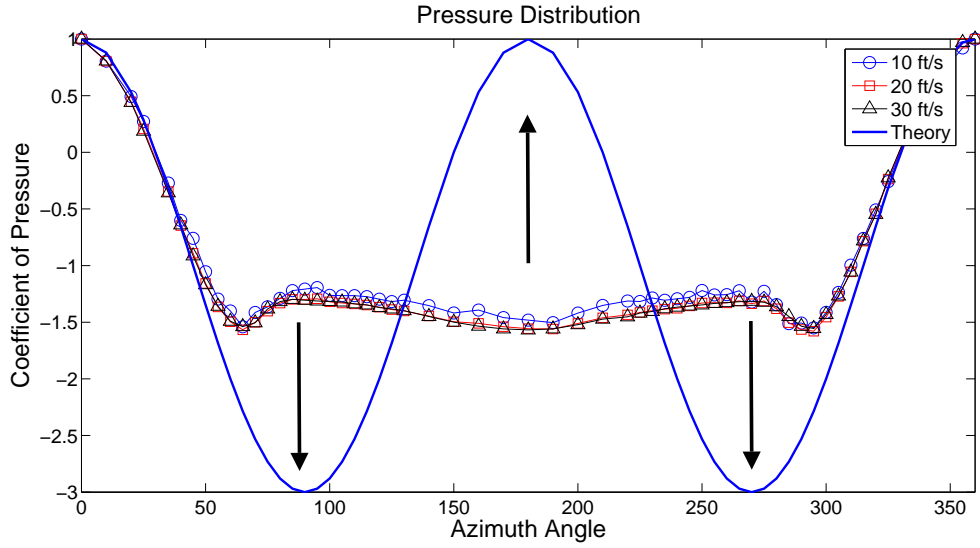
Chapter 4

Synthetic Jet Actuator Test Results on a Circular Cylinder

For this research, active flow control actuators are being used to reduce pressure drag by changing the time-averaged pressure distribution such that it approaches the inviscid theoretical pressure distribution solution. The arrows in Figure 4.1 show the directions needed for favorable changes in pressure profiles obtained for flow over the cylinder with no flow control for the three Re flows studied. Also, the location of the onset of flow separation, which is evident from the pressure distribution as the location at which a plateau in the pressure profile first occurs, is expected to shift downstream as indicated in Figure 4.2.

Pressure distribution plots for every case in the test matrix are in Appendix A but specific plots were chosen to illustrate the effects of varying each of the following parameters: applied voltage, actuator position and freestream velocity (Re). Variations in these parameters result in variations in the coefficient of momentum (C_μ) and the distance between the actuator position, θ_a, and the flow separation point, θ_s (SD_c).

To illustrate the unique effect of a synthetic jet actuator, a single case pressure distribution plot (Figure 4.3) shows the inviscid theoretical pressure distribution (solid line) and the distribution with the actuators on (red squares) and the baseline pressure distribution (black circles). The hollow data points indicate interpolated

Figure 4.1: The black arrows show the desired trends in the pressure distribution for delaying flow separation and reducing pressure drag for 10, 20 and 30 ft/s (Re $= 2.4 \times 10^4$, 4.8×10^4 and 7.3×10^4).

data to provide a continuous approximation of the pressure distribution where the actuators blocked the pressure ports. The shaded bands (magenta) on the plots indicate the location of the working actuator(s).

In Figure 4.3, the effect of two actuators on the pressure distribution around a circular cylinder is shown where Re $= 4.8 \times 10^4$ ($U_\infty = 20$ ft/s and onset of flow separation is at 95°), the actuators are at ±80° and the applied voltage is 1000 V_{p-p}. The first noticeable change in the pressure distribution is the decrease in pressure upstream and downstream of the location of the actuators. This shows that the actuators successfully add energy to the boundary layer such that the boundary layer is stable over more of the cylinder surface and flow separation is delayed. The circled portions of the pressure distribution show that the flow separation point
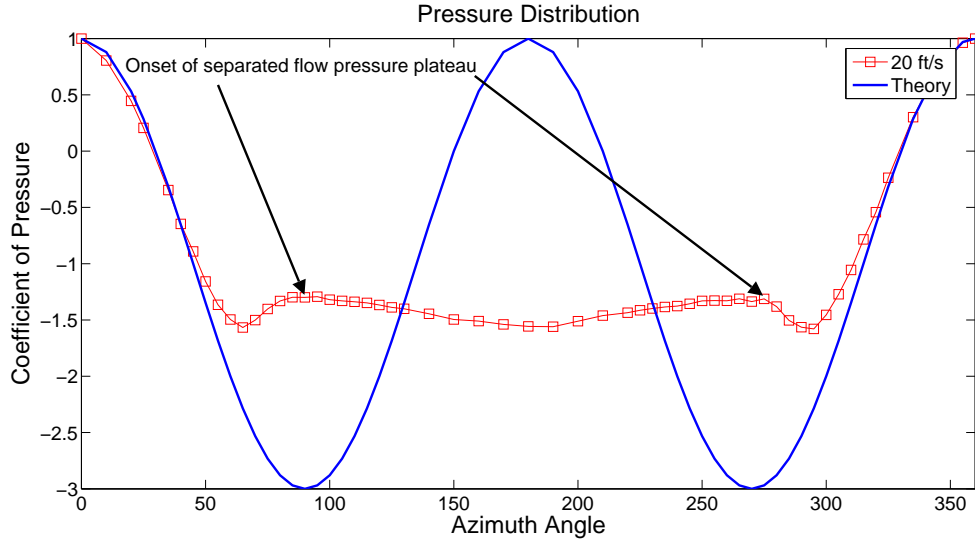
Figure 4.2: The black arrows show the location of the flow separation point for
Re $= 4.8 \times 10^4$ (20 ft/s) at $85°$ corresponding to when the pressure
distribution levels off over the rear half of the cylinder.

moves downstream by $70°$. Also noteworthy, the pressure in the separated flow
region on the rear half of the cylinder increases, which is important for the reduction
in pressure drag because the direction of the resulting force opposes the drag force.
These two changes in the pressure distribution, when compared to the baseline
case, are desirable trends resulting in a shift toward the inviscid theoretical pressure
distribution case and a reduction in the pressure drag.

During testing, one actuator failed because the voltage supplied to the actuator
exceeded the maximum allowable voltage. This led to testing the effect of one
working actuator on the circular cylinder. Interestingly, for some actuator angular
positions, the single actuator was able to produce almost symmetric changes in
the pressure distribution with comparable effectiveness as two actuators as shown

72
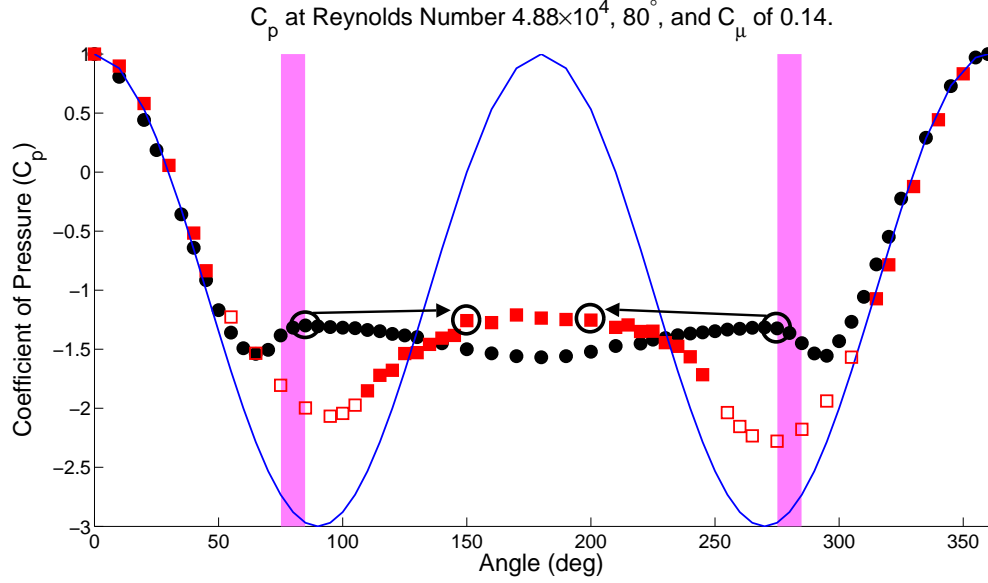
Figure 4.3: Pressure distribution showing the effect of two synthetic jet actuators placed at $\pm 80°$ and with an applied voltage of 1000 V_{p-p} and Re = 4.8×10^4 ($U_\infty = 20$ ft/s and $SD_c = 0.16$).

in Figure 4.4. For the same flow and actuation conditions as in Figure 4.3, the pressure decreases at the location of the actuator and also on the other side of the cylinder as well as increasing the pressure in the separated flow region. Similar results were also reported in a paper by Amitay [6] and they suggested the cause was suction forces from the actuated side pulling the streamlines on the opposite side of the cylinder closer to the surface. Therefore, both sides of the cylinder had a delay in flow separation.

The following sections will illustrate the changes in the pressure distribution when the following parameters are varied: the applied voltage, position of the actuator on the cylinder, and freestream Reynolds number. Each case will show a waterfall plot of the pressure distributions and also a plot to show the percentage of
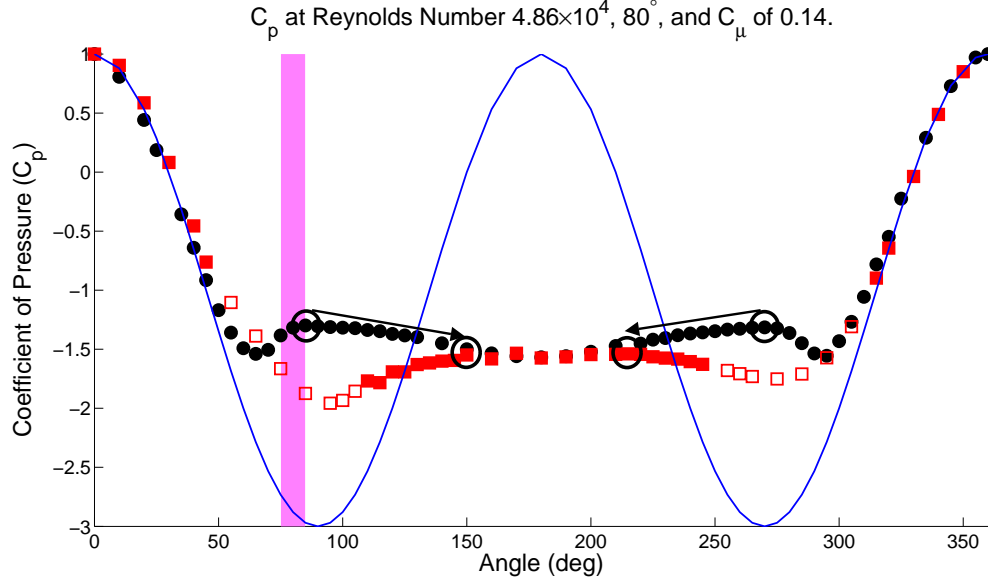
Figure 4.4: Pressure distribution showing the effect of one synthetic jet actuator placed at $+80°$ and with an applied voltage of 1000 V_{p-p} and Re $= 4.8 \times 10^4$ ($U_\infty = 20$ ft/s and $SD_c = 0.16$).

pressure drag reduction compared to the baseline case with no actuators installed as each parameter changes. The ANOVA table for the synthetic jet actuators on the circular cylinder is given in Table 4.1. The mean square error used to compute the confidence interval is 1.75.

4.1   Variation with Applied Voltage

Figure 4.5 shows the variation in the pressure distribution as the maximum applied voltage is increased from $200V_{p-p}$ to $1000V_{p-p}$. Reynolds Number is 7.3×10^4 ($U_\infty = 30$ ft/s and flow separation onset at $85°$) and the actuator location is $\pm 60°$ ($SD_c = 0.29$). At the lowest applied voltage, the pressure distribution is very similar to the baseline case. As the voltage is increased, two significant changes occur: the

ANOVA Table					
Source	DF	Type I SS	Mean Square	F Value	Pr > F
Position	4	11166.27010	2791.56753	1590.71	<.0001
Voltage	4	15481.04595	3870.26149	2205.38	<.0001
Velocity	2	3370.77903	1685.38952	960.38	<.0001
Position*Voltage	16	1660.35593	103.77225	59.13	<.0001
Position*Velocity	8	3394.87112	424.35889	241.81	<.0001
Voltage*Velocity	8	955.29778	119.41222	68.04	<.0001
Position*Voltage*Velocity	32	3626.98877	113.34340	64.59	<.0001

Table 4.1: ANOVA Table for synthetic jet actuators on the circular cylinder.

pressure in the separated region increases and the pressure at the actuator locations decreases. As stated before, both of these changes are desirable.

Figure 4.6 shows the variation in the percentage drop in pressure drag as the applied voltage is increased. The combination of increased pressure in the separated flow region and decreased pressure near the actuators, as seen in Figure 4.5, results in an almost linear increase in pressure drag reduction as the applied voltage increases to $600V_{p-p}$ after which it appears to be approaching a constant value.

The increase in voltage is similar to increasing C_{μ} and these results suggest that the highest C_{μ} achievable by the actuators will produce the most reduction in pressure drag. However, based on Amitay [6], there is a maximum achievable influence, above which increasing C_{μ} or the applied voltage does not provide any additional performance benefit. Figure 4.7 shows the change in the pressure dis-
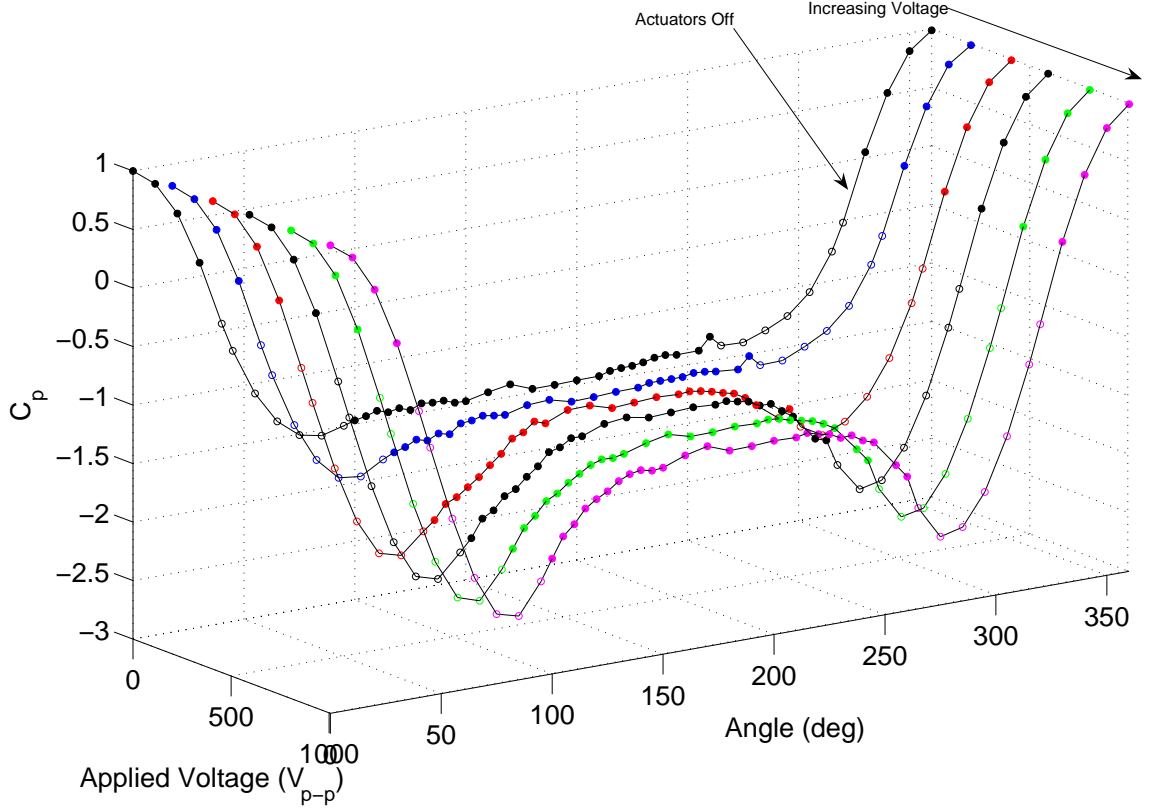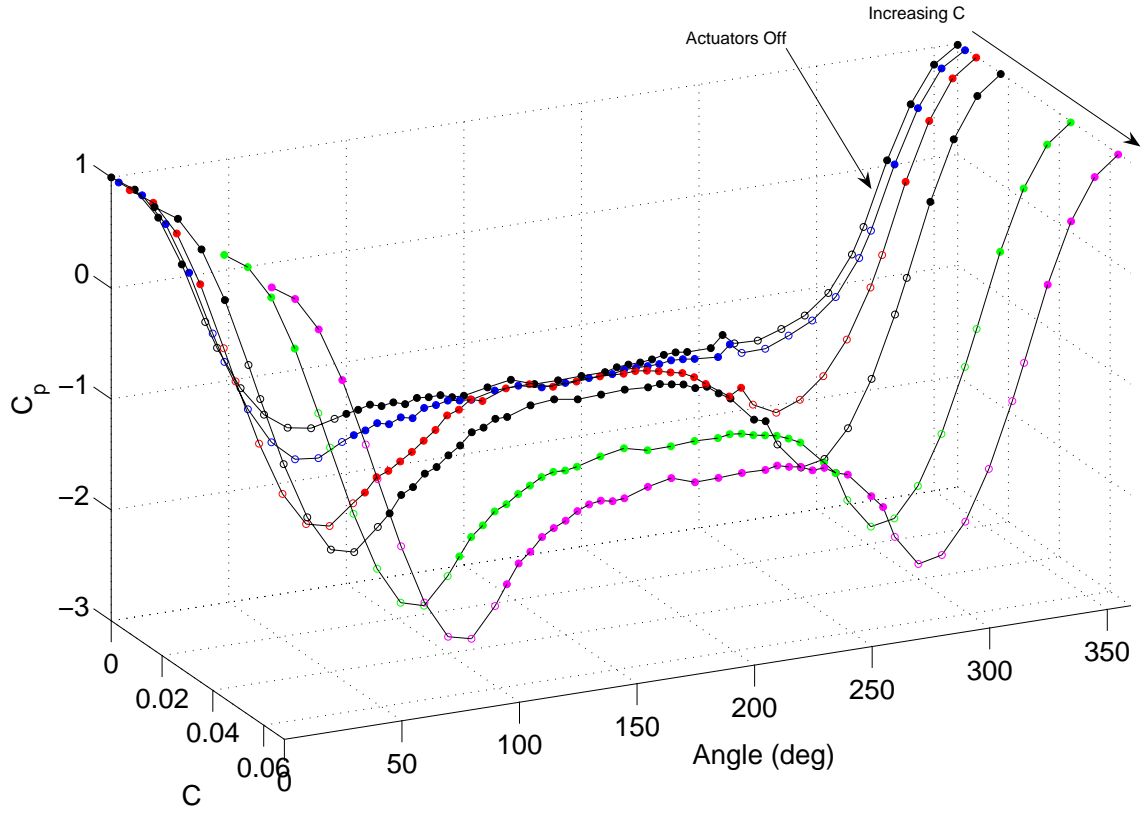
Figure 4.5: Waterfall plot of the variation in the pressure distribution as the maximum applied voltage is increased from 200 V_{p-p} to 1000 V_{p-p}. (Re $= 7.3 \times 10^4$, $U_\infty = 30$ ft/s, $\theta_s = 85°$, $\theta_a = \pm 60°$, $SD_c = 0.29$)

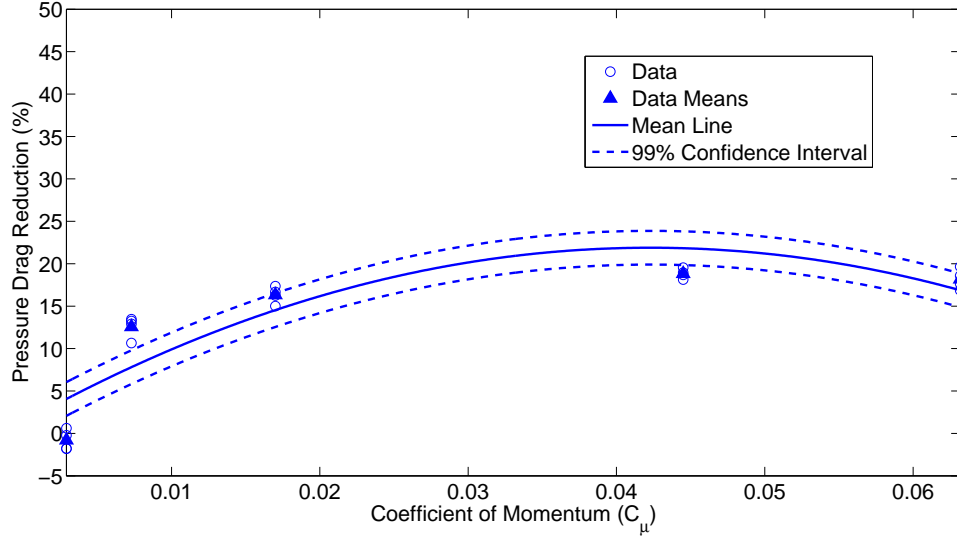tribution as C_μ increases from 0.003 to 0.063. There is a significant change in the pressure distribution for a small change in C_μ and very little change as C_μ continues to increase over an order of magnitude.

The change in the percentage of pressure drag reduction reflects the same trend in Figure 4.8. There is a rapid increase in pressure drag reduction for small changes in C_μ and very gradual increase in pressure drag reduction as C_μ continues to increase.
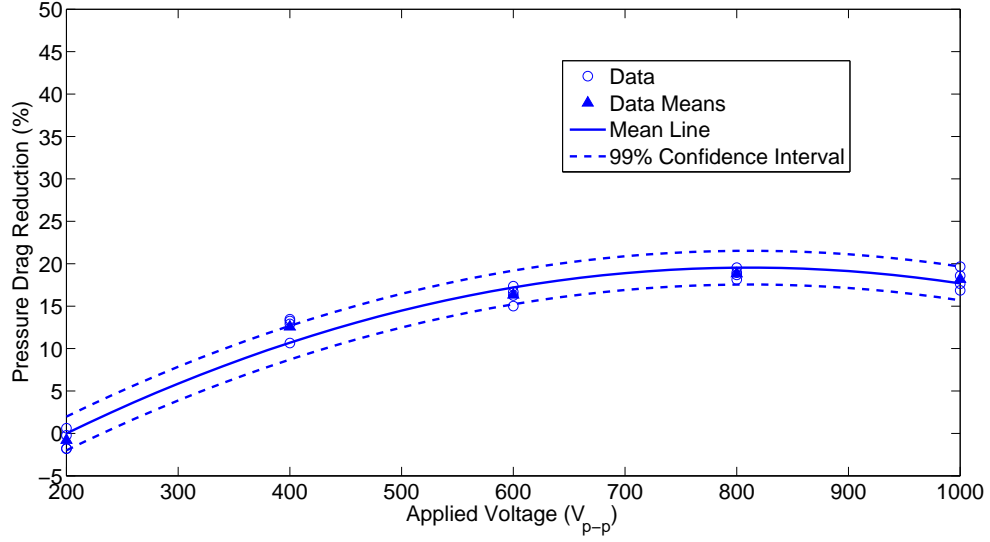
Figure 4.6: Variation in the percentage of pressure drag reduction as the maximum applied voltage is increased from 200 V_{p-p} to 1000 V_{p-p}. (Re = 7.3×10^4, $U_\infty = 30$ ft/s, $\theta_s = 85°$, $\theta_a = \pm60°$, $SD_c = 0.29$)

4.2   Variation with Reynolds Number

The Reynolds number for these tests were $Re = 2.4 \times 10^4$, 4.8×10^4 and 7.3×10^4 corresponding to freestream velocities of 10, 20 and 30 ft/s, respectively. The locations corresponding to the onset of separated flow at these Re were 100°, 95° and 85°, respectively. Because the actuators add a fixed amount of energy to the flow for a given applied voltage, increasing the freestream velocity (comparable to decreasing C_μ) should reduce the apparent effectiveness of the actuators.

Figure 4.9 shows the change in the pressure distribution as velocity is increased. The actuator position is $\pm80°$ and the applied voltage is $1000V_{p-p}$. As the velocity increases, the pressure near the location of the actuators is at a minimum for the 20 ft/s case. The maximum pressure in the separated flow region remains relatively

77

Figure 4.7: Waterfall plot of the variation in the pressure distribution as the coefficient of momentum (C_μ) increases from 0.003 to 0.063. (Re = 7.3×10^4, $U_\infty = 30$ ft/s, $\theta_s = 85°$, $\theta_a = \pm 60°$, $SD_c = 0.29$)

Figure 4.8: Variation in the percentage of pressure drag reduction as the coefficient of momentum (C_μ) increases from 0.003 to 0.063. (Re $=$ 7.3×10^4, $U_\infty = 30$ ft/s, $\theta_s = 85°$, $\theta_a = \pm 60°$, $SD_c = 0.29$)

constant but the flow separation point moves downstream slightly. Despite the increasing velocity, the actuators do not show the expected decreased affect on the pressure distribution.

Figure 4.10 shows the variation in the percentage of drag reduction as velocity increases. An increase in effectiveness from Re $= 2.4 \times 10^4$ to 4.8×10^4 and a slight decrease in effectiveness from 4.8×10^4 to 7.3×10^4 fail to show that the effectiveness of the actuator decreases with increased velocity. The discrepancy can be explained by examining the relative magnitude of the influence of the variation in flow velocity compared to the influence of the variation in angular position relative to the flow separation point. As is discussed in Section 4.3, the latter influence, in fact, appears to be the larger of the two.
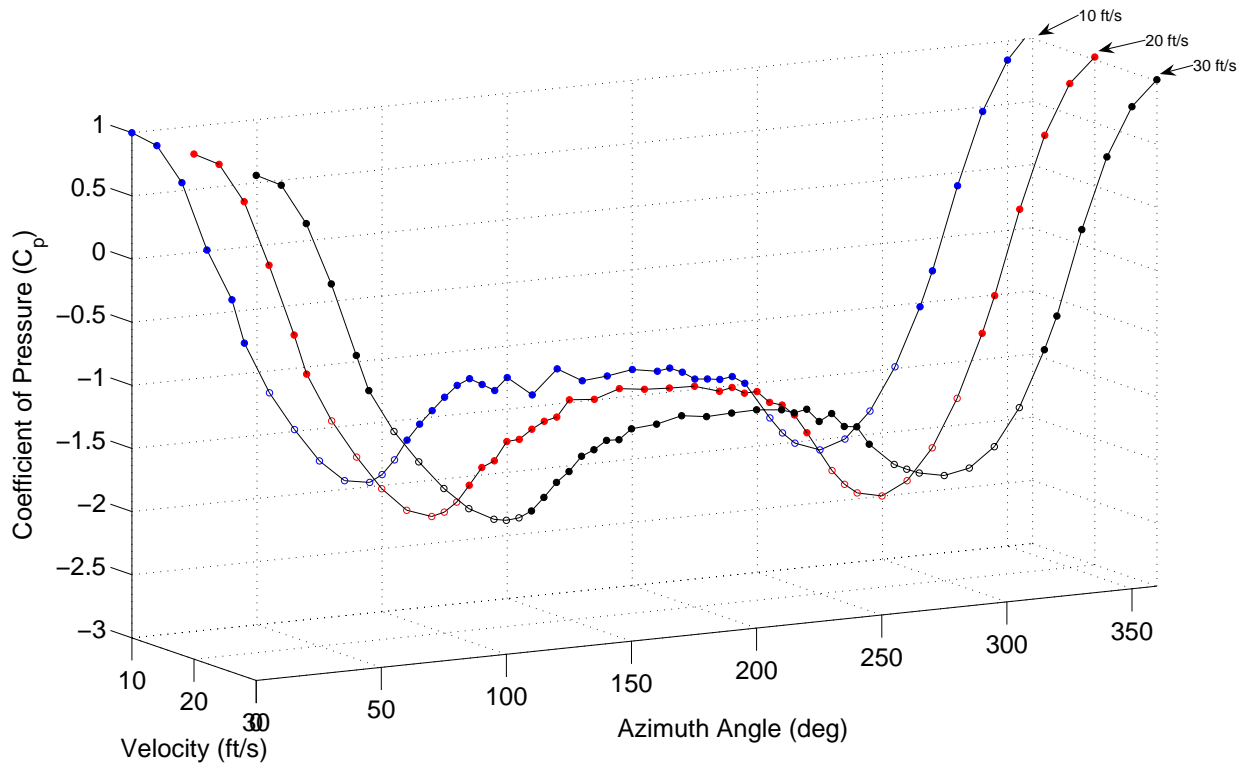
Figure 4.9: Waterfall plot of the variation in the pressure distribution as the Reynolds number is increased from 2.4×10^4 to 7.3×10^4. ($\theta_a = \pm 80°$, $V = 1000\ V_{p-p}$)
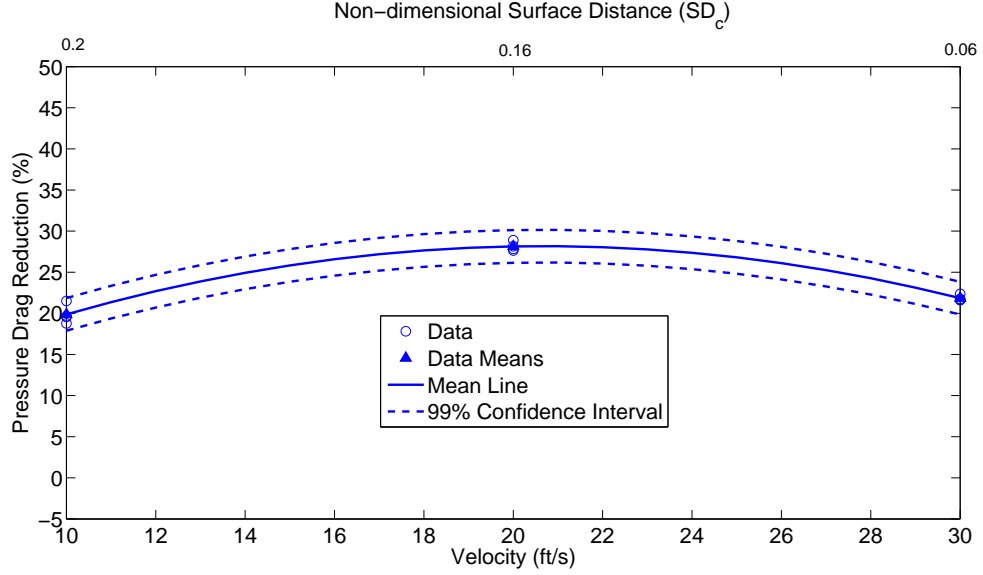
Figure 4.10: Variation in the percentage of pressure drag reduction as the Reynolds number is increased from 2.4×10^4 to 7.3×10^4 and SD_c decreases. ($\theta_a = \pm 80°$, $V = 1000 \ V_{p-p}$)

Figure 4.11 shows a detailed view of the pressure distribution while changing only the Re (cross flow velocity) to allow one to observe how the separation angle changes. At 10, 20 and 30 ft/s, the separation point is at $\pm 95°$ - $100°$, $\pm 95°$ and $\pm 85°$, respectively. This follows the trend seen in Figure 1.7 where the flow separation point moves upstream as the Re increases for $50,000 < Re < 100,000$. Therefore, as Re increases and the actuator position is held constant, the distance between the separation point and actuator location decreases and SD_c becomes an influential performance parameter. For this case, the percentage of pressure drag reduction is highest at $SD_c = 0.16$.

As the velocity increases, C_μ decreases, however Figures 4.12 and 4.13 do not indicate a trend depending on changing C_μ, although again the SD_c value of 0.16
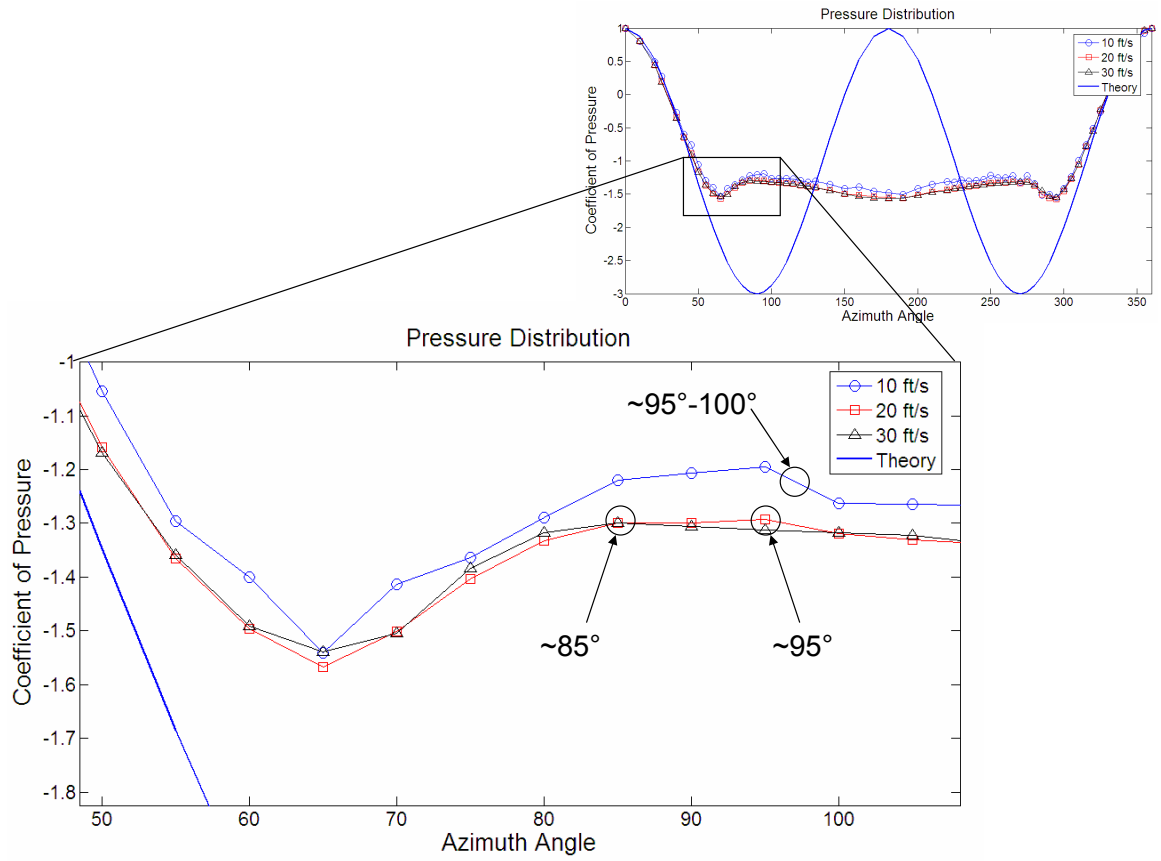
Figure 4.11: Pressure distribution for Re $= 2.4 \times 10^4$, 4.8×10^4 and 7.3×10^4 (10, 20 and 30 ft/s, respectively) and a detailed view to show the change in the pressure distribution corresponding to the onset of flow separation at 95° - 100°, 95°, and 85° as the velocity increases.
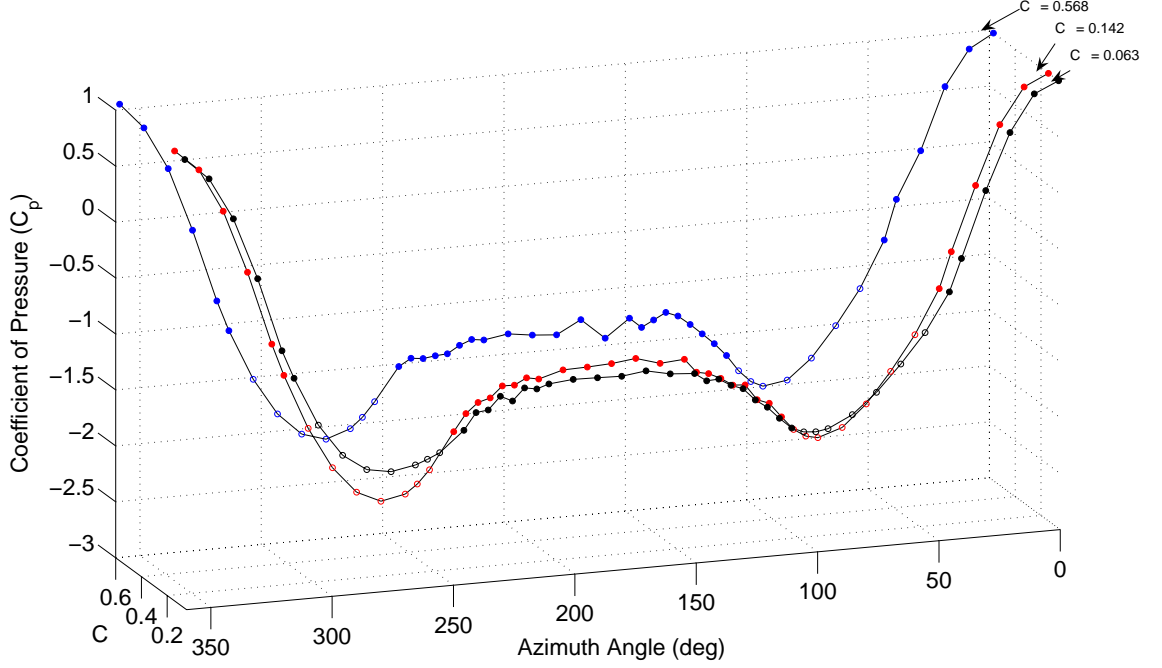
Figure 4.12: Waterfall plot of the variation in the percentage of pressure drag

reduction as C_μ decreases from 0.568 to 0.063. ($\theta_a = \pm 80°$, V =

1000 V_{p-p})

maximizes drag reduction. This suggests that SD_c is more important for analyzing

the changes in the pressure distribution and percentage of pressure drag reduction

than C_μ.

4.3 Variation with Actuator Position

Figure 4.14 shows the variation in the pressure distribution as the actuator

angular positions moves downstream from $\pm 50°$ to $\pm 90°$ (Re = 4.8×10^4, $U_\infty =$

20 ft/s, $\theta_s = 95°$, V = 1000 V_{p-p}). Up to a position of $\pm 80°$, the pressure in the

separated flow region increases slightly and the pressure near the actuators decreases.

Beyond an actuator position of 70°, the pressure near the actuators starts to increase
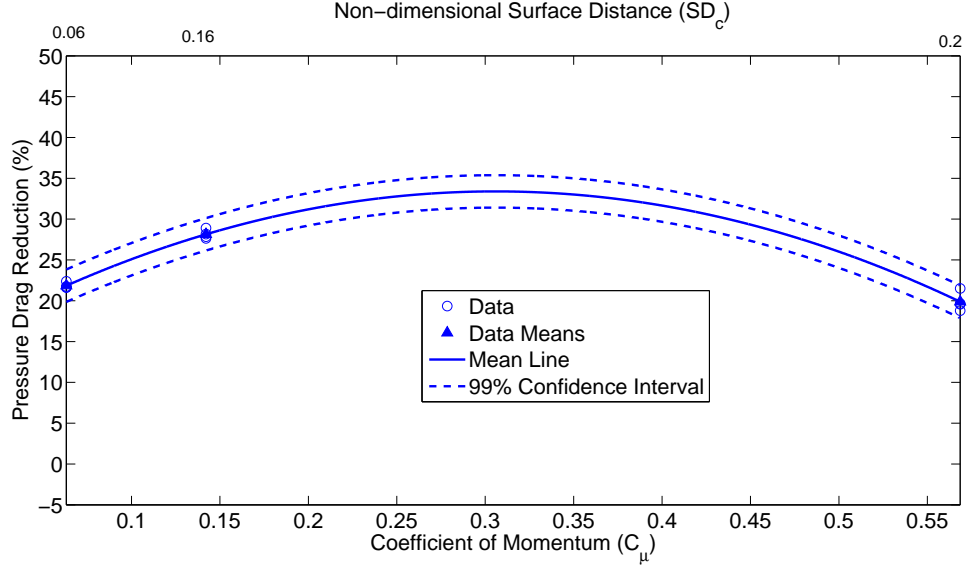
Figure 4.13: Variation in the percentage of pressure drag reduction as C_μ increases from 0.063 to 0.568 and SD_c increases from 0.06 to 0.2. ($\theta_a = \pm 80°$, V = 1000 V_{p-p})

and the pressure in the separated flow region decreases indicating a loss of actuator effectiveness at these angles.

Figure 4.15 shows the corresponding percentage drop in pressure drag as the actuator position moves downstream. The percentage drop starts to increase and then remains fairly constant between 60° and 80°. At 90°, the percentage drop decreases. The percentage drag reduction is also plotted with an axis showing the non-dimensional surface distance (SD_c) described in Section 3.5. The actuators are most effective between the SD_c values 0.16 and 0.37.
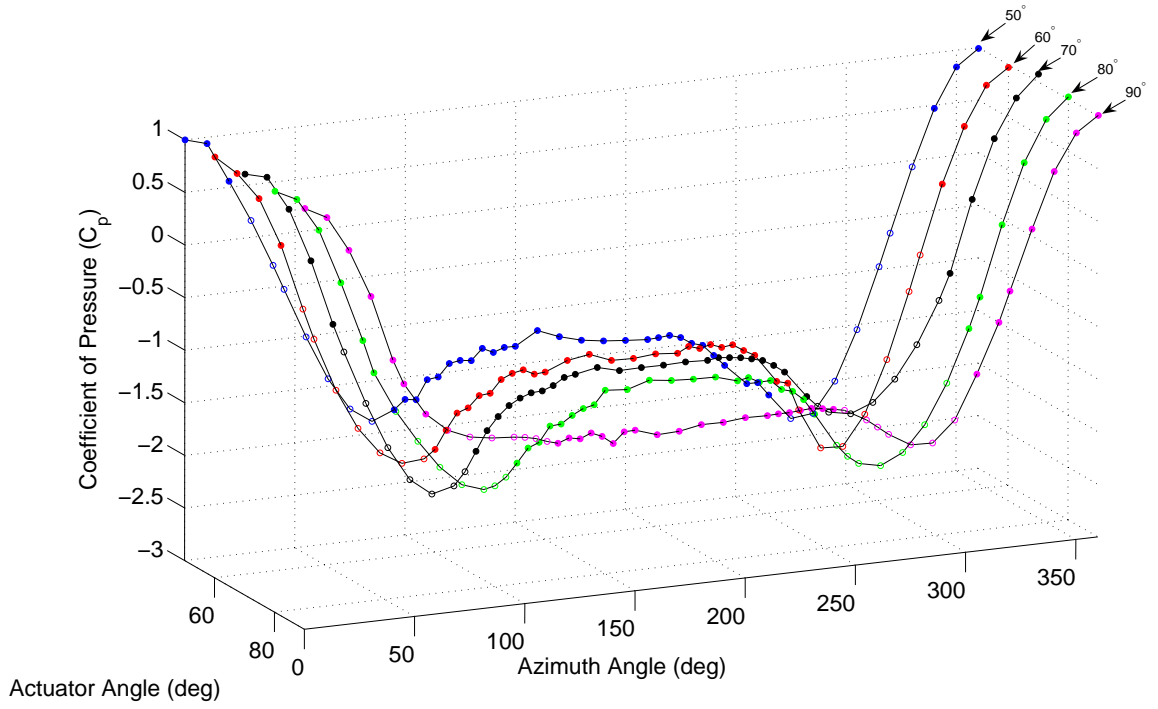
Figure 4.14: Waterfall plot of the variation in the pressure distribution as the actuator angular position moves downstream from $\pm 50°$ to $\pm 90°$. ($U_\infty = 20$ ft/s, Re $= 4.8 \times 10^4$, $\theta_s = 95°$, V $= 1000\ V_{p-p}$, $C_\mu = 0.14$)
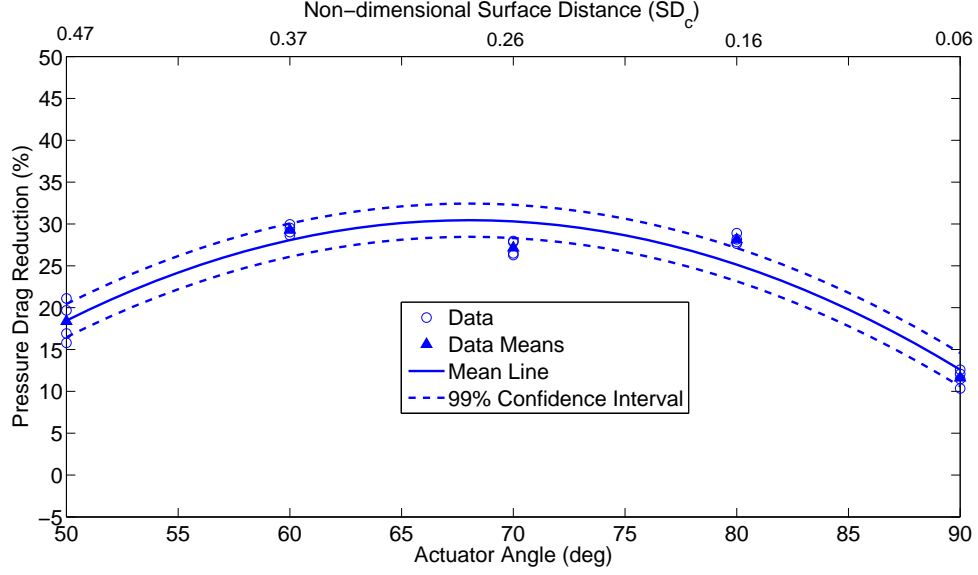
Figure 4.15: Variation in the percentage of pressure drag reduction as the actuator angular position moves downstream from $\pm 50°$ to $\pm 90°$. (U_∞ = 20 ft/s, Re = 4.8×10^4, $\theta_s = 95°$, V = 1000 V_{p-p}, $C_\mu = 0.14$)

4.4 SD_c vs. C_μ

As discussed in the previous sections, two factors have a significantly greater influence on the effectiveness of the actuators for reducing pressure drag: the momentum coefficient (C_μ) and the non-dimensional distance between the flow separation point and the actuator position (SD_c). The following contour plots show the effect of both parameters on the percentage of drag reduction for each velocity. The black points on the contour plot represent the actual SD_c and C_μ values for which the percentages of pressure drag reduction were taken.

Figure 4.16 shows the variation in C_μ and SD_c for a flow velocity of 10 ft/s. As C_μ increases, there is a sudden increase in the percentage of pressure drag reduction up to $C_\mu = 0.1$. As SD_c increases and for C_μ values above 0.1, the percentage of
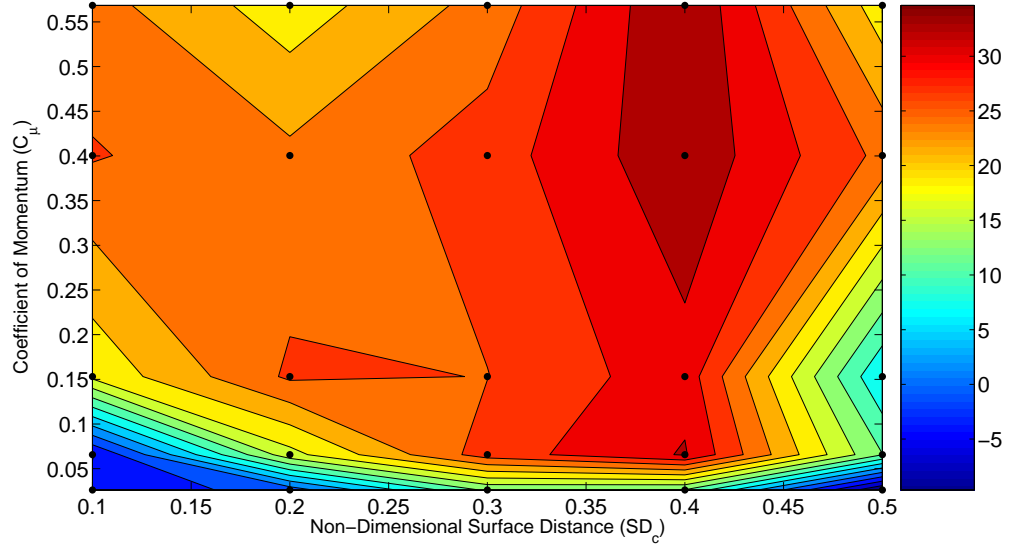
Figure 4.16: Non-dimensional surface distance (SD_c) vs. C_μ and the corresponding percentage of pressure drag reduction (color bar) for synthetic jet actuation at $\mathrm{Re} = 2.4 \times 10^4$ $(U_\infty = 10$ ft/s$)$.

pressure drag reduction is already above 15% but still increases until $SD_c = 0.4$. At this value, there is a very clear peak in actuator performance. For $SD_c > 0.4$ the percentage of pressure drag reduction starts to decrease.

Figure 4.17 shows the variation in the percentage of pressure drag reduction as C_μ and SD_c increase. As C_μ increases, there is a rapid increase in pressure drag reduction up to $C_\mu = 0.2$ for $SD_c > 0.15$. For $SD_c < 0.15$, C_μ has little influence on the percentage of pressure drag reduction. As SD_c increases and C_μ is above 0.2, there is an increase in pressure drag reduction up to $SD_c = 0.15$ where the pressure drag reduction plateaus until SD_c is larger than 0.4 and the pressure drag reduction begins to decrease. There is clearly a region of comparable effectiveness between SD_c values of 0.15 and 0.4.
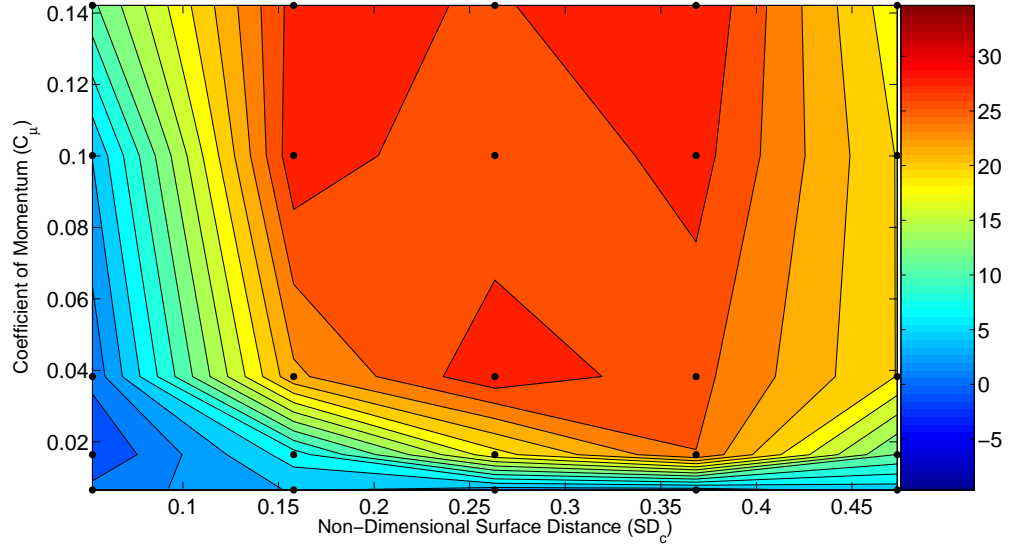
Figure 4.17: Non-dimensional surface distance (SD_c) vs. C_μ and the corresponding percentage of pressure drag reduction (color bar) for synthetic jet actuation at $\mathrm{Re} = 4.8 \times 10^4$ ($U_\infty = 20$ ft/s).

Figure 4.18 shows the variation in the percentage of pressure drag reduction for the 30 ft/s case. As C_μ and SD_c increase, the percentage of pressure drag reduction increases until a general plateau of performance is achieved and the percentage of pressure drag reduction is above 18% corresponding to C_μ values above 0.1 and SD_c values above 0.15. Within the plateau region, there appears to be a peak in actuator performance for $SD_c = 0.18$ and again for $SD_c = 0.4$.

Based on all three plots (Figures 4.16 - 4.18), the percentage of pressure drag reduction is highest for SD_c values between 0.15 and 0.4 and for C_μ values above 0.01.
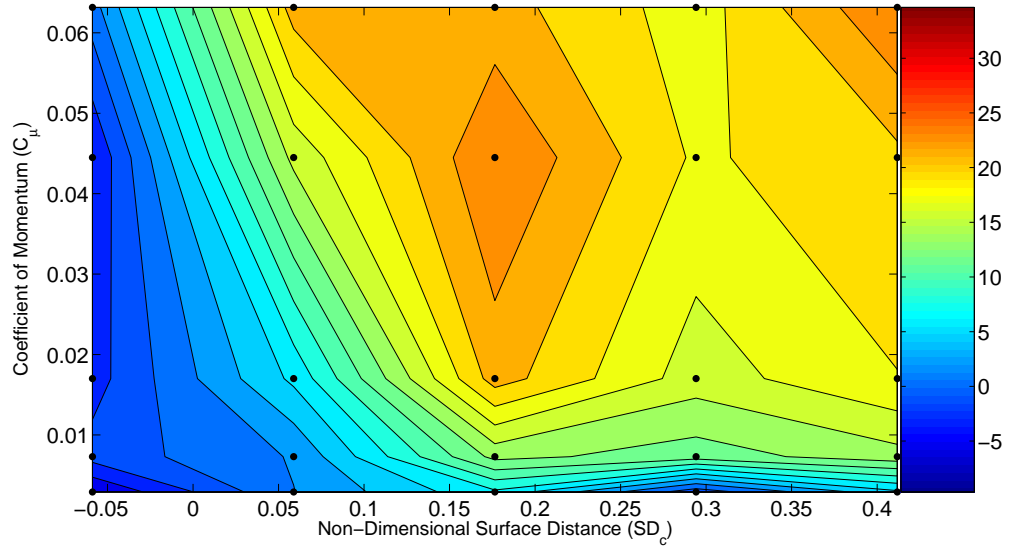
Figure 4.18: Non-dimensional surface distance (SD_c) vs. C_μ and the corresponding percentage of pressure drag reduction (color bar) for synthetic jet actuation at Re $= 7.3 \times 10^4$ $(U_\infty = 30$ ft/s).

4.5 Summary of Observations for Synthetic Jet Actuators on a Circular Cylinder

Chapter 4 shows the effect of varying applied voltage, Re and synthetic jet actuator position on the pressure distribution and the percentage of pressure drag reduction. In summary:

1) As voltage (C_μ) increases, the pressure distribution is increasingly influenced and the percentage of drag reduction increases especially beyond C_μ values of 0.2, above which the drag reduction values remained relatively constant.

2) As the freestream velocity increases, the variation in the pressure distribution and percentage pressure drag reduction do not follow the expected trend

of decreasing effectiveness. Actuator effectiveness is actually dependant on the fixed location of the actuator relative to the changing location of flow separation (SD_c) in addition to the momentum coefficient (C_μ).

3) As the actuator angular position moves downstream, the actuator effectiveness increases until a maximum is achieved based on the location of the actuator relative to the separation point.

4) A non-dimensional surface distance parameter (SD) is used to nondimensionalize the distance between the actuator location and the location of flow separation. There is an apparent optimal range for peak actuator performance between $SD_c = 0.15$ and 0.4, approximately.

Chapter 5

Plasma Actuator Test Results on a Circular Cylinder

For this research, active flow control actuators are being used to reduce pressure drag by changing the time-averaged pressure distribution such that it approaches the inviscid theoretical pressure distribution solution. The arrows in Figure 5.1 show the directions needed for favorable changes in pressure profiles obtained for flow over the cylinder with no flow control for the three Re flows studied. Also, the location of the onset of flow separation, which is evident from the pressure distribution as the location at which a plateau in the pressure profile first occurs, is expected to shift downstream as indicated in Figure 5.2.

Pressure distribution plots for every case in the test matrix are in Appendix A but specific plots were chosen to illustrate the effects of varying each of the following parameters: applied voltage, actuator position and freestream velocity (Re). Variations in these parameters result in variations in the coefficient of momentum (C_μ) and the distance between the actuator position, θ_a, and the flow separation point, θ_s (SD_c).

To illustrate the unique effect of a synthetic jet actuator, a single case pressure distribution plot (Figure 4.3) shows the inviscid theoretical pressure distribution (solid line) and the distribution with the actuators on (red squares) and the baseline pressure distribution (black circles). The hollow data points indicate interpolated

Figure 5.1: The black arrows show the desired trends in the pressure distribution for delaying flow separation and reducing pressure drag for 10, 20 and 30 ft/s (Re = 2.4×10^4, 4.8×10^4 and 7.3×10^4).

data to provide a continuous approximation of the pressure distribution where the actuators blocked the pressure ports. The shaded bands (magenta) on the plots indicate the location of the working actuator(s).

In Figure 5.3, the pressure distribution plot shows the effect of two plasma actuators placed at $\pm 80°$ with an applied voltage of $11.7\mathrm{k}V_{p-p}$ and Re = 2.4×10^4 ($U_\infty = 10$ ft/s and flow separation at $100°$). The plasma actuators cause the pressure near the actuators to decrease significantly and the pressure in the separated flow region to increase between $150°$ and $210°$. As mentioned before, these are both beneficial effects when trying to reduce pressure drag.

Unique to the plasma actuation pressure distributions, a plateau in the pressure distribution is seen in the presence of a strong pressure gradient. This plateau
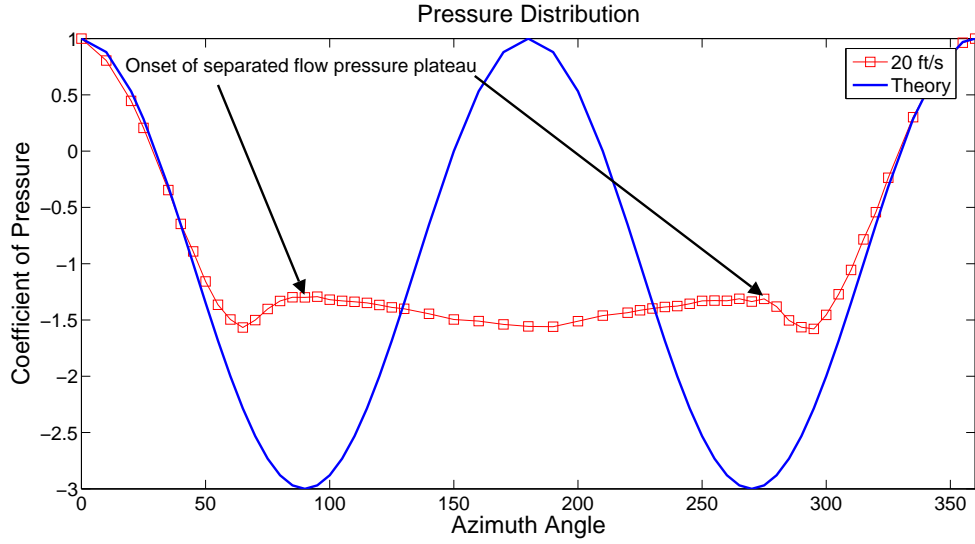
Figure 5.2: The black arrows show the location of the flow separation point for $\text{Re} = 4.8 \times 10^4$ (20 ft/s) at $85°$ corresponding to when the pressure distribution levels off over the rear half of the cylinder.

is indicative of a laminar separation bubble based on two observations: 1) a separation bubble is a region of constant pressure and 2) the location of the plateau lies on the theoretical pressure distribution [16]. Beyond the separation bubble, the flow reattaches as turbulent flow and a less severe adverse pressure gradient is present. The separation bubble exists with plasma actuation because the momentum added to the flow field by these actuators acts along the flow surface which contributes to the formation of a very steep adverse pressure gradient over a large portion of the cylinder surface. In contrast, the synthetic jet actuators used introduced momentum normal to the flow field, which promoted formation of a shallower pressure gradient over a smaller portion of the cylinder surface and therefore, evidence of a separation bubble is not present. An example of a laminar separation bubble on the
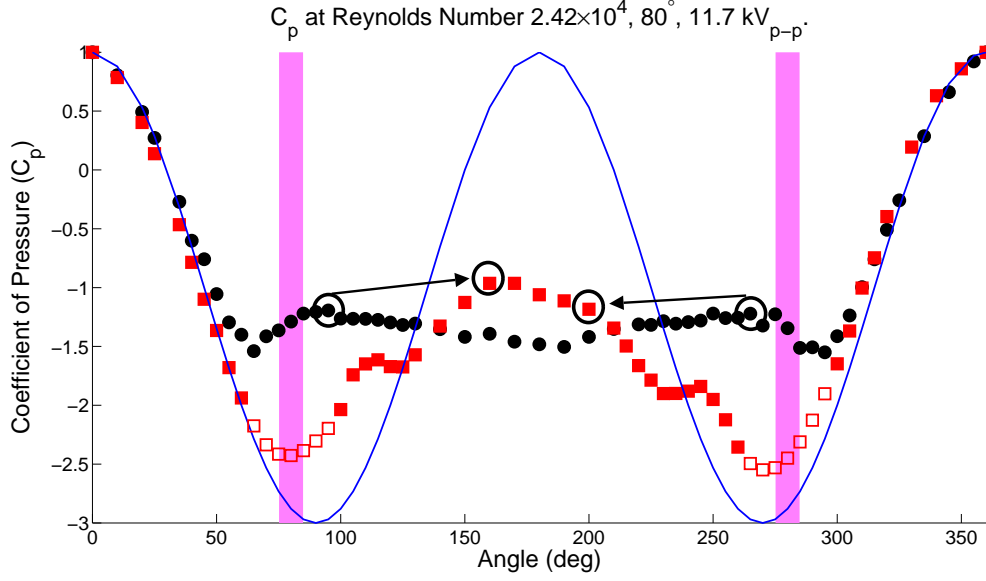
Figure 5.3: Pressure distribution showing the effect of two plasma actuators placed at $\pm 80°$ and with an applied voltage of 11.8kV_{p-p} and $\text{Re} = 2.4 \times 10^4$ ($U_\infty = 10$ ft/s, $\theta_s = 100°$, $SD_c = 0.2$).

pressure distribution of an NACA $66_3 - 018$ (Figure 5.5), shows a similar plateau in the pressure distribution along the adverse pressure gradient and also that the plateau intersects the theoretical inviscid pressure distribution for the airfoil. As with airfoils, the following data will show that a laminar separation bubble results in a reduction in actuator effectiveness for reducing pressure drag and, therefore, is not desirable.

In Figure 5.6, the pressure distribution plot shows the effect of one plasma actuator placed at $80°$ with an applied voltage of 11.8kV_{p-p} and $\text{Re} = 2.4 \times 10^4$ ($U_\infty = 10$ ft/s and flow separation occurs at $100°$). The actuator causes a decrease in pressure at the location of the actuator and a small increase in pressure in the separated flow region. This shows that plasma actuators only affect the actuated
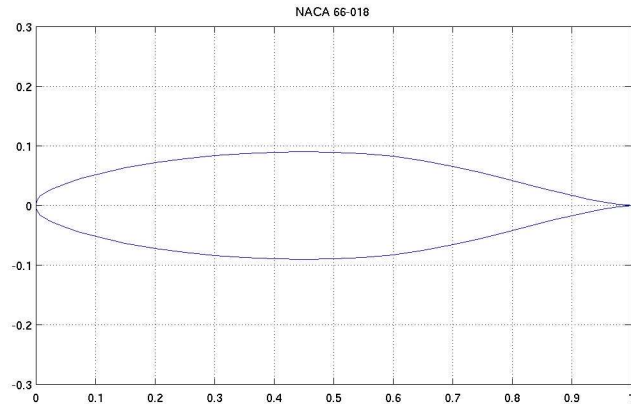
Figure 5.4: NACA $66_3 - 018$ airfoil shape [15].
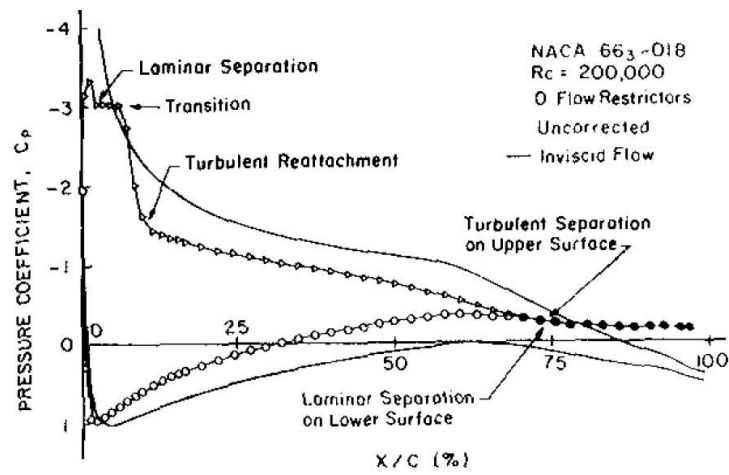
Figure 5.5: Pressure distribution over an NACA $66_3 - 018$ airfoil with a laminar separation bubble indicated by the plateau of constant pressure along the adverse pressure gradient [16].

95
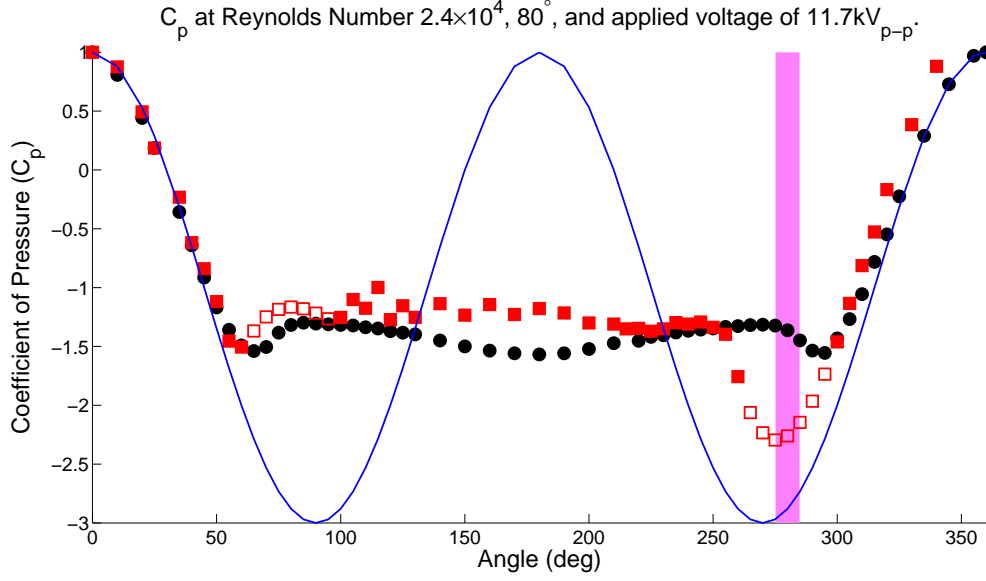
Figure 5.6: Pressure distribution showing the effect of one plasma actuator placed at $\pm 80°$ and with an applied voltage of $11.8 kV_{p-p}$ and Re $= 2.4 \times 10^4$ ($U_\infty = 10$ ft/s, $\theta_s = 100°$, SD $= 0.2$).

side of the cylinder. Also, the pressure drop at the actuator location is not as large as the pressure drop in the two actuator case (Figure 5.3) and there is no evidence of a laminar separation bubble suggesting that the effect of both actuators combine to create a stronger effect (i.e. a steeper adverse pressure gradient).

The following sections will illustrate the changes in the pressure distribution when the following parameters are varied: the applied voltage, position of the actuator on the cylinder, and freestream Reynolds number. Each case will show a waterfall plot of the pressure distributions and also a plot to show the percentage of pressure drag reduction compared to the baseline case with no actuators installed as each parameter changes. The ANOVA table for the synthetic jet actuators on the circular cylinder is given in Table 5.1. The mean square error used to compute

ANOVA Table					
Source	DF	Type I SS	Mean Square	F Value	Pr > F
Position	4	3381.633789	845.408447	139.76	<.0001
Voltage	6	8477.704801	1412.950800	233.58	<.0001
Velocity	2	1286.302564	643.151282	106.32	<.0001
Position*Voltage	24	2186.421674	91.100903	15.06	<.0001
Position*Velocity	8	1625.964169	203.245521	33.60	<.0001
Voltage*Velocity	12	954.954857	79.579571	13.16	<.0001
Position*Voltage*Velocity	48	4062.815832	84.641997	13.99	<.0001

Table 5.1: ANOVA Table for plasma actuators on the circular cylinder.

the confidence interval is 6.05.

5.1 Variation with Applied Voltage

The voltage applied to the actuators was varied from 2.8kV_{p-p} to 11.8kV_{p-p} at increments of 1.4kV_{p-p}. Figure 5.7 shows the effect of increasing the applied voltage to the actuator on the pressure distribution. The actuator angular position is $\pm 80°$ and Re $= 2.4 \times 10^4$ ($U_\infty = 10$ ft/s and the onset of flow separation occurs at $100°$). As the voltage increases, the pressure in the separated flow region gradually increases and the pressure at the location of the actuators decreases. These are both beneficial trends toward reducing pressure drag because, with each increase in applied voltage, the pressure distribution approaches the shape of the inviscid theoretical pressure distribution. At applied voltages above 10kV_{p-p} for Re $= 2.4 \times 10^4$, evidence of a
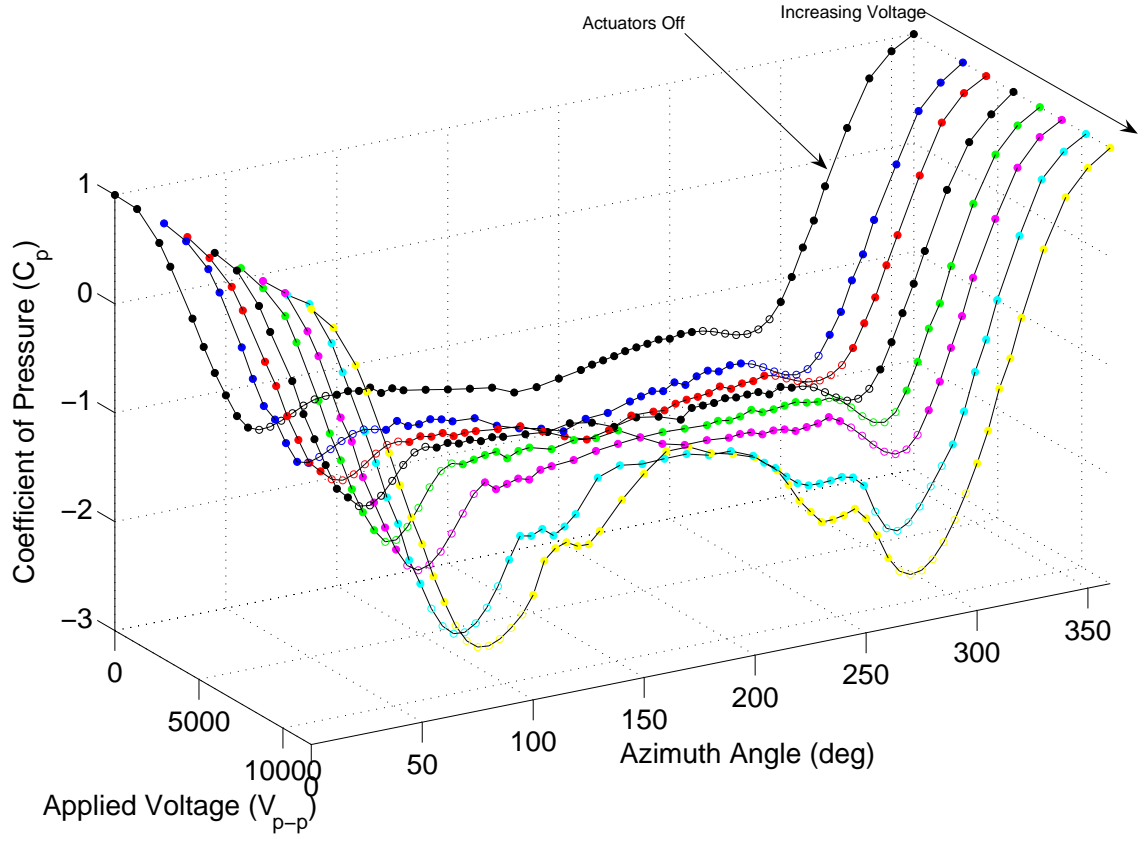
Figure 5.7: Waterfall plot of the variation in the pressure distribution as the maximum applied voltage is increased from 2.8kV_{p-p} to 11.8kV_{p-p}. (Re $= 2.4 \times 10^4$, $U_\infty = 10$ ft/s, $\theta_s = 100°$, $\theta_a = \pm 80°$, $SD_c = 0.2$)

laminar separation bubble appears which leads to a reduction in the impact of the actuator on reducing drag.

Figure 5.8 shows the variation of the pressure drag reduction percentage as the applied voltage increases. At the lowest voltage, there is no change in pressure drag until the applied voltage reaches 6kV_{p-p} and then the percentage of pressure drag reduction increases up to almost 9kV_{p-p}. Beyond 9kV_{p-p}, the pressure drag reduction decreases due to the presence of laminar separation bubbles on either side of the cylinder.

98
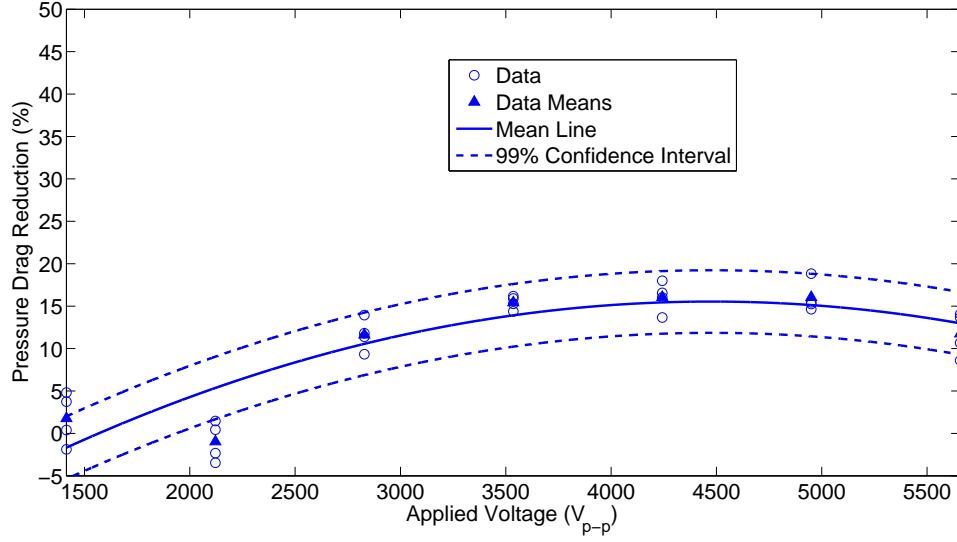
Figure 5.8: Variation in the percentage of pressure drag reduction as the maximum applied voltage is increased from $2.8\mathrm{k}V_{p-p}$ to $11.8\mathrm{k}V_{p-p}$. (Re $= 2.4 \times 10^4$, $U_\infty = 10$ ft/s, $\theta_s = 100°$, $\theta_a = \pm80°$, $SD_c = 0.2$)

5.2 Variation with Reynolds Number

Figure 5.9 shows the change in the pressure distribution as Re increases from 2.4×10^4 to 7.3×10^4 ($U_\infty = 10$ ft/s to 30 ft/s). The applied voltage is $11.8\mathrm{k}V_{p-p}$ and actuator angular position is $\pm90°$. As velocity increases, the pressure at the location of the actuators increases and the maximum pressure in the region of separated flow remains constant. There is a sudden change in the shape of the pressure distribution between 10 ft/s and 20 ft/s due to the strong effectiveness of the actuators at 10 ft/s and also the presence of a separation bubble. Because the actuators add a fixed amount of energy independent of the freestream velocity, C_μ essentially decreases as the velocity increase; therefore, a decrease in actuator effectiveness is expected. However, Figure 5.9 shows that this is not necessarily the case.
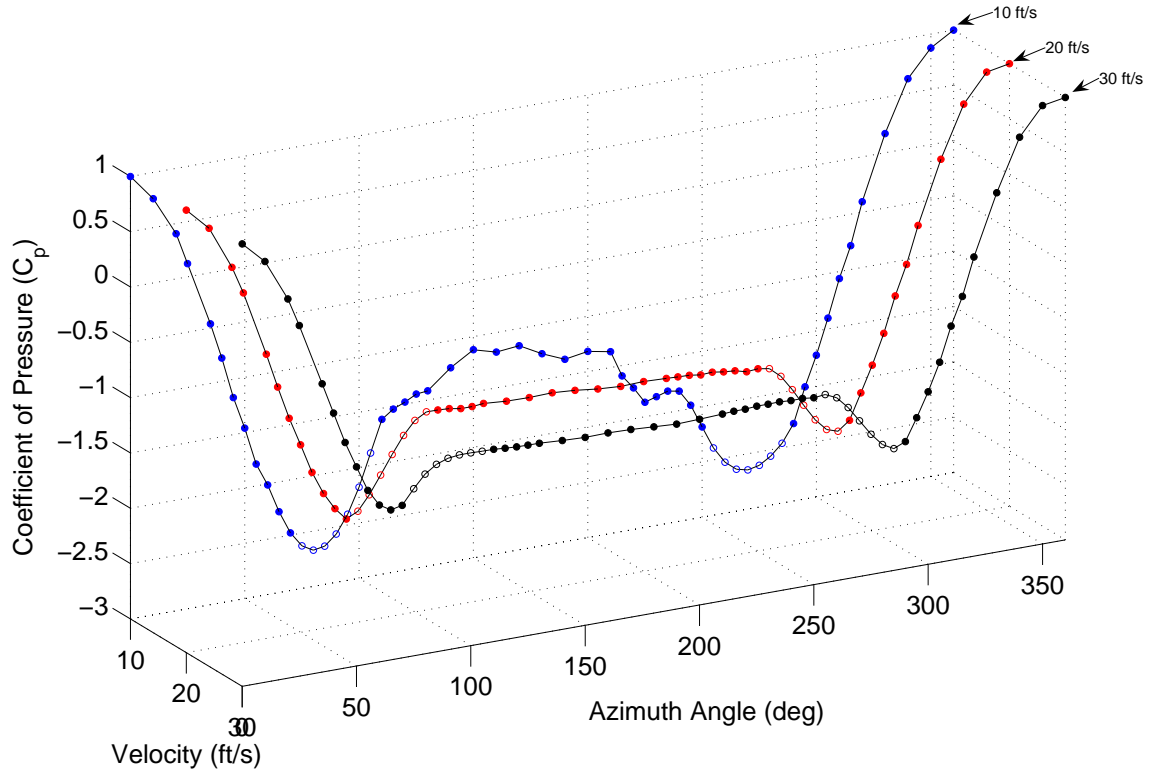
Figure 5.9: Waterfall plot of the variation in the pressure distribution as Re increases from 2.4×10^4 to 7.3×10^4 ($U_\infty = 10$ ft/s to 30 ft/s, $\theta_a = \pm 90°$, V = 11.8kV_{p-p}).
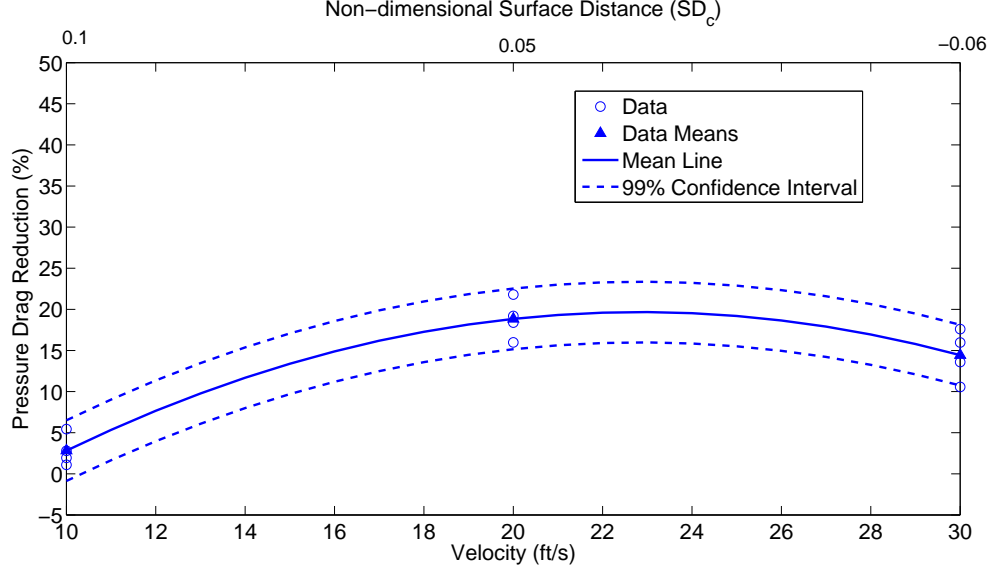
Figure 5.10: Variation in the percentage of pressure drag reduction as Re increases from 2.4×10^4 to 7.3×10^4 ($U_\infty = 10$ ft/s to 30 ft/s, $\theta_a = \pm 90°$, V = $11.8\text{k}V_{p-p}$).

Figure 5.10 shows the change in the percentage of pressure drag reduction as the velocity increases. The percentage of pressure drag reduction increases from 10 ft/s to 20 ft/s because the laminar separation bubble is no longer present. Between 20 ft/s and 30 ft/s, the pressure drag reduction decreases likely due to the decreasing C_μ.

The increase in pressure drag reduction from 10 to 20 ft/s is unexpected when only considering the change in C_μ. By also considering the non-dimensional surface distance parameter, SD_c, it appears that this increase is also due to the change in the distance between the actuator position and flow separation point as the flow velocity increases.

Figure 5.11 shows a detailed view of the pressure distribution while changing

only the Re (cross flow velocity) to allow one to observe how the separation angle changes. At 10, 20 and 30 ft/s, the separation point is at $\pm95°$ - $100°$, $\pm95°$ and $\pm85°$, respectively. This follows the trend seen in Figure 1.7 where the flow separation point moves upstream as the Re increases for $50,000 < Re < 100,000$. Therefore, as the velocity increases and the actuator position is held constant, the distance between the separation point and actuator location decreases and SD_c becomes a valuable parameter. For this case, the percentage of pressure drag reduction is highest at $SD_c = 0.05$.

5.3   Variation with Actuator Position

Figure 5.12 shows the variation in the pressure distribution as the actuator position moves downstream from $\pm50°$ to $\pm90°$. The applied voltage is 10.3kV_{p-p} and Re $= 7.3 \times 10^4$ ($U_\infty = 30$ ft/s). The minimum pressure near the location of the actuators decreases up to $70°$ and then increases as the actuator angle approaches $90°$. The pressure in the separated flow region increases up to $60°$ and then decreases as the actuator angle approaches $90°$. This variation in the pressure distribution is reflected in the pressure drag reduction plot.

Figure 5.13 shows the variation in the percentage of pressure drag reduction as the actuator angle position moves downstream in 30 ft/s flow. A maximum pressure drag reduction is reached at $70°$ ($SD_c = 0.18$), beyond which, the percentage of pressure drag reduction decreases. This suggests the proximity of the actuator momentum infusion into the flow relative to the location of flow separation for the
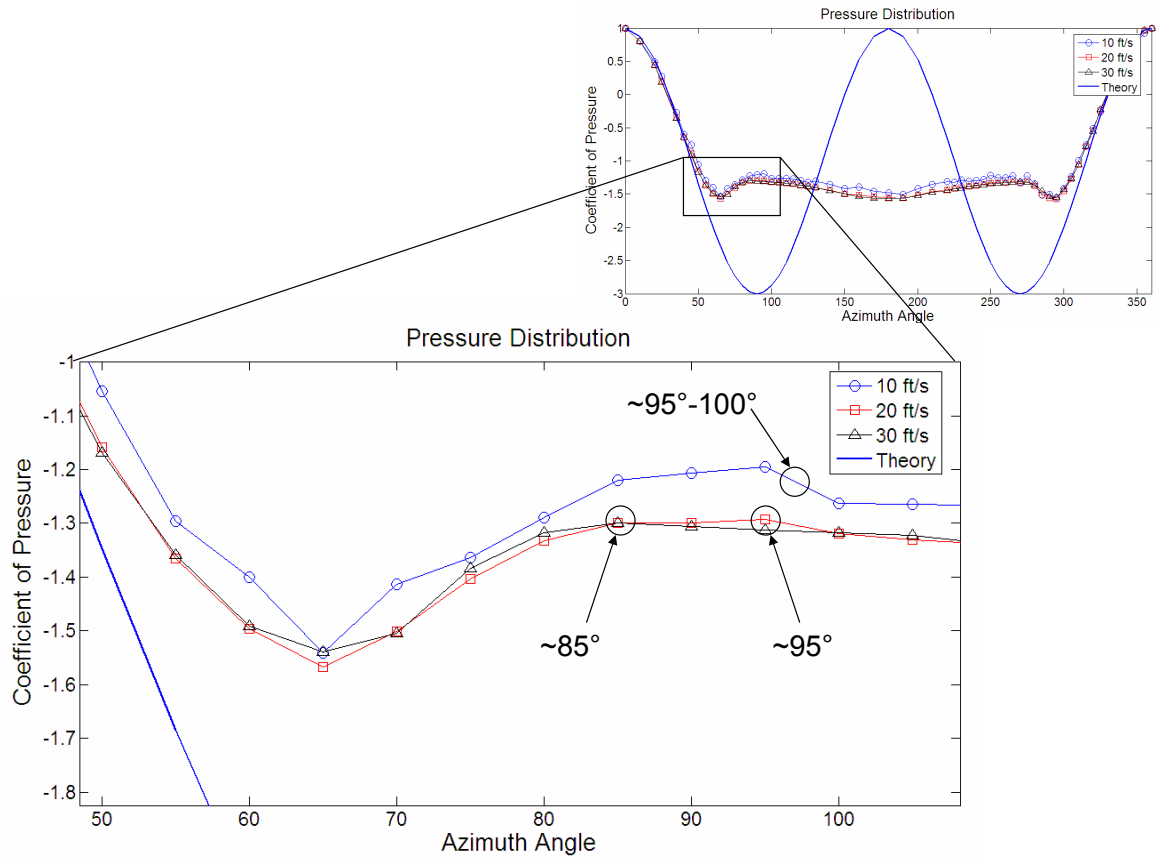
Figure 5.11: Pressure distribution for 10, 20 and 30 ft/s ($Re = 2.4 \times 10^4$, 4.8×10^4 and 7.3×10^4) and a detailed view to show the change in the pressure distribution corresponding to the onset of flow separation at 95° - 100°, 95°, and 85° as the velocity increases.
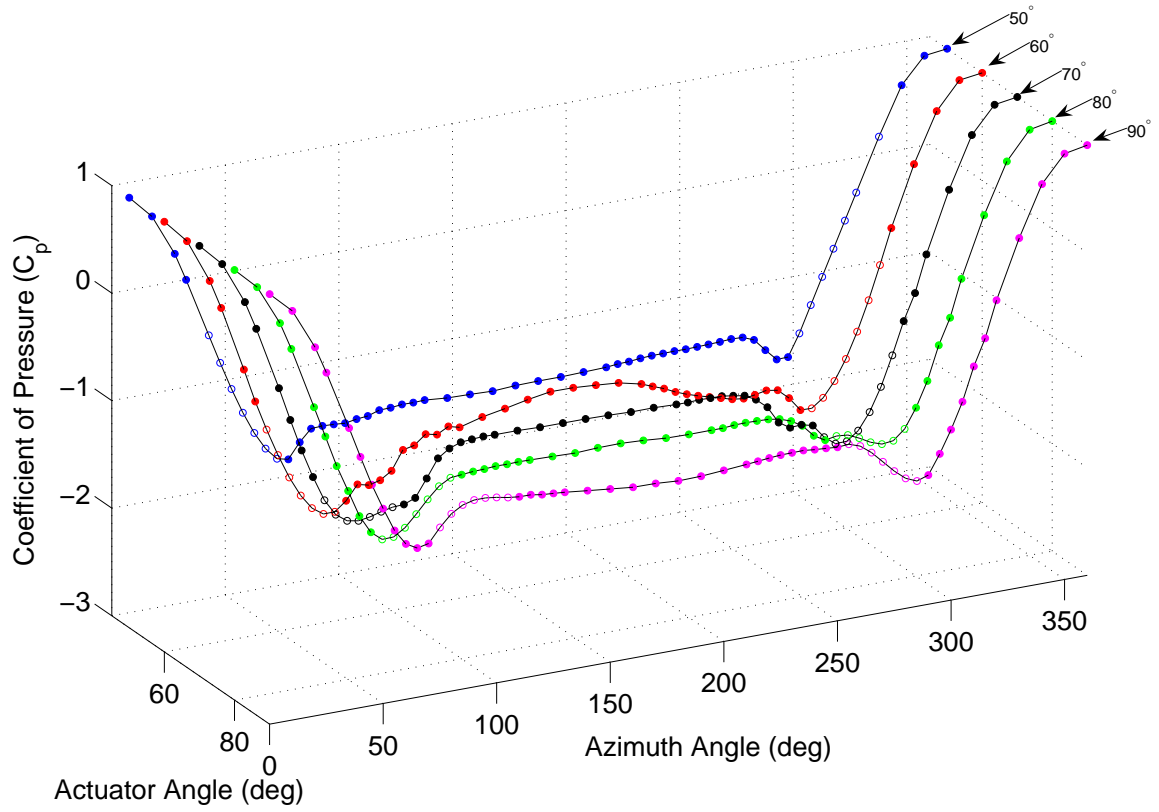
Figure 5.12: Waterfall plot of the variation in the pressure distribution as the actuator angle moves downstream from $\pm 50°$ to $\pm 90°$. (Re $= 7.3 \times 10^4$, $U_\infty = 30$ ft/s, $\theta_s = 85°$, V $= 10.3\text{k}V_{p-p}$)
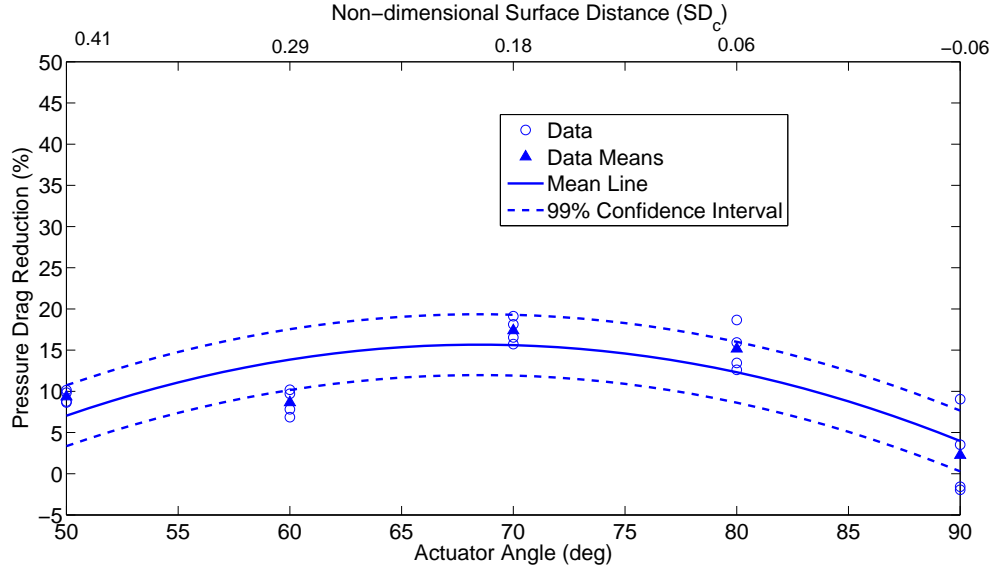
Figure 5.13: Variation in the percentage of pressure drag reduction as the actu-

ator angle moves downstream from $\pm50°$ to $\pm90°$. (Re $= 7.3 \times 10^4$,

$U_\infty = 30$ ft/s, $\theta_s = 85°$, V $= 10.3\text{k}V_{p-p}$)

un-controlled case, as described by SD_c, will be a useful non-dimensional parameter

for optimization of actuator placement.

5.4 SD_c vs. Applied Voltage

As discussed in the previous sections, two factors influence the effectiveness

of the actuators for reducing pressure drag: the applied voltage (comparable to the

momentum coefficient, C_μ) and the distance between the flow separation point and

the actuator position (SD_c). The following contour plots show the effect of both

parameters on the percentage of pressure drag reduction for each velocity. The black

points on the contour plot represent the actual SD_c and C_μ values for which the

percentages of pressure drag reduction were taken.
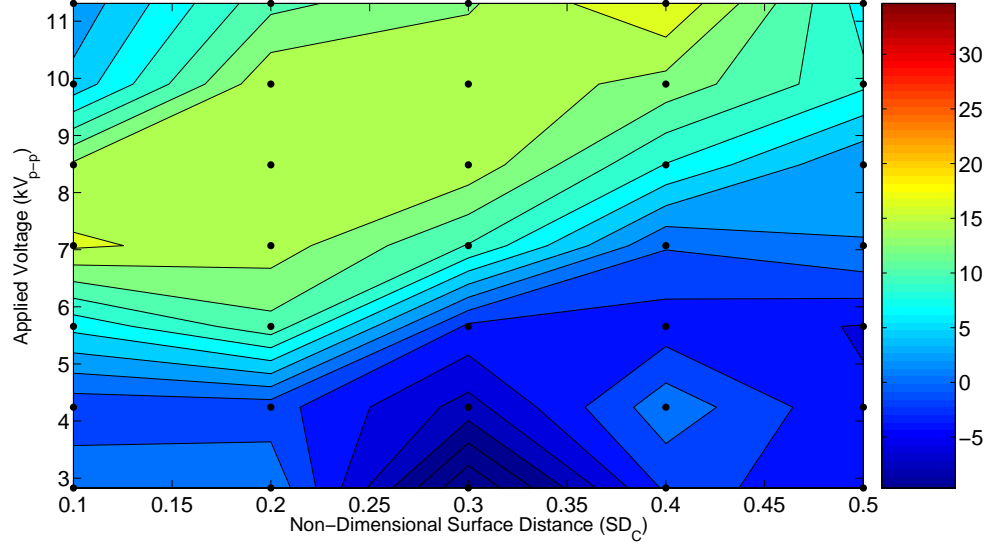
Figure 5.14: Non-dimensional surface distance (SD_c) vs. applied voltage and the corresponding percentage of pressure drag reduction (color bar) for plasma actuation at Re $= 2.4 \times 10^4$ ($U_\infty = 10$ ft/s).

Figure 5.14 shows the variation in the percentage of pressure drag reduction for a flow velocity of 10 ft/s. For low voltages, there is almost no change in the pressure drag for all SD_c values. However, above 6kV_{p-p} at low SD_c values and 9kV_{p-p} for high SD_c values, the percentage of pressure drag starts to increase. The necessary voltage for increasing pressure drag reduction is for $SD_c = 0.2$. As the applied voltage continues to increase for low SD_c values, the peak pressure drag reduction is quickly achieved at 8kV_{p-p}, beyond which, the pressure drag reduction decreases. This decrease is due to the presence of laminar separation bubbles for these operating conditions. As voltage increases, the highest percentage of pressure drag reduction moves from $SD_c = 0.1$ to $SD_c = 0.4$.

Figure 5.15 shows the variation in the pressure drag reduction for 20 ft/s flow.
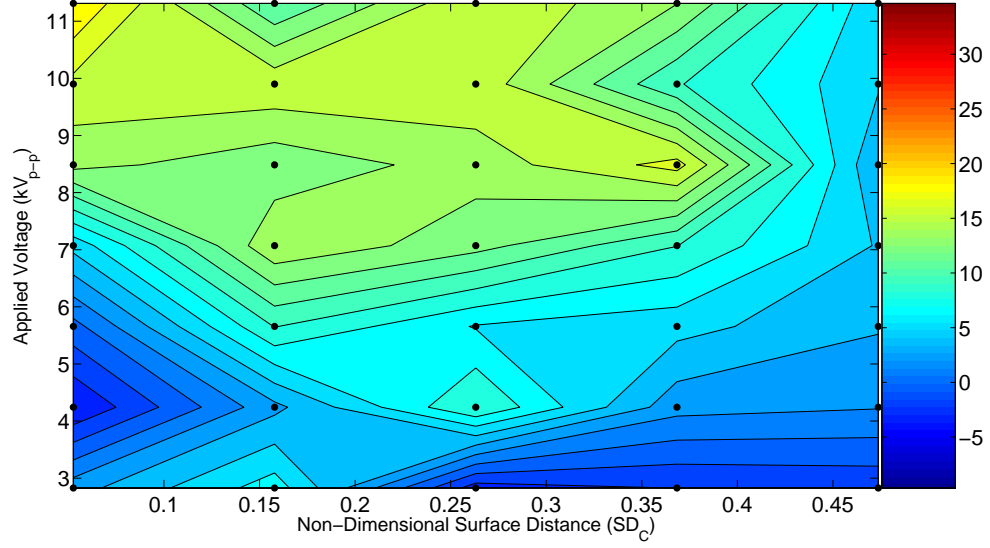
Figure 5.15: Non-dimensional surface distance (SD_c) vs. applied voltage and the corresponding percentage of pressure drag reduction (color bar) for plasma actuation at Re $= 4.8 \times 10^4$ ($U_\infty = 20$ ft/s).

For all SD_c values below 0.45, increasing the applied voltage results in a steady increase in pressure drag reduction. For SD_c values greater than 0.45, the actuators have little effect on the pressure drag because they are located too far from the flow separation point. For applied voltages above 8kV_{p-p}, there are two peaks in pressure drag reduction at $SD_c = 0.05$ and 0.25.

Figure 5.16 shows a very obvious optimal set of operating conditions where the applied voltage is between 6 and 9kV_{p-p} and $SD_c = 0.18$. As SD_c increases above 0.18, there is a steady decrease in pressure drag reduction, independent of the applied voltage. However, for SD_c values below 0.18, the percentage of pressure drag reduction decreases with decreasing SD_c but the rate at which it decreases is less for high voltages than for lower voltages. Based on all three plots, SD_c
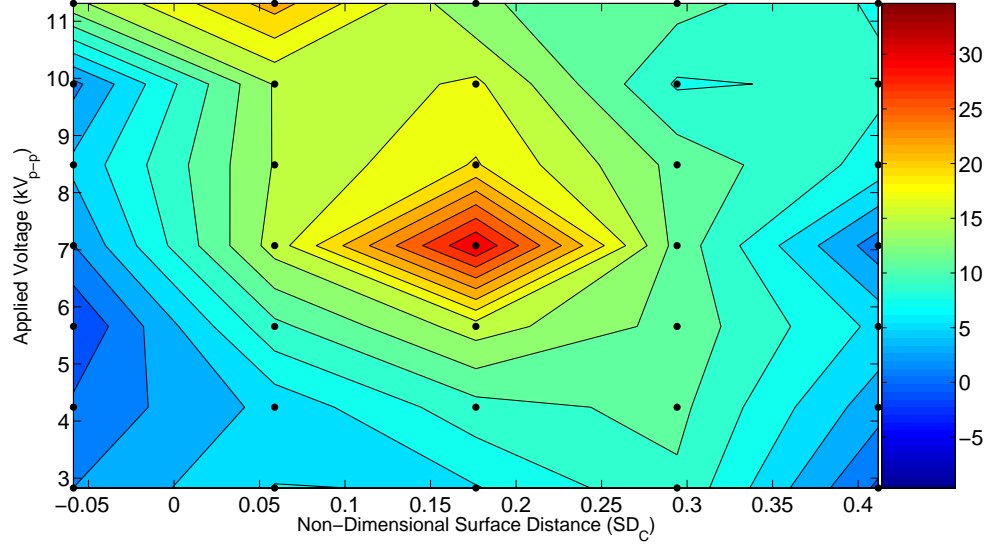
Figure 5.16: Non-dimensional surface distance (SD_c) vs. applied voltage and the corresponding percentage of pressure drag reduction (color bar) for plasma actuation at Re = 7.3×10^4 ($U_\infty = 30$ ft/s).

values from 0 to 0.35 will result in substantial pressure drag reduction, especially at $SD_c = 0.2$. Also, as the applied voltage increase, the percentage of pressure drag reduction increases as well. However, an upper limit is suggested in Figure 5.14 as very high applied voltages at low SD_c values results in a laminar separation bubble. Although never measured in this research, other research shows that C_μ is around O(10^{-7}) to O(10^{-5}) for plasma actuators and could support the decreasing range of actuator effectiveness as velocity increases. The high voltages used in the plasma actuators precluded use of a velocity sensor in close proximity to the devices, and thus values of C_μ were not available for the plasma actuators. It is expected that drag reduction associated with interaction between C_μ and SD_c may have exhibited stronger correlation than voltage and SD_c.

5.5 Summary of Observations for Plasma Actuators on a Circular Cylinder

Chapter 5 shows the effect of varying applied voltage, Re and plasma actuator position on the pressure distribution and the percentage of pressure drag reduction. In summary:

1) As the applied voltage (C_μ) increases, the pressure distribution is increasingly influenced and the percentage of pressure drag reduction increases until a laminar separation bubble appears, causing a decrease in pressure drag reduction.

2) As the freestream velocity increases, Reynolds number increases, but the variation in the pressure distribution and percentage of pressure drag reduction did not follow the expected trend. Instead the combined effect of velocity change on both C_μ and on SD_c appears to influence performance, with the resultant trends relatively flat as velocity changed. The originally expected trend focused only on that as Reynolds number increased, C_μ would decrease, and actuator effectiveness for drag reduction would decrease. The unanticipated trend was that as Reynolds number increased, the location of flow separation moved closer to the actuator, and actuator effectiveness increased. These effects appears to be offsetting, and actuator effectiveness remained fairly constant over the range of Reynolds numbers tested.

3) As the actuator angular position moves downstream, the actuator effectiveness increases until a maximum is achieved based on the location of the actuator

relative to the separation point (SD_c).

4) Plasma actuation results in a very steep adverse pressure gradient over a significant portion of the cylinder surface resulting in a laminar separation bubble and increased pressure drag for $SD_c < 0.2$ and V $> 10\text{k}V_{p-p}$.

5) SD_c values from 0 to 0.35 (especially at $SD_c = 0.2$) result in the most significant percentage of pressure drag reduction. Increased applied voltage generally results in increased pressure drag reduction except at SD_c above 0.45.

Chapter 6

Test Results on the Tail Boom Model

The purpose of active flow control actuators is to change the time-averaged pressure distribution such that it approaches a shape that indicates zero pressure drag and no flow separation as shown in Figure 6.1. This figure shows an *estimated* inviscid theoretical pressure distribution (solid blue line) which is based on the circular cylinder theoretical pressure distribution for the circular portions of the tail boom and results in CD = $7 \times 10^{-4} \approx 0$. The pressure distribution over the linear section of the model was assumed be the same as seen in the experimental data because viscous effects would be insignificant at this location. In addition, the onset of flow separation location is expected to change such that the portions of the pressure distribution indicated on Figure 6.2, corresponding to the baseline flow separation location, move downstream. Notice that the pressure distribution is shown similar to the method used to show a circular cylinder pressure distribution. Because this shape is symmetric, the top and bottom pressure distributions are similar and, therefore, plotted against the chordwise position (x/c) from 0 to 1 back to 0 again.

Figure 6.1 also shows the experimental viscous pressure distribution for the three velocity cases where Re = 2.3×10^4, 4.8×10^4 and 7.3×10^4 corresponding to 7.3 ft/s, 14.6 ft/s and 22.2 ft/s, respectively. The pressure distribution over the
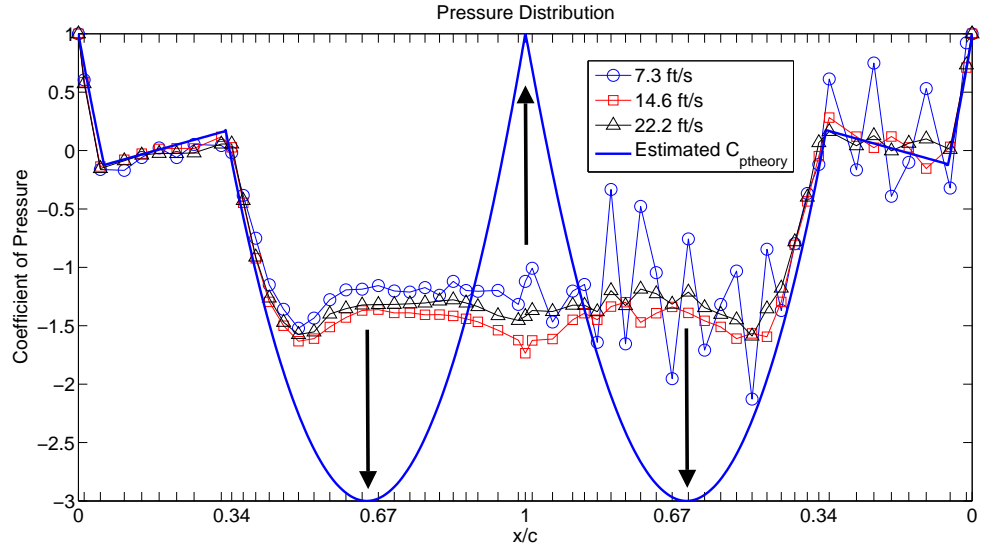
Figure 6.1: The black arrows show the desired trends in the pressure distribution for delaying flow separation and reducing pressure drag for 7.3, 14.6 and 22.2 ft/s (Re = 2.4×10^4, 4.8×10^4 and 7.3×10^4).
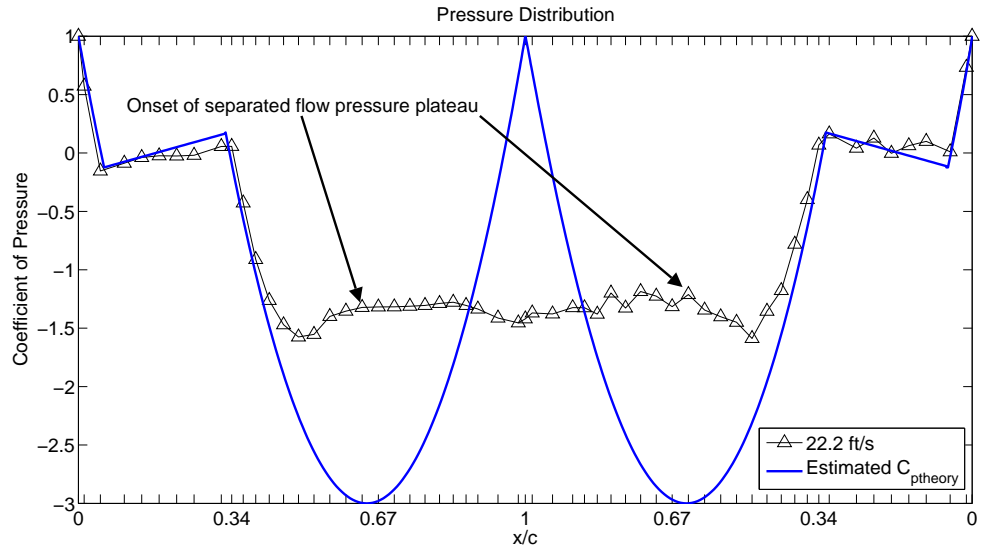
Figure 6.2: The black arrows show the location of the flow separation point for Re = 7.3×10^4 (22.2 ft/s) at x/c = 0.74 corresponding to when the pressure distribution levels off over the rear half of the cylinder.

front portion of the model follows the inviscid theoretical pressure distribution up to x/c≈ 0.43. Beyond this point, the pressure distribution starts to deviate from the estimated theoretical distribution due to viscous effects. The flow eventually separates from the model around x/c = 0.67 for the 7.3 ft/s and 14.6 ft/s cases and at x/c = 0.74 in the 22.2 ft/s case. As addressed in Chapter 3, one of the ESP modules returned irregular data and the effect of which is seen in the 7.3 ft/s case, the lowest velocity tested, where the data is highly irregular on one side of the pressure distribution (x/c = 1 to 0). ESP data from the other side (x/c = 0 to 1), however, is very regular and therefore, the drag reduction data was calculated based on the pressure distribution data from x/c = 0 to 1.

Figure 6.3 shows the positions of the pressure ports and the corresponding numbers on the tail boom model. The ports are more concentrated where the flow is expected to separate to ensure higher resolution when detecting flow separation. The x/c values corresponding to the port locations are referenced when discussing the actuator locations. The actuator location corresponds to the pressure port where the synthetic jet actuator slots were machined (thus, replacing the pressure port) and the plasma actuator electrodes overlapped. Pressure distribution plots for every case in the test matrix are in Appendix A but specific plots were chosen to illustrate the effects of varying each of the following parameters: applied voltage, actuator position and freestream velocity (Re). To the author's knowledge, there are no other sources providing similar data and, therefore, this data is new.

The following sections will illustrate the changes in the pressure distribution when the following parameters are varied: the applied voltage, position of the ac-
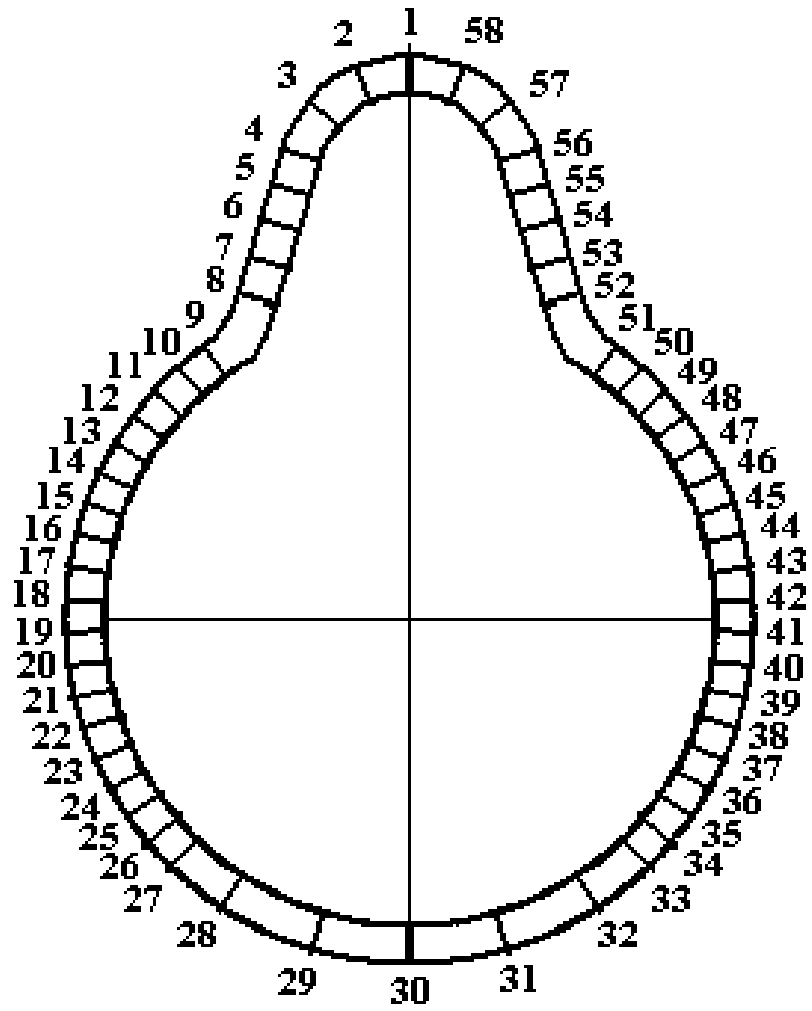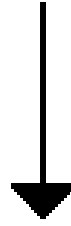
Figure 6.3: Port locations and corresponding port number definitions for the tail boom model.

tuator on the cylinder, and freestream Reynolds number for each type of actuator. Each case will show a waterfall plot of the pressure distributions and also a plot to show the percentage of pressure drag reduction compared to the baseline case with no actuators installed as each parameter changes.

6.1   Synthetic Jet Actuator Data

To illustrate the effect of the synthetic jet actuators on the tail boom pressure distribution, Figure 6.4 shows the change in the pressure distribution when the actuators are placed at x/c = 0.56, actuated using $1000V_{p-p}$ and Re $= 7.3 \times 10^4$ ($U_\infty = 22.2$ ft/s). The actuator off pressure distribution is represented by the black circles and the actuator on pressure distribution is represented by the red squares. The hollow points represent interpolated data to show an approximation of the pressure distribution over the blocked pressure ports. The magenta band shows the location of the actuators. The SJAs cause the pressure distribution near the actuator location to decrease slightly, although this is based on interpolation points and the actual effect may be more or less. The actuators also cause the pressure in the separated flow region (x/c = 1.0) to increase which leads to a reduction in pressure drag.

The ANOVA table for the synthetic jet actuators on the circular cylinder is given in Table 6.1. The mean square error used to compute the confidence interval is 2.45.
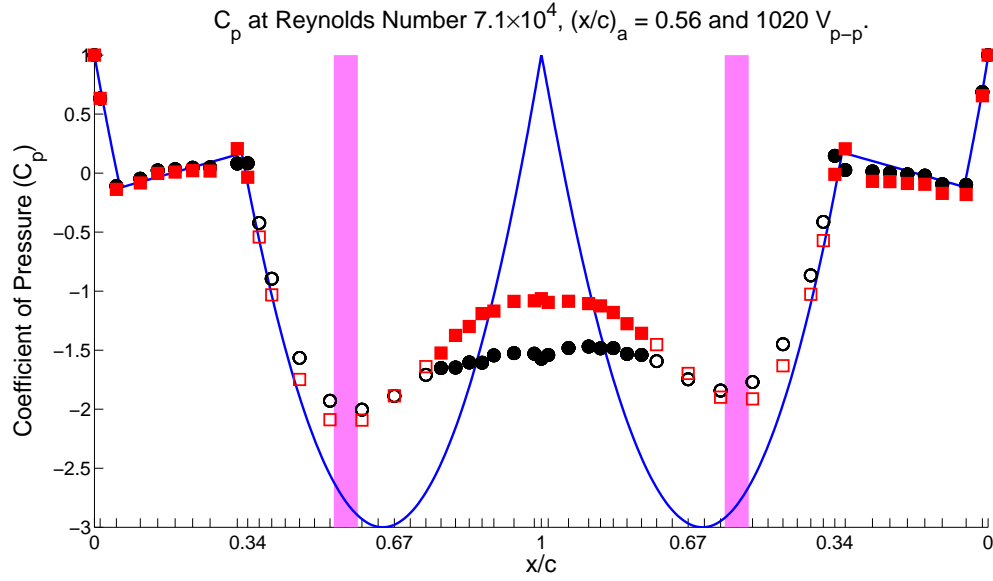
Figure 6.4: Pressure distribution showing the effect of two synthetic jet actuators on the tail boom pressure distribution when placed at $(x/c)_a = 0.56$ with an applied voltage of 1000 V_{p-p} and Re $= 7.3 \times 10^4$. ($U_\infty = 22.2$ ft/s, $(x/c)_s = 0.74$, $SD_{TB} = 0.11$)

ANOVA Table					
Source	DF	Type I SS	Mean Square	F Value	Pr > F
Position	4	41072.05620	10268.01405	4194.99	<.0001
Voltage	4	7554.86810	1888.71703	771.63	<.0001
Velocity	2	2948.44730	1474.22365	602.29	<.0001
Position*Voltage	16	3366.28180	210.39261	85.96	<.0001
Position*Velocity	8	2980.22052	372.52757	152.20	<.0001
Voltage*Velocity	8	2924.80609	365.60076	149.37	<.0001
Position*Voltage*Velocity	32	4644.80835	145.15026	59.30	<.0001

Table 6.1: ANOVA Table for synthetic jet actuators on the tail boom model.
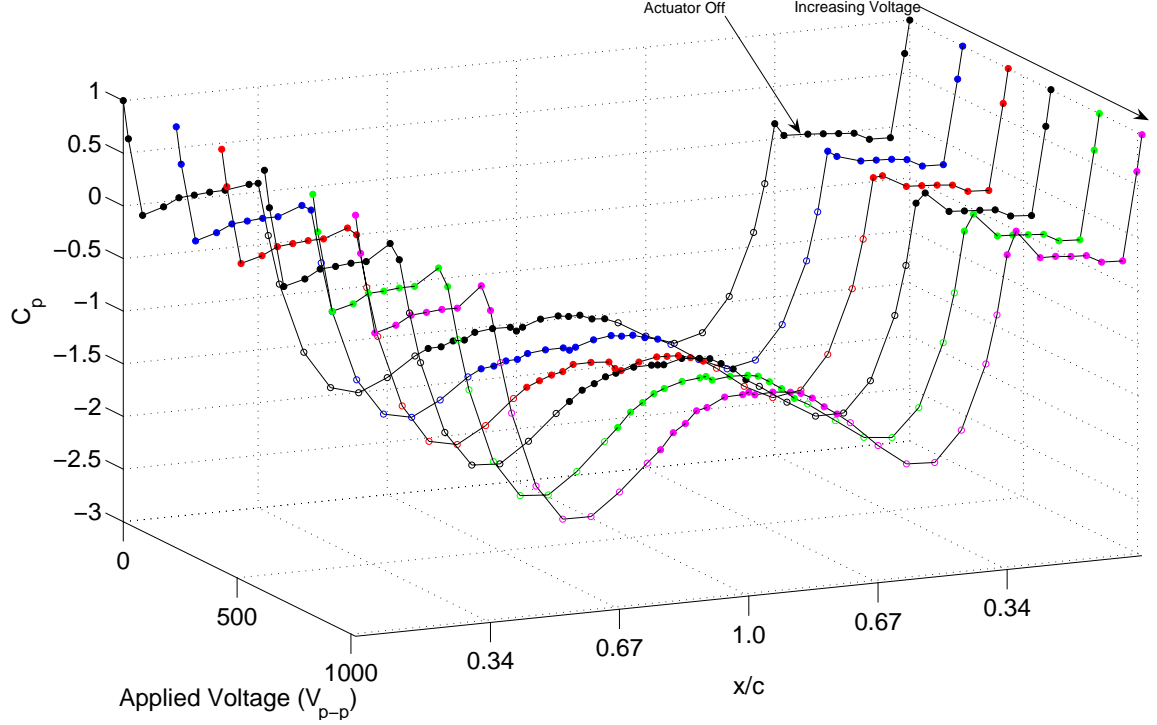
Figure 6.5: Waterfall plot of the variation in the pressure distribution as the applied voltage increases from $200V_{p-p}$ to $1000V_{p-p}$. (Re $= 7.3 \times 10^4$, $U_\infty = 22.2$ ft/s, $(x/c)_s = 0.74$, $(x/c)_a = 0.56$, $SD_{TB} = 0.11$)

6.1.1 Variation with Applied Voltage

Figure 6.5 shows the variation in the pressure distribution around the tail boom as the applied voltage increases from $200V_{p-p}$ to $1000V_{p-p}$ at increments of $200V_{p-p}$. The actuators are located at x/c = 0.56 and Re $= 7.3 \times 10^4$ ($U_\infty = 22.2$ ft/s, $(x/c)_s = 0.74$, $SD_{TB} = 0.11$). At the lowest applied voltage, the pressure distribution resembles the baseline pressure distribution. As the voltage increases, the pressure drops very slightly at the location of the actuators and the pressure in the separated flow region increases.

The corresponding percentage of pressure drag reduction for the pressure dis-
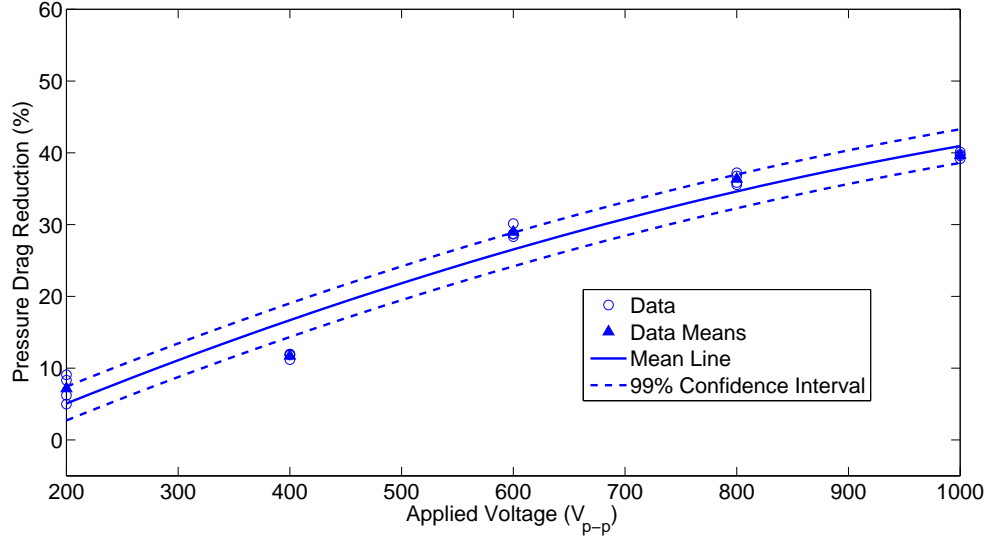
Figure 6.6: Percentage of pressure drag reduction as the applied voltage increases from $200V_{p-p}$ to $1000V_{p-p}$. (Re $= 7.3 \times 10^4$, $U_\infty = 22.2$ ft/s, $(x/c)_s = 0.74$, $(x/c)_a = 0.56$, $SD_{TB} = 0.11$)

tributions in Figure 6.5 is shown in Figure 6.6. As the voltage increases, the percentage of pressure drag reduction increases gradually at first (up to V $= 400V_{p-p}$) and then more quickly. Beyond V $= 600V_{p-p}$, the increasing pressure drag reduction starts to show evidence of a maximum percentage of pressure drag reduction but is not achieved within the voltages tested.

Increasing the applied voltage is similar to increasing the coefficient of momentum (C_μ). Figure 6.7 shows the same pressure distribution data shown in Figure 6.5 plotted using C_μ instead of voltage. This shows that large changes in the pressure distribution occur over a small range of low C_μ values, i.e. C_μ less than 0.022, beyond which, there is little change in the pressure distribution despite large changes in C_μ. This observation is also evident in Figure 6.8 where there is a rapid increase
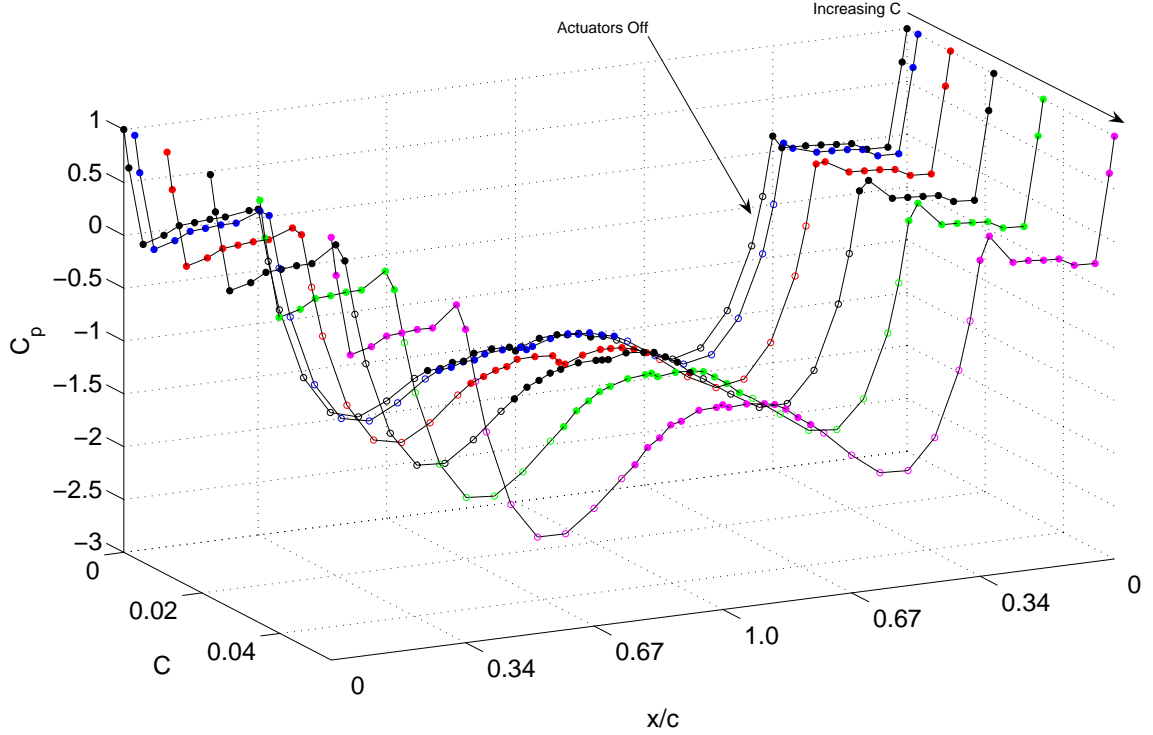
Figure 6.7: Waterfall plot of the variation in the pressure distribution as the coefficient of momentum increases from 0.003 to 0.053. (Re $= 7.3 \times 10^4$, $U_\infty = 22.2$ ft/s, $(x/c)_s = 0.74$, $(x/c)_a = 0.56$, $SD_{TB} = 0.11$)

in the pressure drag reduction up to $C_\mu = 0.022$ after which there is a gradual increase that approaches a local maximum up to $C_\mu = 0.053$.

6.1.2 Variation with Reynolds Number

The actuators were tested in flow velocities of 7.3, 14.6 and 22.2 ft/s to match the Reynolds numbers tested in the circular cylinder cases (Re $= 2.4 \times 10^4$, 4.8×10^4 and 7.3×10^4, $(x/c)_s = 0.67$, 0.67 and 0.74). Figure 6.9 shows the variation in the pressure distribution as Re increases. The actuators are located at $(x/c)_a = 0.49$ and the applied voltage is $1000V_{p-p}$. Increasing the flow velocity while maintaining
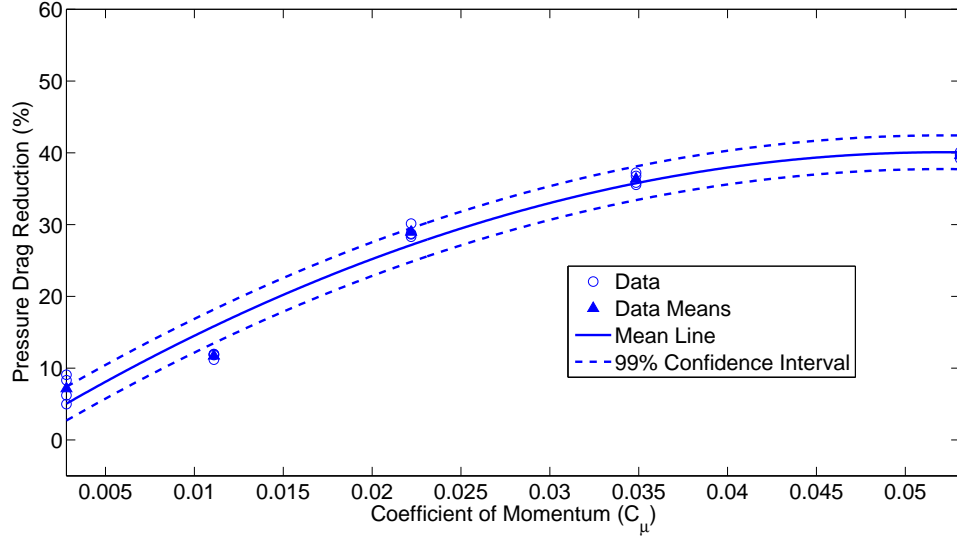
Figure 6.8: Percentage of pressure drag reduction as the coefficient of momentum increases from 0.003 to 0.053. (Re $= 7.3 \times 10^4$, $U_\infty = 22.2$ ft/s, $(x/c)_s = 0.74$, $(x/c)_a = 0.56$, $SD_{TB} = 0.11$)..

the applied voltage is similar to decreasing the momentum coefficient (C_μ). With an initial focus only on this effect, the expected trend was that the pressure distribution would be less effected as the velocity increases. However, the pressure near the location of the actuators decreases from 7.3 ft/s to 14.6 ft/s and increases from 14.6 ft/s to 22.2 ft/s and the pressure in the separated flow region increases with increasing velocity. This unexpected trend is due to the change in the location of flow separation as the velocity increases.

As seen in the circular cylinder cases, the proximity of the actuator to the separation point has a strong effect on the pressure distribution. On the tail boom model, the onset of flow separation occurs at the same location for the 7.3 ft/s and 14.6 ft/s cases $((x/c)_s = 0.67)$ but moves downstream for the 22.2 ft/s case
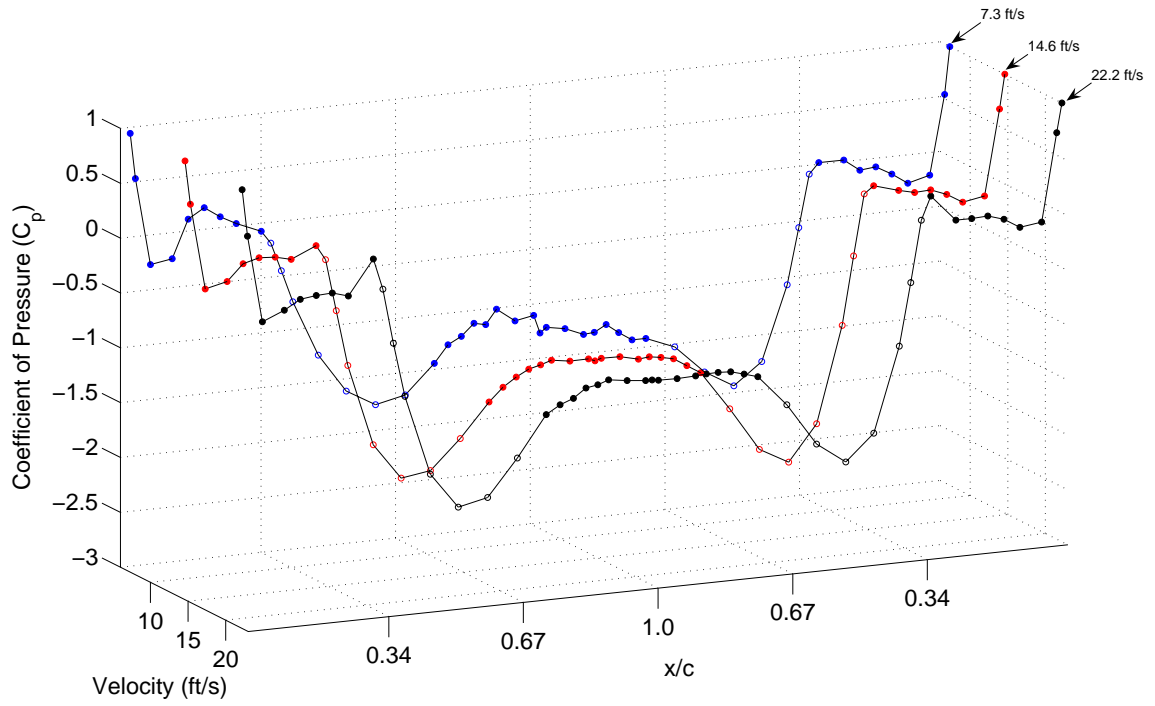
Figure 6.9: Waterfall plot of the variation in the pressure distribution as Re increases from 2.4×10^4 to 7.3×10^4. ($U\infty$ = 7.3 ft/s to 22.2 ft/s, $(x/c)_s$ = 0.67 to 0.71, $(x/c)_a$ = 0.49)

121

$((x/c)_s = 0.74)$ as shown in Figure 6.10. Therefore, as the flow velocity increases, specifically from 14.6 ft/s $(SD_{TB} = 0.18)$ to 22.2 ft/s $(SD_{TB} = 0.23)$, the distance between the actuator and flow separation point increases. This results in a decrease in actuator effectiveness due to the change in proximity between the two points (discussed further in Section 6.4) and the effective decrease in C_μ as the flow velocity increases.

Figure 6.11 shows the corresponding percentage of pressure drag reduction for the pressure distributions in Figure 6.9. From 7.3 ft/s to 14.6 ft/s, the pressure drag reduction increases as a result of the drop in the pressure near the location of the actuators and slight pressure increase in the separated flow region. From 14.6 ft/s to 22.2 ft/s, the pressure drag reduction decreases because the pressure in the separated flow region increases very slightly and the pressure near the location of the actuators increases. As mentioned in the previous paragraph, this is due to the increase in SD_{TB} and decrease in C_μ.

6.1.3   Variation with Actuator Position

Figure 6.12 shows the change in the pressure distribution as the actuator location moves downstream from $(x/c)_a = 0.43$ to 0.71 by two-port increments (equivalent to 11° on the larger diameter part of the model). The applied voltage is $1000V_{p-p}$ $(C_\mu = 0.053)$ and Re $= 7.3 \times 10^4$ $(U_\infty = 22.2$ ft/s, $(x/c)_s = 0.74)$. The pressure near the location of the actuators generally decreases until $(x/c)_a = 0.54$ and then increases at $(x/c)_a = 0.71$. The pressure in the separated flow region
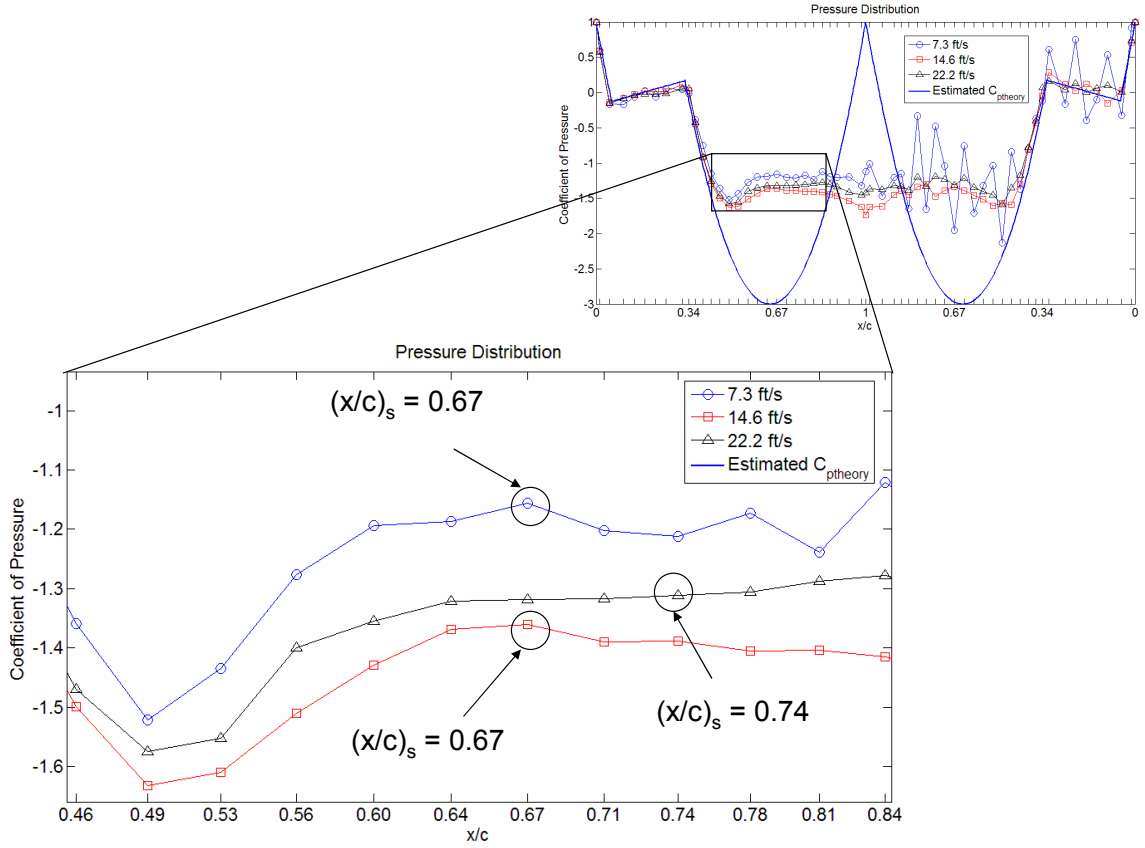
Figure 6.10: Pressure distribution for $\mathrm{Re} = 2.4 \times 10^4$, 4.8×10^4 and 7.3×10^4 (7.3, 14.6 and 22.2 ft/s, respectively) and a detailed view to show the change in the pressure distribution corresponding to the onset of flow separation at $(x/c)_s = 0.67$, 0.67, and 0.74 as the velocity increases.
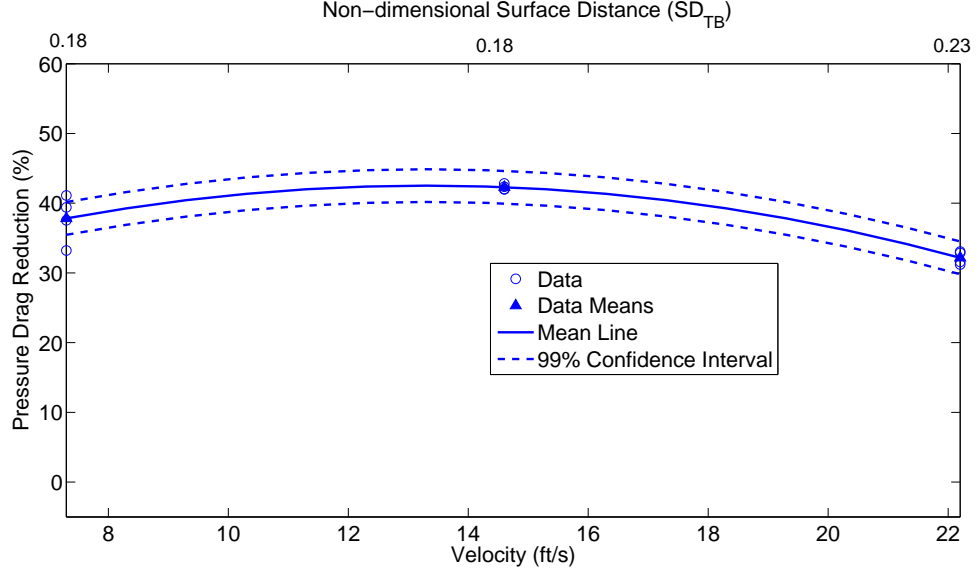
Figure 6.11: Percentage of pressure drag reduction as Re increases from 2.4×10^4 to 7.3×10^4. ($U\infty = 7.3$ ft/s to 22.2 ft/s, $(x/c)_s = 0.67$ to 0.71, $(x/c)_a = 0.49$)

increases from $(x/c)_a = 0.43$ to 0.49. Between $(x/c)_a = 0.49$ and 0.54, the pressure remains fairly constant and then decreases at $(x/c)_a = 0.71$.

Figure 6.13 shows the effect of moving the actuators downstream on the percentage of pressure drag reduction. Pressure drag reduction increases up to $(x/c)_a = 0.54$ and then decreases as $(x/c)_a$ continues to increase. The percentage of pressure drag reduction is also shown with an SD_{TB} on the top axis. This plot shows that the actuators are most effective at $SD_{TB} = 0.17$.

6.1.4 SD_{TB} vs C_μ

As discussed in the previous sections, two factors influence the effectiveness of the actuators for reducing pressure drag: the momentum coefficient (C_μ) and
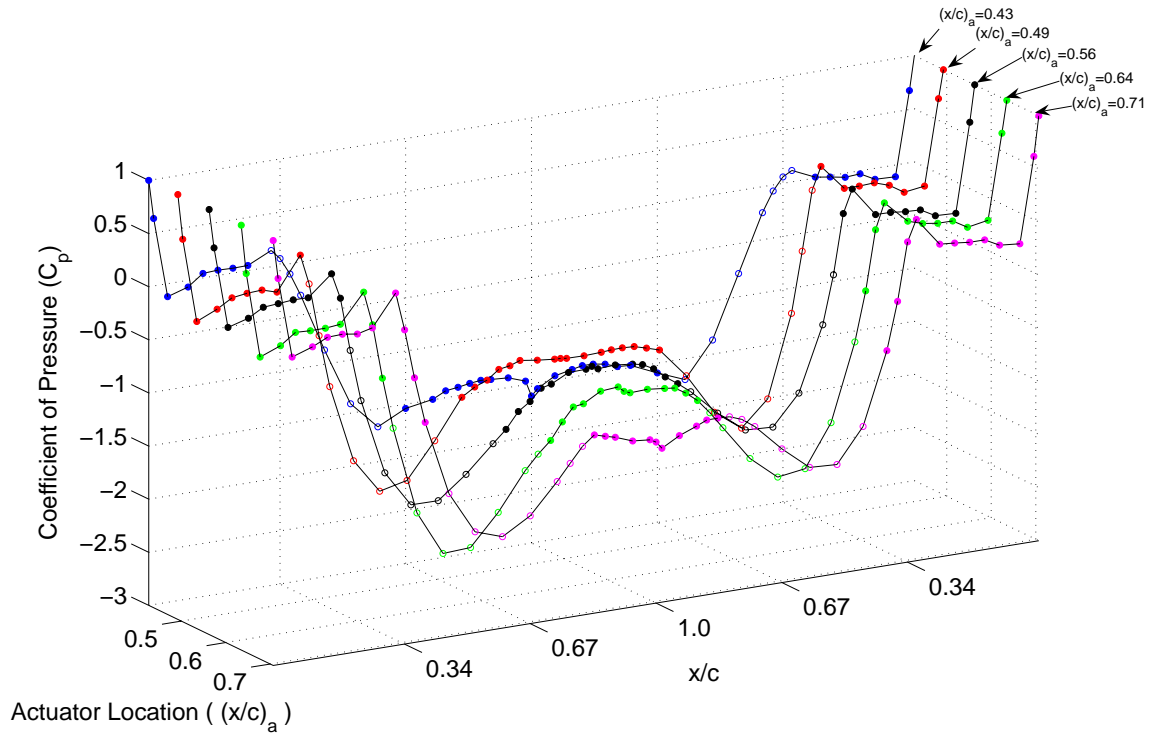
Figure 6.12: Waterfall plot of the variation in the pressure distribution as the actuator position moves downstream from $(x/c)_a = 0.43$ to 0.71. (Re $= 7.3 \times 10^4$, $U_\infty = 22.2$ ft/s, $(x/c)_s = 0.74$, V $= 1000V_{p-p}$, $C_\mu = 0.053$)
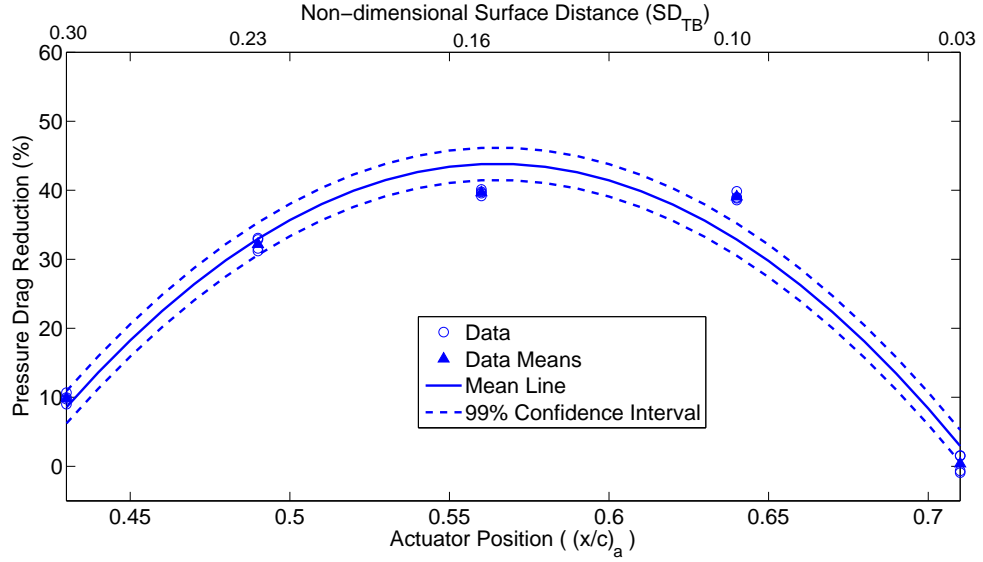
Figure 6.13: Percentage of pressure drag reduction as the actuator position moves downstream from $(x/c)_a = 0.43$ to 0.71. (Re $= 7.3 \times 10^4$, $U_\infty = 22.2$ ft/s, $(x/c)_s = 0.74$, V $= 1000V_{p-p}$, $C_\mu = 0.053$)

the distance between the flow separation point and the actuator position (SD_{TB}). The following contour plots show the effect of both parameters on the percentage of pressure drag reduction for each velocity. The black points on the contour plot represent the actual SD_{TB} and C_μ values for which the percentages of pressure drag reduction were taken.

Figure 6.14 shows the variation in pressure drag reduction with SD_{TB} and C_μ for Re $= 2.4 \times 10^4$ ($U_\infty = 7.3$ ft/s). For constant C_μ, the percentage of pressure drag reduction increases as SD_{TB} increases to 0.18, beyond which pressure drag reduction decreases rapidly. For constant SD_{TB}, the percentage of pressure drag reduction is relatively constant as C_μ increases except at $SD_{TB} = 0.18$ where pressure drag reduction steadily increases. This contour plot clearly shows that the actuators are
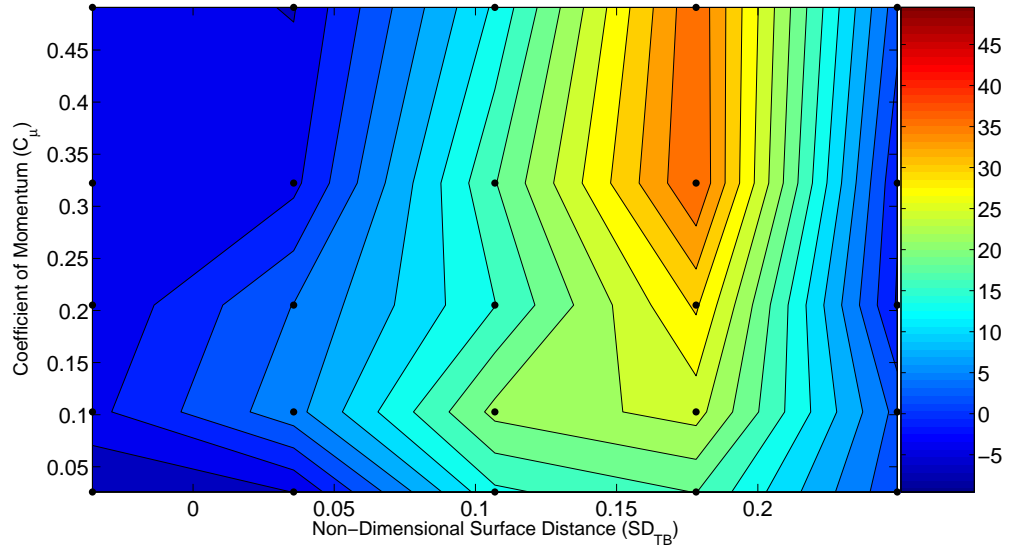
Figure 6.14: Non-dimensional surface distance (SD_{TB}) vs. applied voltage and the corresponding percentage of pressure drag reduction (color bar) for synthetic jet actuation at Re $= 2.4 \times 10^4$ $(U_\infty = 7.3$ ft/s$)$.

most effective at $SD_{TB} = 0.18$ for C_μ values above 0.2.

Figure 6.15 shows the variation in pressure drag reduction with SD_{TB} and C_μ for Re $= 4.8 \times 10^4$ $(U_\infty = 14.6$ ft/s$)$. For constant C_μ, the percentage of pressure drag reduction increases as SD_{TB} increases to 0.18 beyond which pressure drag reduction decreases rapidly (same as Figure 6.14). For constant SD_{TB}, the percentage of pressure drag reduction is relatively constant as C_μ increases above $C_\mu = 0.3$. This contour plot clearly shows, again, that the actuators are most effective at $SD_{TB} = 0.18$ for C_μ values above 0.3.

Figure 6.16 shows the variation in pressure drag reduction with SD_{TB} and C_μ for Re $= 7.3 \times 10^4$ $(U_\infty = 22.2$ ft/s$)$. For constant C_μ, the percentage of pressure drag reduction increases as SD_{TB} increases to 0.10 beyond which pressure drag reduction
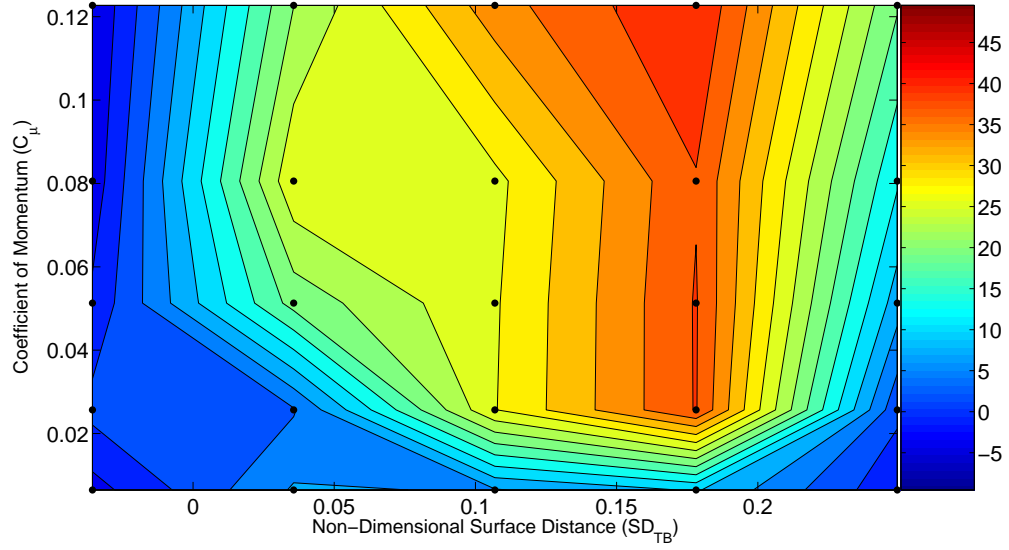
Figure 6.15: Non-dimensional surface distance (SD_{TB}) vs. applied voltage and the corresponding percentage of pressure drag reduction (color bar) for synthetic jet actuation at Re $= 4.8 \times 10^4$ ($U_\infty = 14.6$ ft/s).

is relatively constant up to $SD_{TB} = 0.25$ and then decreases gradually. For constant SD_{TB}, the percentage of pressure drag reduction increases as C_μ increases except for SD_{TB} less than 0.1 and greater than 0.25. This contour plot shows that the actuators are most effective between $SD_{TB} = 0.1$ and 0.25 for C_μ values above 0.2.

Based on all three contour plots (Figures 6.14 - 6.16), the range of SD_{TB} values for which the actuators are most effective centers around $SD_{TB} = 0.18$ but this range expands as velocity increases. This could be due to increased instability in the laminar flow as velocity increases and, therefore, the actuators can influence the boundary layer over a wider range of operating parameters.
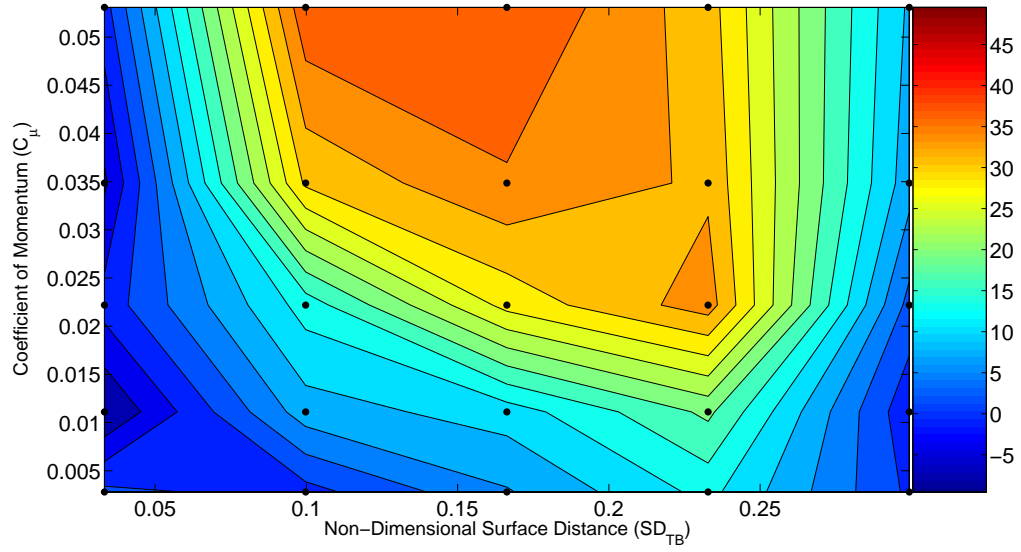
Figure 6.16: Non-dimensional Distance (SD_{TB}) vs. applied voltage and the corresponding percentage of drag reduction (color bar) for synthetic jet actuation at Re $= 7.3 \times 10^4$ ($U_\infty = 22.2$ ft/s).

6.2 Plasma Actuator Data

This section provides results and trends for using plasma actuators on the tail boom model and varying the actuator position, applied voltage and the flow velocity. To illustrate the effect of the plasma actuators on the for a single test case, Figure 6.17 shows the pressure distribution when the actuators are off (black circles), when the actuators are off (red squares) and the estimated inviscid theoretical pressure distribution. The actuators are located at $(x/c)_a = 0.64$, the applied voltage is 11.7kV_{p-p} and Re $= 7.3 \times 10^4$ ($U_\infty = 22.2$ ft/s, $(x/c)_s = 0.74$, $SD_{TB} = 0.10$). The pressure distribution for the actuator off case is similar to the baseline case shown in Figure 6.1 where the flow separates around x/c $= 0.65$. When the actuators are turned on, the pressure drops near the location of the actuators and

129
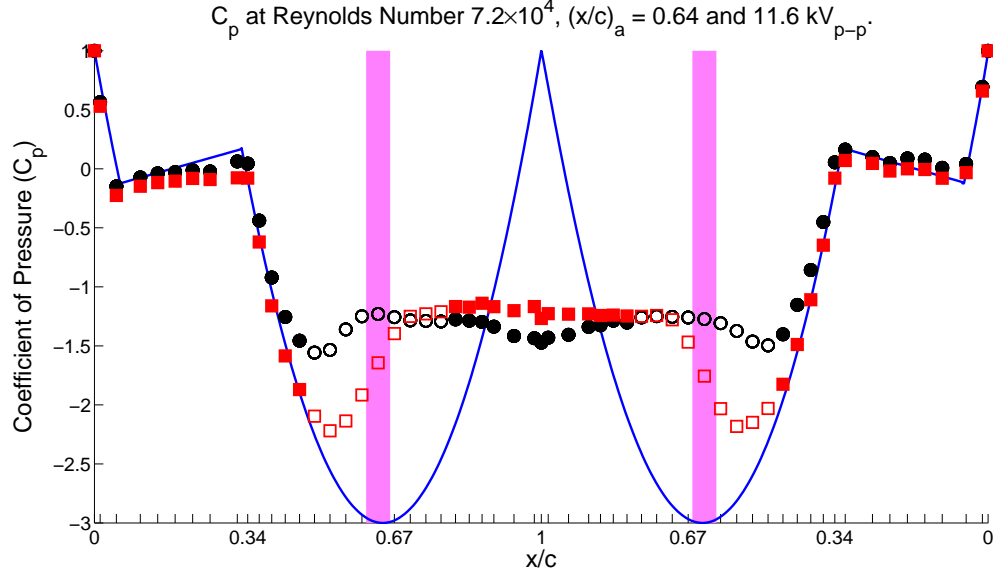
Figure 6.17: Pressure distribution showing the effect of two plasma actuators on the tail boom pressure distribution when placed at $(x/c)_a = 0.64$ with an applied voltage of $11.7 \mathrm{kV}_{p-p}$ and $\mathrm{Re} = 7.3 \times 10^4$. ($U_\infty = 22.2$ ft/s, $(x/c)_s = 0.74$, $SD_{TB} = 0.10$)

the pressure in the separated flow region increases. These changes in the pressure distribution are both beneficial for delaying flow separation and reducing pressure drag. At operating conditions where the pressure near the location of the actuators is significantly decreased ($C_{p_{min}} < -2.5$), there is evidence of a laminar separation bubble indicated by a small region of constant pressure in the presence of an adverse pressure gradient. This unique feature of the pressure distribution due to plasma actuation is discussed in Chapter 5.

The ANOVA table for the synthetic jet actuators on the circular cylinder is given in Table 6.1. The mean square error used to compute the confidence interval is 5.24.

ANOVA Table					
Source	DF	Type I SS	Mean Square	F Value	Pr > F
Position	4	8131.58405	2032.89601	388.14	<.0001
Voltage	6	64885.44305	10814.24051	2064.77	<.0001
Velocity	2	4449.49392	2224.74696	424.77	<.0001
Position*Voltage	24	6476.13334	269.83889	51.52	<.0001
Position*Velocity	8	2094.35025	261.79378	49.98	<.0001
Voltage*Velocity	12	6858.45177	571.53765	109.12	<.0001
Position*Voltage*Velocity	48	18333.84641	381.95513	72.93	<.0001

Table 6.2: ANOVA Table for plasma actuators on the tail boom model.

6.2.1 Variation with Applied Voltage

Figure 6.18 shows the change in the pressure distribution as the applied voltage increases from $2.8\text{k}V_{p-p}$ to $11.7\text{k}V_{p-p}$ by increments of $1.4\text{k}V_{p-p}$. The actuators are located at $(x/c)_a = 0.64$ and $\text{Re} = 7.3 \times 10^4$ ($U_\infty = 22.2$ ft/s, $(x/c)_s = 0.74$, SD_{TB} = 0.10). As the applied voltage increases, the pressure near the actuators decreases dramatically and the pressure in the separated flow region increases gradually. Also, the onset of flow separation moves downstream indicating that flow separation is delayed. All of these changes in the pressure distribution are beneficial for decreasing pressure drag.

Figure 6.19 shows the change in the percentage of pressure drag reduction as the applied voltage is increased. The percentage of pressure drag reduction is relatively constant up to $7\text{k}V_{p-p}$, beyond which, the pressure drag reduction increases
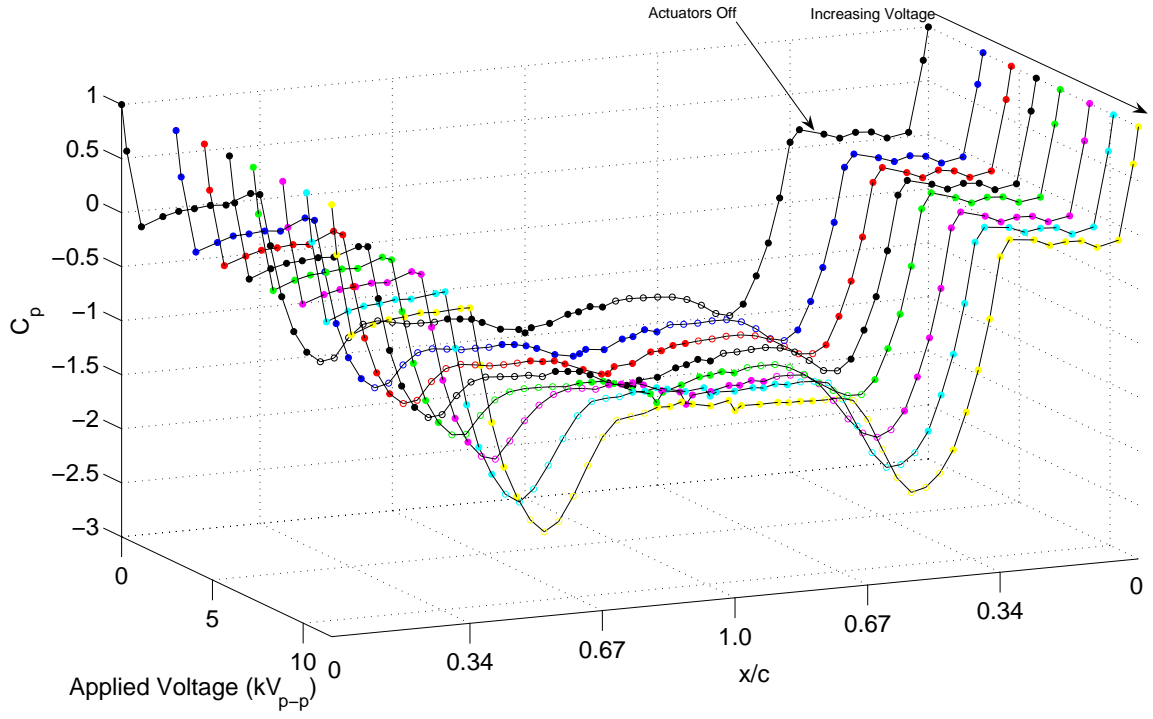
Figure 6.18: Waterfall plot of the variation in the pressure distribution as the applied voltage increases from $2.8 \text{k}V_{p-p}$ to $11.7 \text{k}V_{p-p}$. (Re $= 7.3 \times 10^4$, $U_\infty = 22.2$ ft/s, $(x/c)_s = 0.74$, $(x/c)_a = 0.64$, $SD_{TB} = 0.10$)
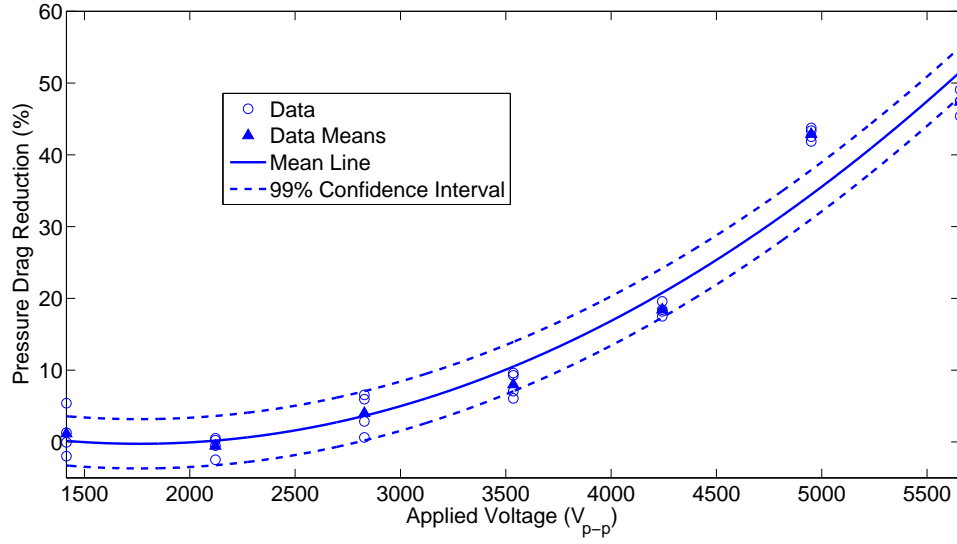
Figure 6.19: Percentage of pressure drag reduction as the applied voltage increases from $2.8\text{k}V_{p-p}$ to $11.7\text{k}V_{p-p}$. (Re $= 7.3 \times 10^4$, $U_\infty = 22.2$ ft/s, $(x/c)_s = 0.74$, $(x/c)_a = 0.64$, $SD_{TB} = 0.10$)

until the applied voltage reaches $10\text{k}V_{p-p}$ and then starts to level off. Increasing the applied voltage is similar to increasing C_μ and, as seen in previous sections where voltage is varied, there is a maximum attainable effectiveness when increasing C_μ has no additional benefit. The change in the pressure drag reduction at the highest applied voltages starts to show the same trend.

6.2.2 Variation with Reynolds Number

Figure 6.20 shows the change in the pressure distribution as Re increases from 2.4×10^4 to 7.3×10^4 ($U\infty = 7.3$ ft/s to 22.2 ft/s, $(x/c)_s = 0.67$ to 0.74). The actuators are located at $(x/c)_a = 0.49$ and the applied voltage is $10.3\text{k}V_{p-p}$. As the velocity increases, the momentum coefficient is effectively decreasing and a decrease
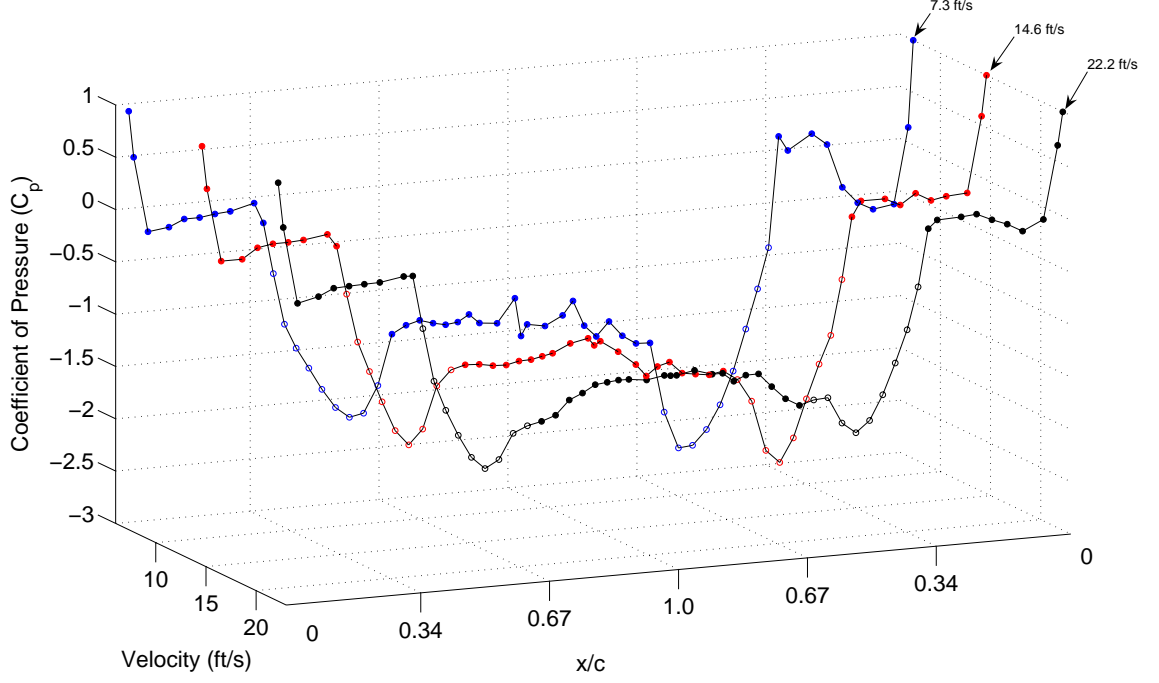
Figure 6.20: Waterfall plot of the variation in the pressure distribution as Re increases from 2.4×10^4 to 7.3×10^4. ($U_\infty = 7.3$ ft/s to 22.2 ft/s, $(x/c)_s = 0.67$ to 0.74, $(x/c)_a = 0.49$, V $= 10.3 \mathrm{k} V_{p-p}$)

in actuator effectiveness is expected. However, as the velocity increases, there is a slight pressure increase in the separated flow region but, for the most part, there is no change in the pressure distribution.

Figure 6.21 shows the percentage of pressure drag reduction as the flow velocity increases. There is almost no change in the pressure drag reduction as velocity increases. As mentioned before, C_μ is not the only parameter affecting actuator performance. As velocity increases, the location corresponding to the onset of flow separation changes (See Figure 6.10). In this case, increasing velocity increases the distance between the actuator location and the flow separation point and, thereby, increasing SD_{TB}. The decrease in C_μ and increase in SD_{TB} seem to balance the
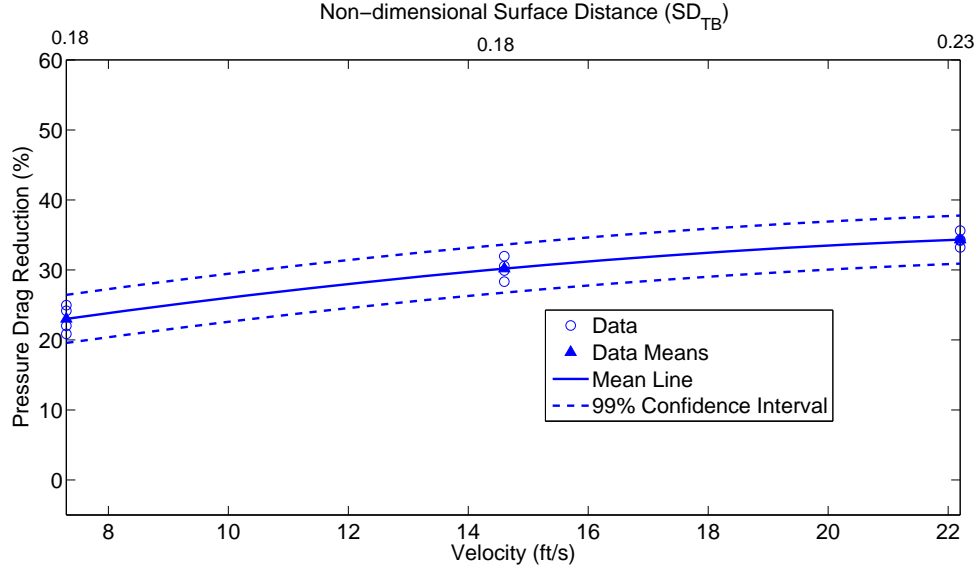
Figure 6.21: Percentage of pressure drag reduction as Re increases from 2.4×10^4 to 7.3×10^4. ($U_\infty = 7.3$ ft/s to 22.2 ft/s, $(x/c)_s = 0.67$ to 0.74, $(x/c)_a = 0.49$, V $= 10.3 \text{k}V_{p-p}$)

actuator effectiveness such that there is no change in pressure drag reduction.

6.2.3   Variation with Actuator Position

Figure 6.22 shows the variation in the pressure distribution as the actuator position moves downstream from $(x/c)_a = 0.43$ to 0.71. The applied voltage is $11.7 \text{k}V_{p-p}$ and Re $= 7.3 \times 10^4$ ($U_\infty = 22.2$ ft/s, $(x/c)_s = 0.74$). As the port location moves downstream, the pressure near the location of the actuators generally decreases until the actuators are at $(x/c)_a = 0.64$ but increases at $(x/c)_a = 0.71$. The pressure in the separated flow region also increases from $(x/c)_a = 0.64$ but decreases at $(x/c)_a = 0.71$.

At $(x/c)_a = 0.56$, there is evidence, based on the pressure distribution, of de-
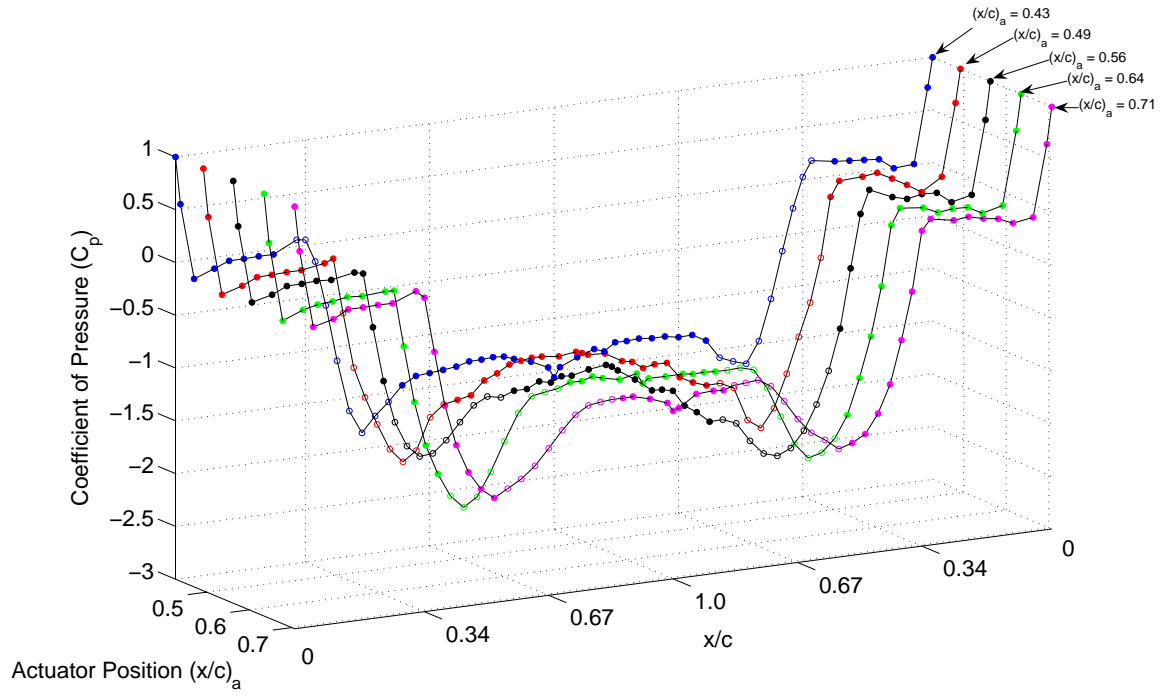
Figure 6.22: Waterfall plot of the variation in the pressure distribution as the

actuator position moves downstream from $(x/c)_a = 0.43$ to 0.71.

(Re $= 7.3 \times 10^4$, ($U_\infty = 22.2$ ft/s, $(x/c)_s = 0.74$, V $= 11.7$kV_{p-p})
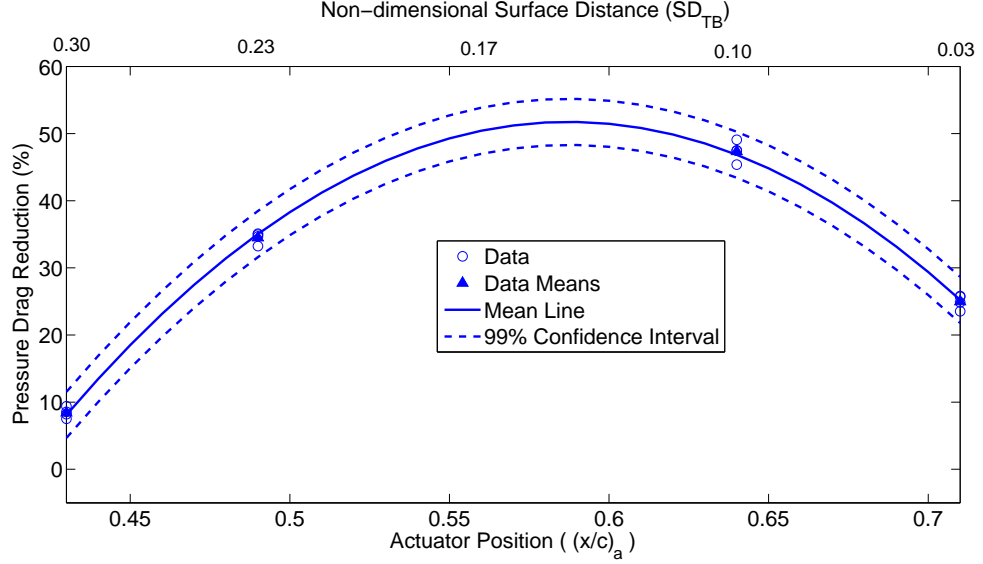
Figure 6.23: Percentage of pressure drag reduction as the actuator position moves downstream from $(x/c)_a = 0.43$ to 0.71. (Re $= 7.3 \times 10^4$, ($U_\infty = 22.2$ ft/s, $(x/c)_s = 0.74$, V $= 11.7\text{k}V_{p-p}$)

creased effectiveness on one side (x/c $= 0$ to 1.0) and increased effectiveness on the other side (x/c $= 1.0$ to 0) of the model. This appears to be due to asymmetries in the actuator construction and placement. Because the drag coefficient is calculated based on the pressure distribution from x/c $= 0$ to 1.0, Figure 6.23 shows a decrease in actuator effectiveness at this point ($(x/c)_a = 0.56$). This also affected the polynomial fit of the mean line such that the values for $(x/c)_a = 0.49$ and 0.64 were excluded from the confidence interval. This point is not representative of the true trend and is believed to be higher than the value presented. Therefore, this point was not used in calculating the quadratic fit and the pressure drag reduction increases from $(x/c)_a = 0.49$ to 0.64 and decreases at $(x/c)_a = 0.71$. The peak in pressure drag reduction data corresponds to $SD_{TB} = 0.10$.

6.2.4 SD_{TB} vs. Applied Voltage

As discussed in the previous sections, two factors influence the effectiveness of the actuators for reducing pressure drag: the applied voltage (similar to (C_μ)) and the distance between the flow separation point and the actuator position (SD_{TB}). The following contour plots show the effect of both parameters on the percentage of pressure drag reduction for each velocity. The black points on the contour plot represent the actual SD_{TB} and C_μ values for which the percentages of pressure drag reduction were taken.

Figure 6.24 shows the variation in pressure drag reduction as SD_{TB} and applied voltage for Re $= 2.4 \times 10^4$ ($U_\infty = 7.3$ ft/s). For constant applied voltage, there is relatively little change in the pressure drag reduction as SD_{TB} increases for applied voltages below $8V_{p-p}$. For an applied voltage around $9kV_{p-p}$, the pressure drag reduction is largest at $SD_{TB} = 0.05$. For the highest applied voltage, the pressure drag reduction is largest for SD_{TB} greater than 0.15.

Figure 6.25 shows the variation in pressure drag reduction as SD_{TB} and applied voltage for Re $= 4.8 \times 10^4$ ($U_\infty = 14.6$ ft/s). For constant applied voltage, pressure drag reduction is fairly constant as SD_{TB} increases except at applied voltages above $8kV_{p-p}$ where there is a peak in pressure drag reduction at $SD_{TB} = 0.05$. As the applied voltage increases above $8kV_{p-p}$, the peak pressure drag reduction occurs over a slightly wider range of SD_{TB} values. For a constant SD_{TB}, is fairly constant up to an applied voltage of $6kV_{p-p}$, beyond which, the pressure drag reduction quickly increases until the maximum effectiveness for that SD_{TB} value is achieved.
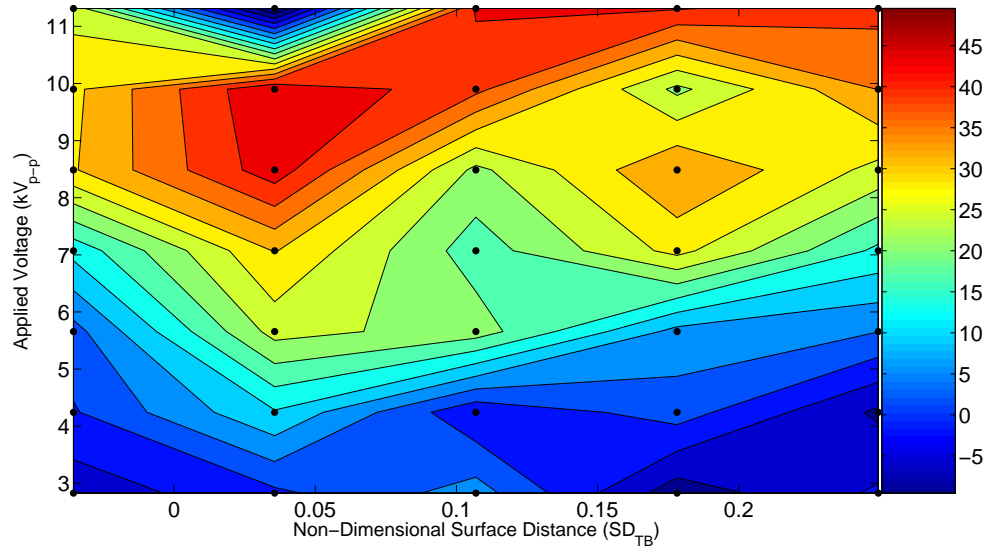
Figure 6.24: Non-dimensional surface distance (SD_c) vs. applied voltage and the corresponding percentage of pressure drag reduction (color bar) for plasma actuation at Re = 2.4×10^4 (U_∞ = 7.3 ft/s).
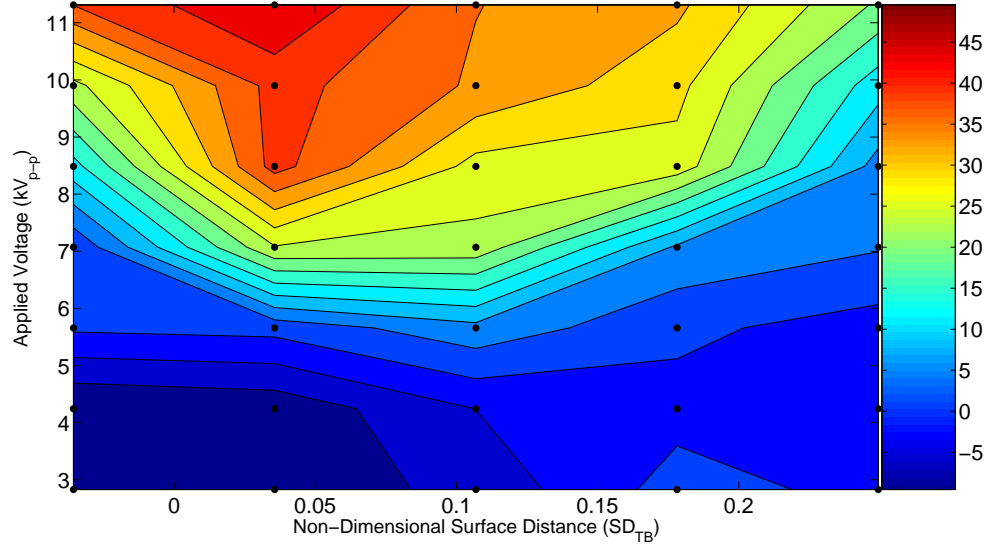
Figure 6.25: Non-dimensional surface distance (SD_c) vs. applied voltage and the corresponding percentage of pressure drag reduction (color bar) for plasma actuation at Re = 4.8×10^4 (U_∞ = 14.6 ft/s).
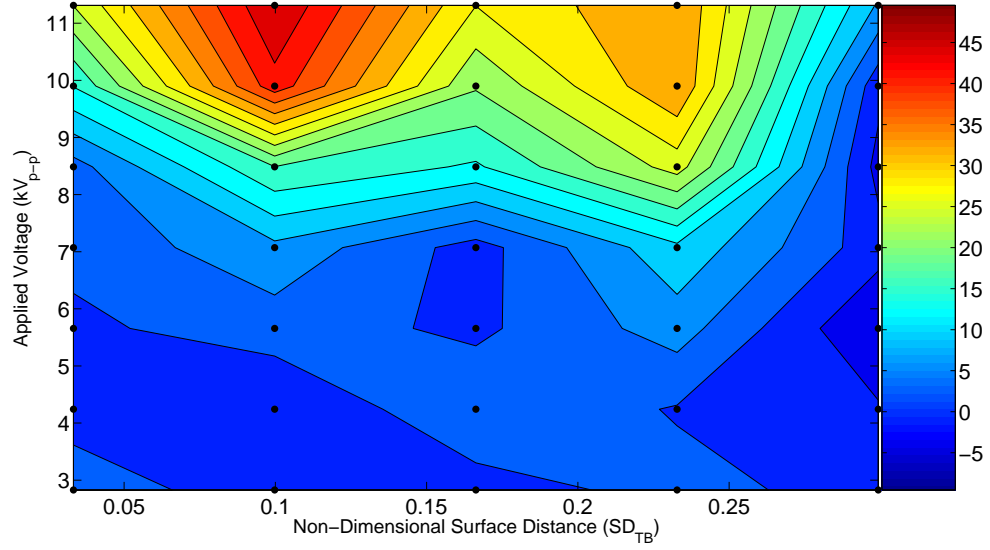
Figure 6.26: Non-dimensional surface distance (SD_c) vs. applied voltage and the corresponding percentage of pressure drag reduction (color bar) for plasma actuation at Re = 7.3×10^4 (U_∞ = 22.2 ft/s).

Figure 6.26 shows the variation in pressure drag reduction as SD_{TB} and applied voltage for Re = 7.3×10^4 (U_∞ = 22.2 ft/s). For constant applied voltage, the pressure drag reduction is relatively constant as SD_{TB} increases for applied voltages below 8kV_{p-p}. For applied voltages above 8kV_{p-p}, pressure drag reduction increases quickly up to SD_{TB} = 0.15 and starts to decrease significantly past SD_{TB} = 0.35. However, there is a dip in the pressure drag reduction at SD_{TB} = 0.25.

Based on all three plots (Figures 6.24 - 6.26), the minimum applied voltage for significant pressure drag reduction increases as velocity increases which agrees with the trend of decreased actuator performance as C_μ decreases. There appears to be little connection in actuator performance between applied voltage and SD_{TB} values when looking at these three plots. Although never measured in this research,

other research shows that C_μ is around O(10^{-7}) to O(10^{-5}) for plasma actuators and could support the decreasing range of actuator effectiveness as velocity increases. The high voltages used in the plasma actuators precluded use of a velocity sensor in close proximity to the devices, and thus values of C_μ were not available for the plasma actuators. It is expected that drag reduction associated with interaction between C_μ and SD_{TB} may have exhibited stronger correlation than voltage and SD_{TB}. In general, however, when the actuators are closer to the flow separation point, the maximum pressure drag reduction occurs at a lower applied voltage than when the actuators are farther from the flow separation point. This trend is due to localized influence of the plasma actuators. When the actuators are close to the location corresponding to the minimum pressure coefficient, they have a large effect on $C_{p,min}$. When the actuators are closer to the rear half of the model, they affect the pressure in the separated flow region which has a slightly stronger influence on the total pressure drag reduction.

6.3 Summary of Observations for Synthetic Jet and Plasma Actuators on a Tail Boom Shape

Chapter 6 shows the effect of varying applied voltage, Re and actuator position on the pressure distribution and the percentage of pressure drag reduction for each type of flow control device. In summary:

1) For synthetic jet actuation:

a) As voltage (C_μ) increases, the pressure distribution is increasingly influenced

and the percentage of pressure drag reduction increases, especially beyond C_μ values above 0.2.

b) As the freestream velocity increases, the variation in the pressure distribution and percentage of pressure drag reduction do not follow the expected trend of decreasing effectiveness. Actuator effectiveness is actually dependant on the fixed location of the actuator relative to the changing location of flow separation (SD_c) in addition to the momentum coefficient (C_μ).

c) As the actuator angular position moves downstream, the actuator effectiveness increases until a maximum is achieved based on the location of the actuator relative to the separation point.

d) There is an apparent optimal range for peak actuator performance between $SD_{TB} = 0.10$ and 0.25, approximately.

2) For plasma actuation the same trends are seen as in the synthetic jet actuation except:

a) The minimum applied voltage required for significant pressure drag reduction increases with increasing velocity which matches the trend of decreased actuator performance as C_μ decreases.

b) The effect of the plasma actuators on the pressure distribution and pressure drag reduction depends on SD_{TB}. For relatively low values of SD_{TB}, the actuators affect the pressure in the separated flow region and result in higher pressure drag reduction results at lower applied voltages than for relatively high values of SD_{TB}.

Chapter 7

Conclusions and Future Work

7.1   Conclusions

This thesis has provided valuable insight on a number of trends and character-
istics of the effect of synthetic jet and plasma actuation on the pressure distribution
associated with flow over bluff body shapes. The primary contribution of this work
is the pressure distribution data associated with these two very different actuators
for varied applied voltage, actuator position and flow velocity on a circular cylin-
der and 2D extrusion of a rotorcraft tail boom cross section. Two non-dimensional
parameters were also used to evaluate the effect of the actuators: the coefficient
of momentum (C_μ) and the non-dimensional distance between the location of the
actuator and the flow separation point (SD).

Both bluff body shapes were tested in freestream conditions where Re $=$
2.4×10^4, 4.8×10^4 and 7.3×10^4. For the circular cylinder model, these Re values
corresponded to $U_\infty = 10$, 20 and 30 ft/s and flow separation locations at 100°, 95°
and 85°, respectively. The actuators were placed from $\pm 50°$ to $\pm 90°$ at 10° incre-
ments. The applied voltages for the synthetic jets were from $200V_{p-p}$ to $1000V_{p-p}$
at increments of $200V_{p-p}$. The applied voltages for the plasma actuators were from
$2.8kV_{p-p}$ to $11.8kV_{p-p}$ at increments of $1.4kV_{p-p}$.

On the tail boom model, the Re values listed above corresponded to $U_\infty =$

7.3, 14.6 and 22.2 ft/s and flow separation locations at $(x/c)_s = 0.67$, 0.67 and 0.74. The actuators were placed at $(x/c)_a = 0.43$, 0.49, 0.56, 0.64, 0.71. The synthetic jet and plasma actuators were operated at the same applied voltages as stated above.

Two symmetrically placed synthetic jet actuators on the circular cylinder decrease the pressure near the location of the actuators and increase the pressure in separated flow region over the rear half of the cylinder. As the applied voltage increases, the effectiveness of the actuators also increases as does the percentage of pressure drag reduction. Increasing the applied voltage is similar to increasing C_μ. Up to $C_\mu = 0.02$, the pressure drag reduction increases and for C_μ values greater than 0.02, there is little additional pressure drag reduction. As flow velocity increases, both C_μ and SD_c are affected. C_μ decreases as velocity increases and SD_c decreases because the flow separation point moves closer to the actuator position as velocity increases. Of the two parameters, actuator effectiveness is more influenced by the variation in SD_c. As the position of the actuators moves downstream, the actuator effectiveness depends on SD_c. Contour plots showing the change in the pressure drag reduction as C_μ and SD_c reveal that the highest percentage of pressure drag reduction is achieved for SD_c values between 0.15 and 0.4. These results are well summarized in Figures 4.16 - 4.18.

At some angular positions, operating one synthetic jet actuator has the same effect on the pressure distribution as operating two actuators. A similar affect was reported in Amitay [6] and it was suggested that suction forces from the actuated side of the cylinder caused the streamlines from the unactuated side to be drawn closer to the cylinder surface. This results in attached flow over the unactuated side

side of the cylinder.

The plasma actuators on the circular cylinder decrease the pressure near the location of the actuators and increases the pressure in the separated flow region over the rear half of the cylinder. As the applied voltage increases, the effectiveness of the actuators increases by further decreasing the pressure near the actuators and increasing the pressure in the separated flow region. However, when Re is low such that a high applied voltage results in a very steep adverse pressure gradient, evidence of a laminar separation bubble appears on the pressure distribution. The presence of the separation bubble forces boundary layer transition to turbulent flow but, overall, results in a decrease in drag reduction. As the flow velocity increases, the actuator effectiveness is influenced by the movement of the flow separation point upstream thereby decreasing SD_c and, in addition, the value of C_μ decreases. Similar to the synthetic jet actuation results, plasma actuator drag reduction is influenced by SD_c at high C_μ values and by C_μ just outside of the optimal ranges of SD_c. As the actuator location moves downstream, the percentage of drag reduction reaches a local maximum between $SD_c = 0.2$ and 0.4. These results are well summarized in Figures 5.14 - 5.16. When operating one plasma actuator, the actuator only affects the pressure distribution near the location of the actuator and increases the base pressure on the same side as the actuator.

On the tail boom model, the synthetic jet actuators have a very similar effect on the pressure distribution as on the circular cylinder as C_μ and SD_{TB} varied. The results of synthetic jet actuation on the tail boom model are well summarized using contour plots (Figures 6.14 - 6.16) of the percentage of drag reduction as C_μ

145

and SD_{TB} increase. These plots show that actuation is most effective for C_μ values greater than 0.2 and for SD_{TB} values between 0.10 and 0.25. In addition, the range of SD_{TB} values for which the actuators are most effective increases as Re increases and the minimum C_μ where increased drag reduction occurs decreases. These effects are due to the increase in boundary layer instabilities as velocity increases which allows the actuators to have an effect over a wider range of SD_{TB} and C_μ values.

The effects of the plasma actuators on the pressure distribution over the tail boom model were also very similar to their effect on the circular cylinder as the applied voltage and SD_{TB} were varied. The results of plasma actuation on the tail boom model are well summarized using contour plots (Figures 6.24 - 6.26 of the percentage of pressure drag reduction as the applied voltage and SD_{TB} are varied. These plots show that, as velocity increases, the minimum C_μ required for significant drag reduction increases. Also, the range of effective values of SD_{TB} decreases as velocity increases. This effect is opposite of the synthetic jet actuation effect and due to the low induced body force produced by the plasma actuators.

7.2   Future Work

The results presented in this thesis provide a foundation for evaluating the potential of using synthetic jet and plasma actuators on bluff body shapes. Many of the variables used to show trends and observations made in this thesis are over a small range. Future work is required for a more complete analysis of the potential and limitations of the actuators on bluff bodies.

146

In the experimental setup, there are several options that would provide more thorough and simpler data acquisition. To address the problem of blocked pressure ports, there are several options for acquiring a more complete picture of the pressure distribution and resulting drag. Provided the models were constructed using SLA (for manufacturing simplicity), hollow cavities within the thickness of the model wall leading from the pressure port to the bottom of the model would allow the pressure distribution to be read despite blockages from inside the model. Another option is the use of pressure sensitive paint to not only provide a complete picture of the pressure distribution but also be used as a flow visualization method.

For measuring the drag and drag reduction associated with using flow control, a drag balance would be a direct approach for measuring pressure drag and skin friction drag. The results provided in this thesis report the reduction of pressure drag. However, as stated in Chapter 1, the skin friction drag inherently increases with delayed flow separation meaning the total drag reduction is less than the reported pressure drag reduction.

The SD parameter introduced in this thesis shows promise as a very valuable parameter for predicting the optimal location for actuator placement. SD is defined here as the normalized surface distance, however, the actual mechanism relating the optimal actuator location to the flow separation point may actually be dependent on something more complicated such as the shape of the boundary layer profile at the optimal actuator position. A measurement of boundary layer profiles along a variety of surfaces compared to the actuator effectiveness at those locations would provide insight for the relationship between the two sets of results.

Other avenues of future work include investigation of the anomaly of actuator performance for the plasma actuators on the circular cylinder at 30 ft/s. It is possible that there is another parameter, such as the Strouhal number, that varies throughout these tests that was not considered but, in this particular case, is very important. In addition, a more complete analysis of the results including complete statistical analysis to understand the correlation between the results. The SAS software produced a large amount of results but only the means and confidence intervals were used. The rest of the results indicate if the apparent optimal positions are actually unique results or if they are relatively similar to other results indicating a large percentage of pressure drag reduction.

Toward a more practical and meaningful results for the industrial aerospace community, the actuators need to be tested at higher Reynolds numbers and the development of using the actuators in arrays. As the results indicate, the plasma actuators affect the pressure distribution locally whereas the synthetic jet actuators affect the pressure distribution globally. An array of one type of actuator or a combination of both types of actuators would lead to even greater flow control authority. As mentioned in the beginning of the thesis, the motivation for this research was an interest in using the synthetic jet or plasma actuators on an AH-64 Apache tail boom to alleviate aerodynamic forcing from the rotor. Because the induced flow from the rotor and the shape of the tail boom are three-dimensional, the flow conditions along the length of the tail boom vary. Once the effect of the actuators on the tail boom shape is fully characterized, arrays of actuators and sensors can be mounted to control the flow separation and pressure drag on the tail

boom.

Because these actuators are influential in low Re conditions, future work should be directed toward testing the actuators on UAVs and MAVs. They actuators are light and compact making them easy to install on a small aircraft. An issue with these actuators that will need to be addressed, especially the plasma actuators, is supplying them with the required voltage signal. The plasma actuators require very high voltage at a very high frequency and, to date, the power supplies for such requirements are heavy and weight requirements for UAVs and MAVs are low. Future work could also involve developing a lightweight power supply to power the actuators.

Appendix A

Pressure Distribution Plots

The following pressure distribution plots show the effect of using synthetic jet or plasma actuators on the circular cylinder or tail boom model. The title of each plot indicates the Reynolds Number, actuator position, and C_μ (for the synthetic jet actuator cases) or the applied voltage (for the plasma actuator cases). Each figure contains:

    1) a solid blue line representing the inviscid theoretical pressure distribution over the model,

    2) magenta bands indicating the location of the actuators on the model,

    3) solid black dots with error bars representing the pressure distribution over the model when the actuators are off and the black dots without error bars are interpolated points.

    4) solid red squares with error bars representing the pressure distribution over the model when the actuators are on and the red squares without error bars are interpolated points.
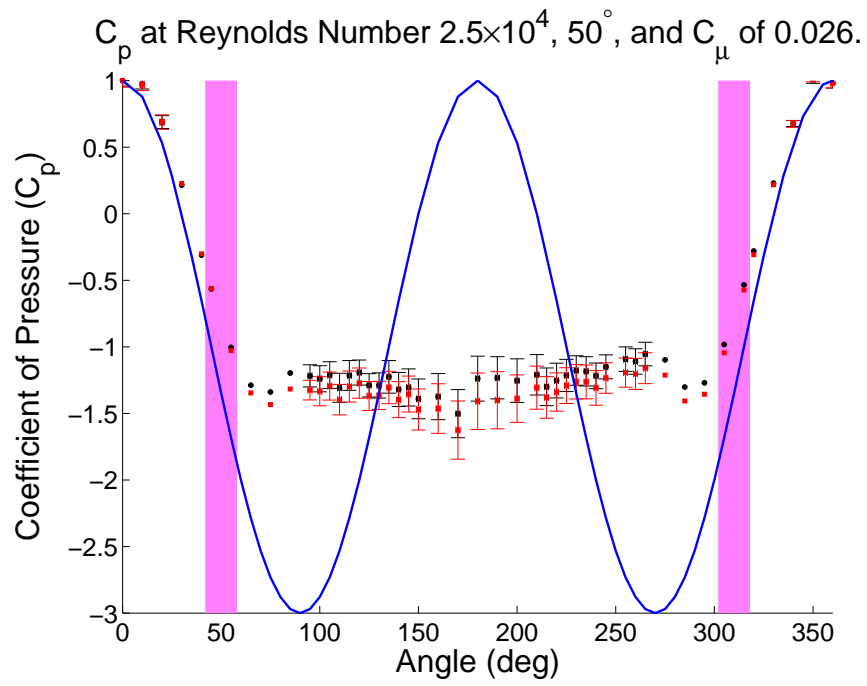
Figure A.1: Synthetic Jet Actuators on a Circular Cylinder.
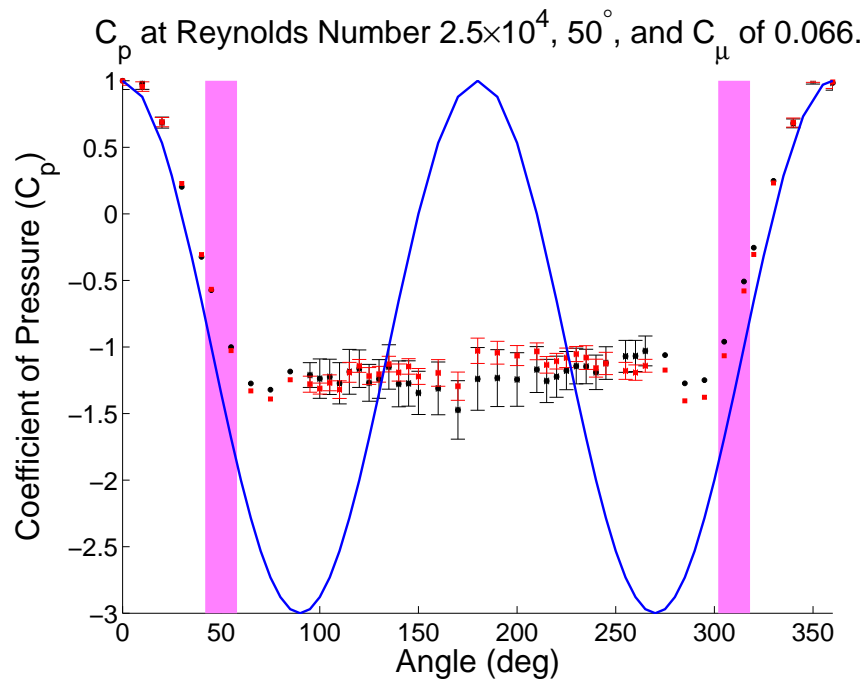
Figure A.2: Synthetic Jet Actuators on a Circular Cylinder.
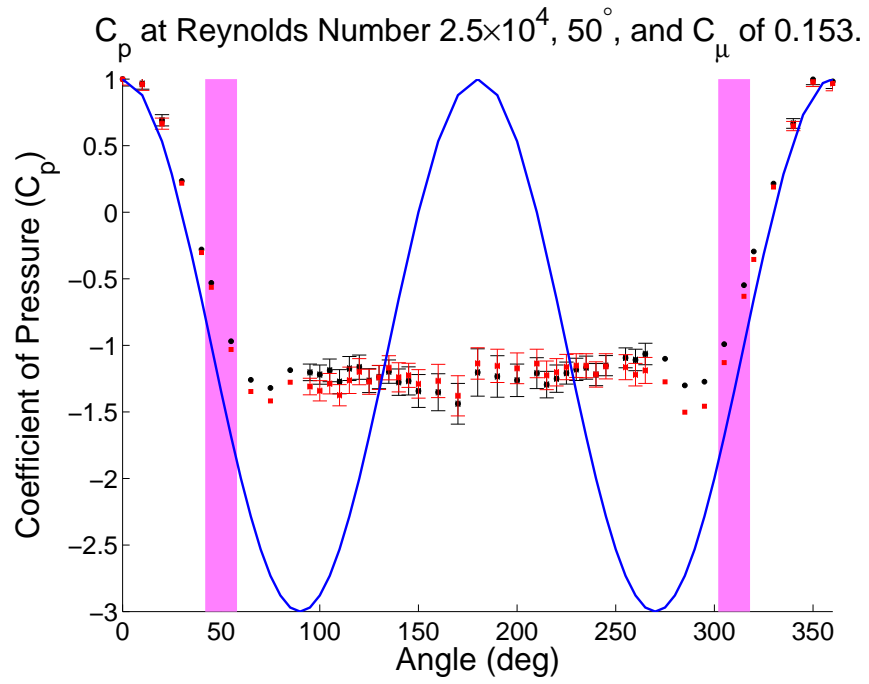
Figure A.3: Synthetic Jet Actuators on a Circular Cylinder.
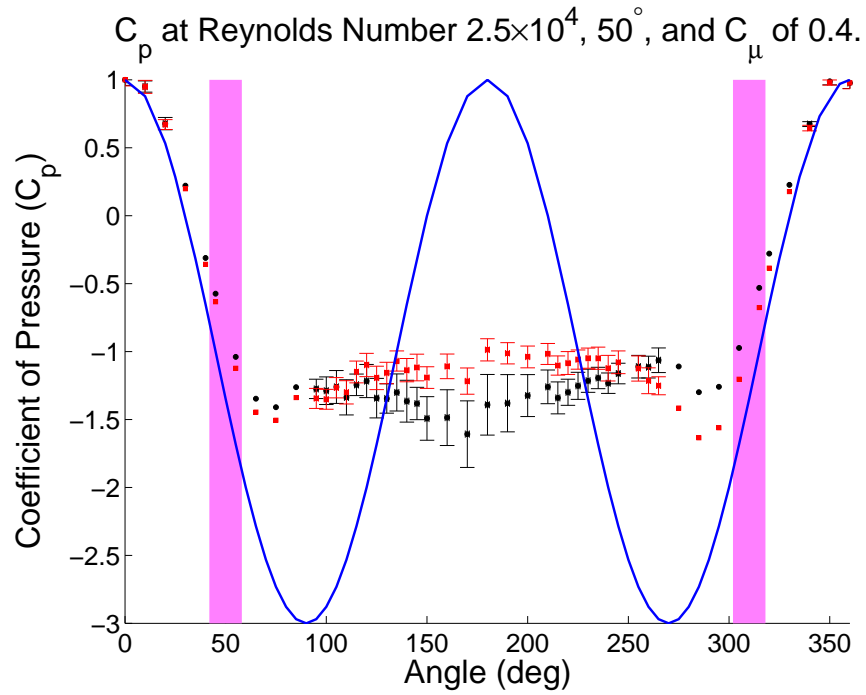
Figure A.4: Synthetic Jet Actuators on a Circular Cylinder.
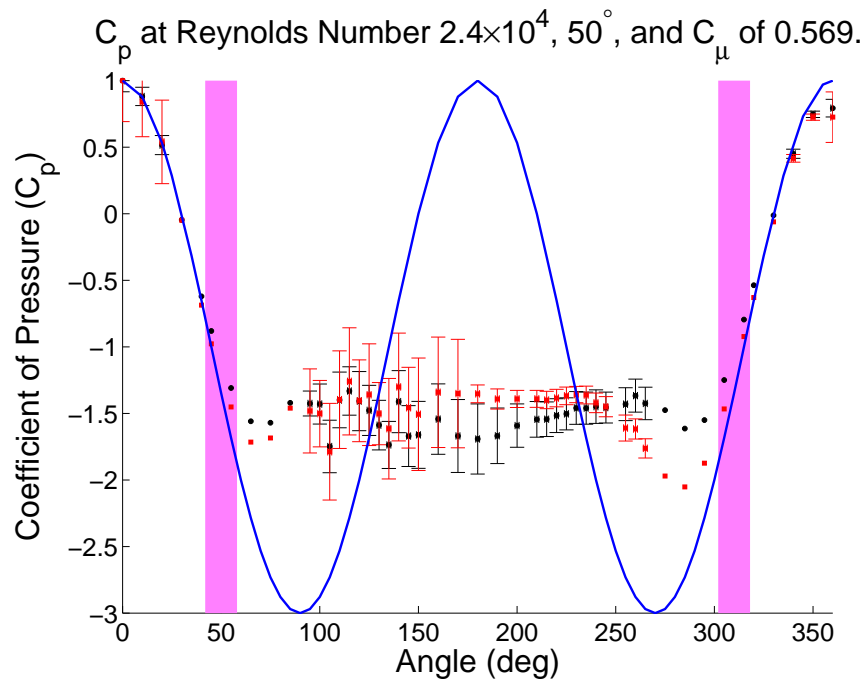
Figure A.5: Synthetic Jet Actuators on a Circular Cylinder.
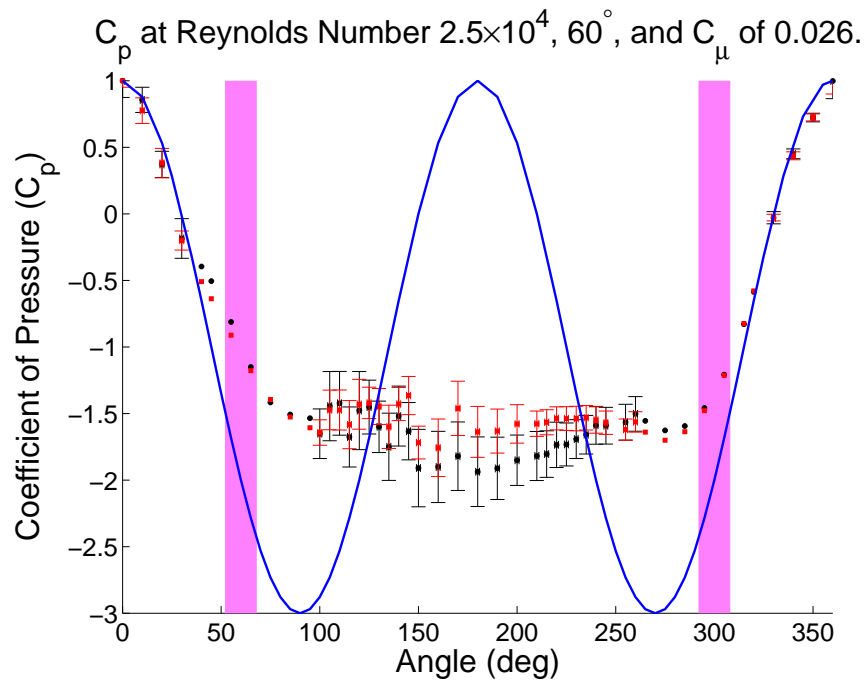
Figure A.6: Synthetic Jet Actuators on a Circular Cylinder.
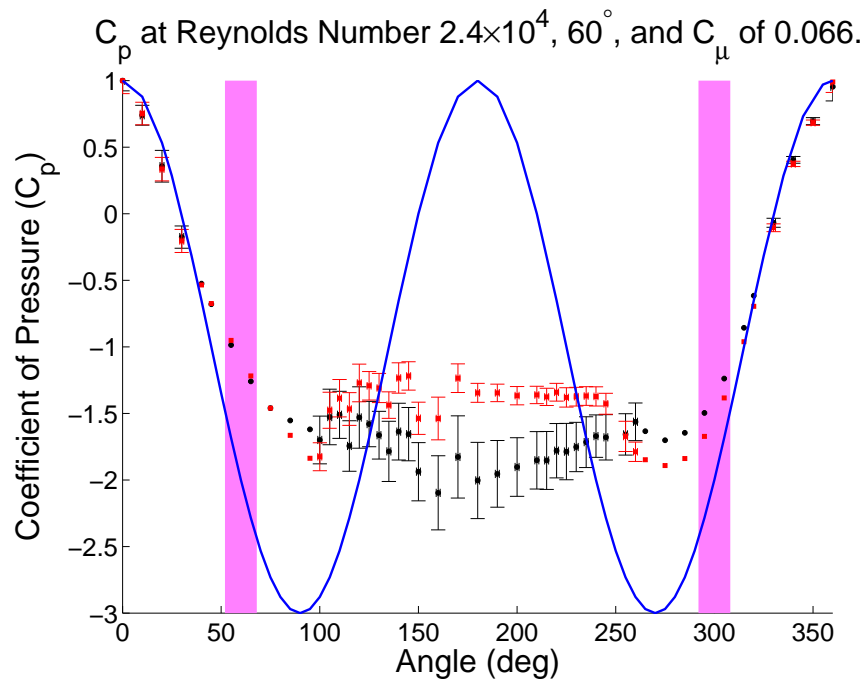
Figure A.7: Synthetic Jet Actuators on a Circular Cylinder.
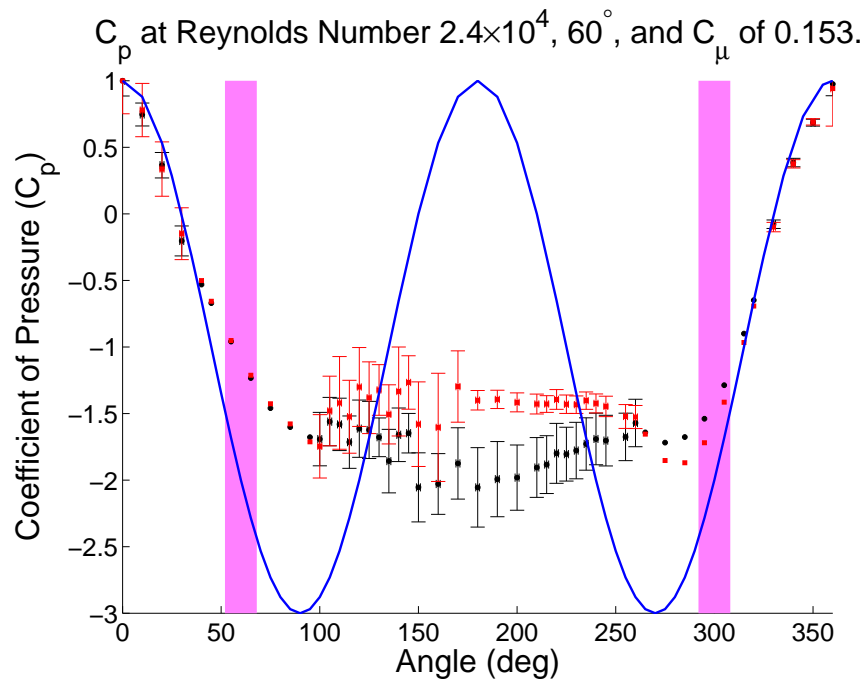
Figure A.8: Synthetic Jet Actuators on a Circular Cylinder.
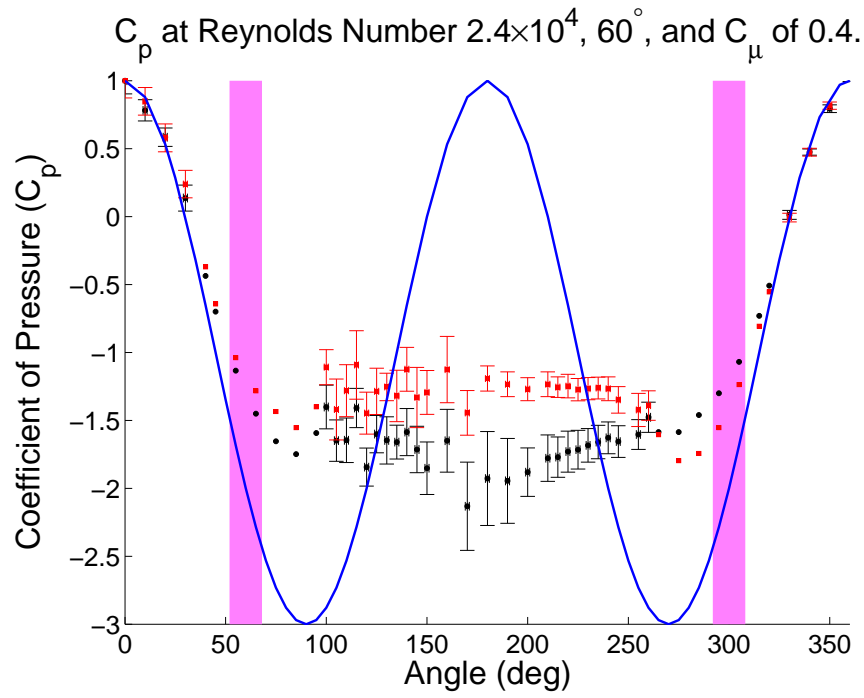
Figure A.9: Synthetic Jet Actuators on a Circular Cylinder.
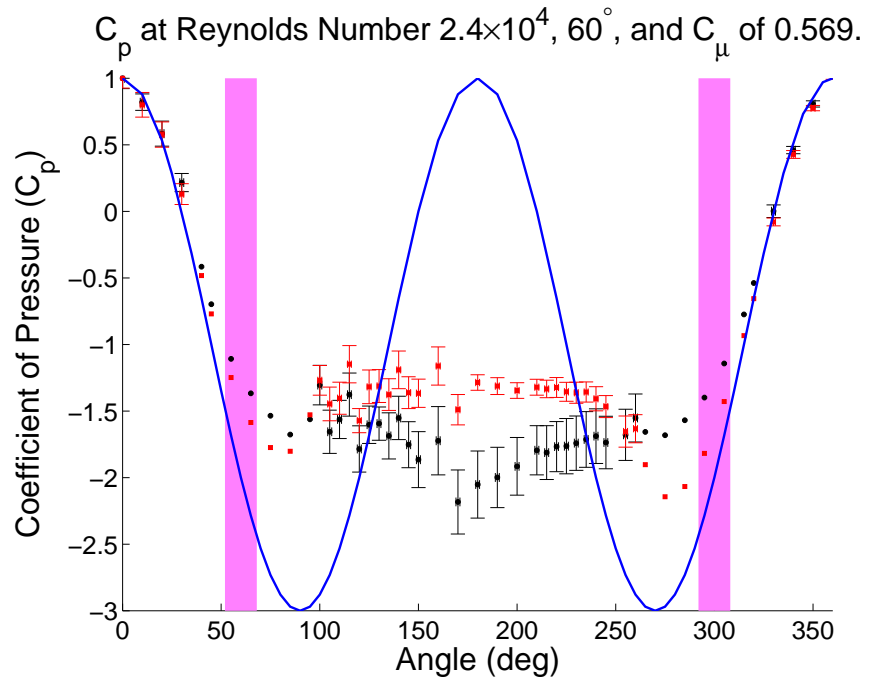
Figure A.10: Synthetic Jet Actuators on a Circular Cylinder.
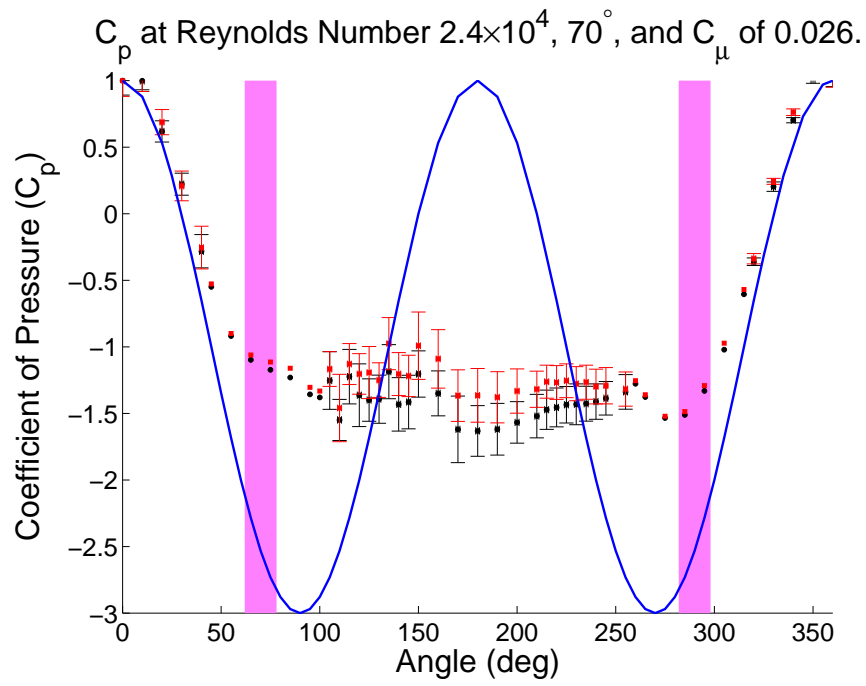
Figure A.11: Synthetic Jet Actuators on a Circular Cylinder.
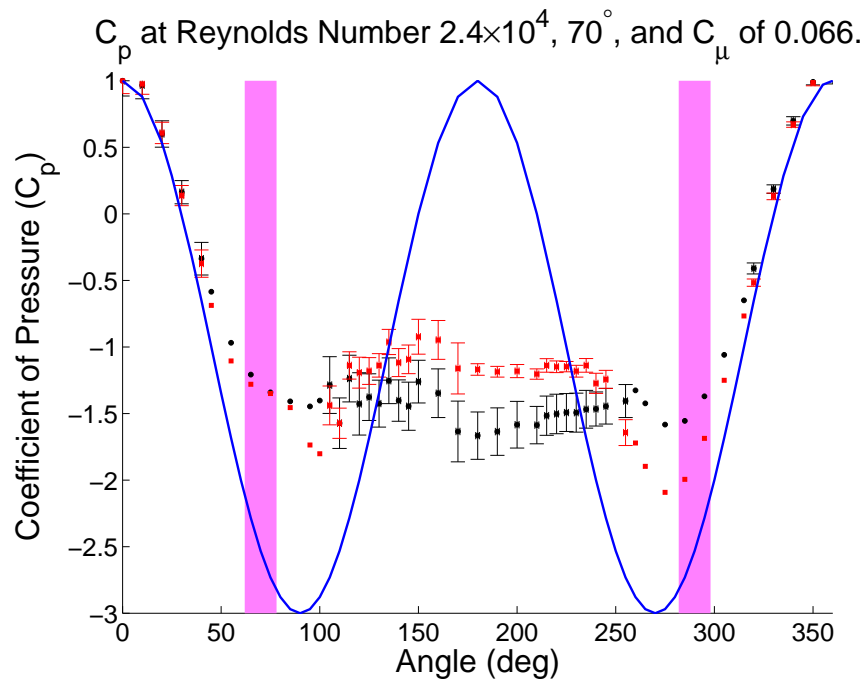
Figure A.12: Synthetic Jet Actuators on a Circular Cylinder.
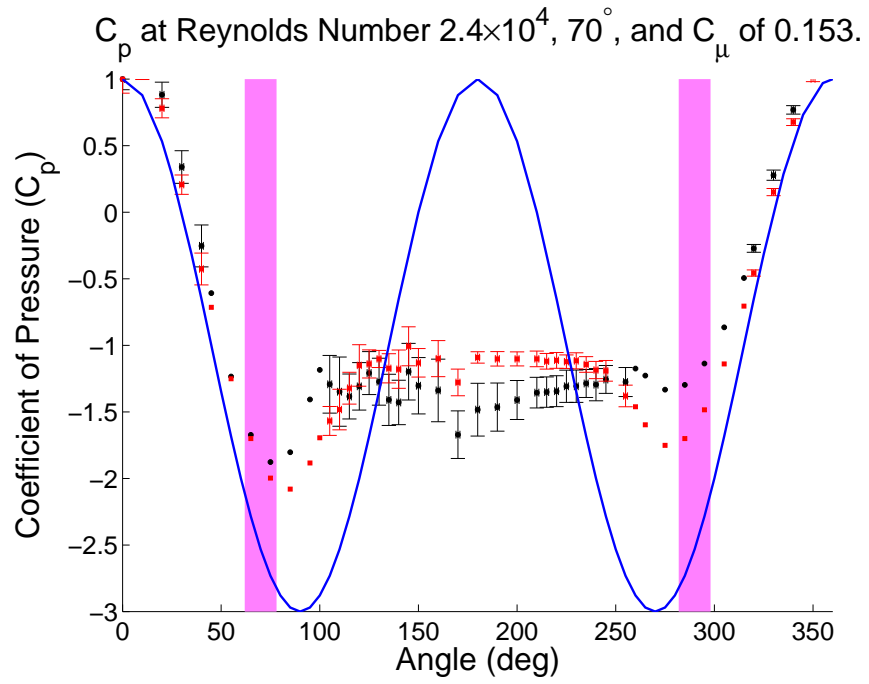
Figure A.13: Synthetic Jet Actuators on a Circular Cylinder.
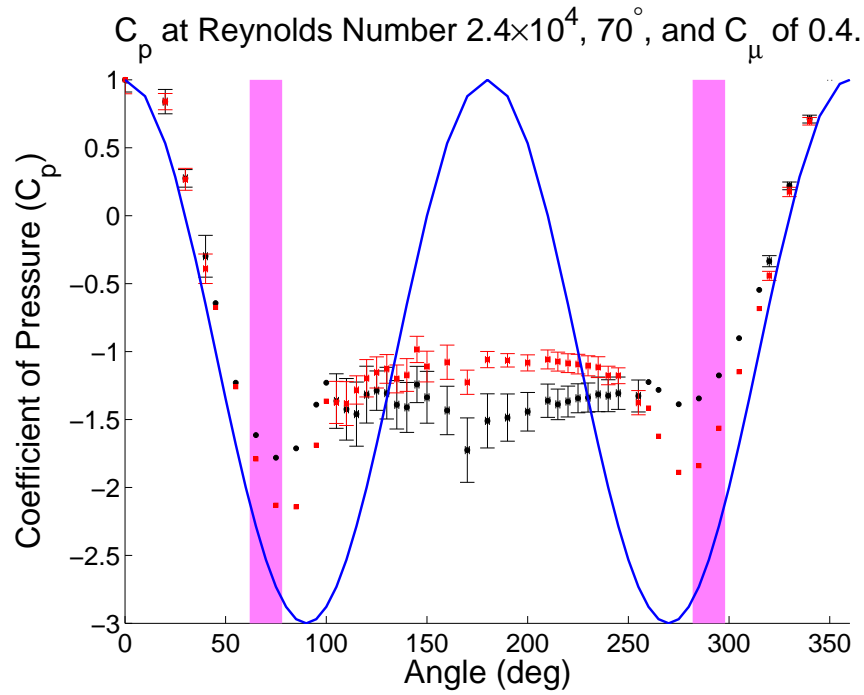
Figure A.14: Synthetic Jet Actuators on a Circular Cylinder.
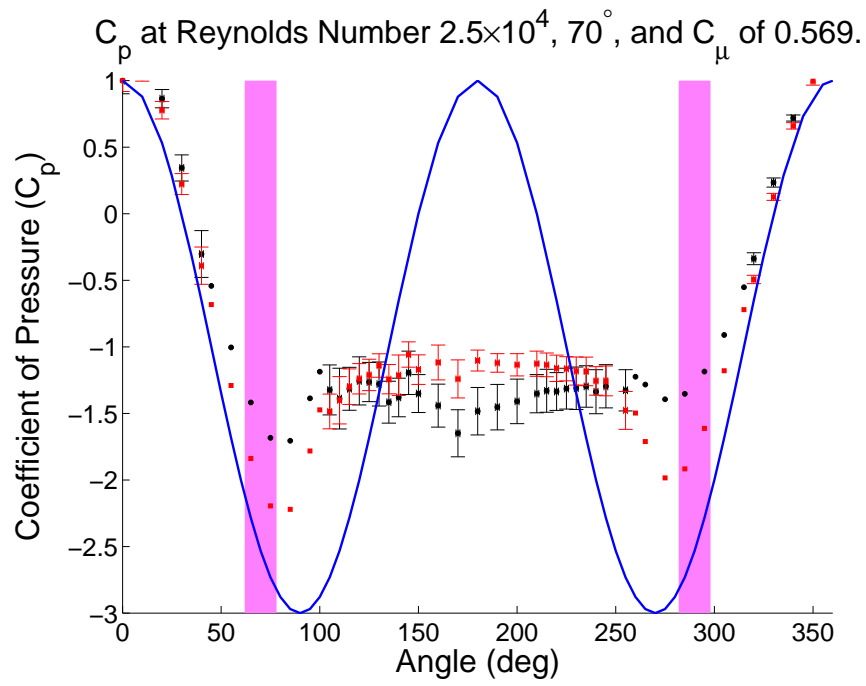
Figure A.15: Synthetic Jet Actuators on a Circular Cylinder.
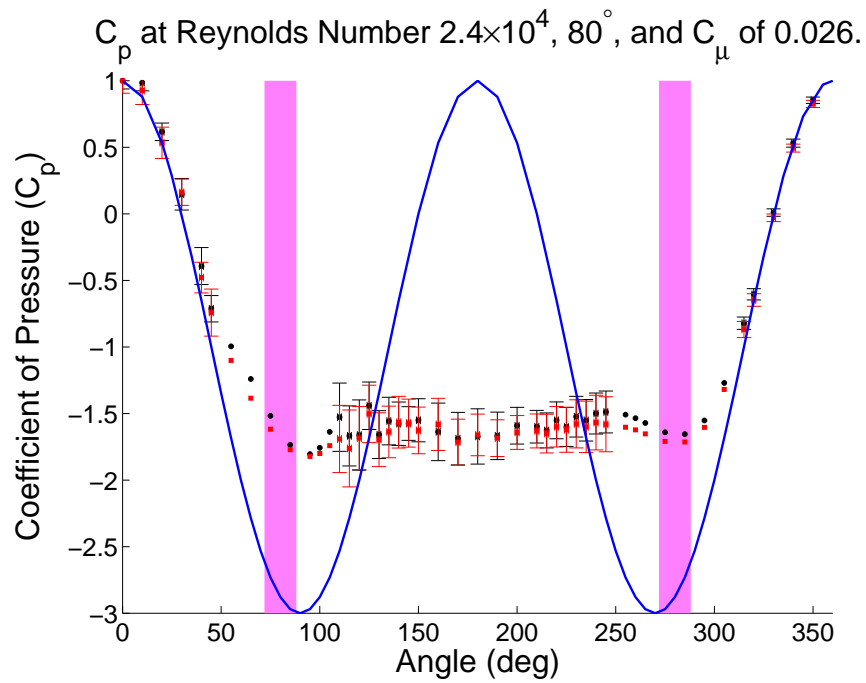
Figure A.16: Synthetic Jet Actuators on a Circular Cylinder.
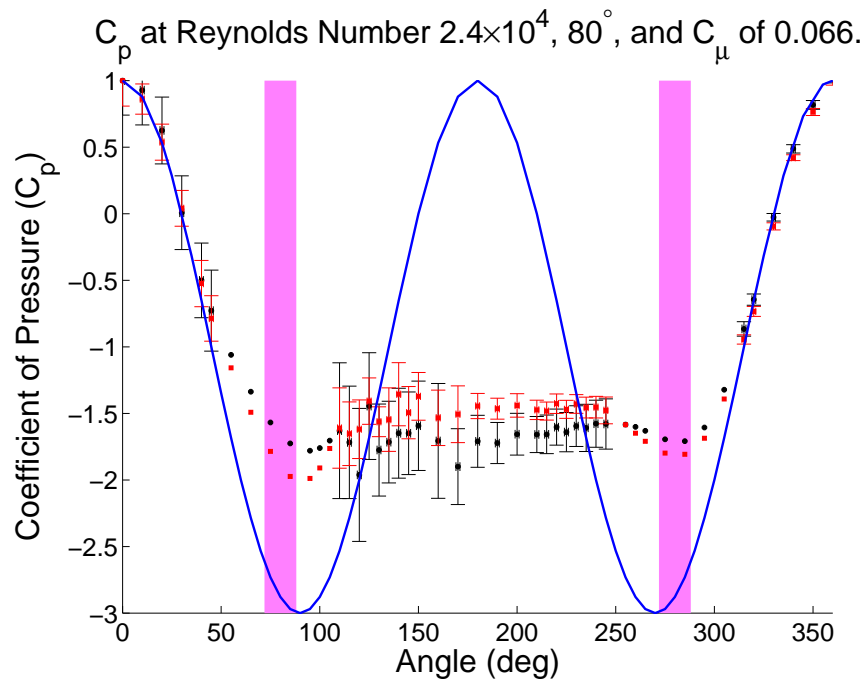
Figure A.17: Synthetic Jet Actuators on a Circular Cylinder.
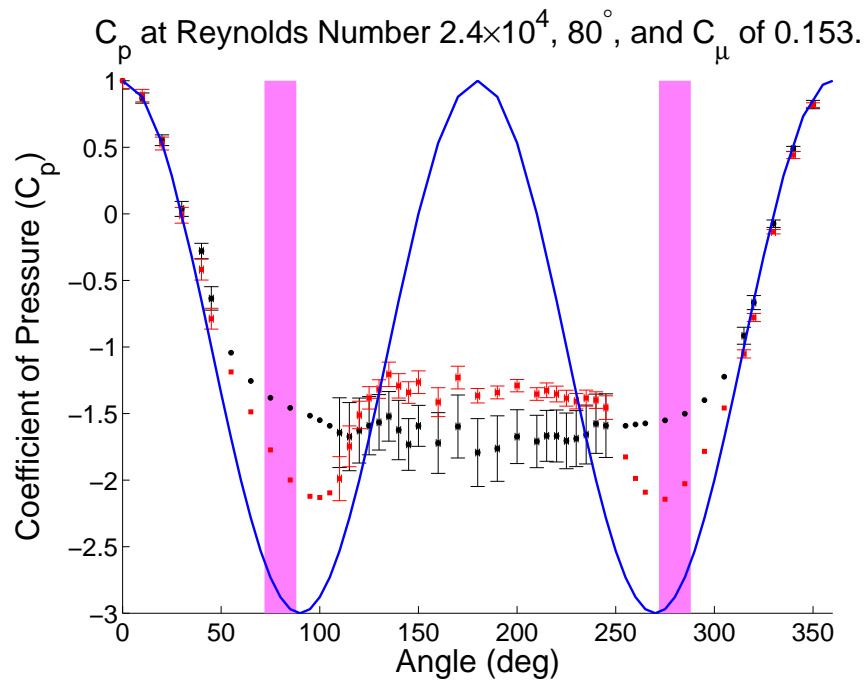
Figure A.18: Synthetic Jet Actuators on a Circular Cylinder.
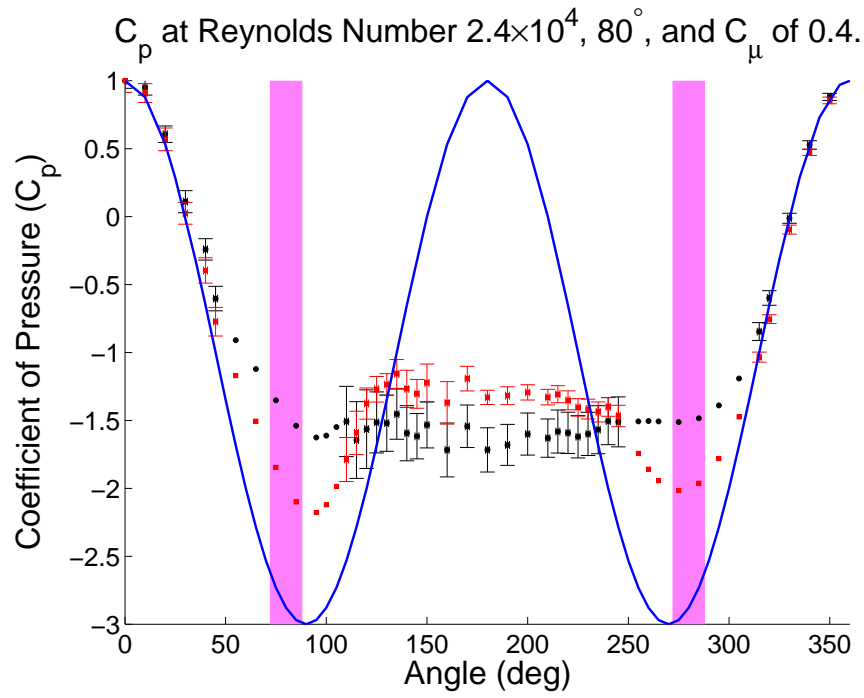
Figure A.19: Synthetic Jet Actuators on a Circular Cylinder.
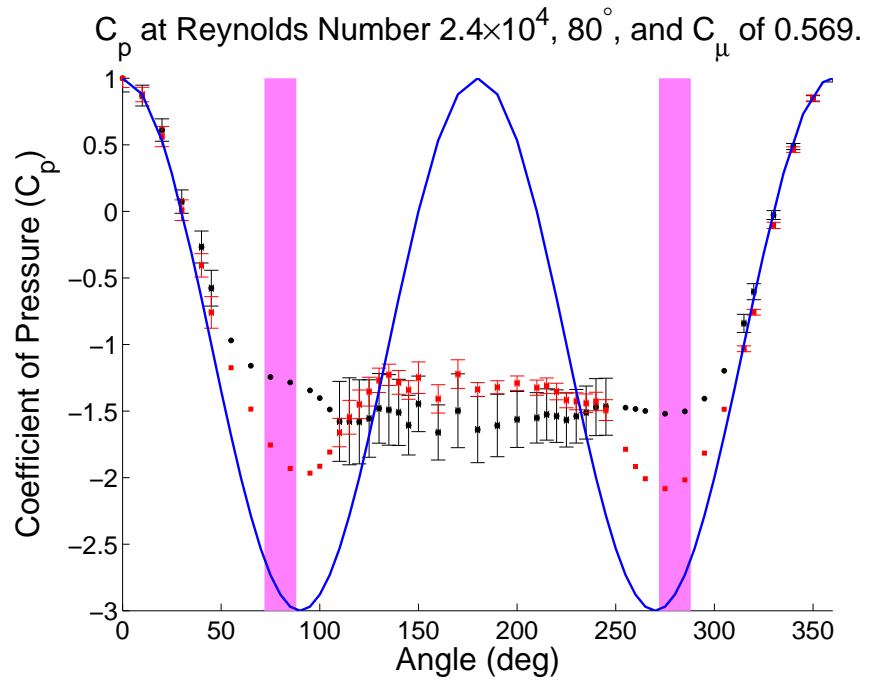
Figure A.20: Synthetic Jet Actuators on a Circular Cylinder.
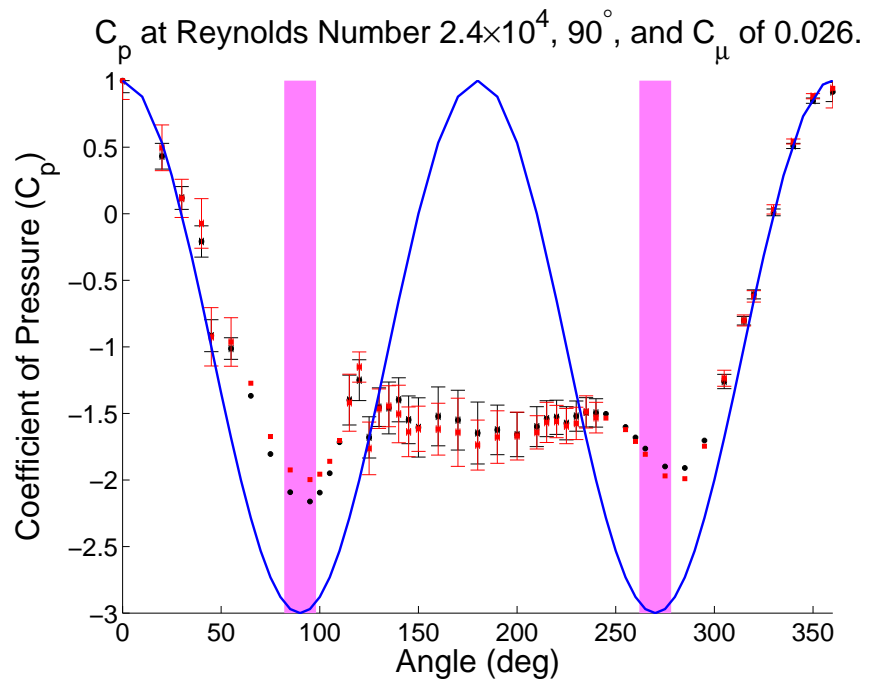
Figure A.21: Synthetic Jet Actuators on a Circular Cylinder.
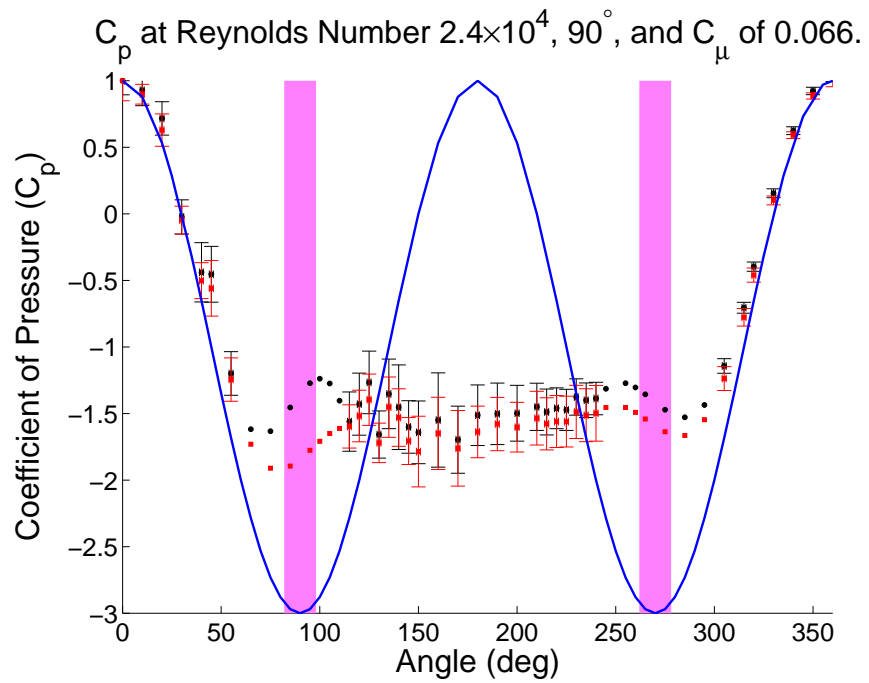
Figure A.22: Synthetic Jet Actuators on a Circular Cylinder.
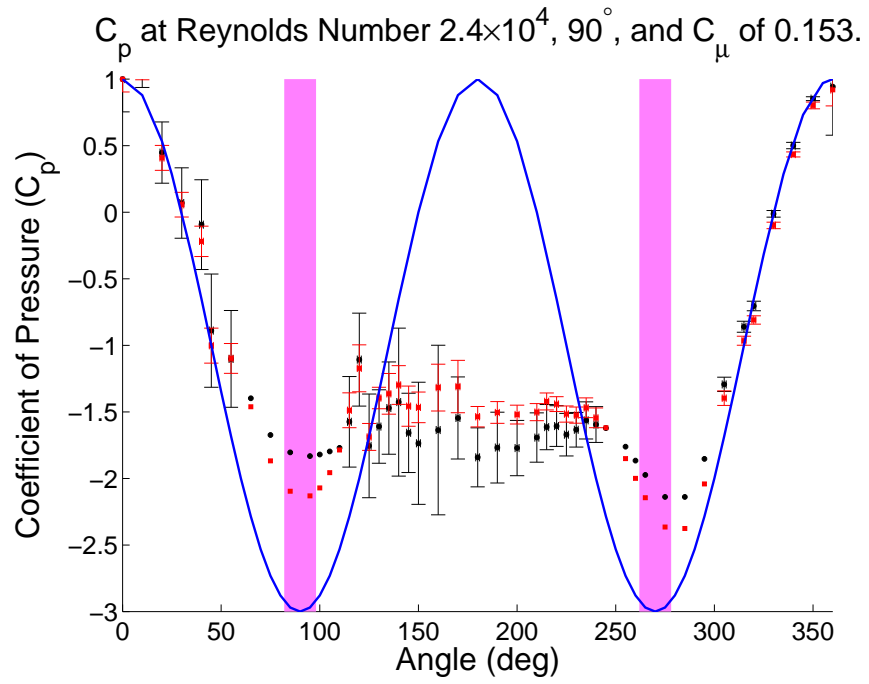
Figure A.23: Synthetic Jet Actuators on a Circular Cylinder.
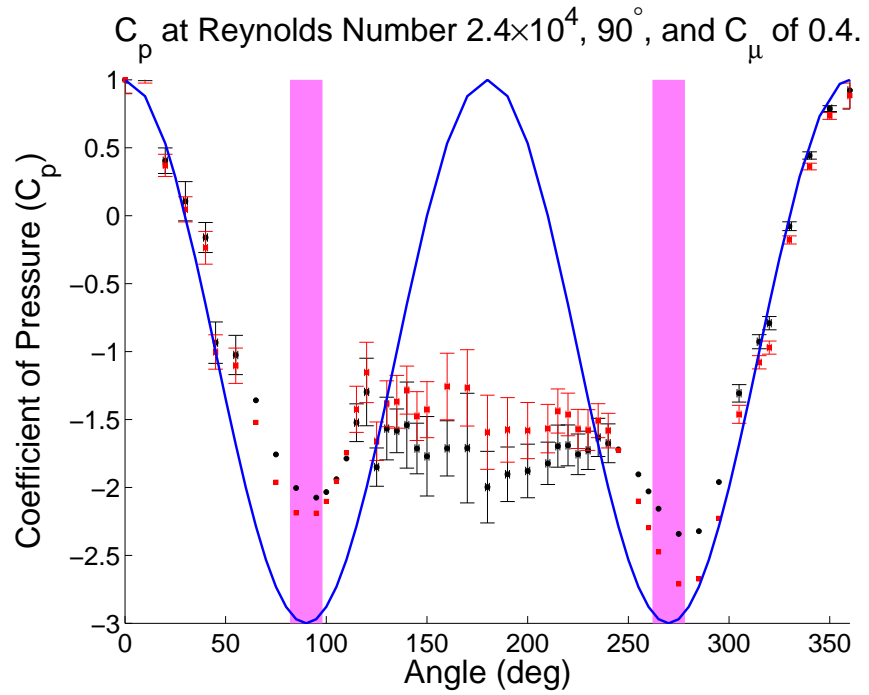
Figure A.24: Synthetic Jet Actuators on a Circular Cylinder.
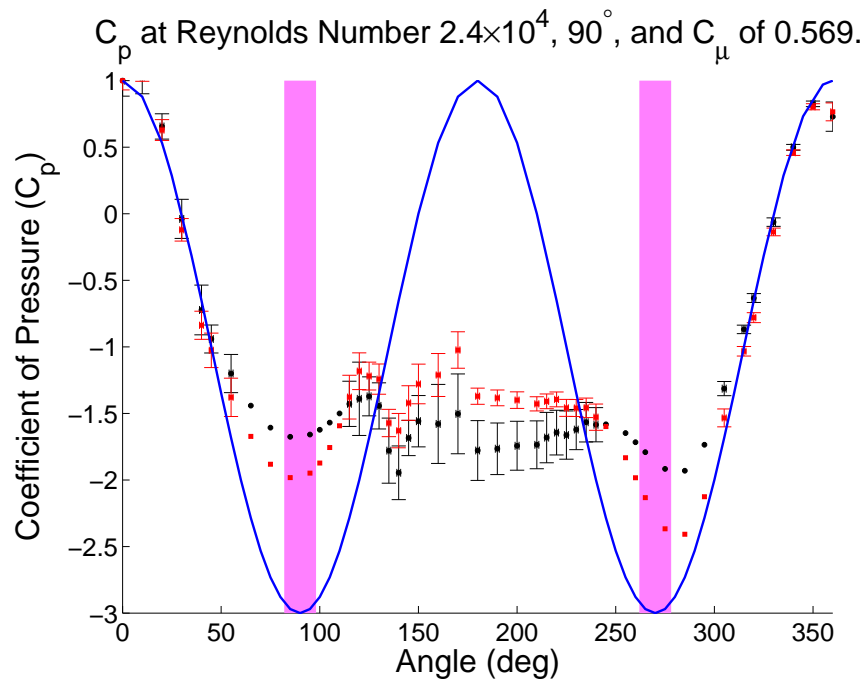
Figure A.25: Synthetic Jet Actuators on a Circular Cylinder.
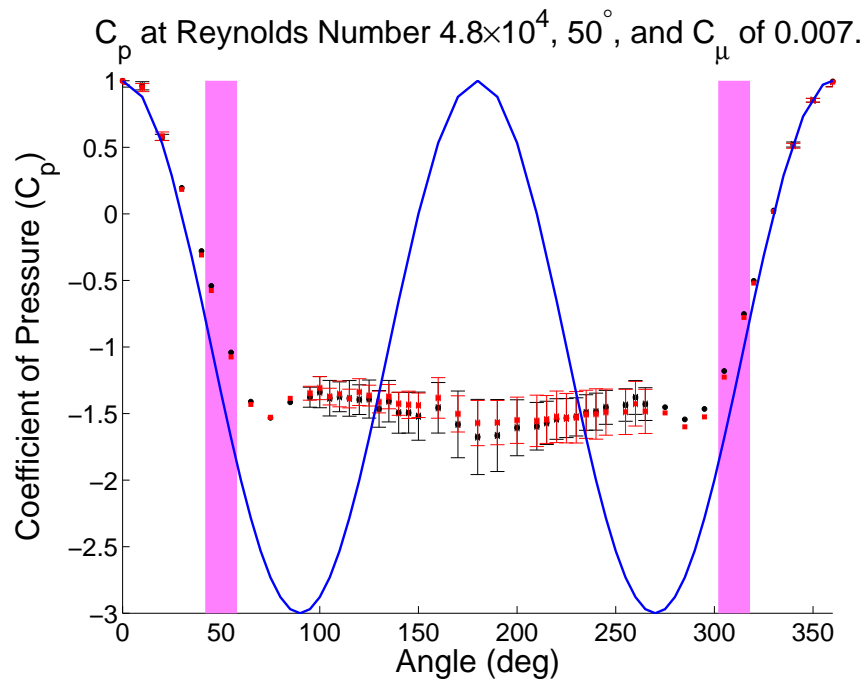
Figure A.26: Synthetic Jet Actuators on a Circular Cylinder.
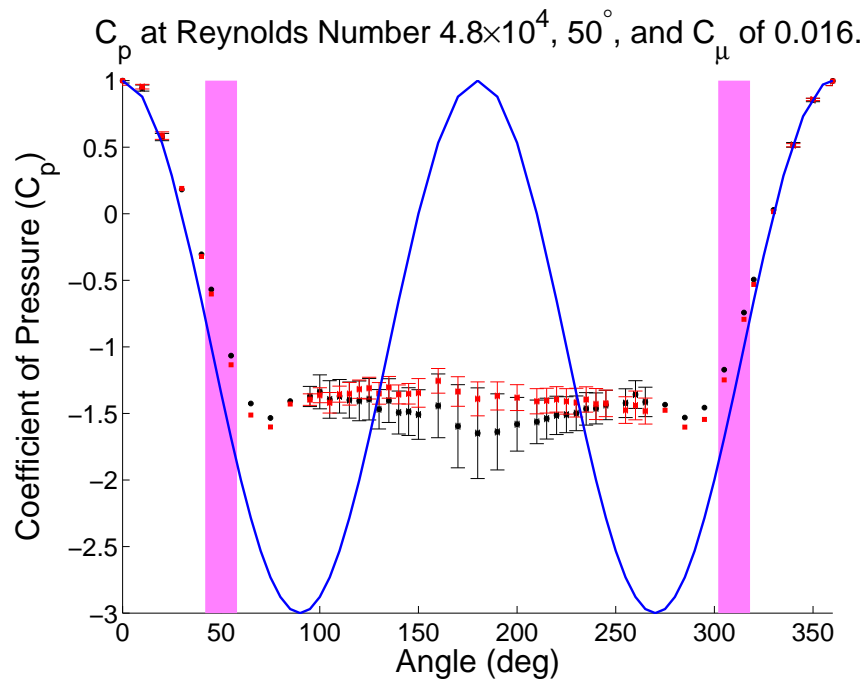
Figure A.27: Synthetic Jet Actuators on a Circular Cylinder.
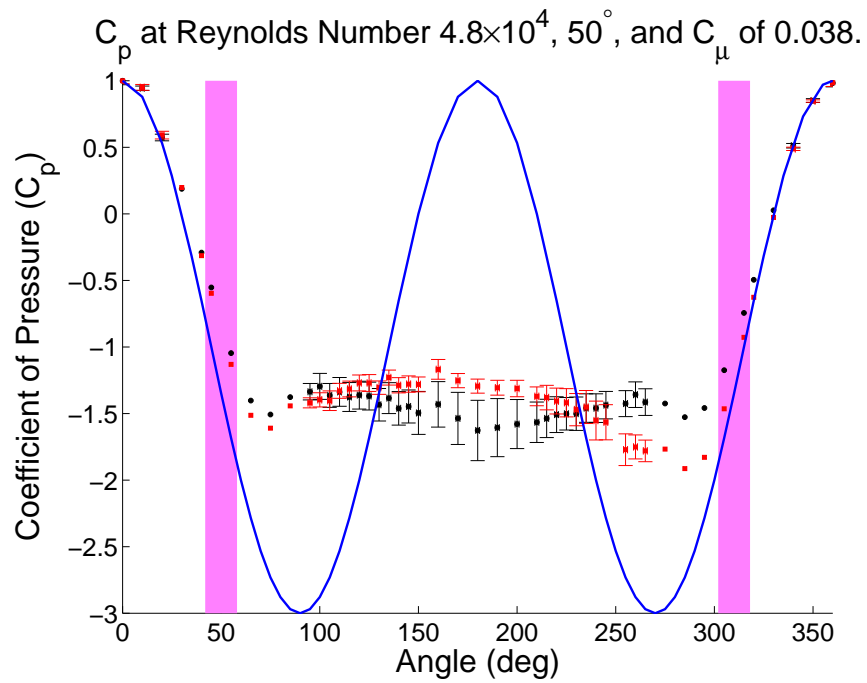
Figure A.28: Synthetic Jet Actuators on a Circular Cylinder.
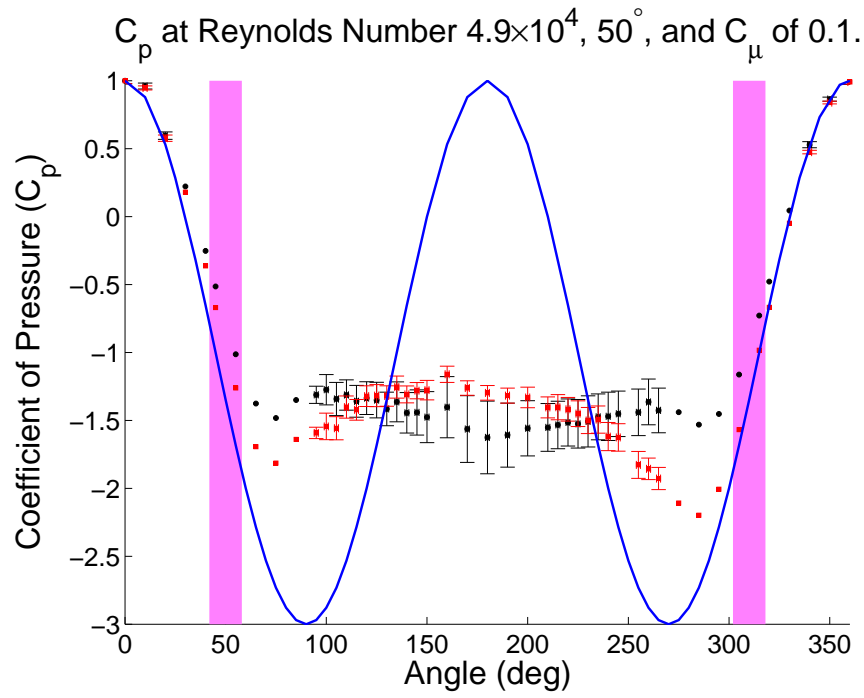
Figure A.29: Synthetic Jet Actuators on a Circular Cylinder.
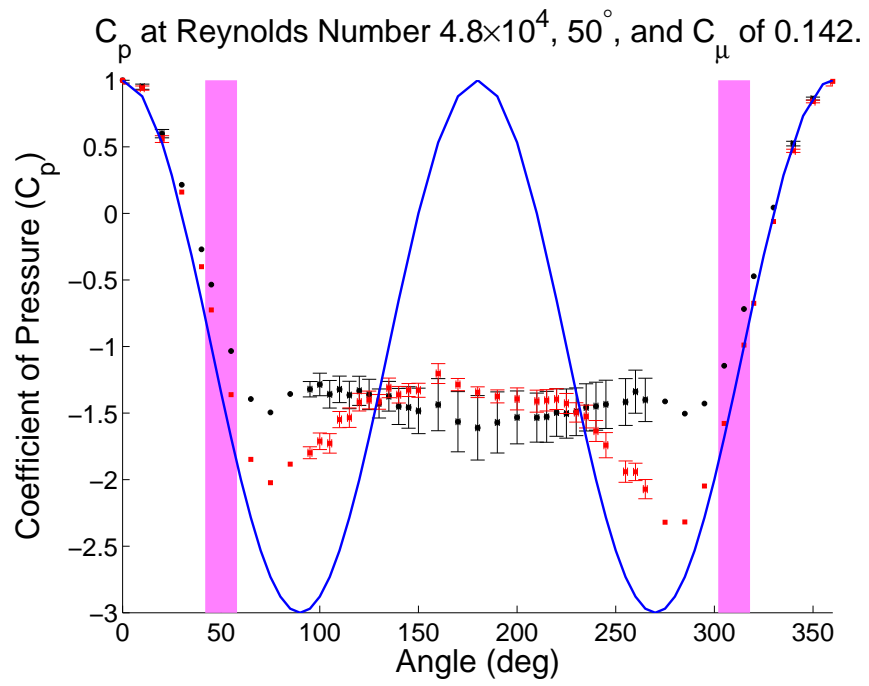
Figure A.30: Synthetic Jet Actuators on a Circular Cylinder.
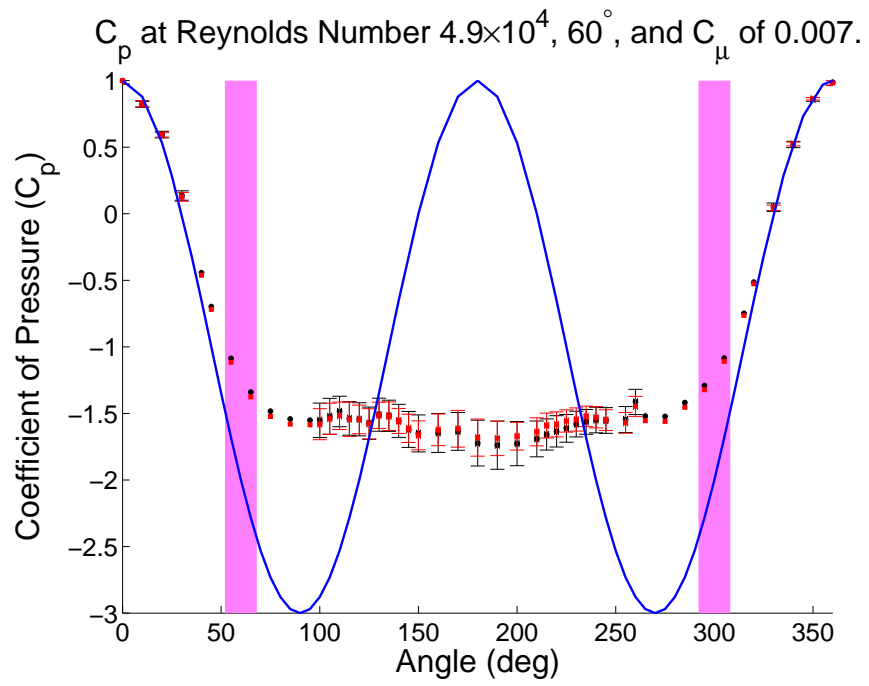
Figure A.31: Synthetic Jet Actuators on a Circular Cylinder.
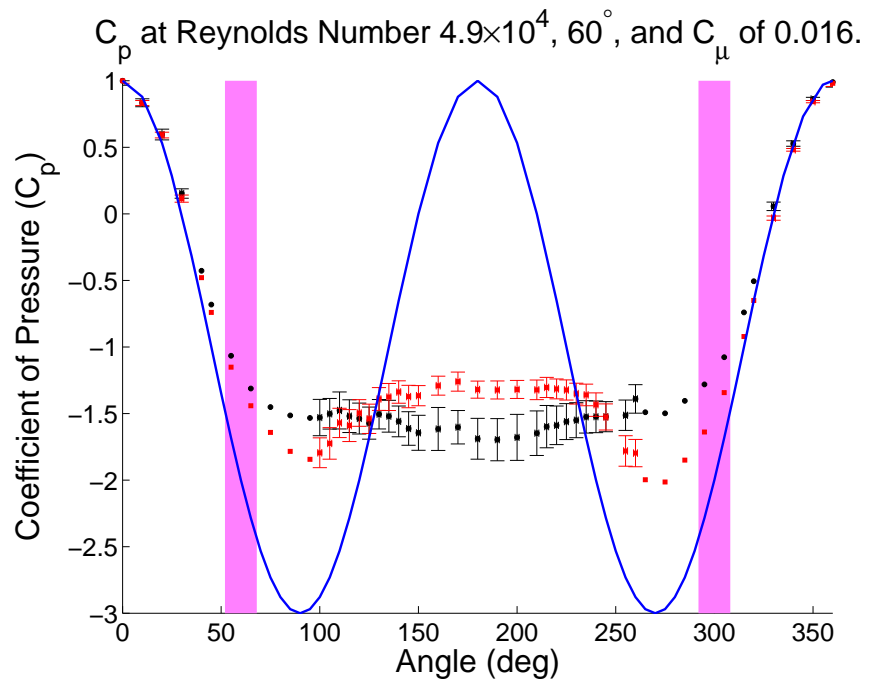
Figure A.32: Synthetic Jet Actuators on a Circular Cylinder.

166
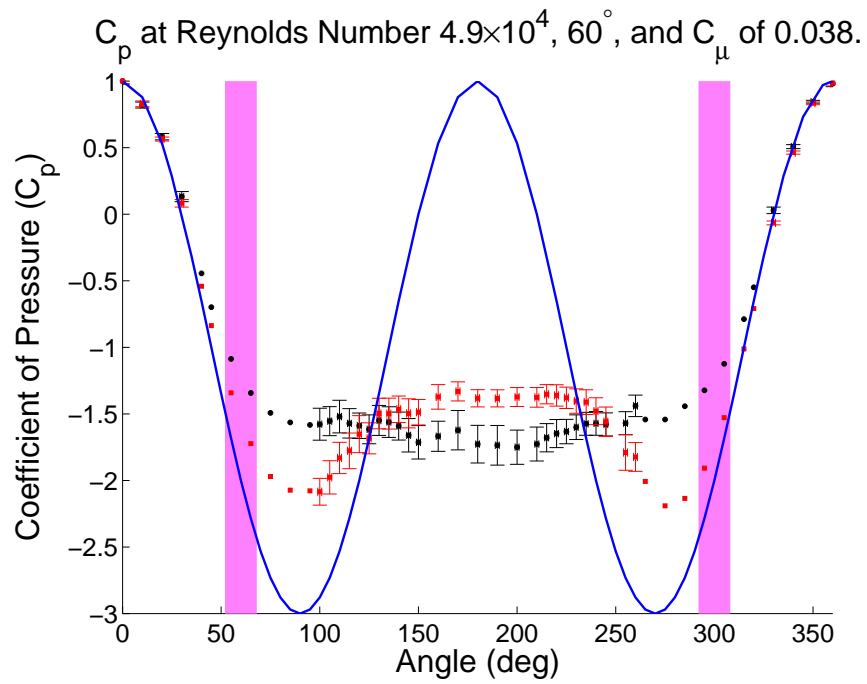
Figure A.33: Synthetic Jet Actuators on a Circular Cylinder.
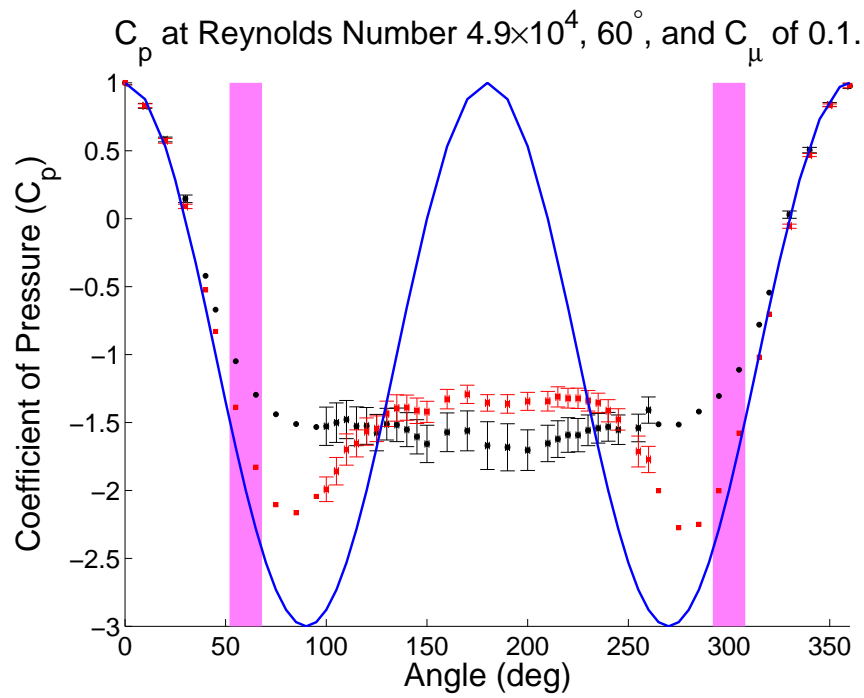
Figure A.34: Synthetic Jet Actuators on a Circular Cylinder.
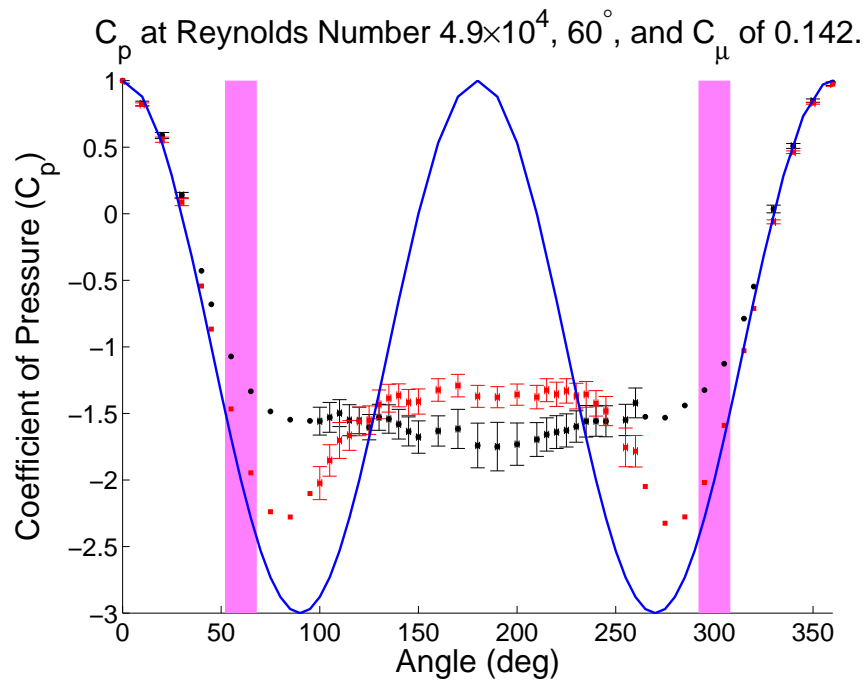
Figure A.35: Synthetic Jet Actuators on a Circular Cylinder.
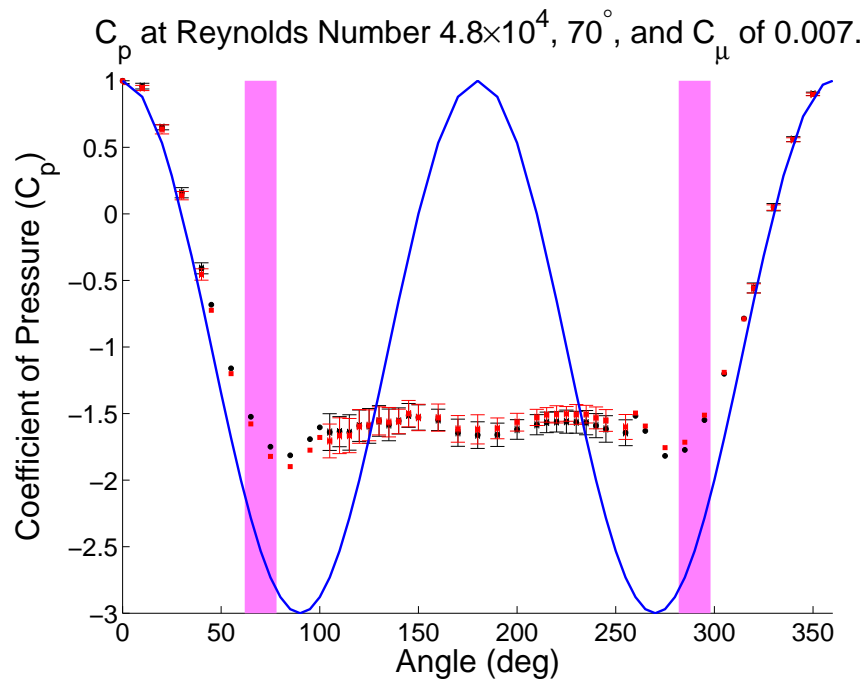
Figure A.36: Synthetic Jet Actuators on a Circular Cylinder.
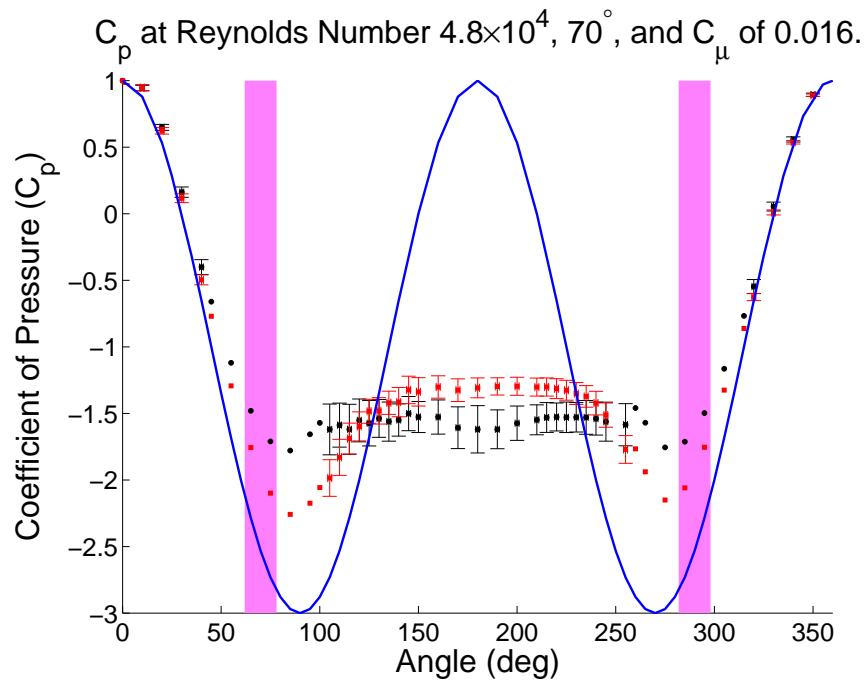
Figure A.37: Synthetic Jet Actuators on a Circular Cylinder.
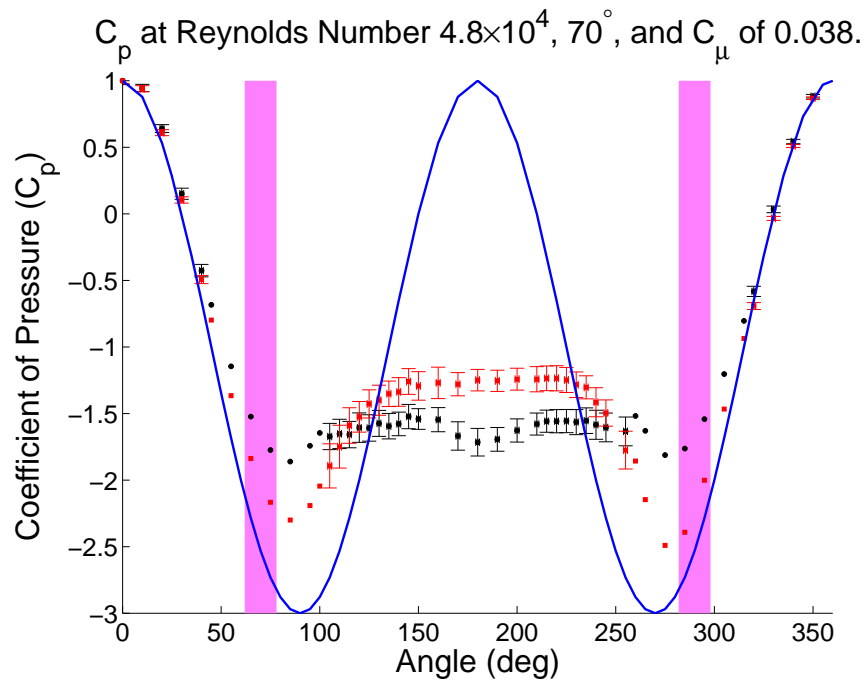
Figure A.38: Synthetic Jet Actuators on a Circular Cylinder.
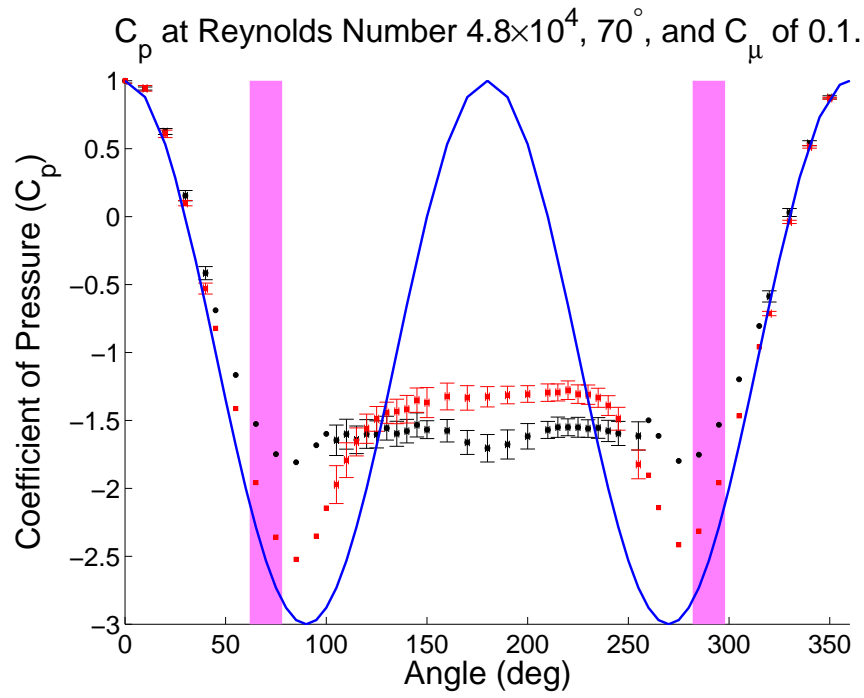
Figure A.39: Synthetic Jet Actuators on a Circular Cylinder.
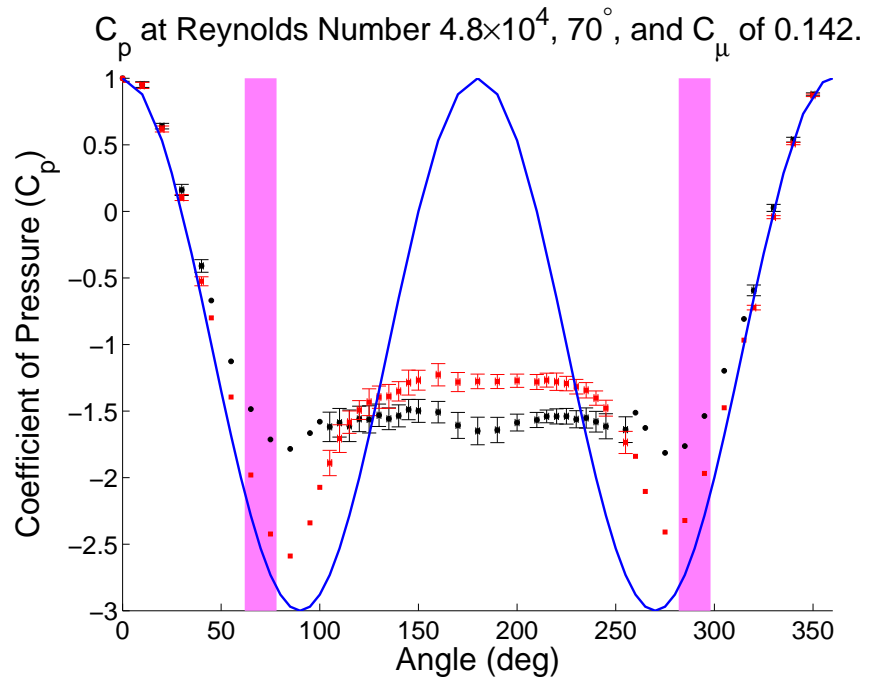
Figure A.40: Synthetic Jet Actuators on a Circular Cylinder.
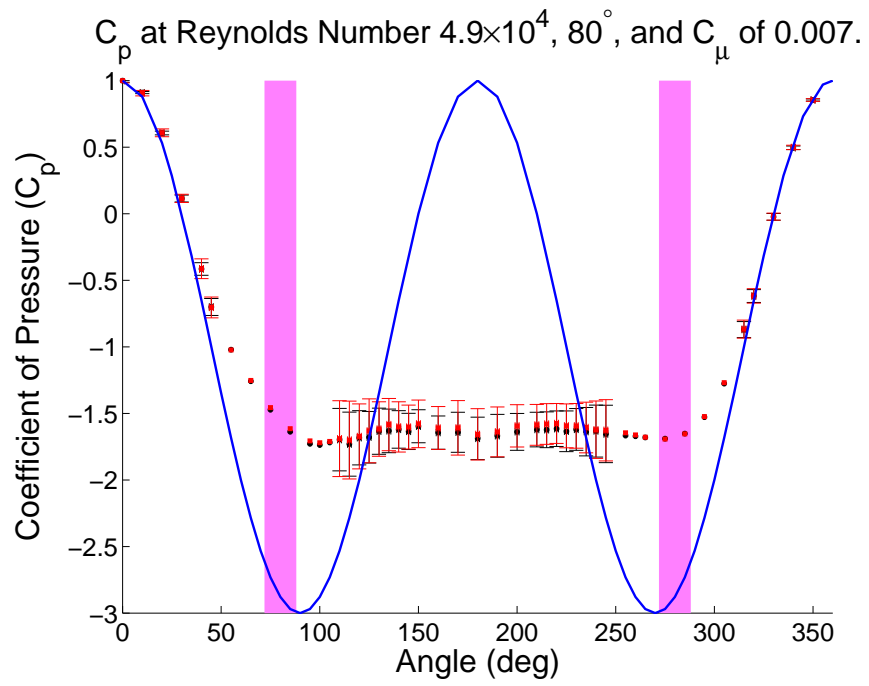
Figure A.41: Synthetic Jet Actuators on a Circular Cylinder.
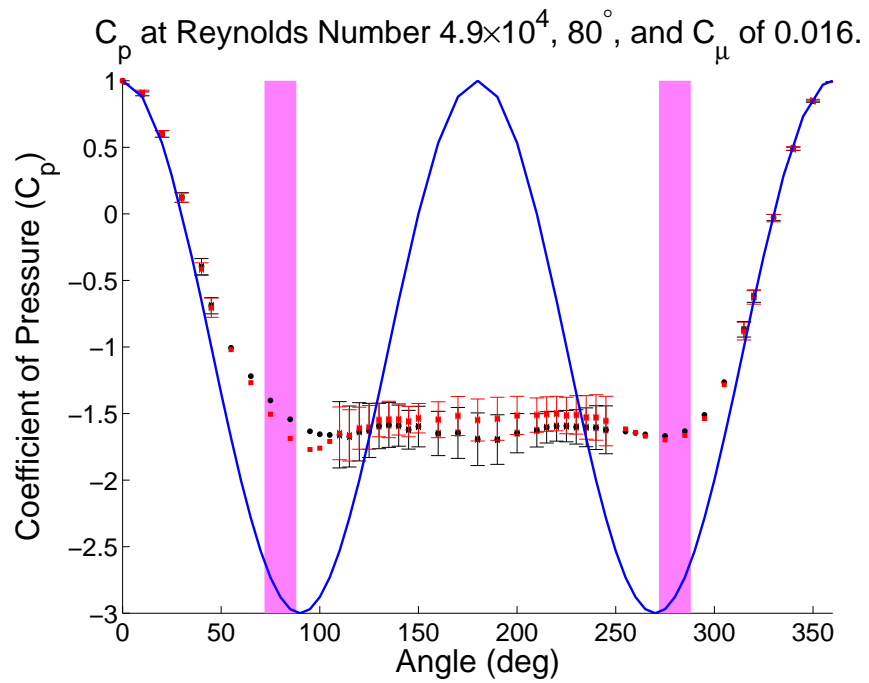
Figure A.42: Synthetic Jet Actuators on a Circular Cylinder.
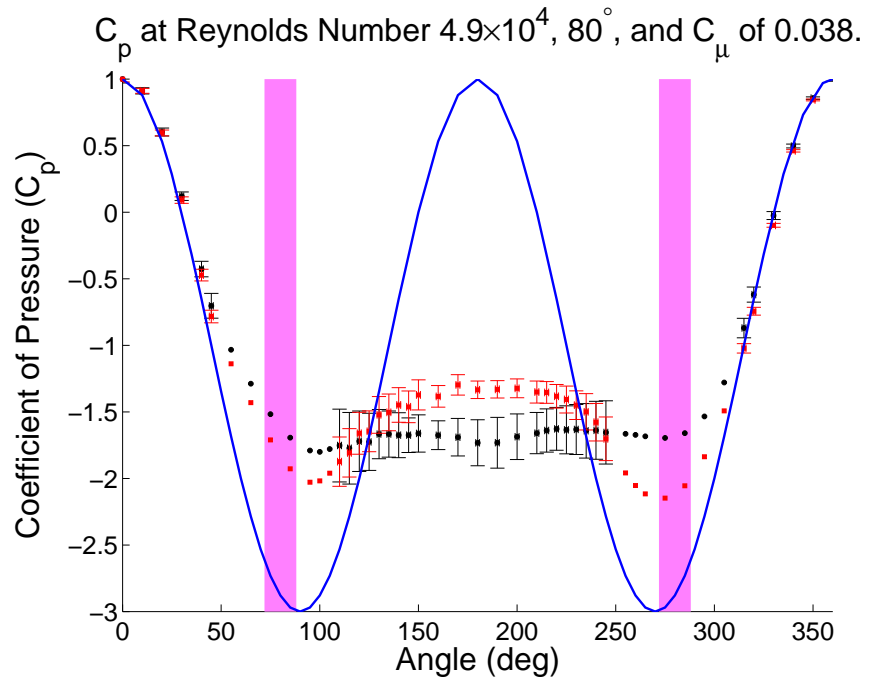
Figure A.43: Synthetic Jet Actuators on a Circular Cylinder.
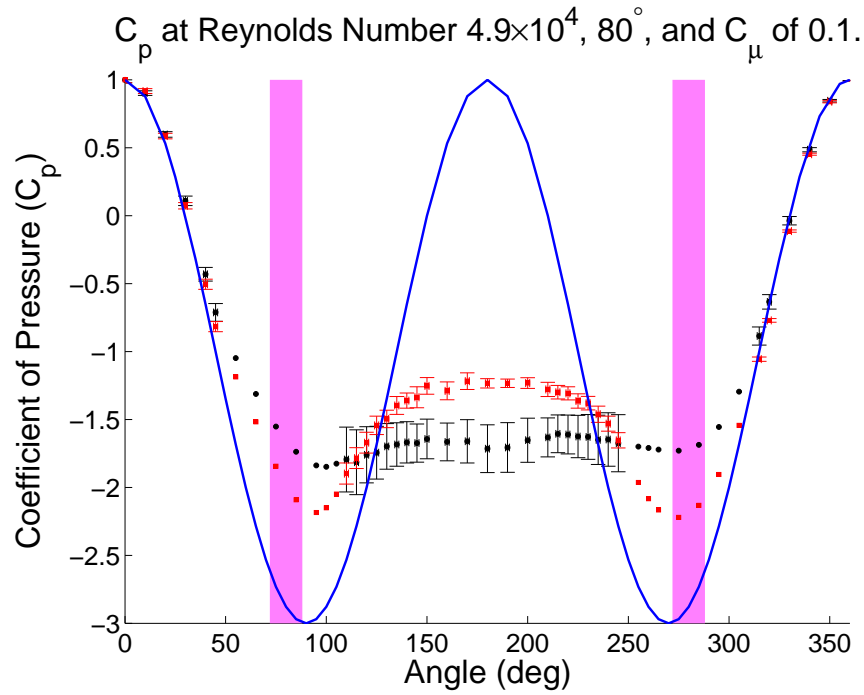
Figure A.44: Synthetic Jet Actuators on a Circular Cylinder.
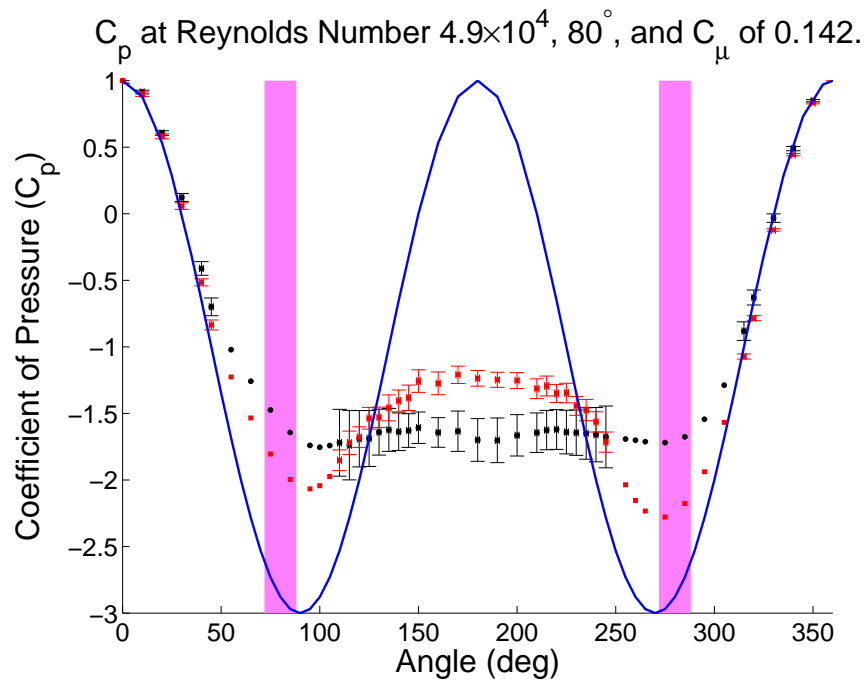
Figure A.45: Synthetic Jet Actuators on a Circular Cylinder.
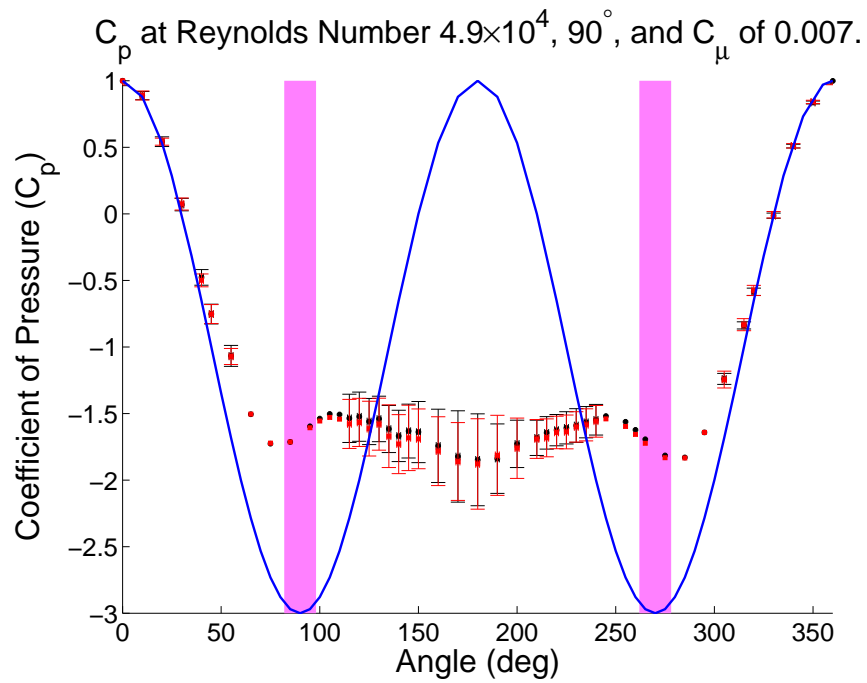
Figure A.46: Synthetic Jet Actuators on a Circular Cylinder.
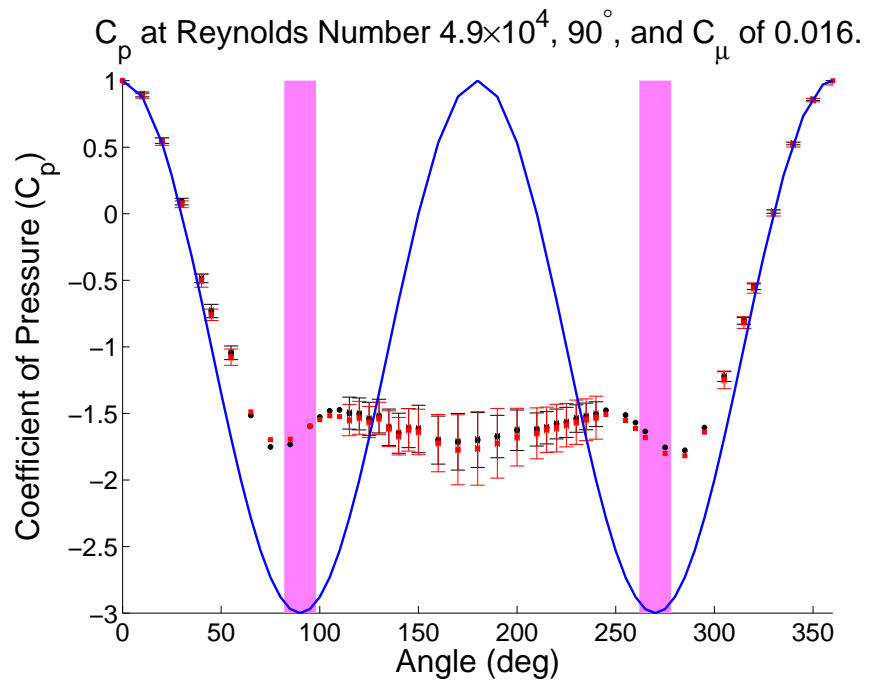
Figure A.47: Synthetic Jet Actuators on a Circular Cylinder.
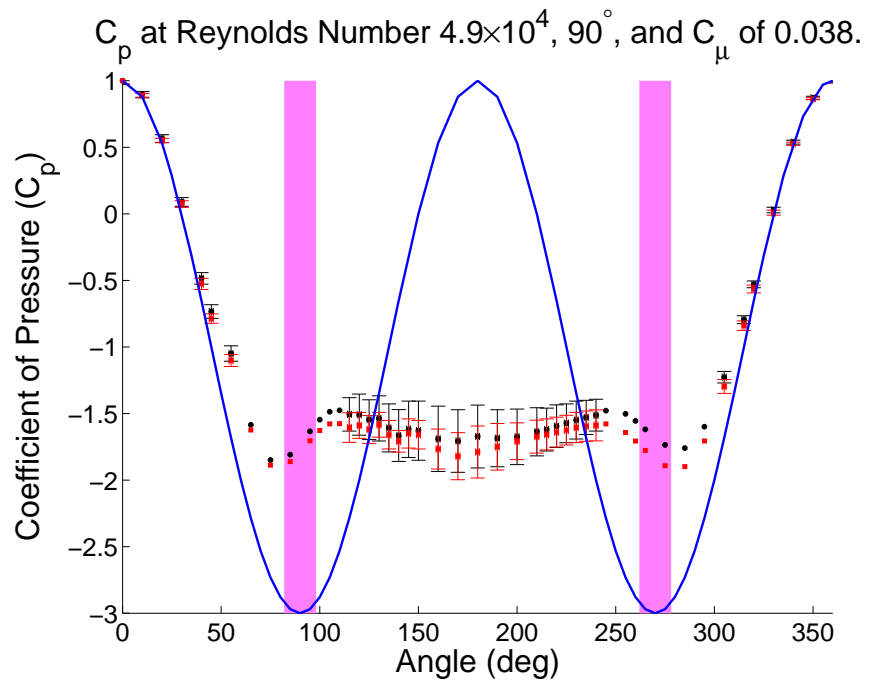
Figure A.48: Synthetic Jet Actuators on a Circular Cylinder.
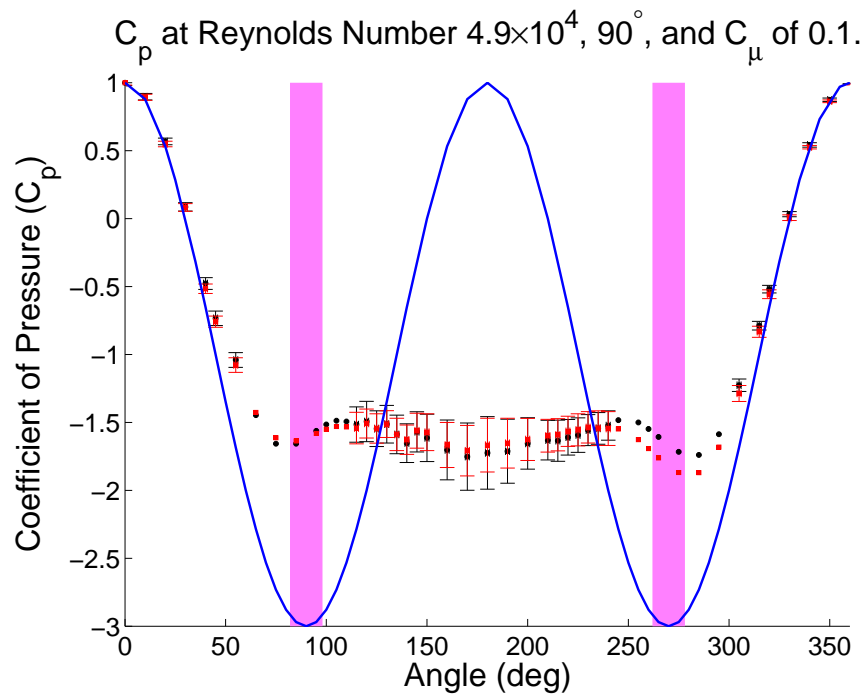
Figure A.49: Synthetic Jet Actuators on a Circular Cylinder.
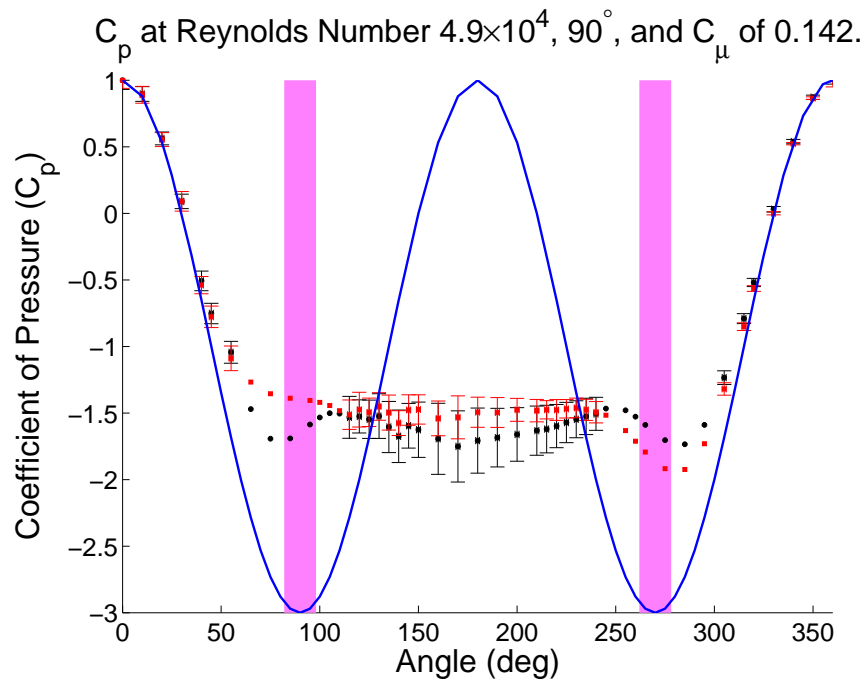
Figure A.50: Synthetic Jet Actuators on a Circular Cylinder.
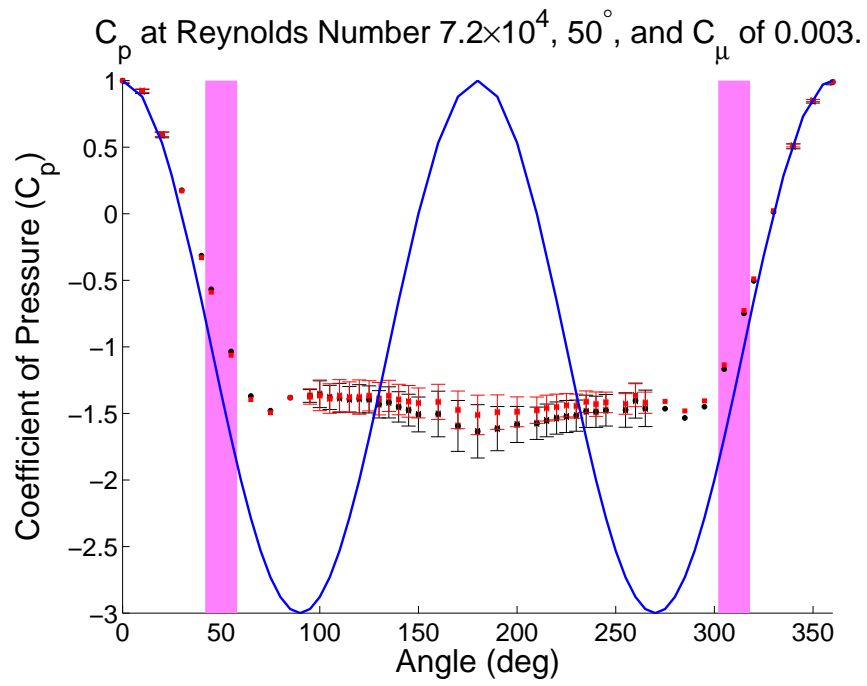
Figure A.51: Synthetic Jet Actuators on a Circular Cylinder.
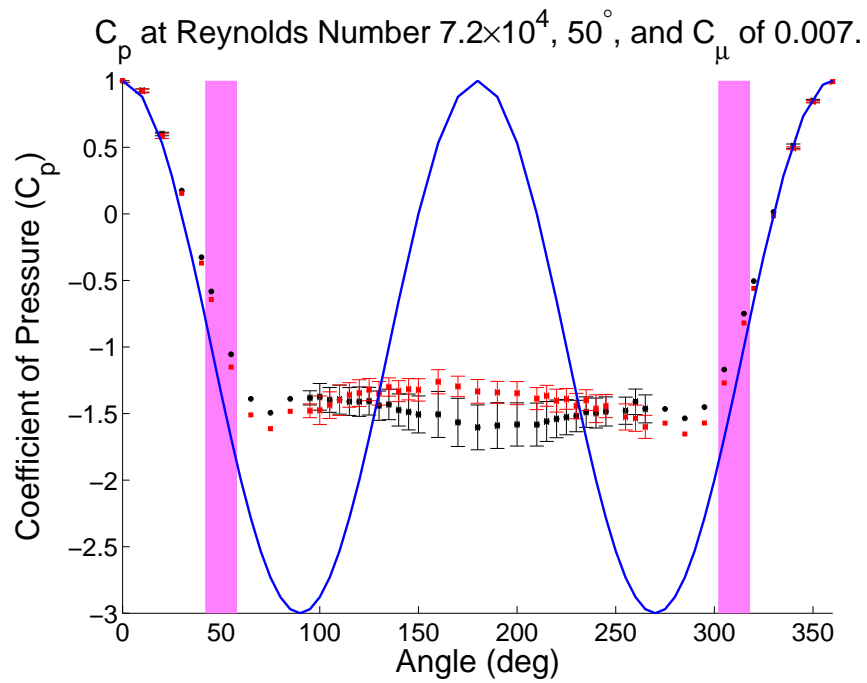
Figure A.52: Synthetic Jet Actuators on a Circular Cylinder.

176
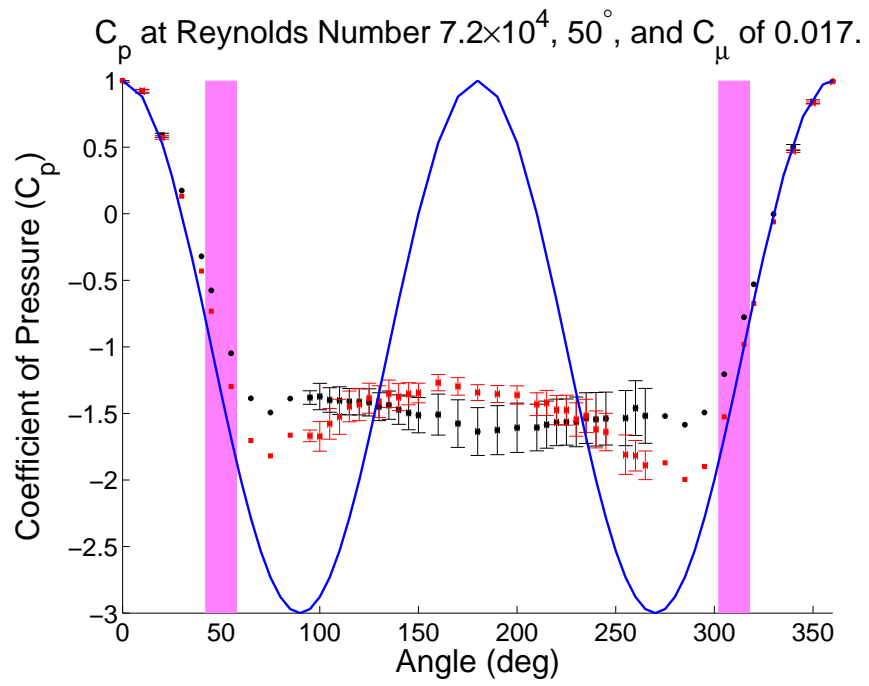
Figure A.53: Synthetic Jet Actuators on a Circular Cylinder.
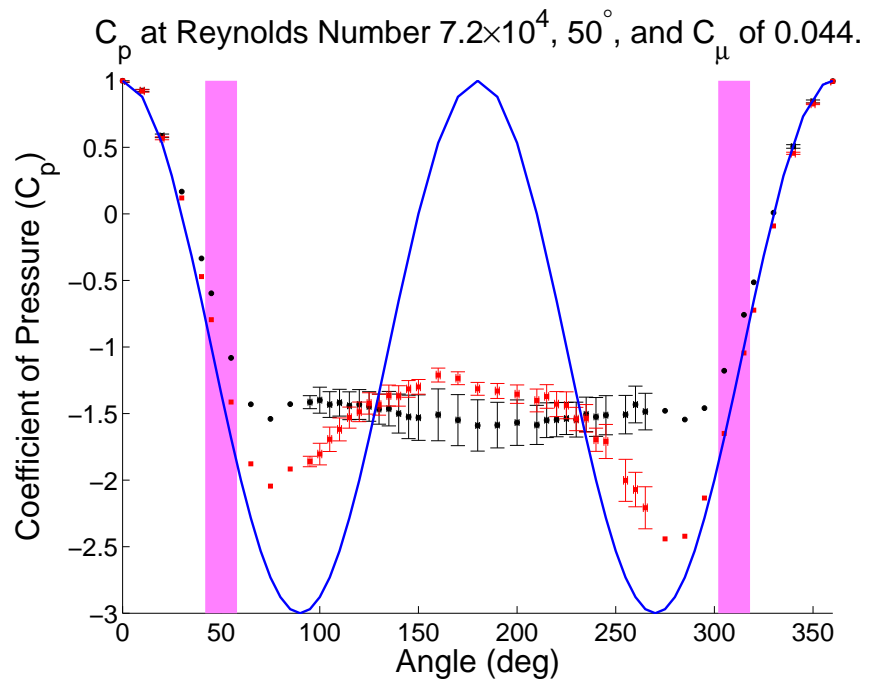
Figure A.54: Synthetic Jet Actuators on a Circular Cylinder.

177
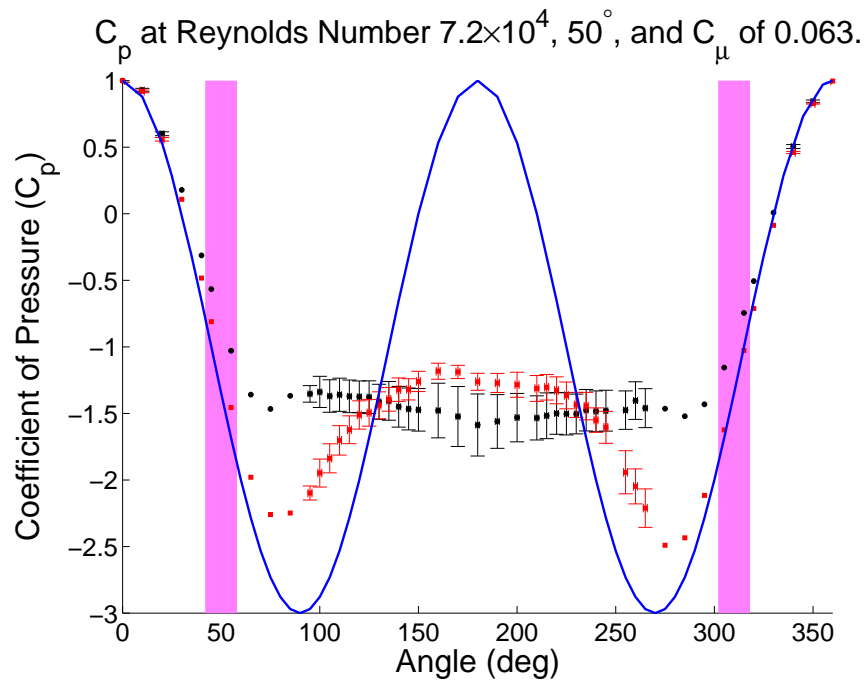
Figure A.55: Synthetic Jet Actuators on a Circular Cylinder.
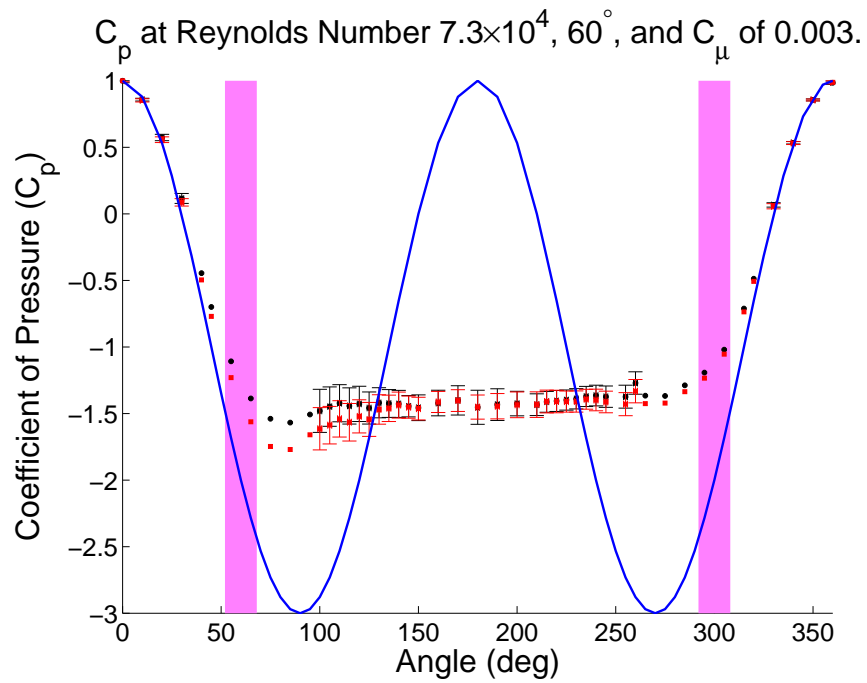
Figure A.56: Synthetic Jet Actuators on a Circular Cylinder.
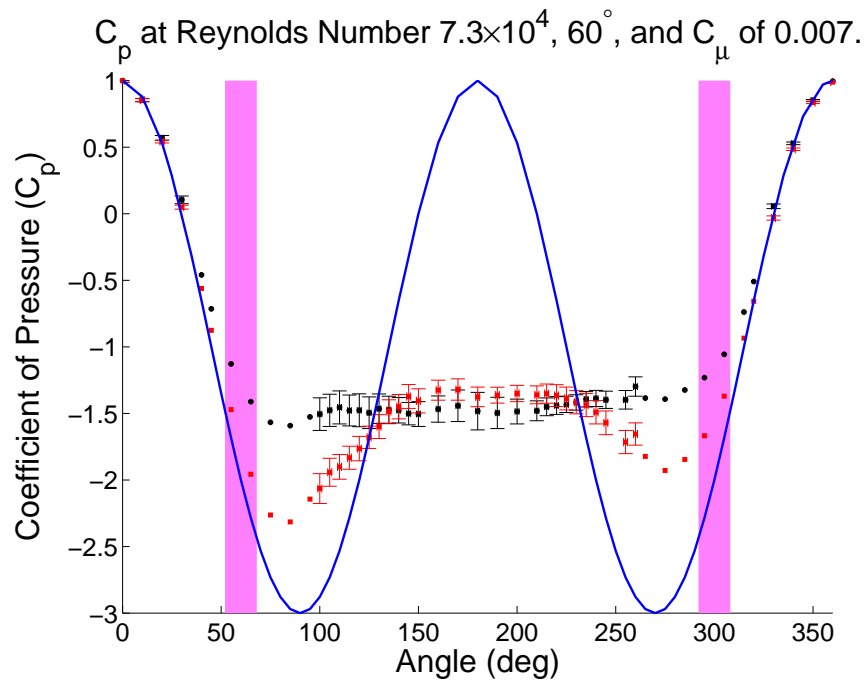
Figure A.57: Synthetic Jet Actuators on a Circular Cylinder.
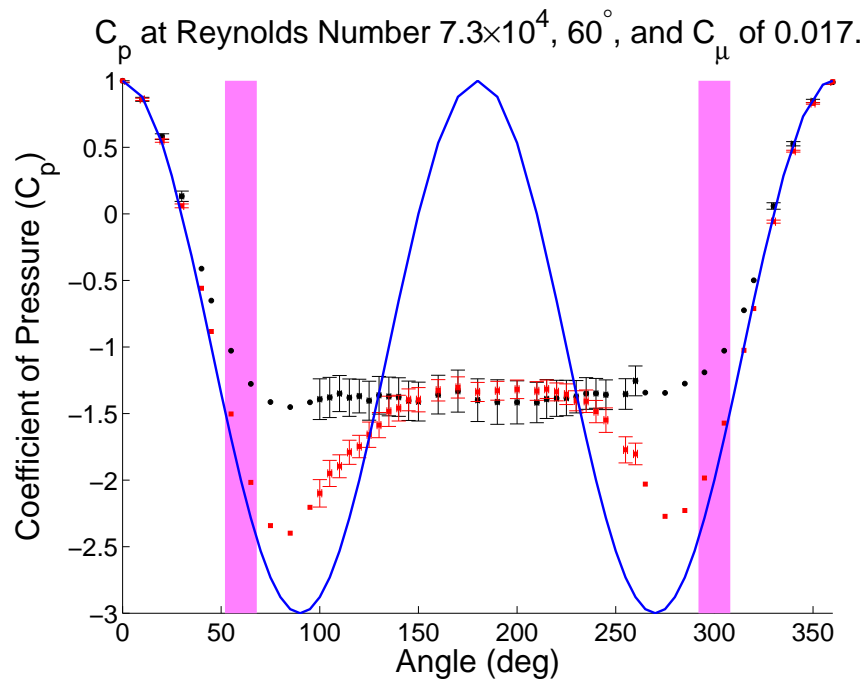
Figure A.58: Synthetic Jet Actuators on a Circular Cylinder.

179
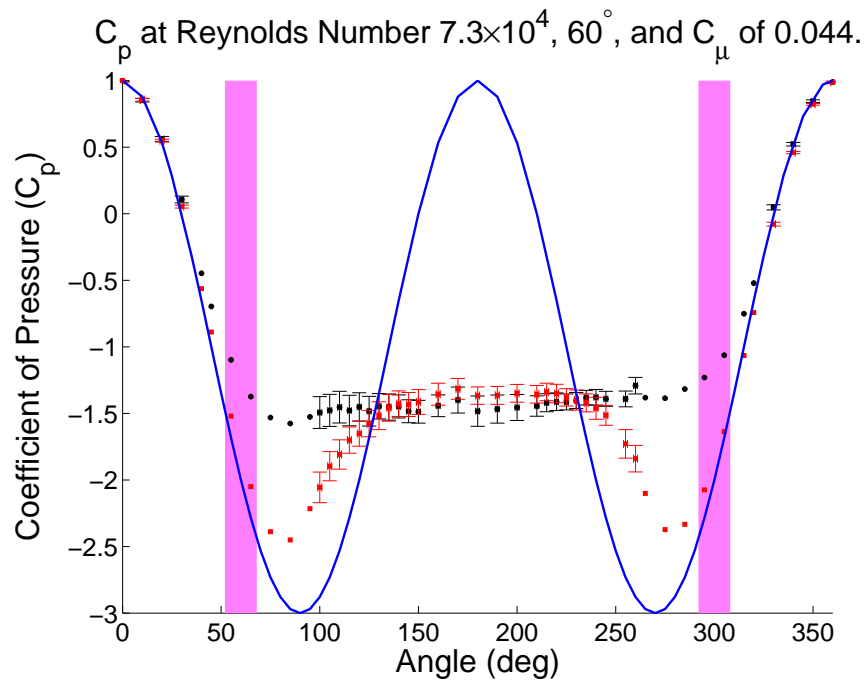
Figure A.59: Synthetic Jet Actuators on a Circular Cylinder.
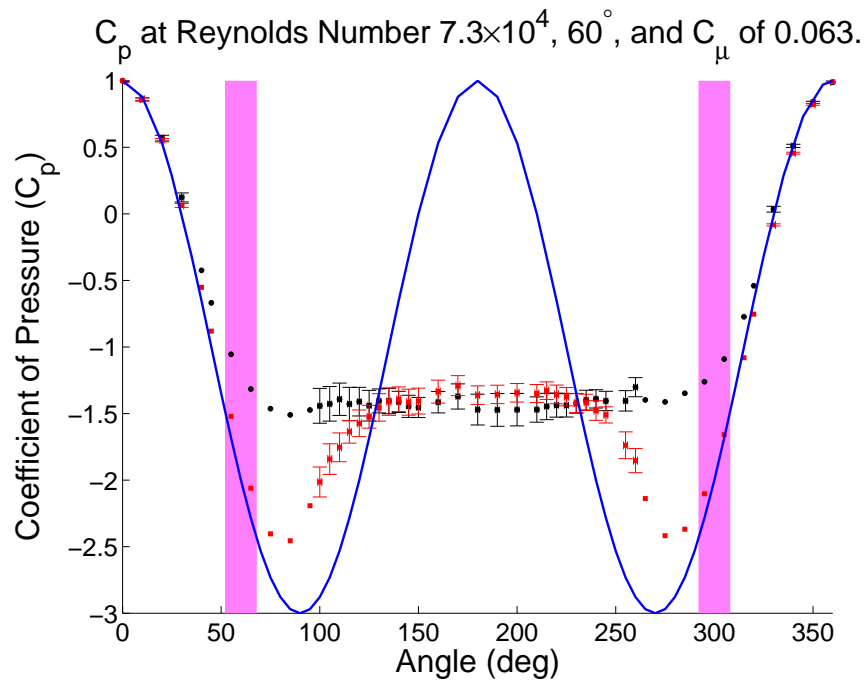
Figure A.60: Synthetic Jet Actuators on a Circular Cylinder.
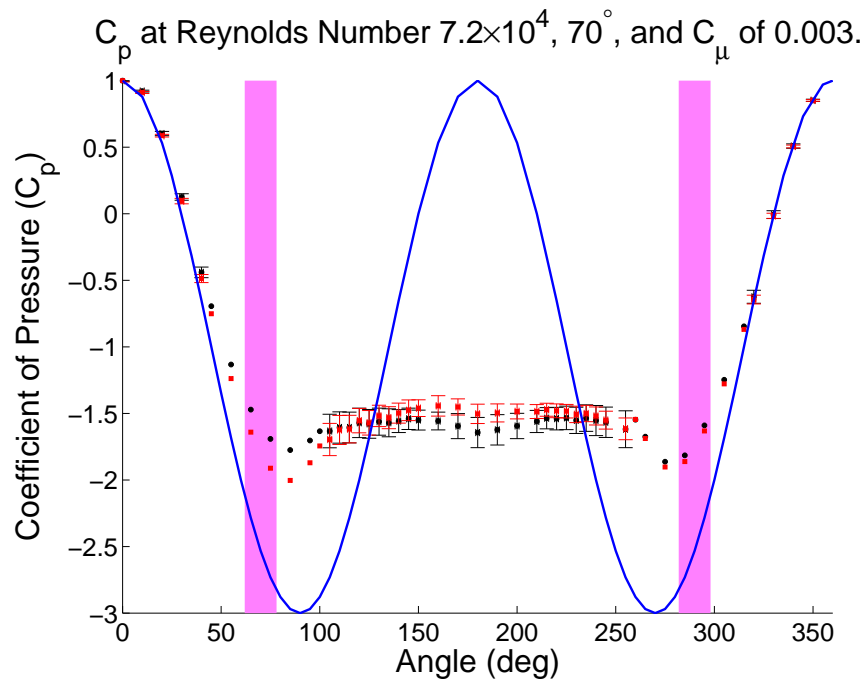
Figure A.61: Synthetic Jet Actuators on a Circular Cylinder.
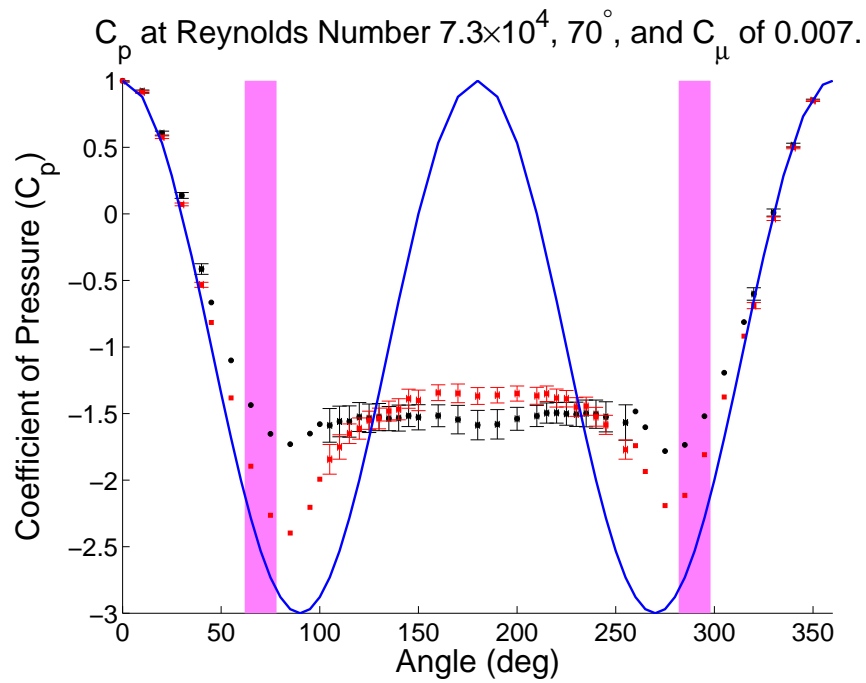
Figure A.62: Synthetic Jet Actuators on a Circular Cylinder.
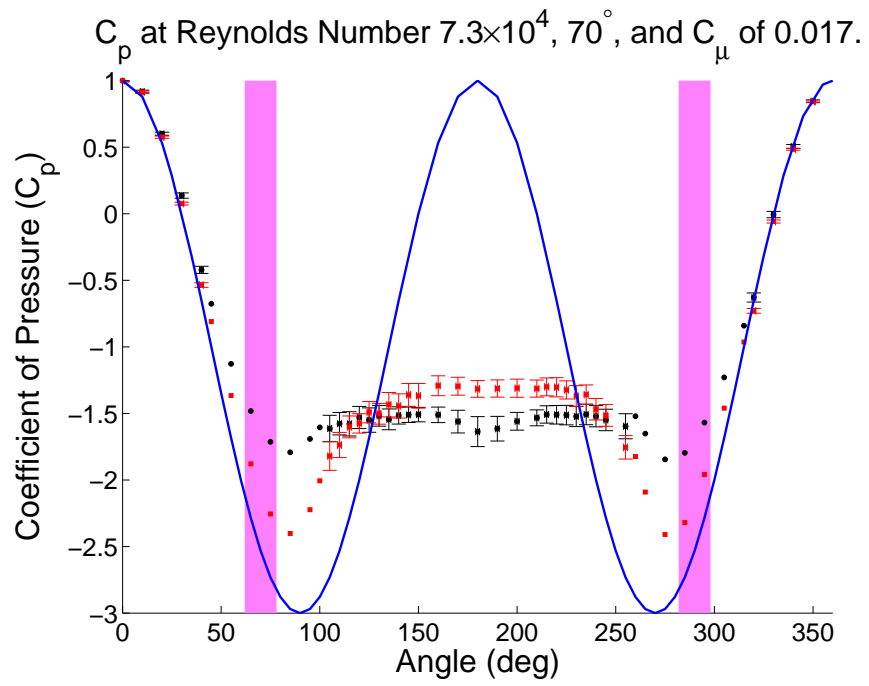
Figure A.63: Synthetic Jet Actuators on a Circular Cylinder.
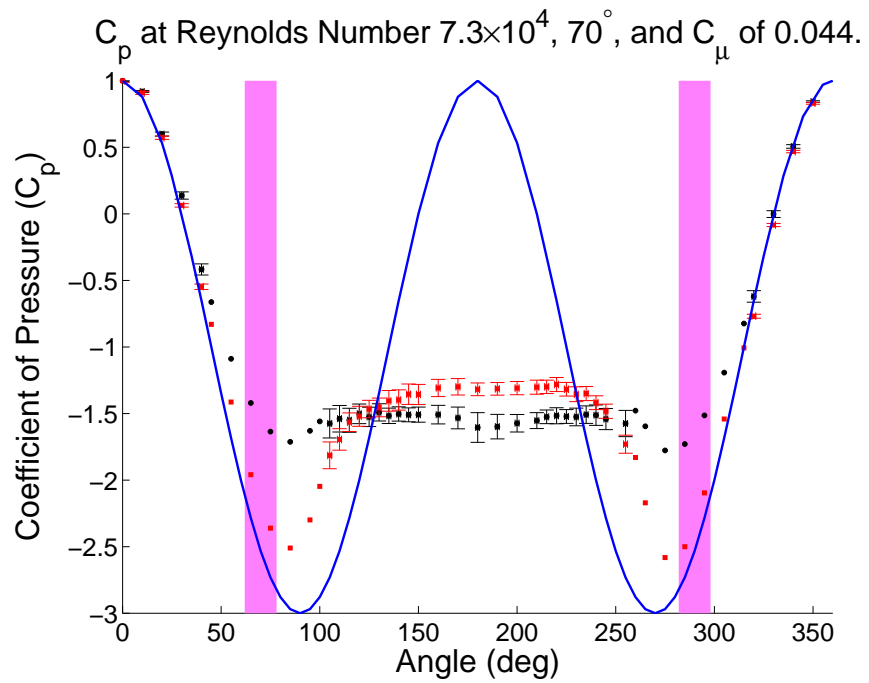
Figure A.64: Synthetic Jet Actuators on a Circular Cylinder.
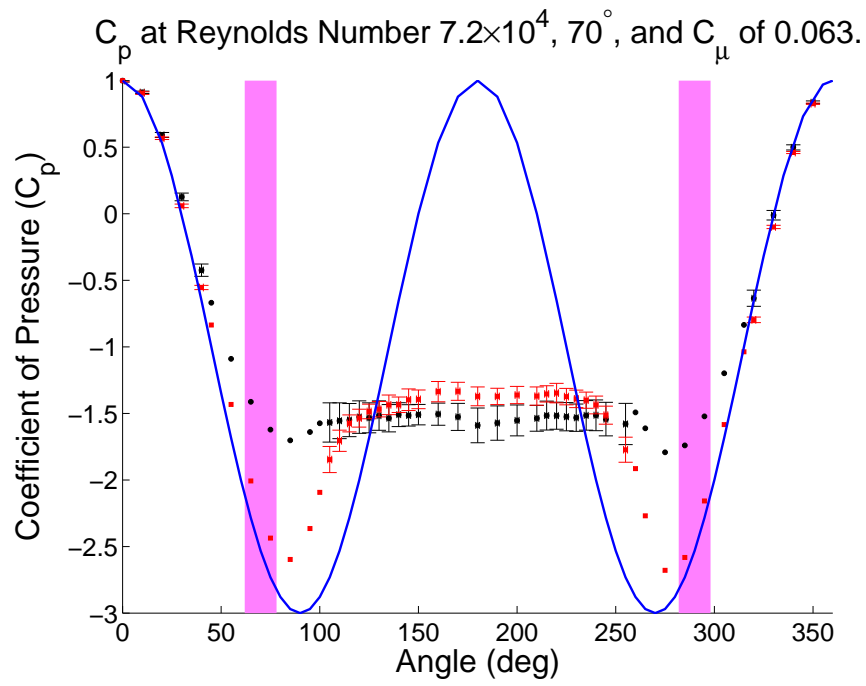
Figure A.65: Synthetic Jet Actuators on a Circular Cylinder.
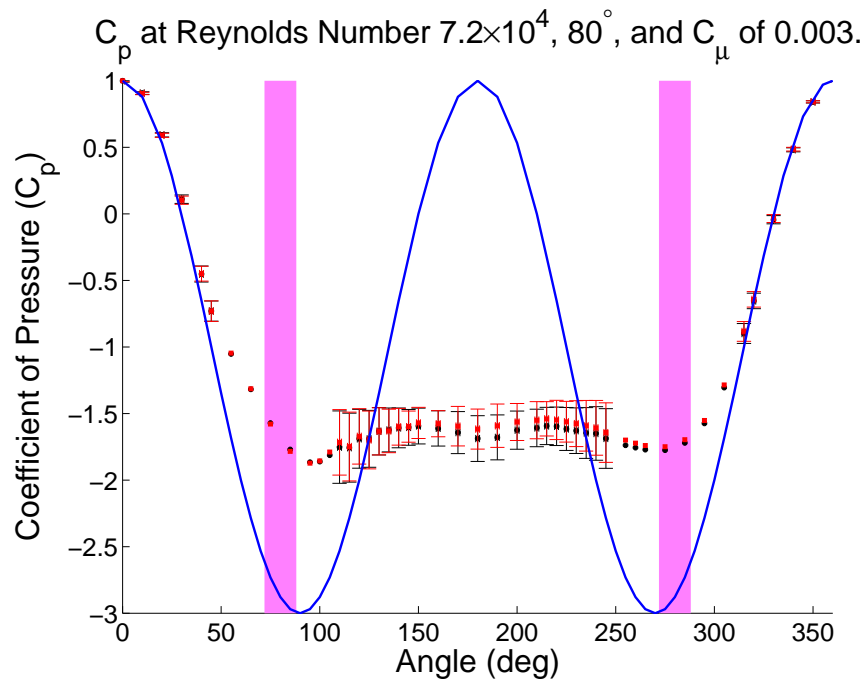
Figure A.66: Synthetic Jet Actuators on a Circular Cylinder.
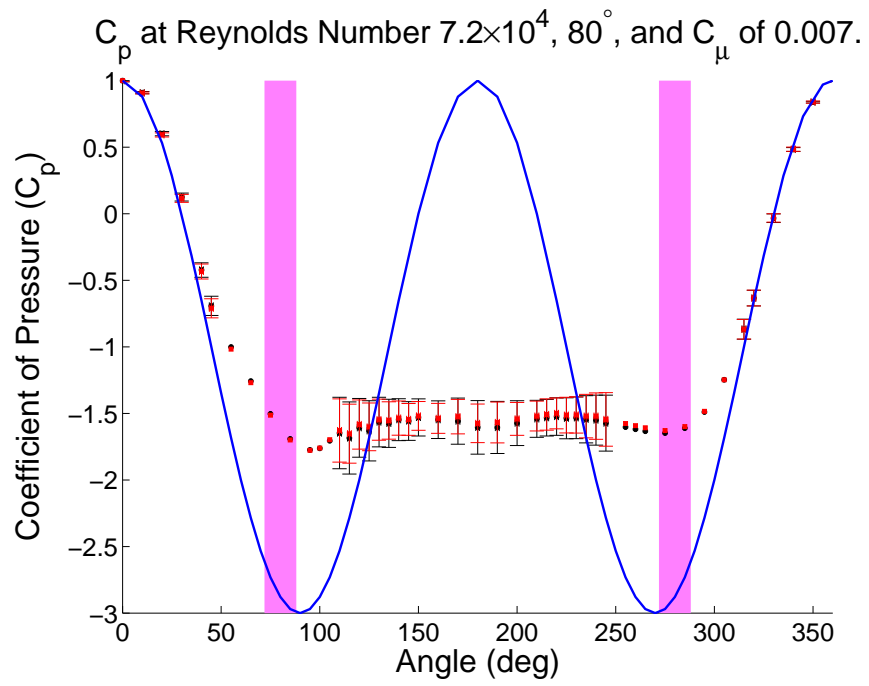
Figure A.67: Synthetic Jet Actuators on a Circular Cylinder.
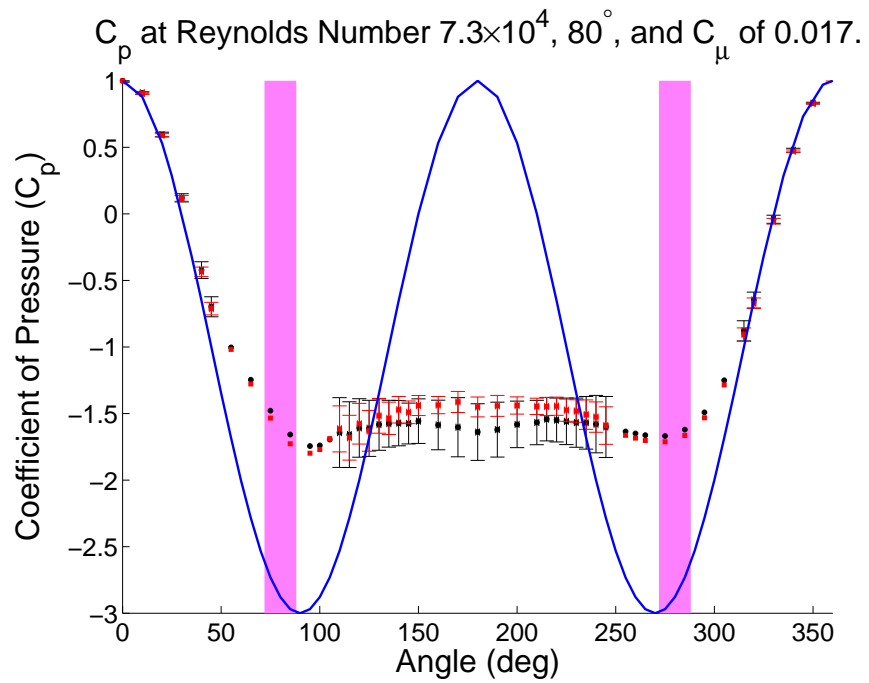
Figure A.68: Synthetic Jet Actuators on a Circular Cylinder.
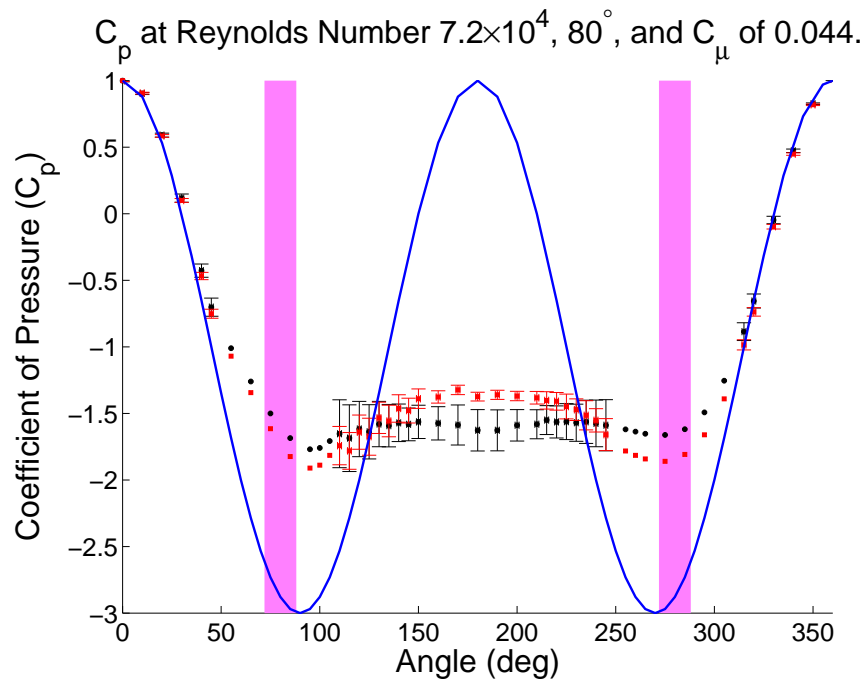
Figure A.69: Synthetic Jet Actuators on a Circular Cylinder.
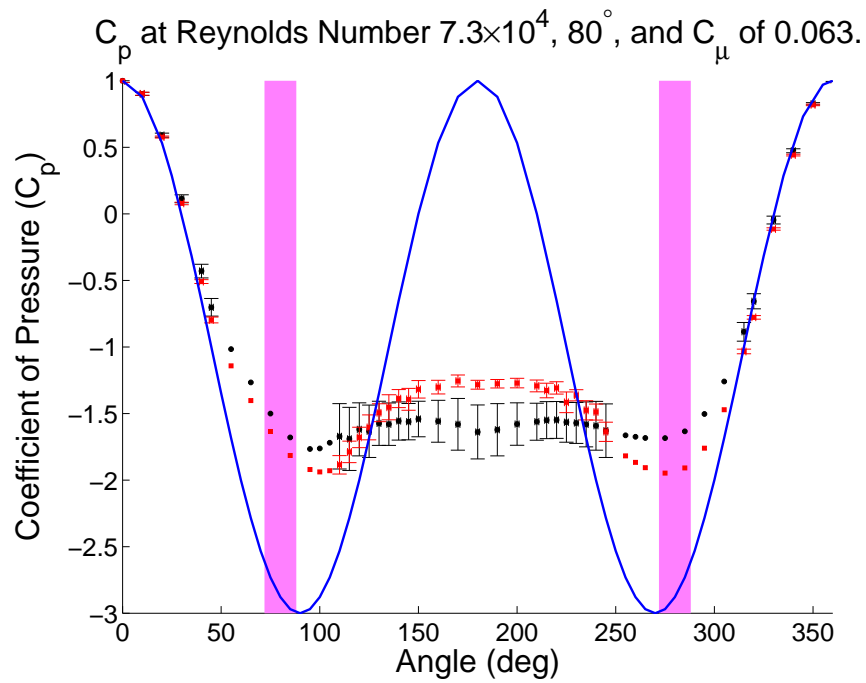
Figure A.70: Synthetic Jet Actuators on a Circular Cylinder.
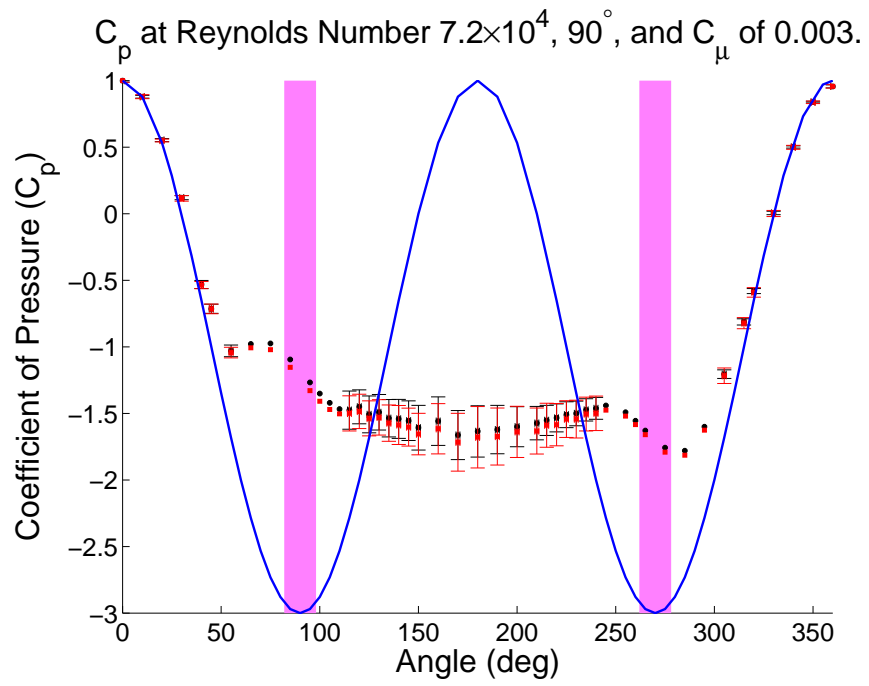
Figure A.71: Synthetic Jet Actuators on a Circular Cylinder.
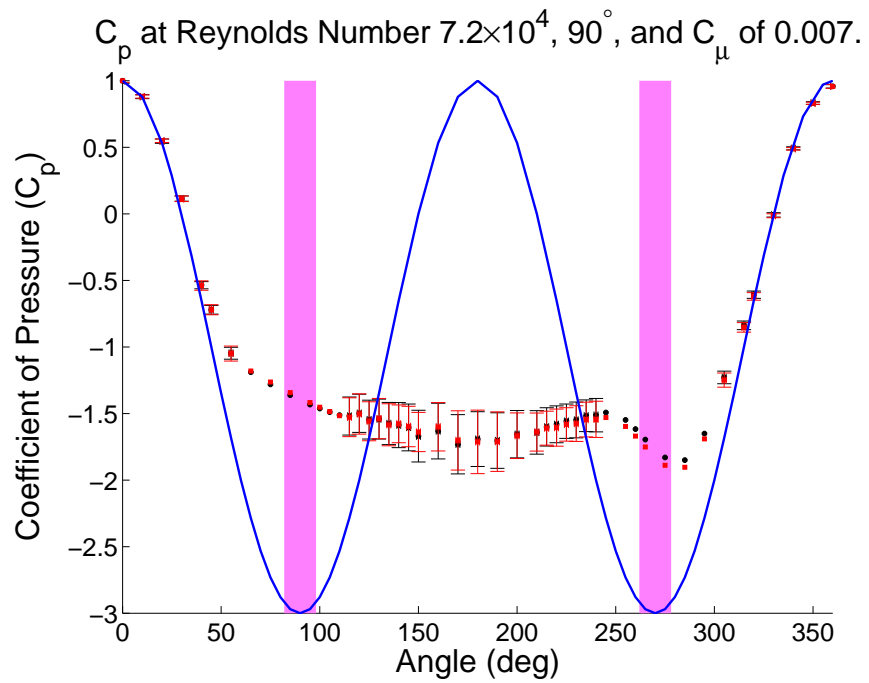
Figure A.72: Synthetic Jet Actuators on a Circular Cylinder.
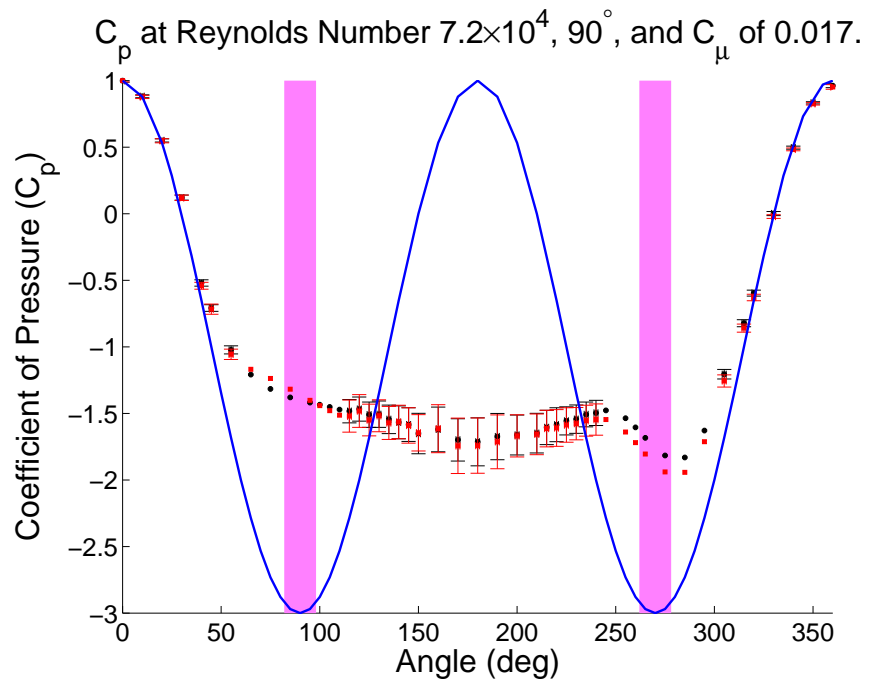
Figure A.73: Synthetic Jet Actuators on a Circular Cylinder.
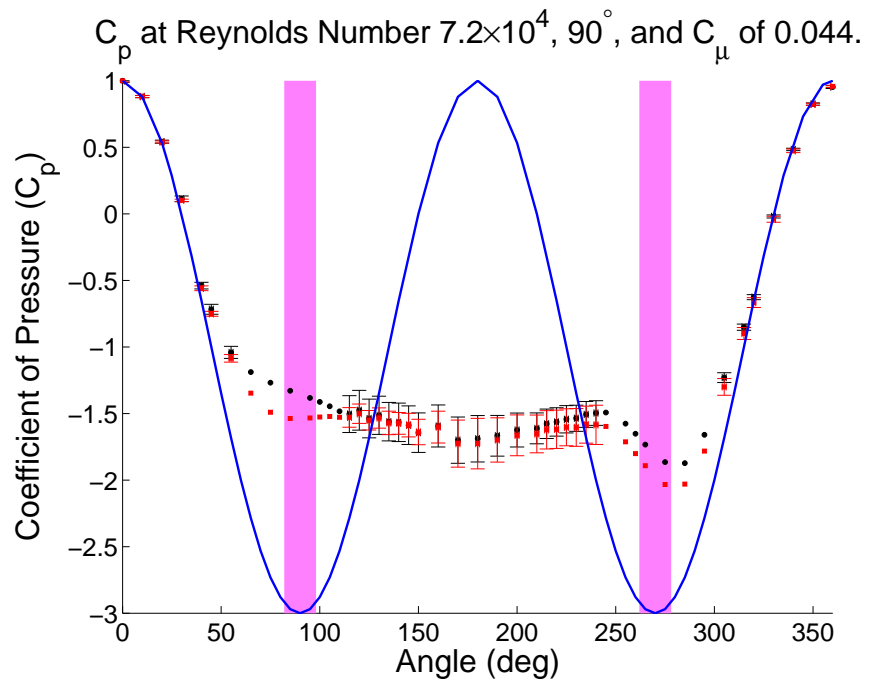
Figure A.74: Synthetic Jet Actuators on a Circular Cylinder.
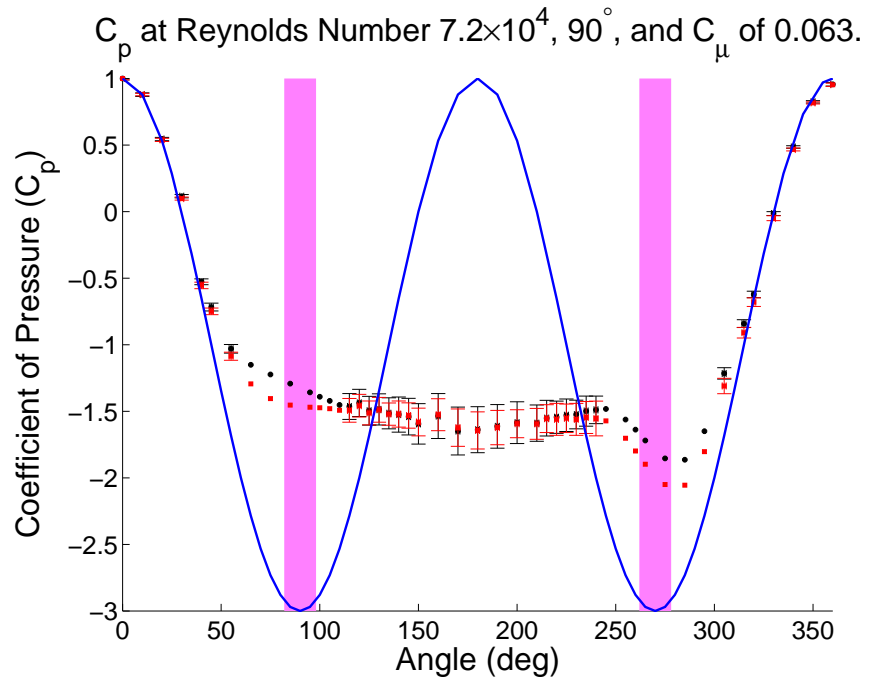
Figure A.75: Synthetic Jet Actuators on a Circular Cylinder.
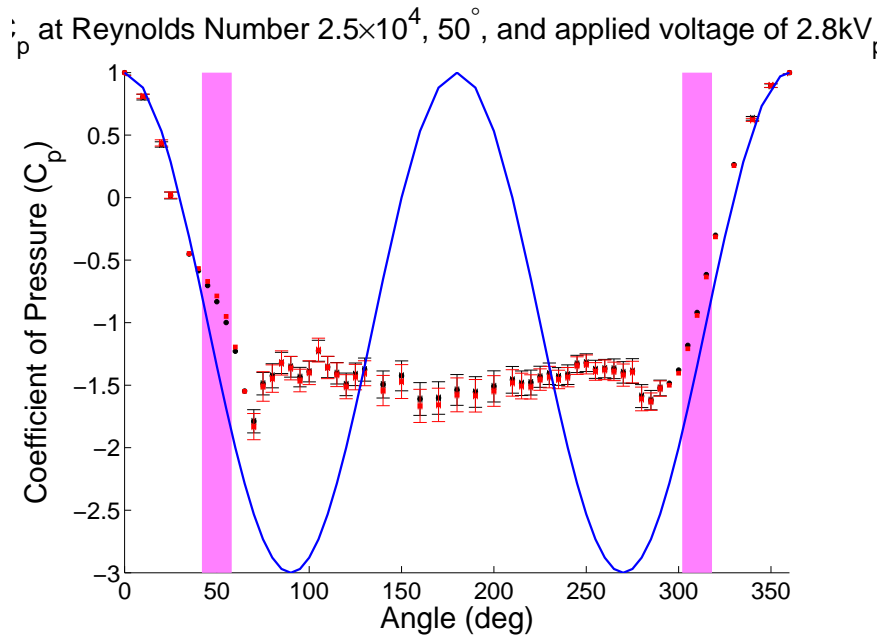
Figure A.76: Plasma Actuators on a Circular Cylinder.
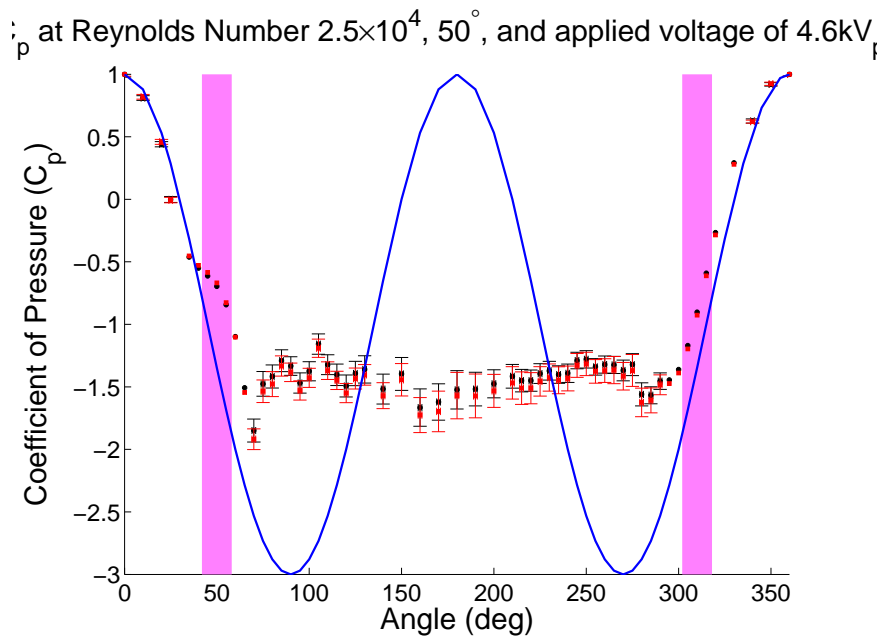
Figure A.77: Plasma Actuators on a Circular Cylinder.
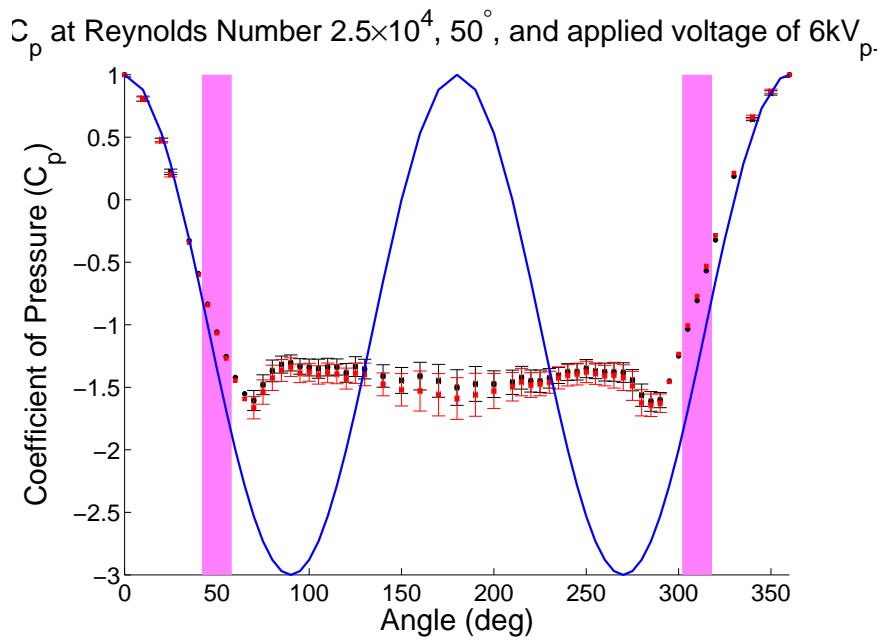
Figure A.78: Plasma Actuators on a Circular Cylinder.
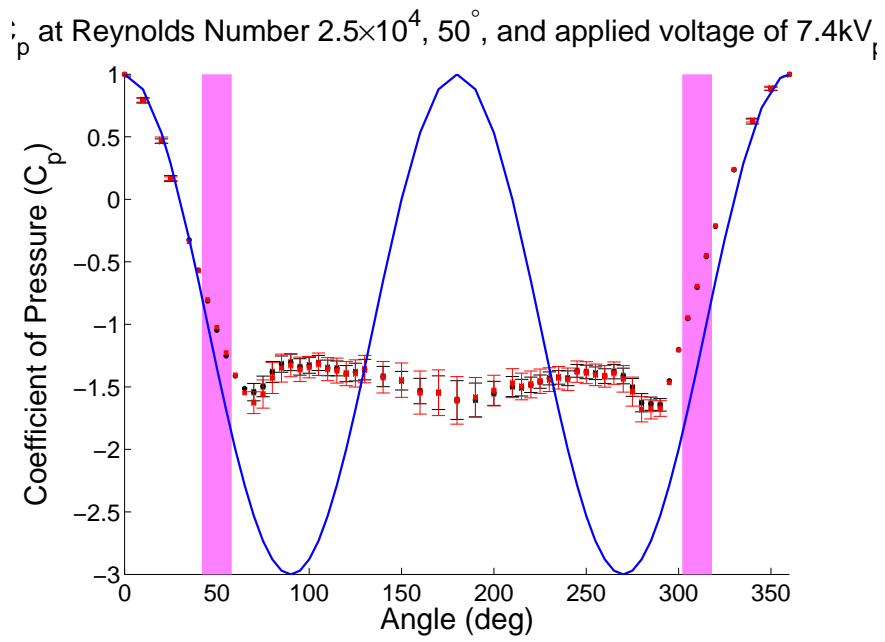
Figure A.79: Plasma Actuators on a Circular Cylinder.
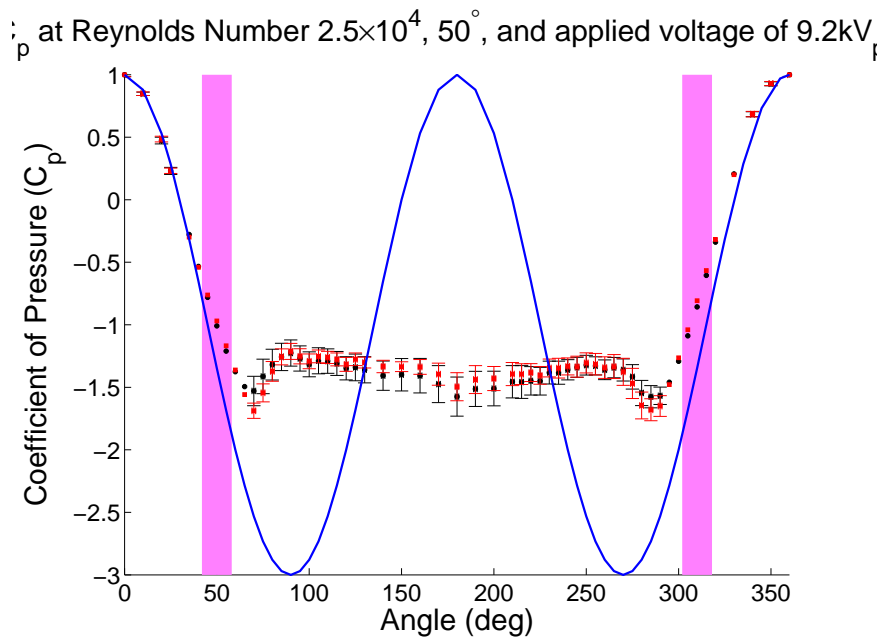
Figure A.80: Plasma Actuators on a Circular Cylinder.

at Reynolds Number 2.5×10⁴, 50°, and applied voltage of 10.3kV
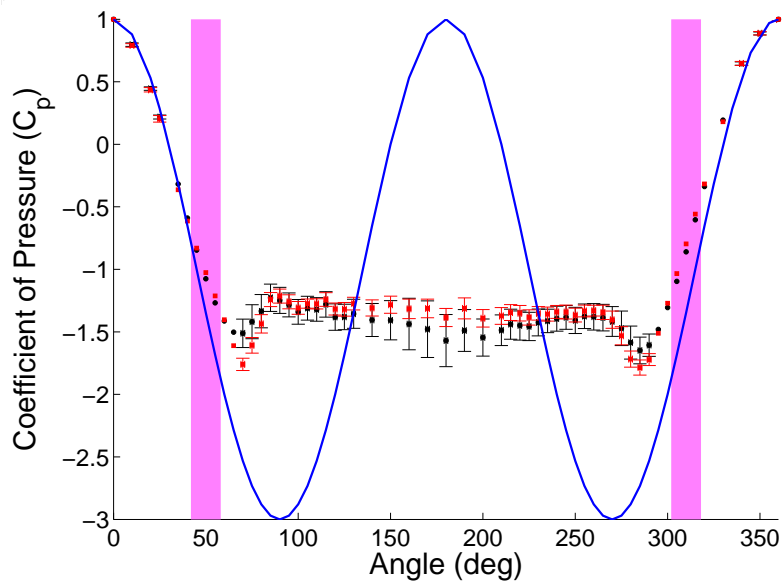
Figure A.81: Plasma Actuators on a Circular Cylinder.

at Reynolds Number 2.5×10⁴, 50°, and applied voltage of 10.3kV
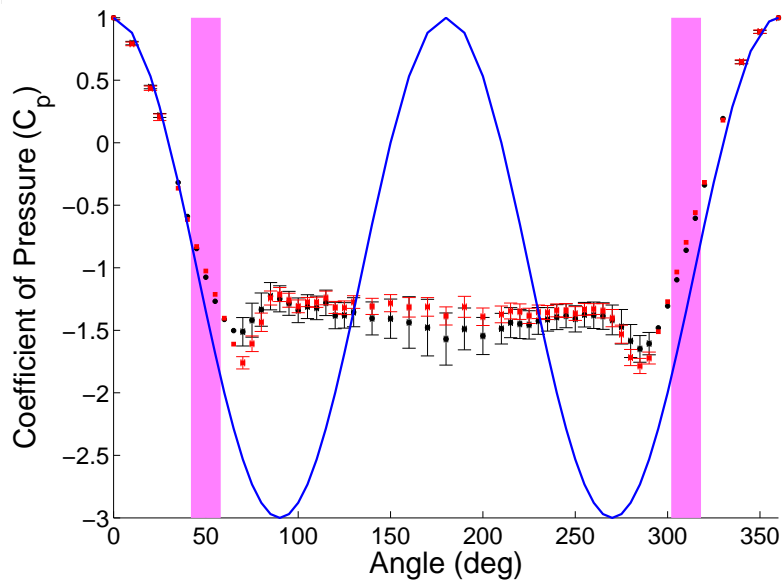
Figure A.82: Plasma Actuators on a Circular Cylinder.
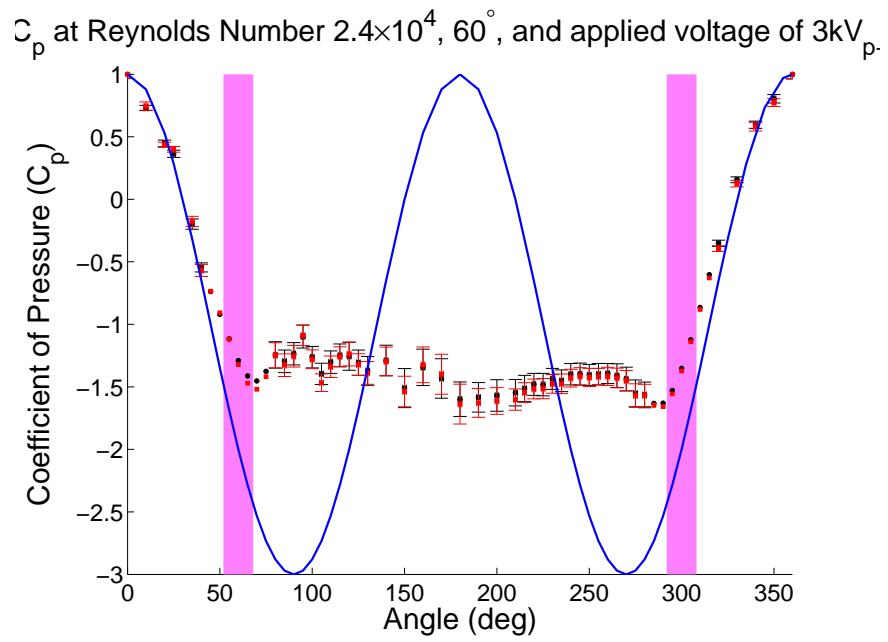
Figure A.83: Plasma Actuators on a Circular Cylinder.
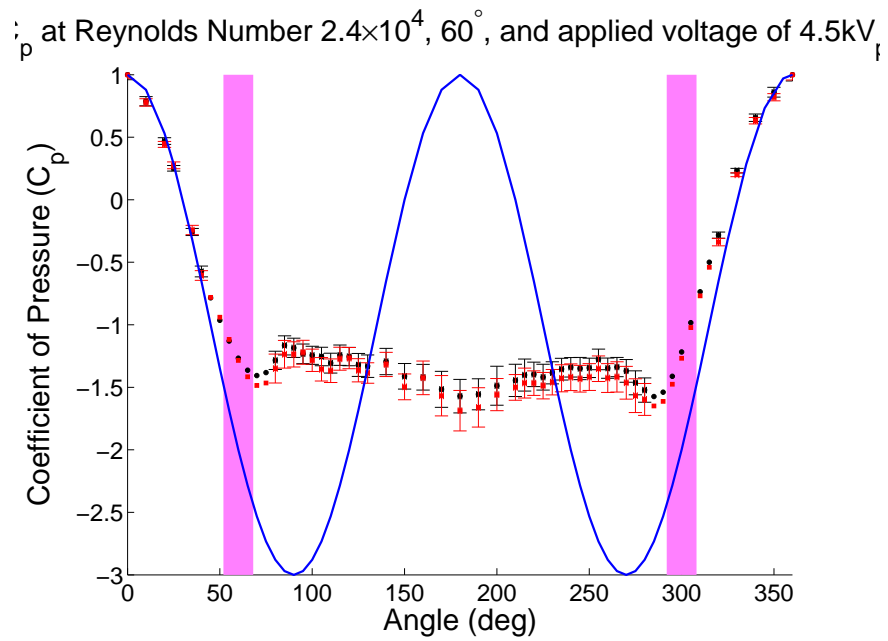
Figure A.84: Plasma Actuators on a Circular Cylinder.
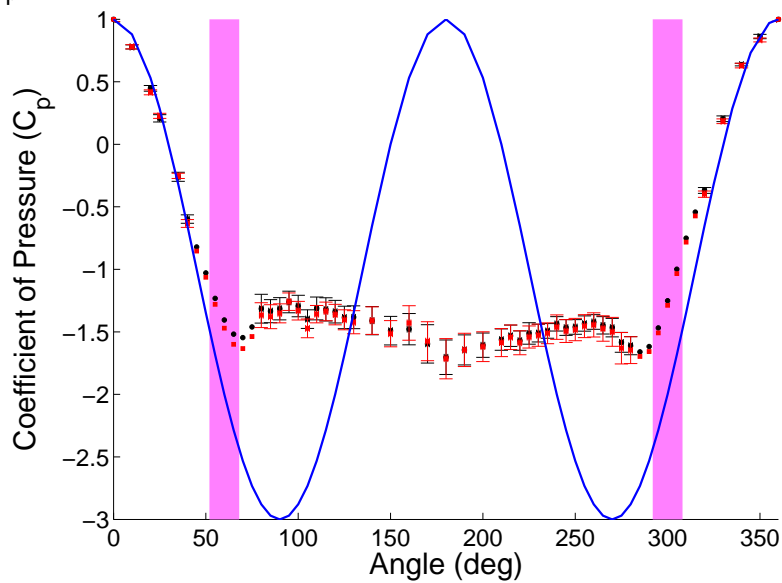
Figure A.85: Plasma Actuators on a Circular Cylinder.
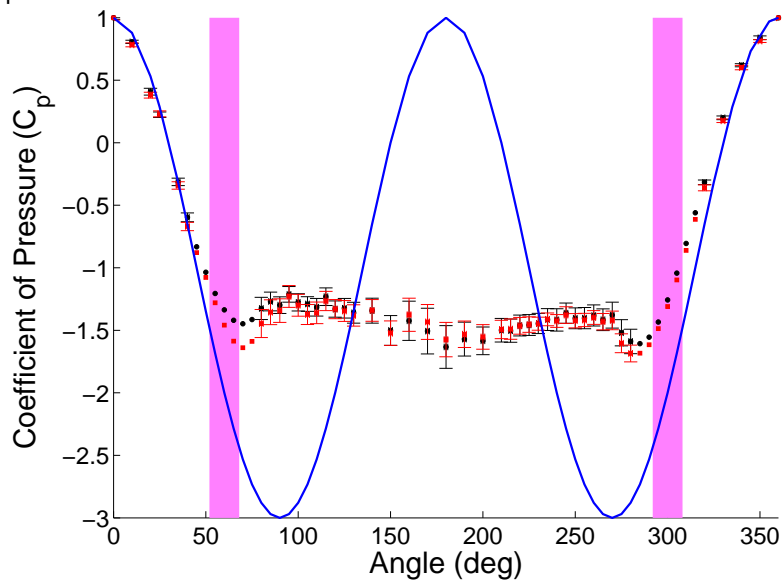
Figure A.86: Plasma Actuators on a Circular Cylinder.

C_p at Reynolds Number 2.4×10^4, $60°$, and applied voltage of 8.9kV
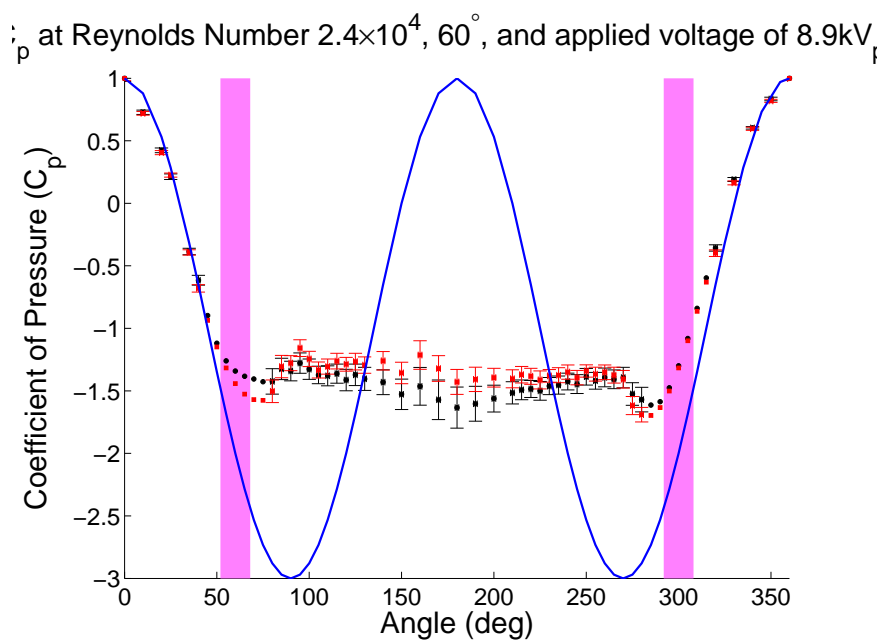
Figure A.87: Plasma Actuators on a Circular Cylinder.

C_p at Reynolds Number 2.4×10^4, $60°$, and applied voltage of 10.3kV
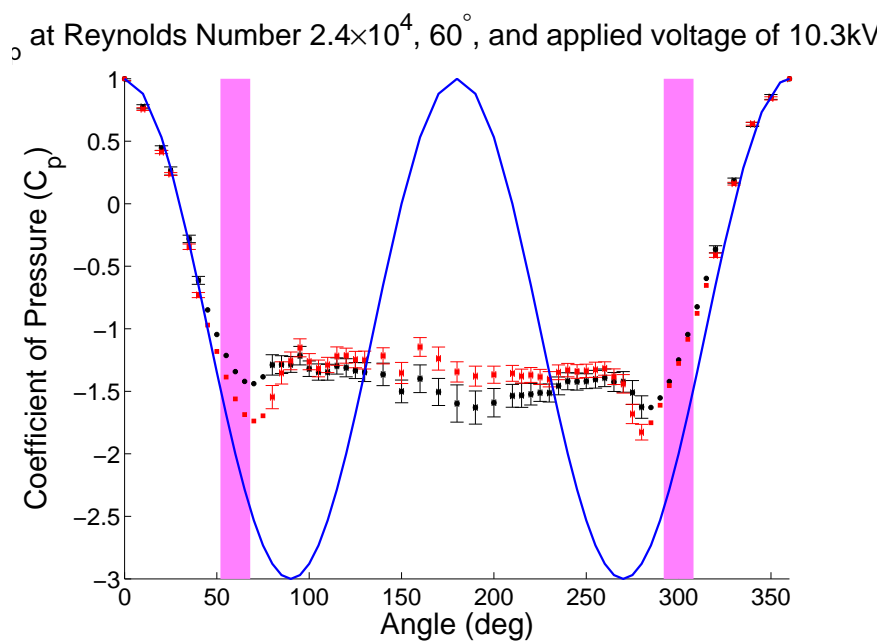
Figure A.88: Plasma Actuators on a Circular Cylinder.
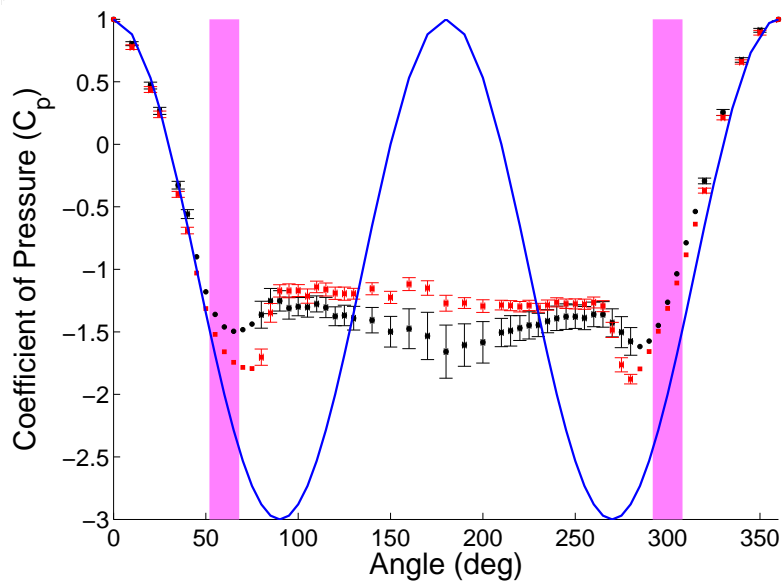
Figure A.89: Plasma Actuators on a Circular Cylinder.
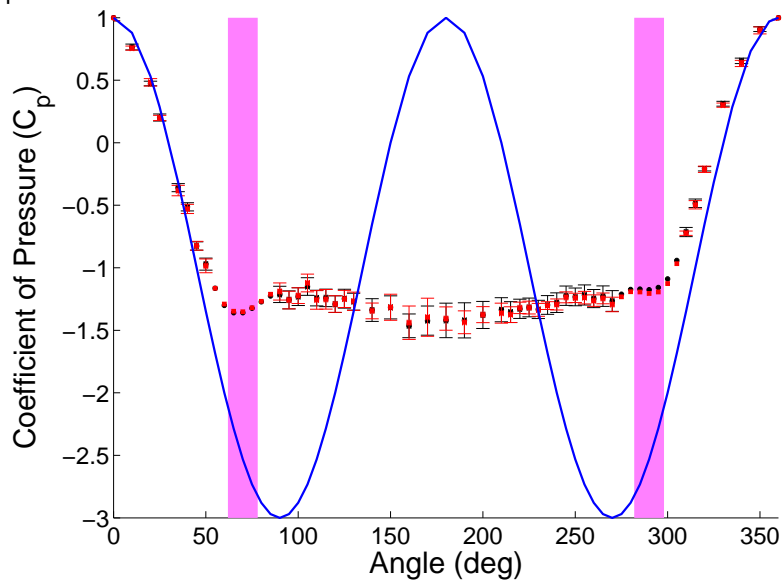
Figure A.90: Plasma Actuators on a Circular Cylinder.
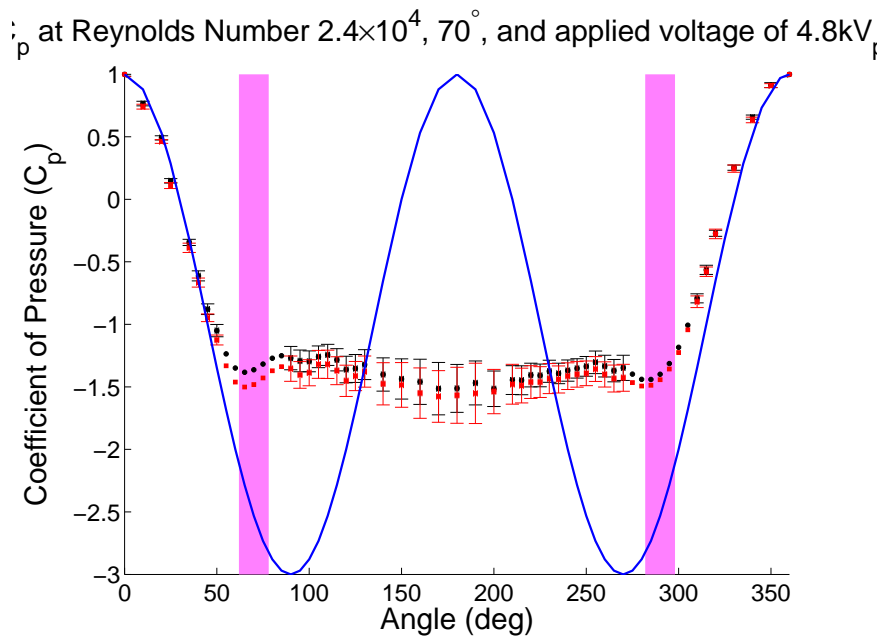
Figure A.91: Plasma Actuators on a Circular Cylinder.
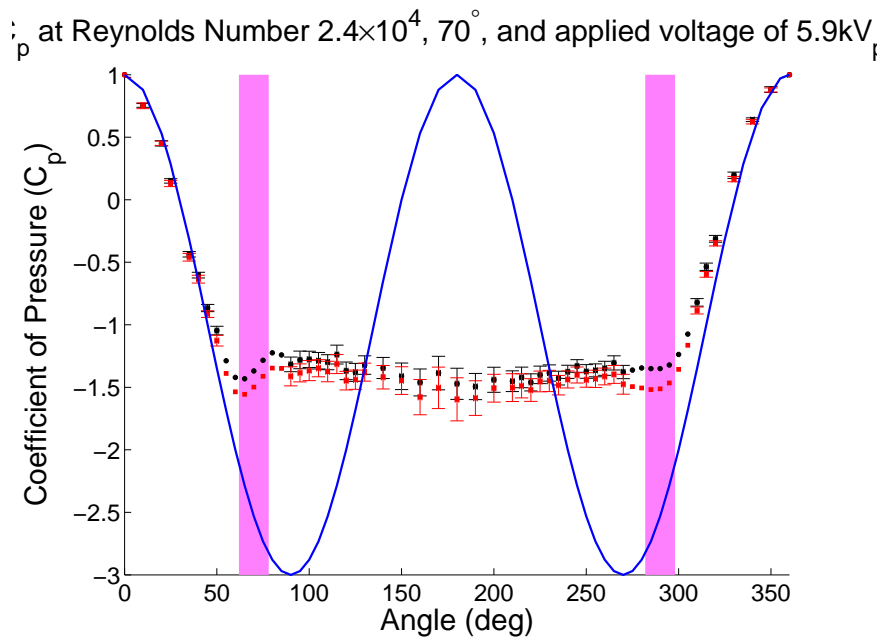
Figure A.92: Plasma Actuators on a Circular Cylinder.
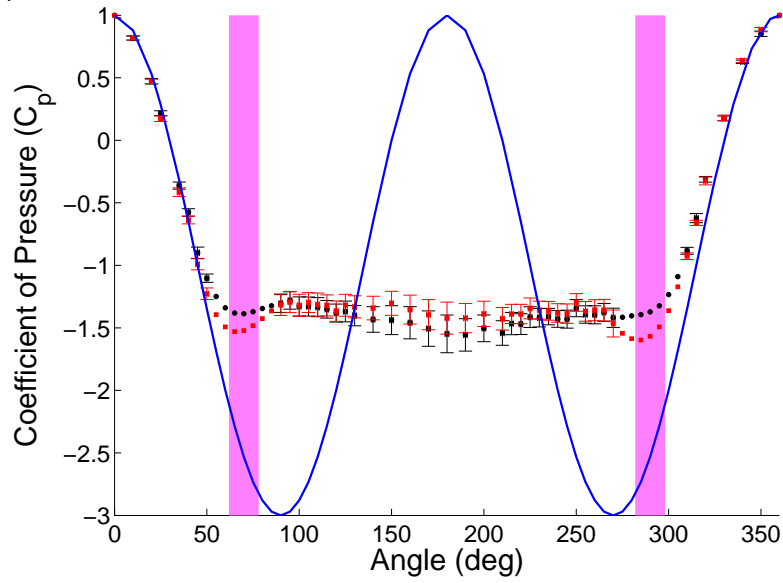
Figure A.93: Plasma Actuators on a Circular Cylinder.
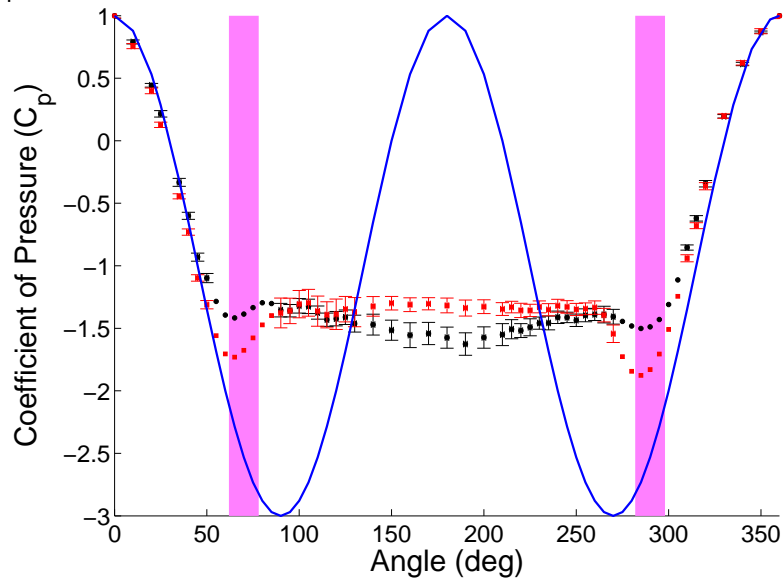
Figure A.94: Plasma Actuators on a Circular Cylinder.

at Reynolds Number 2.4×10^4, 70°, and applied voltage of 10.3kV
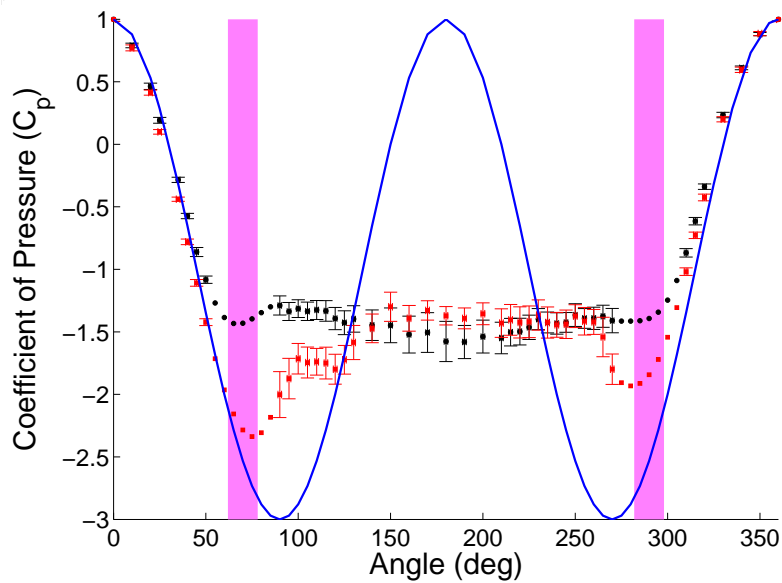
Figure A.95: Plasma Actuators on a Circular Cylinder.

at Reynolds Number 2.4×10^4, 70°, and applied voltage of 11.6kV
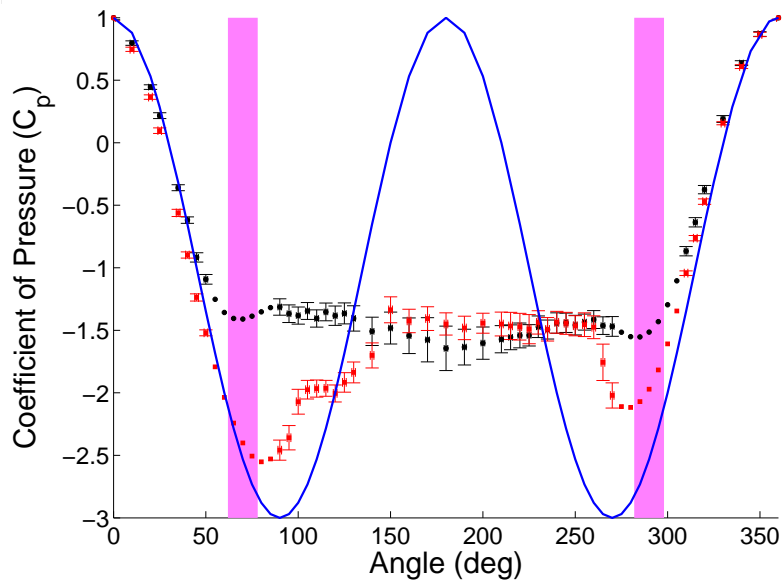
Figure A.96: Plasma Actuators on a Circular Cylinder.
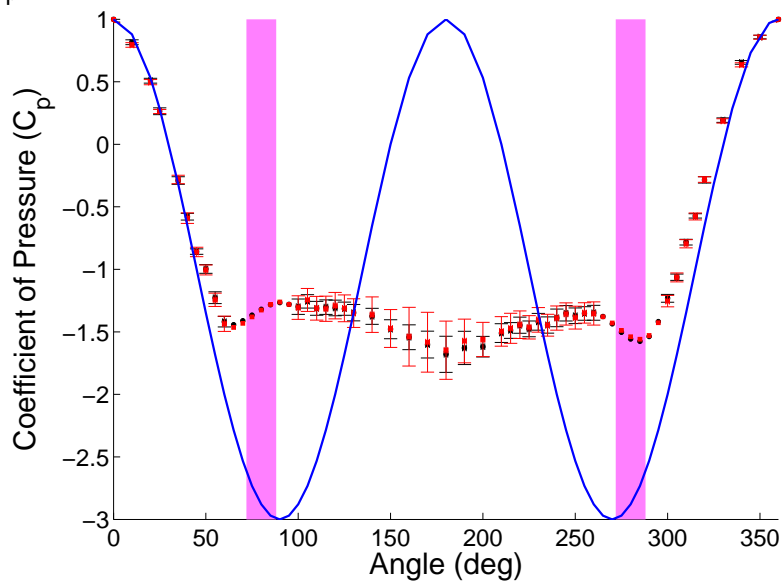
Figure A.97: Plasma Actuators on a Circular Cylinder.
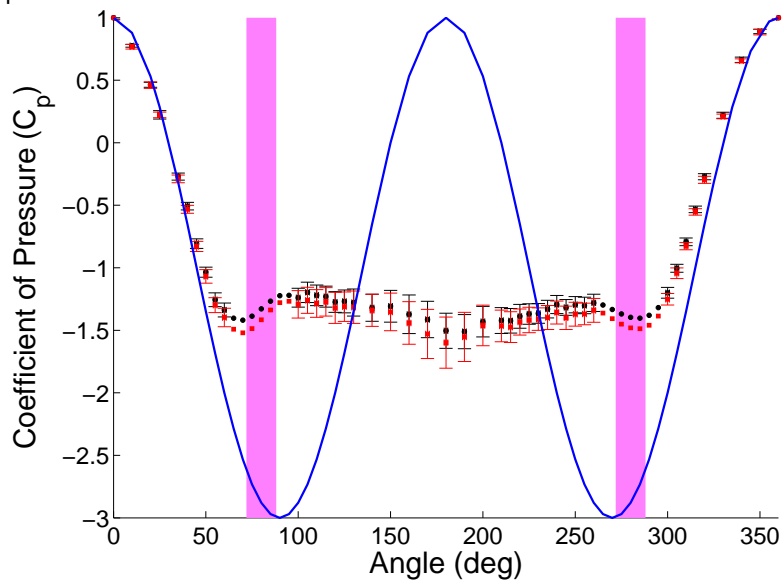
Figure A.98: Plasma Actuators on a Circular Cylinder.
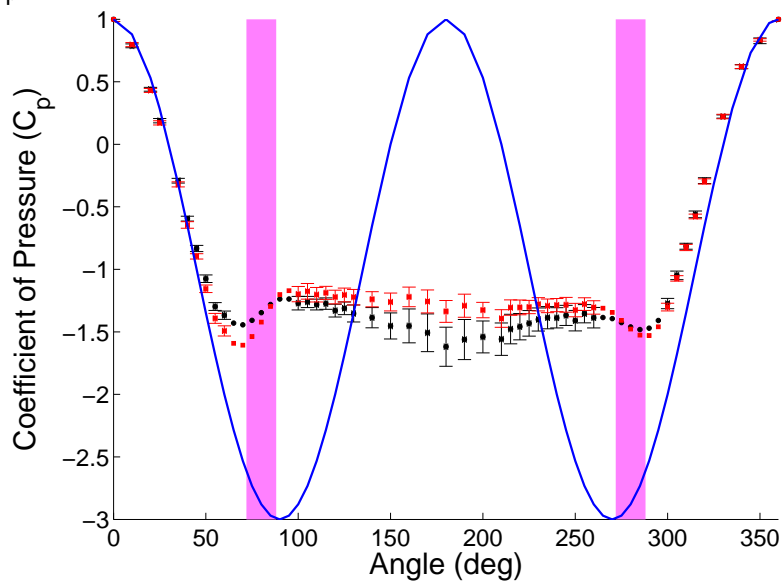
Figure A.99: Plasma Actuators on a Circular Cylinder.
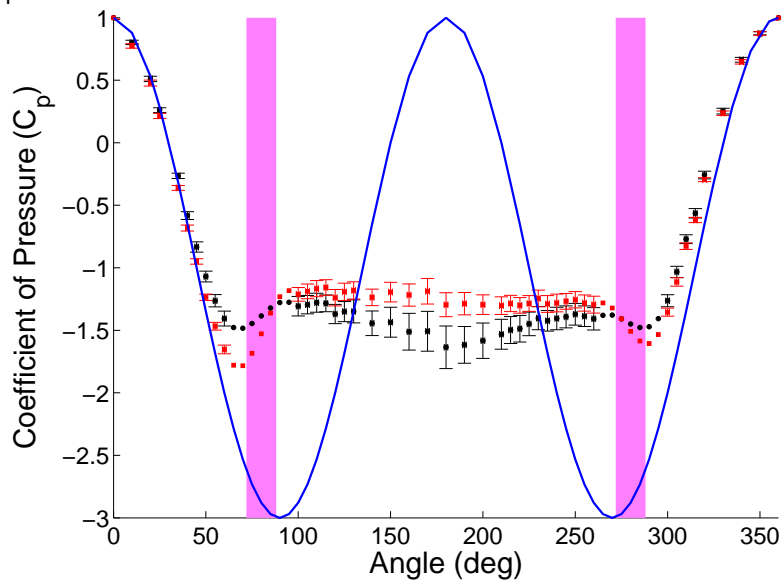
Figure A.100: Plasma Actuators on a Circular Cylinder.

200
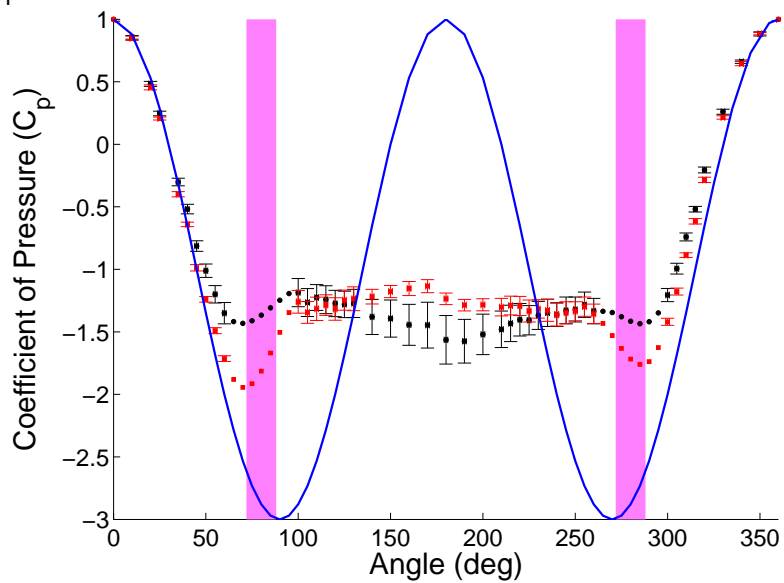
Figure A.101: Plasma Actuators on a Circular Cylinder.
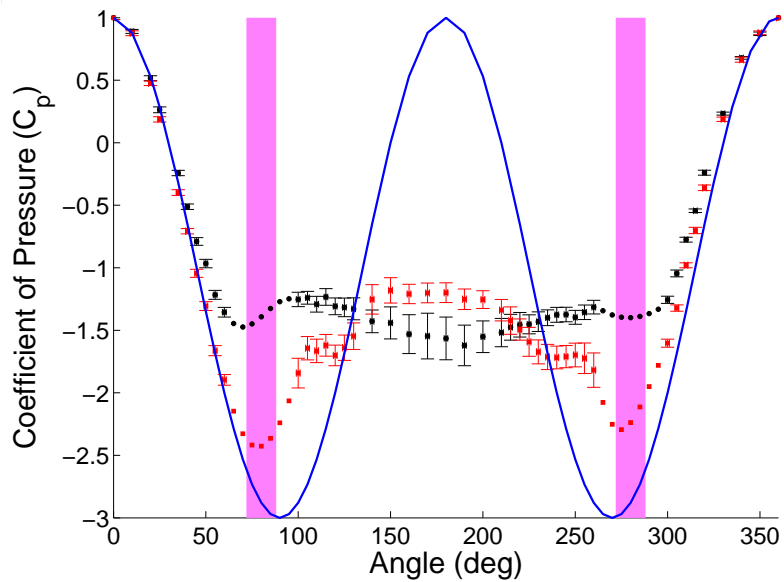
Figure A.102: Plasma Actuators on a Circular Cylinder.
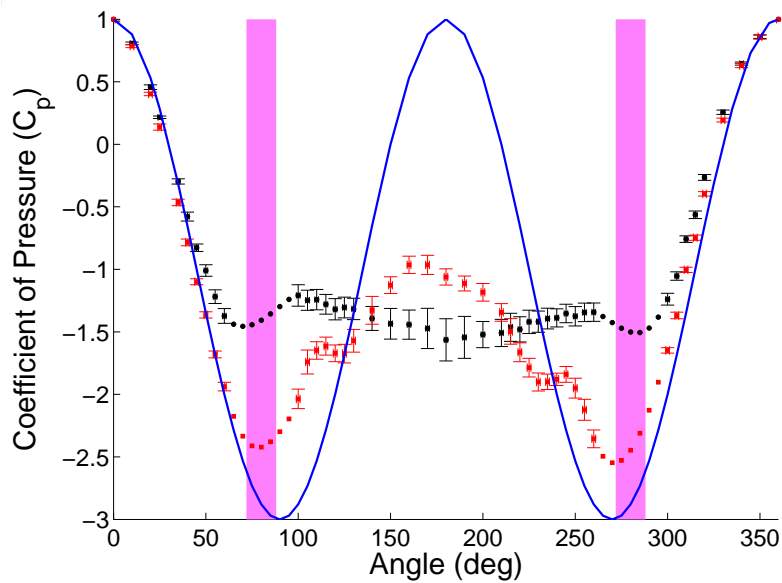
Figure A.103: Plasma Actuators on a Circular Cylinder.
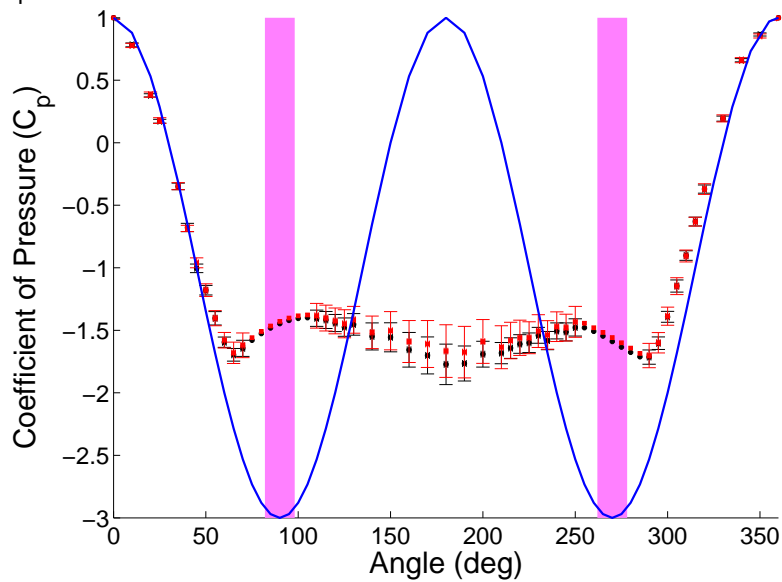
Figure A.104: Plasma Actuators on a Circular Cylinder.
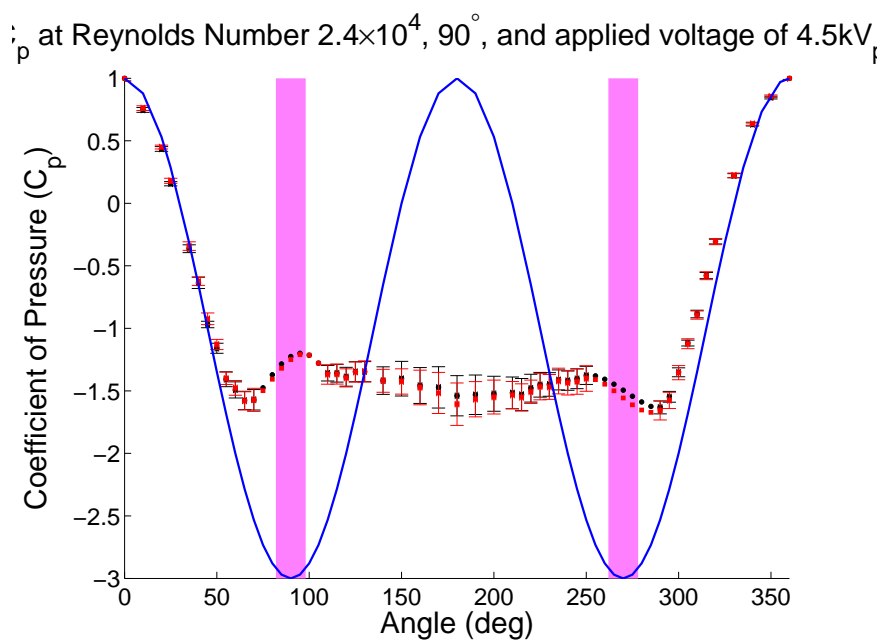
Figure A.105: Plasma Actuators on a Circular Cylinder.
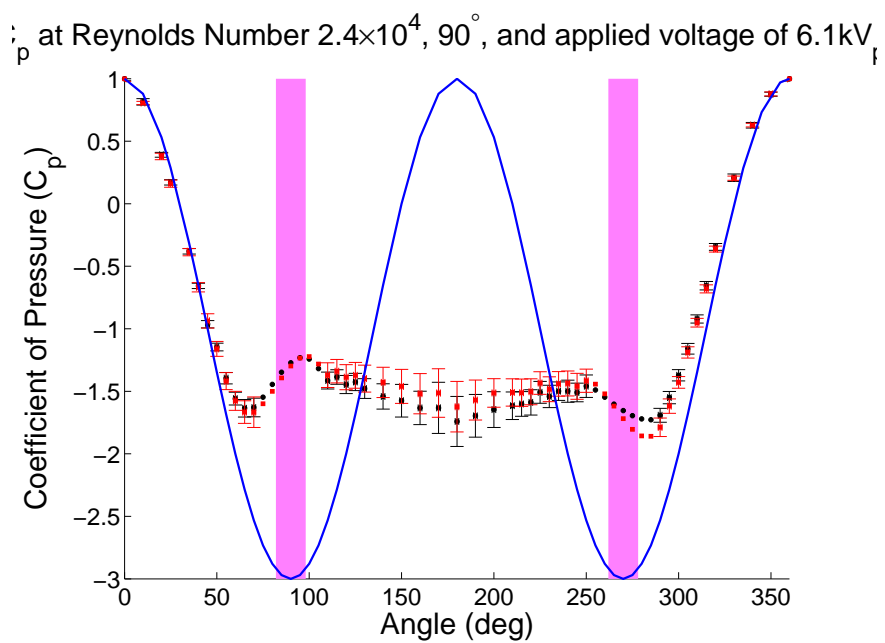
Figure A.106: Plasma Actuators on a Circular Cylinder.
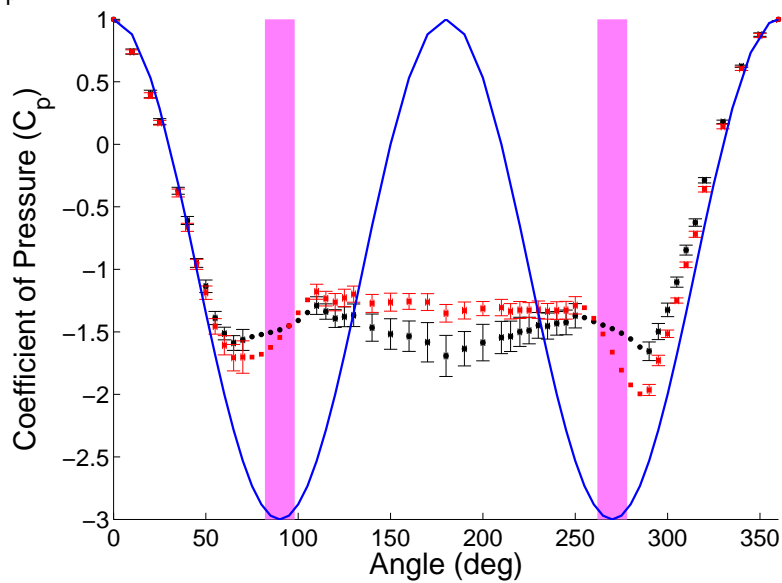
Figure A.107: Plasma Actuators on a Circular Cylinder.
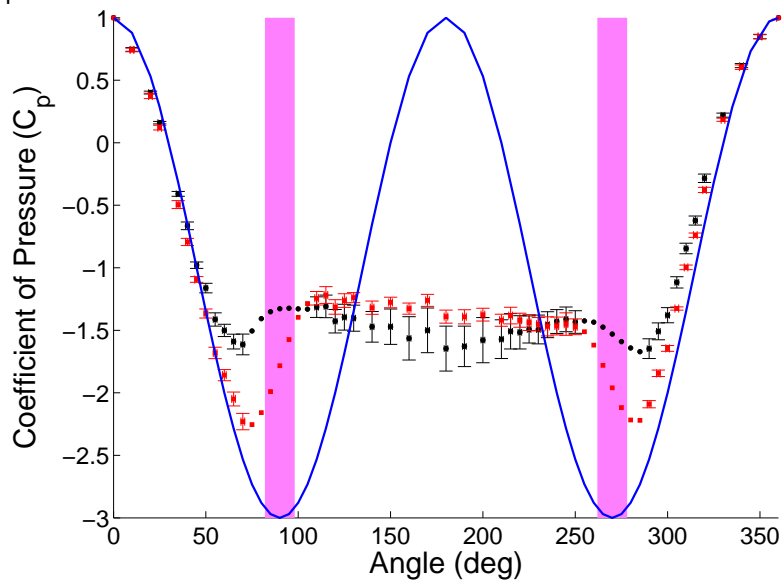
Figure A.108: Plasma Actuators on a Circular Cylinder.
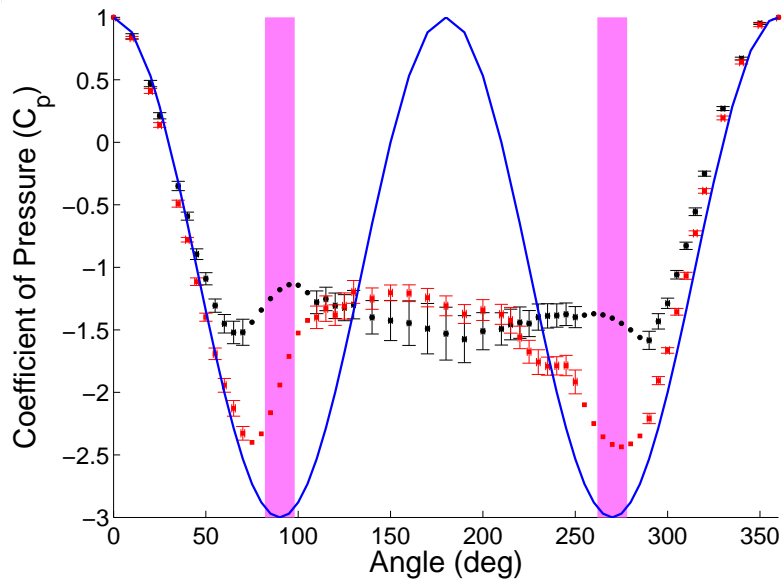
Figure A.109: Plasma Actuators on a Circular Cylinder.
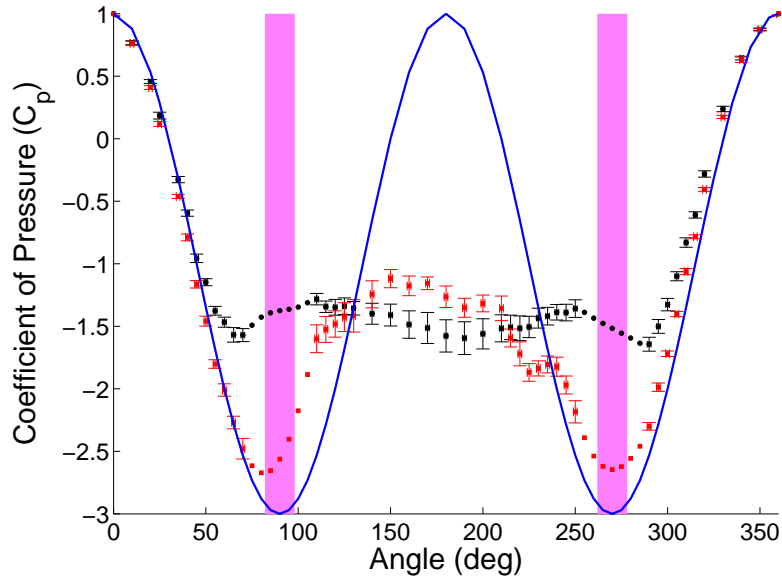
Figure A.110: Plasma Actuators on a Circular Cylinder.

C_p at Reynolds Number 4.8×10^4, $50°$, and applied voltage of 3.2kV$_p$
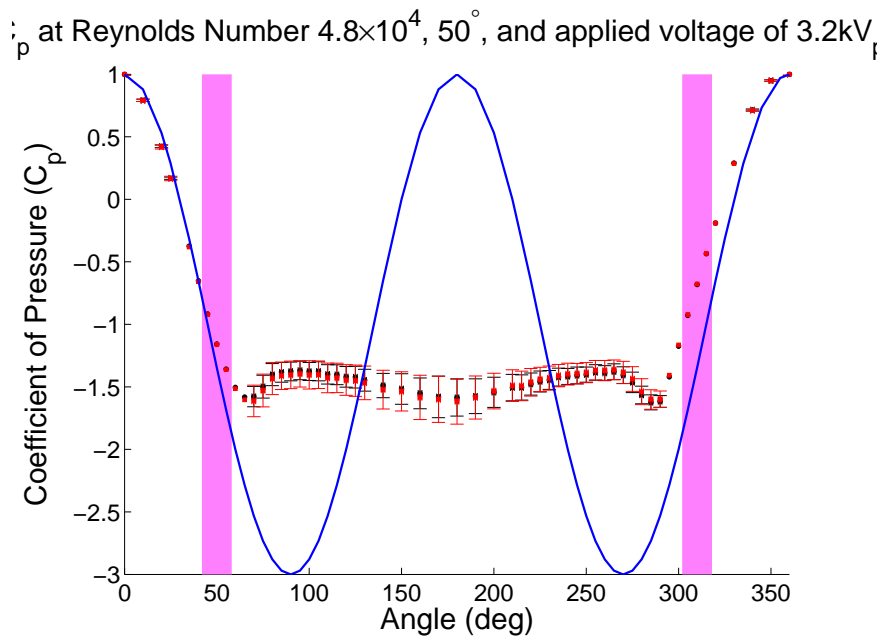
Figure A.111: Plasma Actuators on a Circular Cylinder.

C_p at Reynolds Number 4.9×10^4, $50°$, and applied voltage of 4.4kV$_p$
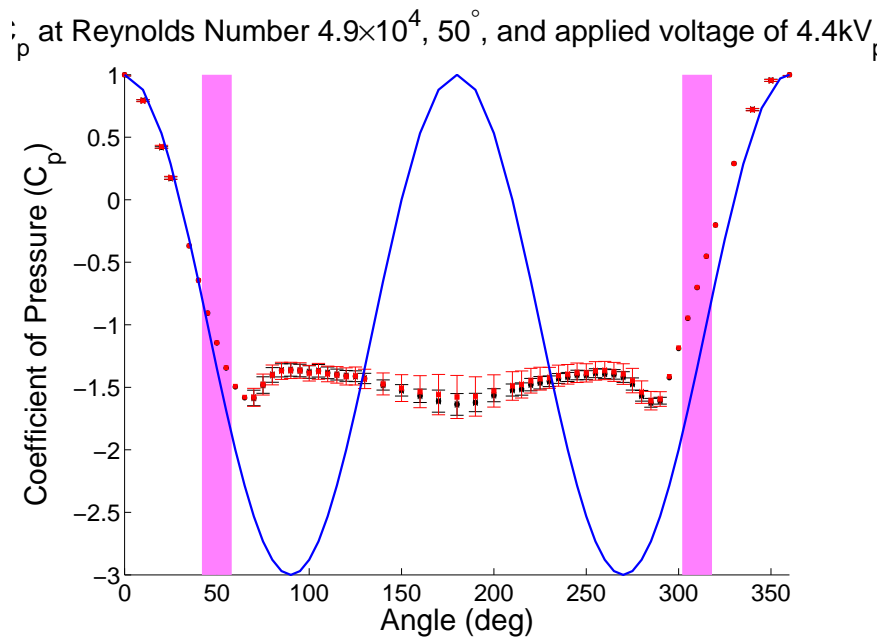
Figure A.112: Plasma Actuators on a Circular Cylinder.
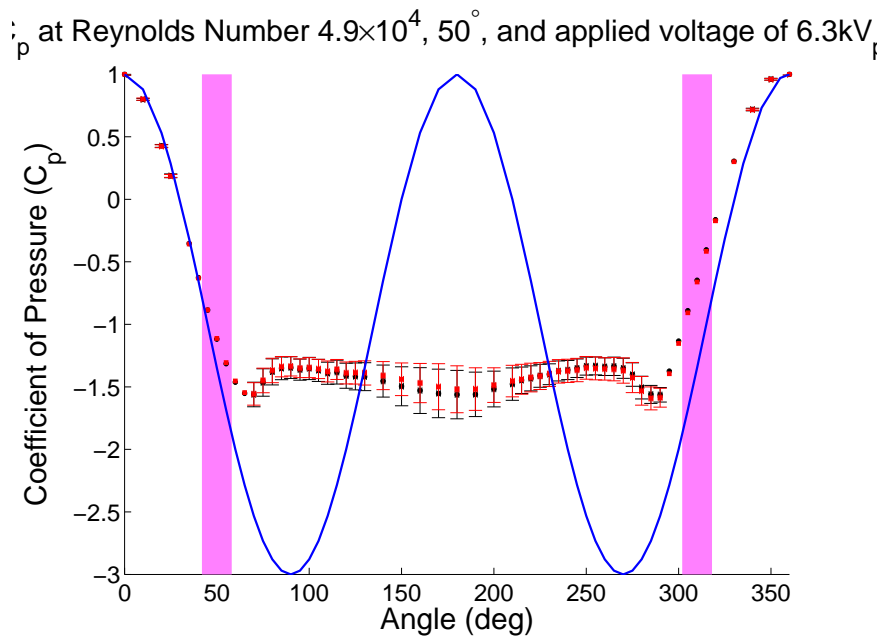
Figure A.113: Plasma Actuators on a Circular Cylinder.
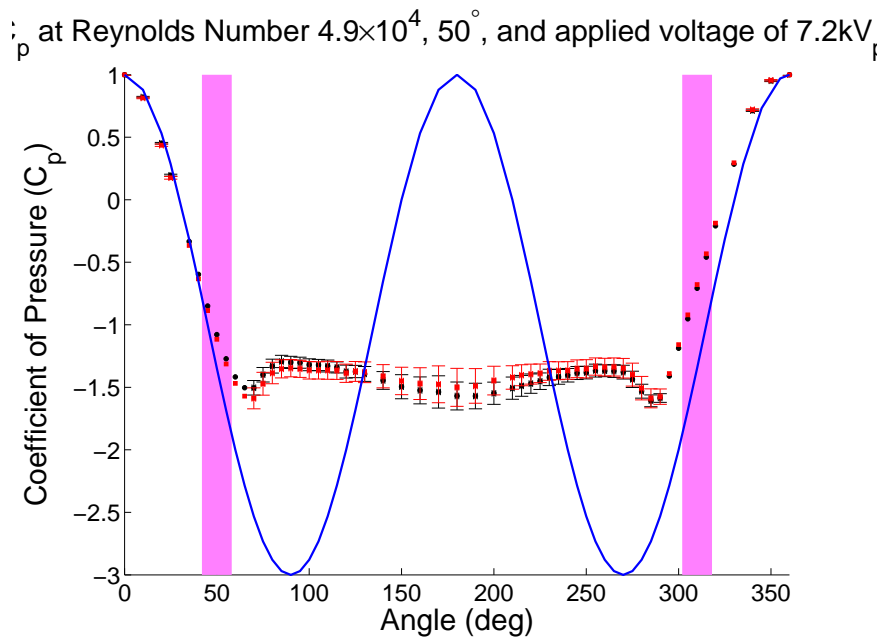
Figure A.114: Plasma Actuators on a Circular Cylinder.

C_p at Reynolds Number 4.9×10^4, 50°, and applied voltage of 8.7kV
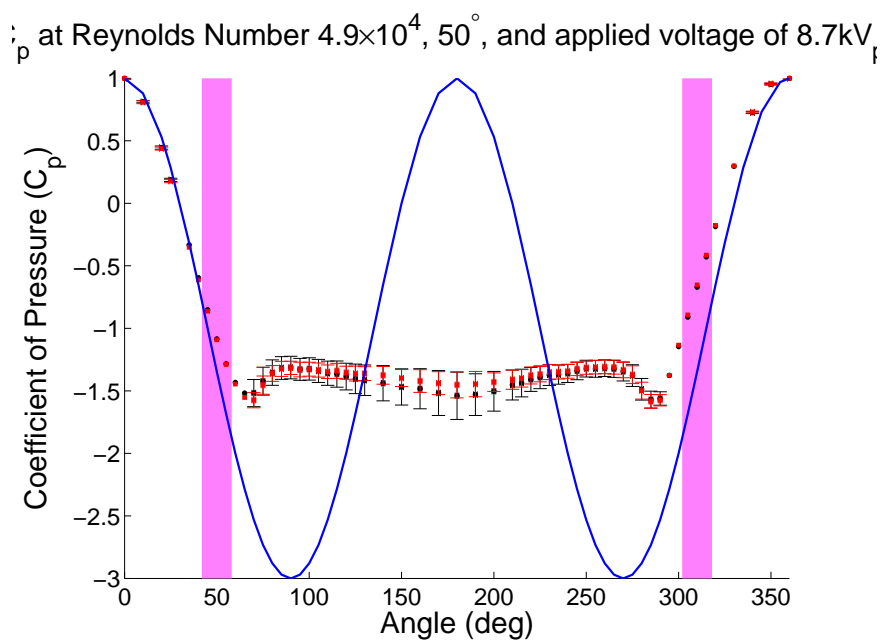
Figure A.115: Plasma Actuators on a Circular Cylinder.

C_p at Reynolds Number 4.9×10^4, 50°, and applied voltage of 10.3kV
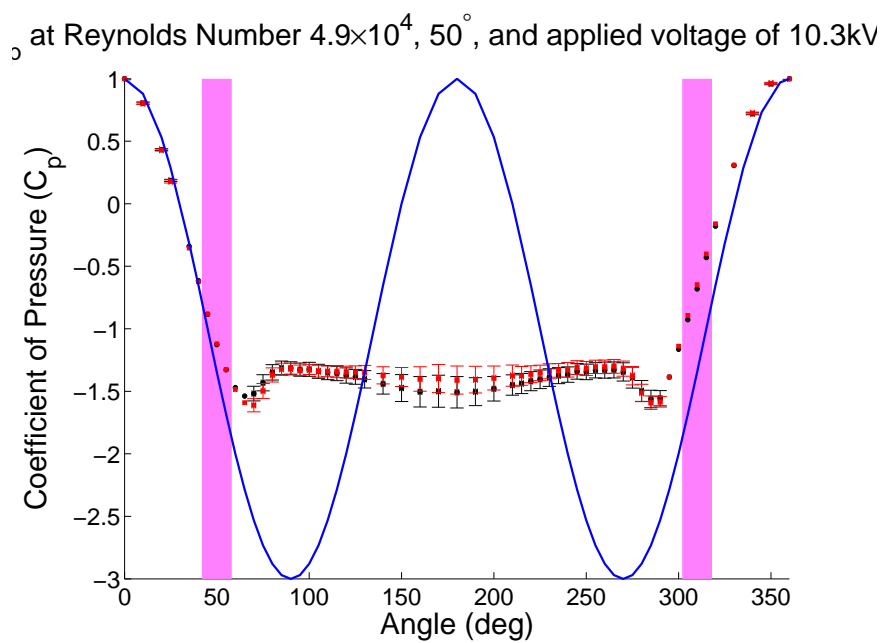
Figure A.116: Plasma Actuators on a Circular Cylinder.
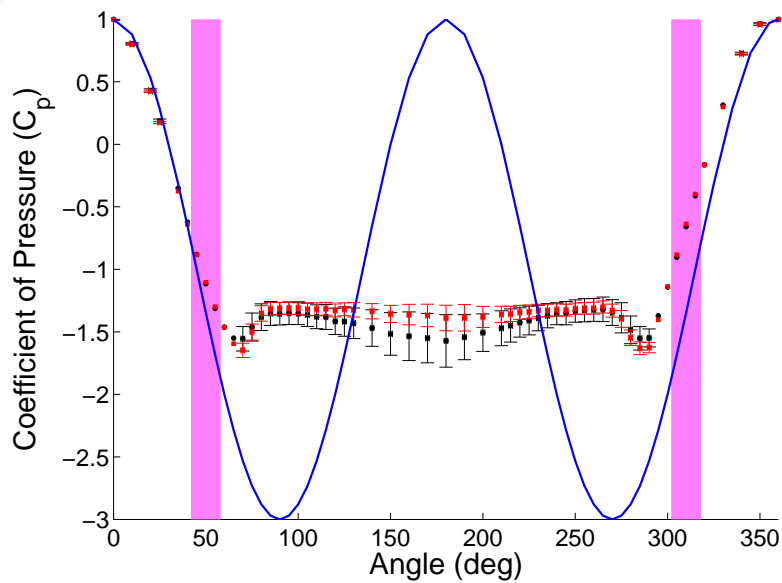
Figure A.117: Plasma Actuators on a Circular Cylinder.

Figure A.118: Plasma Actuators on a Circular Cylinder.
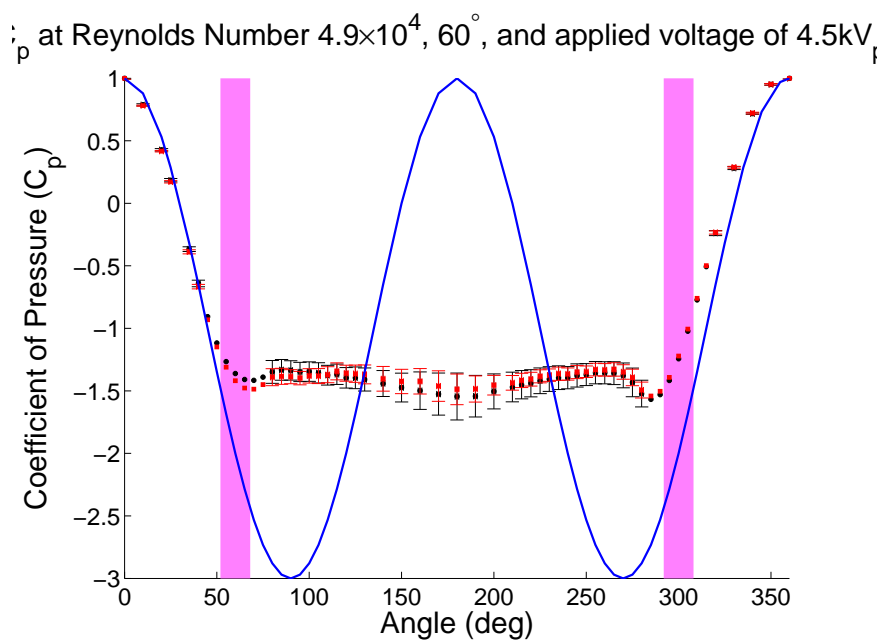
Figure A.119: Plasma Actuators on a Circular Cylinder.
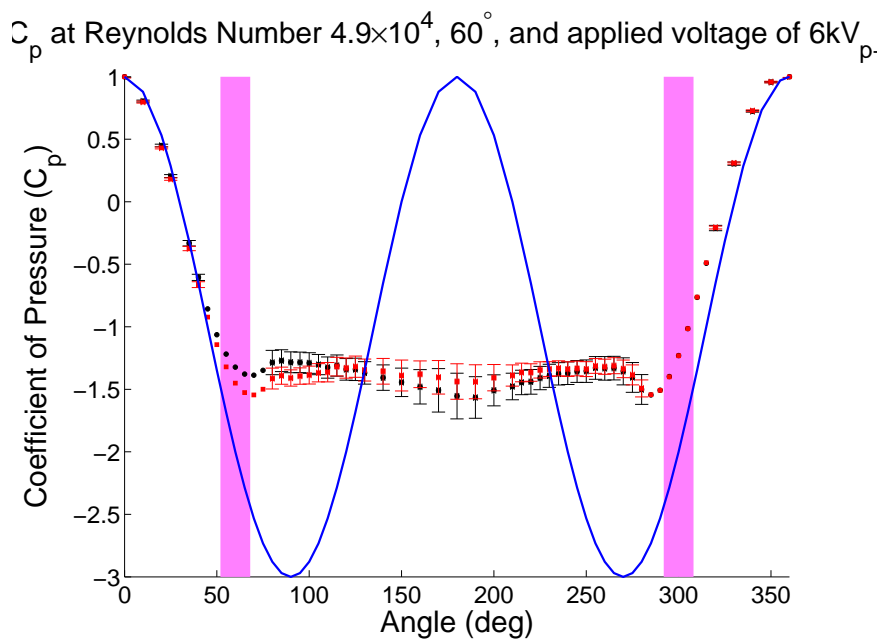
Figure A.120: Plasma Actuators on a Circular Cylinder.
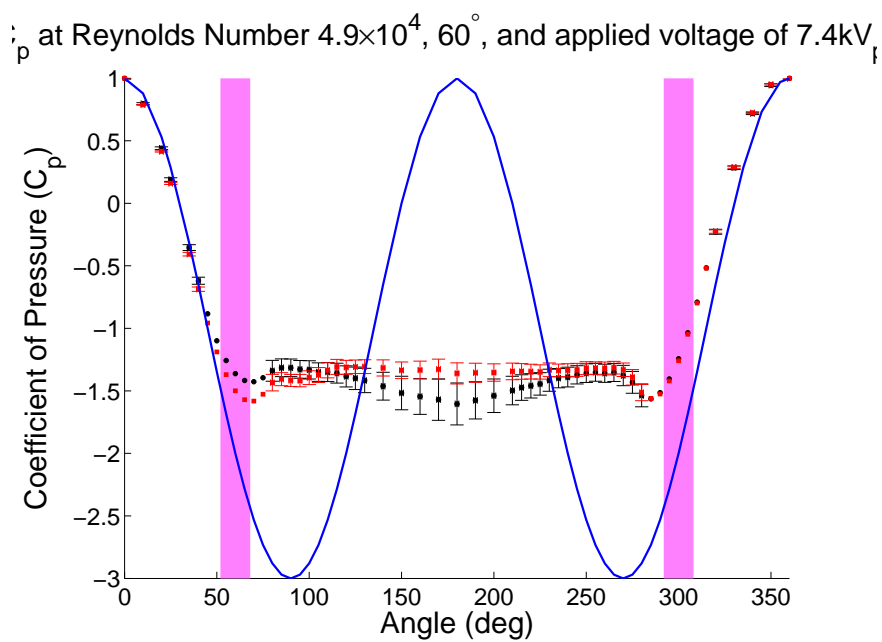
Figure A.121: Plasma Actuators on a Circular Cylinder.
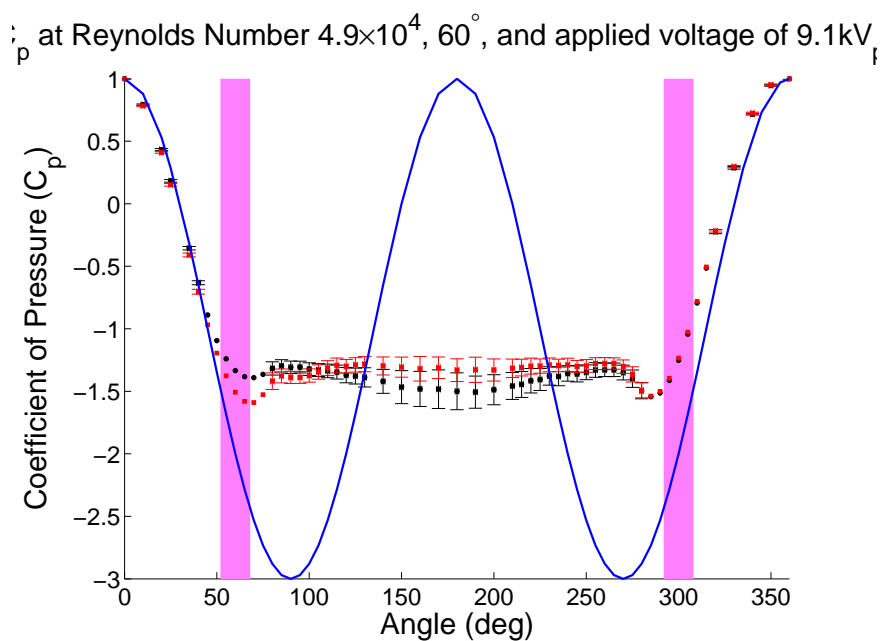
Figure A.122: Plasma Actuators on a Circular Cylinder.

211
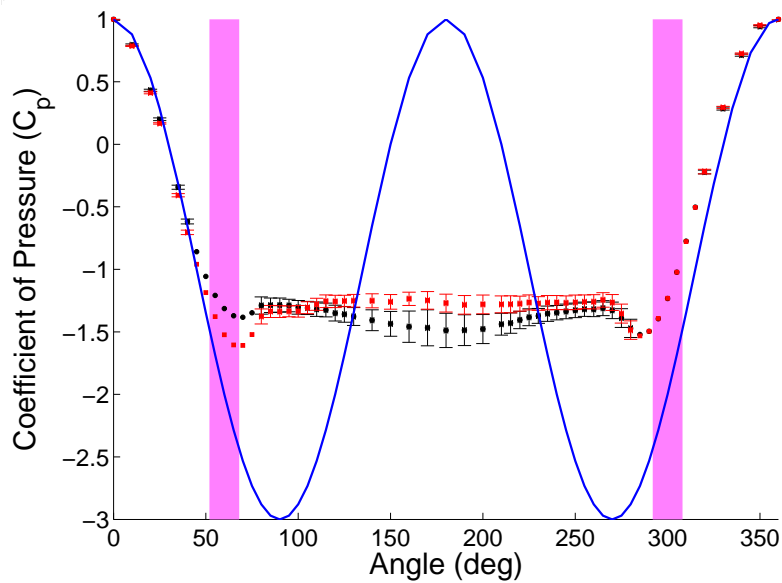
Figure A.123: Plasma Actuators on a Circular Cylinder.
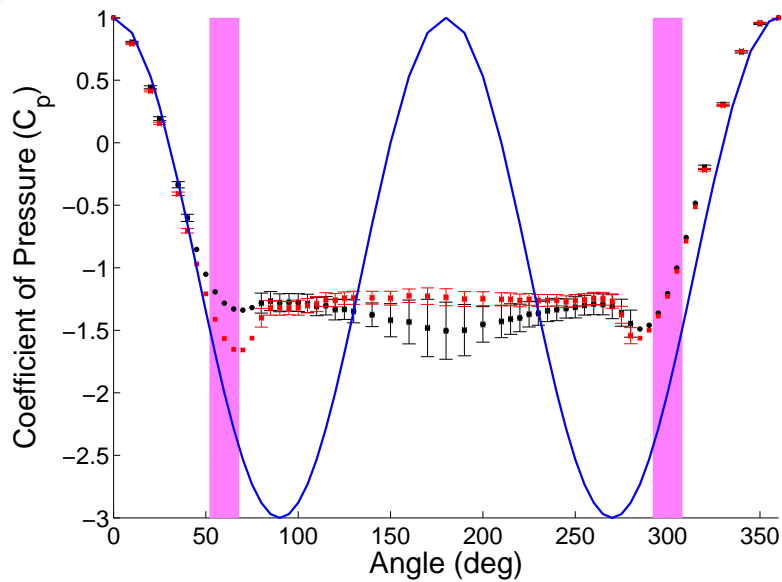
Figure A.124: Plasma Actuators on a Circular Cylinder.
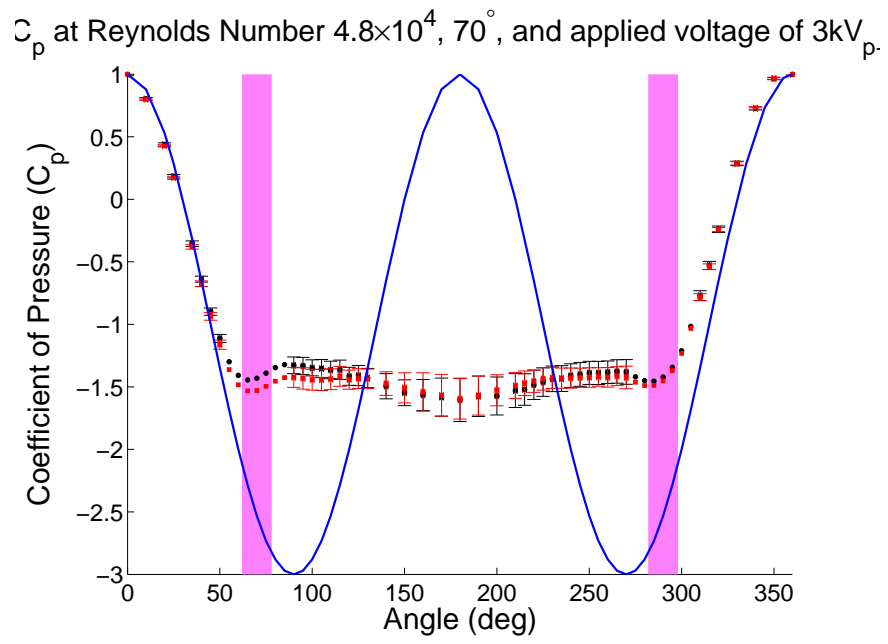
Figure A.125: Plasma Actuators on a Circular Cylinder.
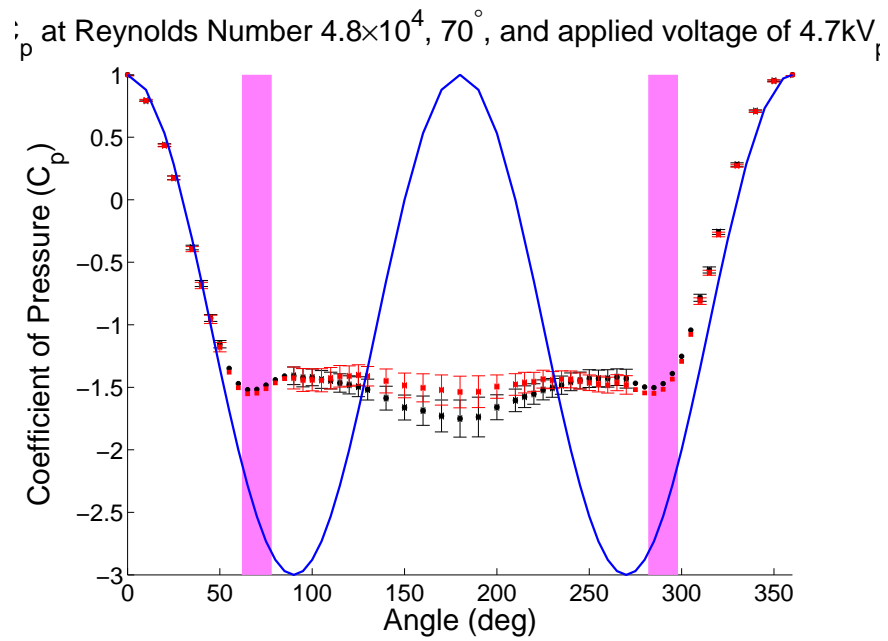
Figure A.126: Plasma Actuators on a Circular Cylinder.
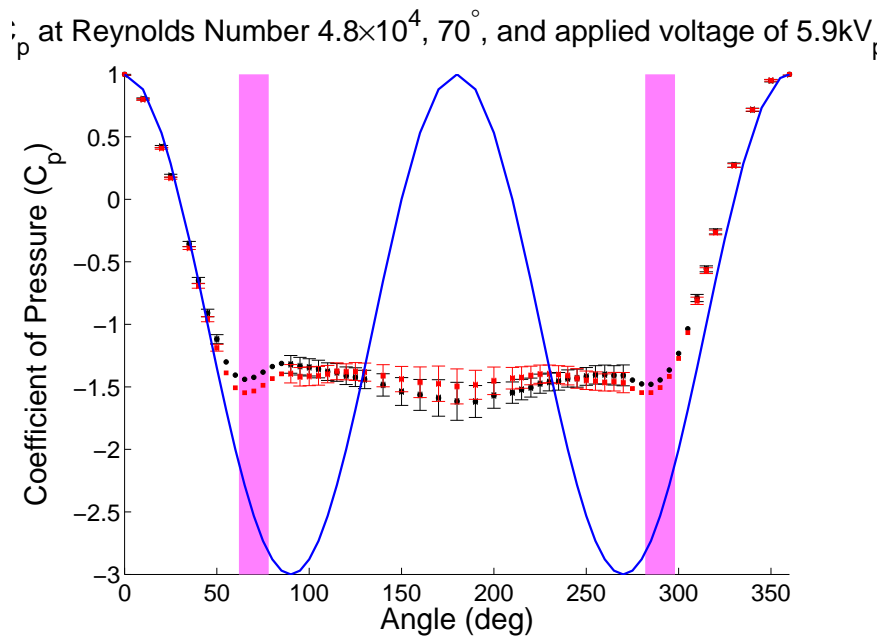
Figure A.127: Plasma Actuators on a Circular Cylinder.
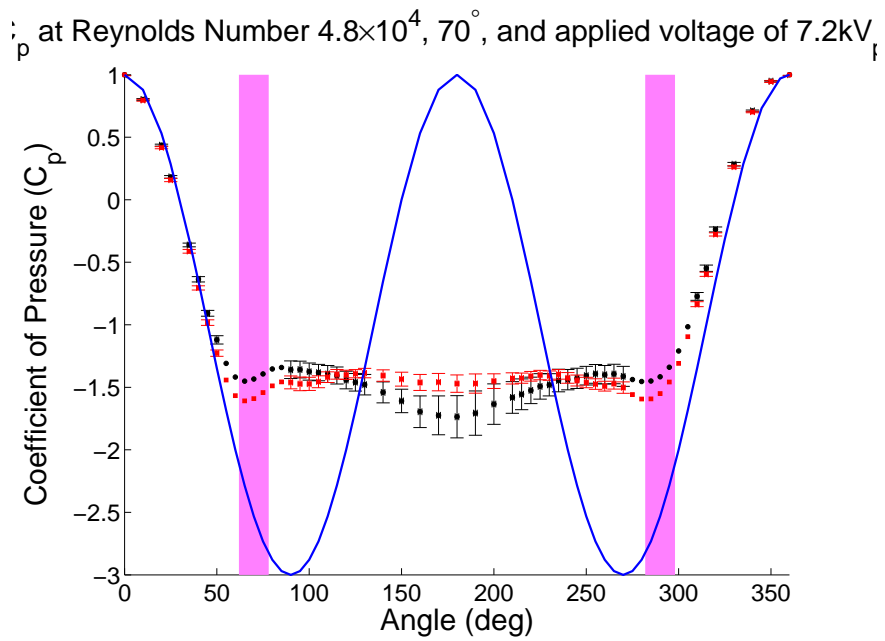
Figure A.128: Plasma Actuators on a Circular Cylinder.
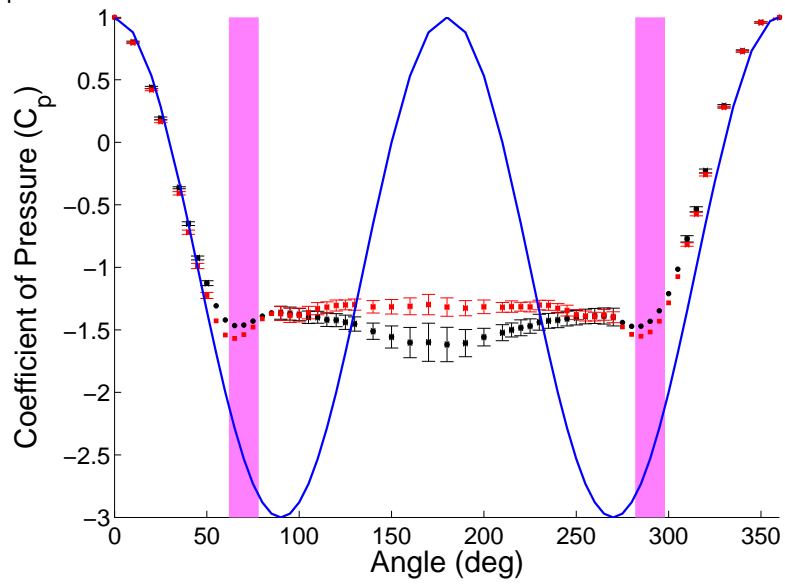
Figure A.129: Plasma Actuators on a Circular Cylinder.
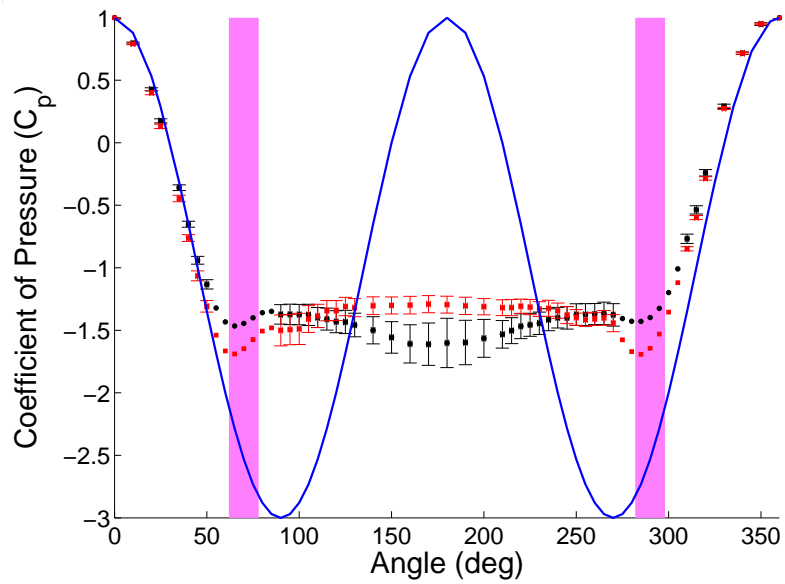
Figure A.130: Plasma Actuators on a Circular Cylinder.
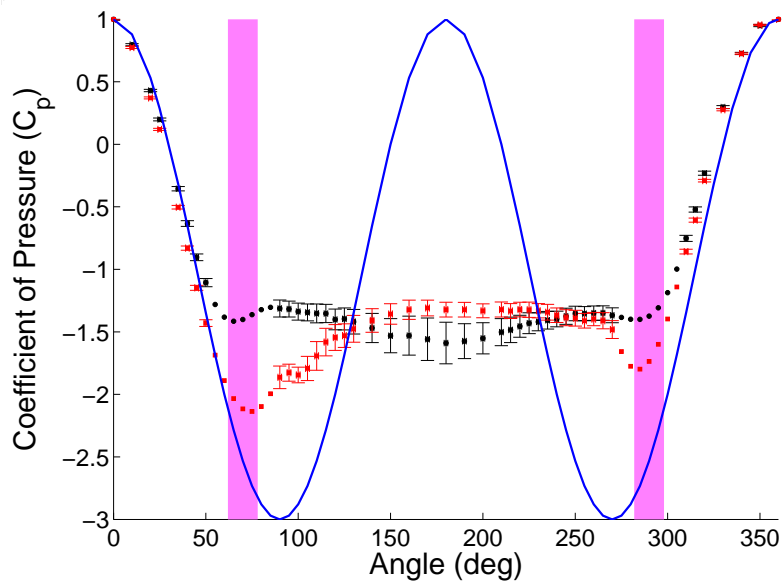
Figure A.131: Plasma Actuators on a Circular Cylinder.
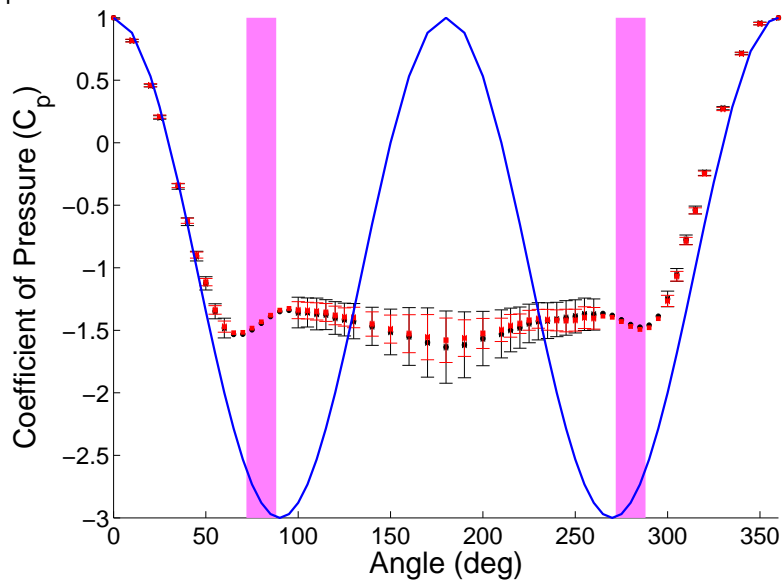
Figure A.132: Plasma Actuators on a Circular Cylinder.

216
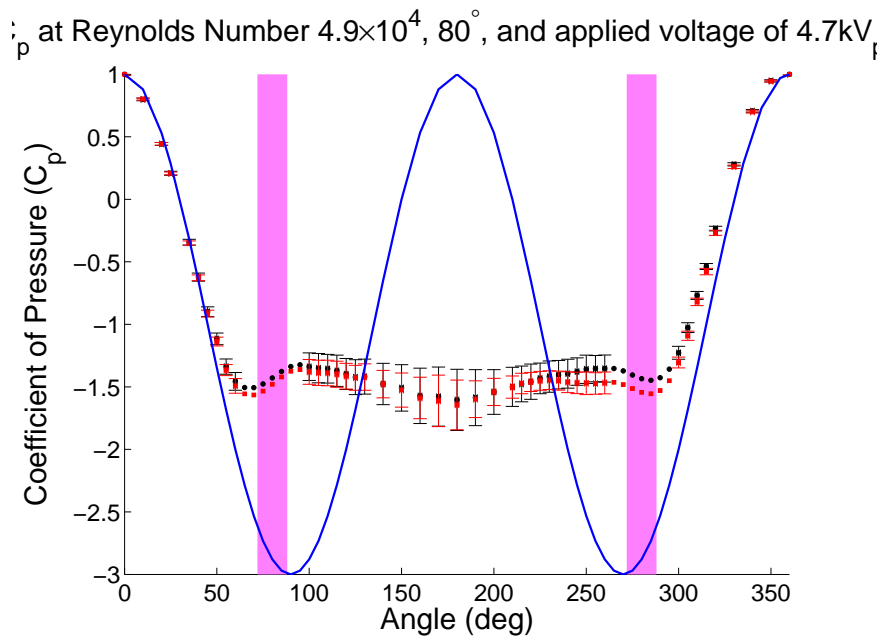
Figure A.133: Plasma Actuators on a Circular Cylinder.
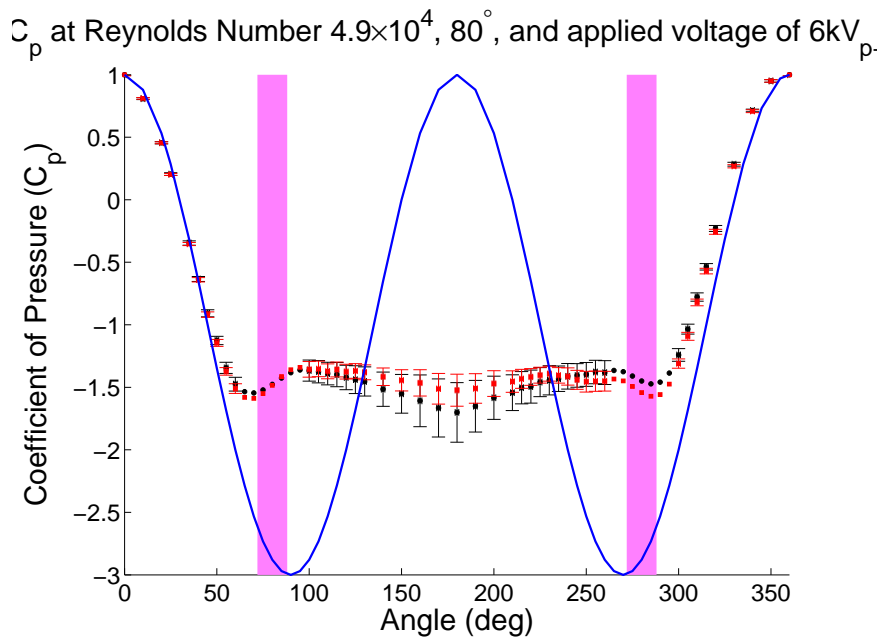
Figure A.134: Plasma Actuators on a Circular Cylinder.
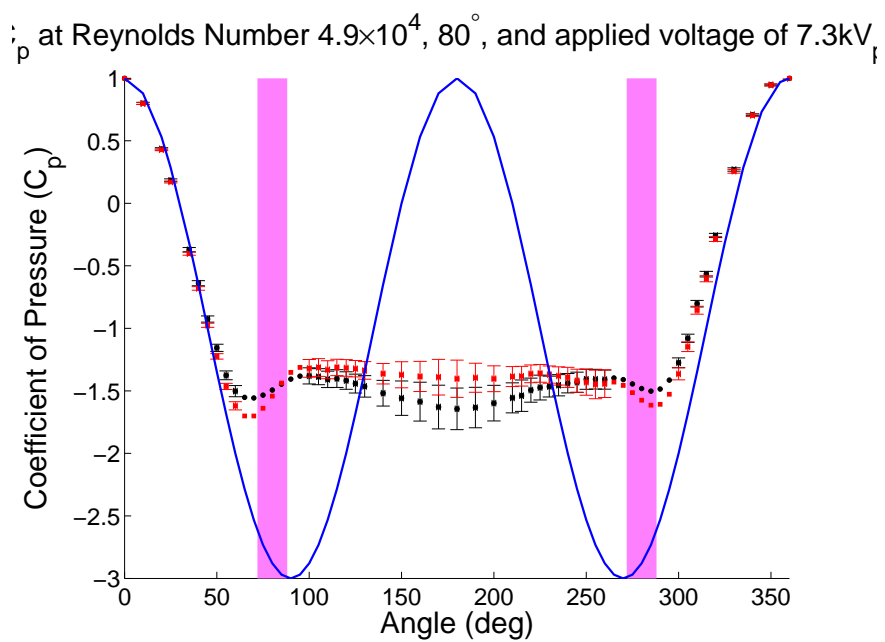
Figure A.135: Plasma Actuators on a Circular Cylinder.
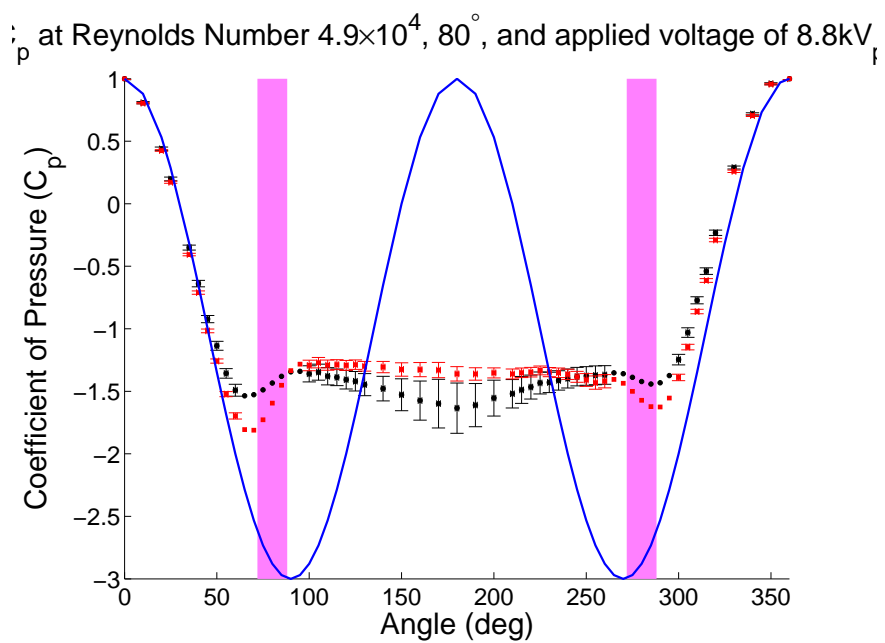
Figure A.136: Plasma Actuators on a Circular Cylinder.
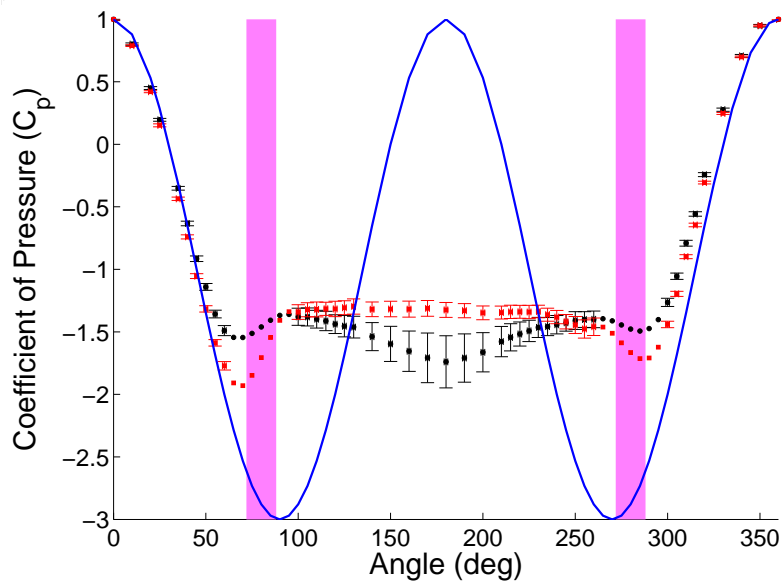
Figure A.137: Plasma Actuators on a Circular Cylinder.
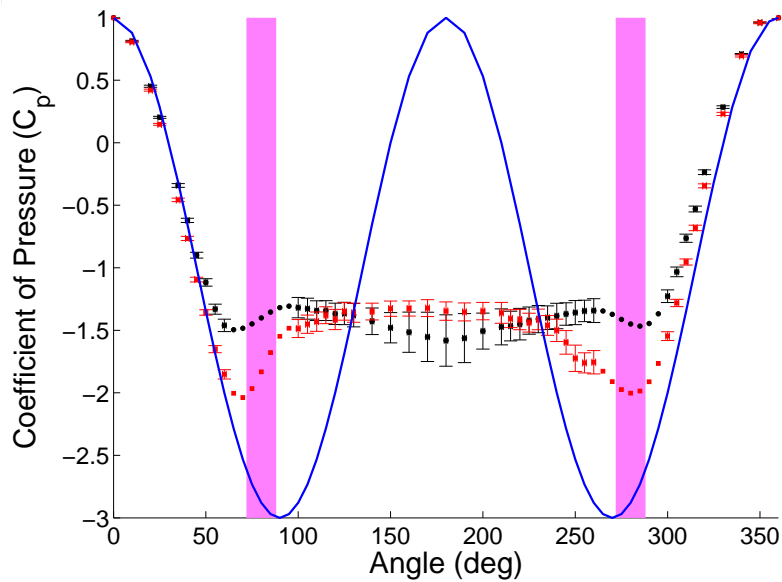
Figure A.138: Plasma Actuators on a Circular Cylinder.
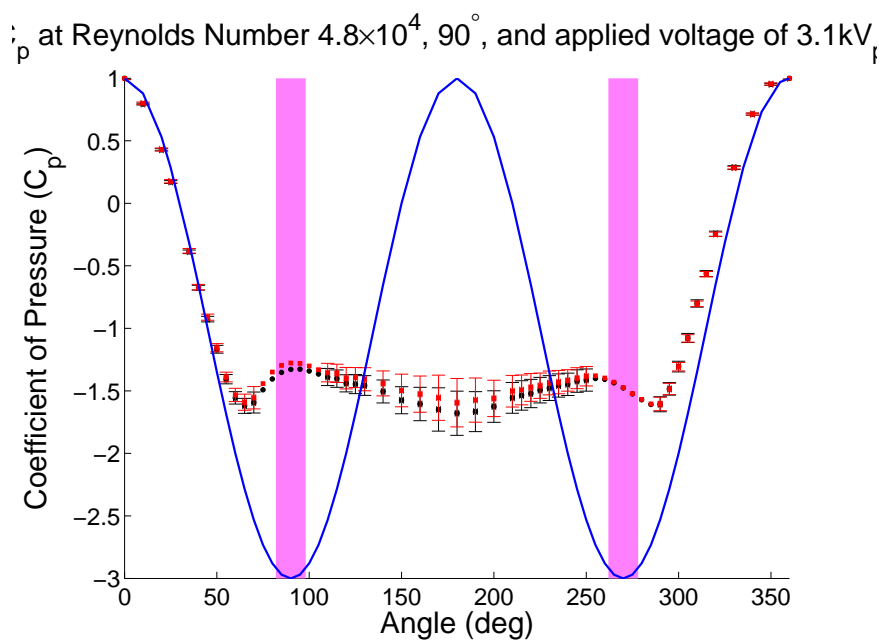
Figure A.139: Plasma Actuators on a Circular Cylinder.
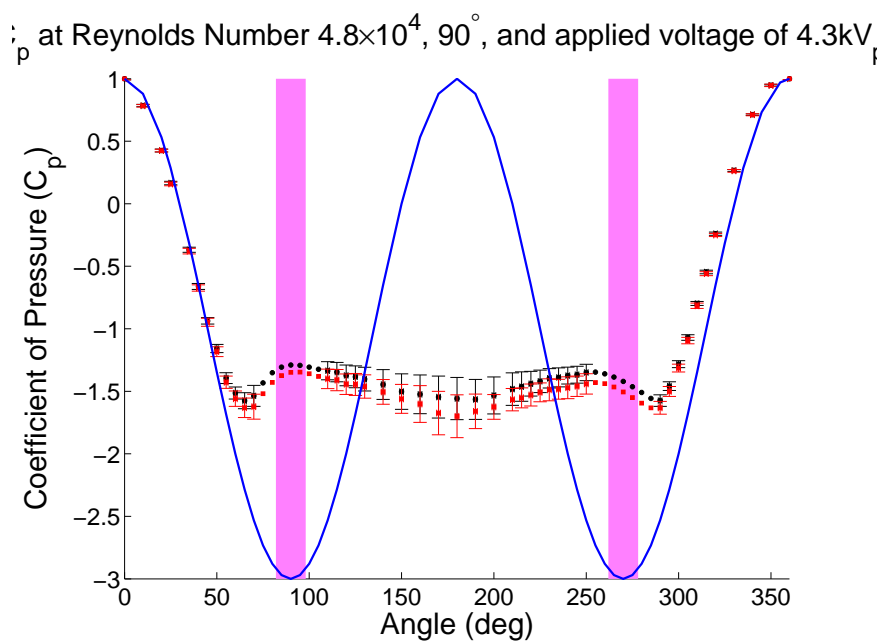
Figure A.140: Plasma Actuators on a Circular Cylinder.
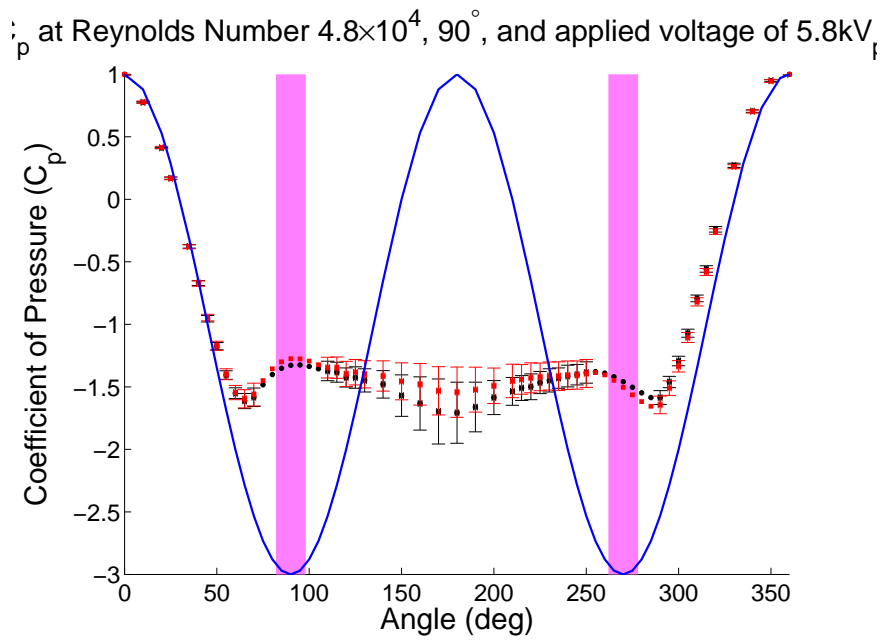
Figure A.141: Plasma Actuators on a Circular Cylinder.
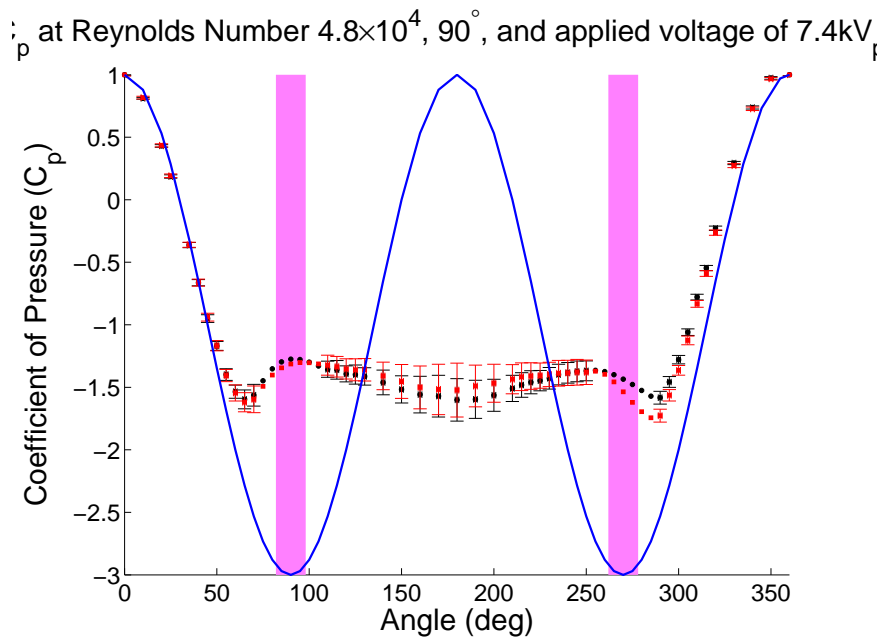
Figure A.142: Plasma Actuators on a Circular Cylinder.
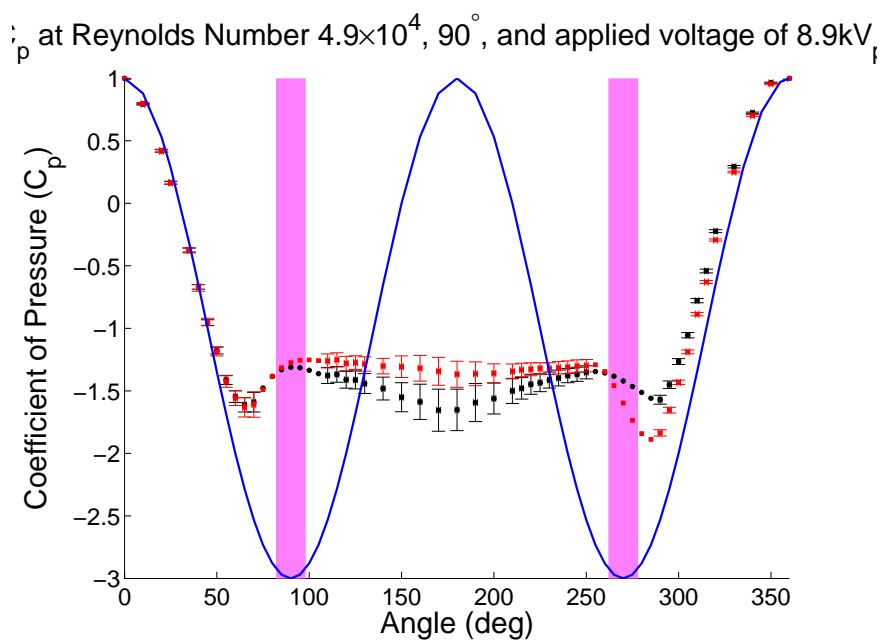
Figure A.143: Plasma Actuators on a Circular Cylinder.
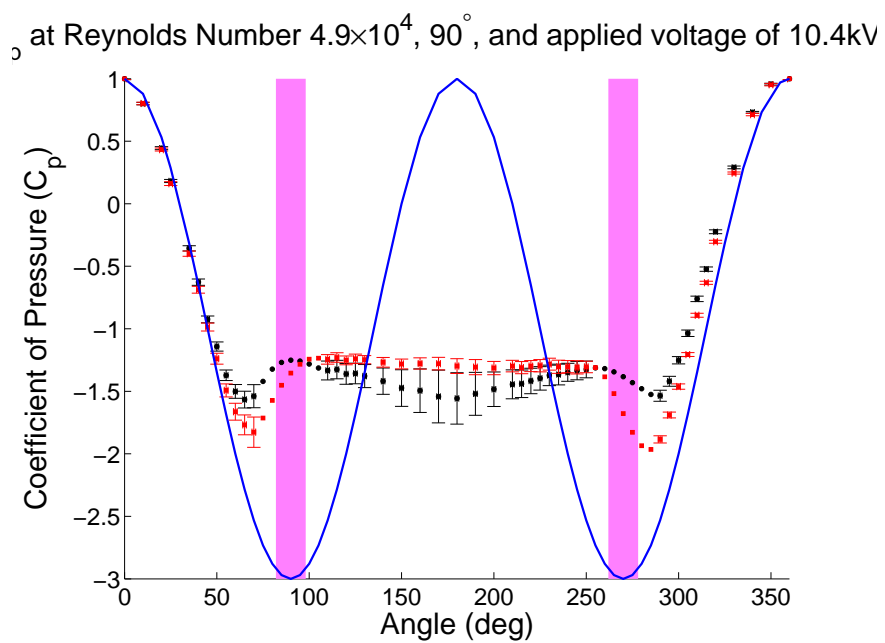
Figure A.144: Plasma Actuators on a Circular Cylinder.

222
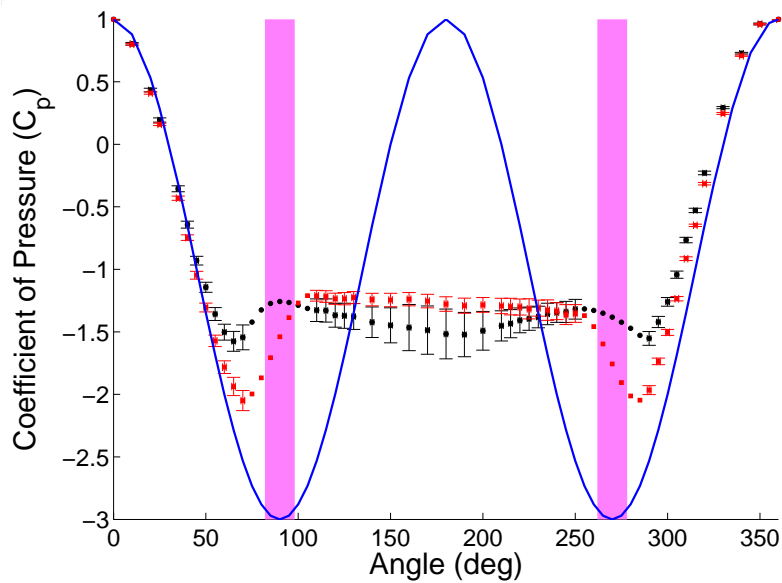
Figure A.145: Plasma Actuators on a Circular Cylinder.
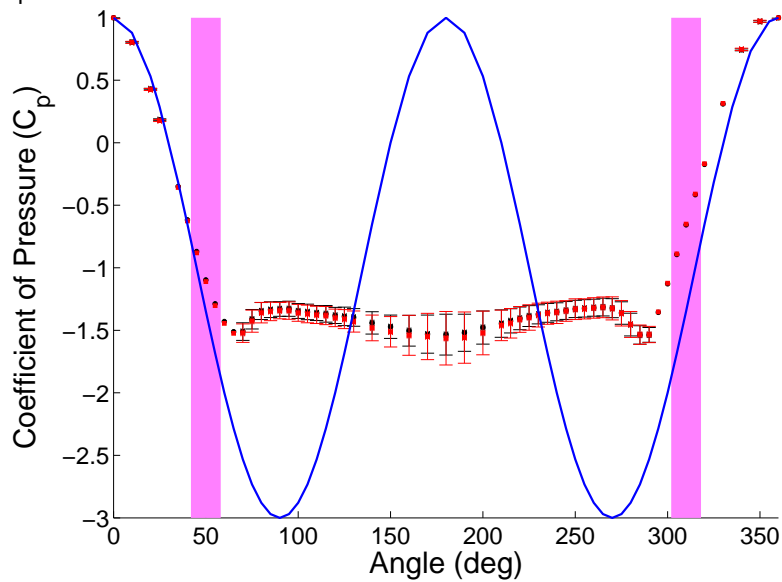
Figure A.146: Plasma Actuators on a Circular Cylinder.
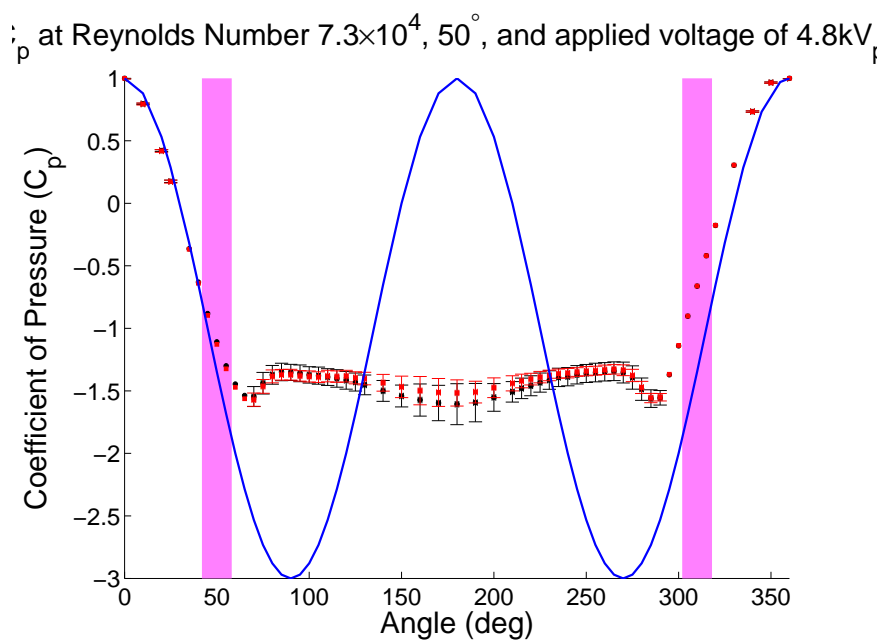
Figure A.147: Plasma Actuators on a Circular Cylinder.
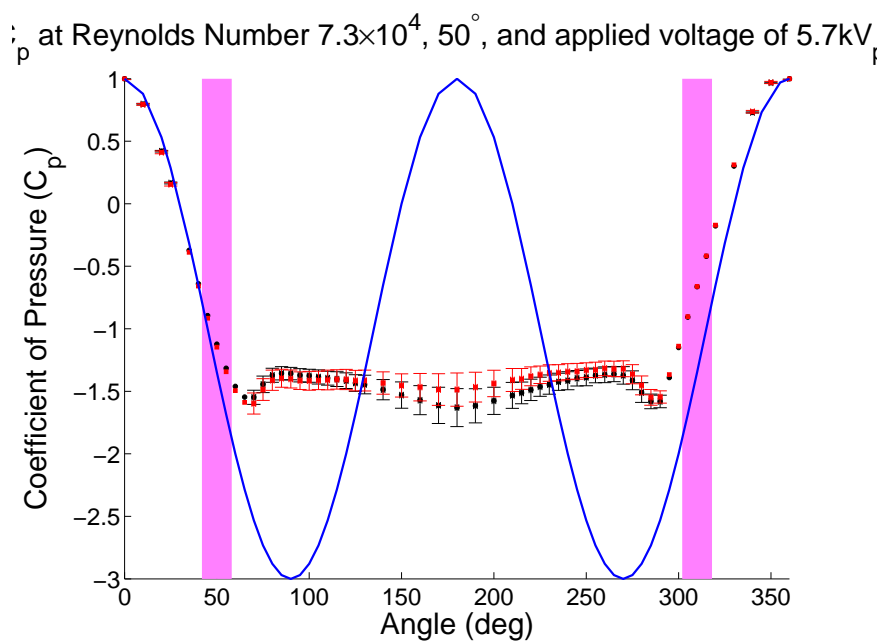
Figure A.148: Plasma Actuators on a Circular Cylinder.
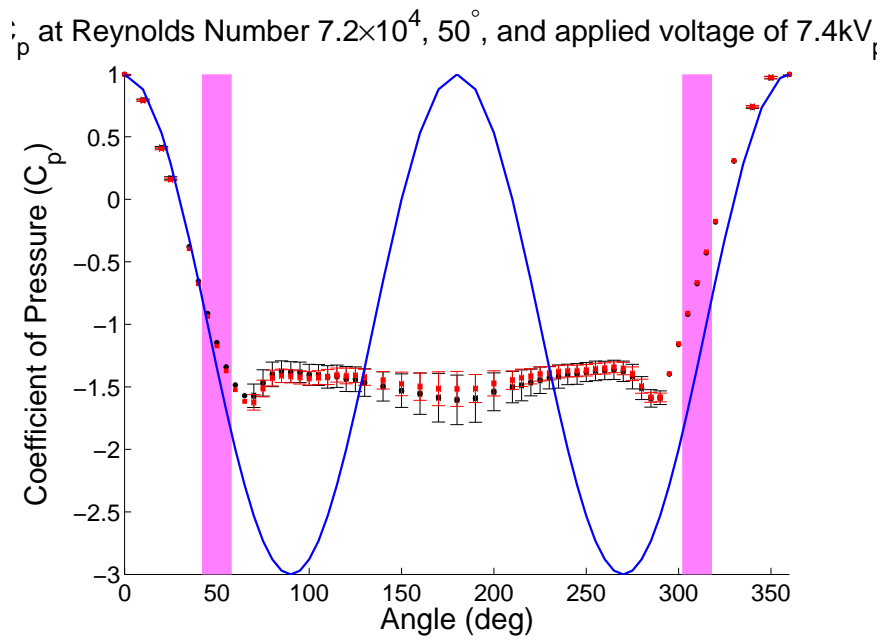
Figure A.149: Plasma Actuators on a Circular Cylinder.
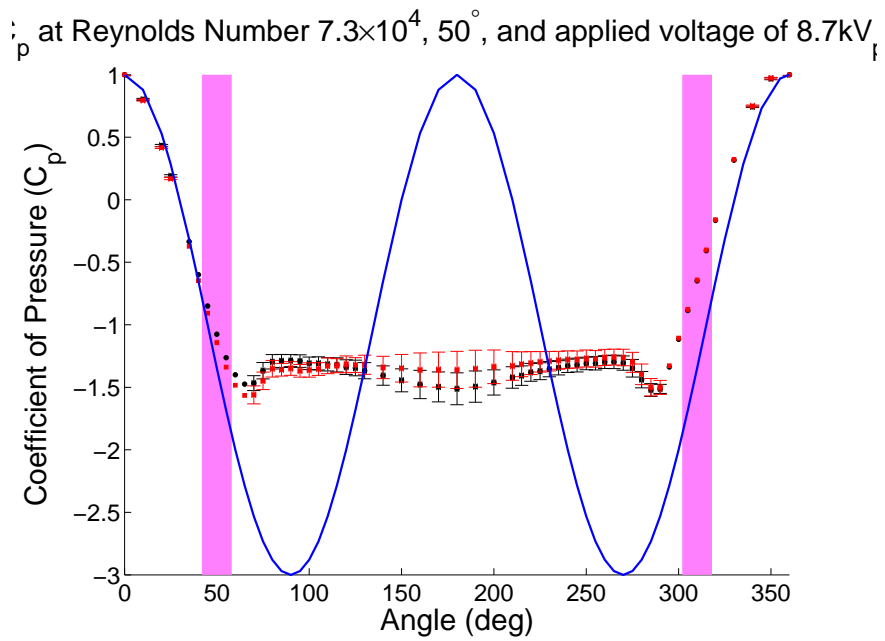
Figure A.150: Plasma Actuators on a Circular Cylinder.

at Reynolds Number 7.2×10^4, 50°, and applied voltage of 10.6kV
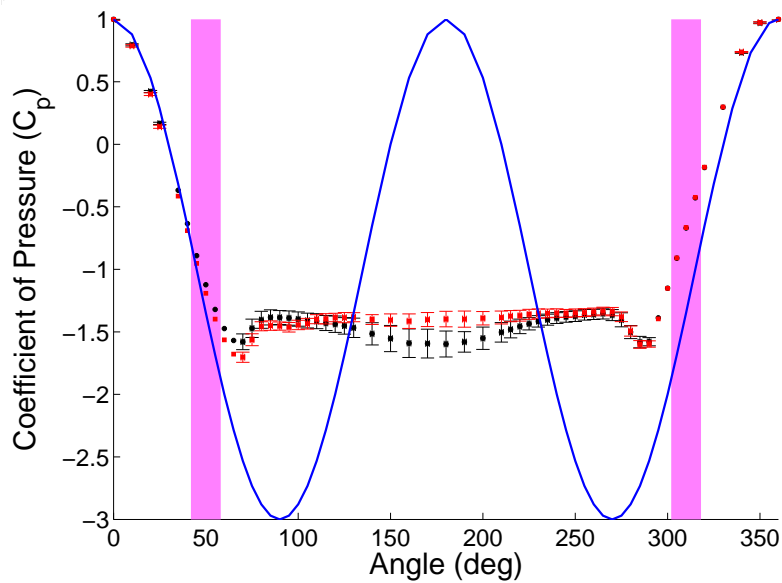
Figure A.151: Plasma Actuators on a Circular Cylinder.

at Reynolds Number 7.2×10^4, 50°, and applied voltage of 11.8kV
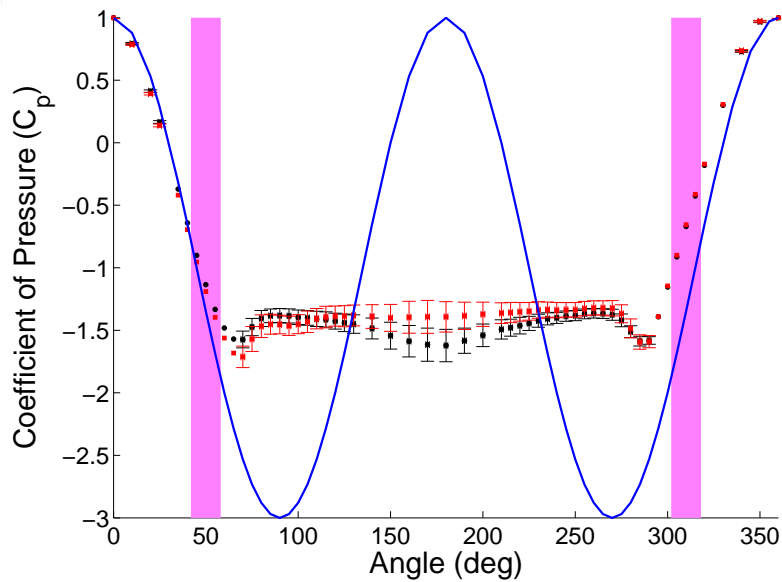
Figure A.152: Plasma Actuators on a Circular Cylinder.
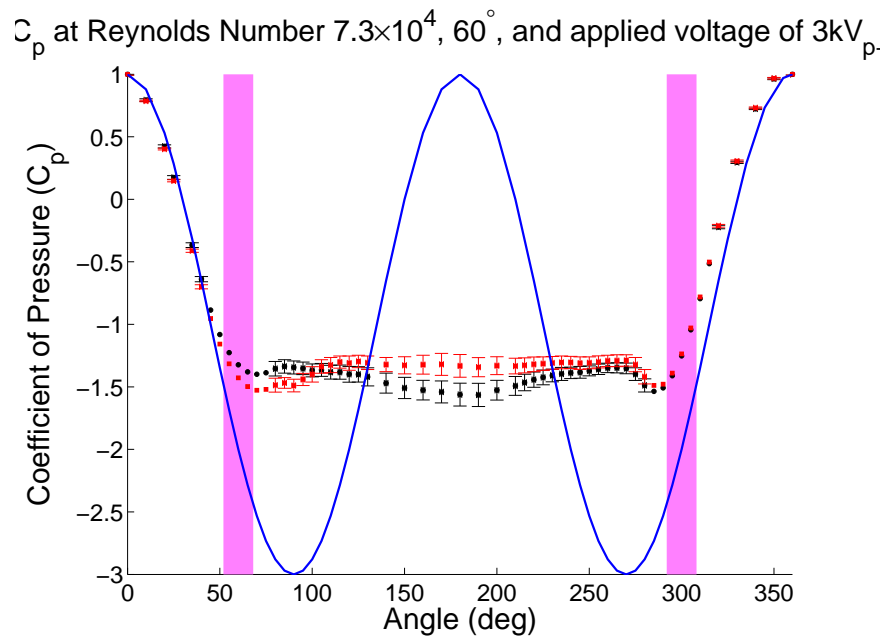
Figure A.153: Plasma Actuators on a Circular Cylinder.
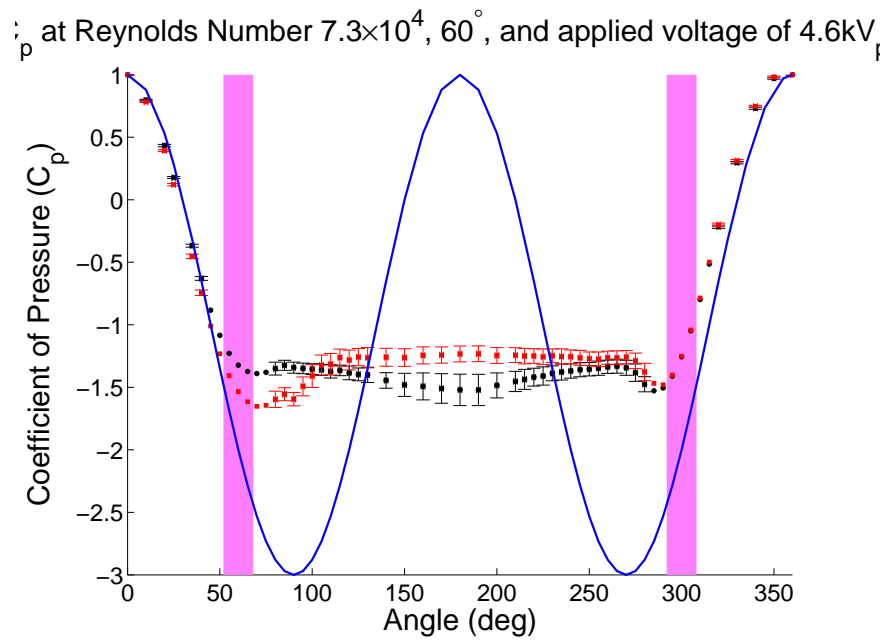
Figure A.154: Plasma Actuators on a Circular Cylinder.
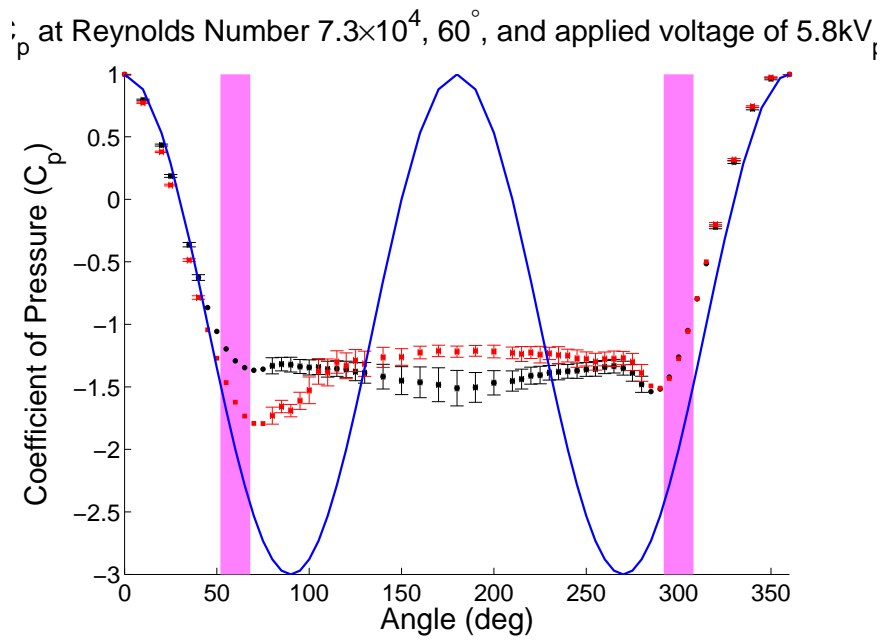
Figure A.155: Plasma Actuators on a Circular Cylinder.
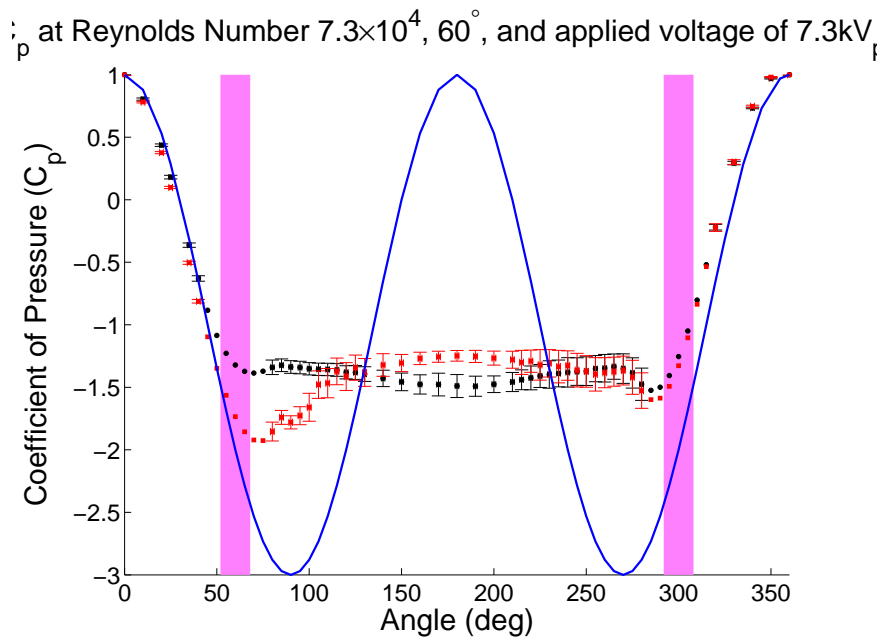
Figure A.156: Plasma Actuators on a Circular Cylinder.
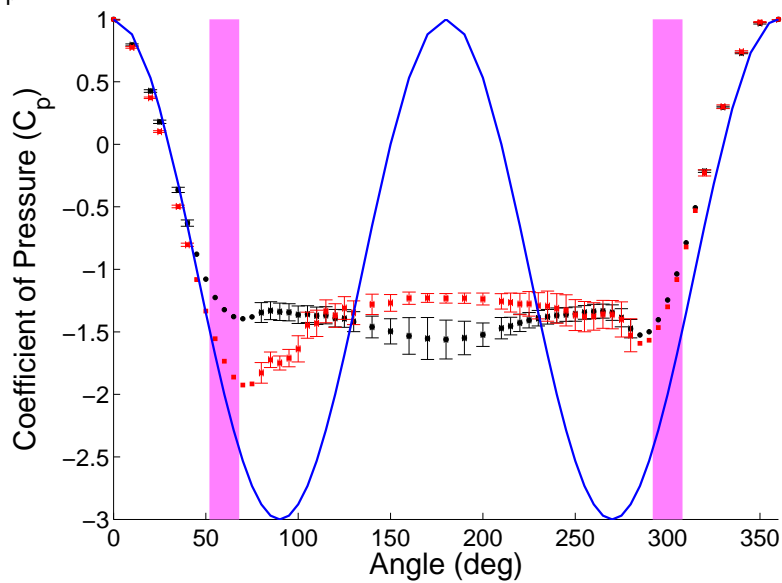
Figure A.157: Plasma Actuators on a Circular Cylinder.
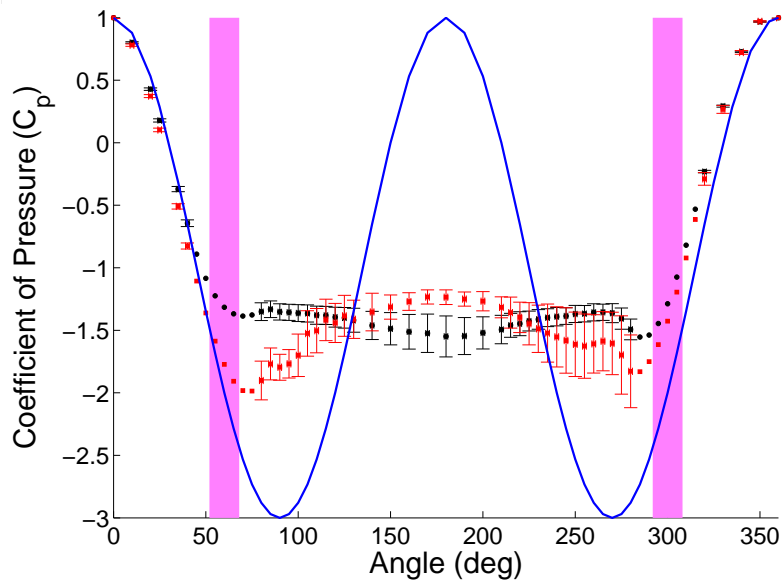
Figure A.158: Plasma Actuators on a Circular Cylinder.
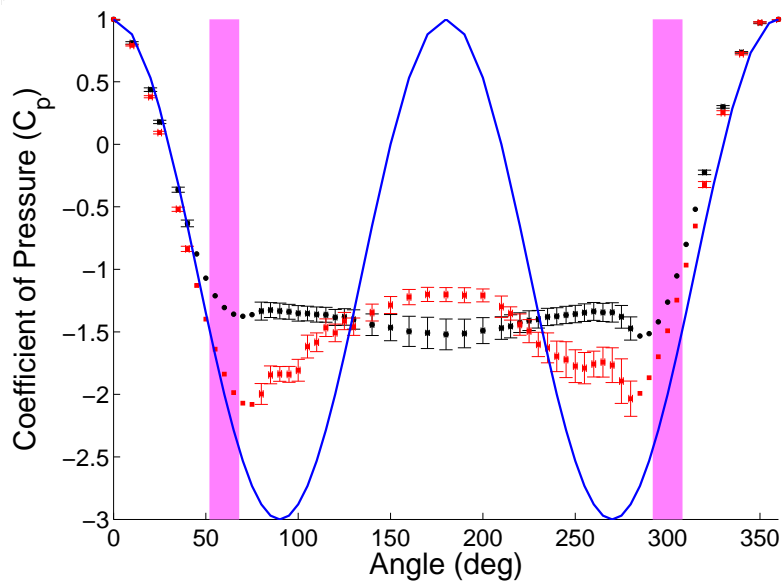
Figure A.159: Plasma Actuators on a Circular Cylinder.
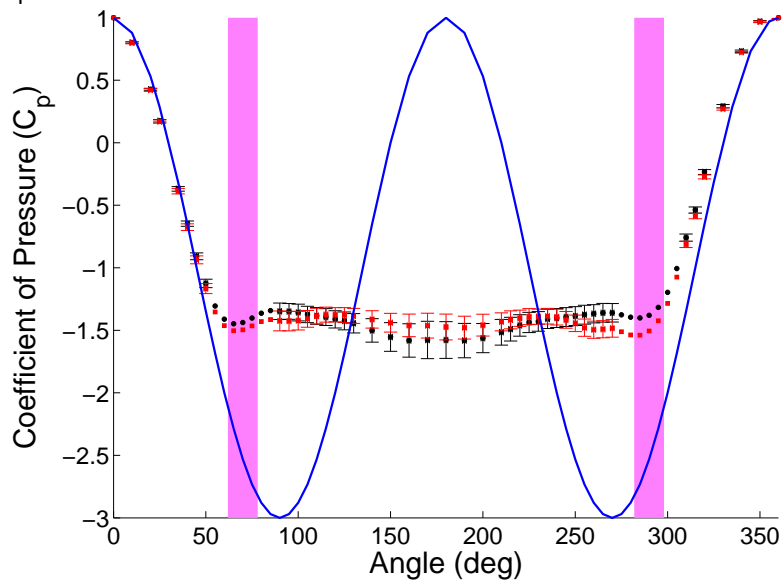
Figure A.160: Plasma Actuators on a Circular Cylinder.
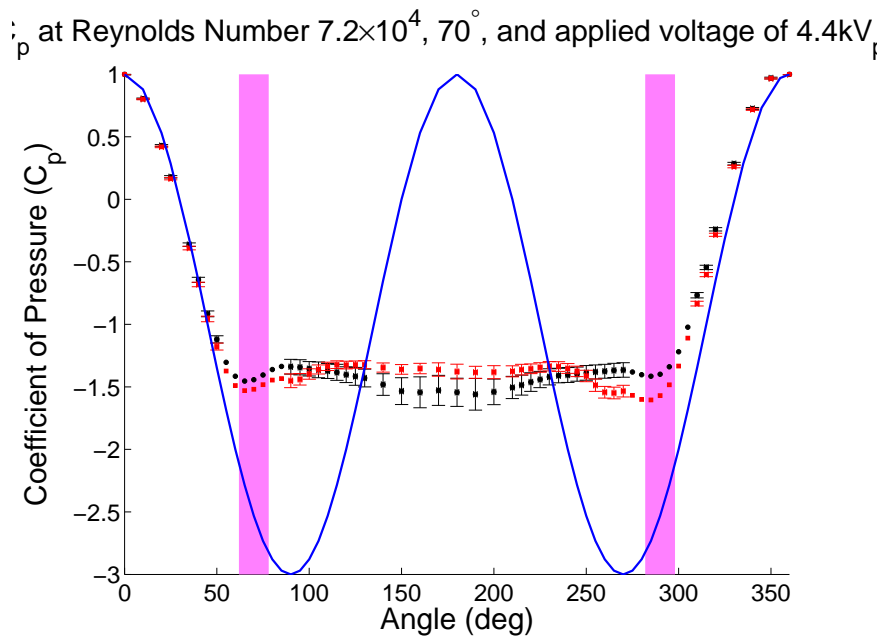
Figure A.161: Plasma Actuators on a Circular Cylinder.
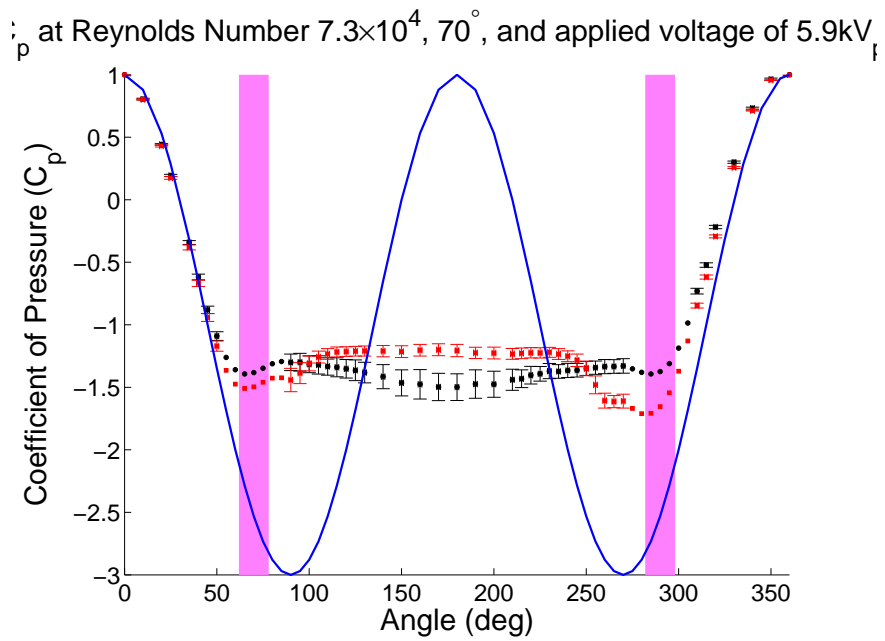
Figure A.162: Plasma Actuators on a Circular Cylinder.

C_p at Reynolds Number 7.3×10^4, $70°$, and applied voltage of 7.3kV
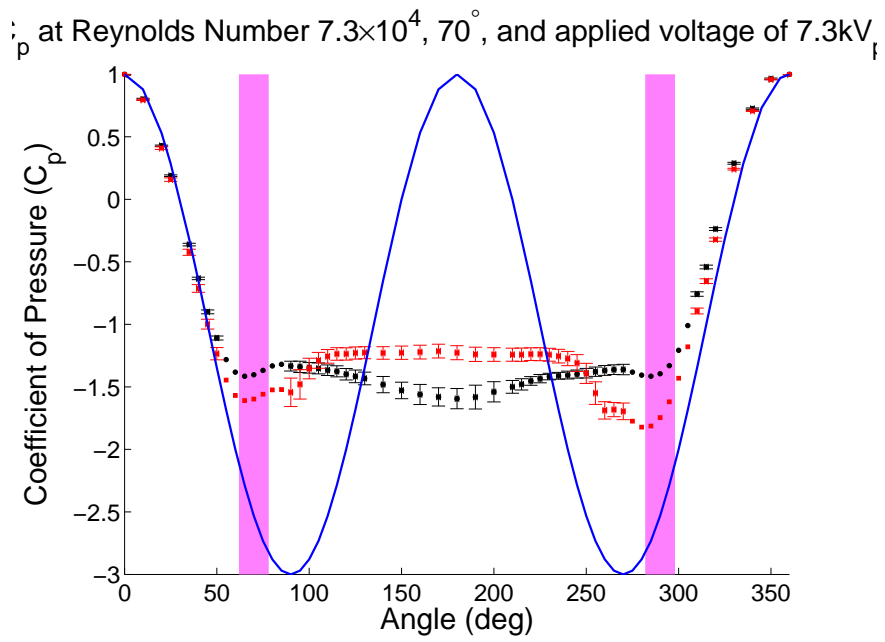
Figure A.163: Plasma Actuators on a Circular Cylinder.

C_p at Reynolds Number 7.3×10^4, $70°$, and applied voltage of 8.8kV
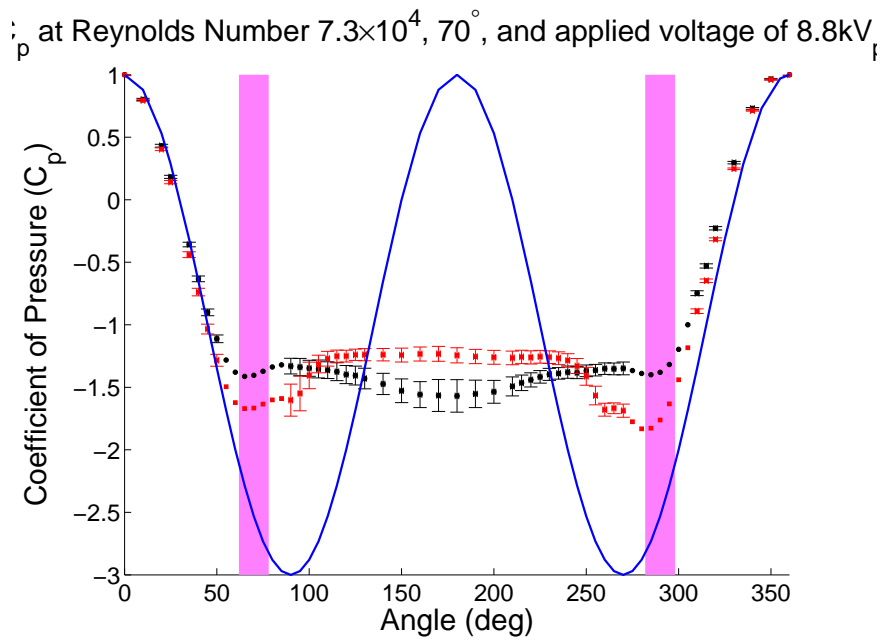
Figure A.164: Plasma Actuators on a Circular Cylinder.
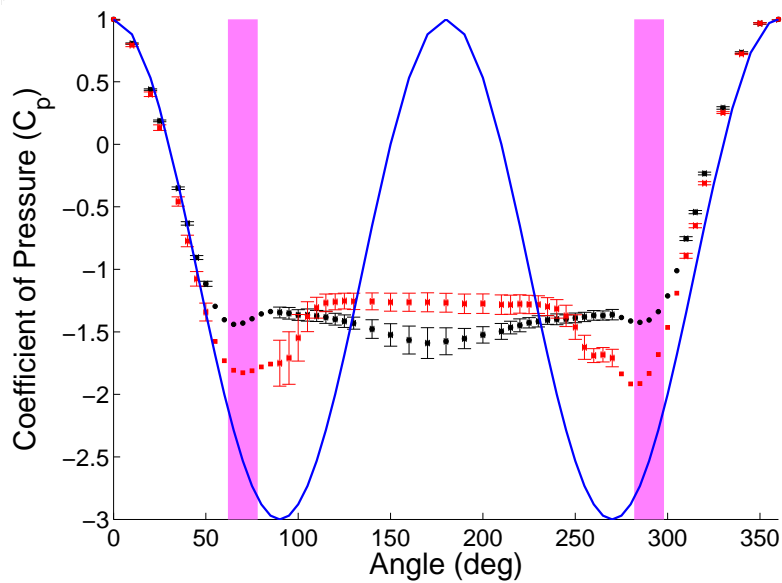
Figure A.165: Plasma Actuators on a Circular Cylinder.
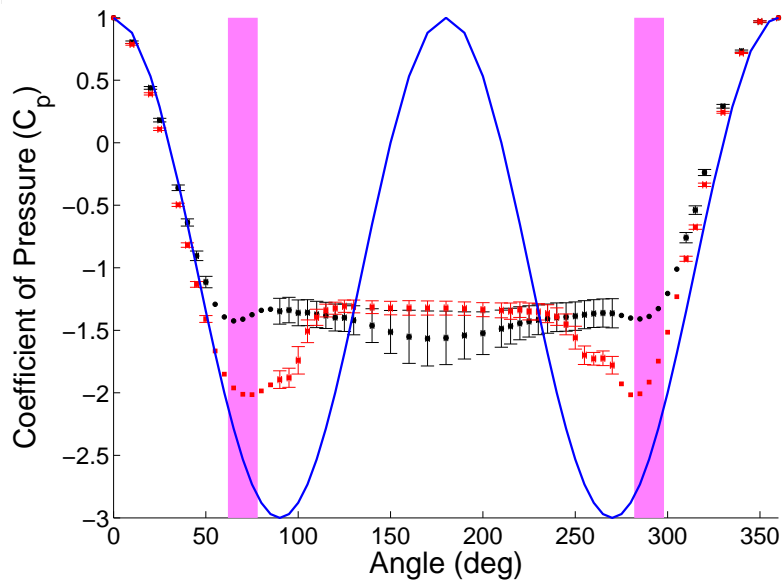
Figure A.166: Plasma Actuators on a Circular Cylinder.
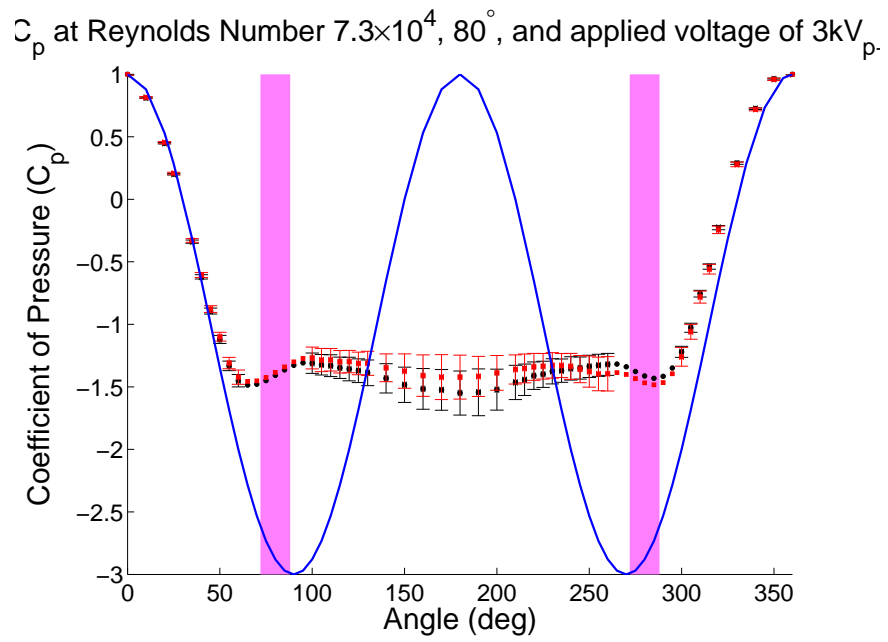
Figure A.167: Plasma Actuators on a Circular Cylinder.
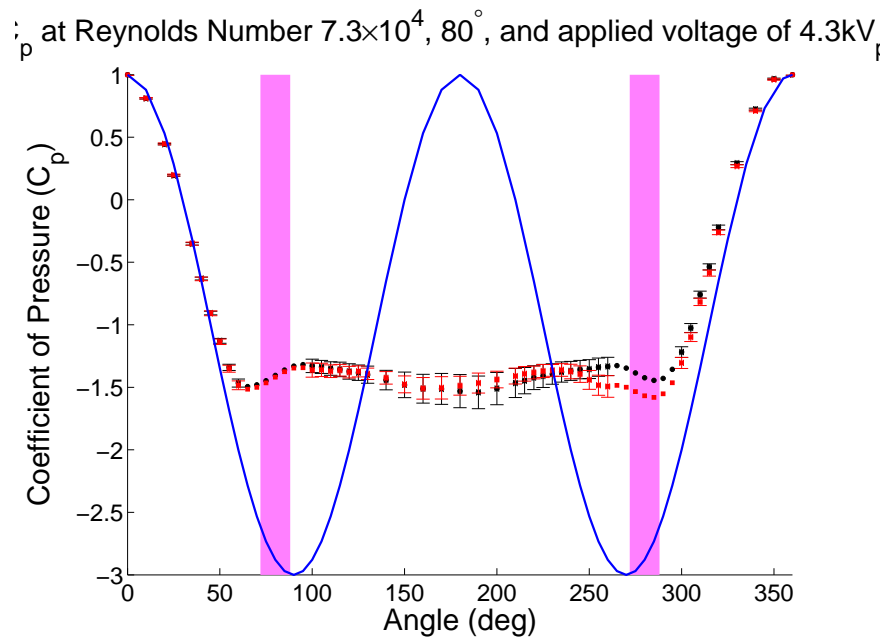
Figure A.168: Plasma Actuators on a Circular Cylinder.
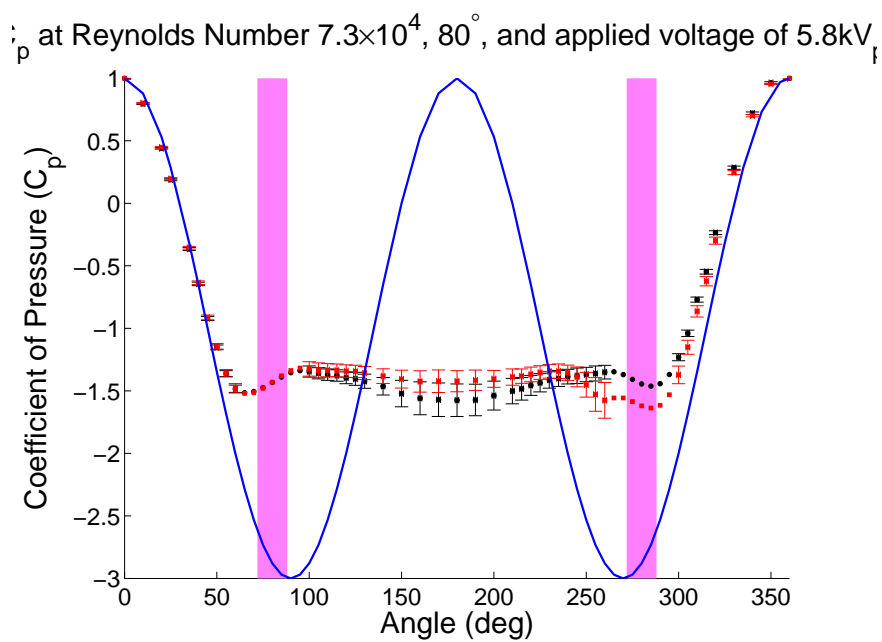
Figure A.169: Plasma Actuators on a Circular Cylinder.
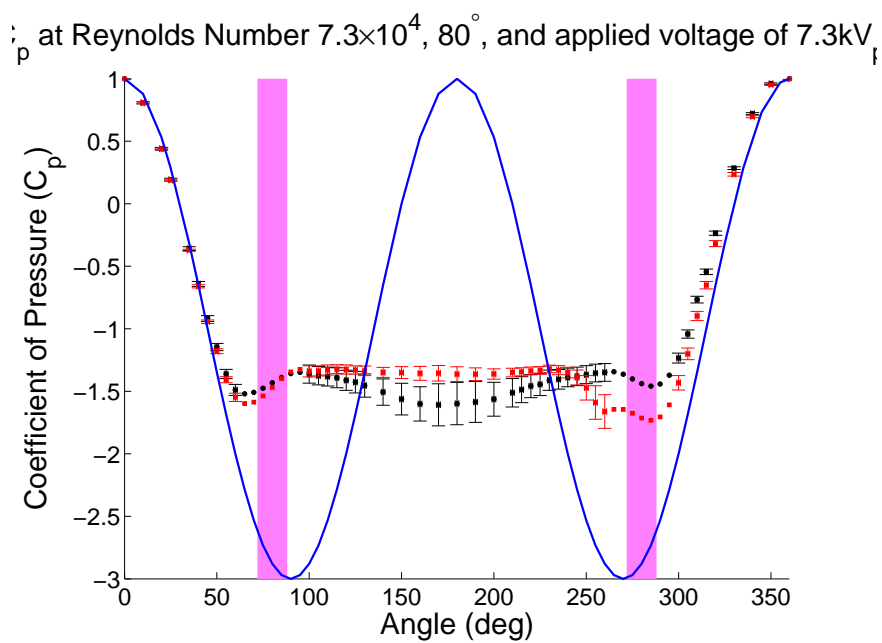
Figure A.170: Plasma Actuators on a Circular Cylinder.
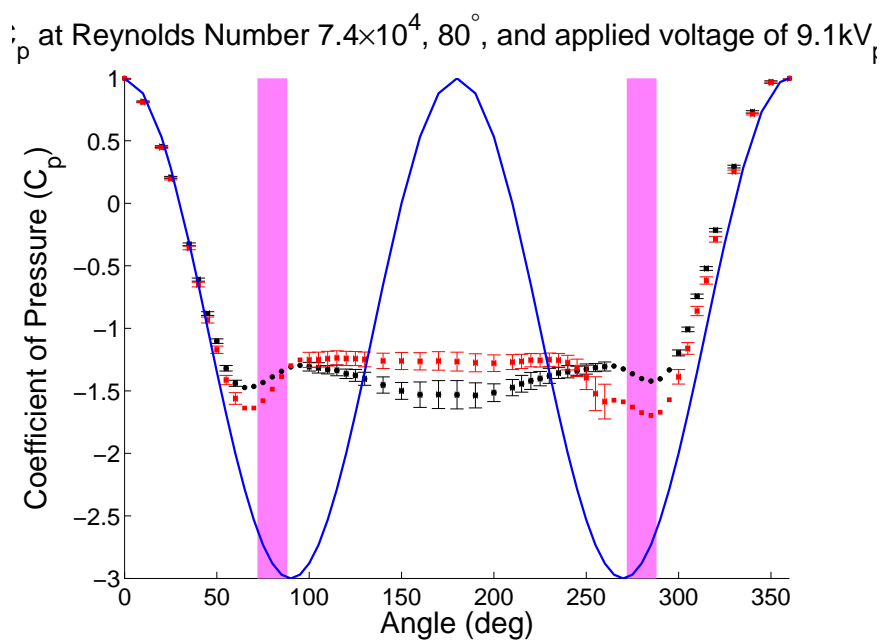
Figure A.171: Plasma Actuators on a Circular Cylinder.
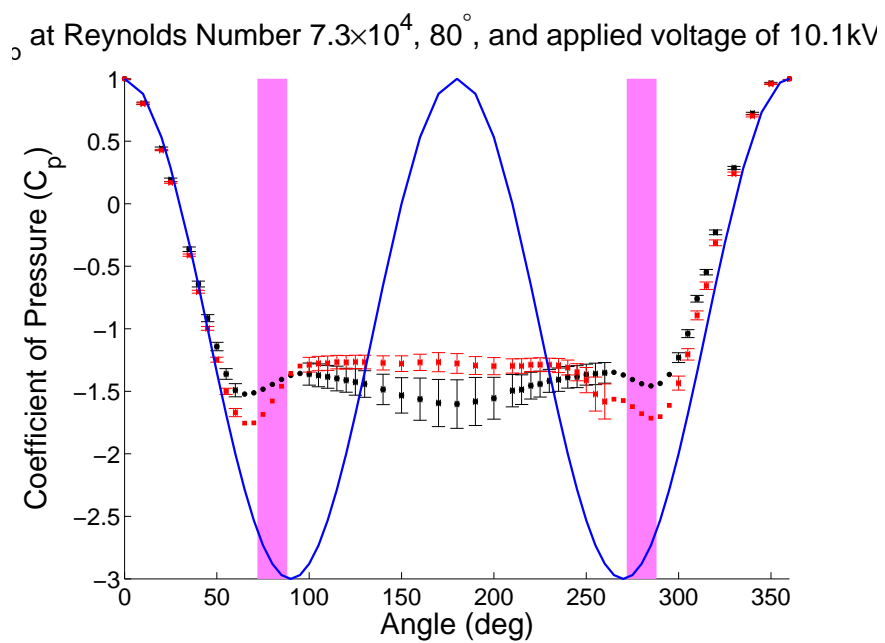
Figure A.172: Plasma Actuators on a Circular Cylinder.
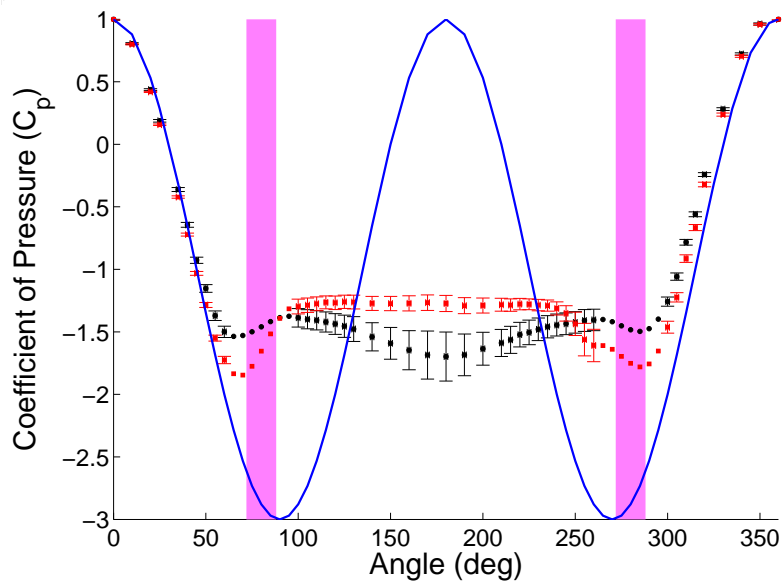
Figure A.173: Plasma Actuators on a Circular Cylinder.

Figure A.174: Plasma Actuators on a Circular Cylinder.
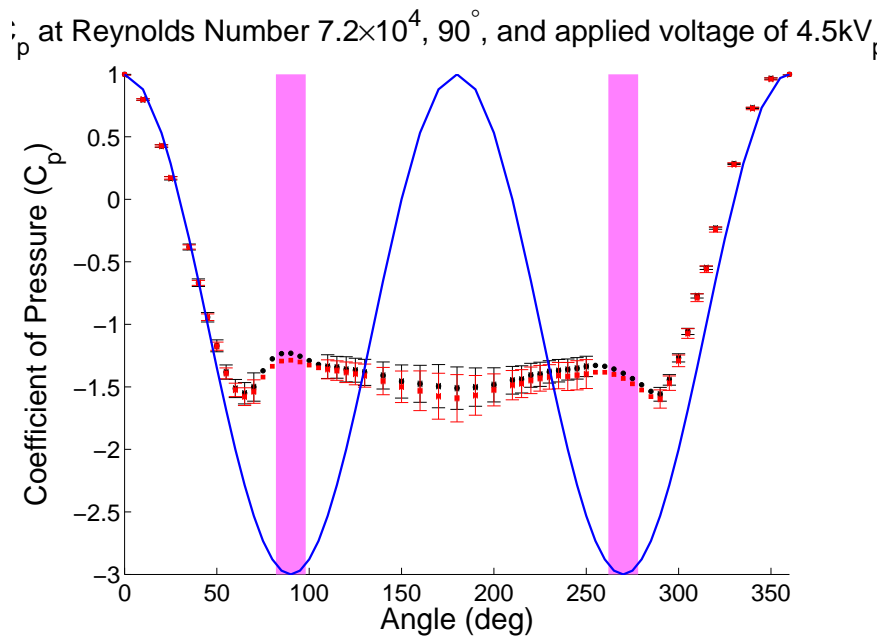
Figure A.175: Plasma Actuators on a Circular Cylinder.
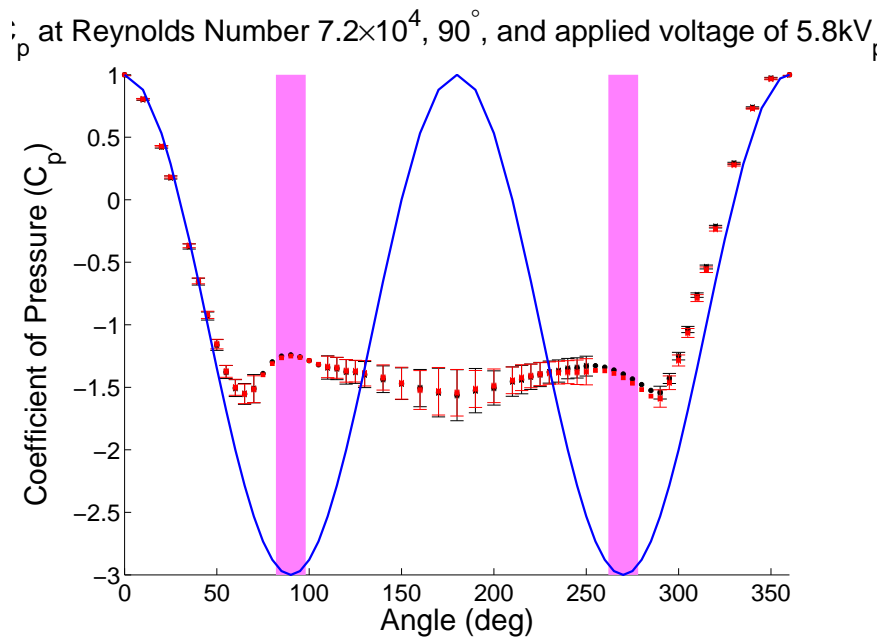
Figure A.176: Plasma Actuators on a Circular Cylinder.
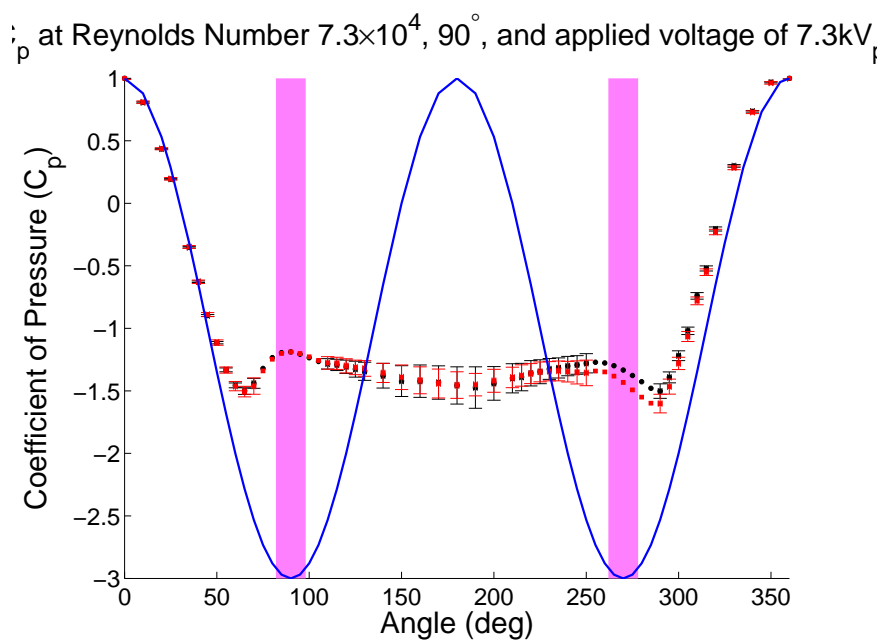
Figure A.177: Plasma Actuators on a Circular Cylinder.
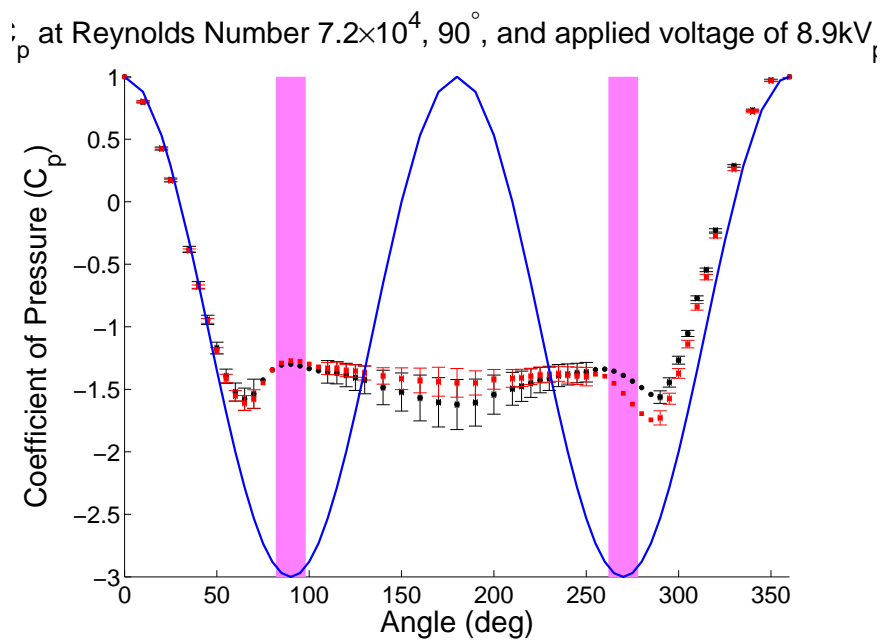
Figure A.178: Plasma Actuators on a Circular Cylinder.

at Reynolds Number 7.3×10⁴, 90°, and applied voltage of 10.3kV
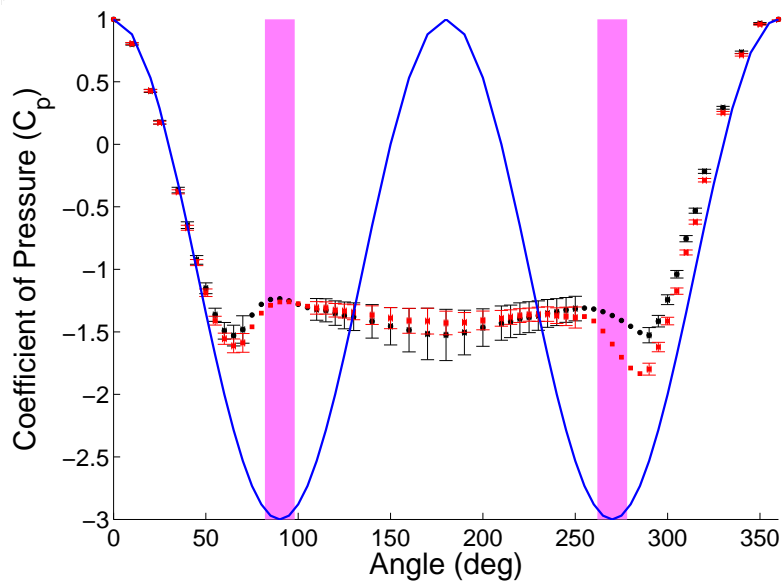
Figure A.179: Plasma Actuators on a Circular Cylinder.

at Reynolds Number 7.2×10⁴, 90°, and applied voltage of 11.6kV
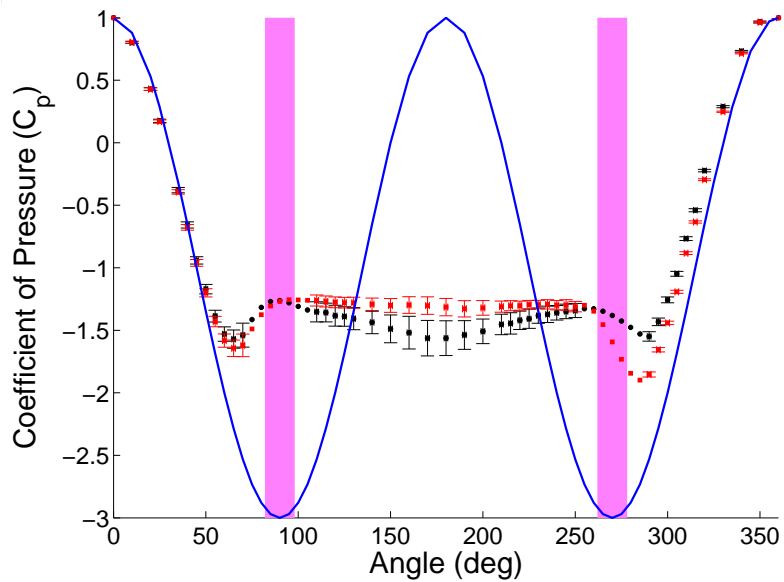
Figure A.180: Plasma Actuators on a Circular Cylinder.
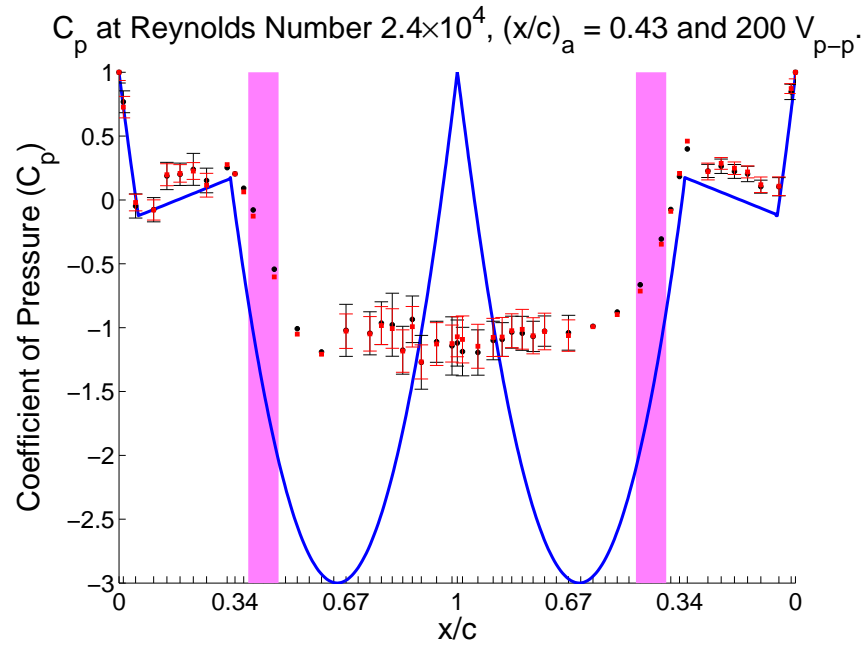
Figure A.181: Synthetic Jet Actuators on a Tail Boom Model.
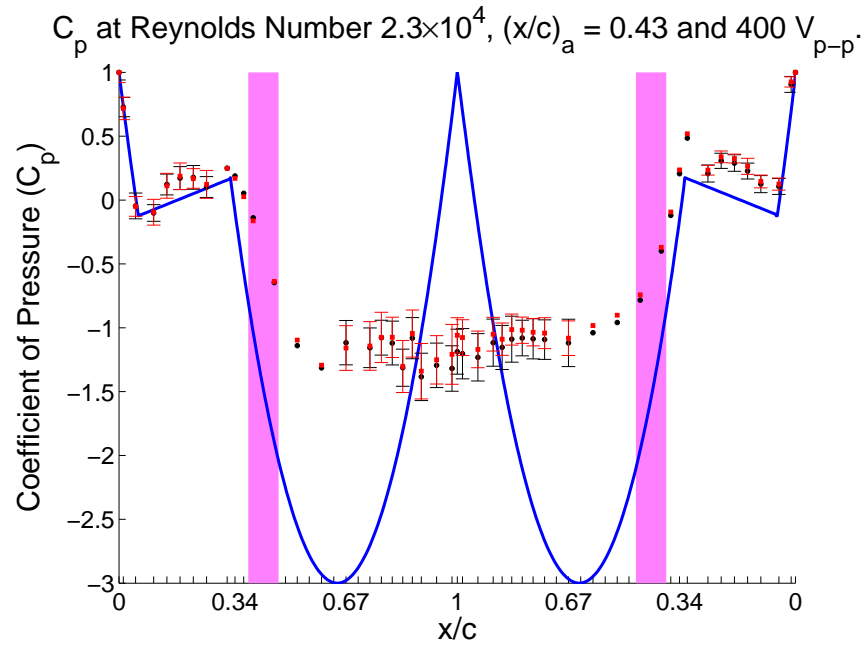
Figure A.182: Synthetic Jet Actuators on a Tail Boom Model.
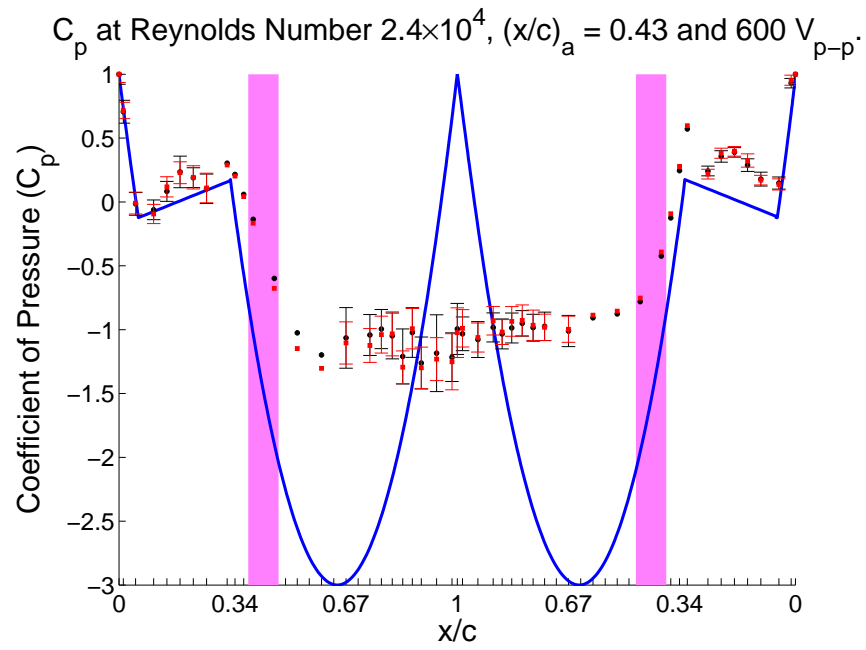
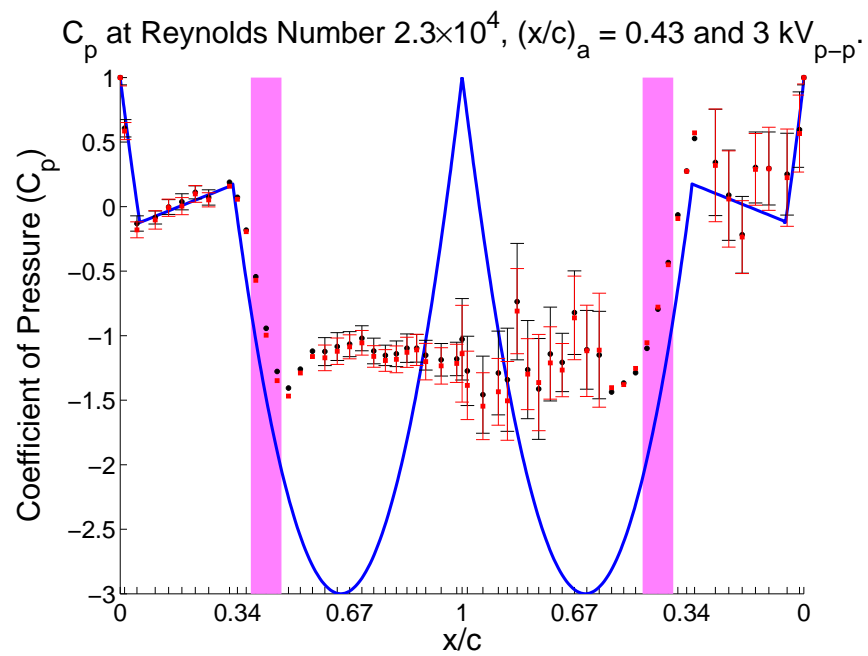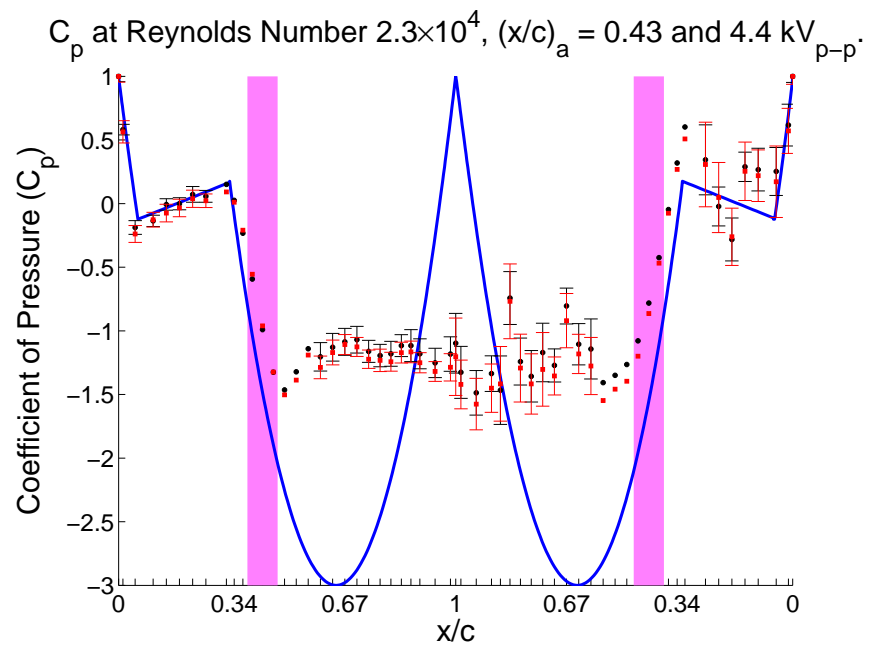**Figure A.183:** Synthetic Jet Actuators on a Tail Boom Model.
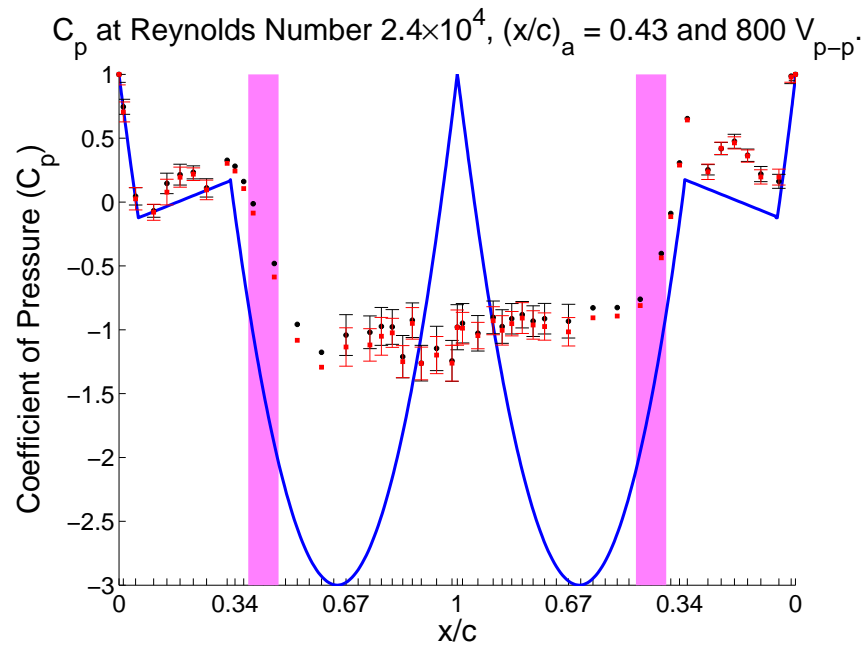
Figure A.184: Synthetic Jet Actuators on a Tail Boom Model.
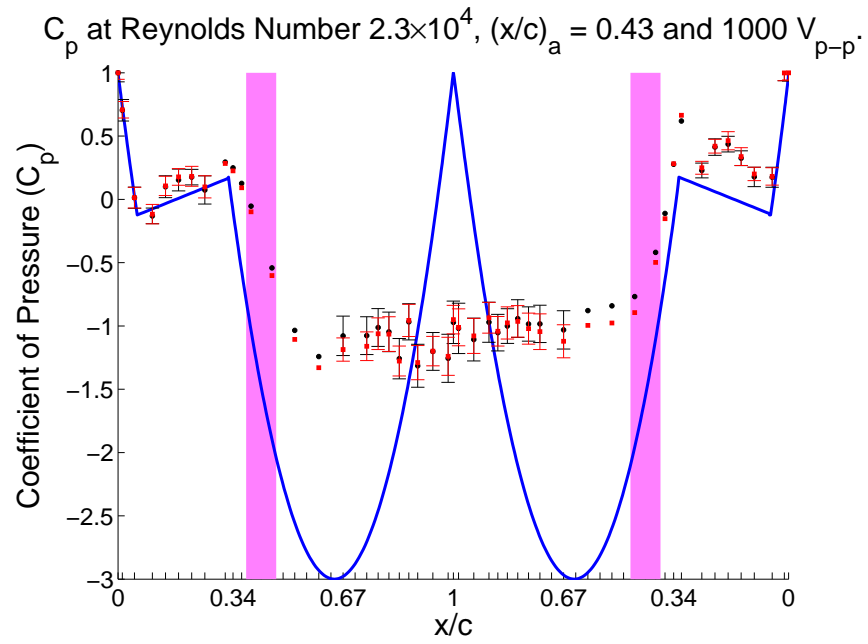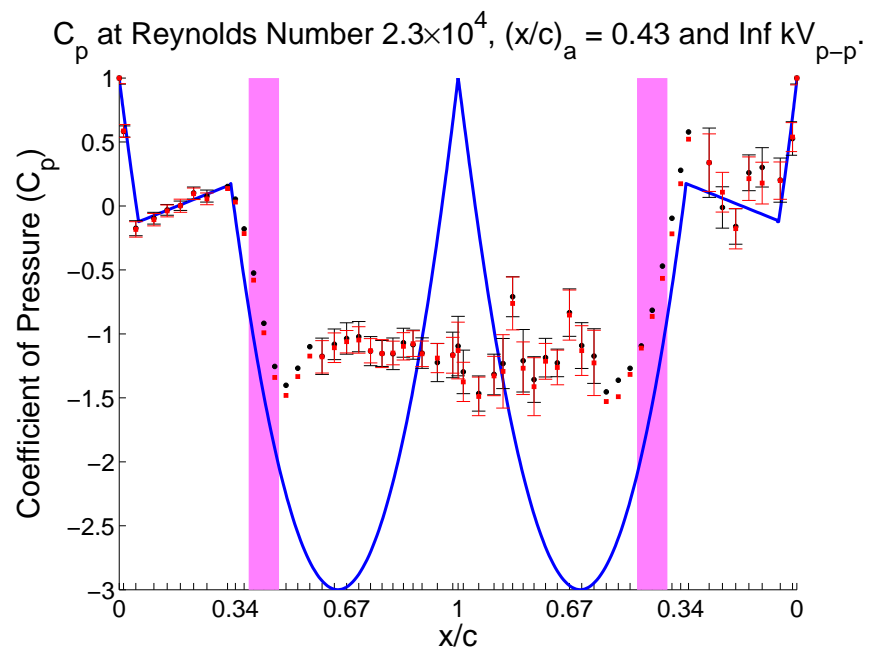
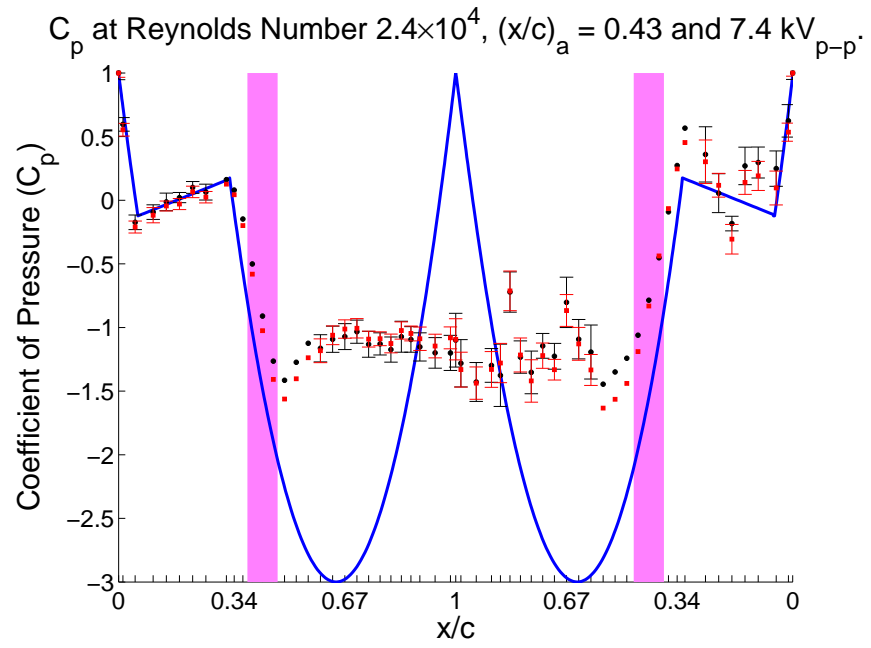**Figure A.185:** Synthetic Jet Actuators on a Tail Boom Model.
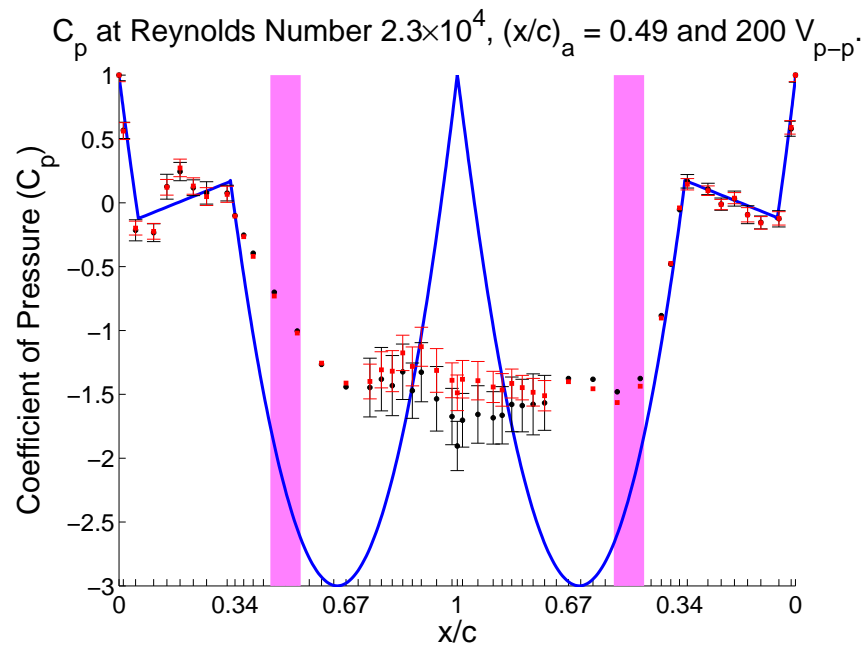
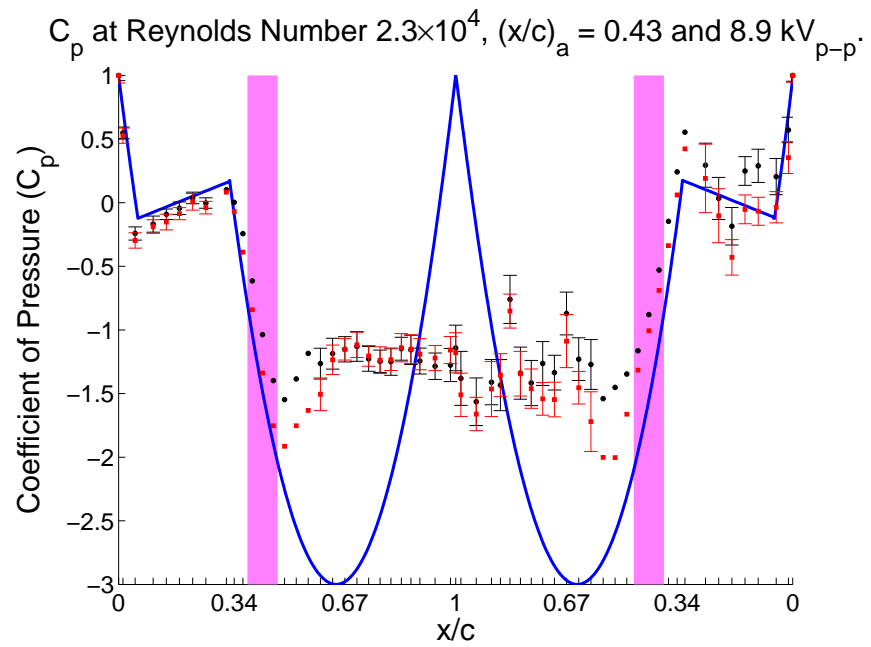**Figure A.186:** Synthetic Jet Actuators on a Tail Boom Model.
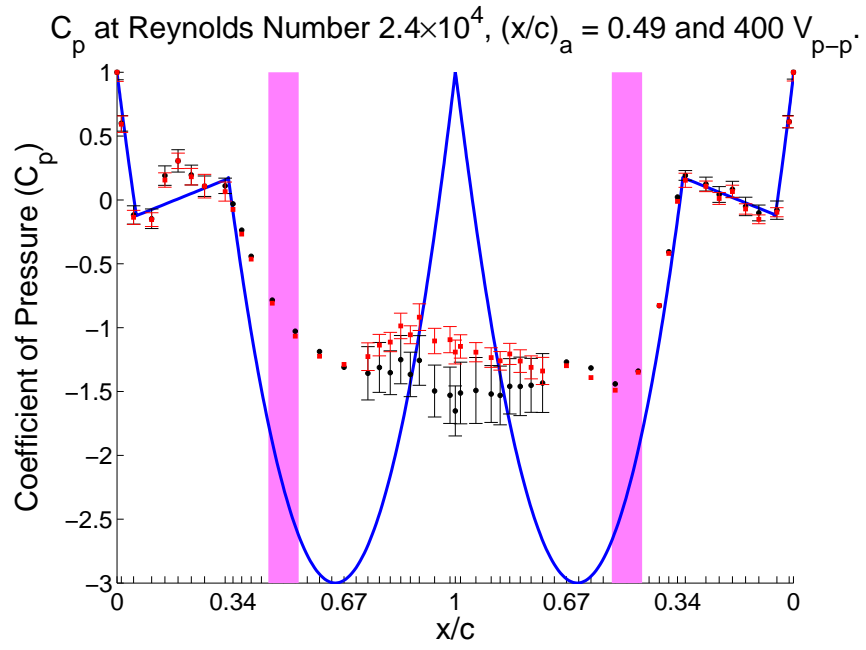
Figure A.187: Synthetic Jet Actuators on a Tail Boom Model.
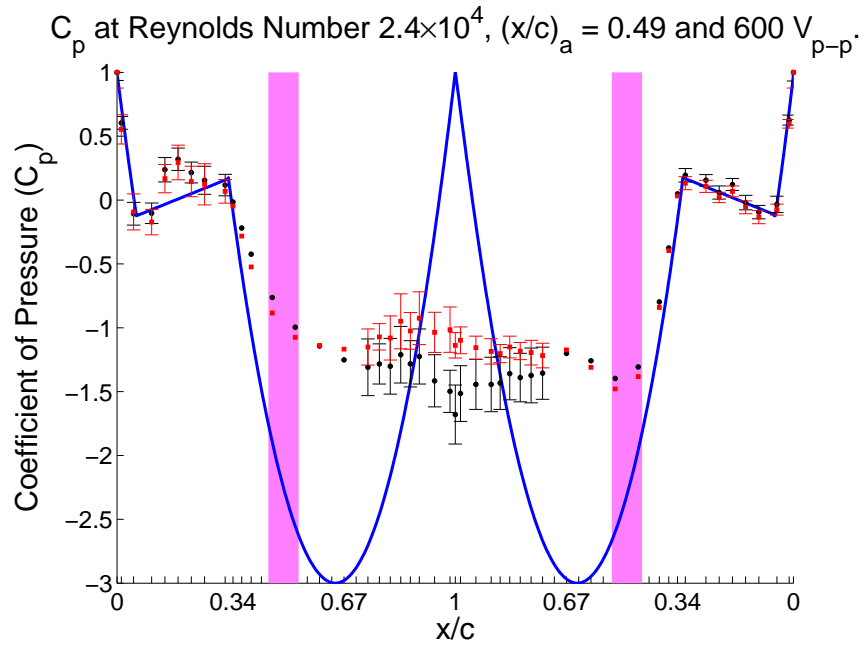
Figure A.188: Synthetic Jet Actuators on a Tail Boom Model.
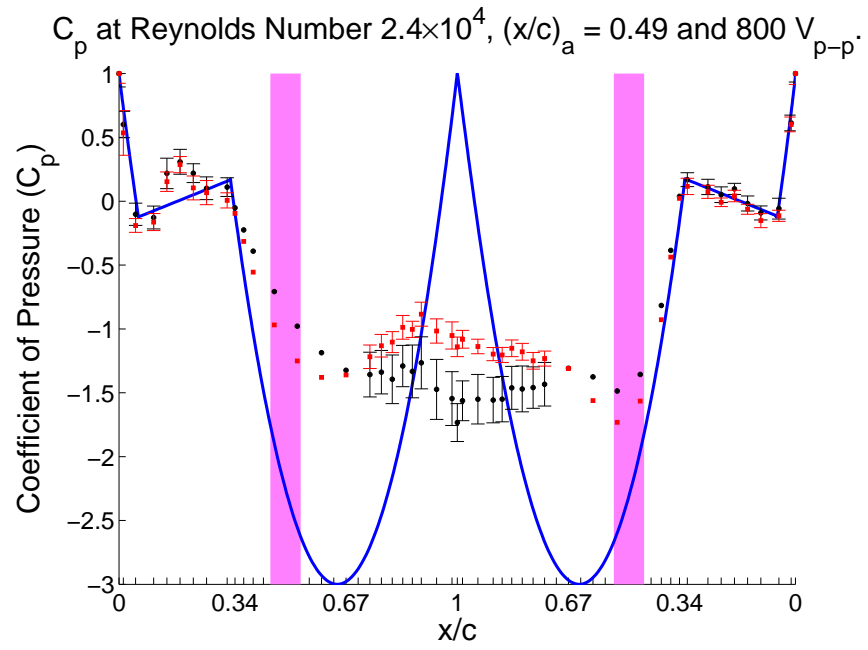
Figure A.189: Synthetic Jet Actuators on a Tail Boom Model.
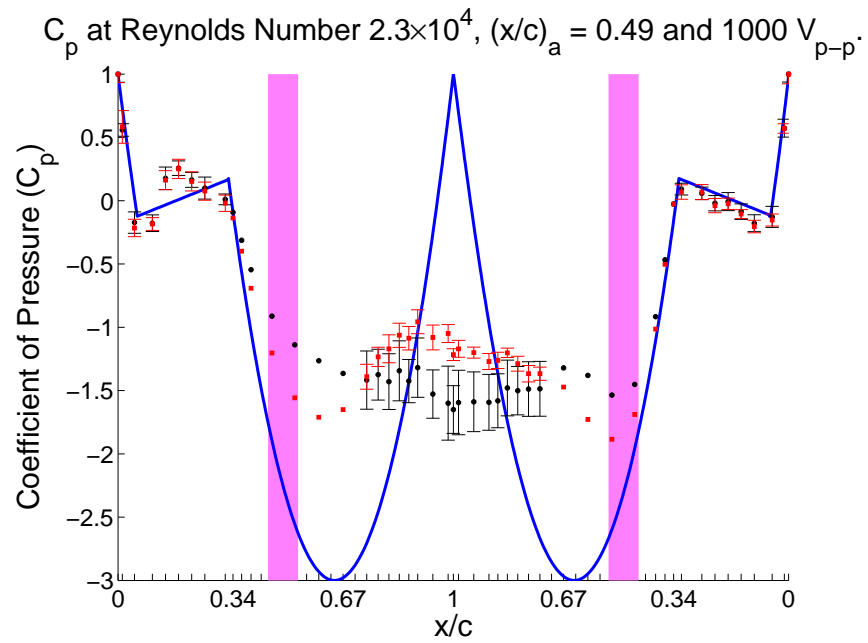
Figure A.190: Synthetic Jet Actuators on a Tail Boom Model.

245
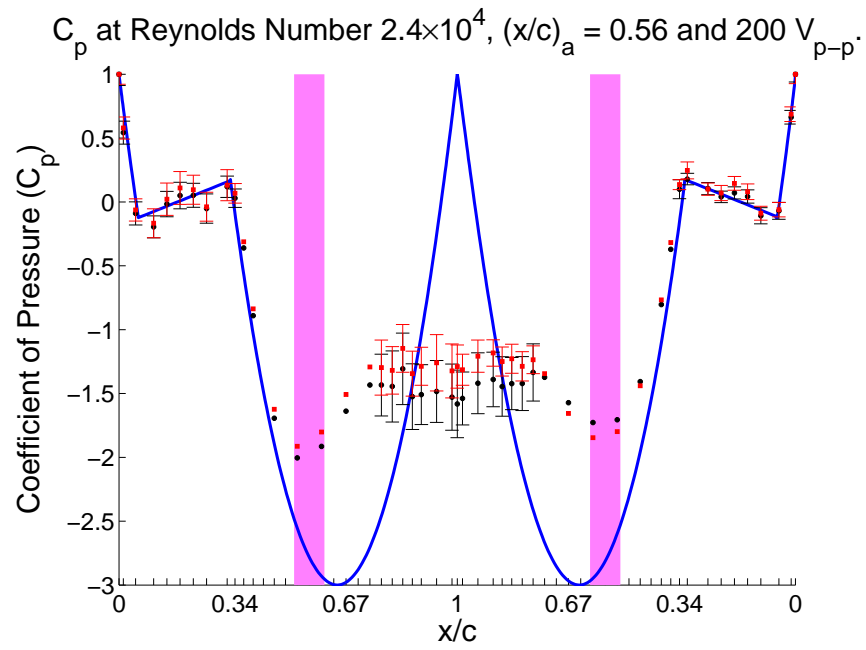
Figure A.191: Synthetic Jet Actuators on a Tail Boom Model.
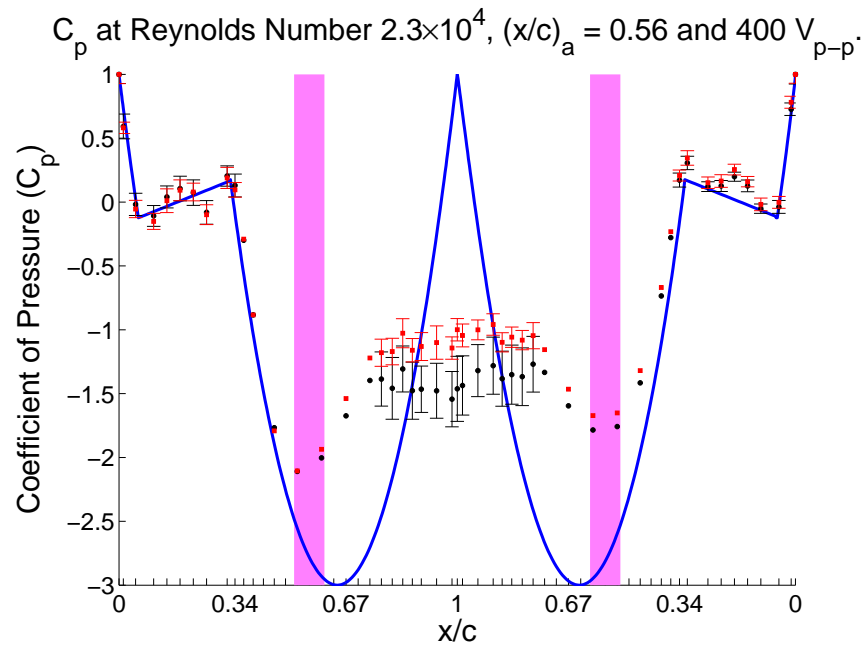
Figure A.192: Synthetic Jet Actuators on a Tail Boom Model.

246
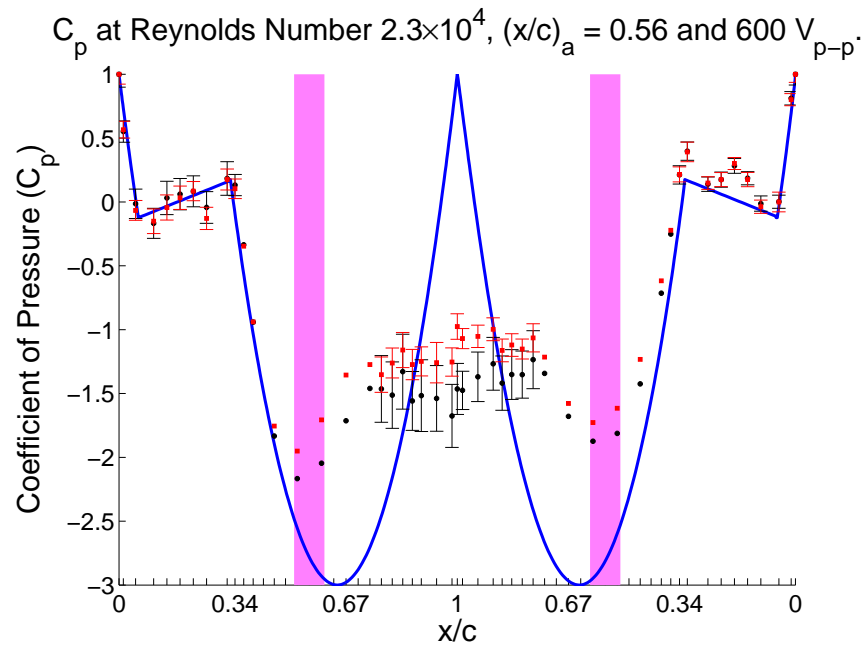
Figure A.193: Synthetic Jet Actuators on a Tail Boom Model.
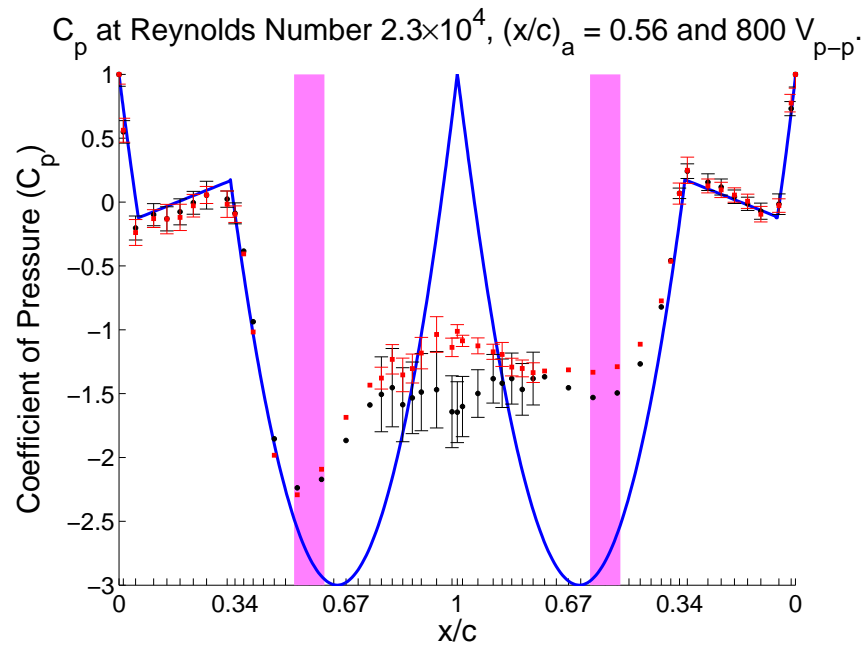
Figure A.194: Synthetic Jet Actuators on a Tail Boom Model.
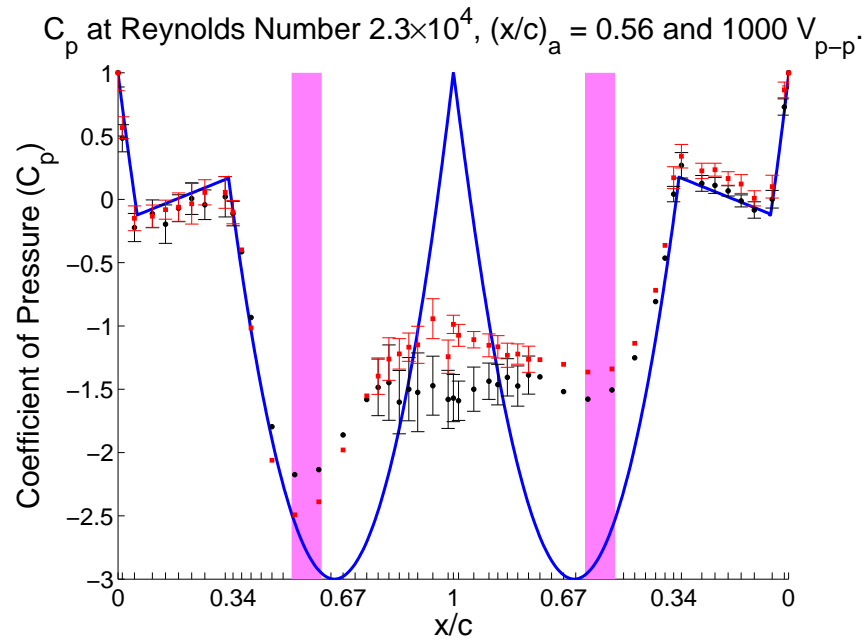
Figure A.195: Synthetic Jet Actuators on a Tail Boom Model.
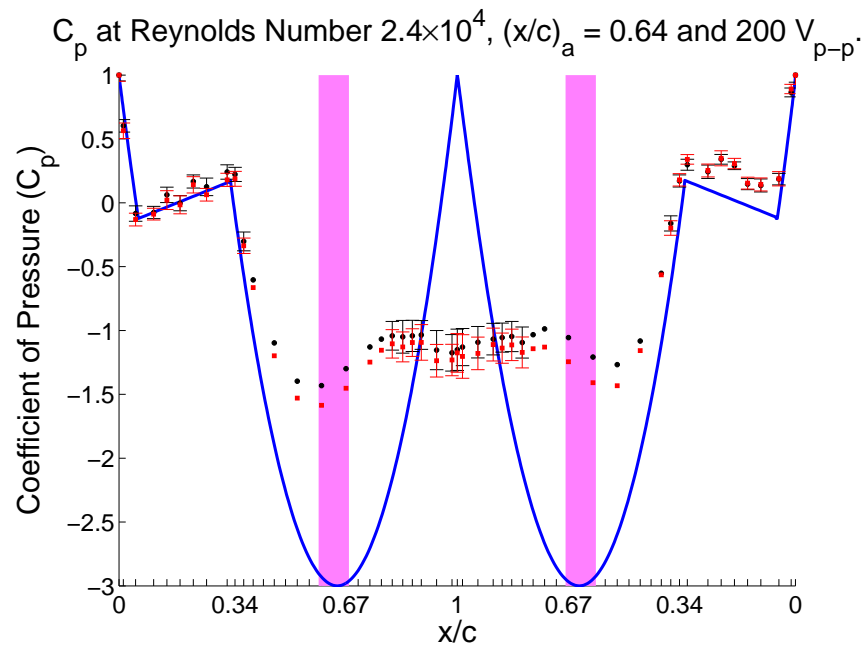
Figure A.196: Synthetic Jet Actuators on a Tail Boom Model.
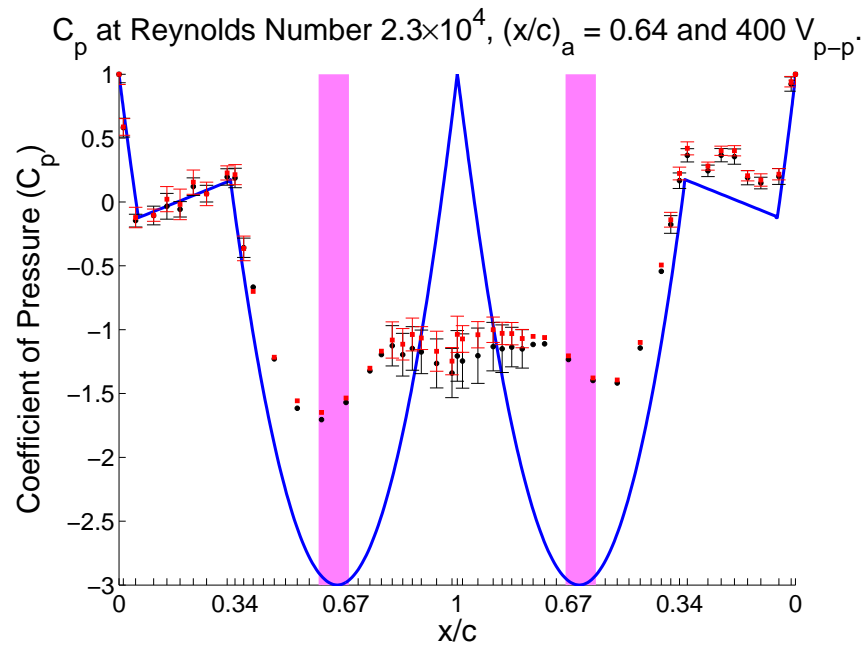
Figure A.197: Synthetic Jet Actuators on a Tail Boom Model.
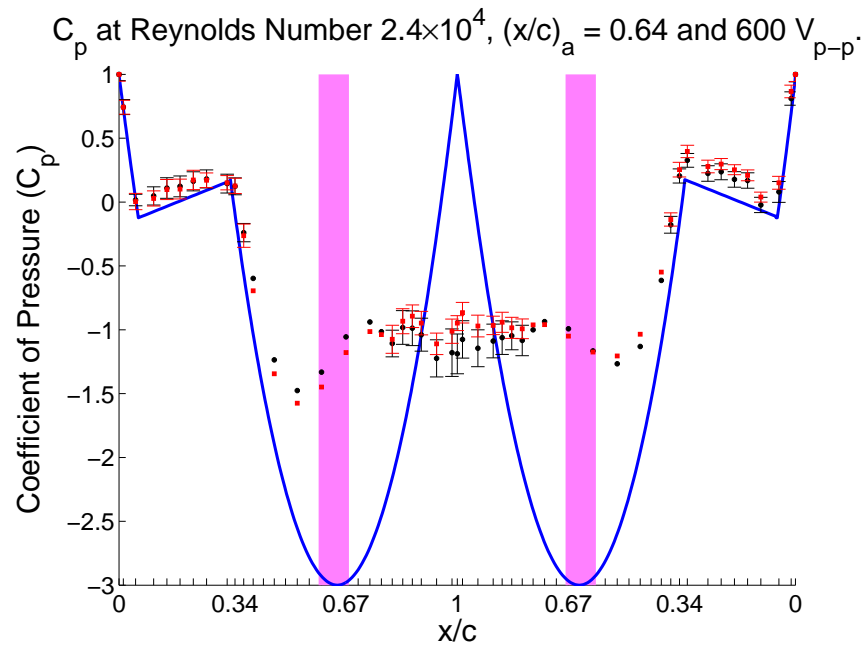
Figure A.198: Synthetic Jet Actuators on a Tail Boom Model.
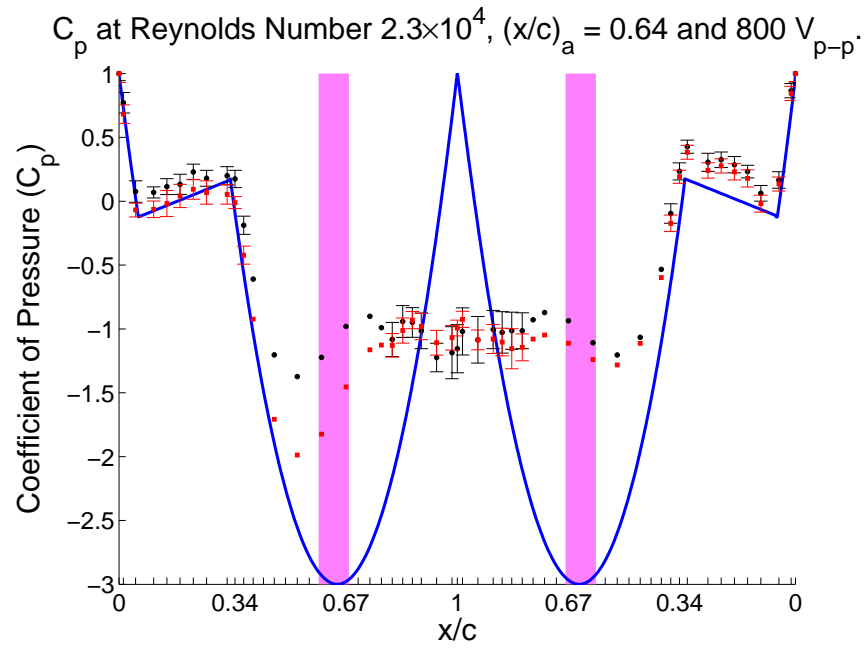
Figure A.199: Synthetic Jet Actuators on a Tail Boom Model.
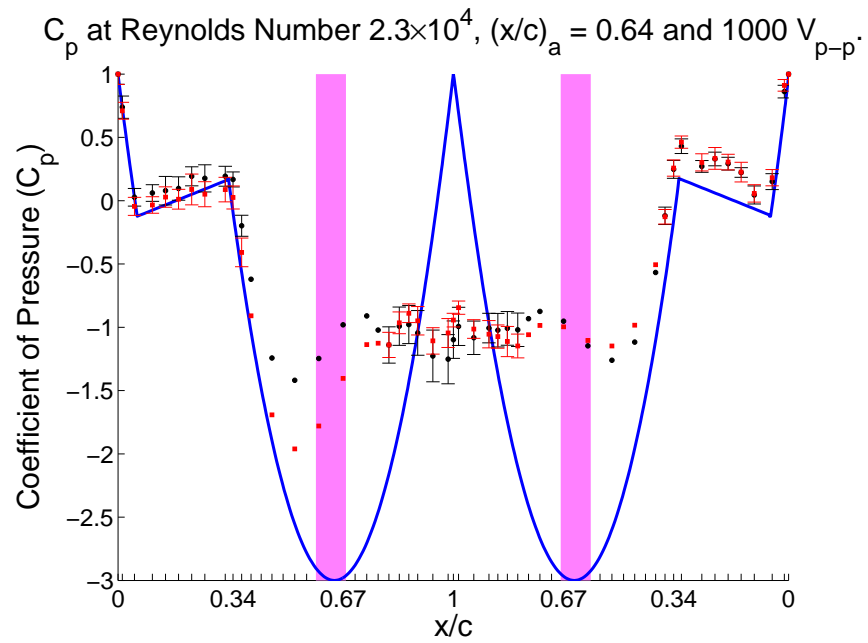
Figure A.200: Synthetic Jet Actuators on a Tail Boom Model.
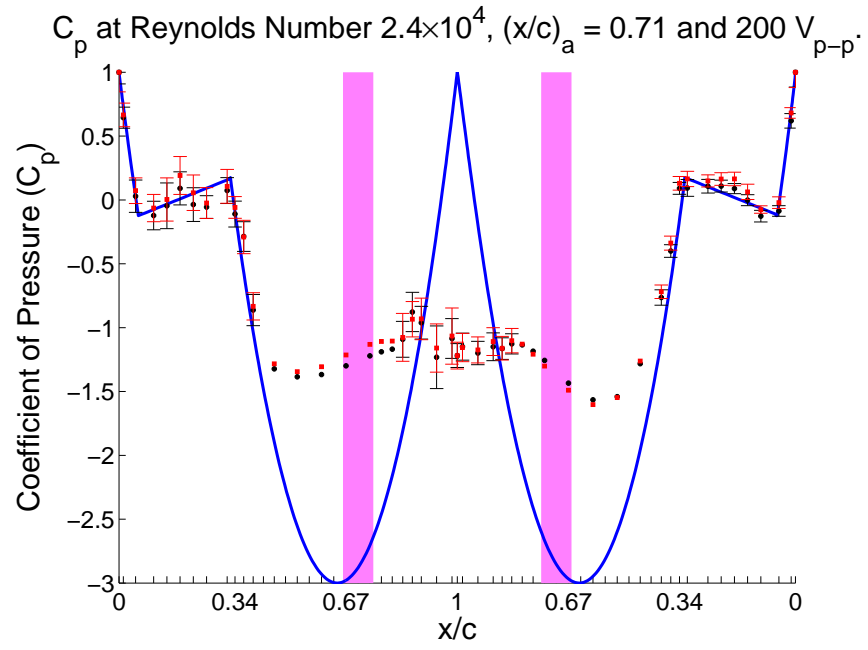
Figure A.201: Synthetic Jet Actuators on a Tail Boom Model.
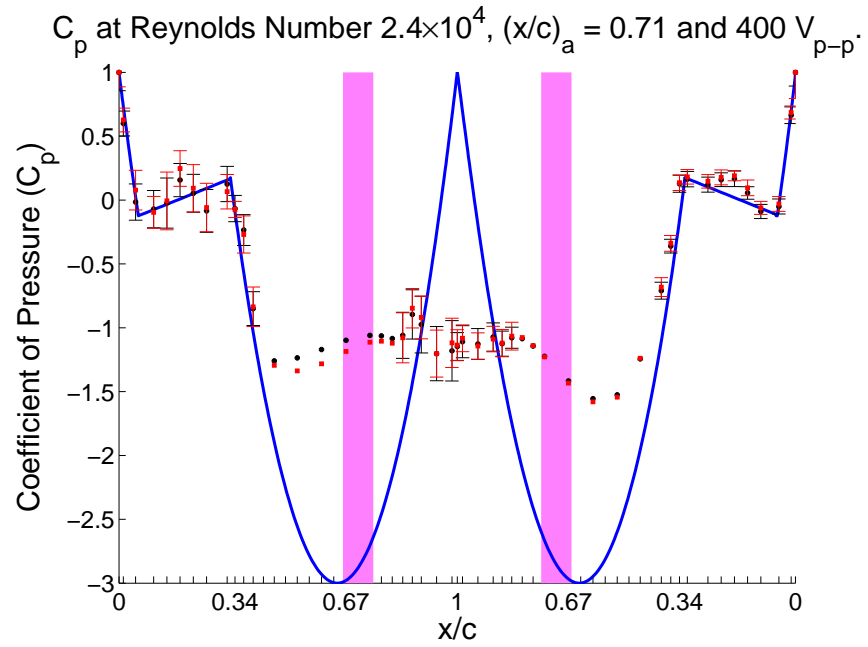
Figure A.202: Synthetic Jet Actuators on a Tail Boom Model.
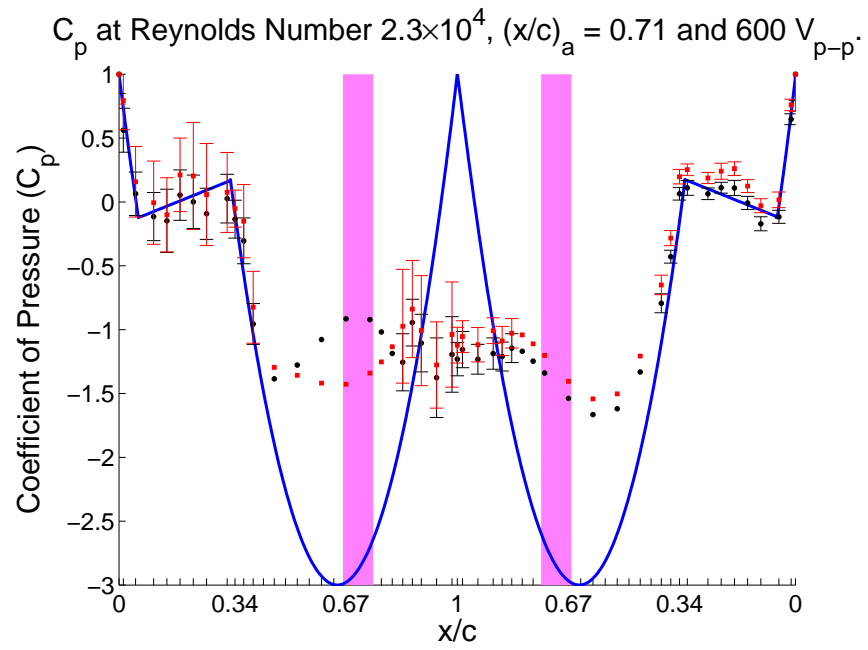
Figure A.203: Synthetic Jet Actuators on a Tail Boom Model.
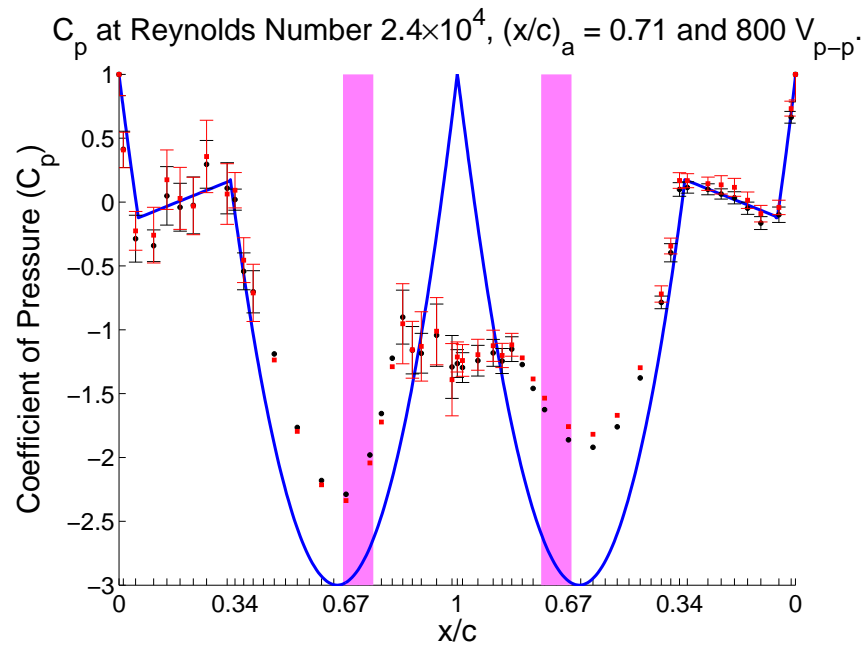
Figure A.204: Synthetic Jet Actuators on a Tail Boom Model.
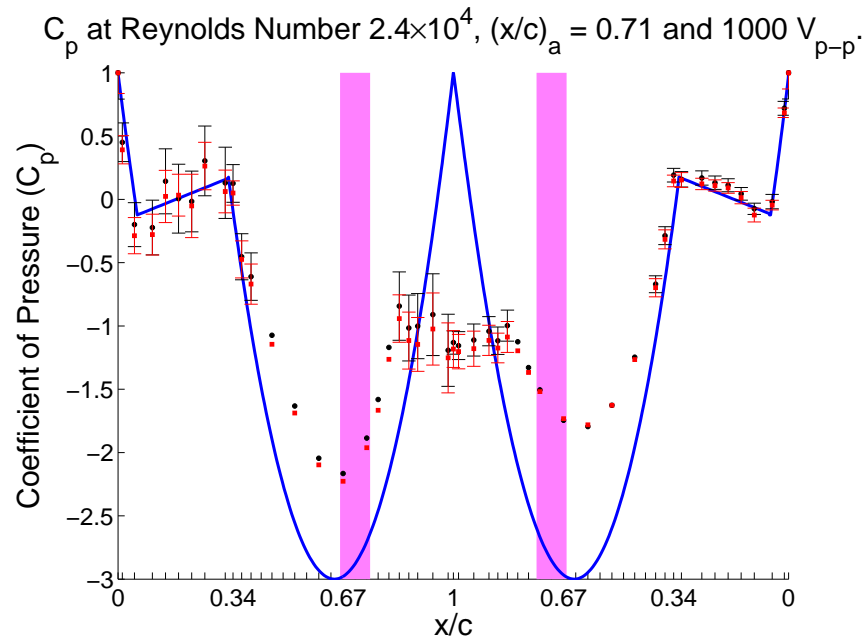
Figure A.205: Synthetic Jet Actuators on a Tail Boom Model.
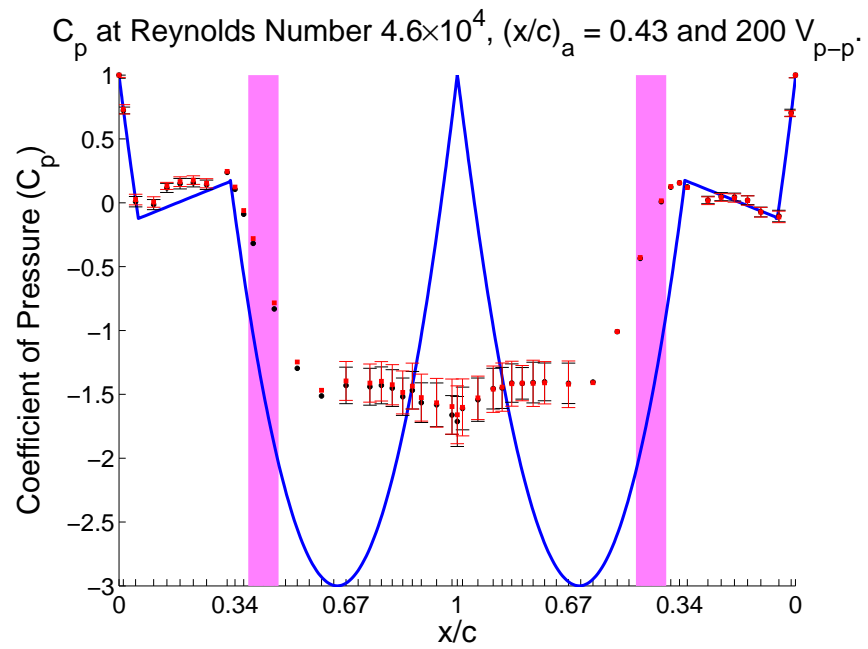
Figure A.206: Synthetic Jet Actuators on a Tail Boom Model.
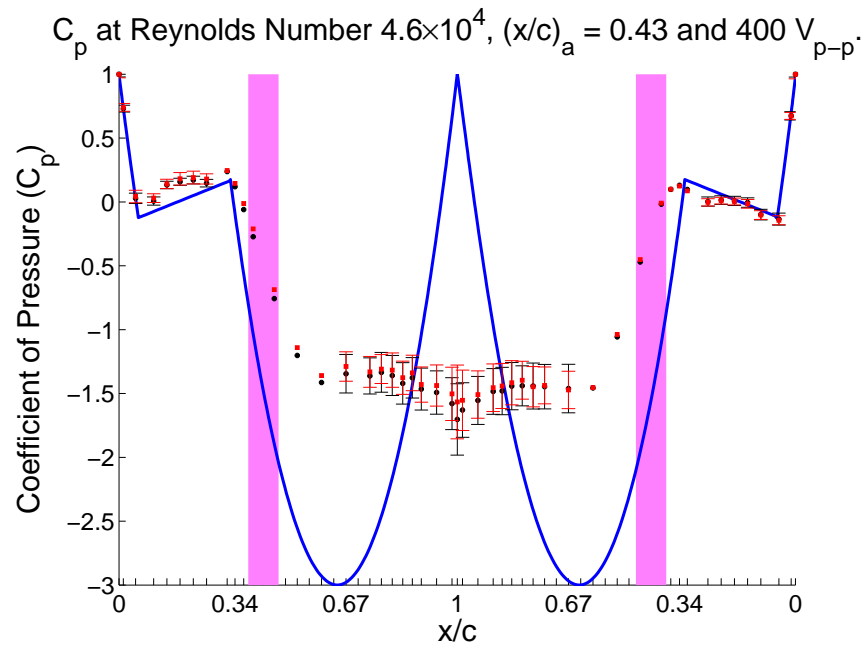
Figure A.207: Synthetic Jet Actuators on a Tail Boom Model.
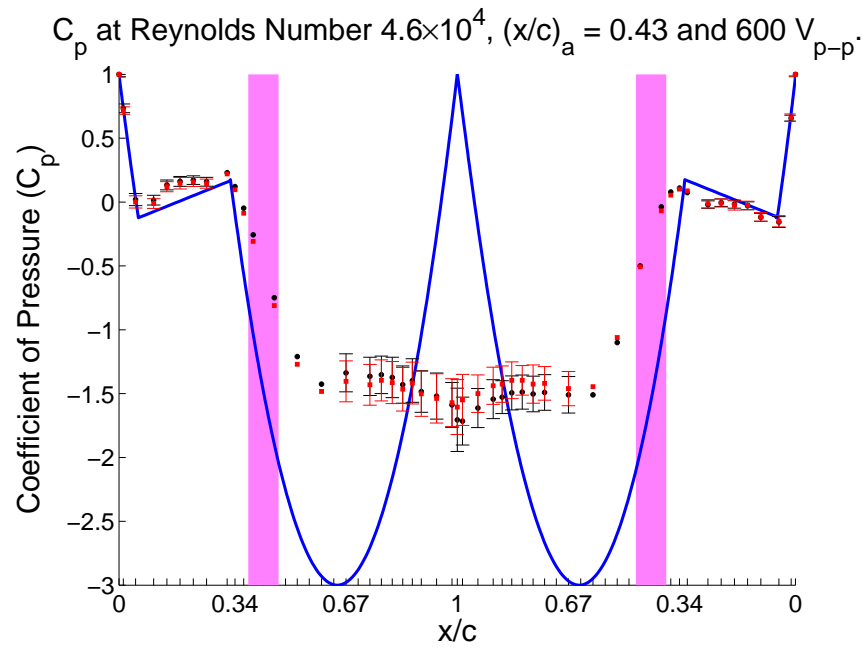
Figure A.208: Synthetic Jet Actuators on a Tail Boom Model.
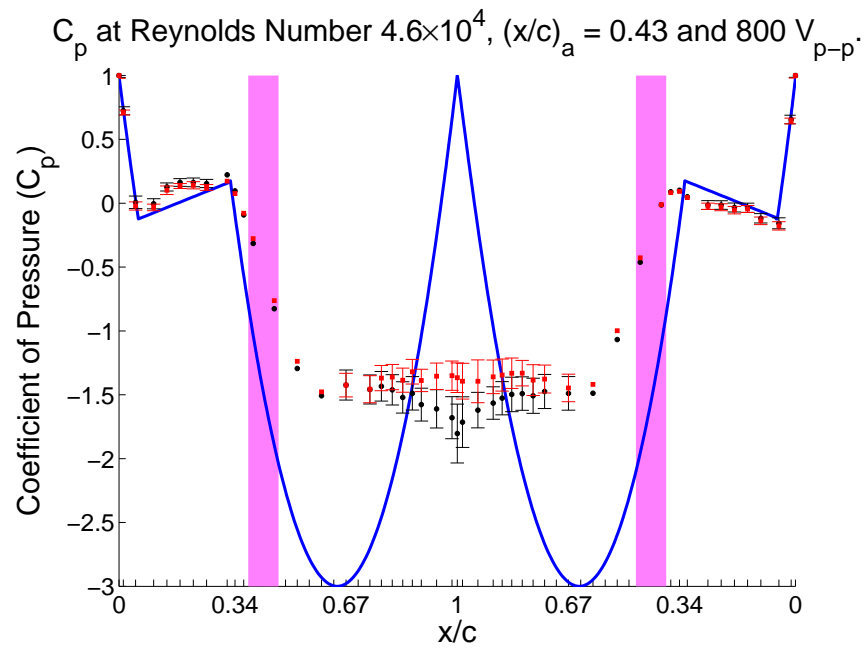
Figure A.209: Synthetic Jet Actuators on a Tail Boom Model.
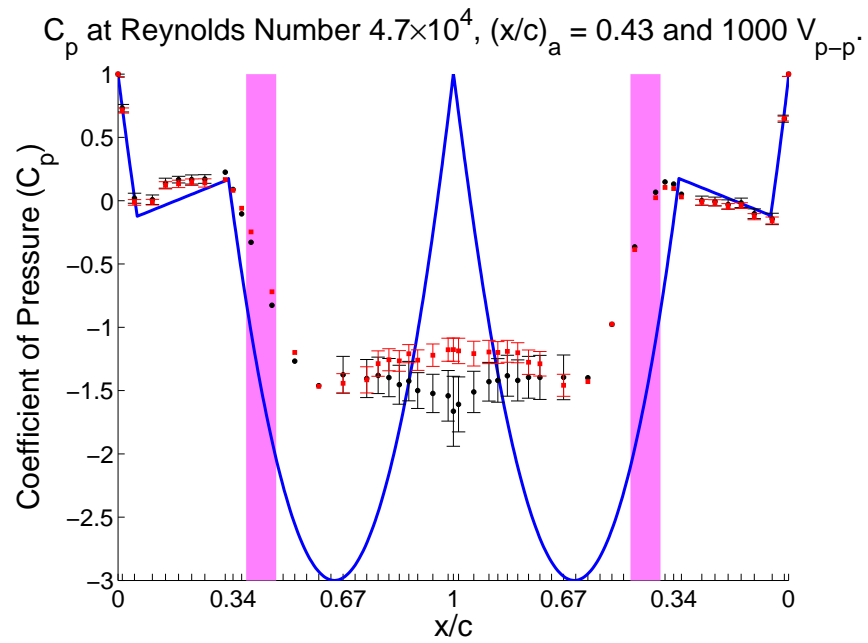
Figure A.210: Synthetic Jet Actuators on a Tail Boom Model.
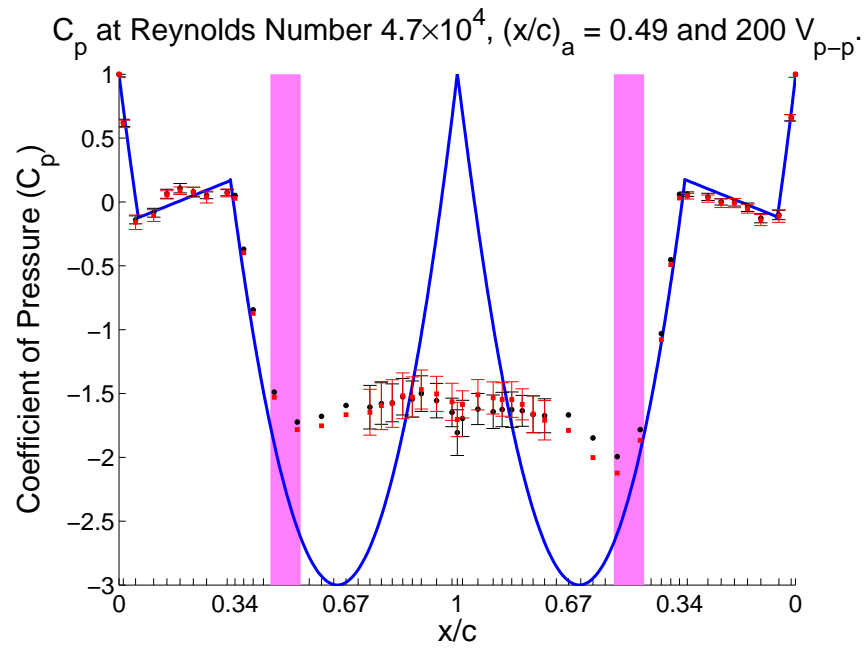
Figure A.211: Synthetic Jet Actuators on a Tail Boom Model.
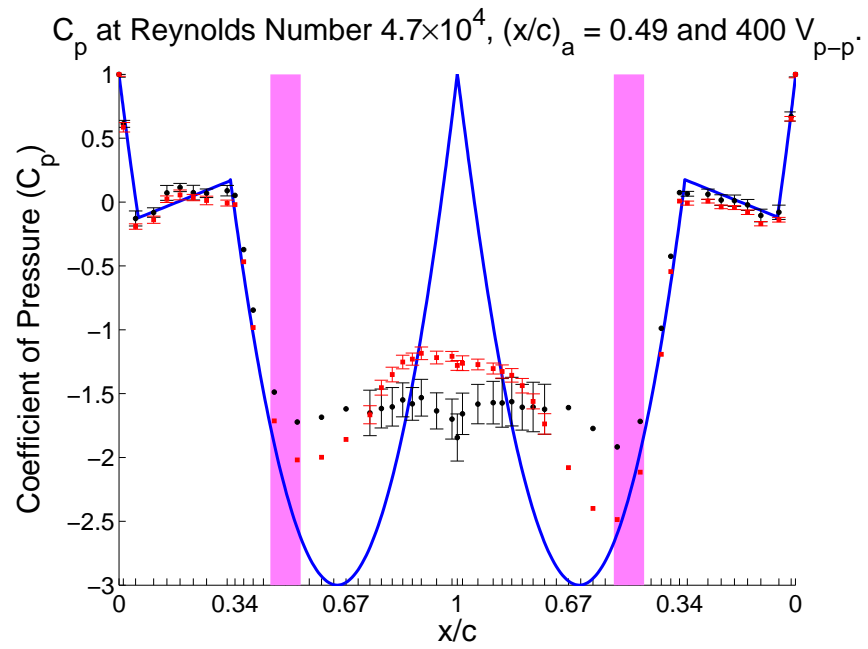
Figure A.212: Synthetic Jet Actuators on a Tail Boom Model.
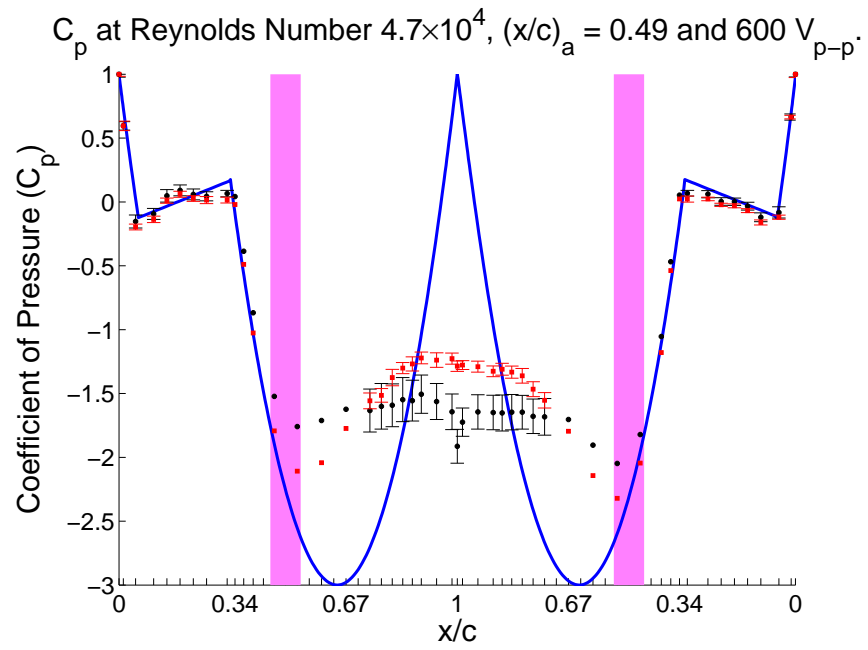
Figure A.213: Synthetic Jet Actuators on a Tail Boom Model.
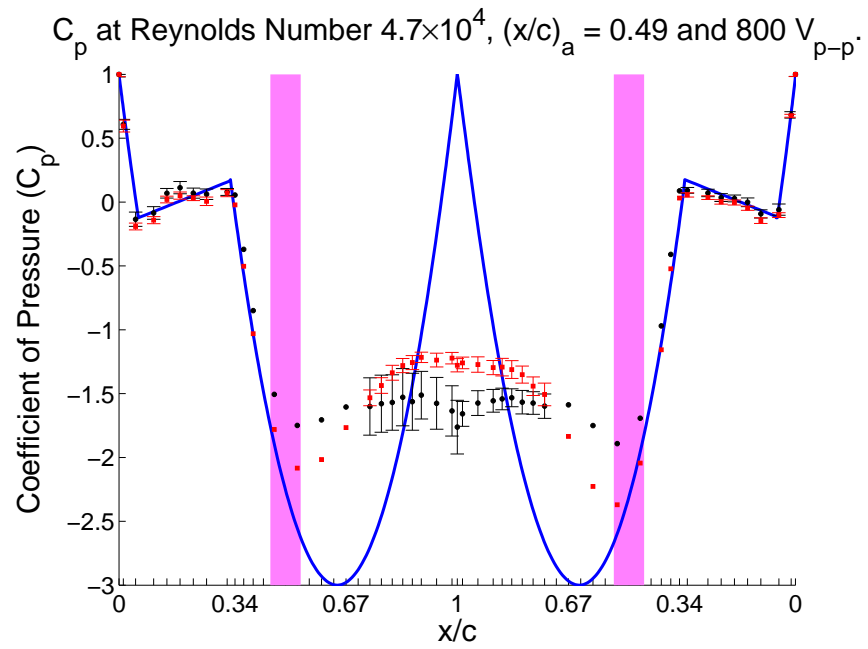
Figure A.214: Synthetic Jet Actuators on a Tail Boom Model.
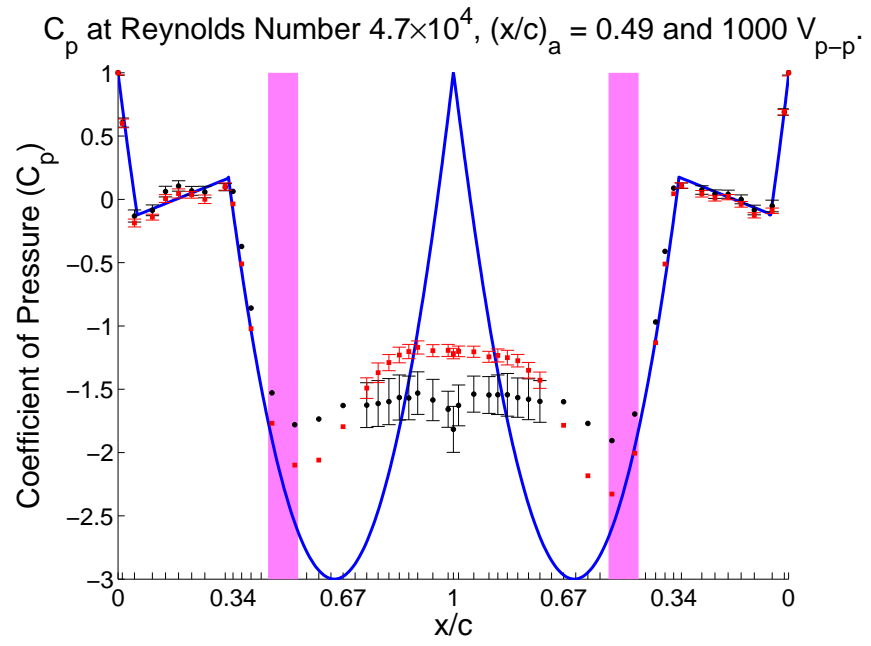
Figure A.215: Synthetic Jet Actuators on a Tail Boom Model.
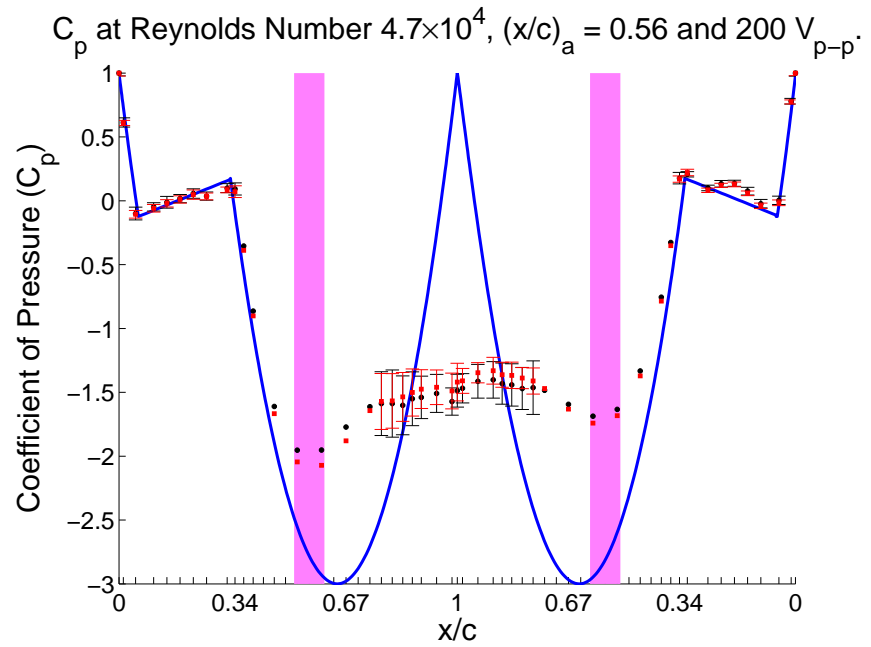
Figure A.216: Synthetic Jet Actuators on a Tail Boom Model.
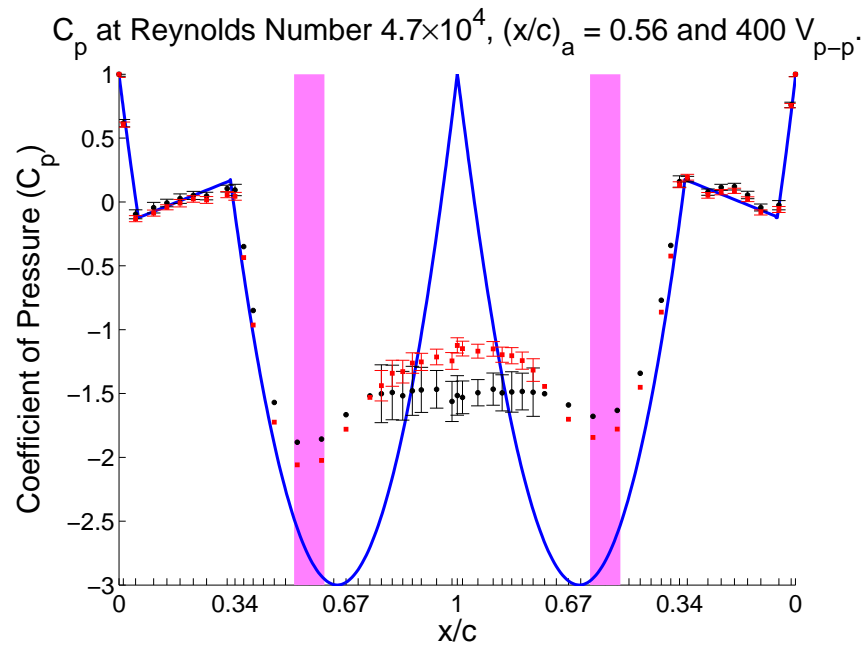
Figure A.217: Synthetic Jet Actuators on a Tail Boom Model.
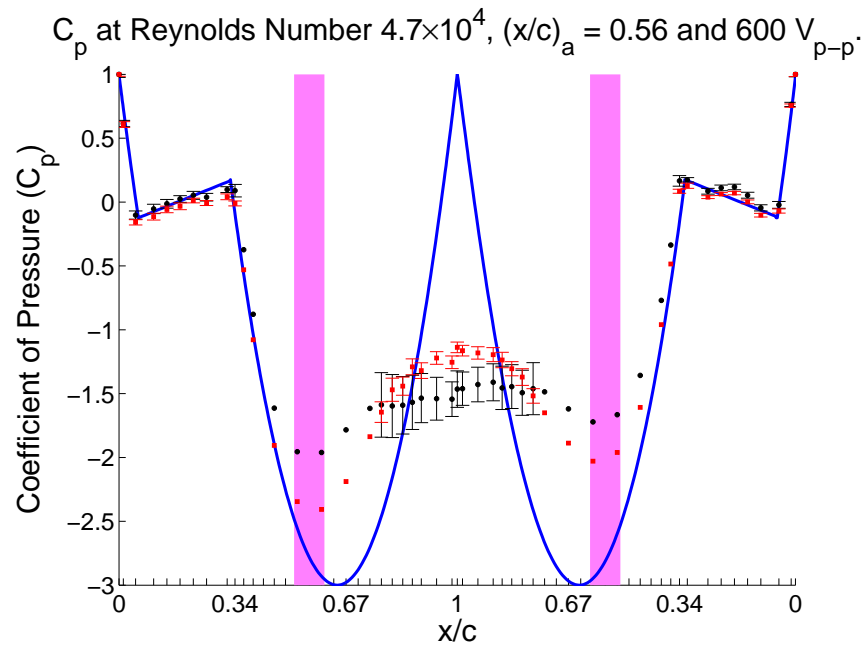
Figure A.218: Synthetic Jet Actuators on a Tail Boom Model.
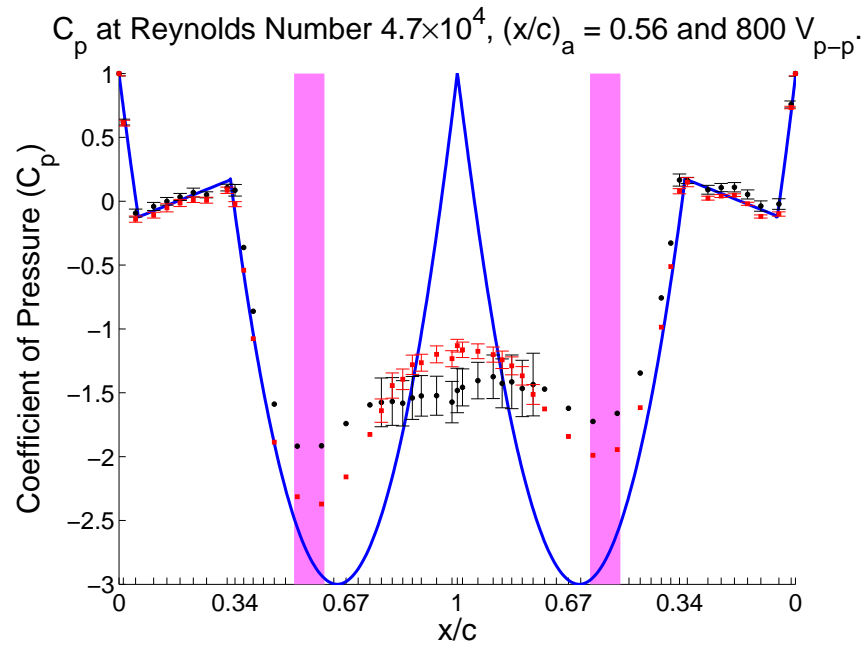
Figure A.219: Synthetic Jet Actuators on a Tail Boom Model.
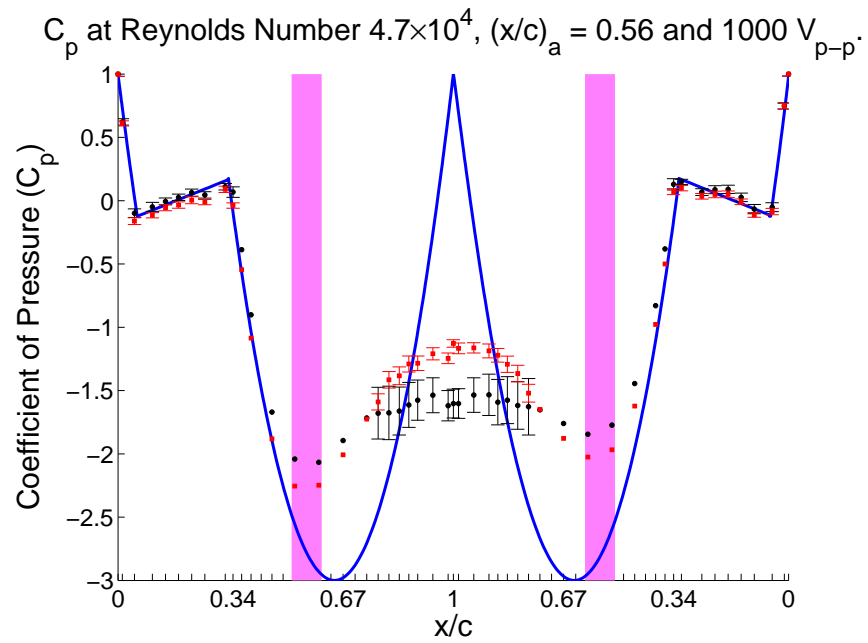
Figure A.220: Synthetic Jet Actuators on a Tail Boom Model.
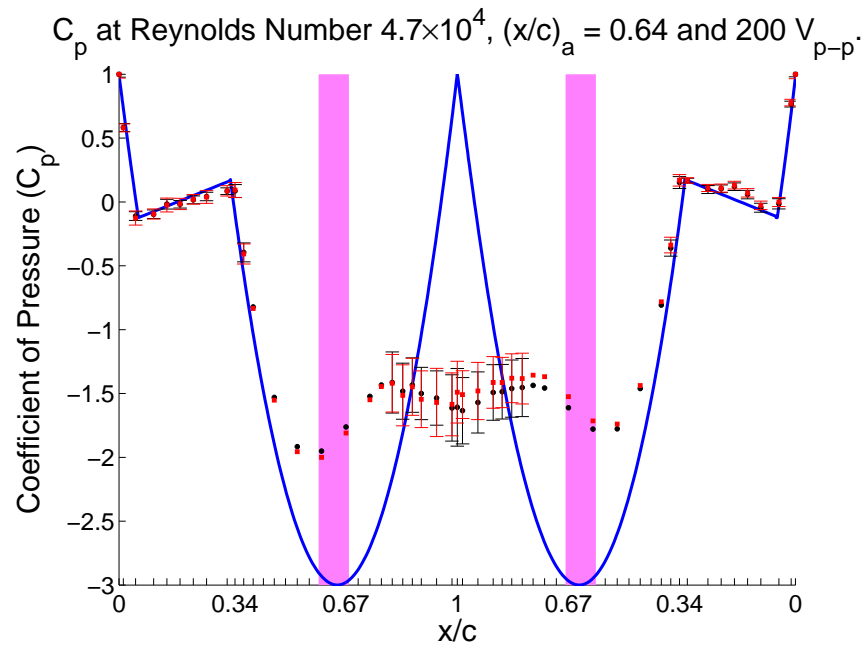
Figure A.221: Synthetic Jet Actuators on a Tail Boom Model.
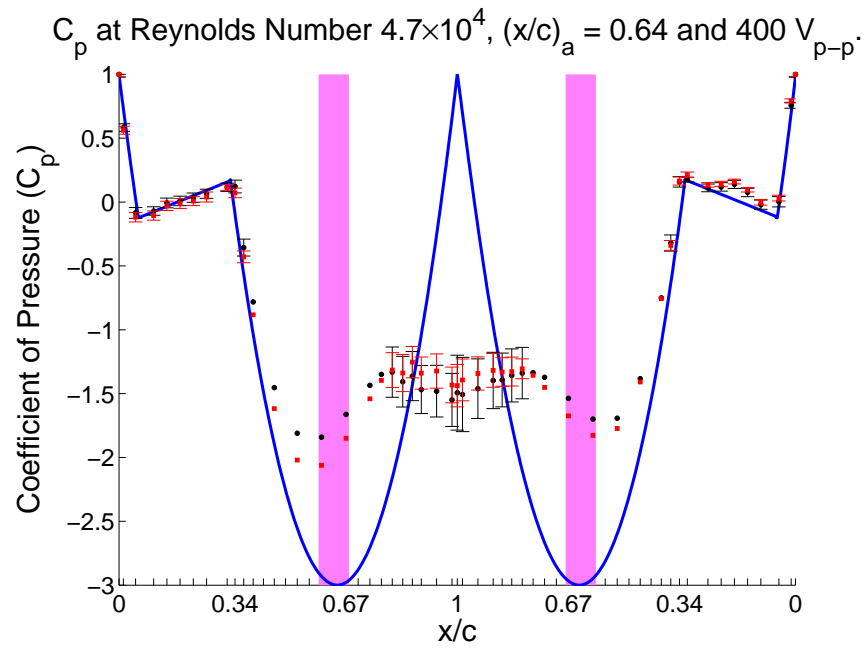
Figure A.222: Synthetic Jet Actuators on a Tail Boom Model.
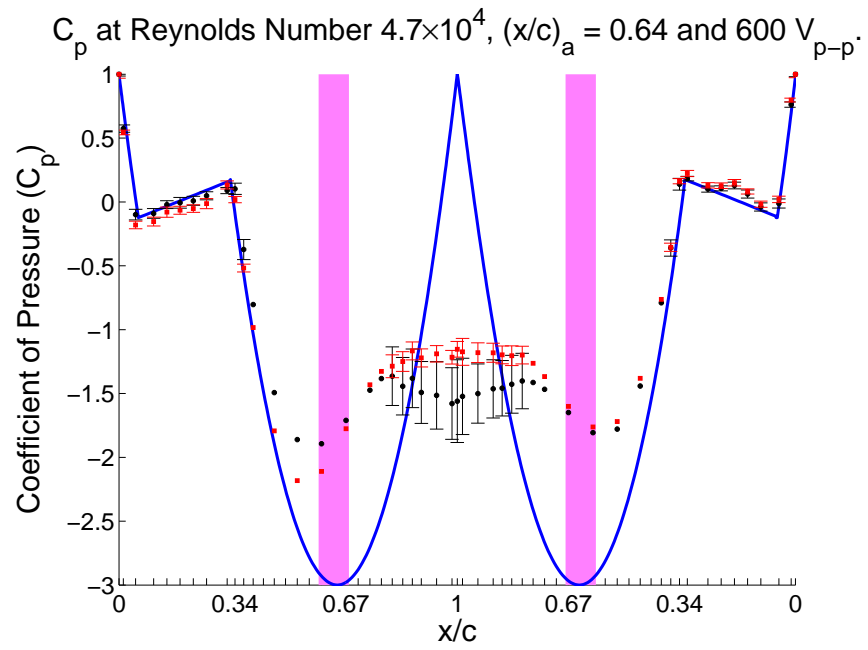
Figure A.223: Synthetic Jet Actuators on a Tail Boom Model.
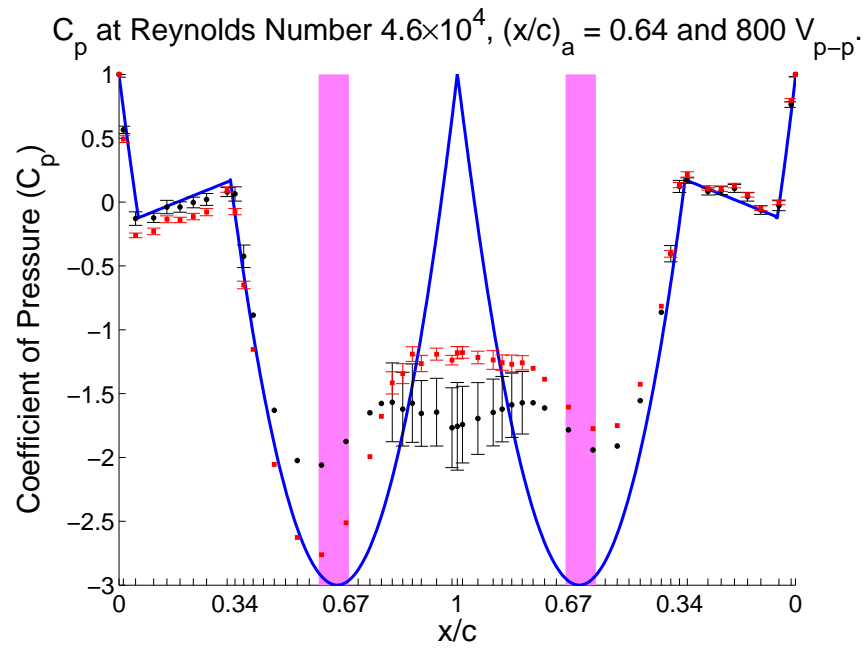
Figure A.224: Synthetic Jet Actuators on a Tail Boom Model.
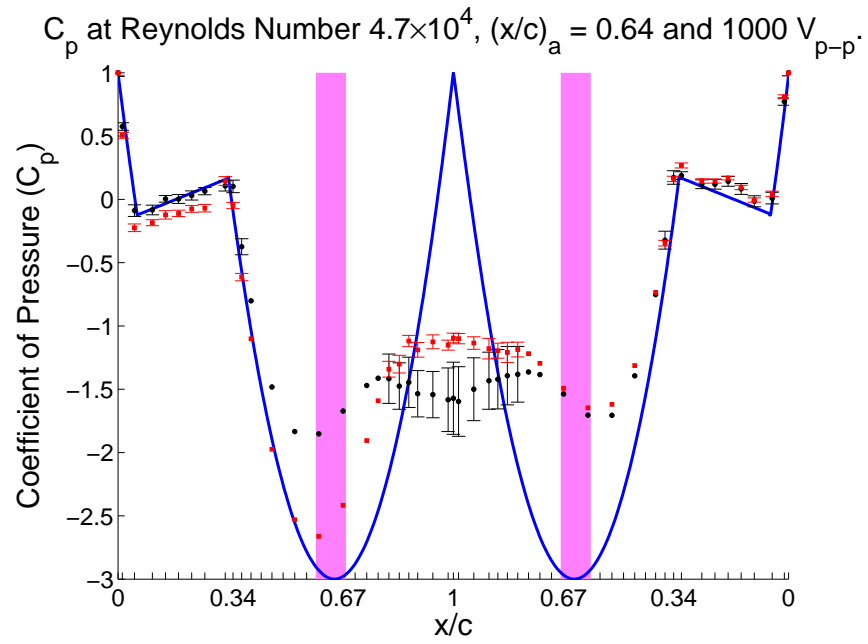
Figure A.225: Synthetic Jet Actuators on a Tail Boom Model.
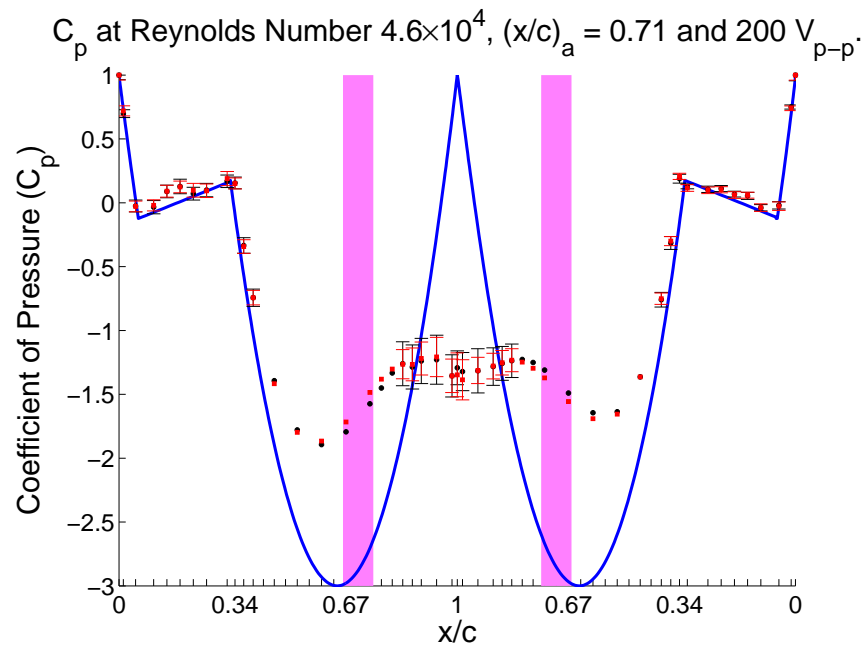
Figure A.226: Synthetic Jet Actuators on a Tail Boom Model.
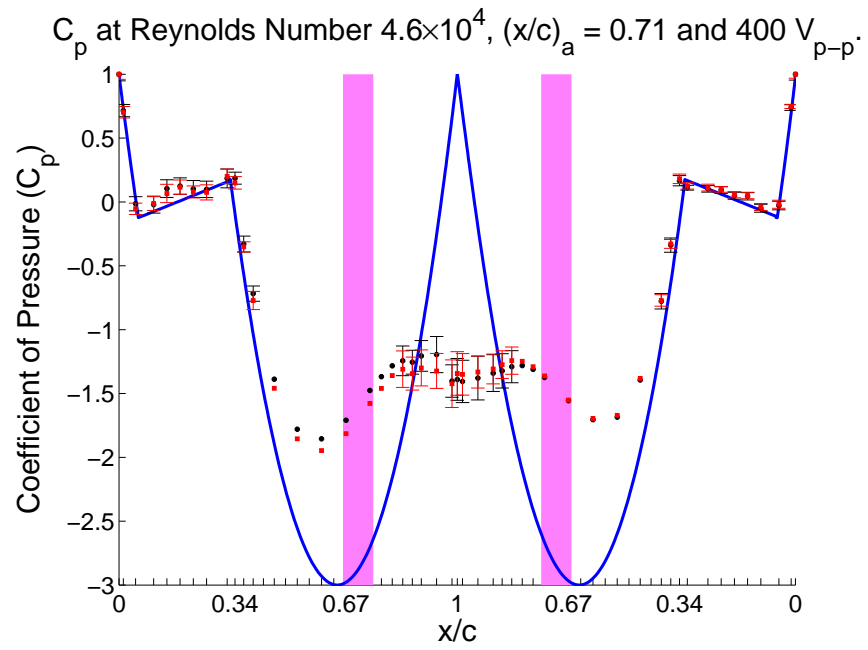
Figure A.227: Synthetic Jet Actuators on a Tail Boom Model.
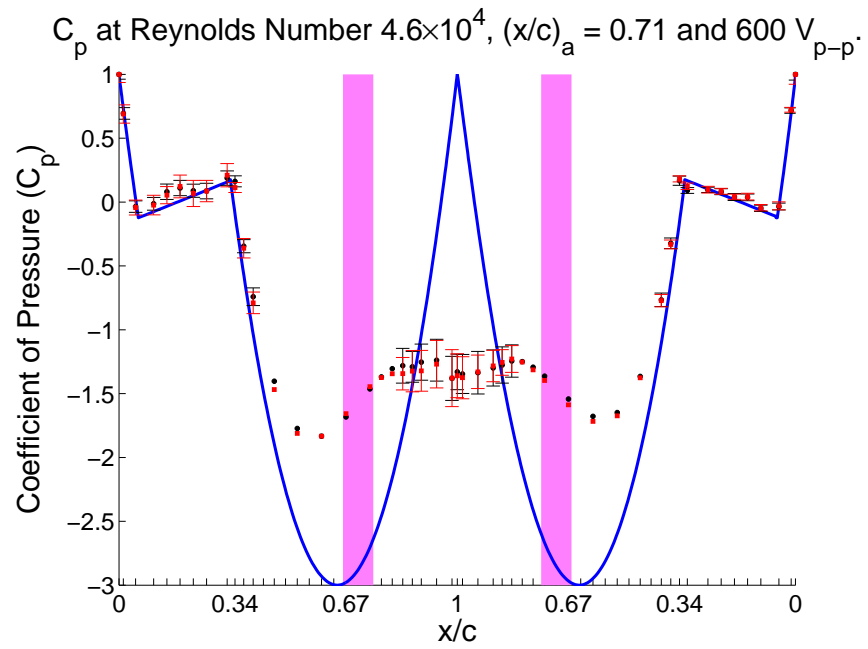
Figure A.228: Synthetic Jet Actuators on a Tail Boom Model.
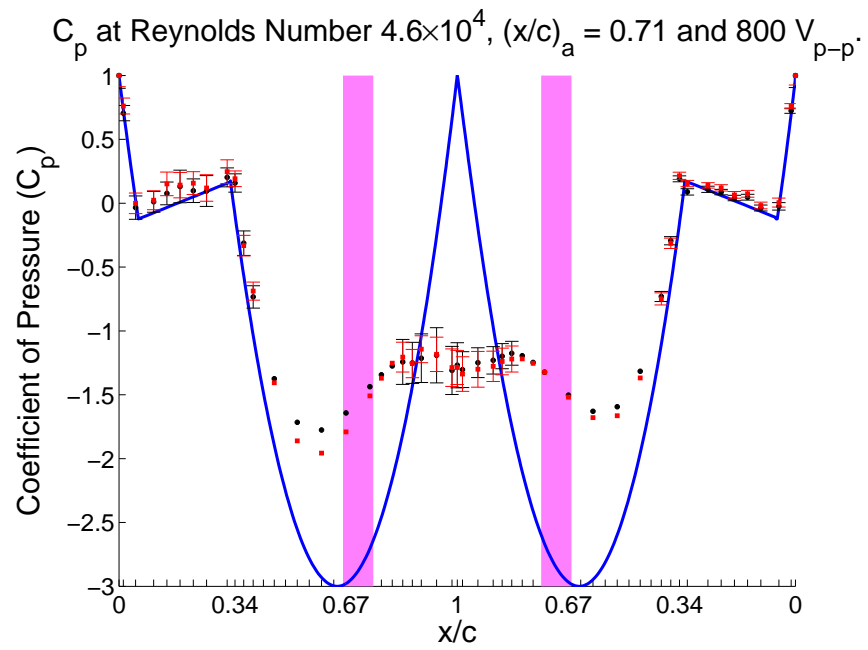
Figure A.229: Synthetic Jet Actuators on a Tail Boom Model.
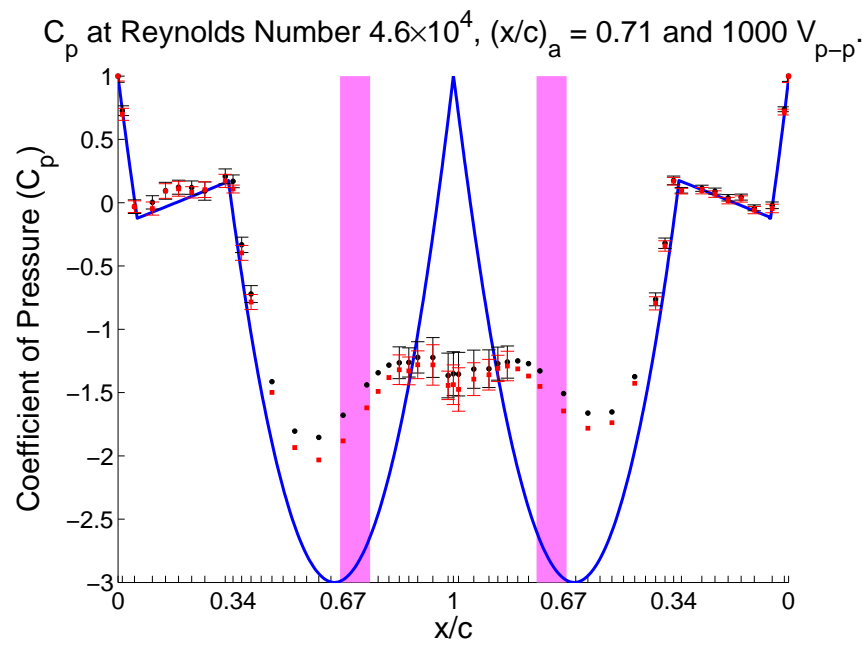
Figure A.230: Synthetic Jet Actuators on a Tail Boom Model.

265
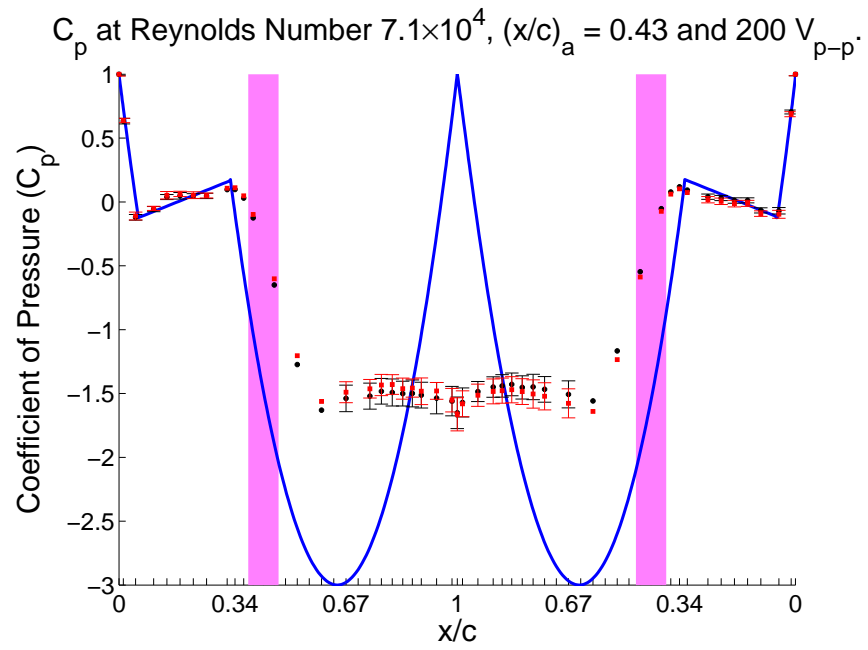
Figure A.231: Synthetic Jet Actuators on a Tail Boom Model.
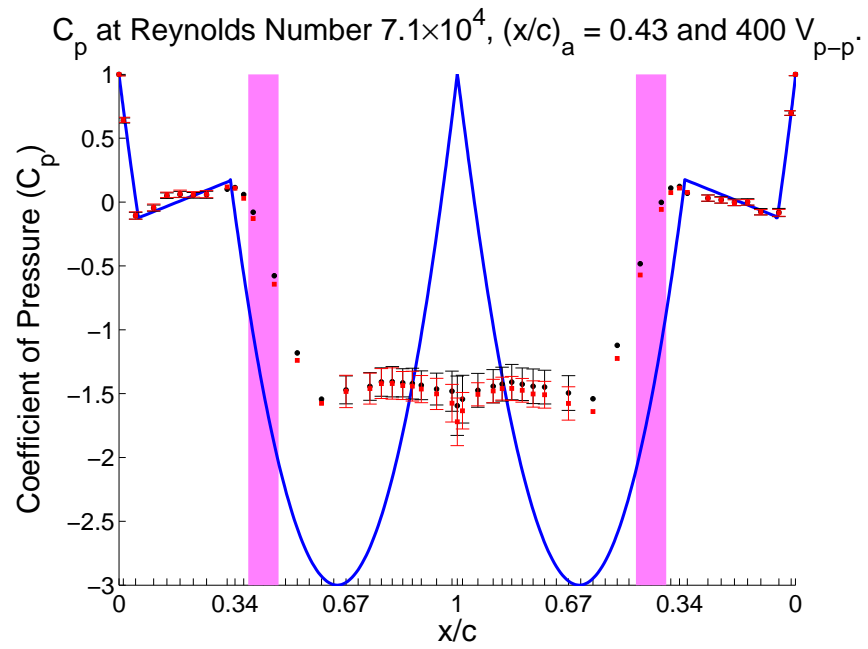
Figure A.232: Synthetic Jet Actuators on a Tail Boom Model.
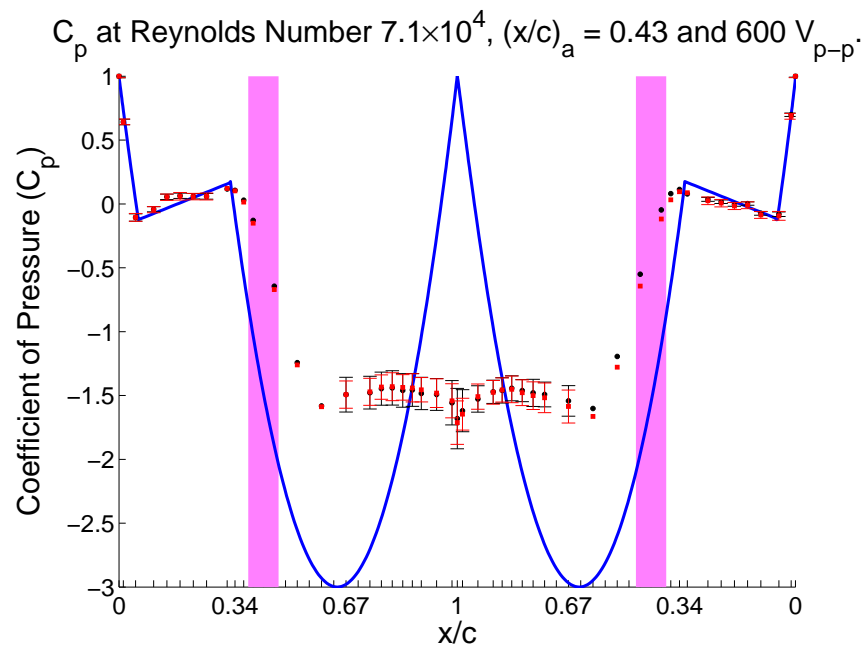
Figure A.233: Synthetic Jet Actuators on a Tail Boom Model.
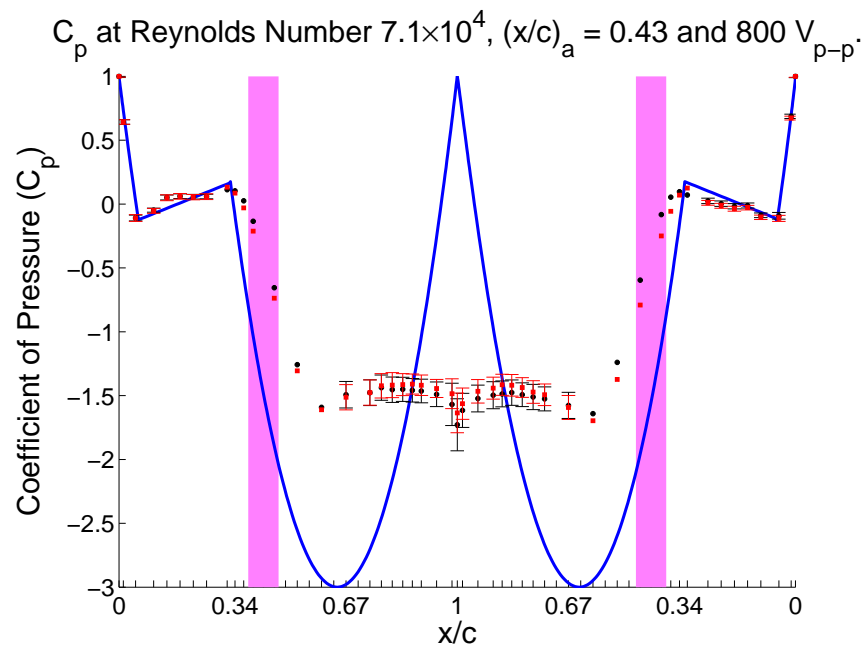
Figure A.234: Synthetic Jet Actuators on a Tail Boom Model.
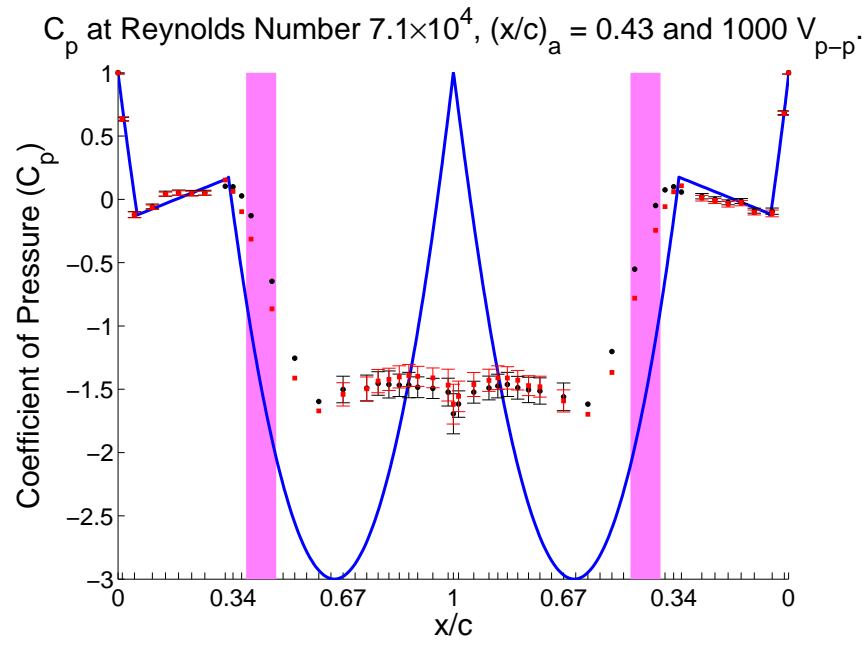
Figure A.235: Synthetic Jet Actuators on a Tail Boom Model.
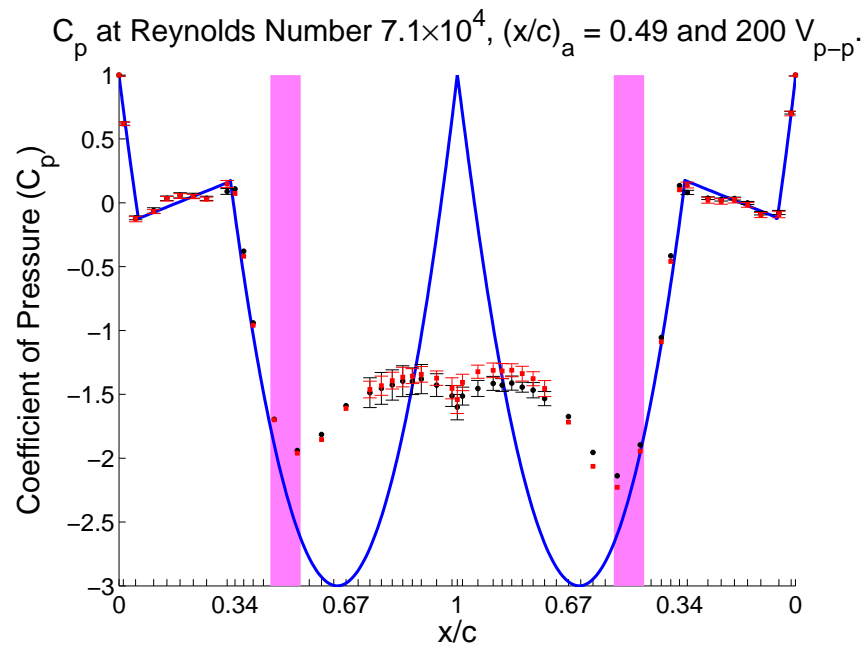
Figure A.236: Synthetic Jet Actuators on a Tail Boom Model.
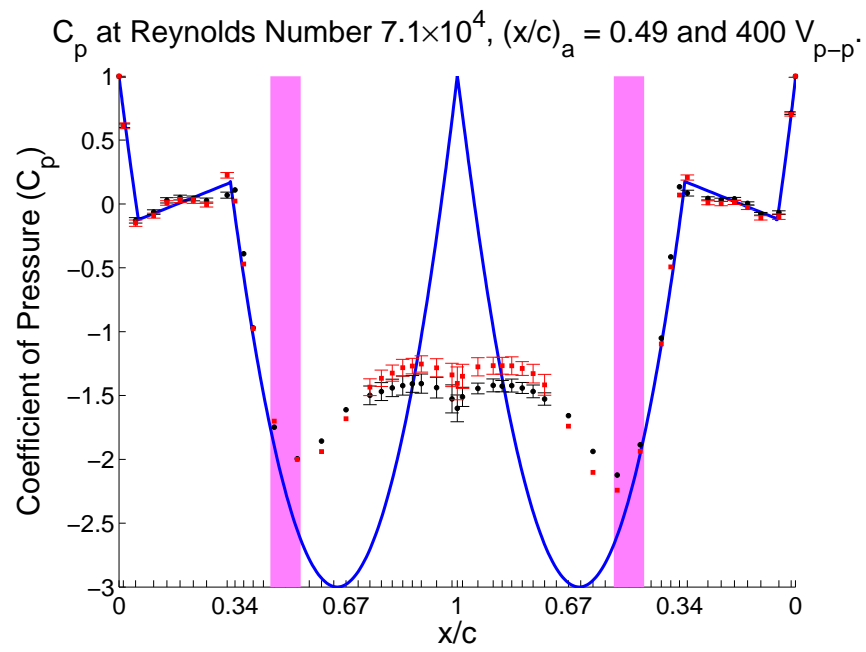
Figure A.237: Synthetic Jet Actuators on a Tail Boom Model.
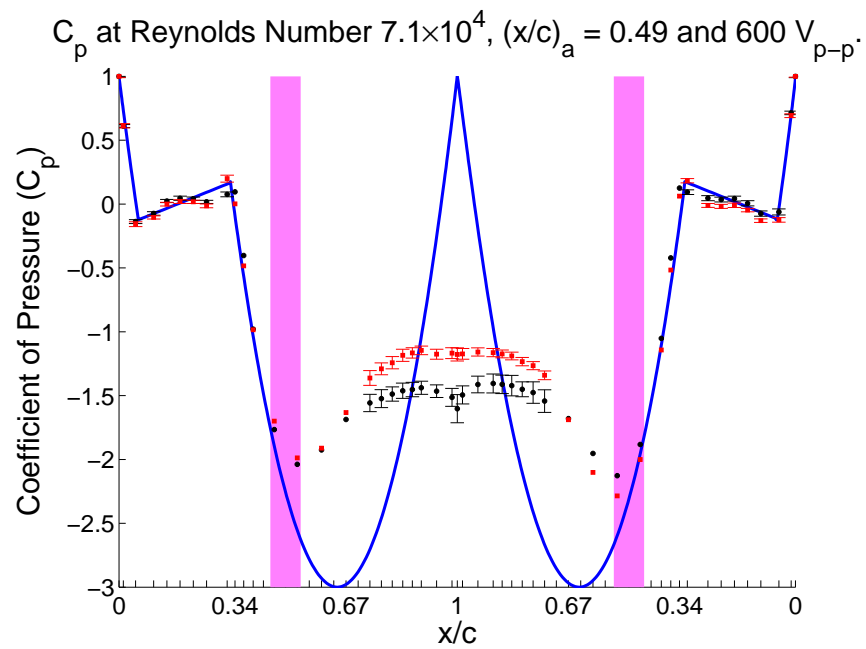
Figure A.238: Synthetic Jet Actuators on a Tail Boom Model.
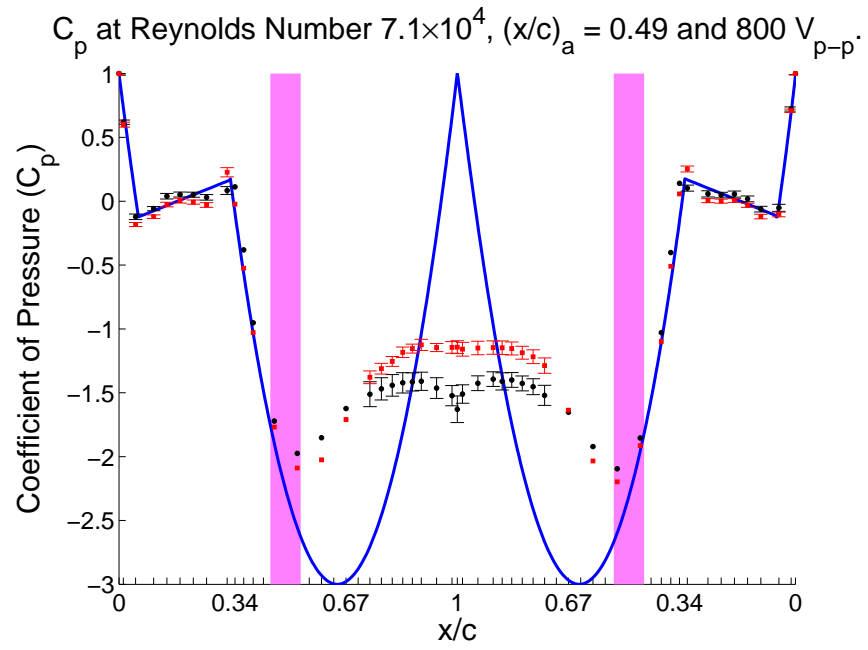
Figure A.239: Synthetic Jet Actuators on a Tail Boom Model.
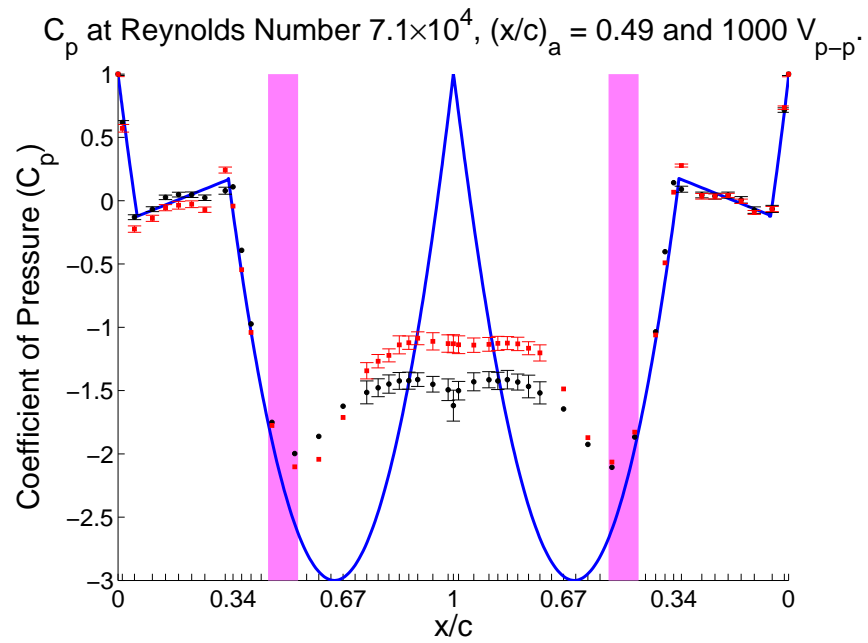
Figure A.240: Synthetic Jet Actuators on a Tail Boom Model.
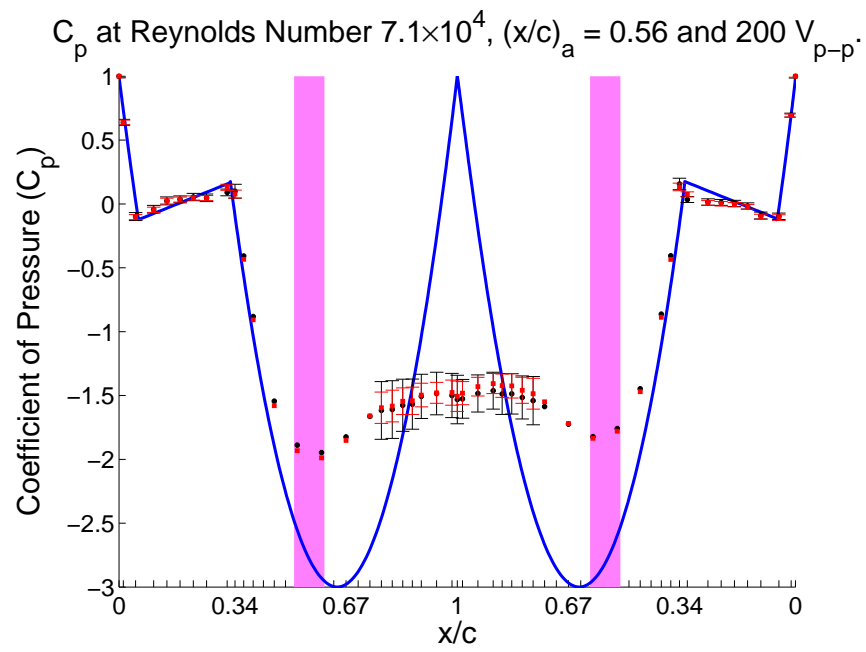
Figure A.241: Synthetic Jet Actuators on a Tail Boom Model.
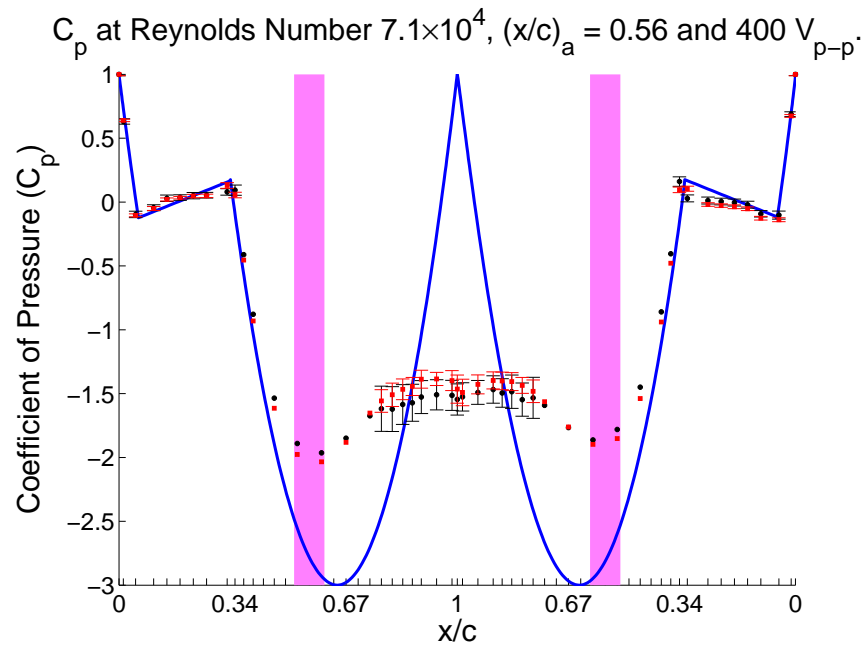
Figure A.242: Synthetic Jet Actuators on a Tail Boom Model.
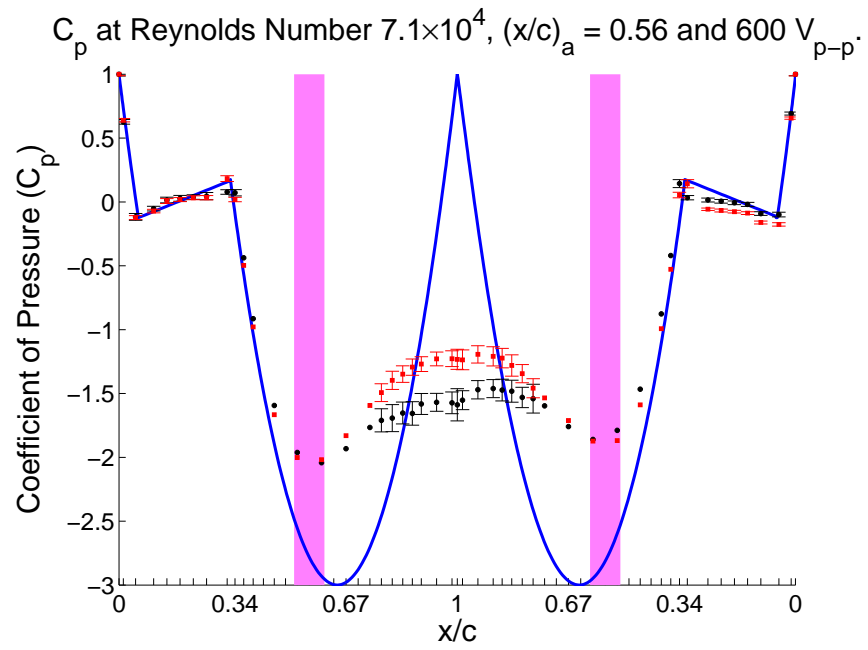
Figure A.243: Synthetic Jet Actuators on a Tail Boom Model.
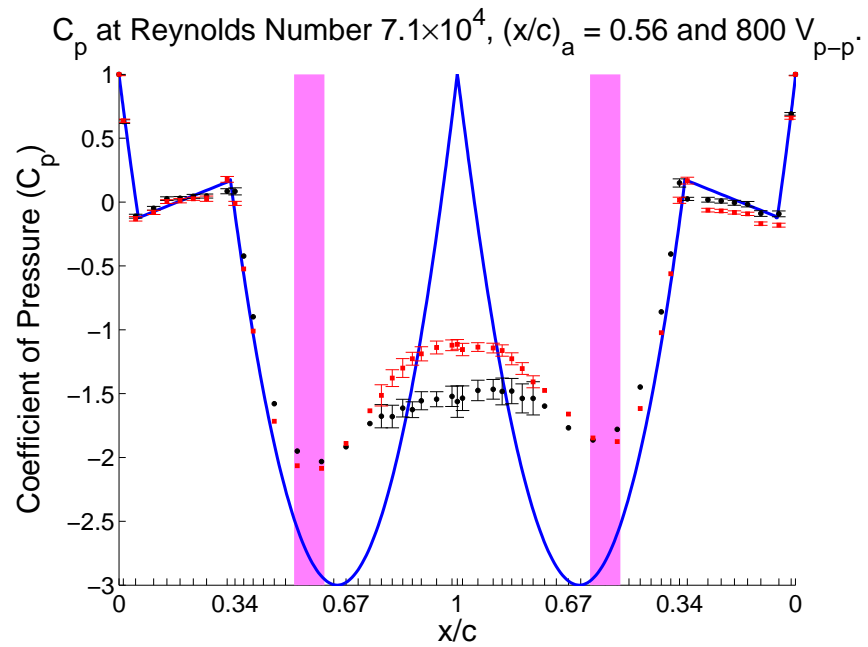
Figure A.244: Synthetic Jet Actuators on a Tail Boom Model.
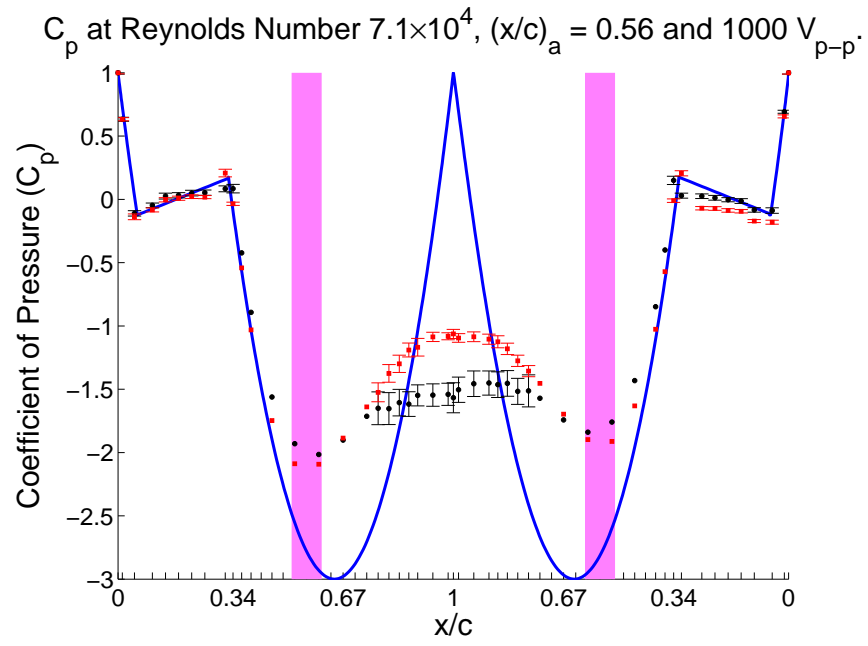
Figure A.245: Synthetic Jet Actuators on a Tail Boom Model.
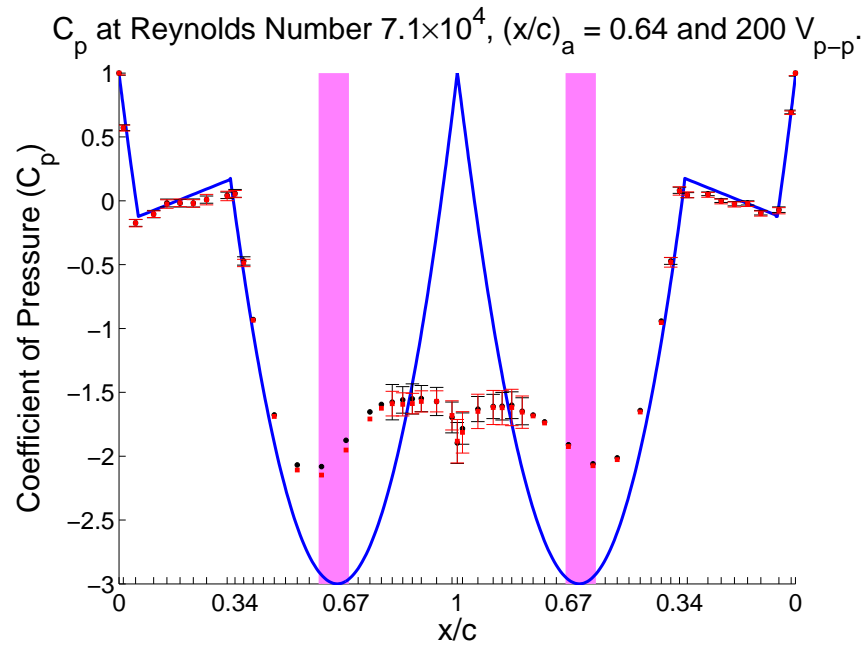
Figure A.246: Synthetic Jet Actuators on a Tail Boom Model.

273
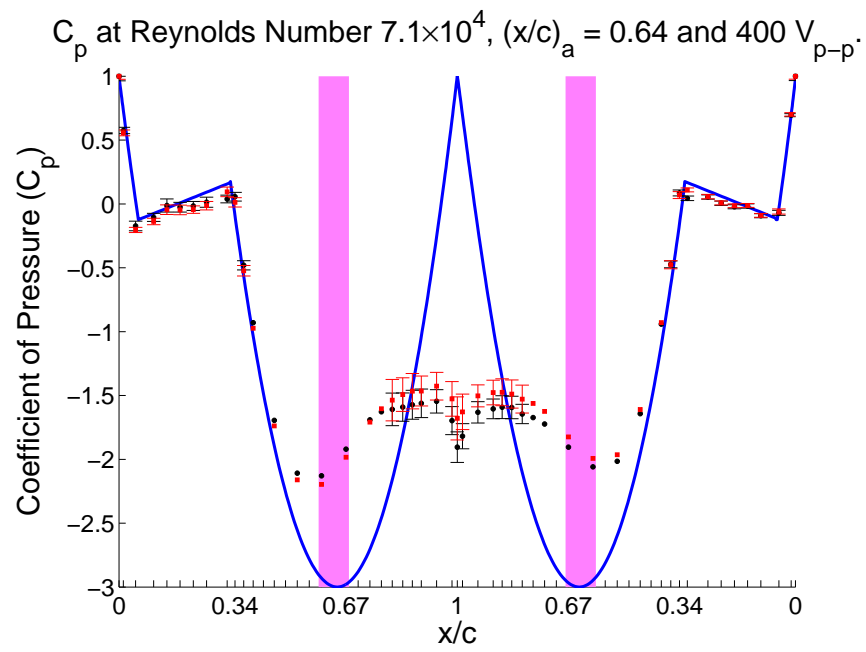
Figure A.247: Synthetic Jet Actuators on a Tail Boom Model.
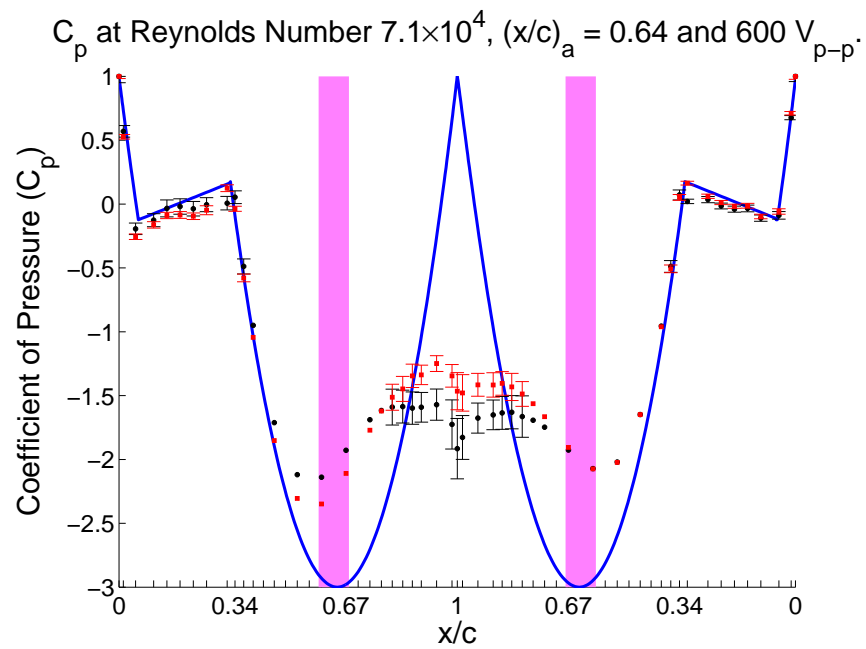
Figure A.248: Synthetic Jet Actuators on a Tail Boom Model.
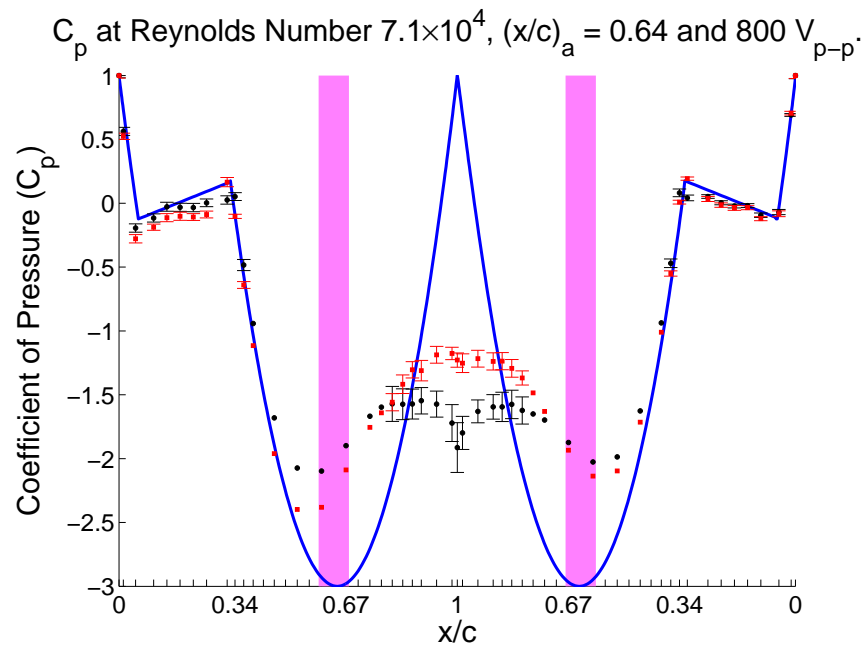
Figure A.249: Synthetic Jet Actuators on a Tail Boom Model.
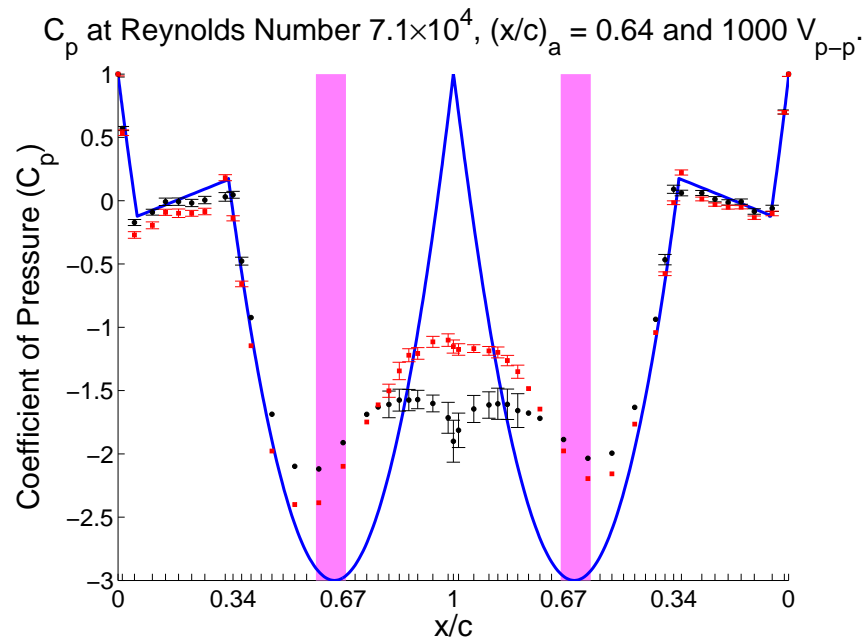
Figure A.250: Synthetic Jet Actuators on a Tail Boom Model.
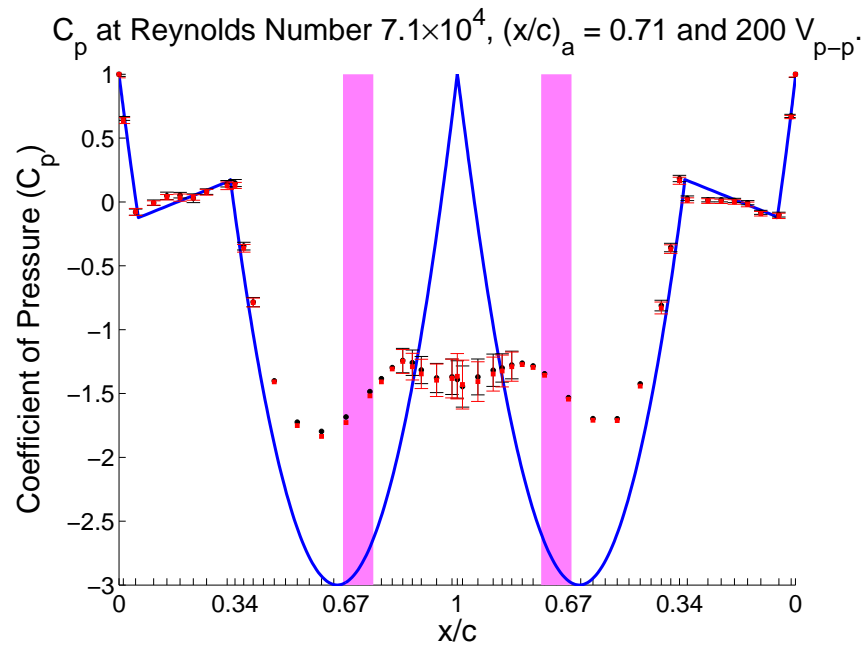
Figure A.251: Synthetic Jet Actuators on a Tail Boom Model.
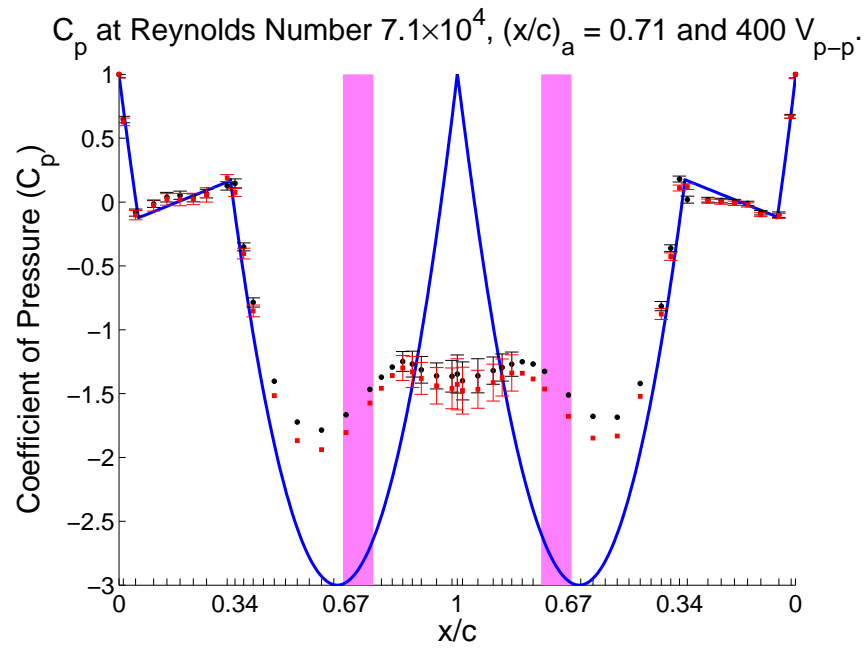
Figure A.252: Synthetic Jet Actuators on a Tail Boom Model.
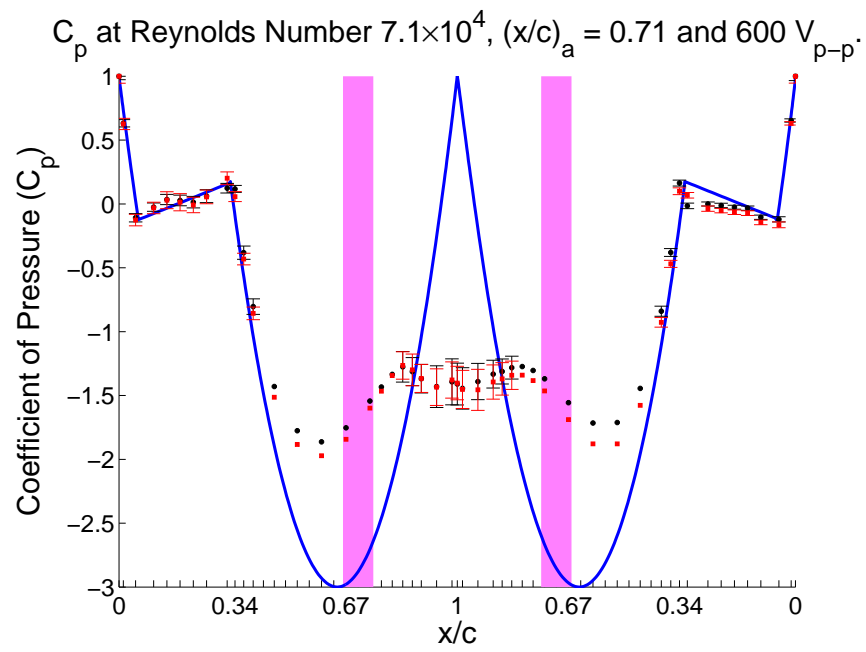
Figure A.253: Synthetic Jet Actuators on a Tail Boom Model.
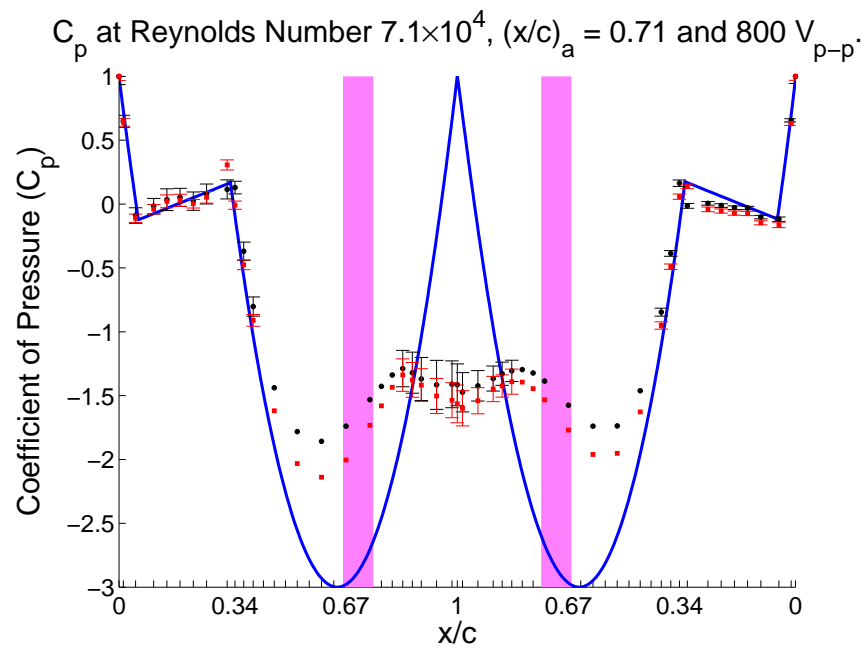
Figure A.254: Synthetic Jet Actuators on a Tail Boom Model.
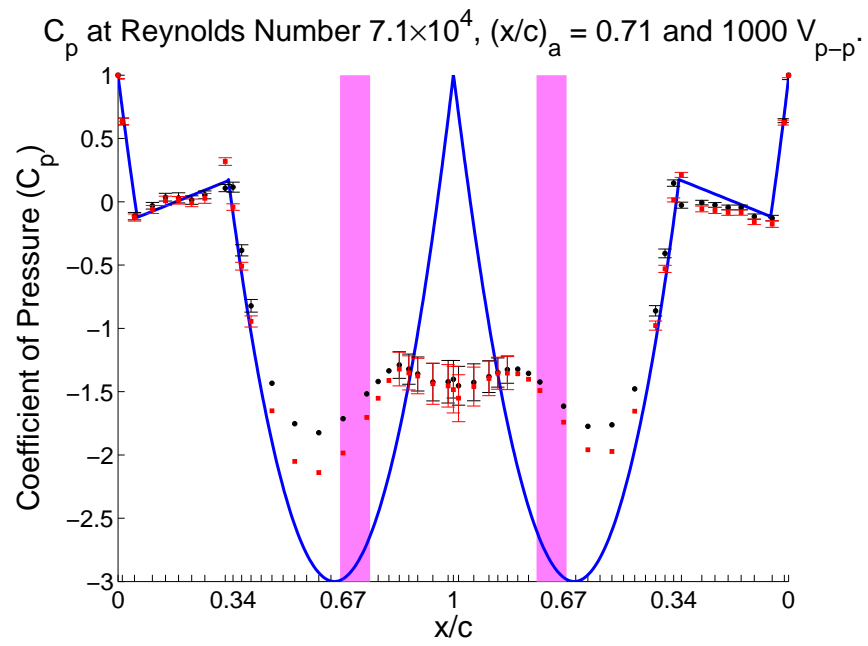
Figure A.255: Synthetic Jet Actuators on a Tail Boom Model.

Figure A.256: Plasma Actuators on a Tail Boom Model.
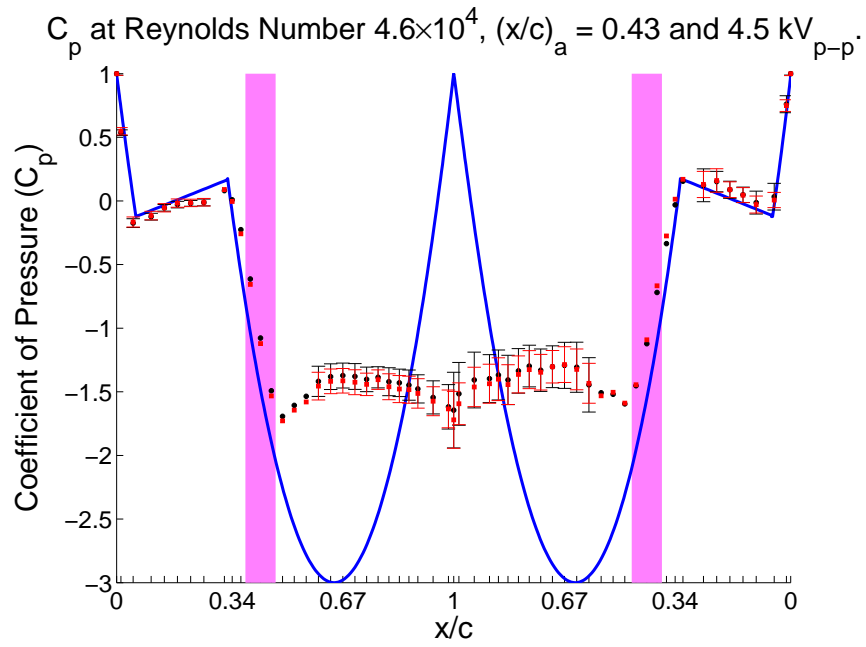
Figure A.257: Plasma Actuators on a Tail Boom Model.

Figure A.258: Plasma Actuators on a Tail Boom Model.

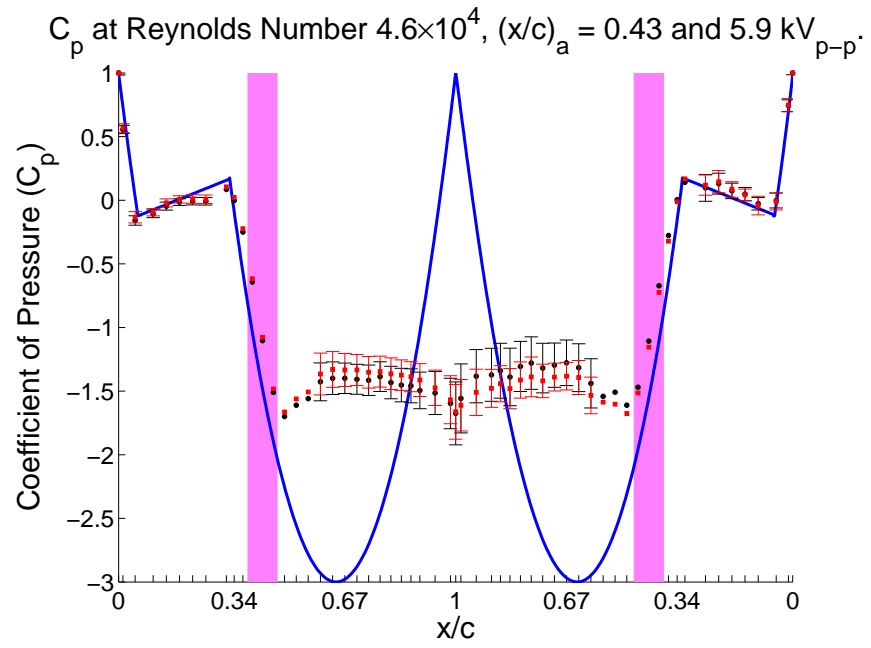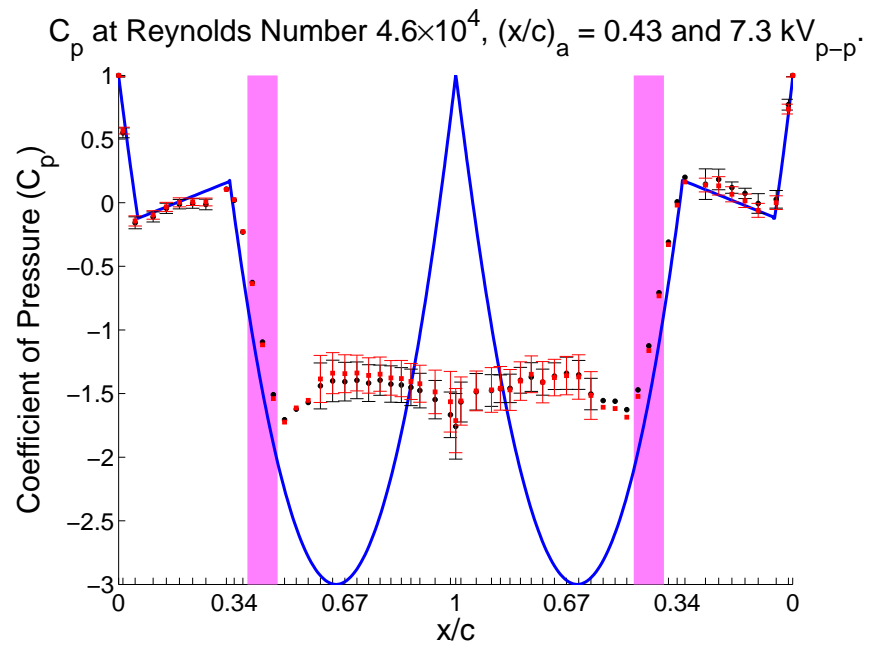**Figure A.259:** Plasma Actuators on a Tail Boom Model.

Figure A.260: Plasma Actuators on a Tail Boom Model.
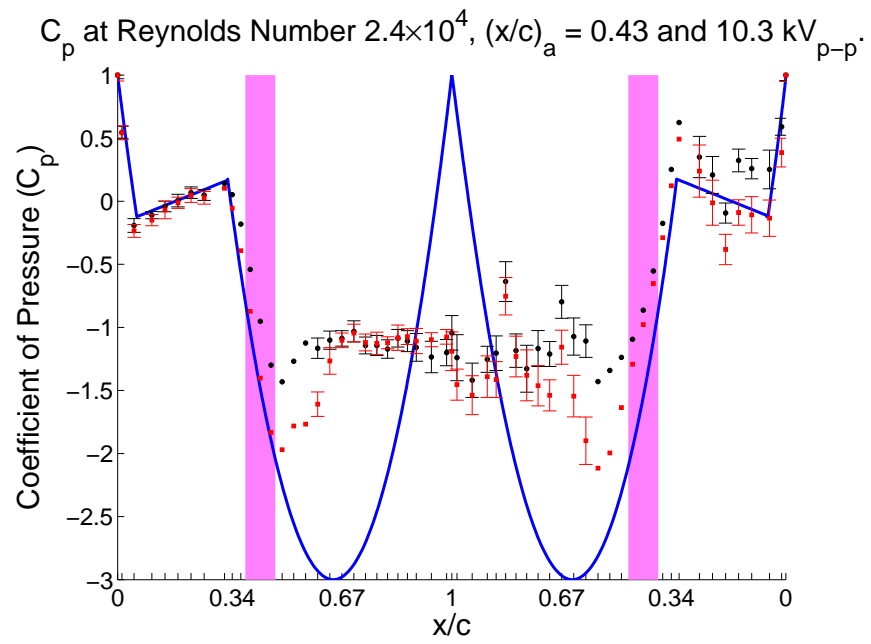
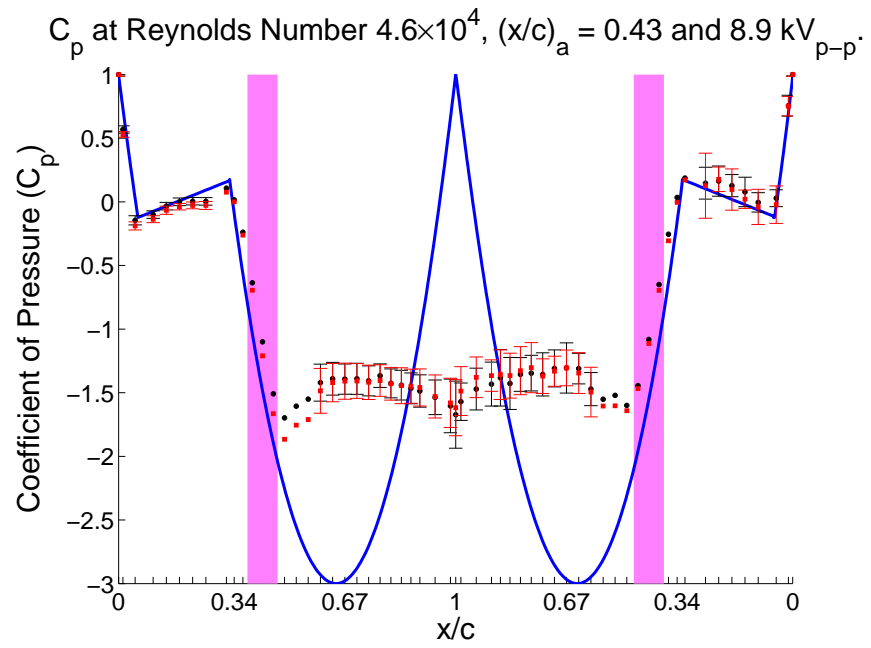**Figure A.261:** Plasma Actuators on a Tail Boom Model.
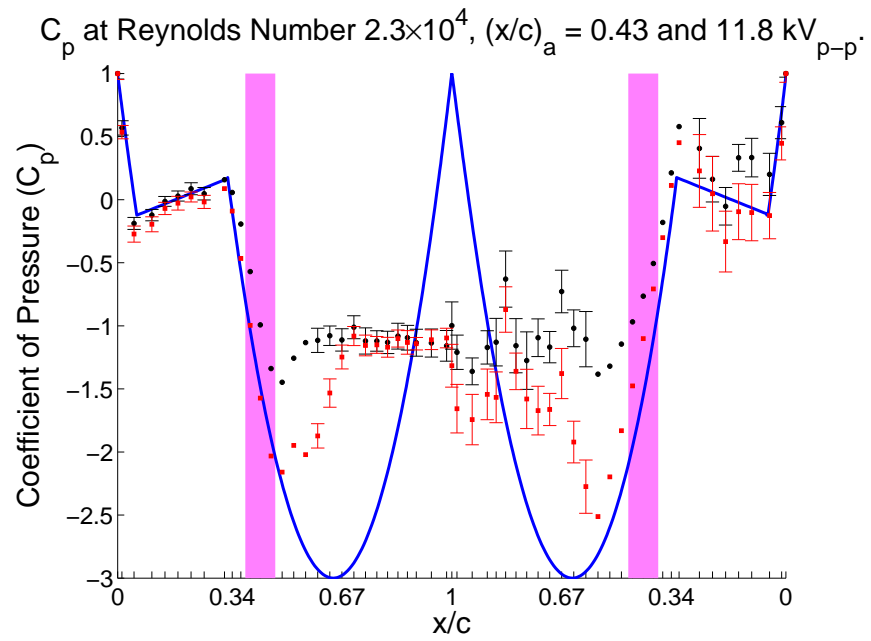
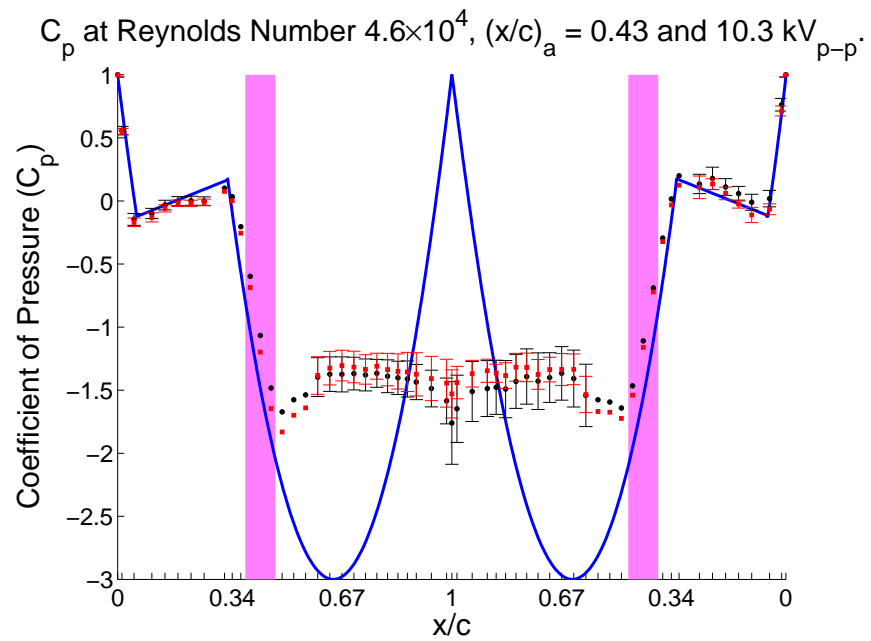**Figure A.262:** Plasma Actuators on a Tail Boom Model.
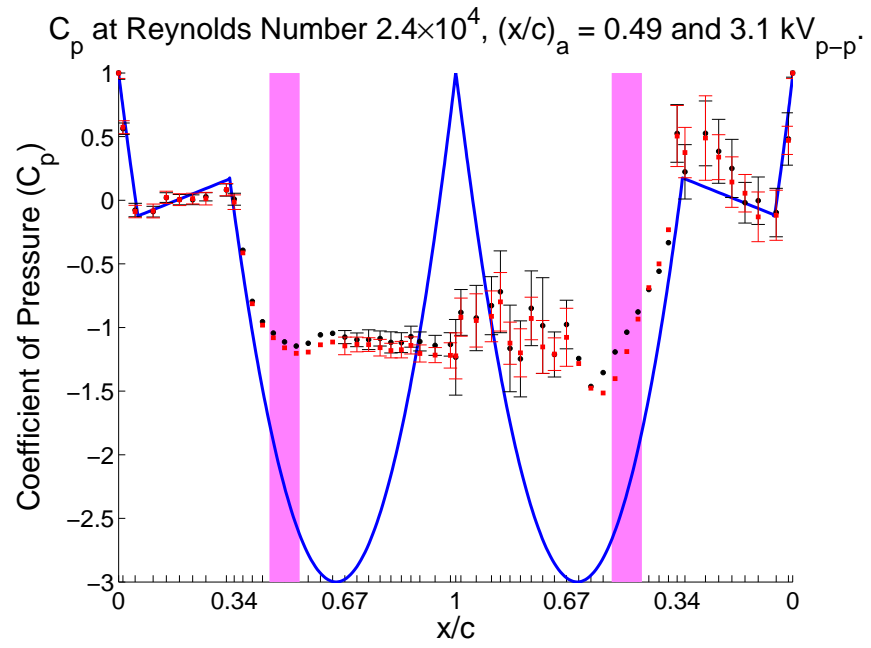
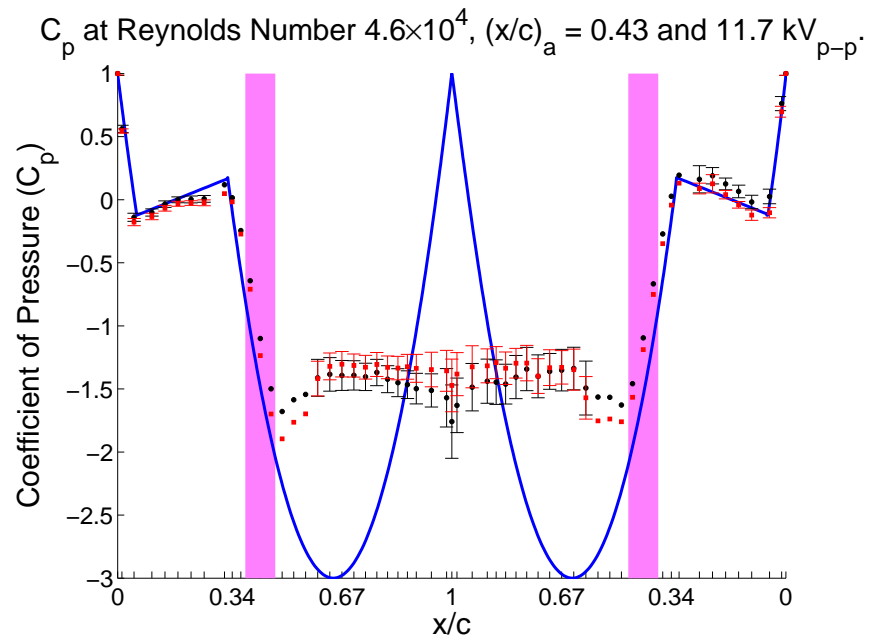**Figure A.263:** Plasma Actuators on a Tail Boom Model.
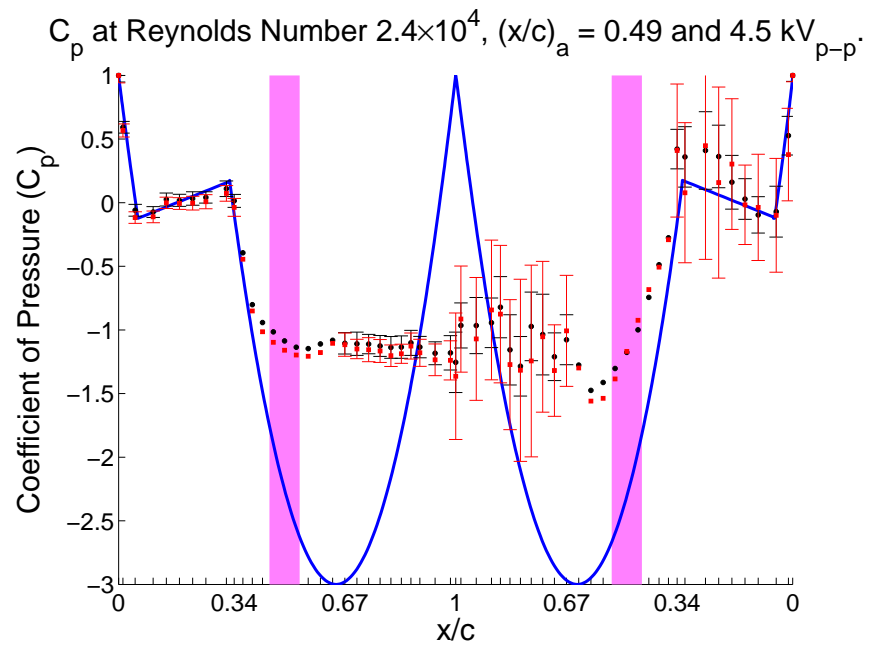
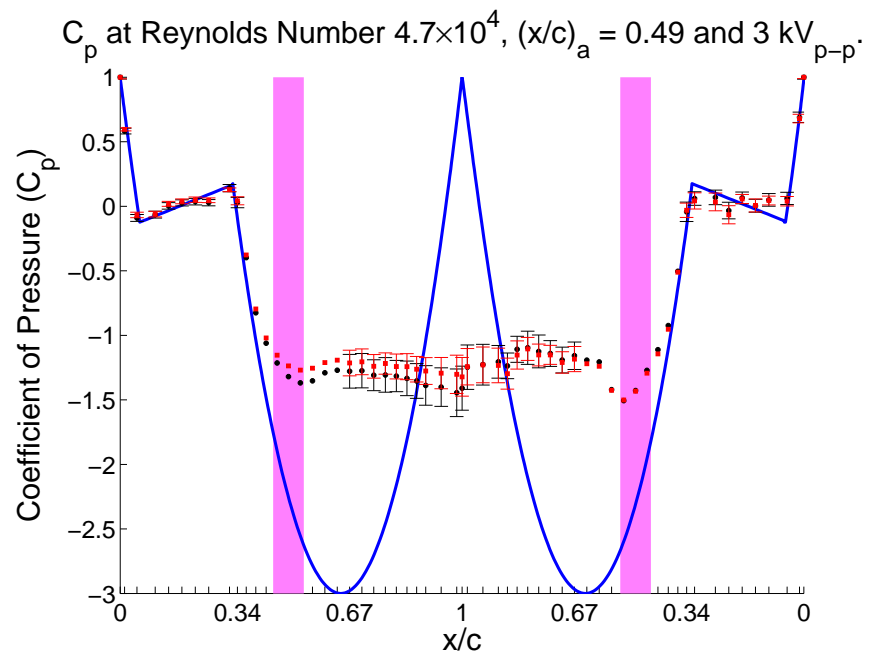**Figure A.264:** Plasma Actuators on a Tail Boom Model.
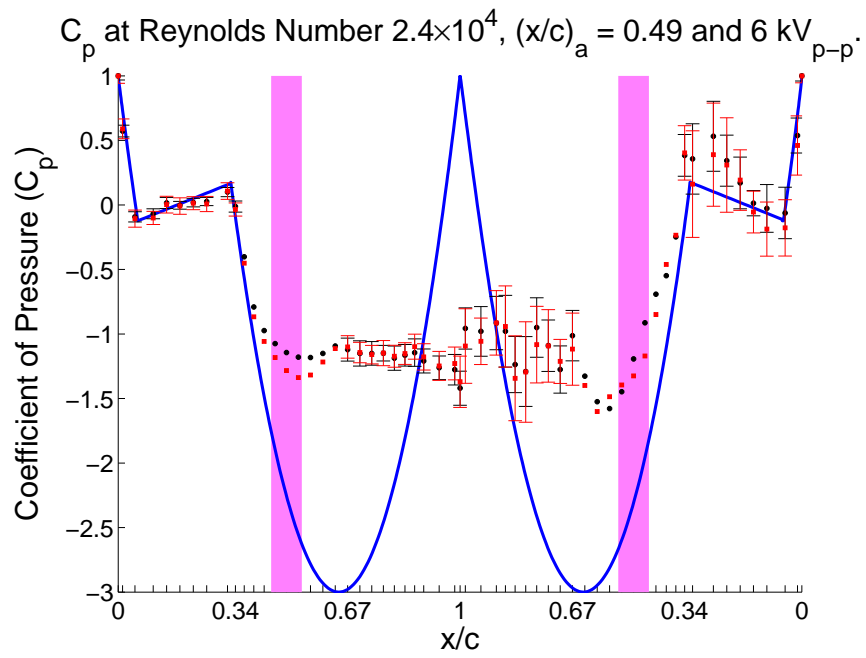
Figure A.265: Plasma Actuators on a Tail Boom Model.
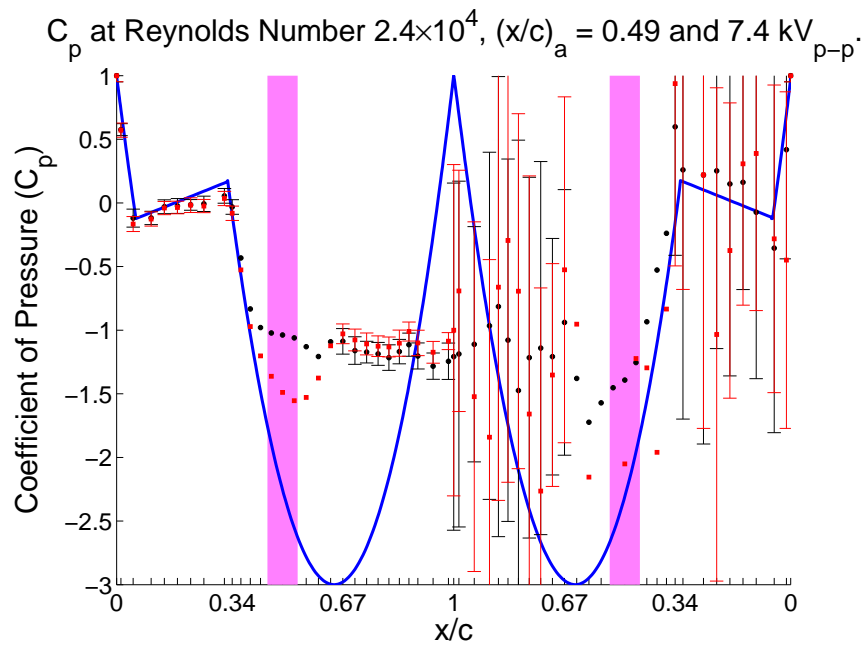
Figure A.266: Plasma Actuators on a Tail Boom Model.

283
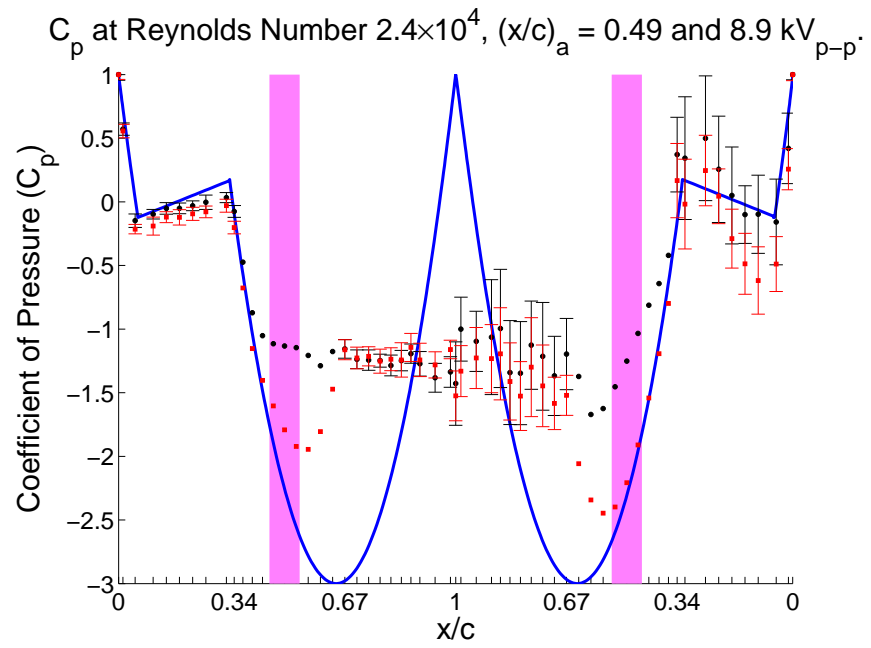
Figure A.267: Plasma Actuators on a Tail Boom Model.
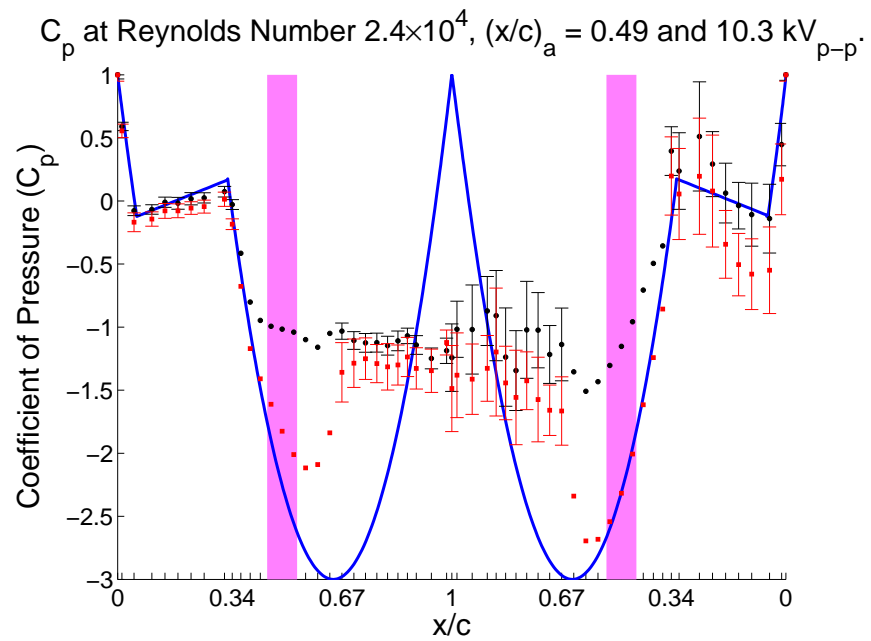
Figure A.268: Plasma Actuators on a Tail Boom Model.
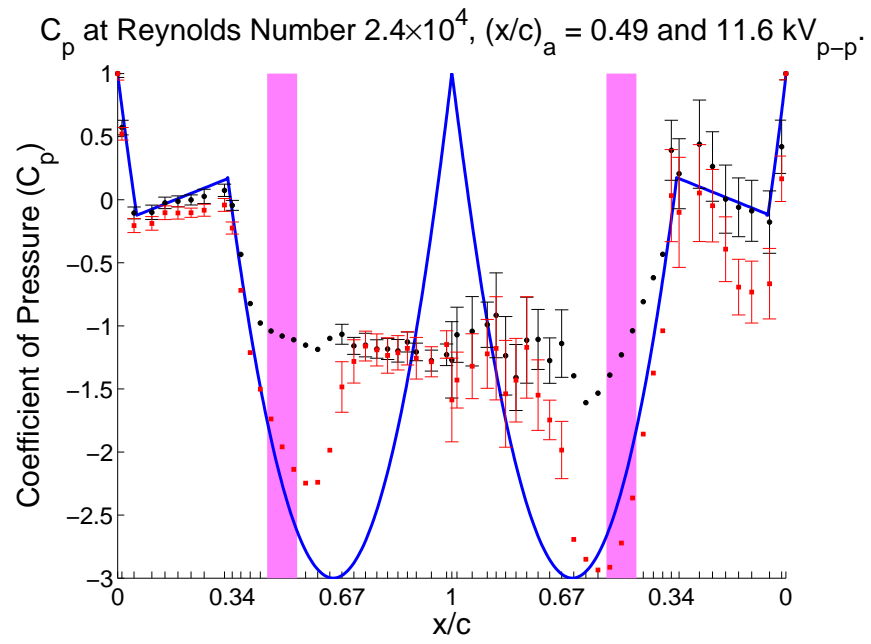
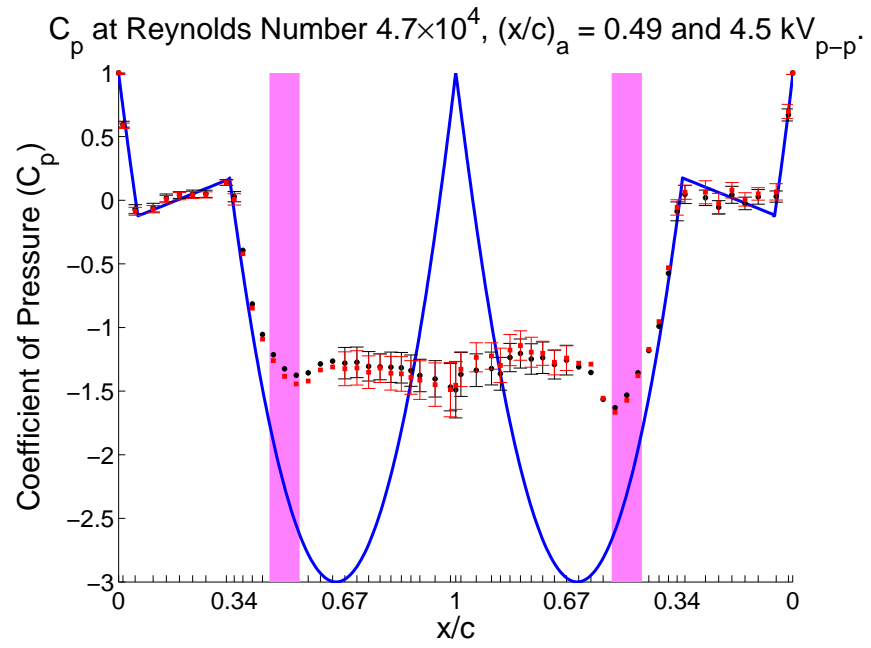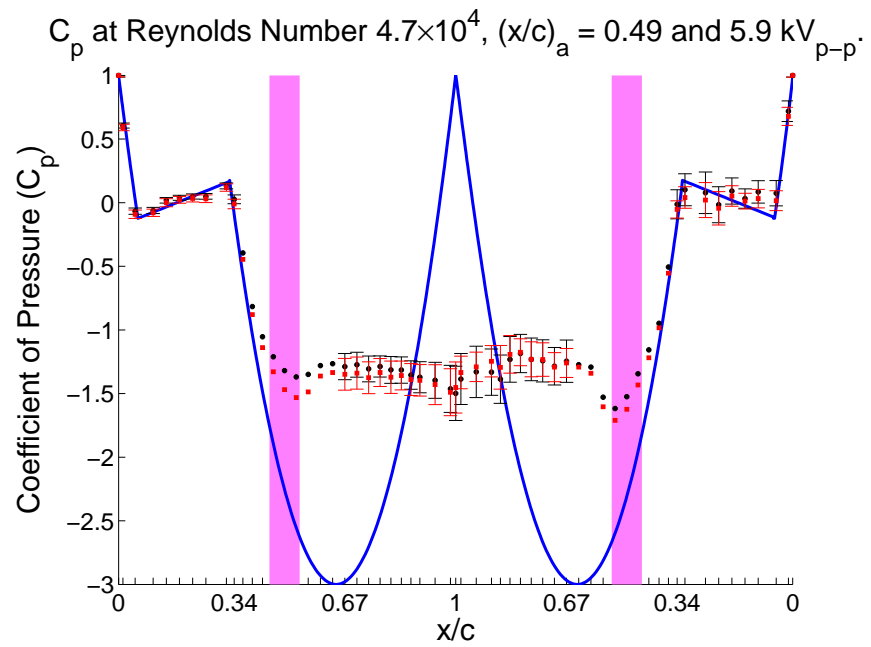**Figure A.269:** Plasma Actuators on a Tail Boom Model.
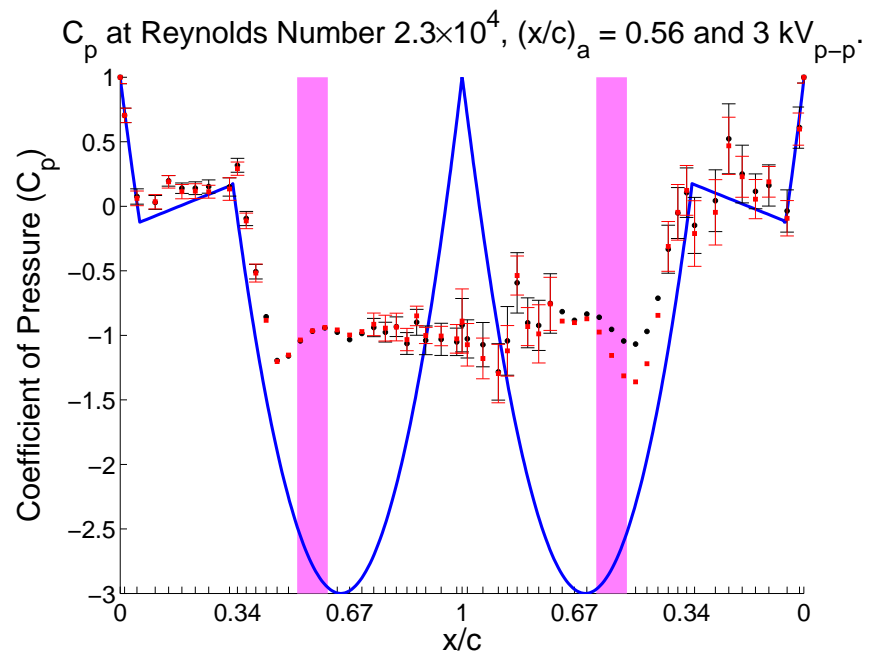
Figure A.270: Plasma Actuators on a Tail Boom Model.
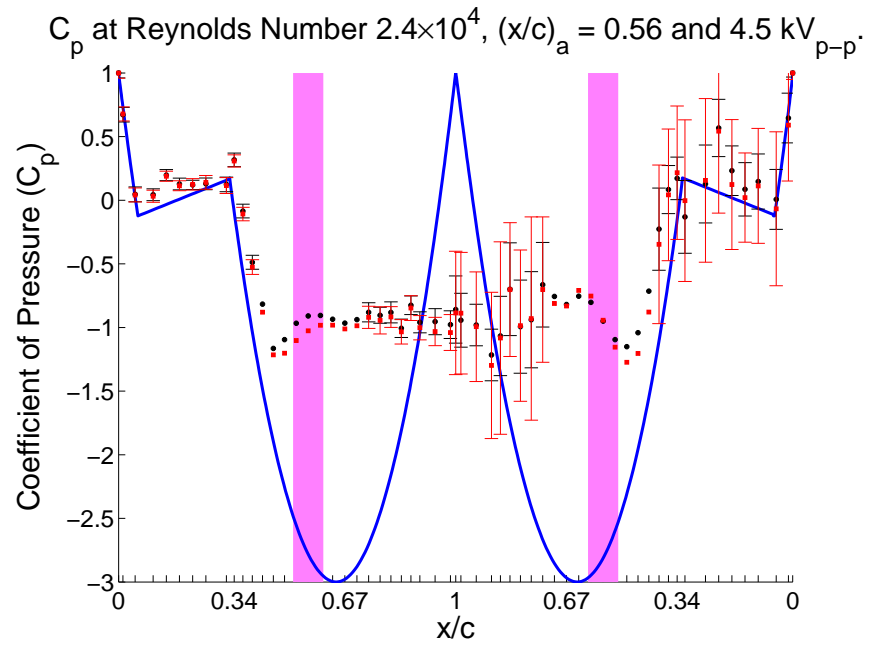
Figure A.271: Plasma Actuators on a Tail Boom Model.
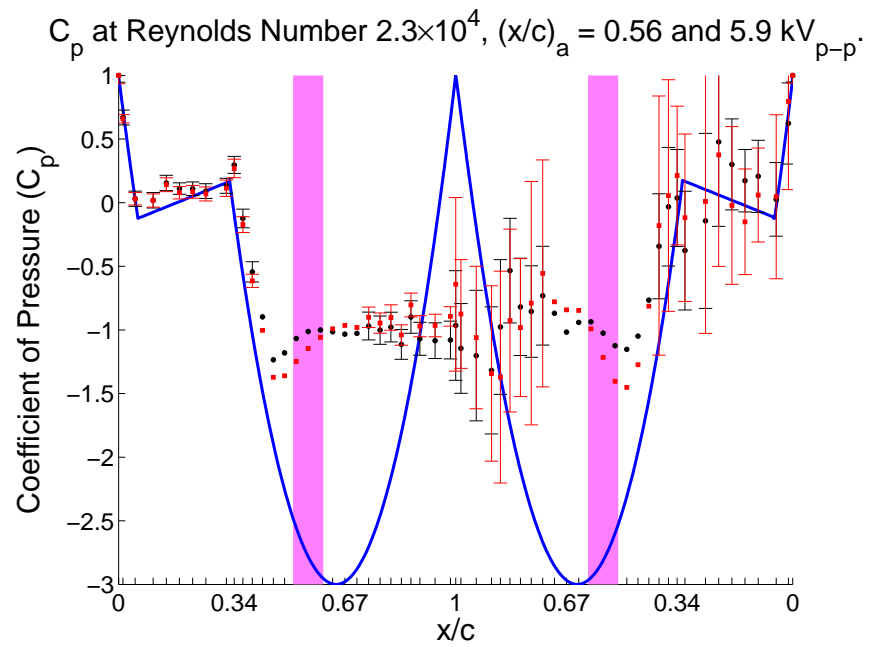
Figure A.272: Plasma Actuators on a Tail Boom Model.
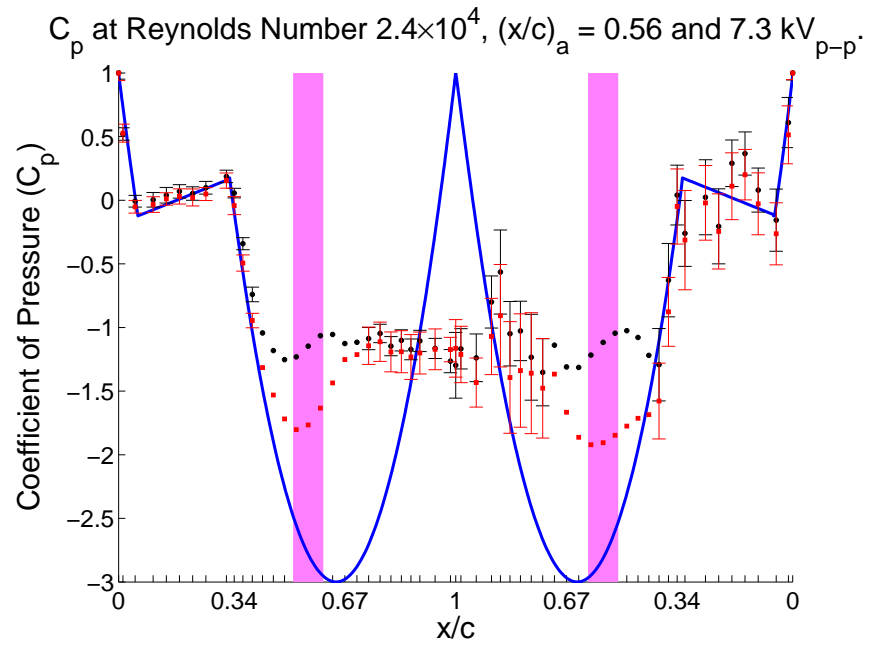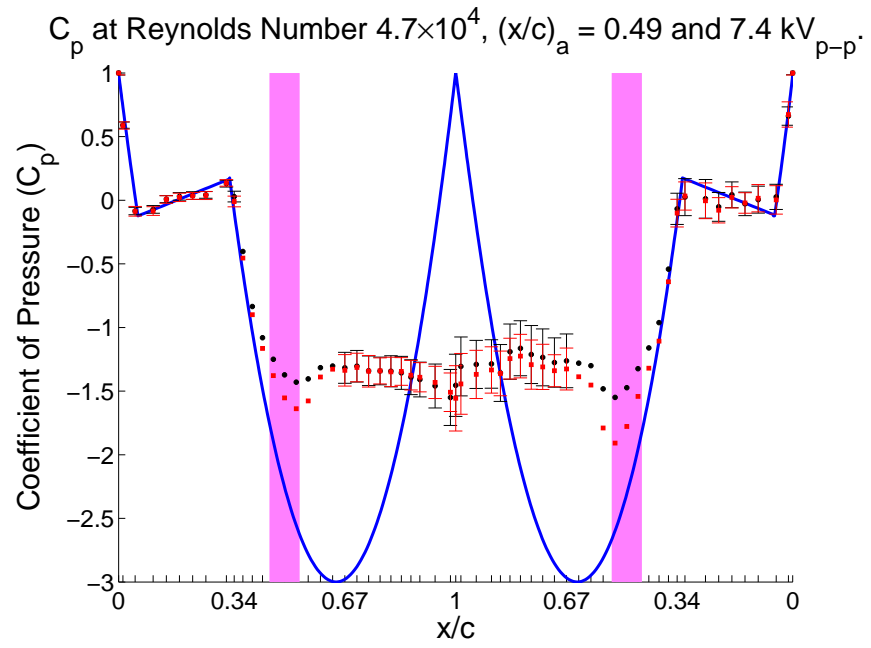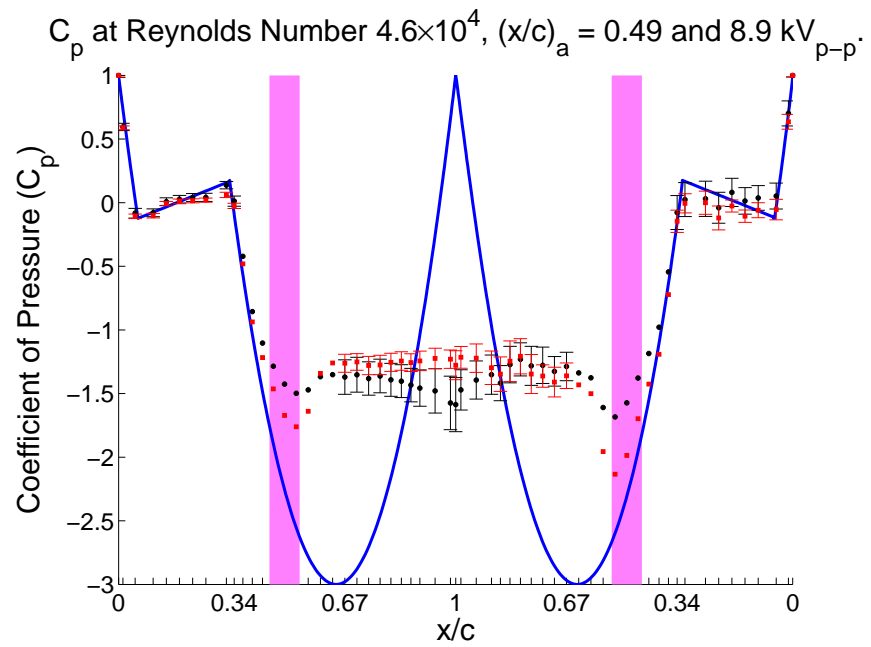
Figure A.273: Plasma Actuators on a Tail Boom Model.
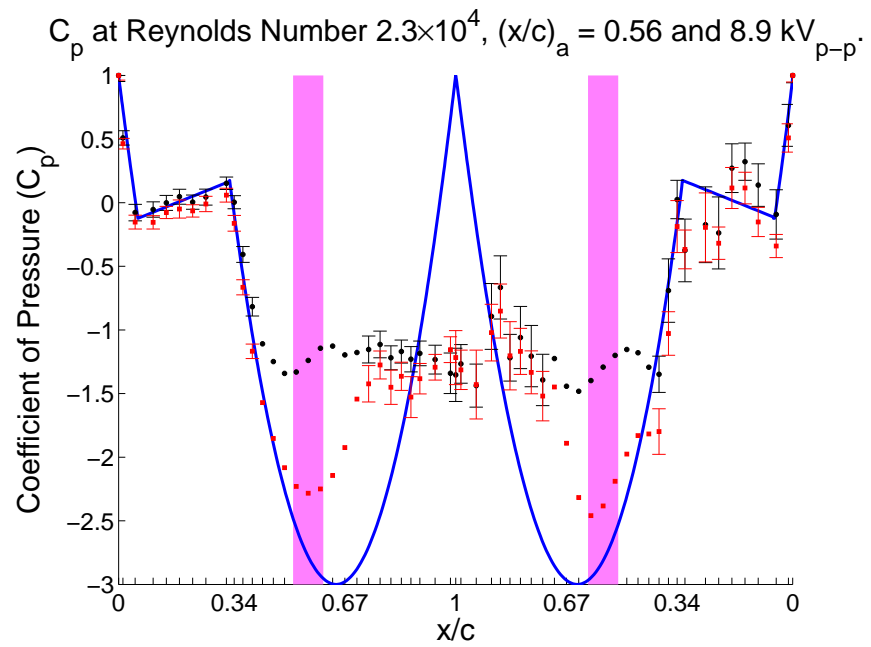
Figure A.274: Plasma Actuators on a Tail Boom Model.
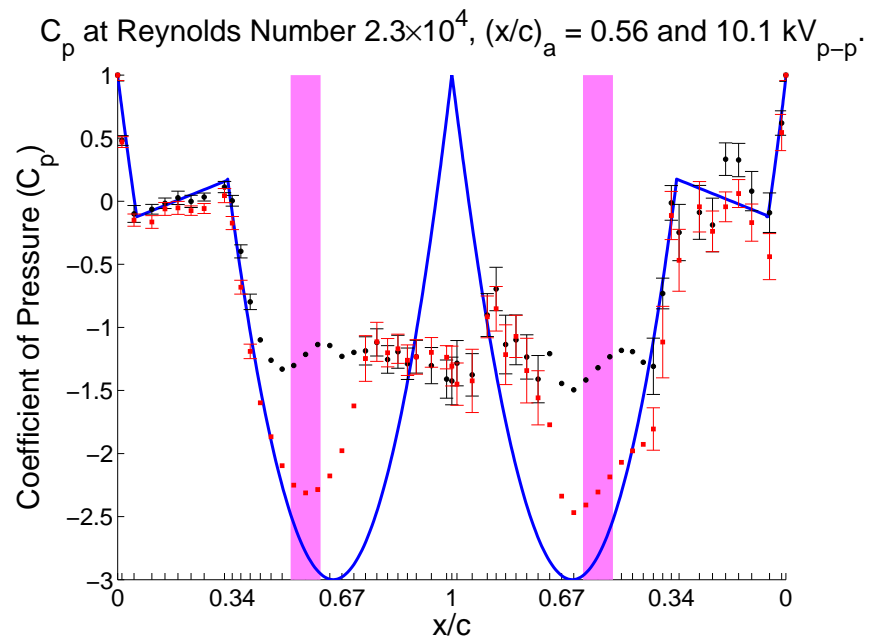
Figure A.275: Plasma Actuators on a Tail Boom Model.
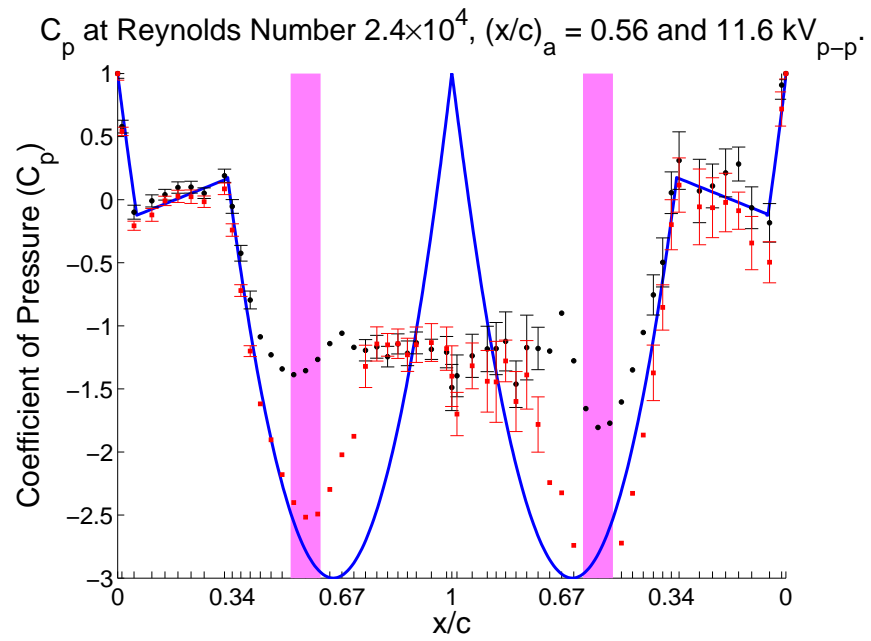
Figure A.276: Plasma Actuators on a Tail Boom Model.
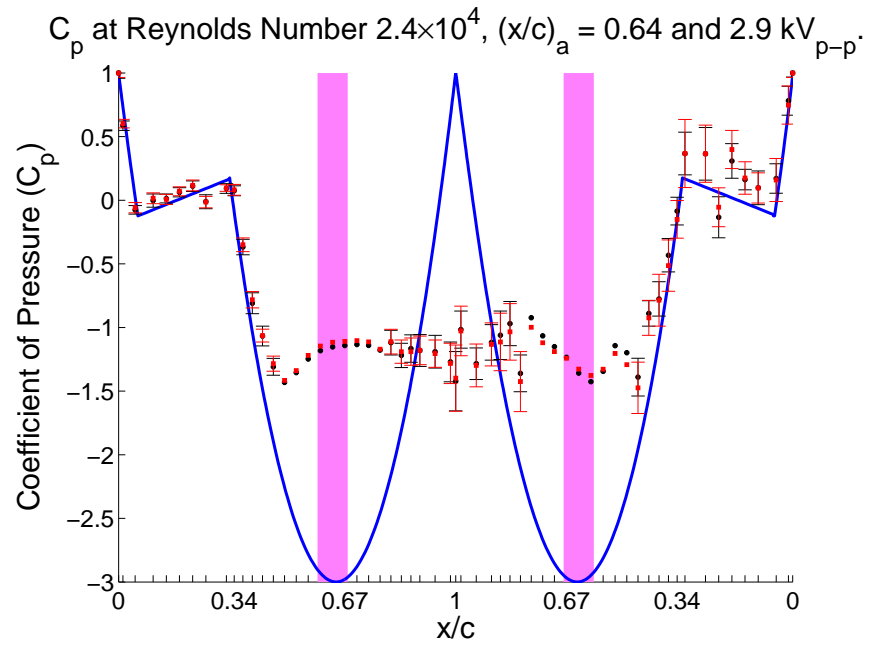
Figure A.277: Plasma Actuators on a Tail Boom Model.
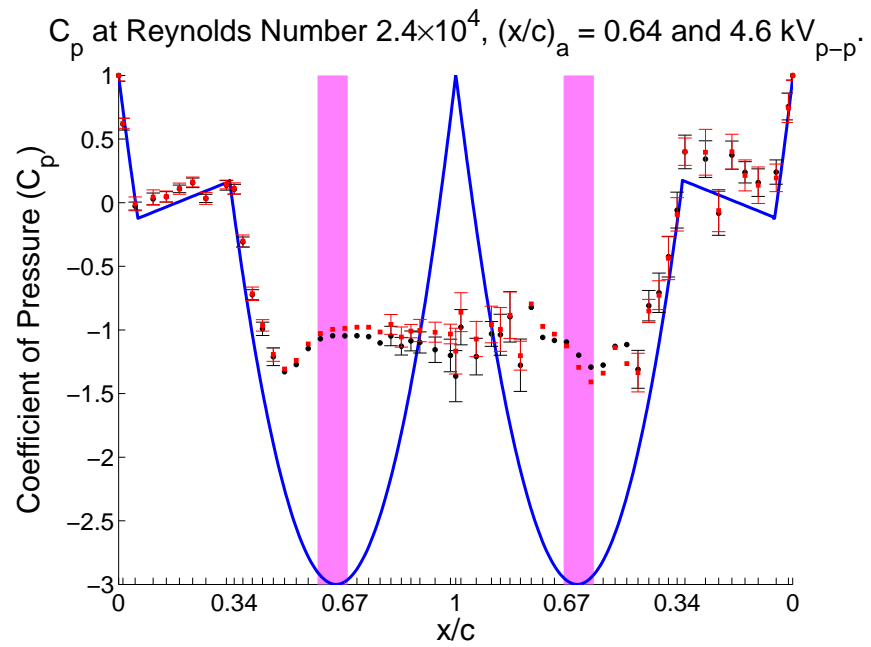
Figure A.278: Plasma Actuators on a Tail Boom Model.
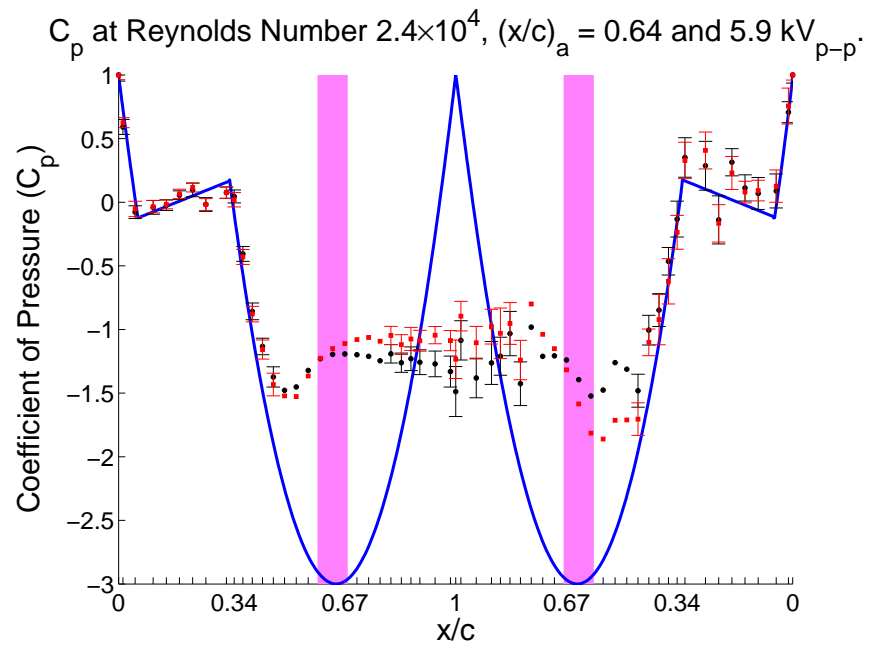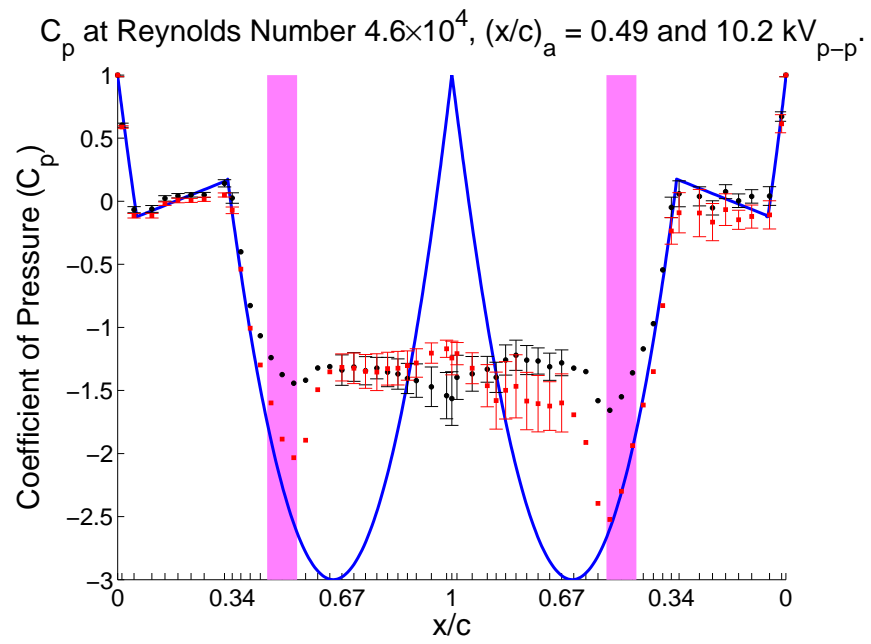
Figure A.279: Plasma Actuators on a Tail Boom Model.
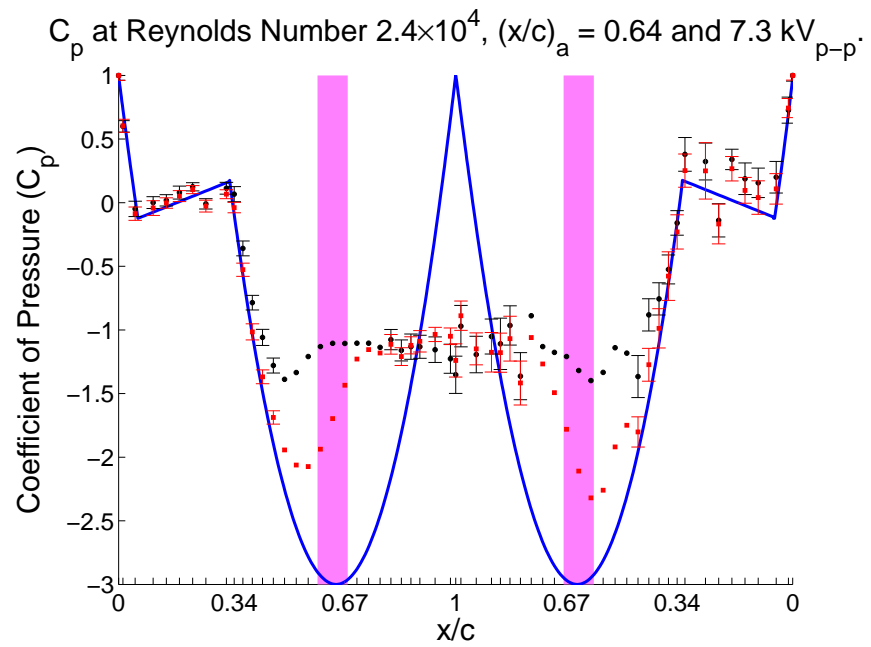
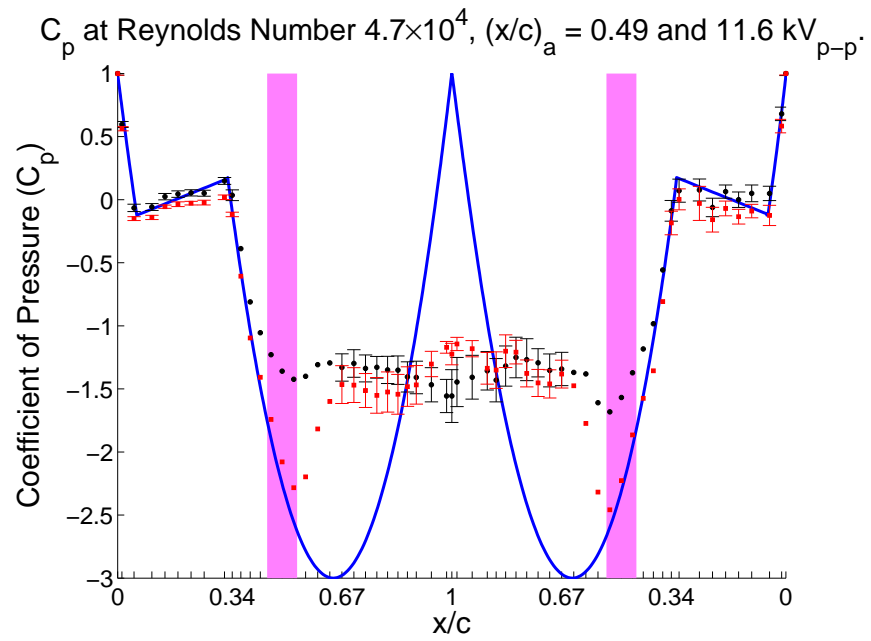**Figure A.280:** Plasma Actuators on a Tail Boom Model.
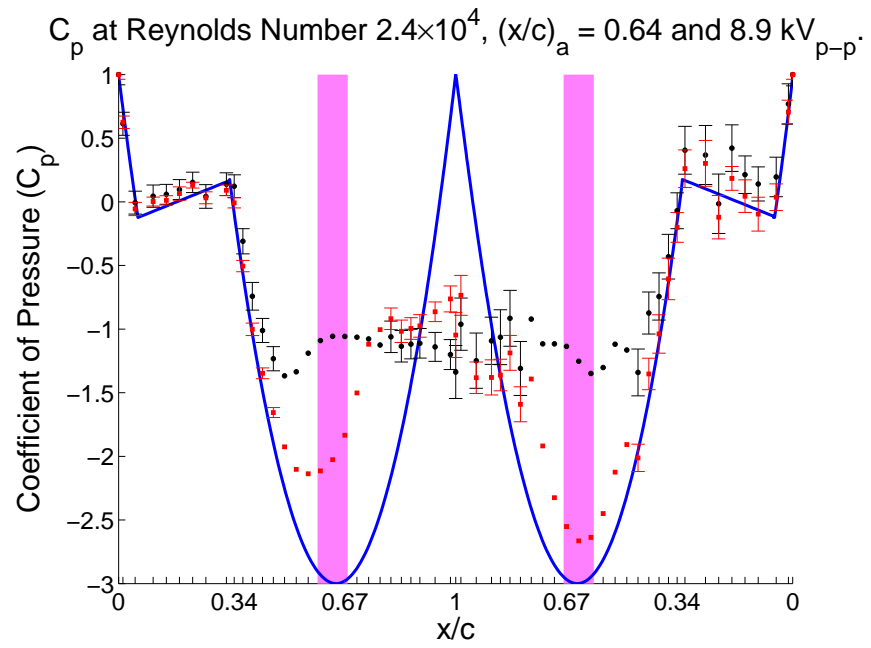
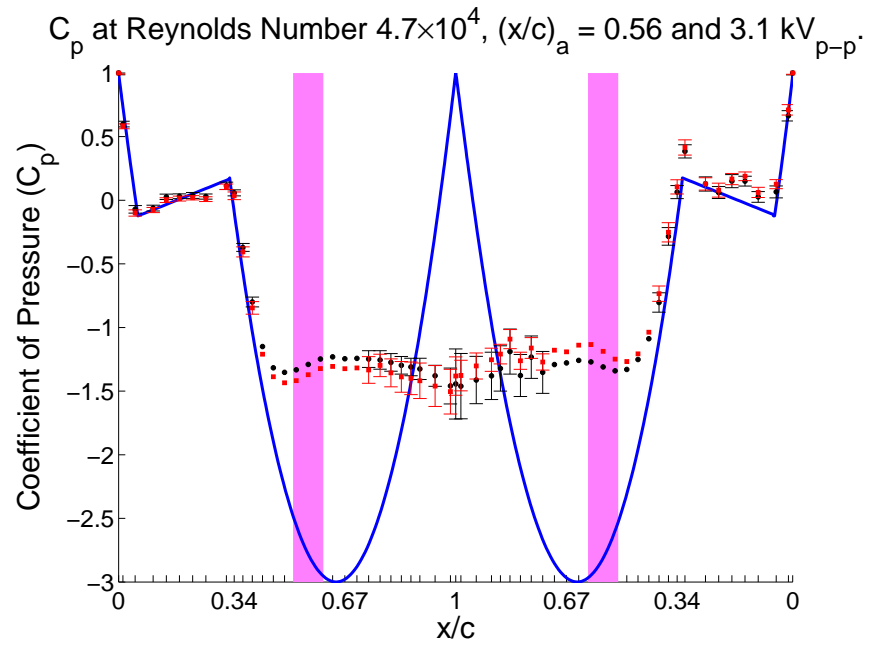**Figure A.281:** Plasma Actuators on a Tail Boom Model.
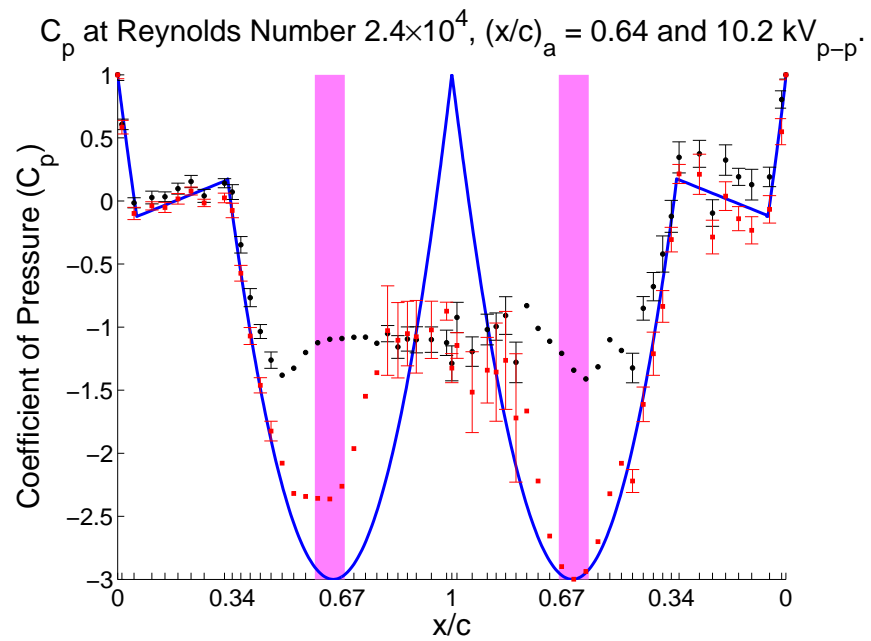
Figure A.282: Plasma Actuators on a Tail Boom Model.
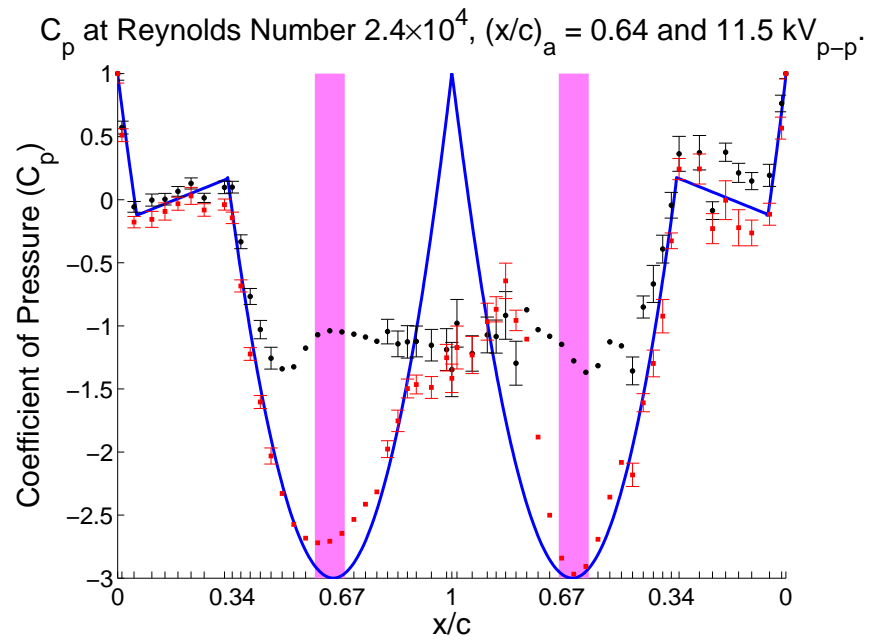
Figure A.283: Plasma Actuators on a Tail Boom Model.
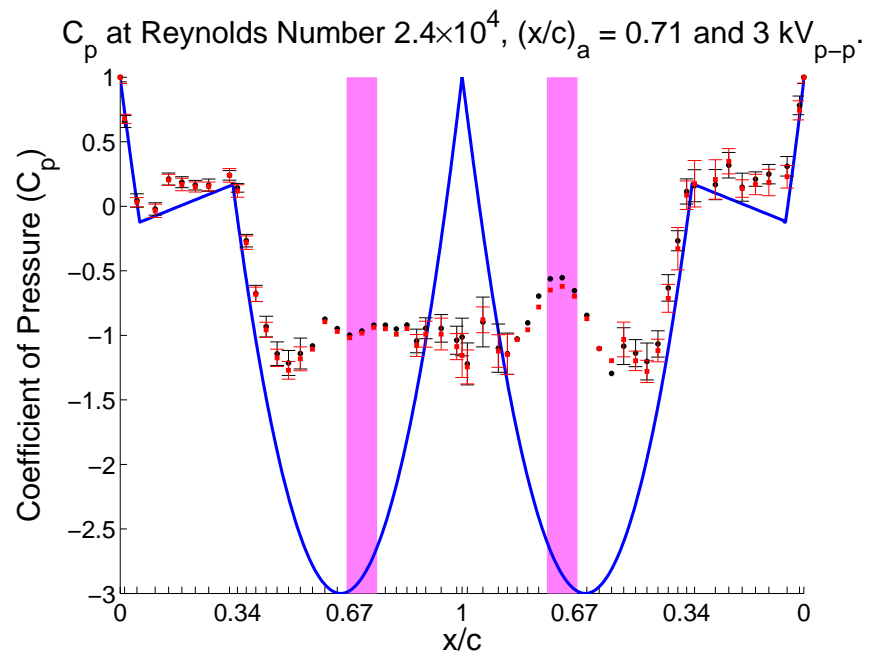
Figure A.284: Plasma Actuators on a Tail Boom Model.
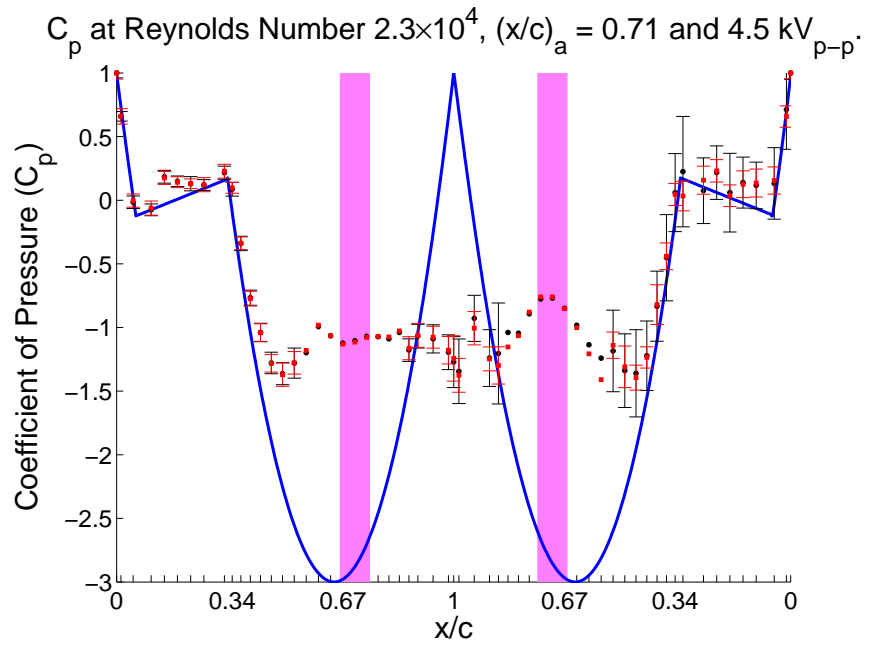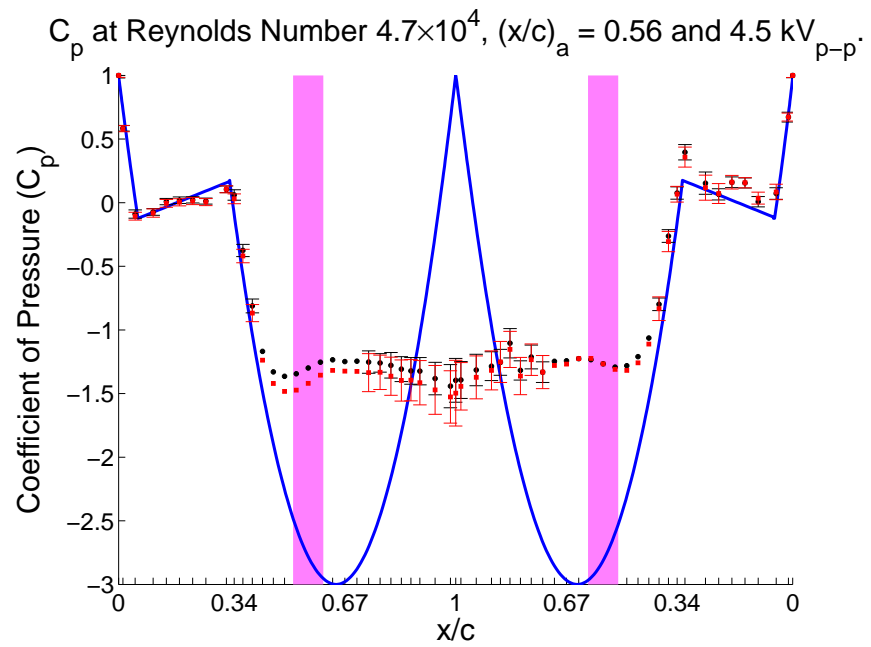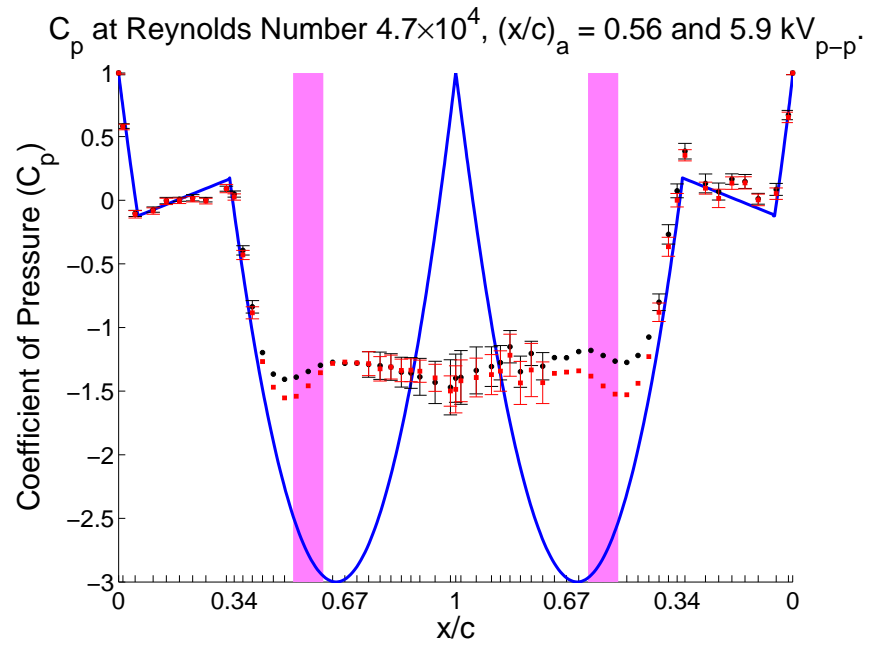
Figure A.285: Plasma Actuators on a Tail Boom Model.
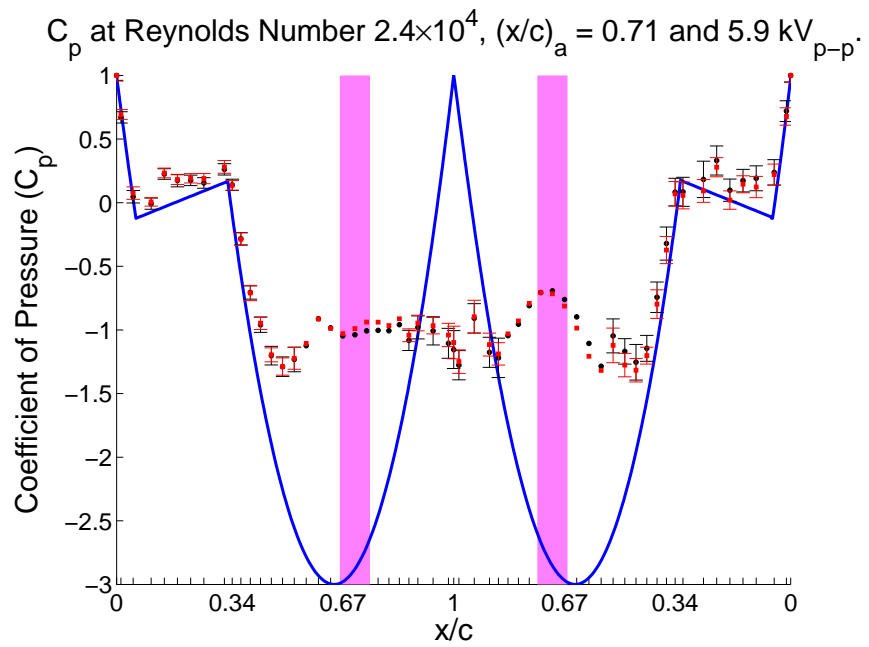
Figure A.286: Plasma Actuators on a Tail Boom Model.
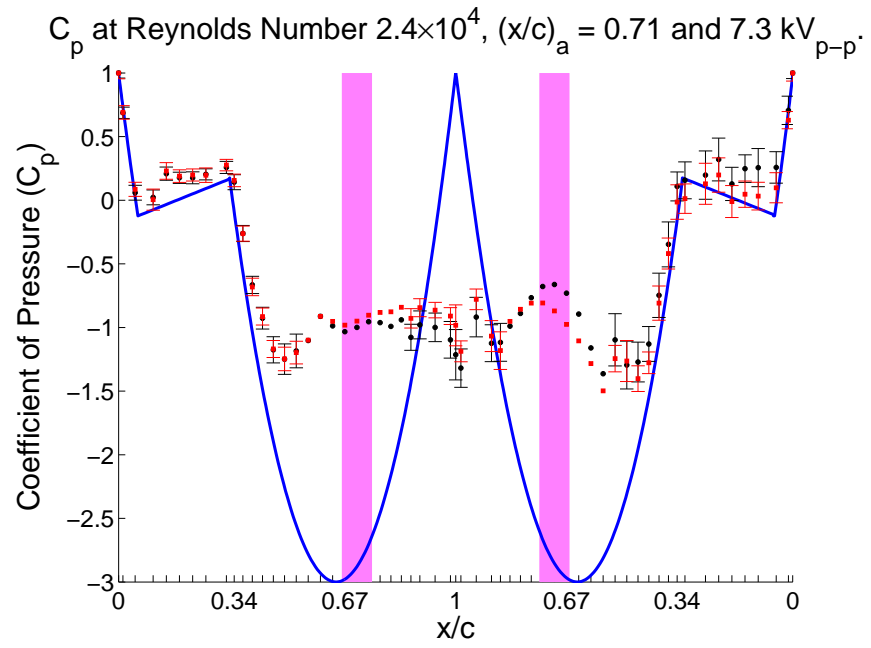
Figure A.287: Plasma Actuators on a Tail Boom Model.
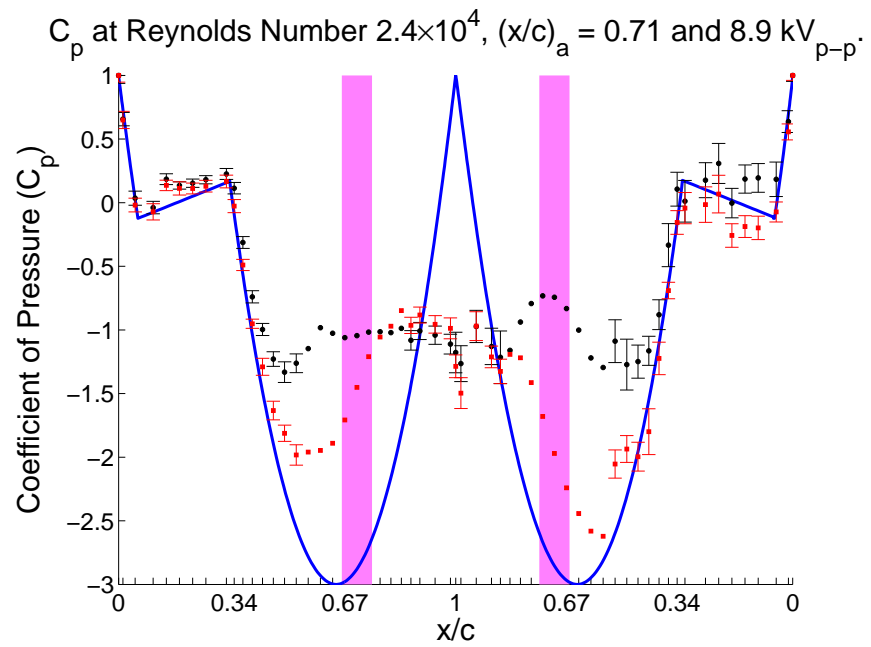
Figure A.288: Plasma Actuators on a Tail Boom Model.
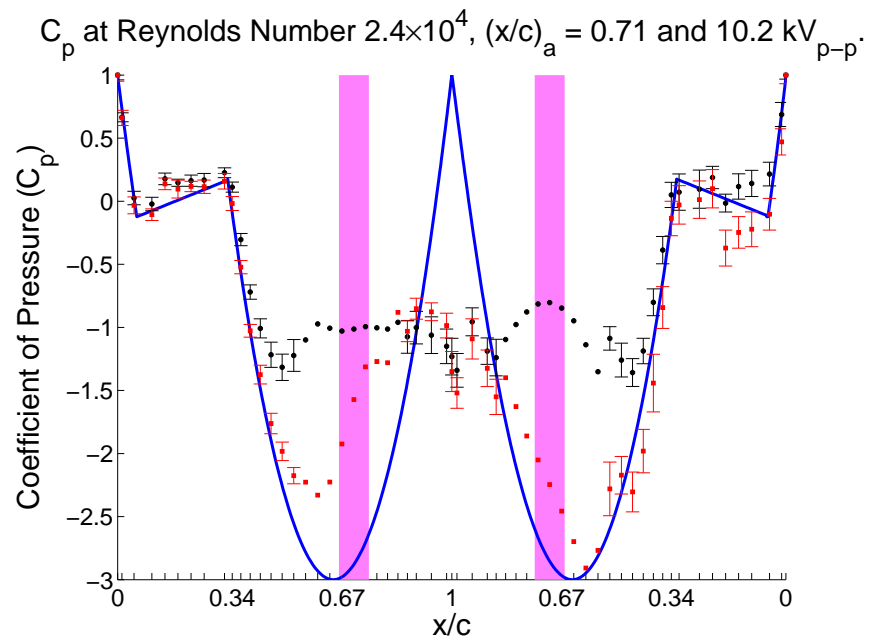
Figure A.289: Plasma Actuators on a Tail Boom Model.
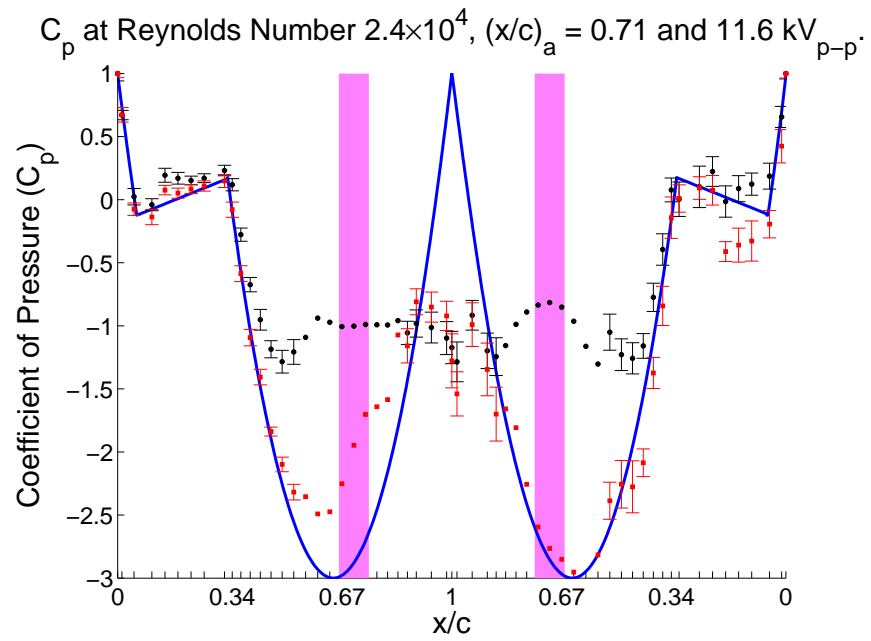
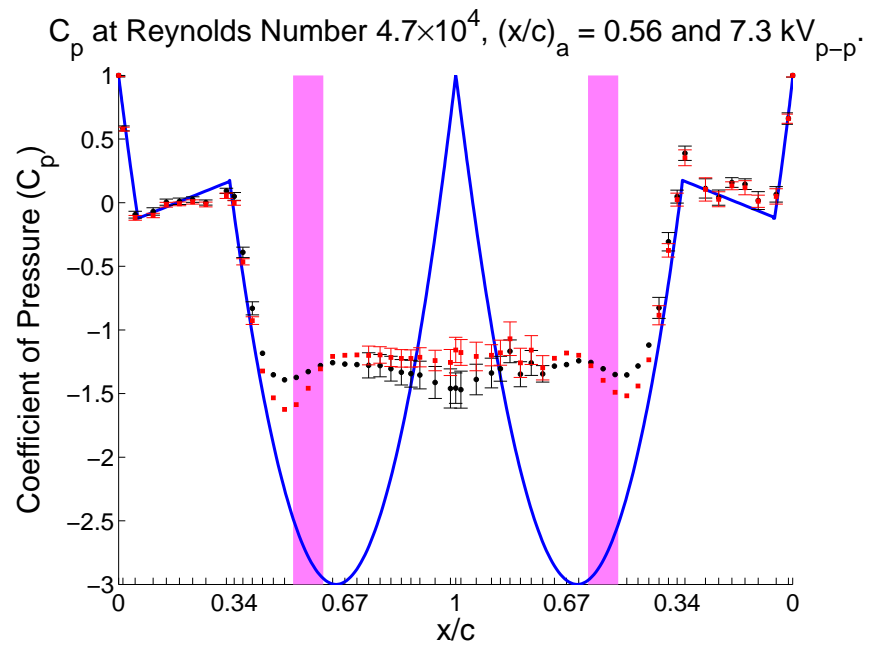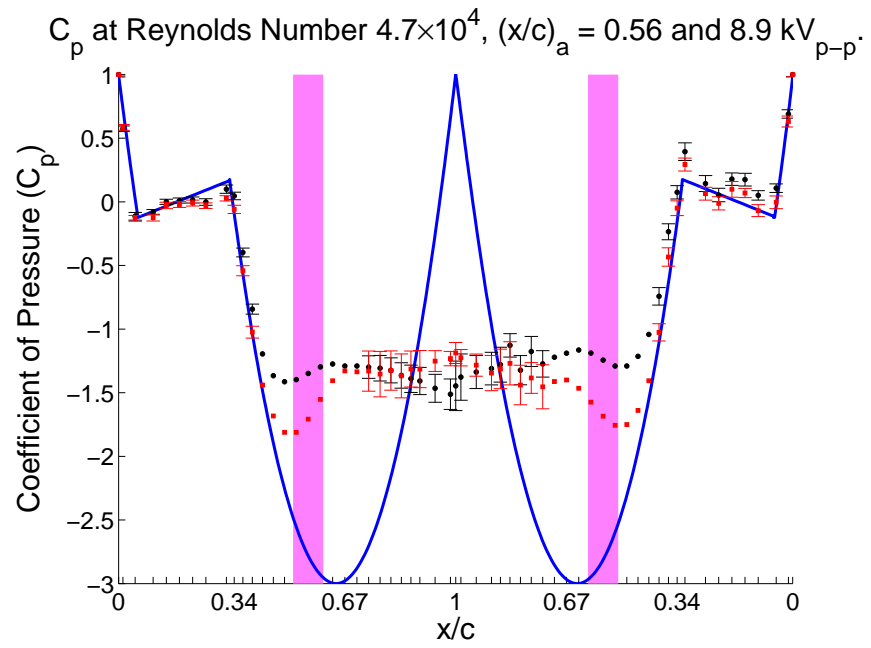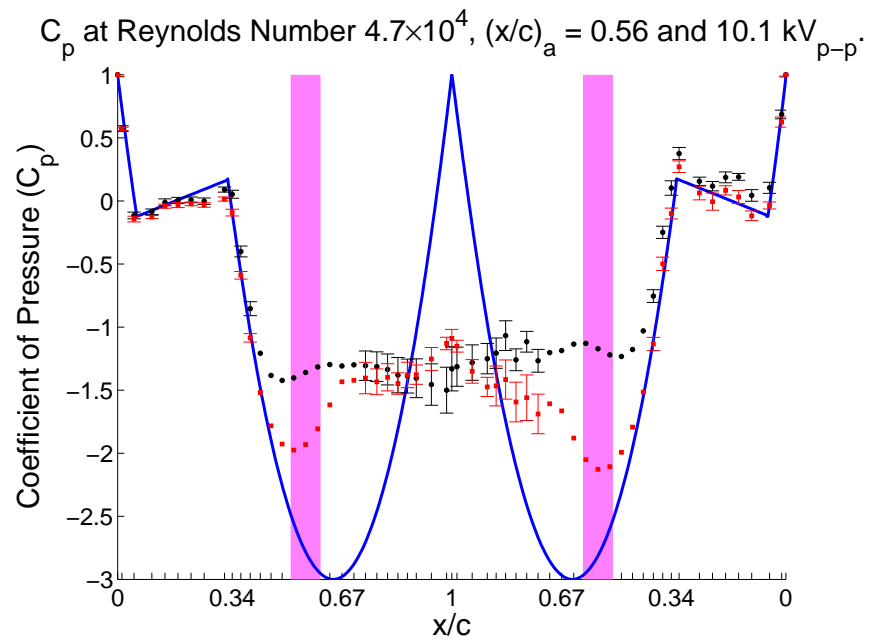**Figure A.290:** Plasma Actuators on a Tail Boom Model.
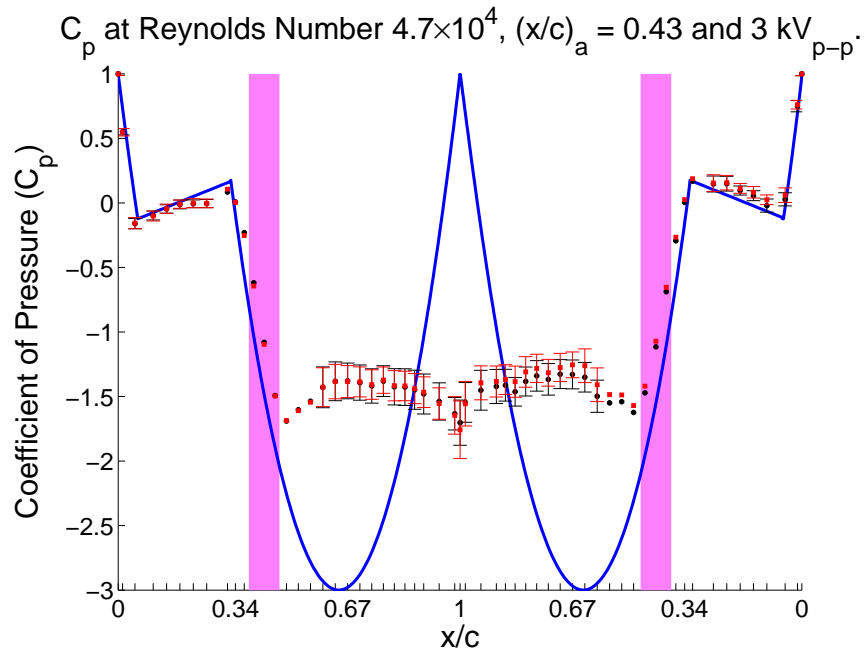
Figure A.291: Plasma Actuators on a Tail Boom Model.

Figure A.292: Plasma Actuators on a Tail Boom Model.

Figure A.293: Plasma Actuators on a Tail Boom Model.

Figure A.294: Plasma Actuators on a Tail Boom Model.

Figure A.295: Plasma Actuators on a Tail Boom Model.

Figure A.296: Plasma Actuators on a Tail Boom Model.
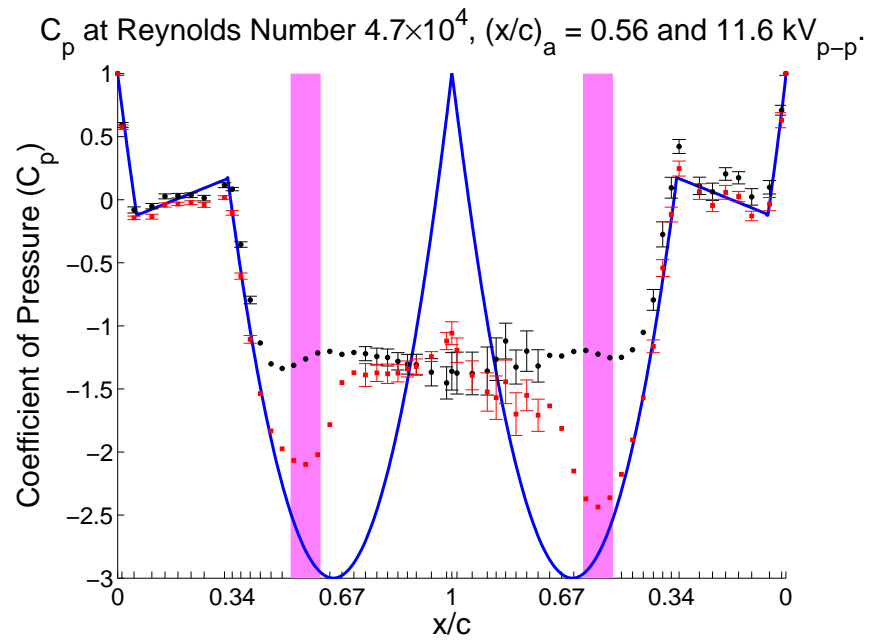
Figure A.297: Plasma Actuators on a Tail Boom Model.

Figure A.298: Plasma Actuators on a Tail Boom Model.

Figure A.299: Plasma Actuators on a Tail Boom Model.

Figure A.300: Plasma Actuators on a Tail Boom Model.
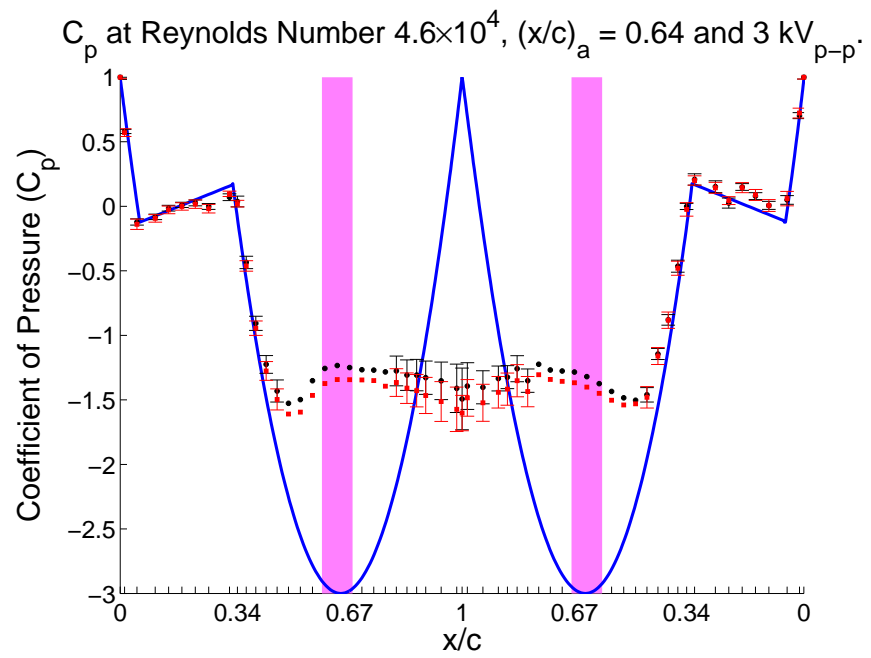
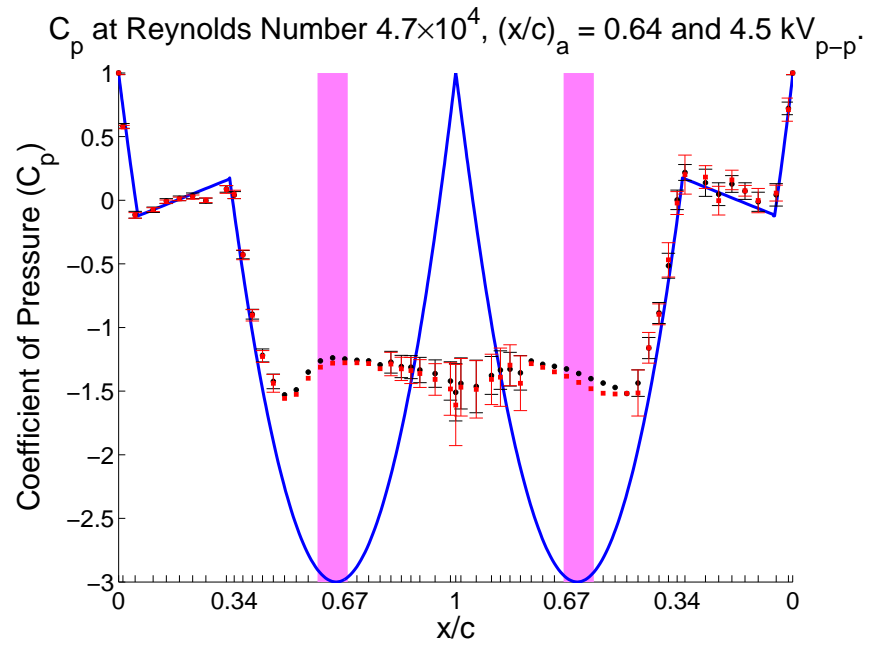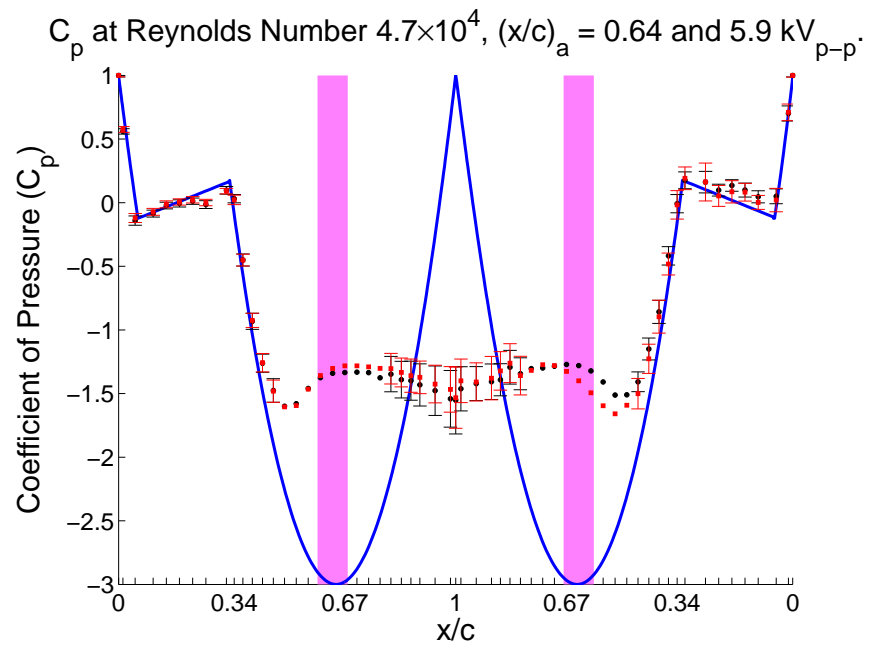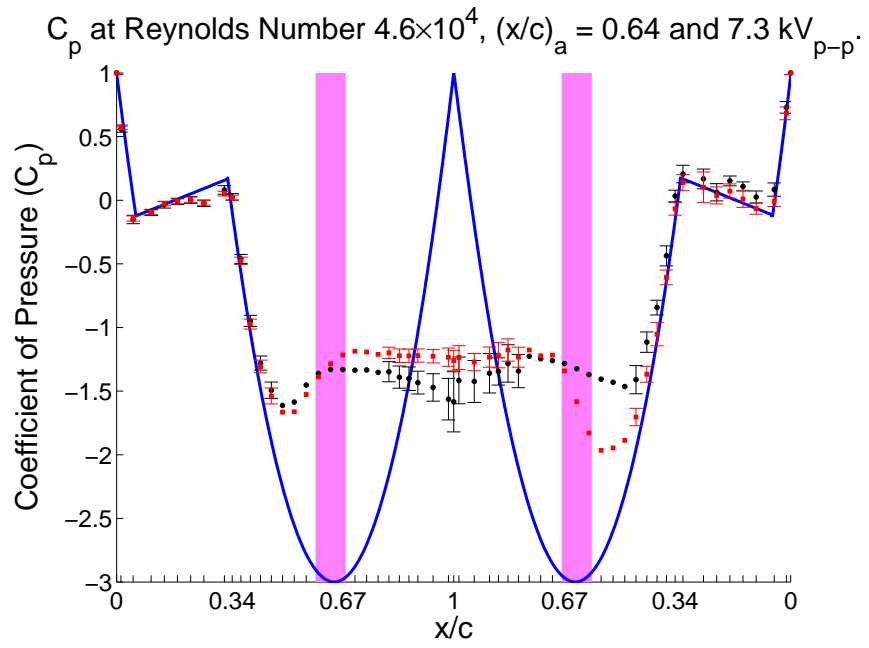**Figure A.301:** Plasma Actuators on a Tail Boom Model.

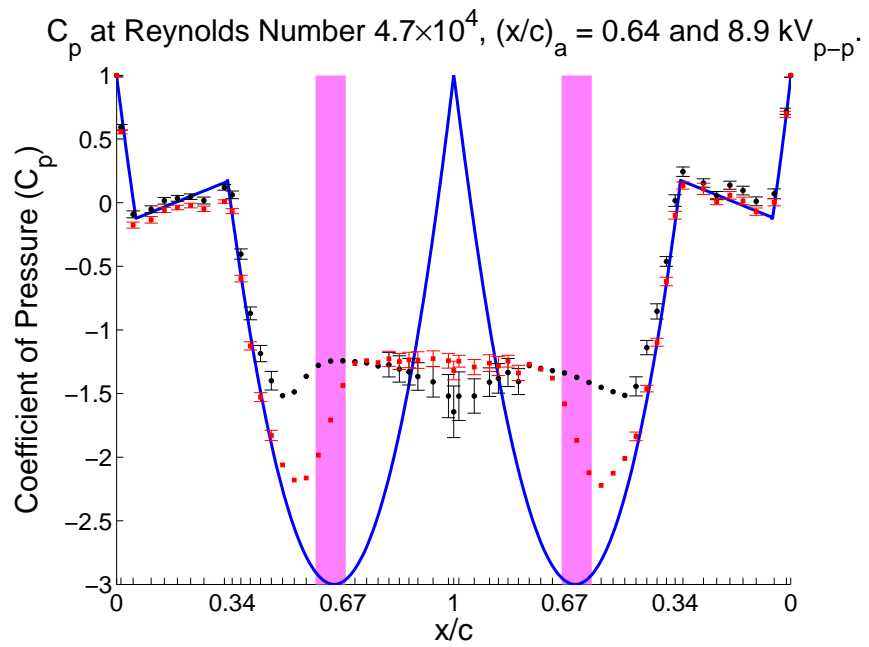**Figure A.302:** Plasma Actuators on a Tail Boom Model.

Figure A.303: Plasma Actuators on a Tail Boom Model.

Figure A.304: Plasma Actuators on a Tail Boom Model.

Figure A.305: Plasma Actuators on a Tail Boom Model.

Figure A.306: Plasma Actuators on a Tail Boom Model.

Figure A.307: Plasma Actuators on a Tail Boom Model.

Figure A.308: Plasma Actuators on a Tail Boom Model.

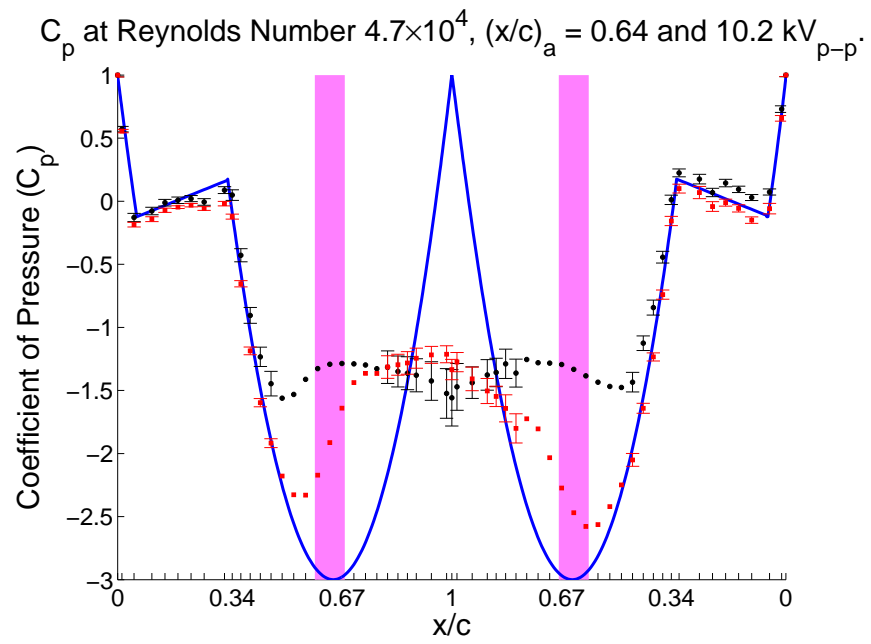**Figure A.309:** Plasma Actuators on a Tail Boom Model.

Figure A.310: Plasma Actuators on a Tail Boom Model.

Figure A.311: Plasma Actuators on a Tail Boom Model.

Figure A.312: Plasma Actuators on a Tail Boom Model.

Figure A.313: Plasma Actuators on a Tail Boom Model.
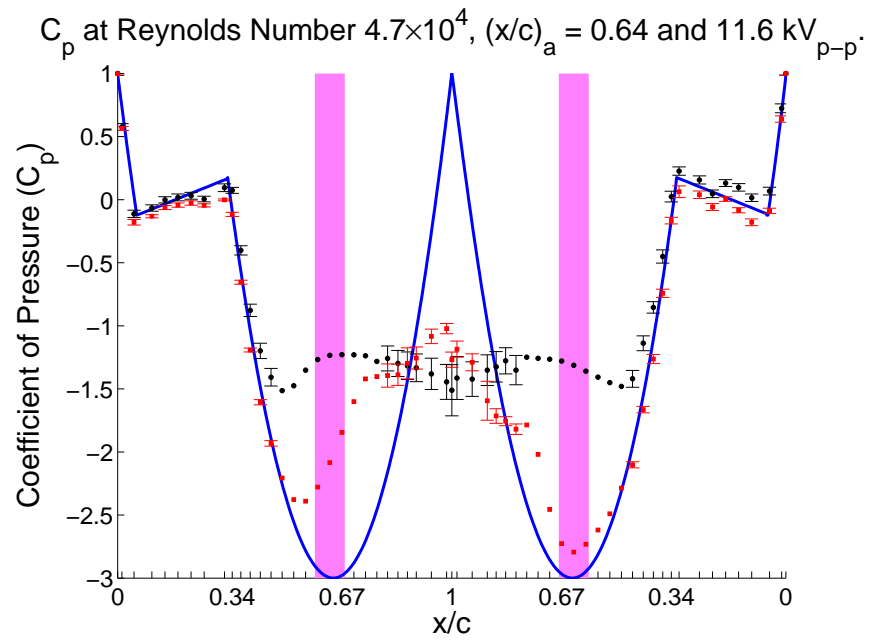

Figure A.314: Plasma Actuators on a Tail Boom Model.

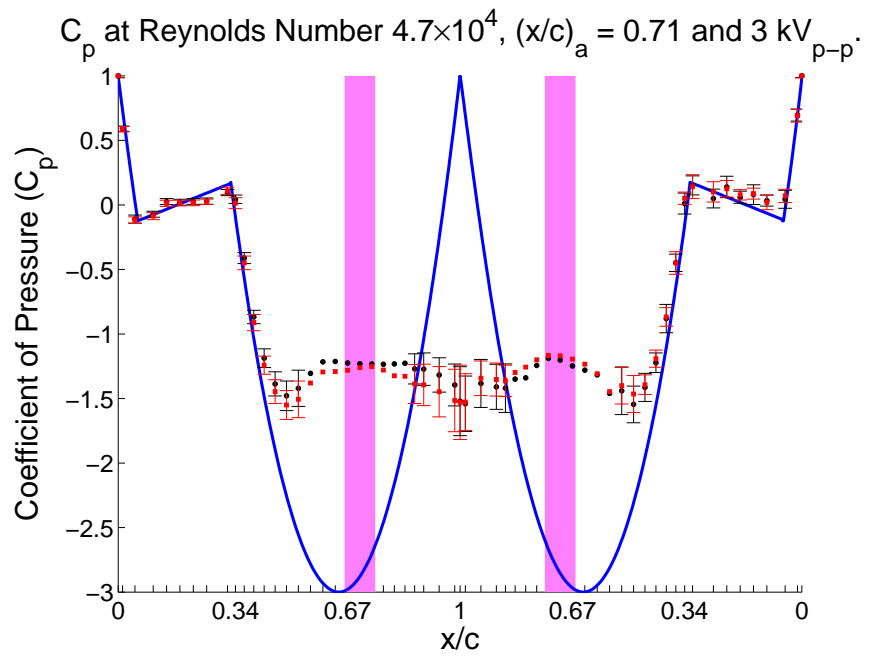**Figure A.315:** Plasma Actuators on a Tail Boom Model.

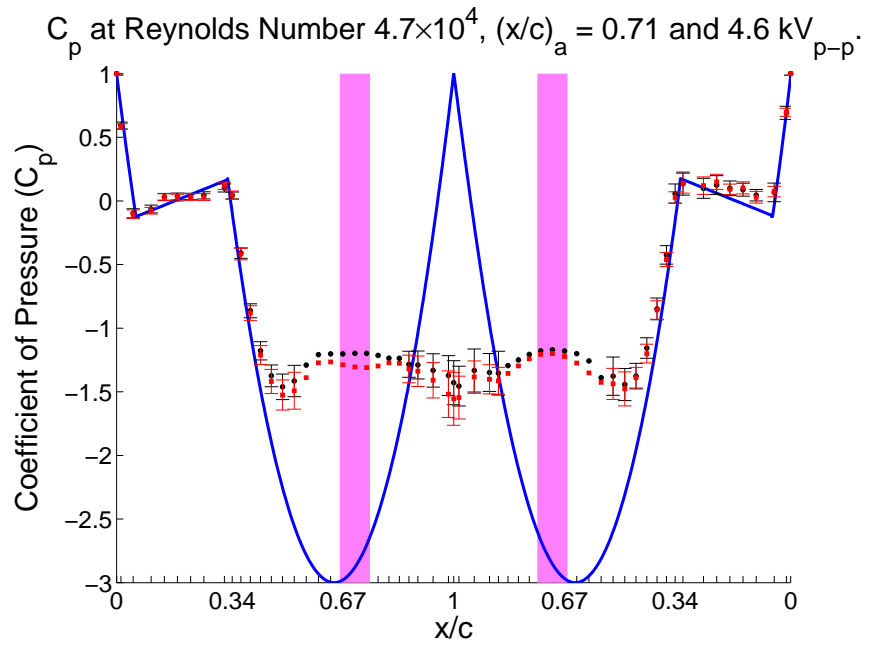**Figure A.316:** Plasma Actuators on a Tail Boom Model.

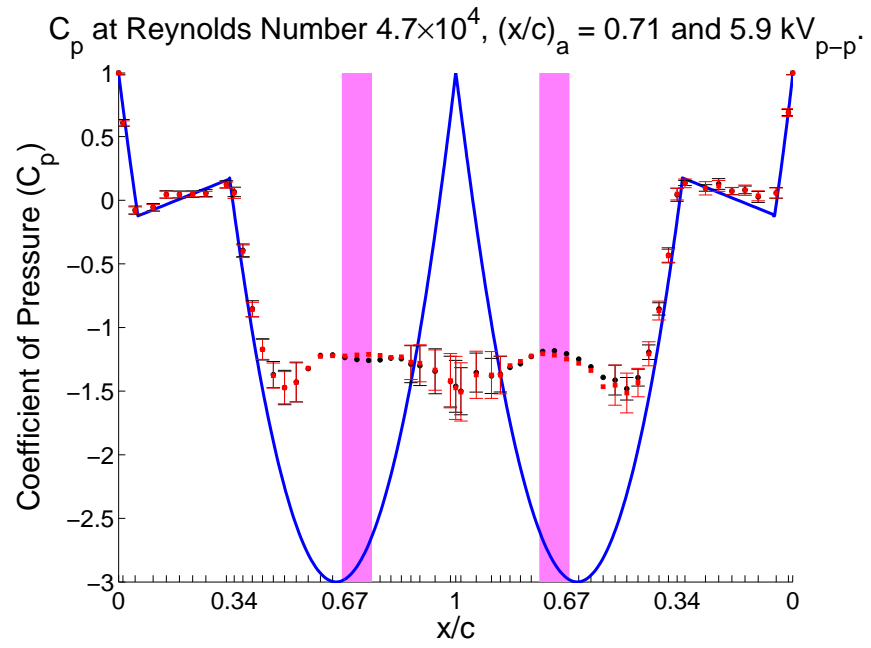**Figure A.317:** Plasma Actuators on a Tail Boom Model.

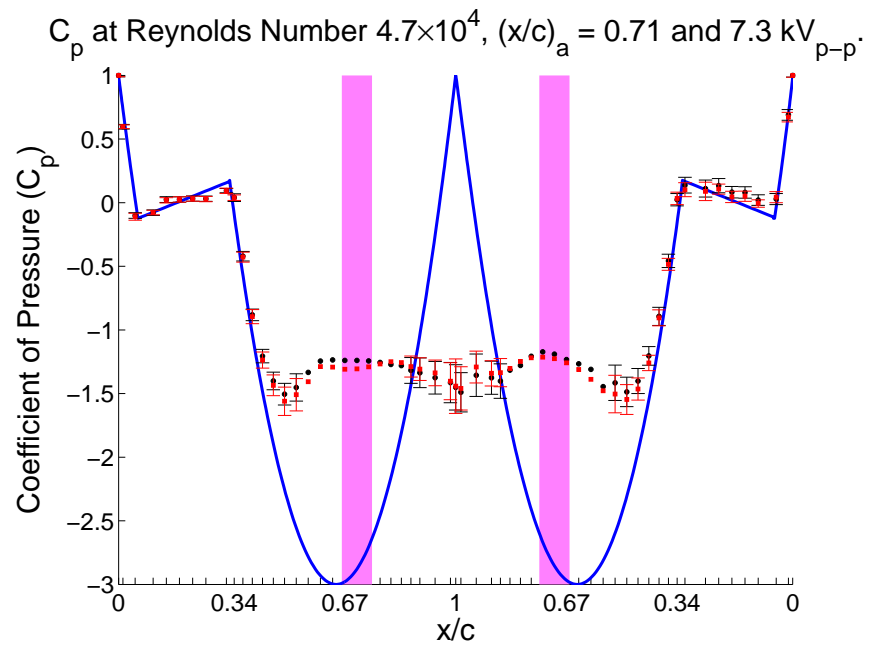**Figure A.318:** Plasma Actuators on a Tail Boom Model.

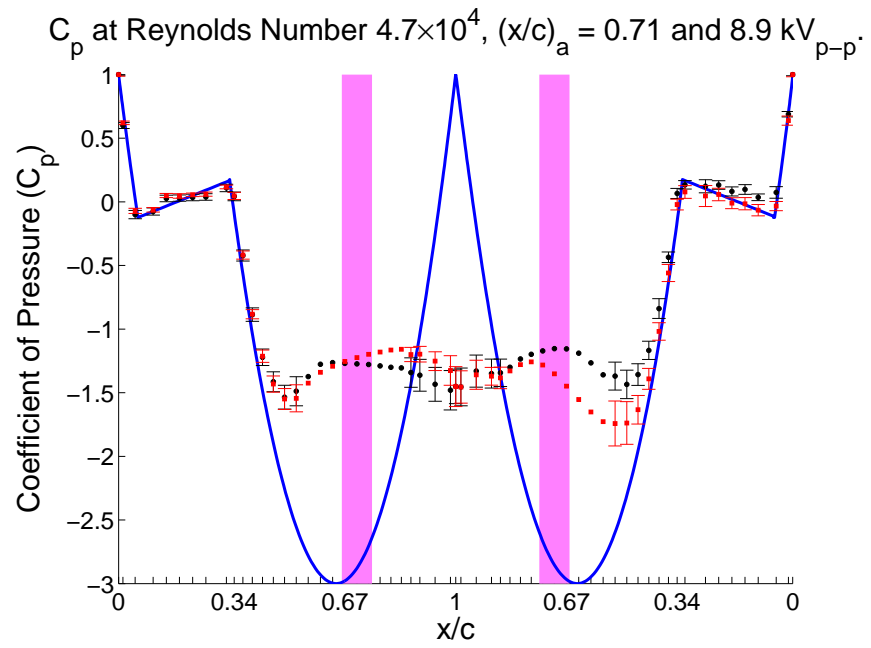**Figure A.319:** Plasma Actuators on a Tail Boom Model.

Figure A.320: Plasma Actuators on a Tail Boom Model.

Figure A.321: Plasma Actuators on a Tail Boom Model.

Figure A.322: Plasma Actuators on a Tail Boom Model.

Figure A.323: Plasma Actuators on a Tail Boom Model.
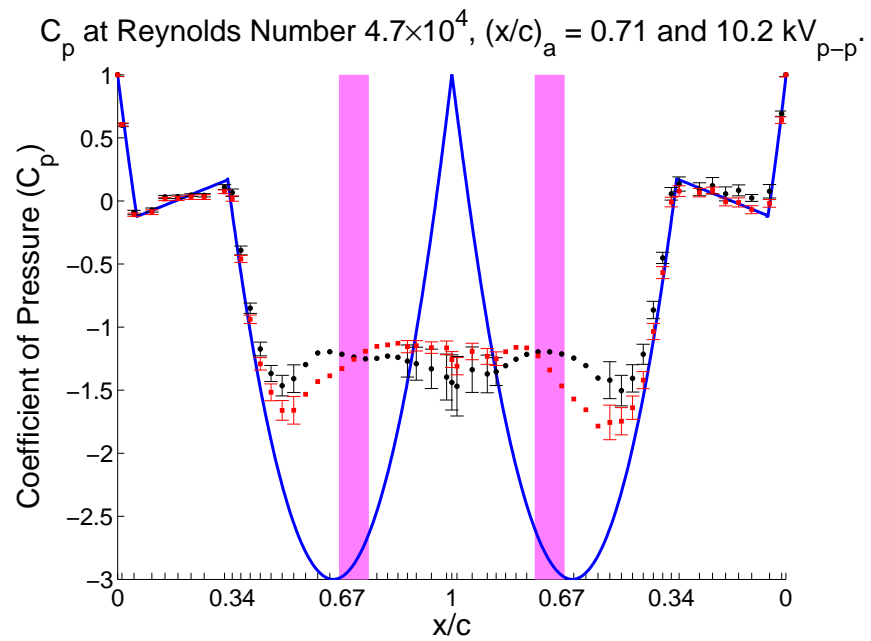

Figure A.324: Plasma Actuators on a Tail Boom Model.

Figure A.325: Plasma Actuators on a Tail Boom Model.

Figure A.326: Plasma Actuators on a Tail Boom Model.

Figure A.327: Plasma Actuators on a Tail Boom Model.

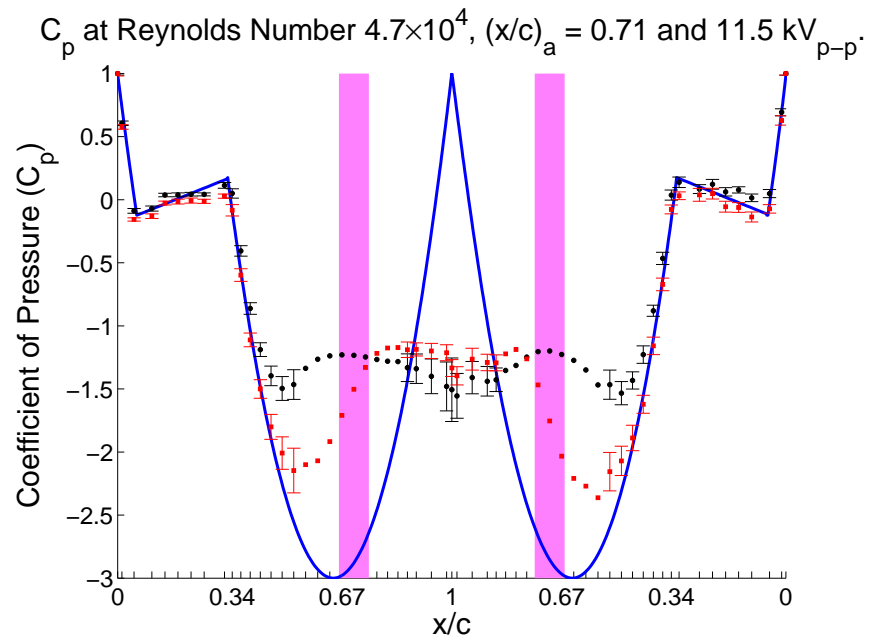**Figure A.328:** Plasma Actuators on a Tail Boom Model.

Figure A.329: Plasma Actuators on a Tail Boom Model.
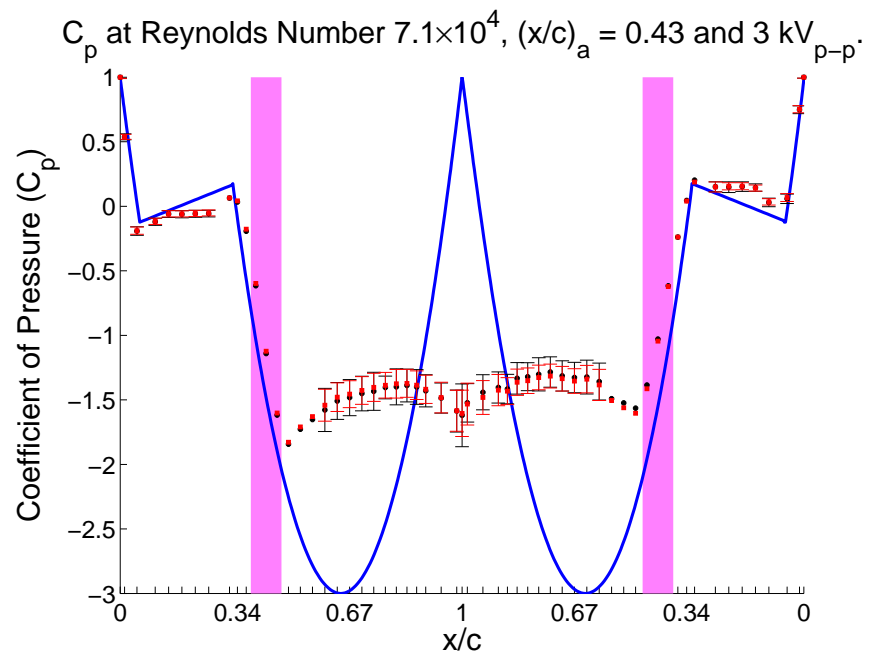

Figure A.330: Plasma Actuators on a Tail Boom Model.

Figure A.331: Plasma Actuators on a Tail Boom Model.

Figure A.332: Plasma Actuators on a Tail Boom Model.

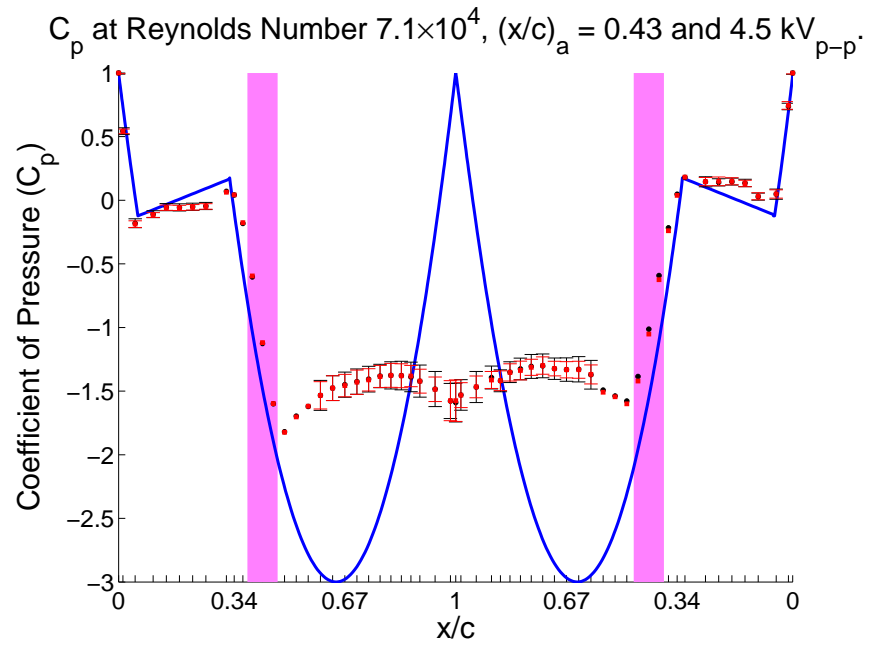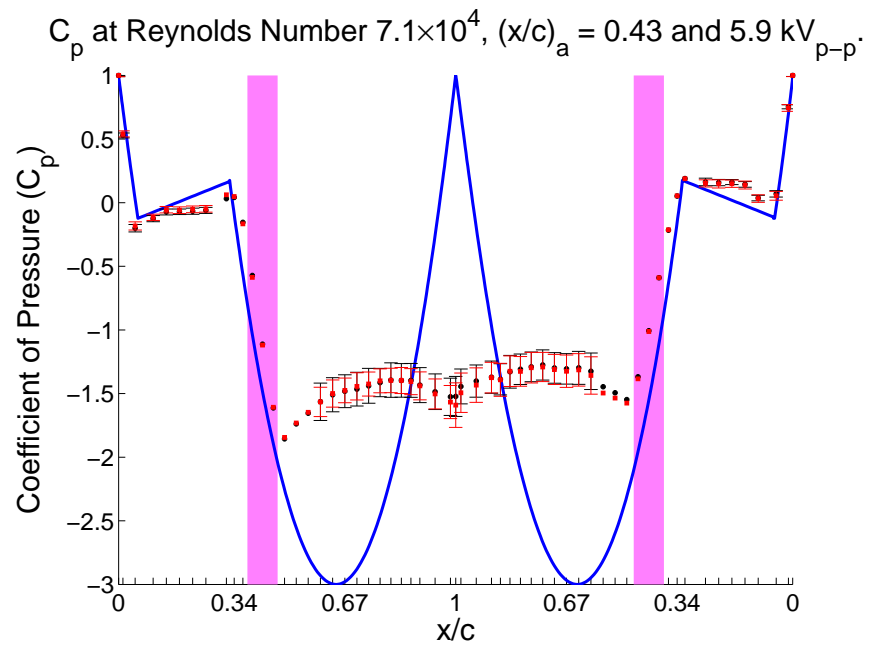**Figure A.333:** Plasma Actuators on a Tail Boom Model.

Figure A.334: Plasma Actuators on a Tail Boom Model.

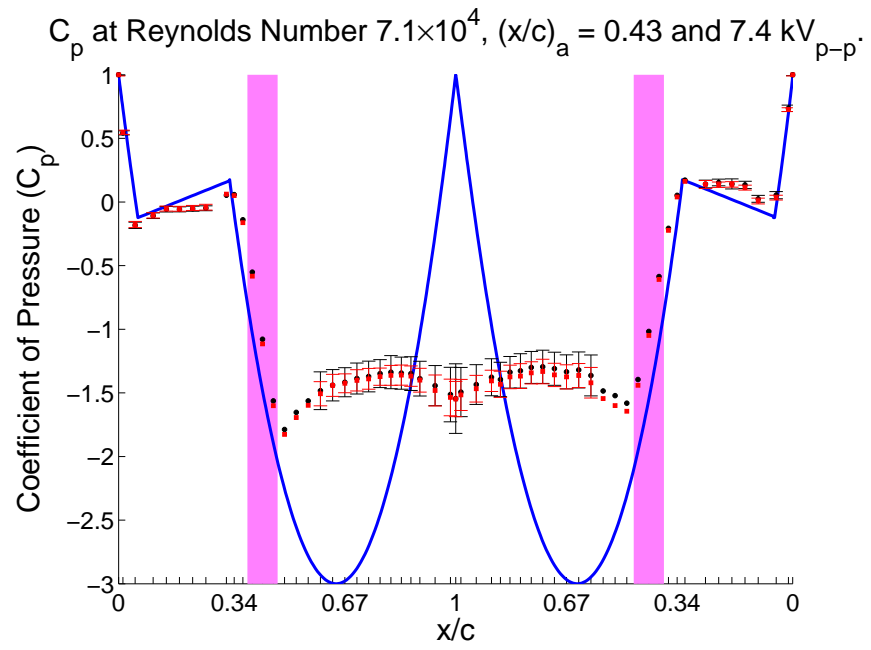**Figure A.335:** Plasma Actuators on a Tail Boom Model.

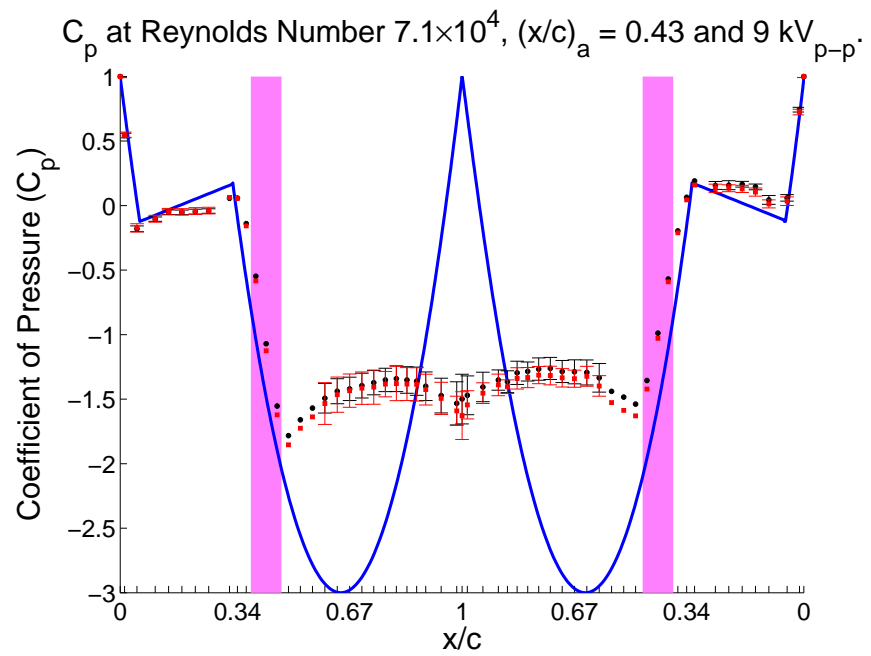**Figure A.336:** Plasma Actuators on a Tail Boom Model.

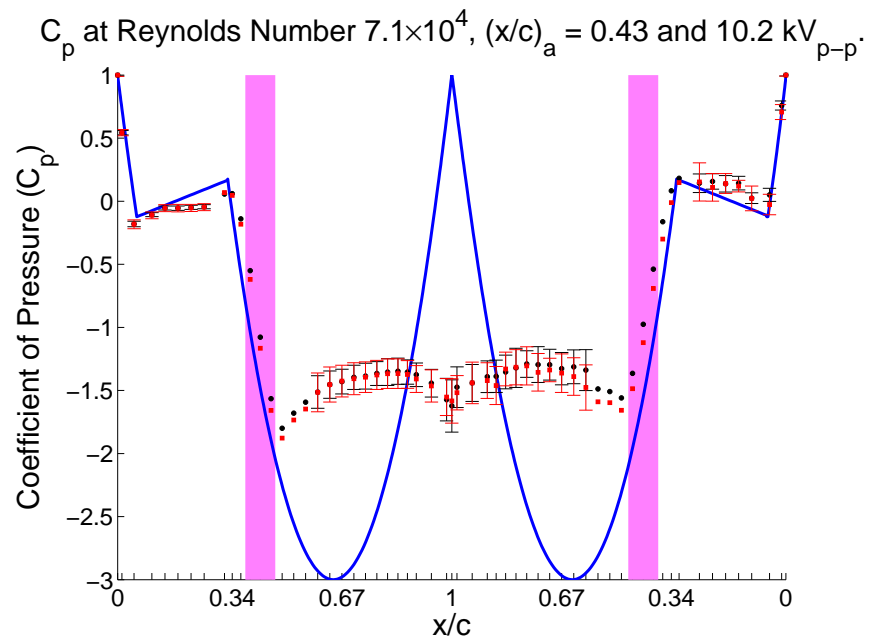**Figure A.337:** Plasma Actuators on a Tail Boom Model.

Figure A.338: Plasma Actuators on a Tail Boom Model.

Figure A.339: Plasma Actuators on a Tail Boom Model.

Figure A.340: Plasma Actuators on a Tail Boom Model.

Figure A.341: Plasma Actuators on a Tail Boom Model.

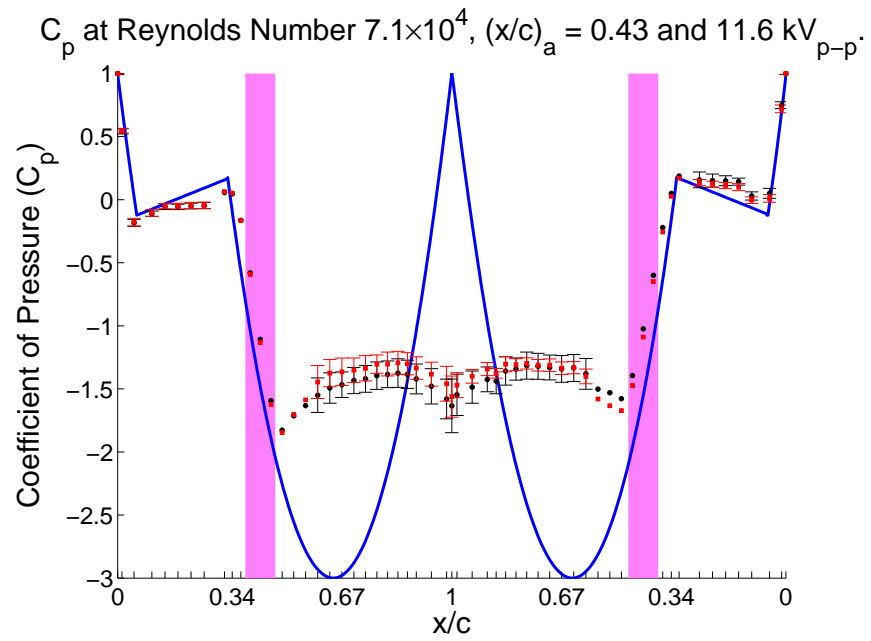**Figure A.342:** Plasma Actuators on a Tail Boom Model.
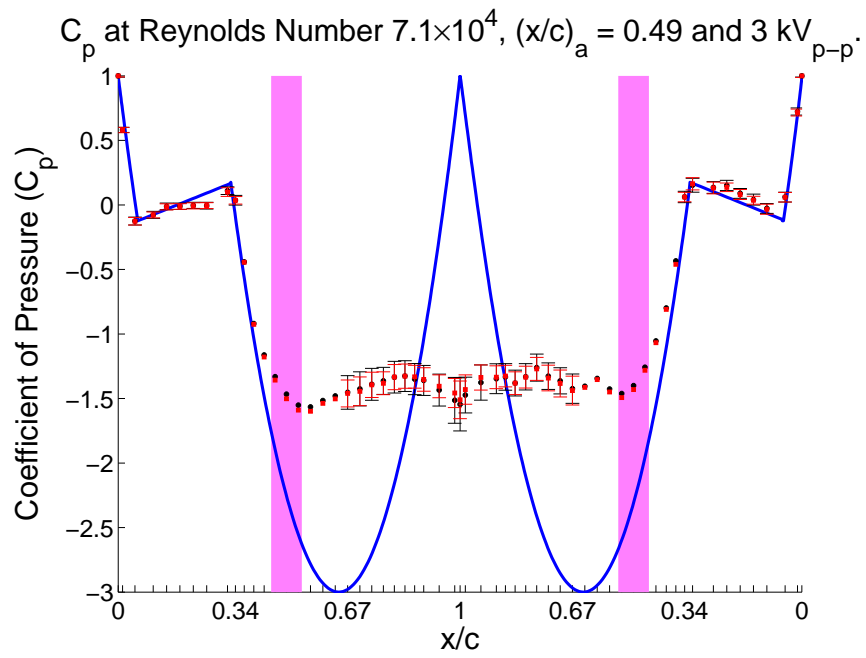
Figure A.343: Plasma Actuators on a Tail Boom Model.

Figure A.344: Plasma Actuators on a Tail Boom Model.

Figure A.345: Plasma Actuators on a Tail Boom Model.

Figure A.346: Plasma Actuators on a Tail Boom Model.

Figure A.347: Plasma Actuators on a Tail Boom Model.

Figure A.348: Plasma Actuators on a Tail Boom Model.

Figure A.349: Plasma Actuators on a Tail Boom Model.

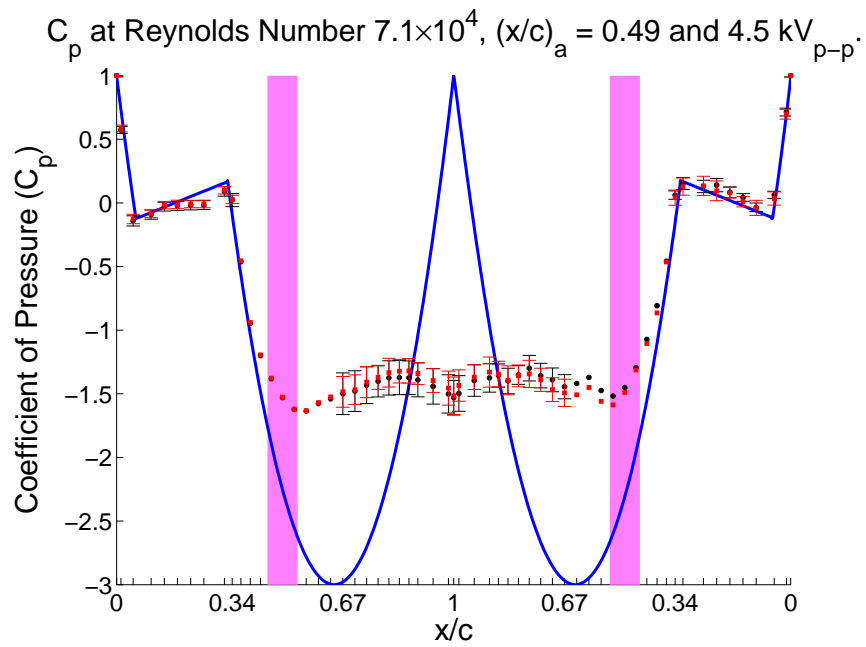**Figure A.350:** Plasma Actuators on a Tail Boom Model.

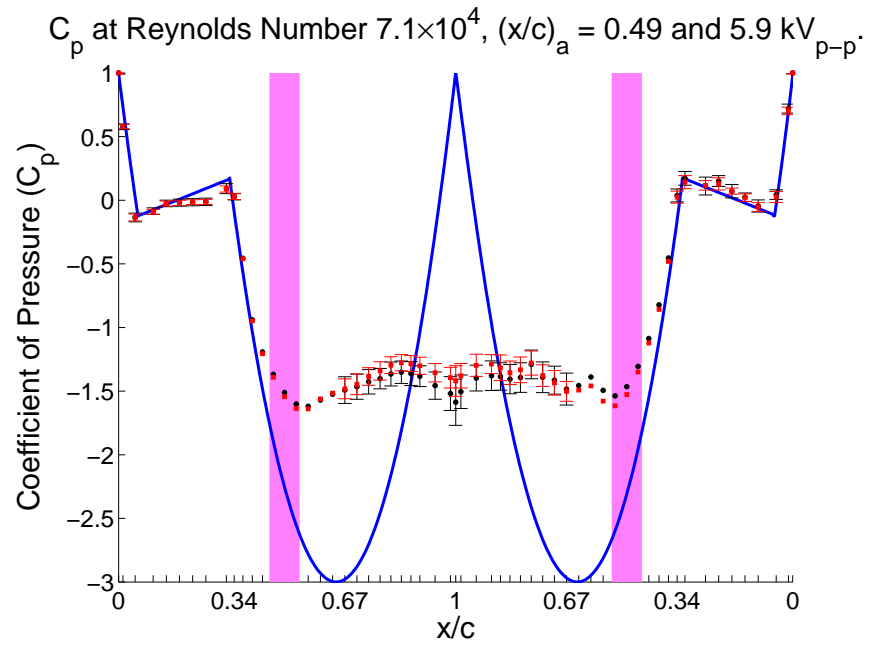**Figure A.351:** Plasma Actuators on a Tail Boom Model.

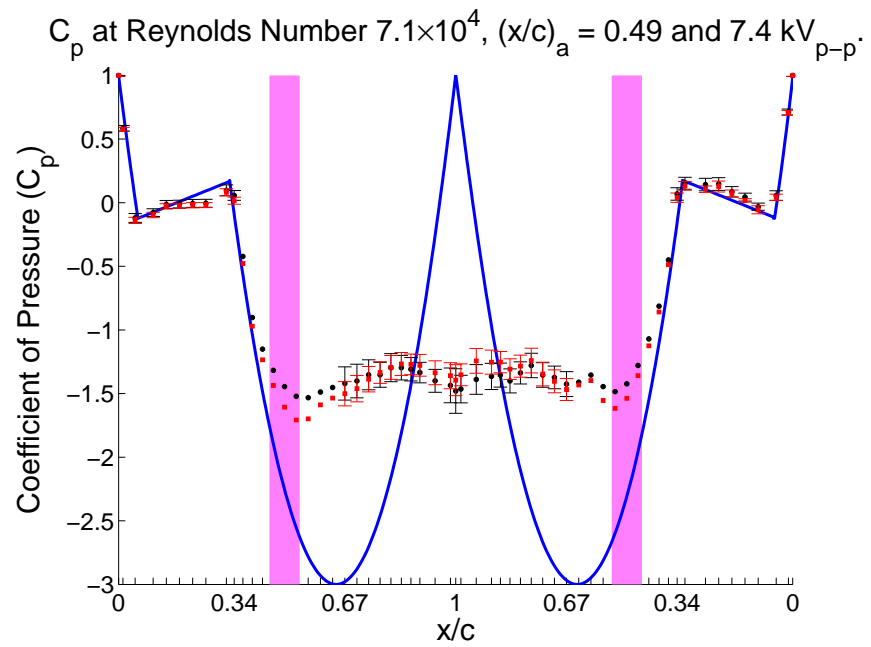**Figure A.352:** Plasma Actuators on a Tail Boom Model.

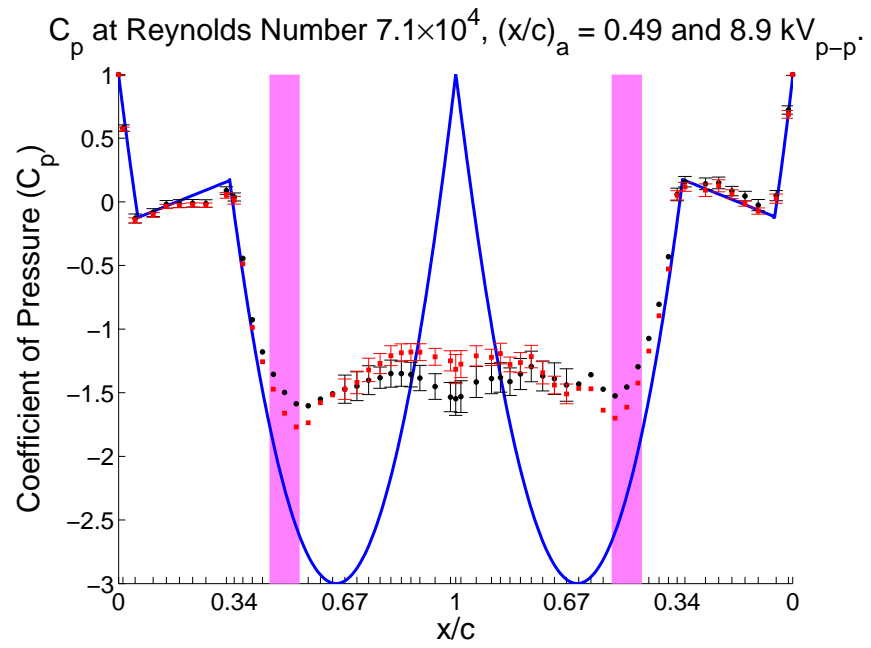**Figure A.353:** Plasma Actuators on a Tail Boom Model.
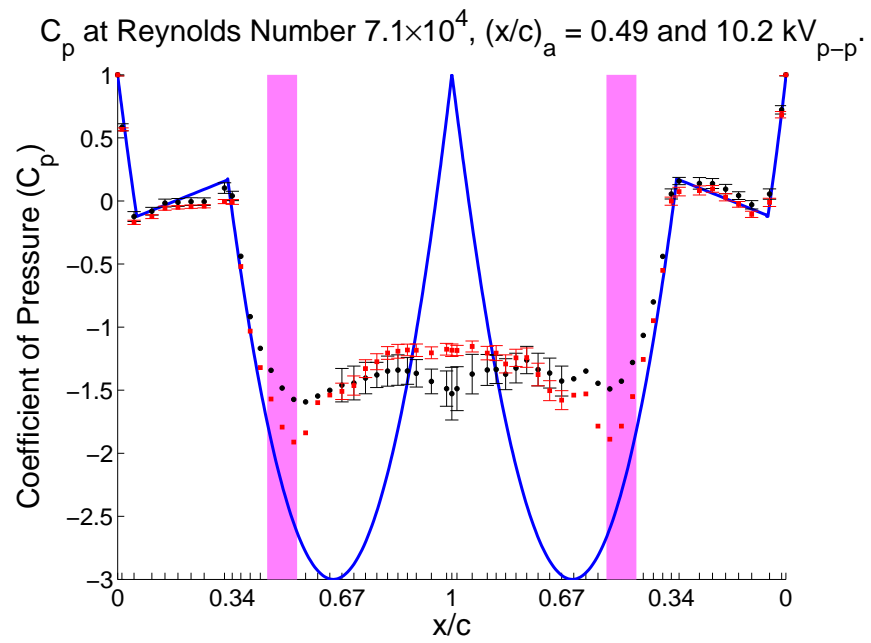

Figure A.354: Plasma Actuators on a Tail Boom Model.

Figure A.355: Plasma Actuators on a Tail Boom Model.
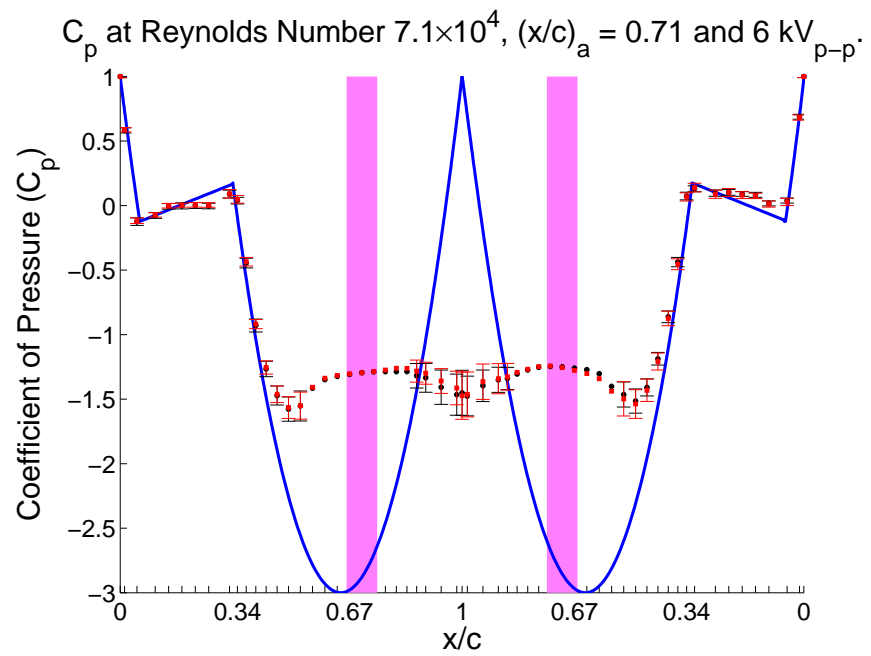
Figure A.356: Plasma Actuators on a Tail Boom Model.

328
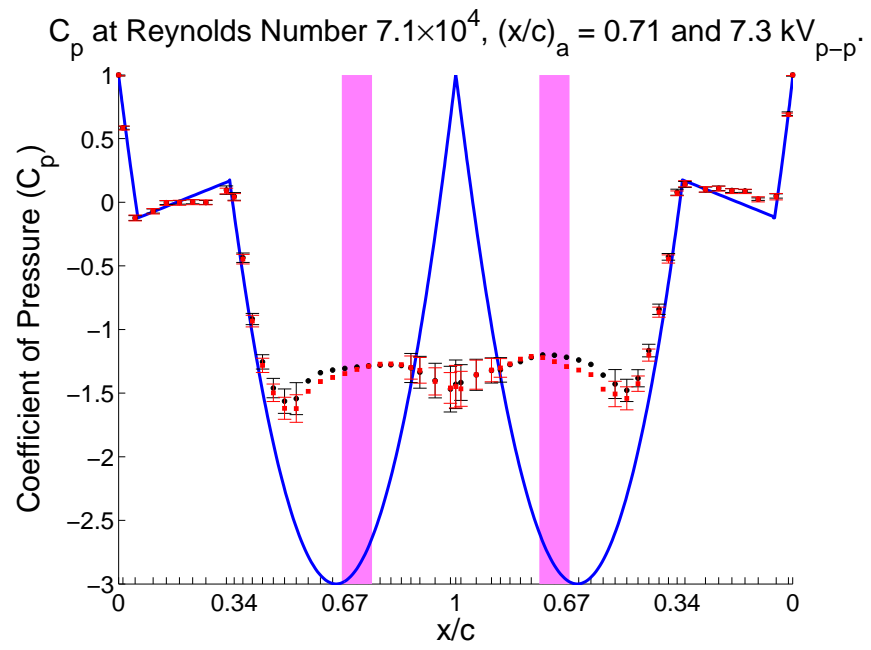
Figure A.357: Plasma Actuators on a Tail Boom Model.
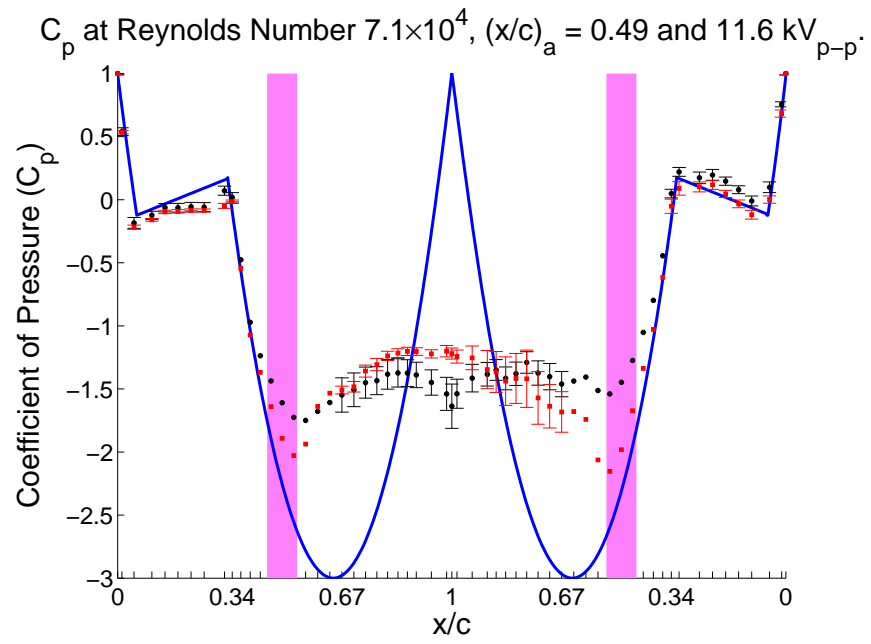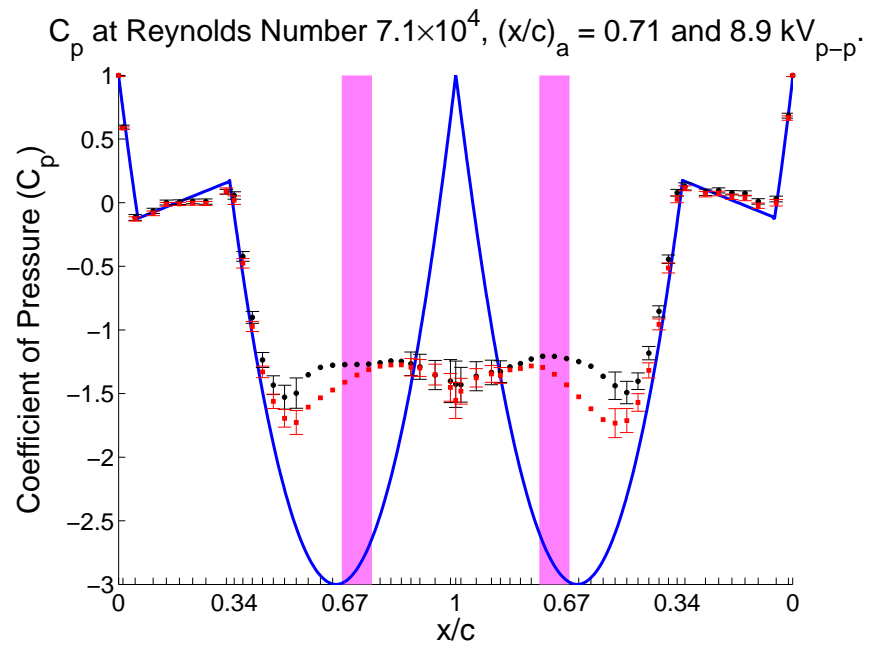

Figure A.358: Plasma Actuators on a Tail Boom Model.

329
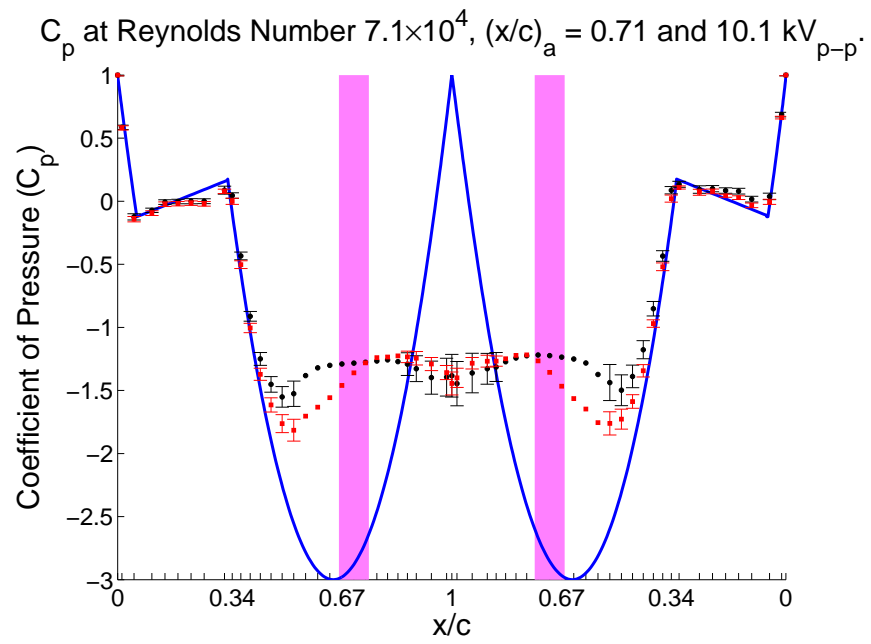
Figure A.359: Plasma Actuators on a Tail Boom Model.

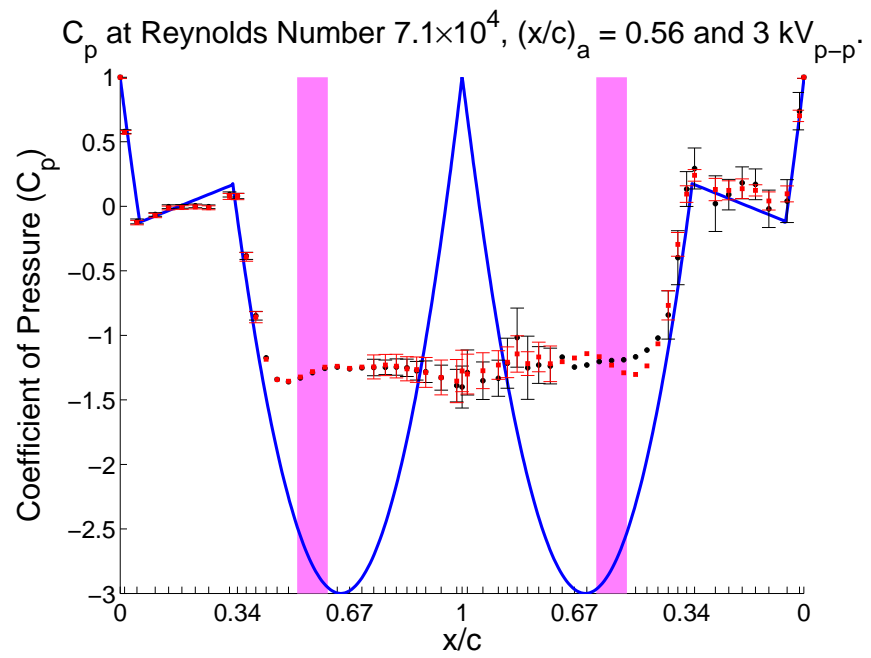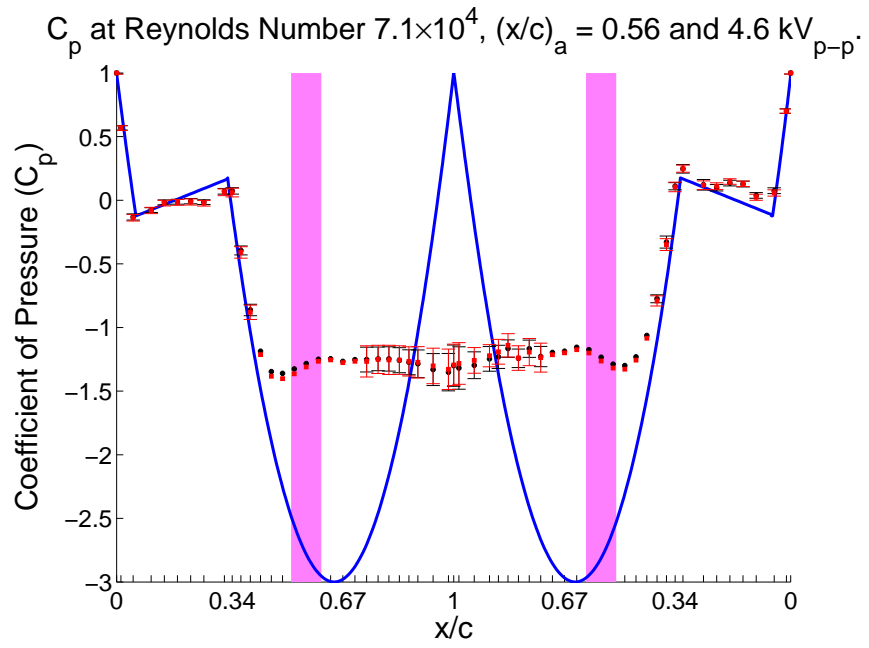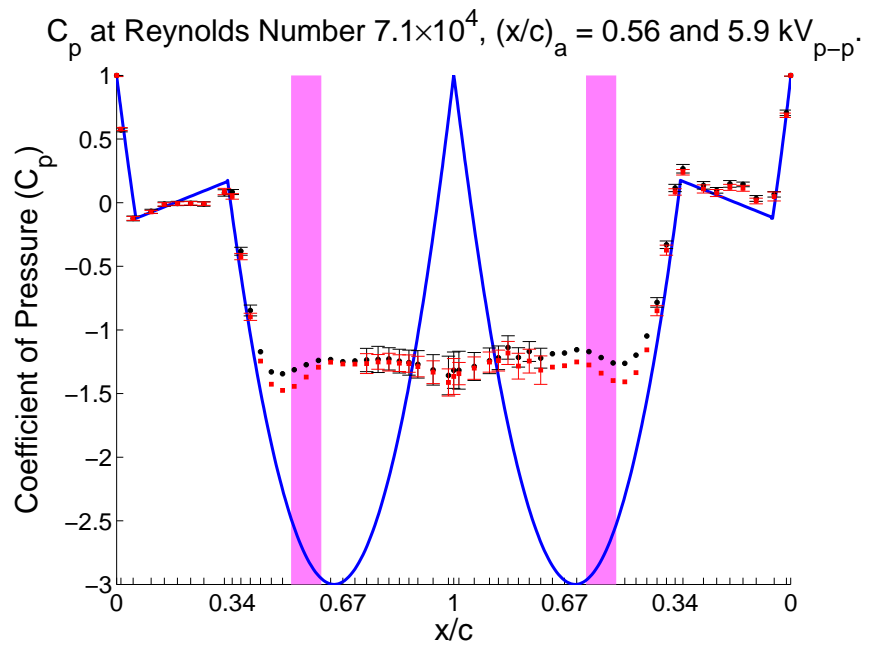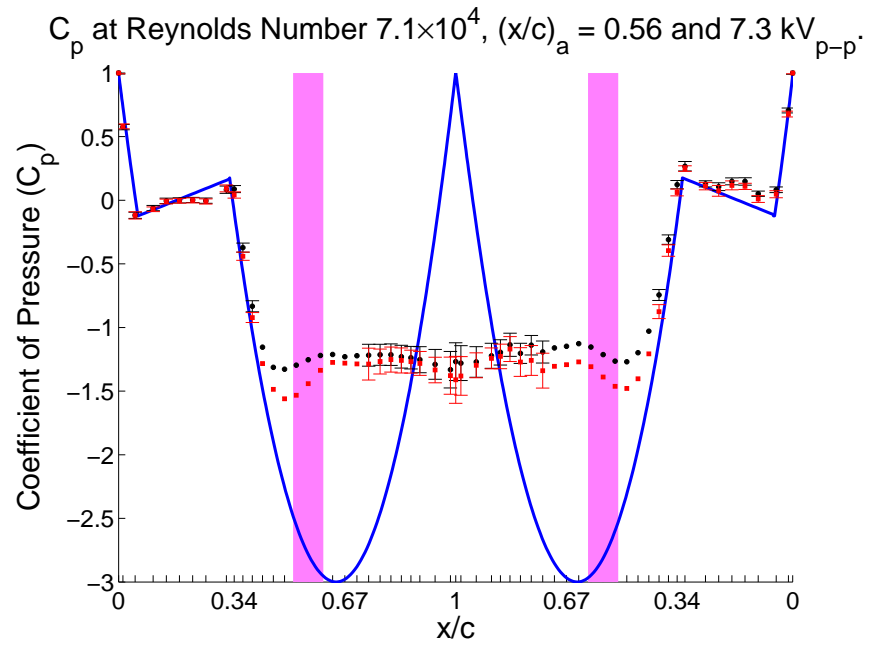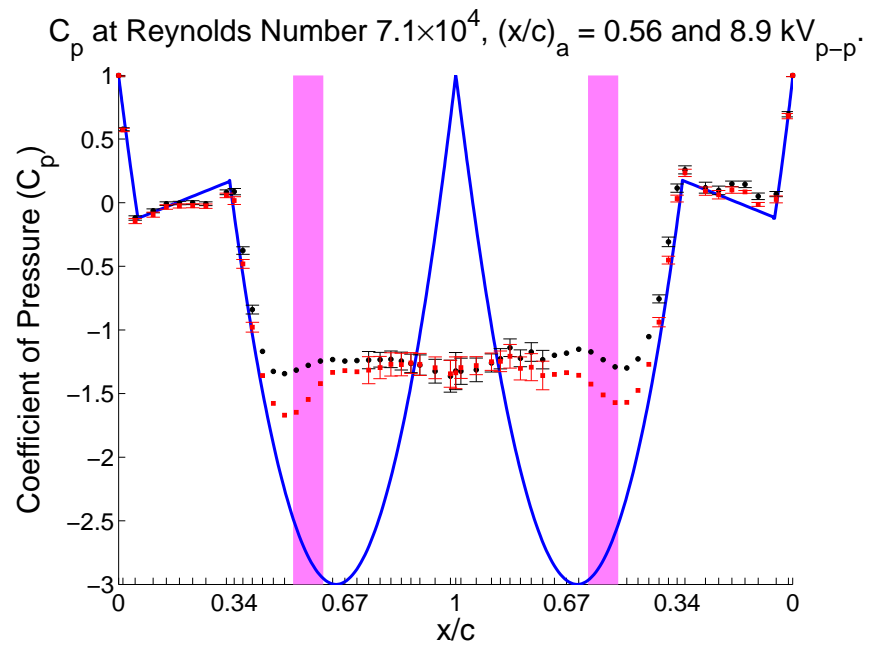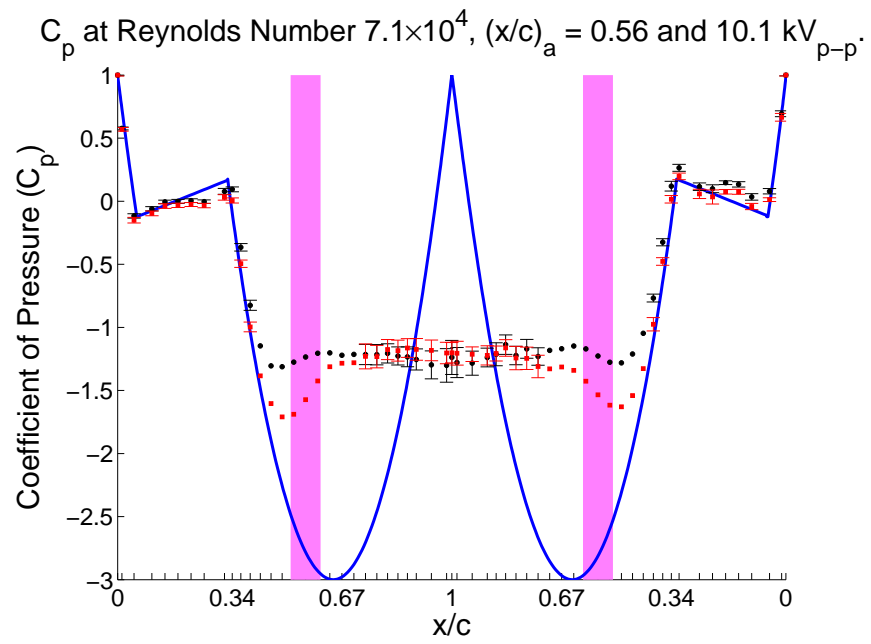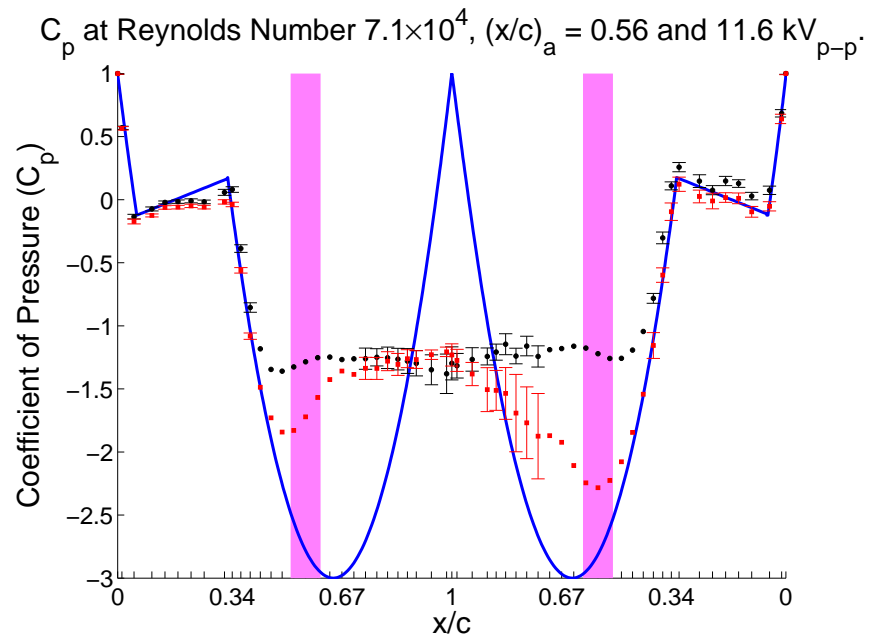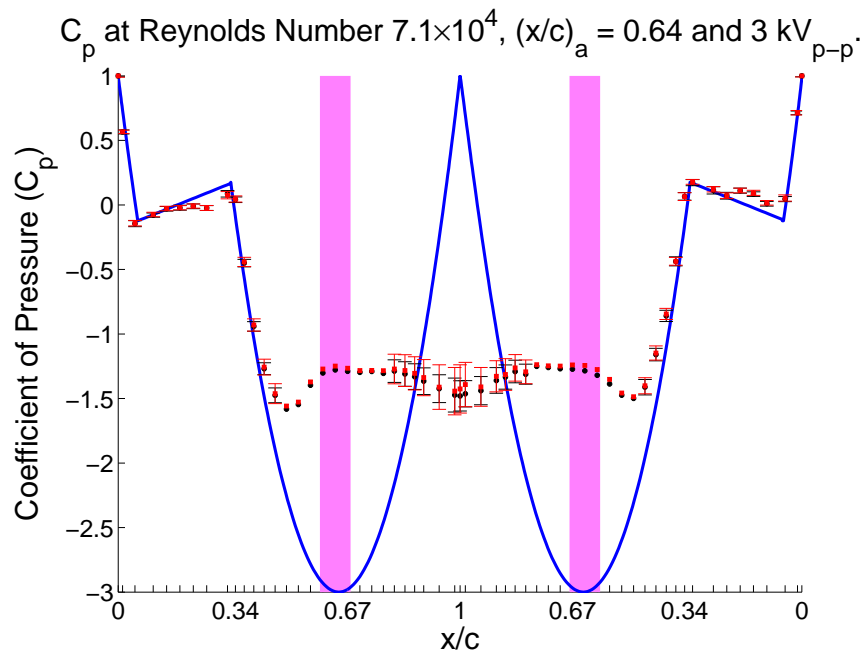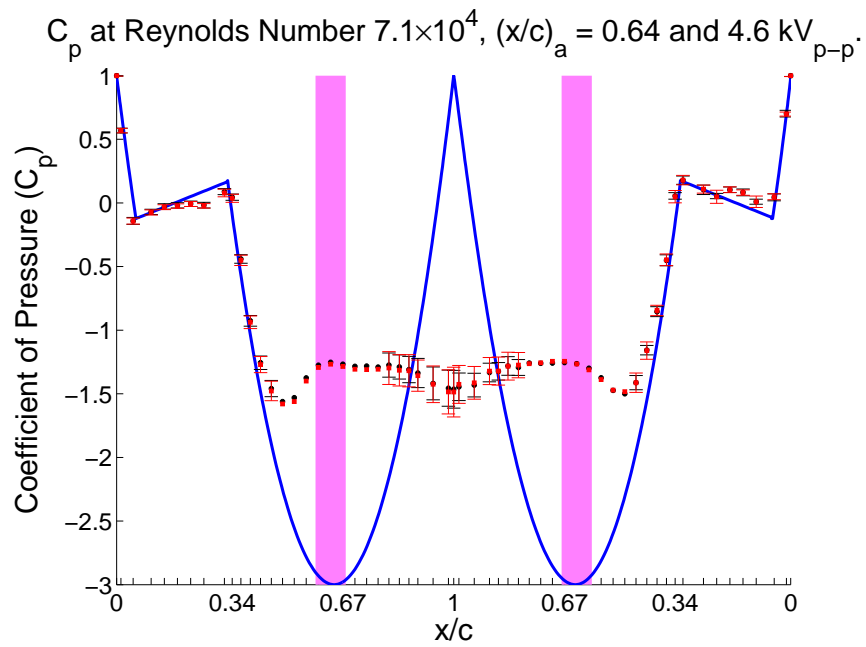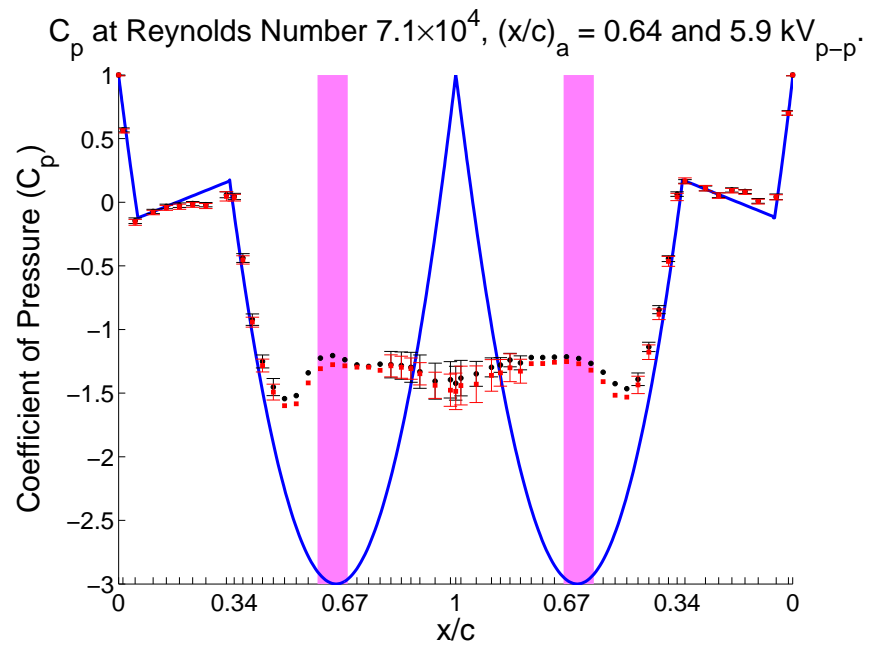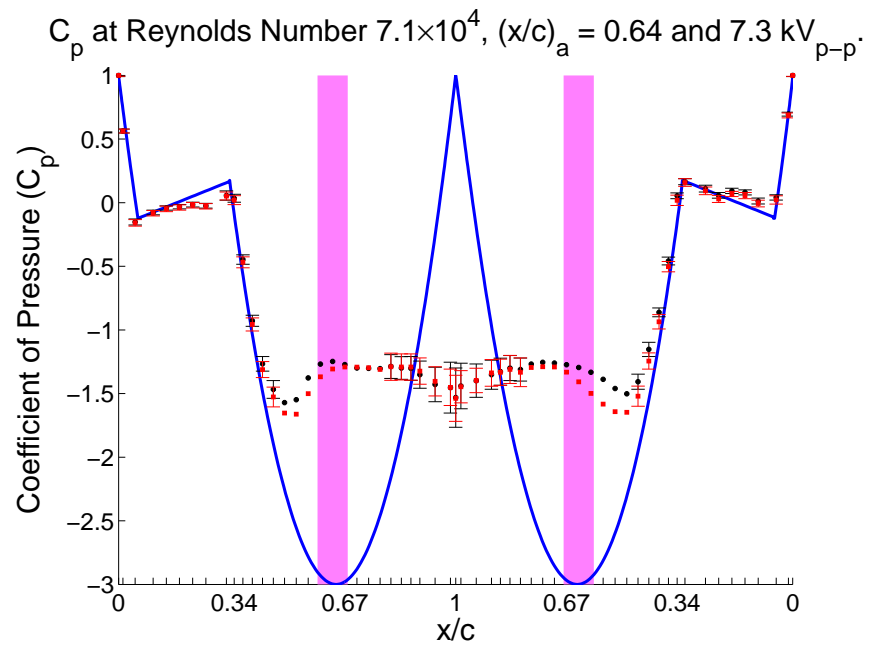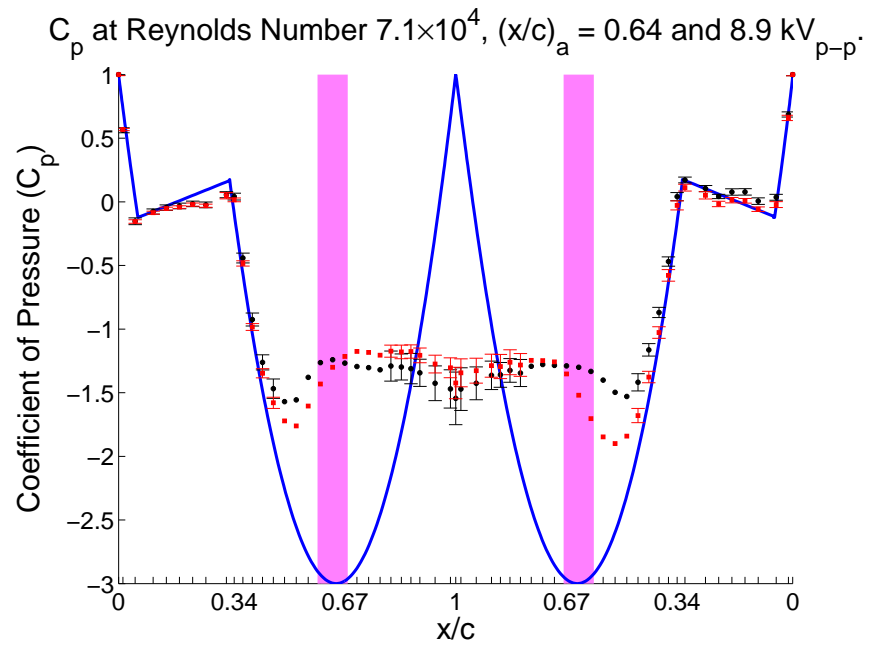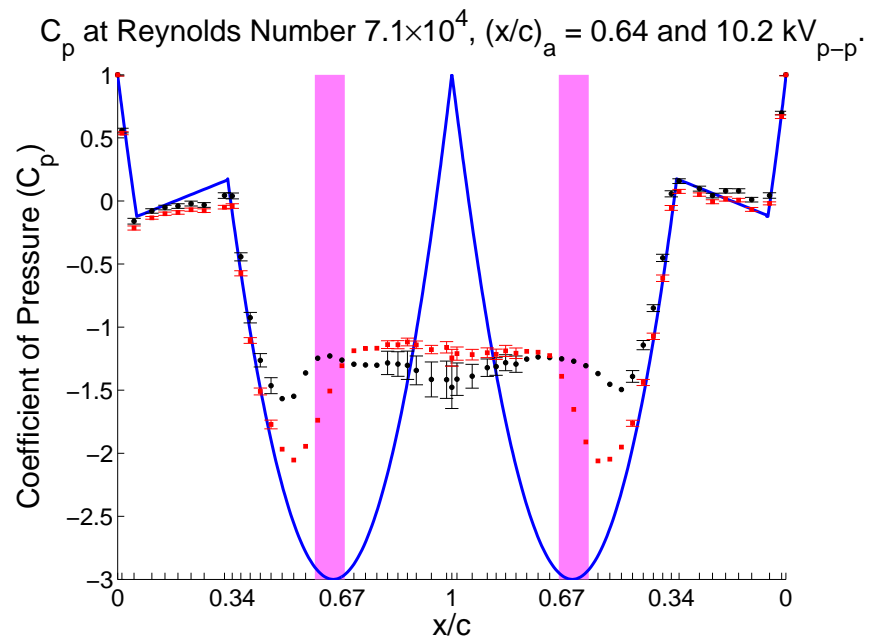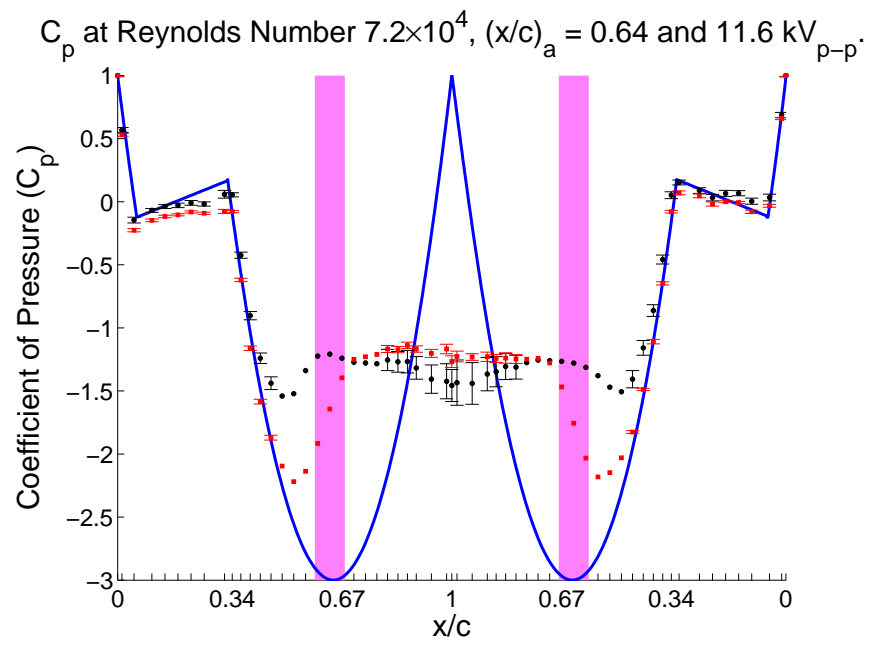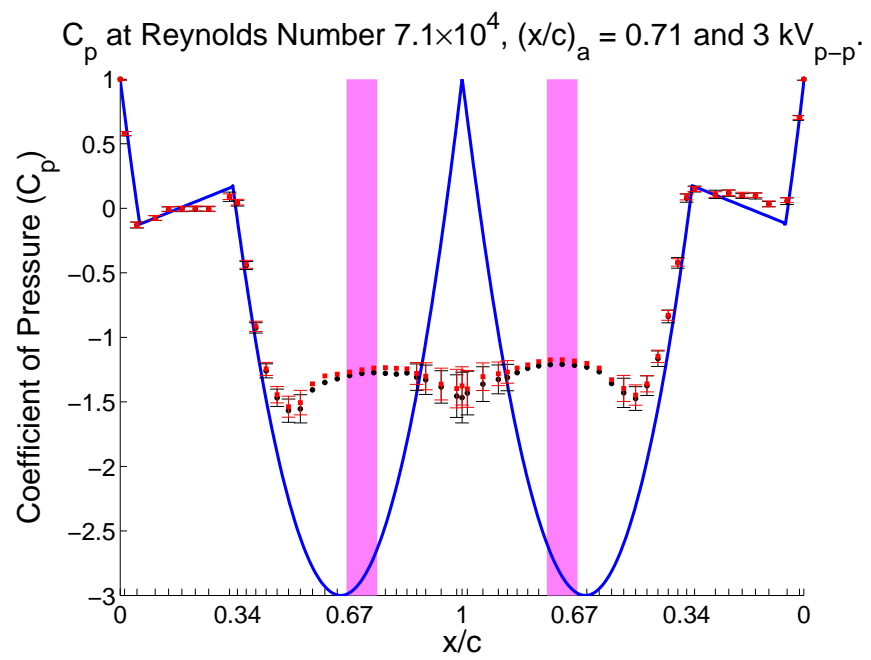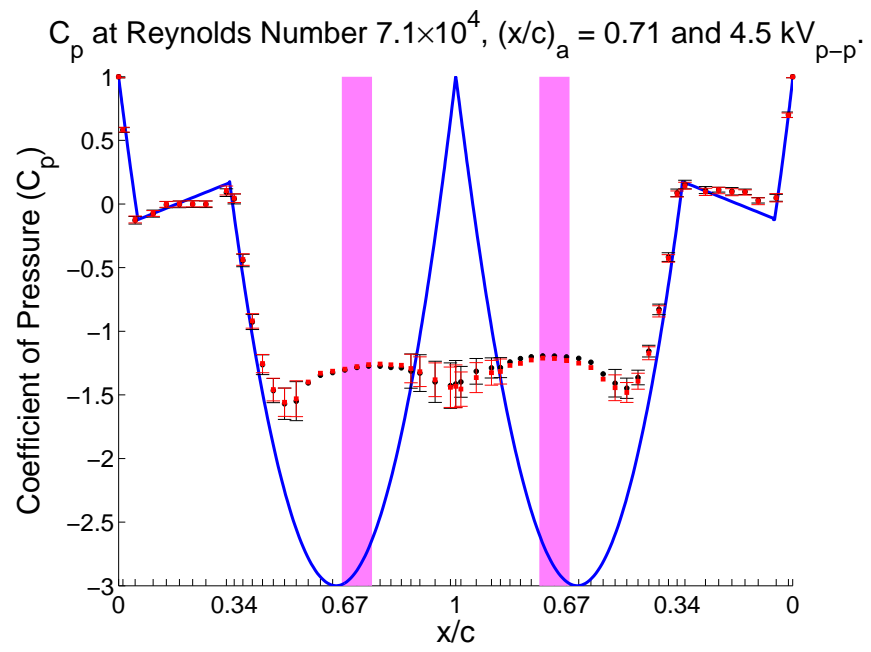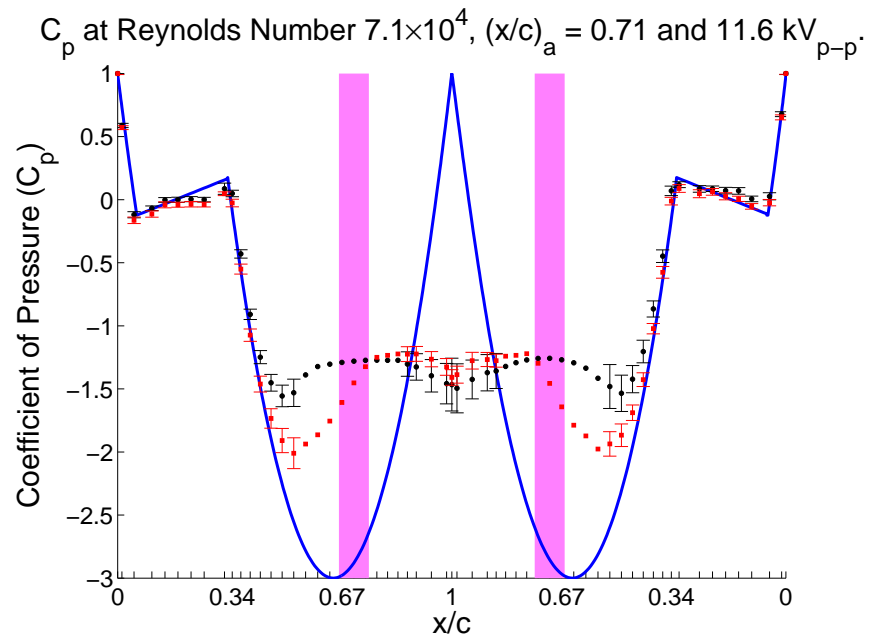**Figure A.360:** Plasma Actuators on a Tail Boom Model.

Bibliography

[1] Anderson, J. D., *Fundamentals of Aerodynamics*, McGraw Hill, 3rd ed., 2001.

[2] Schlichting, H. and Gersten, K., *Boundary Layer Theory*, Springer-Verlag, 8th ed., 2003.

[3] Sumer, M., *Hydrodynamics Around Cylindrical Surfaces*, World Scientific Publishing Company, 1997.

[4] Answers.com, "Boundary-layer flow." http://www.answers.com/topic/boundary-layer.

[5] Achenbach, E., "Distribution of local pressure and skin friction around a circular cylinder in cross-flow up to Re = 5,000,000," *Journal of Fluid Mechanics*, 1968.

[6] Amitay, M., Honohan, A. M., Trautman, M., and Glezer, A., "Modification of the aerodynamic characteristics of bluff bodies using fluidic actuators," *AIAA Fluid Dynamics Conference*, 1997.

[7] Glezer, A., Amitay, M., and Honohan, A. M., "Aspects of Low- and High-Frequency Actuation for Aerodynamic Flow Control," *AIAA Journal*, Vol. 43, No. 7, 2005.

[8] Taubert, L., Kjellgren, P., and Wygnanski, I., "Generic Bluff Bodies with Undetermined Separation Location," *1st Flow Control Conference*, 2002, AIAA Paper 2002-3068.

[9] Morel-Fatio, S., Pines, D. J., and Kiddy, J., "UAV Performance Enhancements with Piezoelectric Synthetic Jet Actuators," *41st Aerospace Sciences Meeting and Exhibit*, January 2003.

[10] Glezer, A. and Amitay, M., "Synthetic Jets," *Annual Review of Fluid Mechanics*, Vol. 34, 2002.

[11] Jabbal, M. and Zhong, S., "The Near Wall Effect of Synthetic Jets in a Laminar Boundary Layer," *3rd AIAA Flow Control Conference*, 2006, AIAA Paper 2006-3180.

[12] Enloe, C. L., McLaughlin, T. E., VanDyken, R. D., Kachner, K. D., Jumper, E. J., and Corke, T. C., "Mechanisms and Responses of a Single Dielectric Barrier Plasma Actuator," *41st AIAA Aerospace Sciences Meeting and Exhibit*, 2003, AIAA Paper 2003-1021.

[13] Font, G. I., "Boundary Layer Control with Atmospheric Plasma Discharges," *40th AIAA/ASME/SAE/ASEE Joint Propulsion Conference and Exhibit*, July 2004.

[14] "AAAC Research Facilities," Tech. rep., Aerodynamics, Aerothermodynamics, and Acoustics Competency, 2002-2003.

[15] Selig, M., "UIUC Airfoil Database," Internet, 2006, http://www.ae.uiuc.edu/m-selig/ads/afplots/naca66-018.gif.

[16] Schmidt, G. S. and Mueller, T. J., "A Study of the Laminar Separation Bubble on an Airfoil at Low Reynolds Numbers Using Flow Visualization Techniques." *AIAA Journal*, 1987, AIAA Paper 1987-242.

[17] Sarioglu, M. and Yavuz, T., "Subcritical Flow Around Bluff Bodies," *AIAA Journal*, Vol. 40, No. 7, July 2002, pp. 1257–1268.

[18] Munska, M. D. and McLaughlin, T. E., "Circular Cylinder Flow Control Using Plasma Actuators," *43rd AIAA Aerospace Sciences Meeting and Exhibit*, 2005, AIAA Paper 2005-141.

[19] McLaughlin, T. E., Felker, B., Avery, J. C., and Enloe, C. L., "Further Experiments in Cylinder Wake Modification with Dielectric Barrier Discharge Forcing," *44th AIAA Aerospace Sciences Meeting and Exhibit*, 2006, AIAA Paper 2006-1409.

[20] Rivir, R. B., Sondergaard, R., Bons, J. P., and Lake, J. P., "Passive and Active Control of Separation in Gas Turbines," *Fluids 2000 Conference and Exhibit*, 2000.

[21] Glezer, A., "Aerodynamic Flow Control Using Synthetic Jets," April 1999, http://www.me.umn.edu/events/seminars/sq99/seminar03.shtml.

[22] McLaughlin, T. E., Munska, M. D., Vaeth, J. P., Dauwalter, T. E., Goode, J. R., and Siegel, S. G., "Plasma-Based Actuators for Cylinder Wake Vortex Control," *2nd AIAA Flow Control Conference*, 2004, AIAA Paper 2004-2129.

[23] Roth, J. R., Sherman, D. M., and Wilkinson, S. P., "Boundary Layer Flow Control with a One Atmosphere Uniform Glow Discharge Surface Plasma," *36th AIAA Aerospace Sciences Meeting and Exhibit*, 1998, AIAA Paper 98-0328.

[24] Bobashev, S. V., D'yakonova, E. A., Erofeev, A. V., Lapushikina, T. A., Maslennikov, V. G., Poniaev, S. A., Sacharov, A. A., and Vasil'eva, R. V., "Shock-tube Facility for MGD Supersonic Flow Control," *AIAA Journal*, 2000, AIAA Paper 2000-2647.

[25] Minucci, M. A. S., Brackon, R. M., Myrabo, L. N., Nagamatsu, H. T., and Shanahan, K. J., "Experimental Investigation of an Electric Arc Simulated "Air Spike" in Hypersonic Flow," *AIAA Journal*, 2000, AIAA Paper 2000-0715.

[26] Adelgren, R. G., Elliott, G. S., and Knight, D., "Energy Deposition in Supersonic Flows," *AIAA Journal*, 2001, AIAA Paper 2001-0885.

[27] Samimy, M., Adamovich, I., Webb, B., Kastner, J., Hileman, J., Keshav, S., and Palm, P., "Development and characterization of plasma actuators for high-speed jet control," *Experiments in Fluids*, 2004.

[28] Bletzinger, P., Ganguly, B. N., Wie, D. V., and Garscadden, A., "Plasmas in high speed aerodynamics," *Journal of Physics D: Applied Physics*, 2005.

[29] Wikipedia, "Double layer." http://en.wikipedia.org/wiki/Double_layer.

[30] Enloe, C. L., McLaughlin, T. E., VanDyken, R. D., Kachner, K. D., Jumper, E. J., Corke, T. C., Post, M., and Haddad, O., "Mechanisms and Responses of a Single Dielectric Barrier Plasma Actuator: Geometric Effects," *AIAA Journal*, Vol. 42, No. 3, 2004.

[31] Enloe, C. L., McLaughlin, T. E., VanDyken, R. D., Kachner, K. D., Jumper, E. J., and Corke, T. C., "Mechanisms and Responses of a Single Dielectric Barrier Plasma Actuator: Plasma Morphology," *AIAA Journal*, Vol. 42, No. 3, 2004.

[32] Enloe, C. L., McLaughlin, T. E., VanDyken, R. D., and Fischer, J. C., "Plasma Structure in the Aerodynamic Plasma Actuator," *42nd AIAA Aerospace Sciences Meeting and Exhibit*, 2004, AIAA Paper 2004-844.

[33] Enloe, C. L., McLaughlin, T. E., Font, G. I., and Baughn, J. W., "Parameterization of Temporal Structure in the Single-Dielectric-Barrier Aerodynamic Plasma Actuator," *AIAA Journal*, 2006.

[34] Corke, T. C. and Matlis, E., "Phased Plasma Arrays for Unsteady Flow Control," *Fluids 2000 Conference and Exhibit*, June 2000.

[35] Porter, C. O., Baughn, J. W., McLaughlin, T. E., Enloe, C. L., and Font, G. I., "Temporal Force Measurements on an Aerodynamic Plasma Actuator," *44th AIAA Aerospace Sciences Meeting and Exhibit*, 2006, AIAA Paper 2006-104.

[36] Post, M. L., *Plasma Actuators for Separation Control on Stationary and Oscillating Airfoils*, Ph.D. thesis, University of Notre Dame, April 2004.

[37] Roth, J. R., Madhan, R. C. M., Yadav, M., Rahel, J., and Wilkinson, S. P., "Flow Field Measurements of Paraelectric, Peristaltic, and Combined Plasma Actuators Based on the One Atmosphere Uniform Glow Discharge Plasma (OAUGDP^{TM}," *42nd AIAA Aerospace Sciences Meeting and Exhibit*, 2004, AIAA Paper 2004-845.

[38] Corke, T. C., He, C., and Patel, M. P., "Plasma Flaps and Slats: An Application of Weakly-Ionized Plasma Actuators," *2nd AIAA Flow Control Conference*, 2004, AIAA Paper 2004-2127.

[39] Hultgren, L. S. and Ashpis, D. E., "Demonstration of Separation Delay with Glow-Discharge Plasma Actuators," *41st AIAA Aerospace Sciences Meeting and Exhibit*, 2003, NASA Technical Memorandum.

[40] Asghar, A. and Jumper, E. J., "Phase Synchronization of Vortex Shedding from Multiple Cylinders Using Plasma Actuators," *41st AIAA Aerospace Sciences Meeting and Exhibit*, 2003, AIAA Paper 2003-1028.